

Structural and Nucleosynthetic Evolution of Metal-poor & Metal-free Low and Intermediate Mass Stars

Simon Wattana Campbell

BSc (Astro Hons), BA (Lang), Dip Eng (Aero)

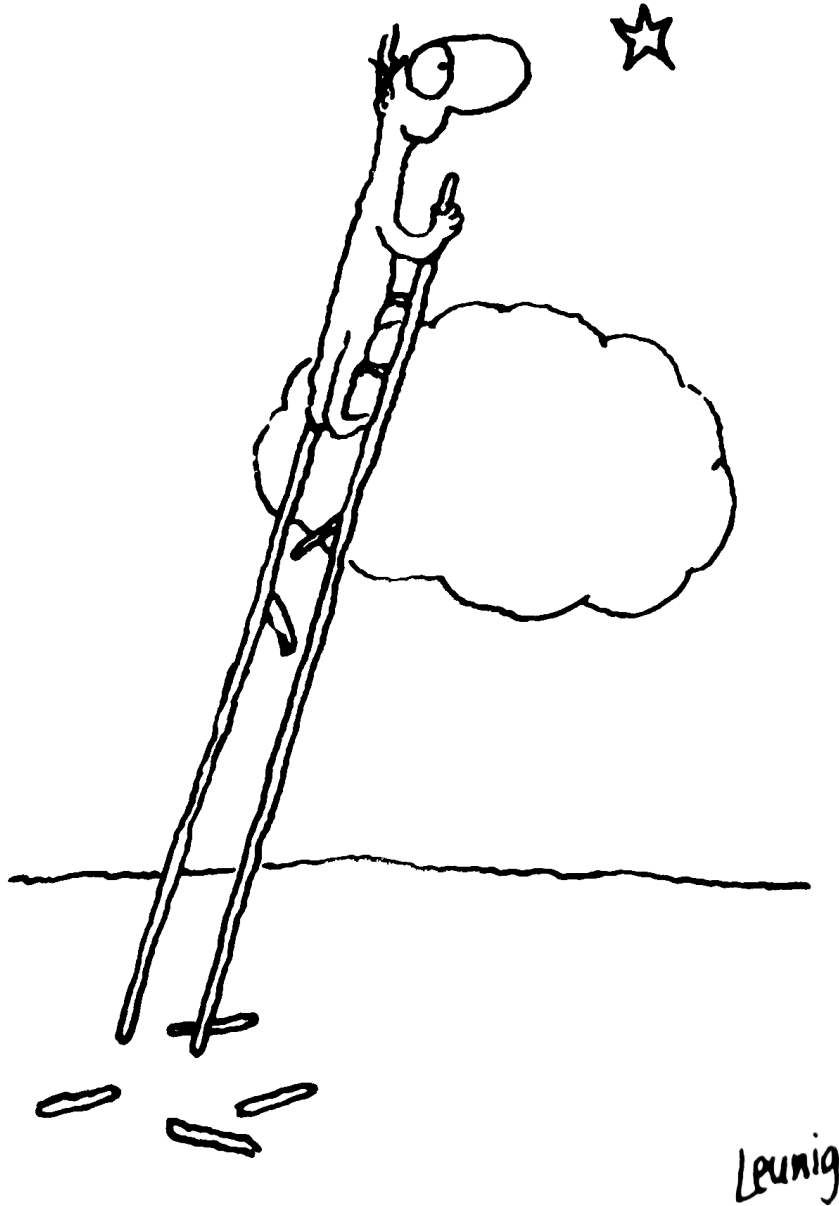
A thesis submitted for the degree of Doctor of Philosophy.

Centre for Stellar and Planetary Astrophysics,

School of Mathematical Sciences,

Monash University, Australia.

March 2007



An apt cartoon from the Melbourne artist Michael Leunig. Reproduced from a coffee mug given to me by Lisa Pinter. We note that the assumptions used in the current work are (usually) more substantial than the support for the ladder!

Contents

Abstract	vii
Statement	viii
Acknowledgements	ix
Publications	xi
I INTRODUCTION	1
1 Setting the Scene	2
1.1 Preface	2
1.2 Layperson’s Introduction to Stars	3
1.3 Synopsis of the Study	6
2 Background	9
2.1 Low Metallicity Observational Evidence	9
2.1.1 Low Metallicity Diagram of the Universe	9
2.1.2 Local Archaeology and the Metal Poor Halo Stars	12
2.1.3 High Redshift: Information from the Young Universe	14
2.2 Big Bang Nucleosynthesis	17
2.2.1 Background	17
2.2.2 Primordial Abundances for the Stellar Models	19
2.3 Previous Theoretical Models of $Z = 0$ and EMP Stars	20
2.3.1 Introduction	20
2.3.2 ZAMS and Beyond: 1960s to 1980s	21
2.3.3 DSF Discovery and DCF Modelling: 1990s to 2001	23
2.3.4 Latest Studies: 2002 to 2006	28
2.3.5 The Current Study In Context	30
II METHOD	32
3 Numerical Codes	33
3.1 Structural Evolution Code	34
3.1.1 History of Development and Basic Assumptions	34
3.1.2 Overview of Numerical Method	35
3.1.3 Included Physics	36
3.2 Nucleosynthesis Code	43
3.2.1 Introduction	43
3.2.2 Code Overview	44
3.2.3 Input Physics	44
3.2.4 NS Code Modifications	48
3.2.5 Yield Calculation and Synthetic Pulses	48

4	Structural Evolution Code Modifications	49
4.1	Time-Dependent Mixing	49
4.1.1	Motivation	49
4.1.2	The Diffusive Mixing Paradigm	49
4.1.3	Choice of Implementation Method	52
4.1.4	Choice of Numerical Method	53
4.1.5	Diffusive Overshoot	61
4.1.6	Semiconvection	74
4.1.7	Summary, Practicalities & Future Work	77
4.2	Opacity	79
4.2.1	Low Temperature: 500 – 8000K	79
4.2.2	Mid Temperature: 8000K – 500MK	80
4.2.3	High Temperature: 500MK – 2000MK	81
4.2.4	Conductive: High T and R	81
4.2.5	Summary, Practicalities and Future Work	81
4.3	CNO Equilibrium with He Burning at $Z = 0$	82
4.3.1	Motivation	82
4.3.2	Equilibrium CNO Burning and Timestepping	83
4.3.3	Dual Burning Modification	84
4.4	Other Modifications	85
III	STELLAR MODEL RESULTS	87
5	Zero Metallicity Stars: Structural Evolution	88
5.1	Background	88
5.1.1	Overview	88
5.1.2	Physical Parameters Used & Initial Composition	89
5.2	Detailed Evolution at $0.85M_{\odot}$	91
5.2.1	Main Sequence to RGB Tip	91
5.2.2	Dual Core Flash	101
5.2.3	Secondary RGB and Core Helium Burning	114
5.2.4	AGB	121
5.2.5	Executive Summary of Peculiar Evolution	127
5.2.6	Comparison With Previous Work	131
5.3	Detailed Evolution at $2.0M_{\odot}$	139
5.3.1	MS and CNO Mini-Flash	139
5.3.2	Core He Burning and Second Dredge-Up	141
5.3.3	TP-AGB: Dual Shell Flashes and Third Dredge-Up	146
5.3.4	Comparison With Previous Work	150
5.4	Overview and Discussion of All $Z = 0$ Models	156
5.4.1	$M = 0.85 M_{\odot}$ to $3.0 M_{\odot}$	156

6	Zero Metallicity Stars: Nucleosynthetic Evolution	160
6.1	Background	160
6.1.1	Initial Composition	160
6.2	Detailed Nucleosynthesis at $M = 0.85 M_{\odot}$	160
6.2.1	First Dredge-Up	161
6.2.2	Dual Core Flash	162
6.2.3	Is the DCF a New s-Process Site?	170
6.2.4	TP-AGB	170
6.2.5	Chemical Yield	173
6.3	Detailed Nucleosynthesis at $M = 2.0 M_{\odot}$	174
6.3.1	Second Dredge-Up	177
6.3.2	Dual Shell Flashes/CNO-PIEs	177
6.3.3	Dual Shell Flashes – Potential s-Process Sites?	187
6.3.4	TP-AGB	190
6.3.5	Chemical Yield	198
6.4	Summary of All $Z = 0$ Models and Yields	200
6.4.1	Low Mass: The $1 M_{\odot}$ Model	201
6.4.2	Intermediate Mass: The $3 M_{\odot}$ Model	203
6.4.3	All $Z = 0$ Yields	203
7	Metal Poor Halo Star Models	217
7.1	Background	217
7.1.1	Introduction	217
7.1.2	Brief Overview of Code Inputs	218
7.1.3	The Grid of Models	221
7.1.4	Initial Composition	221
7.2	Structural Evolution	223
7.2.1	Main Sequence to RGB Tip/Core He Ignition	225
7.2.2	On the Occurrence of Dual <i>Core</i> Flashes	228
7.2.3	On the Occurrence of Dual <i>Shell</i> Flashes	232
7.2.4	Further Evolution in the HR Diagram	232
7.2.5	TP-AGB	238
7.2.6	Mass Loss	244
7.2.7	Table of Lifetimes	250
7.3	Nucleosynthetic Evolution	252
7.3.1	Introduction	252
7.3.2	First Dredge-Up	252
7.3.3	Dual Core Flashes	253
7.3.4	Second Dredge-Up	258
7.3.5	Dual Shell Flashes	260
7.3.6	TP-AGB	261
7.4	Yields	263
7.4.1	Uncertainty in the Yields of the LM, Higher-Z Models	265
7.4.2	Grouping the Models Into Yield Types	265
7.4.3	Some Key Properties of The Yields	266
7.4.4	Elemental Yields: Helium to Phosphorus	270
7.4.5	Nuclidic Yield Tables by Mass Fraction	279

7.5	Comparison with Previous Studies	282
7.5.1	Low Mass Structural Evolution	283
7.5.2	Intermediate Mass Structural Evolution	286
7.5.3	The Polluting Episodes	286
7.6	Comparison with Halo Star Observations	290
7.6.1	Overview	290
7.6.2	Comparisons With Dual Flash Abundances	293
7.6.3	Comparisons With Yields	298
7.6.4	Comparisons with Individual EMP Halo Stars	308
7.6.5	Summary	314
8	Galactic Globular Cluster Stars	317
8.1	Introduction	317
8.1.1	The GC Abundance Anomalies Mystery	317
8.1.2	GC Stellar Models: The Grids and Input Physics	318
8.2	Models of NGC 6752 Stars	319
8.2.1	The Standard Set	319
8.2.2	Models Varying Mass-Loss Rates and Reaction Rates	323
8.3	GC Chemical Evolution with AGB Yields	328
8.3.1	Abstract	328
8.3.2	The Pollution Model	328
8.3.3	Generation B AGB Stars	329
8.3.4	Results	330
8.3.5	Summary	332
8.4	Models of NGC 6752 Stars <i>Without 3DUP</i>	333
8.4.1	Motivation	333
8.4.2	Inhibiting 3DUP	334
8.4.3	The Grid of Models	335
8.4.4	Results	335
8.4.5	Discussion	338
8.4.6	Conclusion	341
8.5	Cyanogen in GC AGB Stars: Observing Project	344
8.5.1	Abstract	344
8.5.2	Introduction	344
8.5.3	Literature Search Results and the Observing Proposal	345
8.5.4	Discussion	346
IV	CONCLUSION	350
9	Summary of $Z = 0$ and EMP Models	351
9.1	Peculiar Evolution	351
9.2	Chemical Pollution	352
9.2.1	Mass-Metallicity Pollution Diagram	352
9.2.2	Extra Channels for Producing CEMPs	354
10	Concluding Remarks	358
10.1	Reflecting on the Journey	358
10.2	Future Work	360

V	APPENDICES	361
A	Yields: Metal-Deficient and $Z = 0$ Models	362
A.1	Plots: Elemental Yields Versus Initial Mass	363
A.2	Plots: Elemental Yields Versus $[\text{Fe}/\text{H}]$	369
A.3	Tables: Nuclidic Yields by Mass Fraction	377
B	Yields: Globular Cluster Models	388
B.1	Tables: Nuclidic Yields by Mass Fraction	389
C	Miscellaneous Material	396
C.1	Surface Opacity Uncertainty in $Z = 0$ AGB Stars	396
C.2	Plots from the Journey	400
	Bibliography	404

Abstract

In this study we have investigated stellar evolution and nucleosynthesis in the low and extremely low metallicity regime – including models of stars with a pure Big Bang composition (i.e. $Z = 0$). The metallicity range of the extremely metal-poor (EMP) models we calculated is $-6.5 < [\text{Fe}/\text{H}] < -3.0$, whilst most of our models are in the mass range $0.85 < M < 3.0 M_{\odot}$. We have also calculated a series of models with a metallicity of $[\text{Fe}/\text{H}] = -1.4$, to compare with observations of abundance patterns in Galactic globular cluster stars.

Many of the extremely metal-poor (EMP) and $Z = 0$ models experience violent evolutionary episodes not seen at higher metallicities. We refer to these events as ‘Dual Flashes’ since they are characterised by peaks in the hydrogen and helium burning luminosities occurring at roughly the same time. Some of the material processed by these events is later dredged up by the convective envelope, causing very significant surface pollution. These events have been reported by previous studies, so our results confirm their occurrence – at least in stellar models.

The novelty of this study is that we have calculated the entire evolution of the $Z = 0$ and EMP models, from the ZAMS to the end of the AGB – including detailed nucleosynthesis. We have also calculated the nucleosynthetic yields, which we make available in the appendices. Although subject to many uncertainties these are, as far as we are aware, the only yields available in this mass and metallicity range.

We find that our models predict an increased number of carbon-rich stars at the lowest metallicities. This is mainly due to the extra pollution provided by the Dual Flash (DF) events – which do not occur in higher metallicity models. This concurs well with the observations that show the proportion of carbon-enhanced metal-poor (CEMP) stars in the Galactic halo to be higher at lower metallicities. It is also found that the pollution arising from the DF events is simultaneously C- and N-rich, as also observed in the CEMP stars. This contrasts with the pollution expected from third dredge-up at low mass, which would be C-rich only. Furthermore, the models predict that the proportion of CEMP stars should continue to increase at lower metallicities. We also compare the chemical pollution arising from our models with the detailed abundance patterns available for some of the most metal-poor CEMP stars, and find mixed results.

In relation to our globular cluster (GC) models we find that our ‘standard’ AGB models have fundamental problems in explaining the GC abundance anomalies, mainly due to the occurrence of third dredge-up (3DUP). As an experimental test we also calculate a series of models in which we ‘turn off’ 3DUP. Here we find that the match with observations is better, but problems still remain. We provide the yields for all these GC models in the appendices.

Finally we note that all these calculations contain many uncertainties. These include the unknown mass-loss rates, uncertain nuclear reaction rates, and the treatment of convection. In the case of the Dual Flash events a further uncertainty is the possibility that full fluid dynamics calculations are really needed to model these violent episodes.

Statement

This thesis contains no material which has been accepted for the award of any other degree or diploma in any university or other institution. To the best of my knowledge this thesis contains no material previously published or written by any other person except where reference is made in the text. The length of this thesis is less than 100,000 words, exclusive of figures, tables, appendices and bibliographies.

Simon Wattana Campbell

Acknowledgements

Firstly I'd like to thank my supervisor – John Lattanzio – of Monash University, Australia, for his support and friendship over the last 4.9 years. Indeed, he certainly deserves thanks right now because he has just read through every word of this thesis – which, as you can see, is no small feat! Particularly since the pace at which I have fired chapters at him has accelerated in the last few months. Even at this 11th hour (well, 27th for me today) he is religiously reading the last sections. I would also like to thank him for encouraging me with the forging of many scientific collaborations, to follow my scientific interests, to attend conferences, and to give seminars. I also think he deserves thanks for maintaining the Stellar Interiors and Nucleosynthesis (SINS) group throughout the years. Our SINS meetings were a key part of my time at Monash. Of course JL is synonymous with port and cheese appreciation (not to mention wine and beer), for which I am all the more educated (thanks to his mum Joy for those P & C nights and BBQs too!).

There are so many friends and colleagues I would like to thank at Monash that I will probably forget someone, so please don't hold it against me! In no particular order: Gareth Kennedy (for many interesting conversations – and inspiring the lecture-hopping culture), John Mansour (for all our long chats about music, bikes, etc.), Johnny Hitti (for those long philosophical arguments – and music appreciation at the NFF etc.), Hamed Moradi (for passionate discussions on religion & politics + organising the soccer – and African music appreciation), Carolyn Doherty (for putting up with my extreme mess in the office – and my hogging of all the Evoln notes), John McCloughan (for all those Cinque Lire cafe trips and organising the happy hours at the Nott), Keith Hsuan (for interesting discussions and an insight into swing dancing), Lisa Elliott (for letting me tag along on those observing trips & sharing travel stories), Amanda Karakas (for the early help with the stellar codes and her very useful thesis), Christian Lerrahn (for some interesting email debates & organising the soccer), Marie Gibbon (for keeping the Global Warming issue alive), Allie Ford (for the vego section of the Maths Dept. BBQs and letting me tag along on the observing run), Juan Oliveros (some more sangria soon!), Charles Morgan (for some interesting discussions), and Paul Lasky and Hannah Schunker for resurrecting Happy Hour. Thanks also to the CSPA staff. All of these people have contributed to helping me survive the PhD. They have also helped put the 'P' into the PhD – through all the great discussions/debates we've had over the years. I've been very lucky to be in an environment so rich with nice, intelligent people. A particular thanks to Gertrude Nayak, who helped me with getting into honours – if that hadn't happened I wouldn't have reached this stage, and the secretaries (Linda, Denise, Barb & Doris et al.). Finally I thank Monash University for the PhD scholarship that supported me financially for 3.5 years.

I have been fortunate enough to have gone to various conferences and visited various universities around the world during my time at Monash (largely thanks to John Lattanzio). In my travels I have met many nice people, such as Onno Pols (thanks for the binary star education even though that work did not end up in this thesis, for looking after me in Utrecht & of course for the Belgian beer education!), Chris Tout (thanks for the hospitality in Cambridge – especially those traditional Cambridge Uni dinners), Jordi Jose (thanks for looking after me in Barcelona), Sandro Chieffi (thanks for the help with the high-T opacity tables), David Yong (always the fellow vegetarian at conferences), Sergio Cristallo (mi hijo), Lionel Siess, Peter Cottrell, Agostino Renda, Jarrod Hurley, Brad Gibson, Yeshe Fenner, Rob Izzard, Axel Bonacic Marinovic, Liz Wylie, Kenji Bekki, and many more. A special thanks to the organisers of the Torino workshops over the years, at Granada (Inma & Carlos & Olga) and Cambridge (Maria, Richard, John & Ross et al.).

As most of this work was done on computers I think it fitting to thank the people that contributed to the open-source software I have used. All of my work has been done using Linux operating systems. A few pieces of software I have made great use of have been: Yorick (for most of

the plots in the thesis), the GNU Image Manipulation Program (GIMP), and LyX (a \LaTeX frontend). I have used LyX to write this entire document – and I can highly recommend it! Thanks to the people that provide those services that are indispensable for astronomers and astrophysicists – the NASA ADS and astro-ph. I also have to thank the excellent staff at the Australian Partnership for Advanced Computing (APAC supercomputer) and also the Victorian version, VPAC. Much of this work was done under the APAC grant Project Code g61 (“Element Production by Intermediate Mass Red-Giant Stars”). Of course a big thanks goes to the original authors of the Stellar codes I have used in this thesis – Peter Wood, Rob Cannon, John Lattanzio, Cheryl Frost, Faulkner & Gingold. Thanks also to the IT guys for support over the years (Jon, Declan, Sean & Mike).

Other friends I would like to thank are the NFF crew (Dave, Claudia, Jan, Pat, Dave & Barb, Suki) – for the great Easter music festivals/get-togethers over the years. It was always a welcome change of scene. Rachel, Matt & Nathan for our pub dinners, Marina for having us over for dinner so often (braving the Vego cooking) and those great African nights full of dancing at the Espy, Mary & Tony for the musical outings. A big thanks to Nim and Man & Manvina for always being great hosts in Malaysia.

I thank my family – Mum & Dave for being so caring, especially all those supportive phone calls and emails, my nomadic brothers Alex and Jeff – it was always nice to see you on your jaunts to Melbourne – hopefully we’ll see more of you two when we move to Asia! Thanks also to our amazing net-surfing, e-mailing, beach-combing Grandma, for her moral support, all the email updates on the family – and lovely luncheons in Anglesea. Two more people I consider family are Lisa’s mum Maria and Lisa’s brother Joe. Maria has been very supportive over the years – making many yummy dinners, and looking after our various animals when we go away. Joe has been there for us too, ever reliable and always willing to help out.

Here I would like to thank the person most central to my life – my loving partner of 13 years, Lisa Pinter. She has supported me emotionally, morally and practically over my many years of study. It has been a very hard road to get the thesis finished this year. I appeared to have had bitten off a bit more than I could chew! Nevertheless, Lisa supported me through the months and months of 7 day weeks (sometimes wisely steering clear of me in my PhD lair!). It was a difficult time for her too. We seem to have both survived though – I think the daily coffee together at Santucci’s helped with that. There is definitely some catching up to do. I have been away in thesis land for quite a while!

Finally we note that the writing of this thesis has been on a laptop in our house which sources most of its *energy from a star!*^a

^aWe have 12×165 Watt solar panels on the roof.

Publications

The following papers were published during the Author's candidature:

Refereed

1. **Origin of Abundance Inhomogeneity in Globular Clusters**
Bekki, K., Campbell, S. W., Lattanzio, J. C., Norris, J. E.
2007, MNRAS, accepted January 2007
2. **The Chemical Evolution of Helium in Globular Clusters: Implications for the Self-Pollution Scenario**
Karakas, A. I., Fenner, Y., Sills, A., Campbell, S. W., Lattanzio, J. C.
2006, ApJ, 652, 1240
3. **Fluorine Abundance Variations in Red Giants of the Globular Cluster M4 and Early-Cluster Chemical Pollution**
Smith, V.V., Cunha, K., Ivans, I.I., Lattanzio, J.C., Campbell, S.W., Hinkle, K.H.
2005, ApJ, 633, 392S
4. **Abundance Anomalies in NGC6752 - Do AGB Stars Have a Role?**
Campbell, S.W., Fenner, Y., Karakas, A.I., Lattanzio, J.C., Gibson, B.K.
2005, Nuclear Physics A, 758, 272
5. **The Evolution of Fluorine in Galactic Systems**
Renda, A., Fenner, Y., Gibson, B.K., Karakas, A.I., Lattanzio, J.C., Campbell, S.W., Chieffi, A., Cunha, K., Smith, V.V.
2005, Nuclear Physics A, 758, 324
6. **Modelling Self-Pollution of Globular Clusters from Asymptotic Giant Branch Stars**
Fenner, Y., Campbell, S.W., Karakas, A.I., Lattanzio, J.C., Gibson, B.K.
2004, MNRAS, 353, 789
7. **On the origin of fluorine in the Milky Way**
Renda, A., Fenner, Y., Gibson, B.K., Karakas, A.I., Lattanzio, J.C., Campbell, S.W., Chieffi, A., Cunha, K., Smith, V.V.
2004, MNRAS, 354, 575

Conference Proceedings

1. **Are There Radical Cyanogen Abundance Differences Between Galactic Globular Cluster RGB and AGB Stars?**
Campbell, S.W., Lattanzio, J. C., Elliott, L. M.
2006, MmSAI, 77, 864
2. **Helium enhancements in globular cluster stars from Asymptotic Giant Branch star pollution**
Karakas, A. I., Fenner, Y., Sills, A., Campbell, S. W., Lattanzio, J. C.
2006, MmSAI, 77, 858
3. **Nucleosynthesis in Early Stars**
Campbell, S.W.
2004, in Carnegie Observatories Astrophysics Series, Vol. 4: Origin and Evolution of the Elements, ed. McWilliam, A., Rauch, M., sympE, 7C

4. **Abundance Anomalies in NGC 6752. Are AGB Stars the Culprits?**
Campbell, S.W., Fenner, Y., Karakas, A.I., Lattanzio, J.C., Gibson, B.K.
2004, MmSAI, 75, 735
5. **The Role of AGB Stars**
Lattanzio, J., Karakas, A., Campbell, S.W., Elliott, L., Chieffi, A.
2004, MmSAI, 75, 322

Part I

INTRODUCTION

Chapter 1

Setting the Scene

“Science is a way of trying not to fool yourself. The first principle is that you must not fool yourself, and you are the easiest person to fool.”

– Richard Feynman

1.1 Preface

The perennial questions of ‘What is out there?’ and ‘Is there any other life in the Universe?’ are not solely the domains of scientists such as astrophysicists and astronomers. They are key questions for humanity. Interest in these questions pervades our society at large. For astronomers and astrophysicists this is frequently evidenced in the reactions of people to their profession. No matter what the age-group a whole series of questions usually ensues. These questions are always very pertinent – and often very difficult to answer. I believe that this great, raw, interest is a healthy sign. Given this passion for the subject of astronomy it would be nice if our education systems reflected this interest and offered greater opportunities for children – and adults – to learn more about the Universe. Exposing people to the amazing reality that is our Universe opens our minds and puts our place in the Universe (and on our planet) into perspective. Furthermore, learning how information about the Universe is gathered by scientists is highly revealing of just how powerful a method Science is for understanding reality.

This thesis represents a tiny step (but hopefully a useful one!) in the process of attempting to understand the Universe. It is predicated on many other small (and some large) steps taken by scientists – and indeed other researchers – before us. The exact topic is necessarily very narrow, highly specialised. However the broader context is easily understandable and, as noted above, of great interest to many people. Therefore, for the non-specialists that have, for some reason, found themselves with a copy of this highly technical monograph, we first provide a section that gives some general information on the important role of stars in our Universe. We also give a non-specialist introduction to the current study towards the end of that section. A more technical introduction is given in Section 1.3.

1.2 A Layperson's Introduction to the Importance of Stars

When talking about stars the image that generally pops into people's minds is that of the night sky filled with millions of pinpoints of light. Practically all of the light that we see in space comes from stars of one sort or another. Some of those stars that we see at night are actually entire *galaxies*. However these galaxies are themselves just collections of many, many stars – like a city is a collection of many, many houses. The galaxies just look like tiny bright dots because they are so far away. Indeed the galaxy that we live in – known as the 'Milky Way' – is one of these collections of stars. It has *billions* of stars. So what are these things called stars that seem to be everywhere in the Universe, shining brightly? The answer to that is best seen during the *day* rather than the night. The star that shines the brightest (at least for us) is our own Sun. It turns out that all those stars in the night sky are just like the Sun – huge bright balls of gas. The only reason the Sun looks so much brighter than all the other stars is because we are so close to it. Indeed, we are so close to it that we can feel the heat from it – and get sunburnt by its UV radiation. So the Sun is our 'pet' star. It also turns out that it is a pretty average star compared to all the other stars out there. It has an average size (which is pretty big!), an average brightness, and even an average age. So there are lots of stars out there quite similar to our Sun. However there are also stars out there that are much bigger and much smaller. Some are much brighter but some are much dimmer. There is even a whole range of colours!

The Light From Stars

A key question that many people ask about stars is 'Why do they shine?'. This is a great question. It took researchers quite a long time to work this out. Back in the early 1900s we had no idea. People suggested that the Sun produces so much heat that it must be burning *coal!* Another theory was that the heat was produced by the slow collapse of the Sun. This is possible, but it turned out that the Sun wouldn't shine for very long in this case – it would have shone for much less time than the Earth has been around – so that theory was rejected too. About 20 years later we still didn't know how the Sun shone. One of the famous astronomers at the time (scientists could be famous back then!), Arthur Eddington, wrote a brief article summarising some of the theories about how the Sun might shine ([Eddington 1919](#)). This is a fascinating article because it shows science at work. Eddington had collected all the evidence about the Sun and worked out the key characteristics of the source of energy – but still didn't know what it actually was. None of the explanations at the time fitted the evidence. It turns out that the reason they couldn't work it out was because the source of energy had not even been discovered on Earth yet – nuclear energy! It is impressive that – even before nuclear energy was discovered – the scientists around that time were saying that it must have been *something* like that. They were calling it 'sub-atomic energy'. Since this energy must be causing the stars to shine so brightly and for so long, it was naturally wondered if humans could harness it, as [Eddington \(1920\)](#) noted:

"If, indeed, the sub-atomic energy in the stars is being freely used to maintain their

great furnaces, it seems to bring a little nearer to fulfillment our dream of controlling this latent power for the well-being of the human race – or for its suicide.”

In this statement he also foreshadowed one of the unfortunate spin-offs of these scientific investigations – the development of nuclear weapons. Interestingly Eddington's comment was made well before nuclear weapons were invented.

So we now know that it is *nuclear energy* that powers the stars. This energy is released in nuclear reactions, and, in particular, nuclear *fusion* reactions. Nuclear fusion simply means that two (sub-atomic) particles are fused together. This usually happens in the very centre of stars – where it is very hot and dense. The sub-atomic particles are moving around so fast that when they collide they stick together. Nuclear fusion has two effects. The first we have already mentioned – that nuclear energy is released, which causes the star to shine. The second is a very important effect – *a new particle is formed* (out of the combination of the two involved in the collision). This is occurring all the time in the Sun. For example, in the Sun there is a lot of hydrogen. When some of these hydrogen nuclei collide they eventually combine to form the next element in the periodic table – helium. Then, if there is a lot of helium (and the temperature is high enough), carbon can be formed, and so on. This is alchemy – turning one element into another. It appears that Nature is doing alchemy all the time, in stars. Indeed, it turns out that almost all elements are made in stars – even gold, silver and uranium! The modern name for this alchemy (or ‘synthesis of the elements’), is *nucleosynthesis*, which is the topic of the next section.

Stellar Alchemy: The Origin of the Elements

Around the late 1930s the picture of stellar nucleosynthesis was beginning to be fleshed out (based on earlier work by researchers such as George Gamow and Ernest Rutherford). In 1939 Hans Bethe published a paper called “Energy Production in Stars” where he proposed that the particular nuclear reactions occurring in stars like the Sun were those that involved hydrogen being ‘burnt’ to helium. He proposed two sets of reactions – the CNO cycles and the proton-proton (p-p) chains. We now know that this is correct – and that it is the p-p chains that provide the most energy in the Sun.

After about 20 more years of research (by many scientists) the famous work called “Synthesis of the Elements in Stars” by Burbidge et al. (1957) (also known as the B²FH paper) really consolidated and clarified our knowledge of the origin of the elements. They investigated all the different types of nuclear reactions that lead to the production of the elements: hydrogen burning, helium burning, neutron capture reactions, etc. It had been discovered that ***stars are the major source of almost all elements*** – except for hydrogen and helium which were the main elements produced by the Big Bang. Our picture of the origin of the elements has not changed much since then, although there has been an explosion of research work into the details of all the different types of stars. The current study is one of these research works.

An interesting consequence of the fact that almost all elements are produced by stars is that everything on Earth must have, at one stage, been made inside a star (apart from the H and He) – including ourselves and the planet itself! This realisation must have inspired that now

famous statement: '*We are all made of stardust*'. We note that the way that the stardust (or gas) gets out of the stars is either through mass loss via stellar winds or violent explosions of stars (i.e. supernovae).

Thus it can be seen that stars are very important objects in the Universe - they provide most of the light that we can see and also produce almost all of the Elements that surround us!

Information from the Starlight

One of the most amazing things about starlight is that it actually contains a huge amount of information. People often ask how astronomers know exactly what a star is made of, or how fast a star is rotating. Both of these pieces of information come from the starlight itself. The best example to explain this is our own star's light – sunlight. Everyone has seen a spectrum of light from the Sun – through a crystal or a rainbow for example. Sunlight is made up of all these colours. The crystal (or water in the case of rainbows) spreads the sunlight out so we can see the array of colours. It was originally thought that the spread of colours was continuous – that there were no breaks in the pattern. However, in 1802 William Wollaston was looking at one of these spectra and noticed that there were lots of little dark lines in it. These are now called 'Fraunhofer lines', after Joseph Fraunhofer who investigated them in detail around 1814. It wasn't for another 60 years before scientists finally figured out what these lines were. The breakthrough came when [Kirchhoff and Bunsen \(1860\)](#) made the discovery that every chemical element has a set of particular colours that it absorbs (and emits). These are called *spectral lines*. [Kirchhoff and Bunsen](#) then realised that these were the lines that people were seeing in the Sun's spectrum. This was a very important breakthrough. It opened up a huge door that has enabled us to explore the Universe in great detail – without having to go anywhere in a spaceship. It turned out that, if we had a powerful enough telescope, it was possible to get chemical information from millions and millions of stars. Indeed, we are still using this method today in exploring the Universe. It has given us a huge amount of information that has enabled astronomers and astrophysicists to develop theories about how the Universe has evolved. Finally we note that the same light can be used to work out how fast a star is moving away from or towards us (by using the Doppler shift) and also how fast it is spinning. It can also be used to work out if the star has a companion star (i.e. a binary star system) – or even a planet!

Computer Simulations of Stars & The Current Study

With all this information being collected from the starlight we have a lot of things that need to be explained. There are still many things that we do not understand about the Universe. However we do know a fair bit about many areas of physics. For example, we have a good understanding of the effects of Gravity, we know a lot about nuclear reactions (through experiments and theory), and we know a lot about how gas behaves. Add to this the fact that these physical laws ('laws of Nature') are, in general, easily described by the language of mathematics, and it appears possible for us to put it all together and work out what is happening inside a star. Indeed, this is the job description of a stellar astrophysicist! In the early days of stellar astrophysics scientists would do all the calculations *by hand*. In some cases the scientists had a whole 'army' of people

that would do the calculations of stars by hand. Naturally the invention of ‘automatic digital computers’ came as a great boon to this area of research. As computers became more capable around the end of the 1950s, many scientists applied them to the problem of stellar evolution (eg. [Haselgrove and Hoyle 1956](#); [Sears 1959](#); [Heney et al. 1959](#)). This led to a great increase in understanding of stars since we could now follow the whole life-cycle of a star with a computer program. This is very handy because stars take millions or billions of years to evolve in reality. As computers became faster and faster so the stellar evolution simulations became faster and more detailed. For example, to calculate the life of the Sun up to its present age would have taken weeks in the 1960s – but now we can calculate it in a matter of minutes, and with much greater precision.

This study is a study in stellar evolution, using computer codes as just described. We look at particular types of stars – stars that were born just after the Big Bang. Thus they are the first generation of stars that ‘lit up’ the Universe. They are also the first generation of stars that released newly-formed elements into the Universe (often referred to as ‘pollution’). We also investigate the second generation of stars. These two groups of stars are of particular interest at the moment because astronomers have discovered a group of stars – in our Milky Way galaxy – that have seen very little pollution. This means that they are extremely old – they are ‘stellar relics’ from the early times of the Universe. Understanding them (through stellar modelling) should give a big insight into the early stages of the evolution of our Galaxy – if not the Universe. Hopefully our models help in some small way.

1.3 Synopsis of the Study

In astronomy and astrophysics elements with atomic numbers greater than that of hydrogen and helium are referred to as ‘metals’. The Big Bang produced only hydrogen and helium (and trace amounts of heavy elements), so the ‘metallicity’ of a star is naturally a measure of how much pollution its gas has been subjected to since the beginning of the Universe. Since the material that pollutes the Universe is primarily produced via nucleosynthesis inside stars, the rate of pollution is dependent on the timescales of stellar evolution. The metallicity of a star is thus often taken as an age indicator (although this does not always hold due to other factors affecting the pollution rate, eg. the local star formation rate). When we talk of metallicity in what follows we shall use the traditional definition – $[\text{Fe}/\text{H}]^a$. We note that this has limitations as a star can be metal-rich in carbon (even super-solar) but still extremely metal-poor in terms of Fe – as seen in the carbon-enhanced metal-poor halo stars.

The main thrust of the current study centres on understanding some of the recent – and not so recent – observations of low and extremely low metallicity stars. The key question is: ‘Can we match theory with observations of these very old stars?’. We investigate three populations of low metallicity stars in particular, the first of which is (so far) unobserved and therefore purely hypothetical:

1. Population III stars ($Z = 0$)

^aWhere $[\text{Fe}/\text{H}]_{star} = \log\left(\frac{N_{Fe}}{N_H}\right)_{star} - \log\left(\frac{N_{Fe}}{N_H}\right)_{\odot}$.

2. Extremely metal-poor stars ($-6.5 < [\text{Fe}/\text{H}] < -3.0$)
3. Mildly metal-poor Galactic Globular Cluster stars ($[\text{Fe}/\text{H}] = -1.4$)

The mass range which we (primarily) explore is $0.85 < M < 3.0 M_{\odot}$. At extremely low metallicities the upper limit at which the core He flash occurs is only $\sim 1.3 M_{\odot}$ (in terms of initial stellar mass). In the current study we define stars above this mass to be intermediate-mass stars, and those below to be low-mass stars. Thus our mass range covers a variety of stars with different evolutionary features.

Although no Pop III stars have been observed to date there are many observations of extremely metal-poor (EMP) stars in the Galactic halo. The observed numbers of these interesting stars has greatly increased in the past decade or so, mainly due to surveys such as the Hamburg/ESO Objective Prism Survey (HES, [Christlieb et al. 1999](#)) and the HK survey ([Beers et al. 1992](#)). As these stars are so metal poor – reaching down to $[\text{Fe}/\text{H}] = -5.4$ ([Frebel et al. 2005b](#)) – they represent a possible link to Pop III. This is due to the fact that the gas from which they formed could only have been enriched by a small number of pollution events – or even a single event. Thus these stars may bear the chemical signatures of Pop III. Another possibility is that these EMP halo stars may actually be members of Pop III themselves. Their envelopes may have accreted heavy element polluted material over their ~ 10 Gyr lifespans. For these reasons we have calculated the series of zero metallicity models (Chapters 5 and 6), as well as the grid of models having metallicities comparable to those of the most metal-poor (EMP) halo stars (Chapter 7). For the initial composition of our EMP stars we mixed the ejecta from a $Z = 0$ supernova model with pristine Big Bang material, to mimic the single pollution event theory mentioned above (see Section 7.1.4 for details).

Making detailed calculations of stars of such low metallicities provided a set of stellar modelling problems that had to be resolved before computation was possible. The key modification was the addition of time-dependent mixing to the structural evolution code. This was needed due to the occurrence of violent hydrogen flashes in these models (which do not occur in higher metallicity models). During these events the evolutionary timesteps become comparable to the mixing turnover timescales, so instantaneous mixing is no longer a valid approximation. These, and other code modifications, are detailed in Chapter 4. The numerical codes which we have used for our study are described in Chapter 3.

A substantial amount of previous work has been done in relation to the modelling of EMP and $Z = 0$ stars. We compile a list of the literature in Table 2.2, which provides a convenient overview of the progress of the field at a glance. Although the structural evolution for these stars has been partly investigated, some uncertainties remain unresolved. We highlight these in the sections in which we compare our results with those in the literature (eg. Sections 5.2.6, 5.3.4 and 7.5). Less work has been done in trying to ascertain what the nucleosynthetic yields of these stars are. Indeed, full nucleosynthetic evolution and yields of low- and intermediate-mass $Z = 0$ and EMP models remains quite an unexplored area. We report on the detailed nucleosynthesis of two of our $Z = 0$ models in Chapter 6 and for some of our EMP models in Section 7.3. Thanks to high resolution spectroscopy now available on large (8-10 m) telescopes there are now detailed abundance observations for a selection of the EMP halo stars. These observations

provide multidimensional constraints on the stellar modelling, since we need to match a range of elemental abundances at once. These abundance patterns provide new insights/clues to the nucleosynthesis occurring inside EMP stars. We compare the nucleosynthetic results of our models with some of these abundance patterns in Section 7.6. In particular we discuss the results of our models in terms of the interesting discovery that the proportion of carbon-enhanced EMP stars increases with decreasing metallicity (see eg. the review by [Beers and Christlieb 2005](#)), in Sections 7.6 and 9.2.2. Taking the structural and nucleosynthetic evolution together, these models, although certainly full of uncertainties, represent the most comprehensive investigation into EMP evolution and nucleosynthesis to date. Although naturally also full of uncertainties, we have provided the yields of all our models in Appendix A. These will be of use to chemical evolution studies of the early Universe. Indeed, they are the only yields at these masses and metallicities of which the Author is aware.

A large part of the Author's time was spent on an interesting low-metallicity tangent. This is reflected by the presence of Chapter 8, in which we explore the intriguing mystery of the Galactic globular cluster abundance anomalies. We quantitatively investigate the popular theory that the abundance anomalies (eg. the Mg-Al and Na-O anticorrelations) originate in AGB stars. On finding that 'standard' AGB models have fundamental problems with producing these anomalies we try another tack in which we artificially 'turn off' third dredge-up in the AGB models (Section 8.4). These models prove to be a better match to the observations but still fall short. Thus the solution to the mystery remains as elusive as ever. We note that we provide the yields for all of these models in Appendix B.

In Chapter 2.1 we give a brief overview of the various observations at low metallicity, to put our modelling in context.

Finally, in Chapter 10, we reflect on the road that lead to this somewhat substantial body of work, and give a list of future research directions. As mentioned there we shall not be lacking of things to do!

Chapter 2

Background

“Our imagination is stretched to the utmost, not, as in fiction, to imagine things which are not really there, but just to comprehend those things which ‘are’ there.”

– Richard Feynman

2.1 Low Metallicity Observational Evidence

First we note that there has been no direct observation of any Population III ($Z = 0$) stars to date. This is probably not surprising since we would expect stars that had been in existence for approximately a Hubble time to have had their surfaces polluted to some degree via accretion from the ISM. Observations of metal-poor objects are however routinely made. These observations can provide indirect information on the nature of the first generation of stars. Metal-poor objects can be observed locally – in old stellar populations – or by ‘looking back in time’ at young objects/systems (ie. at high redshift). In this section we first present the results of a literature search for low metallicity objects, in graphical form. We then go on to describe some of these low metallicity objects, grouped by their locations (i.e. high or low redshift).

2.1.1 Low Metallicity Diagram of the Universe

In Figure 2.1 we provide a diagram that summarises the overall metallicity picture we have of the Universe at the moment, based on a literature search we performed during the course of the current study. It schematically displays the ranges of metallicity present in all low metallicity systems (of which the author is aware). Presenting the metallicity information in this way gives an interesting overview of the metal pollution throughout the Universe. We need to add some caveats though. The ranges displayed are not necessarily definitive in any of the cases – new observations may extend the ranges. They are also affected by observational bias. There are even differences between results in the literature. The median values are also somewhat uncertain but, due to the gaussian-like distributions of most of the object groups (and the log scale), they should be more robust than the spreads.

In the diagram we use the traditional definition of metallicity – $[\text{Fe}/\text{H}]$. As can be seen, each group actually spans at least an order of magnitude in metallicity. The extreme case is the

Galactic halo field stars which, with the current data available, span 6 orders of magnitude. However, the mean metallicity of this group is actually comparable to the Galactic GCs and Damped Ly α systems. It can also be seen that the populations least polluted with Fe (based on observations to date) are the Ly α systems – and the stars that lie in the extremely metal-poor tail of the Galactic halo population (also see Figure 2.2). Iron is commonly accepted to have two main sources – a fast release component via type II supernovae (SNeII) and a delayed release component via type Ia supernovae (SNe-Ia). The delayed release (~ 1 to 3 Gyr) of Fe by SNe-Ia is thought to be the reason for the $[\alpha/\text{Fe}]$ gradient in the Galaxy – as the fresh Fe gets released, $[\alpha/\text{Fe}]$ reduces to \sim Solar. However this probably does not explain the extreme iron deficiency of the field halo stars. In this case the material from which they formed must have been subjected to a very small number of pollution events (possibly only by a single SNI) or have been diluted to a great degree — or both. It is these two populations that should have the most ‘direct’ evidence for the nature of Population III. The Galactic Halo stars will be most useful for comparisons with the stellar models presented in this study (see eg. Section 7.6 on page 290 where we compare our metal-poor and $Z = 0$ models with observations).

We give some information and the data sources for the metallicity diagram here, in order to save space in the caption:

Details for Figure 2.1: Note that the ends of the distributions are not necessarily definitive in any of the cases — new observations may extend the ranges. They are also affected by observational bias and there are differences between results in the literature. The median values are also somewhat uncertain but due to the gaussian-like distributions of most of the object groups (and the log scale) they should be more robust than the spreads. As dust depletion of iron is significant in non-stellar sources (eg. DLA systems), the $[\text{Fe}/\text{H}]$ values have been increased by about 0.4 dex for these objects (which brings the values roughly in line with the observed $[\text{Zn}/\text{Fe}]$ abundances; see eg. Pettini 2004). Also, due to the paucity of $[\text{Fe}/\text{H}]$ values available for Ly α systems, the $[\text{Fe}/\text{H}]$ values for these systems have been derived by scaling from the oxygen and carbon abundances assuming a scaled-Solar metal distribution.

Data sources for Figure 2.1 (from bottom to top): LMC cluster $[\text{Fe}/\text{H}]$ values are from Olszewski (1993) and Olszewski et al. (1996) (metal-poor & metal-rich populations), Extragalactic GC values from Brodie and Strader (2006) (metal-poor & metal-rich populations), Milky Way halo field star values from Allende Prieto et al. (2006), Milky Way GC values from Bica et al. (2006) and Harris (1996) (metal-poor & metal-rich populations), Ly α forest values from Levshakov et al. (2001) and Pettini (2004), Damped Ly α values from Prochaska et al. (2003) and Pettini (2004), SMC cluster values from Olszewski et al. (1996), and Blue Compact Galaxy values from Kunth and Östlin (2000) and Izotov and Thuan (1999).

We now go on to describe some of the low metallicity groups included in the metallicity diagram. In particular we give details on the metal-poor Galactic halo stars and, for some perspective, the low metallicity objects seen at high redshift. These descriptions support the large amount of information condensed in Figure 2.1.

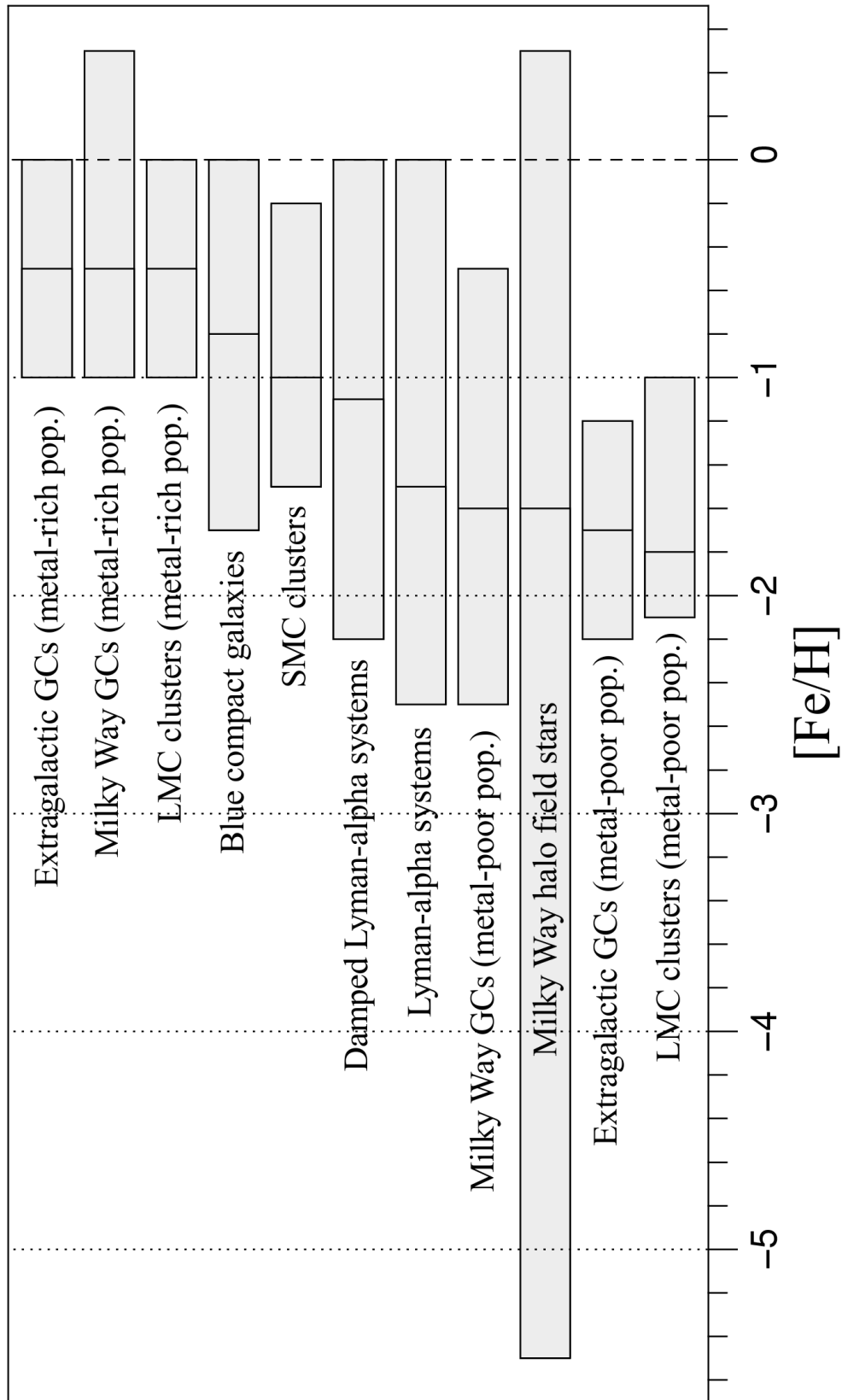


Figure 2.1: A *rough* summary of metallicity, as defined by $[Fe/H]$. The object groups are plotted in order of median metallicity which is denoted by the vertical line in each box. See text for more details on this figure, including data sources.

2.1.2 Local Archaeology and the Metal Poor Halo Stars

Low metallicity near-field objects are useful for studying the chemical history of the early Universe. Indeed, much more detailed information about their chemical composition can be obtained from these objects than from the high-redshift objects because they are so close to us. The same high-resolution instruments that are used to glean information from high redshift objects are able to give much more detail for nearby stars and galaxies. In the case of nearby galaxies the sample is also not limited to very bright objects (or objects in front of bright background objects) as it is at high redshift. The ability to sample smaller objects (even down to individual stars) within galaxies outside the Milky Way also contributes to the wealth of information available for the taking. Much work has been done to try and unravel the chemical history of the Galaxy, and information from the oldest stellar populations in and near our Galaxy provides vital constraints on the theories.

The three most metal-poor, low-redshift groups of objects from Figure 2.1 are:

- The Milky Way Halo field stars
- The metal-poor Globular Clusters (galactic and extragalactic)
- The LMC clusters (low metallicity group)

The lowest metallicity objects known to date are found in the Galactic Halo – the extremely metal-poor Halo stars (EMP halo stars). However the LMC clusters and metal-poor globular clusters (in the Milky Way halo and their counterparts around other galaxies) also have metallicities comparable to the bulk of the field Halo population. All of these object groups provide valuable information about the early chemical history of the Universe, and, at the low-metallicity end of their distributions, they should provide information about the elusive Population III.

For the current study it is the EMP halo stars that are of most interest, as the low-metallicity tail of their distribution represents the most metal-poor objects known in the Universe. Indeed, *the* most metal-poor object is the EMP halo star HE 1327-2326 (Frebel et al. 2005a). Furthermore, much data is currently being collected for these objects, in the form of detailed chemical compositions (eg. Aoki et al. 2006; Spite et al. 2006; Beers et al. 2007; Aoki et al. 2007). This observational data provides stringent constraints on the theoretical models, which we discuss later in this study. For these reasons we now give some background information on this interesting population.

Milky Way Halo Field Stars

The Milky Way halo is a potential source of a great amount of information about the low metallicity Universe. Comprising the lowest metallicity population of our Galaxy, it contains the lowest metallicity objects observed in the Universe to date – with a significant number of stars exhibiting heavy element abundances much lower than those of Ly α systems at high redshift. The halo population falls into two groups – the field stars and the globular clusters (GCs). The GCs are a significant low metallicity group and are the subject of Chapter 8. Here we focus on the field star population.

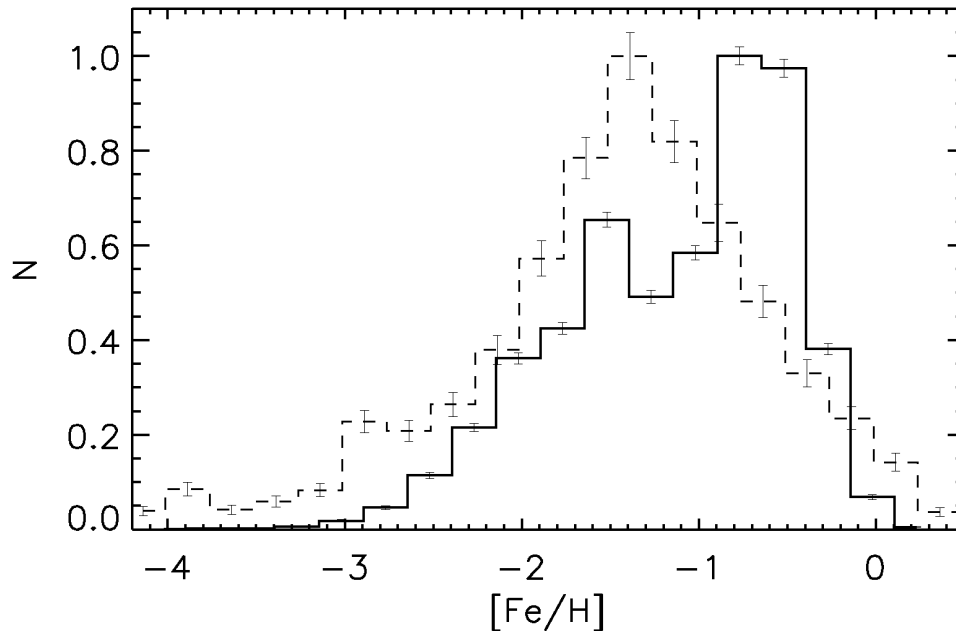


Figure 2.2: Metallicity versus scaled number of stars N for a region of the Milky Way. The two groups of observations are taken at different distances from the galactic plane: within 3 kpc (solid line) and > 8 kpc (dashed line). Observations are from data release 3 of the SDS. [From Beers et al. 2005, with permission]

The halo field star system is generally metal-poor but there is a spread in $[\text{Fe}/\text{H}]$. Beers et al. (2005) have put together a rough metallicity distribution function (MDF) for the halo based on the available (but observationally biased) data. It can be seen in Figure 2.2 that the halo is clearly metal-poor relative to the thick disc population (dashed line). Future surveys with less observational bias will refine the MDF but a significant tail of extremely metal-poor stars is evident already. We note that the extreme tail of the MDF is where the least polluted information about Population III should lie, as these objects have probably only been polluted by a few (or even just one) first generation stars. Thus the chemical composition of their envelopes may reflect that of Pop III ejecta.

The halo field stars have the great advantage of being very close (relative to external galaxies and DLAs for example), enabling observations of very high resolution to be made using 8-10 m class telescopes with spectrographs. Indeed, there has been an explosion of such observations in the last decade as the realisation that extremely metal-poor stars actually exist. It used to be thought that there was a lower cut-off in the MDF at $[\text{Fe}/\text{H}] \sim -2.5$ – ie. that low-mass extremely metal-poor (or $Z=0$) stars never formed (eg. Bond 1981). Subsequent surveys specifically looking at the halo population revealed lower and lower metallicity stars, as the limiting (apparent) magnitudes of the searches increased, indicating that *low-mass very low-metallicity stars did indeed form*.

The two major low-metallicity halo field star surveys to date are the HK and Hamburg/ESO surveys. Originally known as the Preston/Shectman Survey, the HK survey is named after the method of using the H and K calcium lines to select metal-poor stellar candidates (by eye; Beers et al. 1985, 1992). The candidates were then targeted with follow-up medium resolution spectroscopy to confirm if they were really Fe-poor. To date (the data analysis is still in progress) the survey has found ~ 1000 halo stars with $[\text{Fe}/\text{H}] < -2.0$ and ~ 100 with $[\text{Fe}/\text{H}] < -3.0$ (Beers

and Christlieb 2005). The more modern Hamburg/ESO Survey (HES, originally designed as a QSO survey; Wisotzki et al. 1996) is more efficient at finding low metallicity stars. It utilises an automatic/digital selection technique and also reaches down to dimmer stars (with a higher limiting magnitude of $B \sim 17.5$ as compared to $B \sim 15.5$ in the HK survey; Christlieb et al. 1999). So far it has uncovered ~ 200 stars with $[\text{Fe}/\text{H}] < -3.0$.

A very recent development has been the utilisation of the publicly available data collected by the Sloan Digital Sky Survey (SDSS; York et al. 2000). This survey was designed to collect information about QSOs and galaxies but actually contains many Milky Way stars. Beers et al. (2005) note that by SDSS data release 3 (SDSS DR3) there were spectrographic data for 70,000 Milky Way stars available. Analysing this wealth of data Allende Prieto et al. (2006) put together a database with T_{eff} , $\log(g)$ and $[\text{Fe}/\text{H}]$ for more than 20,000 of these stars. Amongst the analysed stars were ~ 2000 stars with $[\text{Fe}/\text{H}] < -2.0$ and ~ 150 stars with $[\text{Fe}/\text{H}] < -3.0$. This dramatically increases the total number of metal poor halo stars known, which now stands at ~ 450 with $[\text{Fe}/\text{H}] \lesssim -3.0$. However, new surveys currently underway and planned for the future will increase the sample size by orders of magnitude. These surveys, such as the Sloan Extension for Galactic Understanding and Exploration (SEGUE, using the same telescope as the SDSS; Beers et al. 2005), and GAIA, the European Space Agency's 3-telescope satellite to be placed at the L2 Earth-Sun Lagrangian point, will most likely uncover stars of much lower metallicity than currently known – or at least increase the sample size at the extremely metal-poor end of the MDF. GAIA will have a limiting magnitude of $V \sim 20$ so will be able to sample the outer halo, which may be more metal-deficient than the inner halo. However, as Beers and Christlieb (2005) note, stars of this magnitude will be very difficult to follow up with the high resolution needed for abundance determination (using current instruments). Also, new telescopes such as the Chinese Large-Area Multi-Object Spectrographic Telescope (LAMOST) will be able to perform rapid searches for metal-poor stars and also to follow-up medium resolution spectroscopy (Zhao 2005). Thus the near future is bright for gaining low-metallicity information from the Galactic halo stars. This should give a much deeper insight into the nature of Population III, and the chemical evolution of the Universe in general.

Finally we note that higher resolution follow-up observations of EMP stars found by the surveys gives us detailed chemical compositions which are readily compared with theoretical stellar and chemical evolution models. Indeed, this is what we do in Section 7.6 on page 290 where we compare our metal-poor (and $Z = 0$) models with the EMP halo star abundance observations from the literature.

2.1.3 High Redshift: Information from the Young Universe

Here we give another perspective on the low-metallicity Universe. There are two main ways in which chemical information is gathered about the young (high redshift) Universe. The first is by directly analysing the light emitted by bright objects at high redshift, such as that from quasars, Seyfert galaxies or Lyman-break galaxies. The second is by analysing the absorption features present in the spectra of the bright objects – absorption that has occurred as the light has travelled from the high-redshift objects through innumerable obstacles (such as intergalactic gas clouds) before finally arriving at Earth.

As the emission features of the bright objects at high redshifts show that they are (in general) quite metal-rich, here we concentrate on the information gathered via absorption features.

Ancient Backlighting: Early Active Galactic Nuclei

It is now generally agreed that quasi-stellar objects (QSOs or ‘quasars’) are the early Universe counterparts to current-day active galactic nuclei (AGN). They are extremely luminous (up to $\sim 10^{14} L_{\odot}$) and the fact that some display variability on the order of weeks implies that they must be very compact. They are thought to be very massive accreting black holes – the majority of their luminosity comes from the accretion of matter rather than thermonuclear reactions, as their spectra are dominated by non-thermal emission (although there is often a thermal/stellar component which is now understood to be that of the surrounding stars of the host galaxy). As these QSOs, or galactic cores, are so luminous, and have been in existence since at least the first 10% of the age of the Universe, they act as useful probes into the high redshift Universe. Indeed, QSOs are now routinely discovered at larger and larger redshifts (eg. in surveys such as the Sloan Digital Sky Survey (SDSS)). The highest redshifted QSO observed to date is *J114816.64 + 525150.3* which has a redshift of 6.4, corresponding to a look-back time of ~ 13 billion years (Fan et al., 2003).

Lyman α Forests

QSOs themselves have some very interesting chemical features. For example they exhibit strong metal emission lines (eg. O, N, Si, Fe, Laor et al. 1995) indicating that there had already been a large amount of nucleosynthesis even by this early stage of the Universe, at least in very dense regions. However, it is the use of QSOs to sample the high redshift inter-galactic medium (IGM) that has provided the most information on low metallicity systems in the early Universe. By the time the strong continuum emission from QSOs reaches Earth, the photons have passed through innumerable obstacles along the line of sight. This gives rise to absorption lines against the background continuum. Furthermore, as the QSO emission has (often) come from the high redshift universe, it has passed through gas clouds and galaxies located at various distances/red shifts along the line of sight. Hydrogen, in addition to being an ubiquitous chemical species in the Universe, also absorbs strongly in the ultraviolet (UV), notably at 1215.67 \AA – the Lyman α ($\text{Ly}\alpha$) line of neutral hydrogen (HI). Although the majority of hydrogen is actually ionised (even in the high redshift IGM), absorption via $\text{Ly}\alpha$ is so strong that even at low HI abundances it will absorb most of the radiation at 1215.67 \AA . As the absorbing gas clouds and galaxies are at differing redshifts, each absorber subtracts a section of the redshifted QSO continuum. The resultant spectrum that we observe thus has multiple sharp HI absorption lines at various offsets to the blue, relative to the QSO continuum, as the intervening absorbers are less redshifted than the QSOs. This multitude of lines reflects the multitude of $\text{Ly}\alpha$ absorbing systems that the radiation has passed through – and is known as the *Ly α forest*. The $\text{Ly}\alpha$ forest was first discovered using optical telescopes. Thus the earliest observations were actually at long look-back times as the $\text{Ly}\alpha$ lines had been shifted from the UV far into the red end of the spectrum. It is now known that the absorbers that produce the $\text{Ly}\alpha$ forests are of low

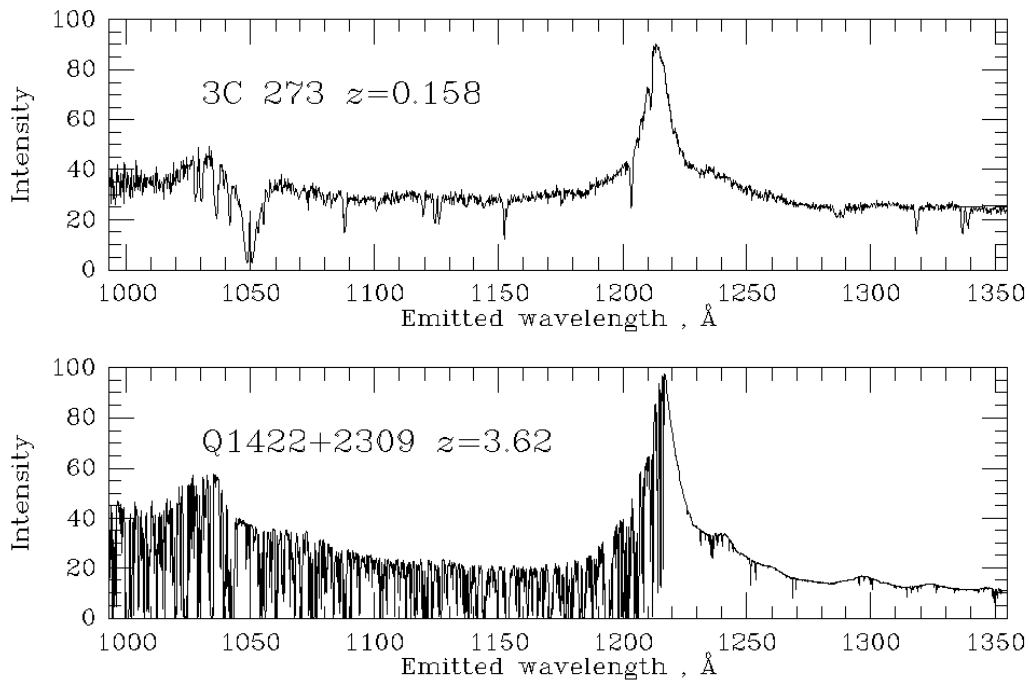


Figure 2.3: The spectra of two QSOs at different redshifts (from the HST and Keck I telescopes, respectively). Both spectra have the same bandwidth range and have been shifted so the scale is approximately in the rest frame of the QSOs (ie. the large QSO Ly α emission lines are at ~ 1215 Å). The second peak at ~ 1026 Å is the QSO Lyman β emission. Most of the absorption line features between these peaks are due to absorbers in the line of sight (IGM, galaxies) and are redshifted to a lesser and lesser extent as one moves from the QSO Ly α emission towards shorter wavelengths. It can be seen that there are many more absorption features at high redshift. [Image courtesy of William Keel, University of Alabama, Tuscaloosa, USA, private communication.]

HI column densities ($10^{12} \lesssim N(\text{HI}) \lesssim 10^{16} \text{ cm}^{-2}$). This distinguishes them from *Damped Ly α* systems as the absorption lines are sharp (ie. not damped). Figure 2.3 shows examples of the Ly α forest at two different redshifts.

A new development in sampling the high redshift IGM is to use Gamma-Ray Bursts (GRBs) as background sources instead of QSOs (Fynbo et al. 2006). In fact all these spectrographic observations are quite a recent development (~ 15 years) and have been made possible by the current generation of 10 metre class telescopes with high resolution spectrographs (eg. HIRES on Keck I). The advent of this technology has drastically increased the distances/redshifts at which we can gain information on chemical abundances (see Pettini 2004 for a recent review), revolutionising our understanding of the chemical evolution of the Universe. In addition to the HI absorption there are also many metal lines observed. Ly α systems are the lowest metallicity systems known at high redshift, having metallicities of $\sim 10^{-2} \rightarrow 10^{-3}$ times solar. They thus represent the closest link we have to Population III at high redshift.

Damped Lyman α Systems

Damped Lyman α systems (DLAs, eg. Wolfe et al. 1986) are the higher-density analog of Ly α systems. Quantitatively they have neutral hydrogen column densities: $N(\text{HI}) \gtrsim 2 \times 10^{20} \text{ cm}^{-2}$. The high density causes broad absorption lines with damping wings. The absorbers appear to be

galaxies in early stages of evolution (although this is somewhat uncertain; see eg. [Pettini 2004](#) for a review). Some have recently been associated with galaxies but it appears some do not have detectable stellar populations. Their metallicities are, in general, higher than Ly α systems but still substantially sub-solar, while their early state of evolution is inferred from their chemical pattern.

Brief Summary of Pollution of the Young IGM

The young intergalactic medium (IGM) was once thought to consist of pristine primordial intergalactic gas clouds, unpolluted by the processes going on in, for example, quasar host galaxies. It is now known that much of the early IGM was polluted (through the methods just discussed above). Depending on the cloud HI column densities, it has been shown that up to 90% of clouds at $z \sim 3$ are polluted with metals such as silicon, carbon and nitrogen ([Songaila and Cowie 1996](#)). Indeed, Figure 1 in [Songaila and Cowie 1996](#) shows the ‘C-IV forest’ – a multitude of instances of a particular carbon line at different redshifts, analogous to the Ly α forest (the C-IV doublet, at $\sim 1550 \text{ \AA}$, is redward of Ly α). The metal abundances in the high-redshift clouds have been found to be $\sim 10^{-1} \rightarrow 10^{-2}$ solar (eg. [Songaila 2001](#)). In terms of their abundance *pattern* they are relatively high in silicon as compared to carbon – at a redshift of ~ 3 the Si/C ratio is ~ 3 times solar ([Songaila and Cowie 1996](#)). This overabundance of Si implies that the stellar source of the pollution was predominantly Type II supernovae (SNeII). Interestingly, this abundance pattern is also reminiscent of the Galactic Halo field population. Despite this clue, the origin of the metal pollution is still unresolved. Some authors suggest that it originates from galactic outflows – galactic winds that, at early epochs, were strong enough to pollute the IGM (eg. [Adelberger et al. 2005](#)), some argue that tidal stripping of galaxies is the only way to inject so much metal into the IGM (eg. [Gnedin 1998](#)), and others argue that there was a *pregalactic* population of stars that initially polluted the Universe at a redshift $\gg 6$. Recent observations that show that metal abundances are roughly constant with redshift ($1.5 < z < 5.5$, [Songaila 2001](#)) – within clouds of similar density – appear to support the hypothesis that the metal pollution was implanted at a very early epoch. [Songaila \(2001\)](#) also notes that the metallicity is so high (carbon $\sim 10^{-2}$ solar) – even at $z \sim 5$ – that the majority of the pollution must have occurred before this epoch. It would be interesting to compare the pollution of the young IGM with that of the EMP Galactic halo stellar population, particularly since so much carbon is seen in both. This is however outside the scope of the current study so we shall investigate this at a later date.

2.2 Big Bang Nucleosynthesis

2.2.1 Background

Apart from predicting the well-known Cosmic Background Radiation, Big Bang Theory also predicts a rapid nucleosynthesis of elements in the first few minutes of the Universe. Big Bang Nucleosynthesis (BBN) is a mature area of research, such that the main elemental predictions have been known since the 1960s (see eg. [Boesgaard and Steigman 1985](#) for a review). Figure

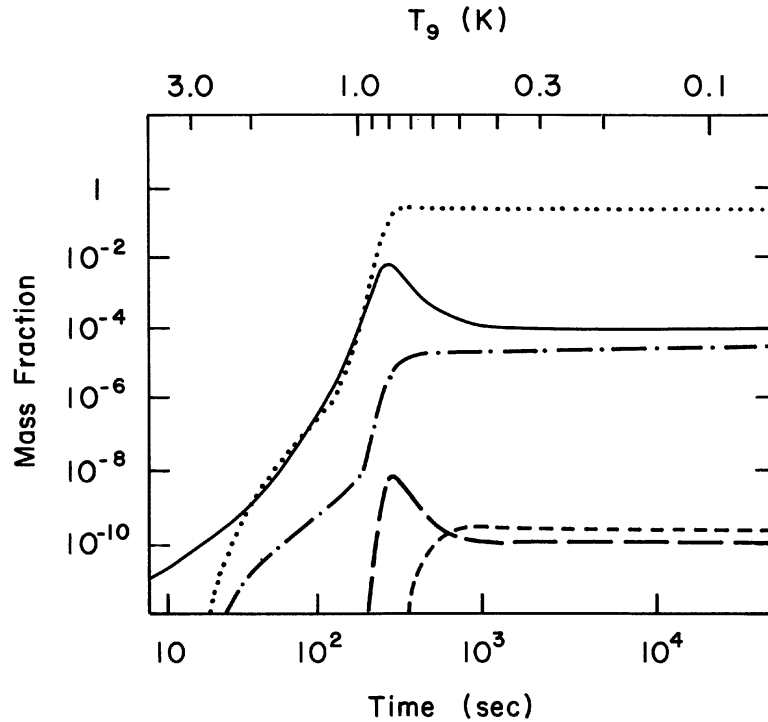


Figure 2.4: The abundance evolution from a Big Bang nucleosynthesis calculation. Nuclides shown are ^4He (dotted line), ^2H (solid), ^3He (dash-dotted), ^7Li (long dashed) and ^7Be (short dashed). This figure is from the annual review by [Boesgaard and Steigman \(1985\)](#).

2.4 shows the results of a typical BBN calculation. As can be seen in the Figure, most of the nucleosynthesis happens in a brief window of time – when the density and temperature are conducive to nuclear reactions. As the universe rapidly expands and cools nuclear reactions are no longer possible and the primordial abundance pattern is essentially ‘frozen’ in. It remains like this until (local) temperatures and densities are again high enough for nuclear reactions – usually in stars.

In the overall picture of the chemical evolution of the Universe it is this primordial mix of isotopes that everything else stems from. The first generation of stars form from this gas and their subsequent evolution is primarily governed by this chemical make-up. Importantly, the nucleosynthesis of fresh nuclei that occurs in these stars is then (usually) released into the interstellar environment via winds or supernovae explosions, polluting the ambient gas that will, in turn, go into the formation of the next generation of stars. Thus it is important to have the initial composition of the first generation correct. There is some debate about the extent to which BBN occurs in a homogeneous gas. Standard BBN (SBBN) assumes the primordial gas is homogeneous. Inhomogeneous BBN (IBBN) theory allows for some regions of higher density in which more advanced nucleosynthesis can occur. Higher abundances of nuclei crucial to determining stellar structure can be produced in IBBN (eg. ^{12}C). Recent studies into IBBN even suggest that *very* heavy nuclei can be formed – through the p-process and r-process. In their IBBN simulations [Matsuura et al. \(2005\)](#) produce heavy elements such as ^{158}Eu and ^{90}Mo at the mass fraction level of $\sim 10^{-8}$. However the size of the regions in which this happens must be kept small so as to stay within the observational evidence constraints. Indeed, current observations of the anisotropies in the Cosmic Microwave Background Radiation (CMB) by the Wilkinson

Nuclide	Primordial Mass Fraction
^1H	0.754992 (0.754796)
^2H	(1.96×10^{-4})
^3He	7.85×10^{-6}
^4He	0.24500
^7Li	(3.13×10^{-10})
^{12}C	0.0
^{14}N	0.0
^{16}O	0.0

Table 2.1: Initial abundances used in the zero-metallicity stellar models, as given by the Standard Big Bang Nucleosynthesis calculations by [Coc et al. \(2004\)](#). This material was also used to dilute SNe ejecta to give the initial composition of our Halo star models. Values in brackets are the abundances used in the nucleosynthesis calculations. ^7Li and ^2H are only used in the nucleosynthesis calculations, as these species are not included in the structure code.

Microwave Anisotropy Probe (WMAP) satellite suggest that SBBN theory is sufficient to explain the primordial abundances ([Lara et al. 2006](#)), even though there may have been small levels of inhomogeneity. For this reason we use abundance predictions from homogeneous/standard BBN theory in the current study.

2.2.2 Primordial Abundances for the Stellar Models

The most abundant nuclei produced by SBBN are ^1H , ^2H , ^3He , ^4He and ^7Li . The recent observations by WMAP have significantly constrained the predictions of SBBN. In [Table 2.1](#) we list all the starting abundances used for the stellar structure models in this study, which are taken from the SBBN calculations of [Coc et al. \(2004\)](#).

Of particular interest is the primordial abundance of ^4He (Y_P). A recent review and study by [Olive and Skillman \(2004\)](#) in light of the recent WMAP observations (from which η , the primordial baryon to photon ratio, is inferred) finds that Y_P gained through observations actually has large errors associated with it. However, even taking into account the errors, the observed Y_P is easily within the error bars of Y_P given by SBBN calculations, as η (the only parameter in the calculations) also has an uncertainty – despite the very detailed observations of WMAP. On reanalysing the observational data [Olive and Skillman \(2004\)](#) find $0.232 \leq Y_P \leq 0.258$. Using the WMAP constraint on η , many authors have revised the SBBN calculations. Using SBBN combined with the WMAP constraint [Coc et al. \(2004\)](#) finds $Y_P = 0.2479 \pm 0.0004$. [Cyburt et al. \(2002\)](#) find $Y_P = 0.2484^{+0.0004}_{-0.0005}$. For the current study we adopt a value of $Y_P = 0.245$ which is roughly in the centre of the observational error bars found by [Olive and Skillman \(2004\)](#) and close to the values given by SBBN + WMAP calculations.

^7Li has long been a contentious issue between observers and SBBN simulators (see eg. the review by [Boesgaard and Steigman 1985](#)). To the current day there remains a strong discrepancy between the observations and the SBBN calculations. Primordial ^7Li is thought to be visible on the surface of (hot) metal-poor Galactic halo stars. The ‘Spite Plateau’, observed by [Spite and Spite \(1982\)](#), shows that there is a very constant abundance of ^7Li across these stars. It is this plateau value that is thought to be the primordial abundance, as there is such a narrow spread between stars (of varying metallicity) that it seems unlikely that any other process

could have produced it. We would expect other processes, such as production in SNe or AGB stars, to have produced a much greater, stochastic, spread. SBBN calculations, which have multiple constraints, predict a higher primordial abundance of ${}^7\text{Li}$ – by a factor of ~ 3 . Although not a very large factor it is still large enough to lie outside the observational errors. As the situation is still unresolved, in the current study we choose to adopt the SBBN prediction for ${}^7\text{Li}$. This decision is lent some weight by the fact that SBBN predictions are supported by other observational evidence, such as ${}^2\text{H}$ (and to some extent ${}^4\text{He}$).

Primordial Abundances of Heavier Nuclei

If trace amounts of heavier nuclei were available in the early Universe this may have a very significant effect on the evolution of zero metallicity stars. In particular, if ${}^{12}\text{C}$ is present at the (mass fraction) level of $10^{-12} \rightarrow 10^{-10}$ then the CNO cycle will be able to operate on the main sequence and during H-shell burning – rather than just the p-p chains. Depending on the actual abundance this would affect the structural evolution, as the efficiency of the CNO cycles increases with the abundance of CNO nuclei. However it is generally accepted that SBBN does not produce significant amounts of nuclei with atomic mass > 7 . For example, [Vangioni-Flam et al. \(2000\)](#) include reactions involving B, Be and C but find that the mass fractions of B and Be produced are of the order 10^{-16} or less. This is 3 orders of magnitude below the lowest abundances of these elements that has been observed (in Galactic Halo stars, see eg. [Boesgaard and King 1993](#)).

2.3 Previous Theoretical Models of $Z = 0$ and Extremely Metal-Poor Stars

2.3.1 Introduction

Here we give an overview of the literature on the subject of zero and very-low metallicity stellar modelling, from its beginnings to the present day. We focus in particular on low- and intermediate-mass stars, as this is the range of interest for the current study. No literature survey is perfect – we may have missed a paper or two in our survey – but we believe the survey does cover the vast majority of the papers published. Importantly, the main developments over the ~ 50 year history of the subject are provided, through the descriptions of the main findings of each paper.

Table 2.2 lists the studies covered in our review. In the table we have also provided some key details of the studies, namely the mass and metallicity ranges of the models, the stages of evolution reached, and the helium content used. The table thus provides a quick overview of the development of the field at a glance.

The whole review is organised chronologically (in the table and the text). The text is divided into three sections. The first section details the early developments whilst the second section details developments in the 1980s, 1990s and early 2000s. The third section is delineated by the start date and end date of the Author’s thesis candidature (i.e. by the time-frame of the current

study). This choice highlights the fact that much work was done in the field during this period, as it has recently been (and still is) a ‘hot topic’ in stellar astrophysics. This is mainly due to the recent discovery of some extremely metal-poor Galactic halo stars, particularly the C-rich star HE0107-5240 (Christlieb et al. 2002).

We also provide a fourth section that places the current study into the context of the development of the field.

2.3.2 ZAMS and Beyond: 1960s to 1980s

The Early Days

Around the same time that it was realised that the newly invented ‘automatic digital computers’ could be applied to the problem of stellar evolution (eg. Haselgrove and Hoyle 1956; Sears 1959; Henyey et al. 1959; Schwarzschild and Selberg 1962), the watershed work of Burbidge et al. (1957) (now known as the B²FH paper) detailed eight nucleosynthetic paths to provide weight to the argument that stars are the origin of most elements in the Universe. Noting that this theory did not explain the production of hydrogen in the Universe, Ezer (1961) constructed some potential primordial ZAMS models composed solely of H (in the mass range 1 – 2000 M_{\odot}). Although the only nuclear reactions included in her models were those of the p-p chains, Ezer found that the central temperatures reached were high enough to initiate the 3α process, thereby producing primary ^{12}C and allowing the CNO cycles to operate.

With the maturing of Big Bang Nucleosynthesis theory (BBN, eg. Peebles 1966; Wagoner 1973) and new observations (eg. Searle and Sargent 1972) it appeared that helium was also one of the main components of the primordial gas, and thus stellar modellers began constructing primordial ZAMS models with metal-free compositions containing $\sim 20\%$ He and $\sim 80\%$ H (eg. Ezer and Cameron 1971; Cary 1974; Castellani and Paolicchi 1975).

Ezer (1972) appears to be the first to evolve a primordial stellar model past the main sequence, taking the evolution of a 3 M_{\odot} , $Z = 0$ star through the core He burning stage. Ezer found that the star spent most of its time on the blue side of the HR diagram and produced ^{12}C in the core towards the end of the MS. She also found that core He ignition occurred while the star was still on the blue side of the HR diagram, thereby preventing the star from reaching the RGB phase. In terms of evolutionary timescales she found that the MS lifetime was considerably longer than that of Pop I models but also that the core He burning phase was a factor of 3 *shorter*. Although the details of some evolutionary features would change in the future, due to improved input physics, the majority of her findings for this model are still indicative of our understanding of $Z = 0$ intermediate mass (IM) stellar evolution today.

At low masses (LM) Wagner (1974) calculated models of metal-poor and extremely metal-poor stars in the mass range $0.65 \rightarrow 2.5 M_{\odot}$ up to and including the RGB in order to investigate their stellar lifetimes and pulsational stability (see Table 2.2 for the metallicity range). Wagner found that the stellar lifetimes were dependent on the metallicity Z and also the H abundance. Low metallicity models had shorter lifetimes than Pop I models if the H content was the same, but lifetimes increased if H was increased.

It wasn't until almost a decade later that the first true $Z = 0$ LM models of advanced stages of evolution were calculated. D'Antona and Mazzetelli (1982) followed the evolution of $0.9 M_{\odot}$ and $1 M_{\odot}$ models up to the end of the RGB. They noticed an important feature of these models – that the tip of the RGB is ~ 1 dex less luminous than stars of Pop I or II. They suggested that this would not affect the observability of primordial low-mass stars as the SGB/RGB lifetime was longer due to the reliance on pp-chain energy production (we note that the lifetime prediction is at odds with the current study's findings). Another very important observation they made was that the core He flash began well off centre. They go on to suggest that it is so off centre that the He convection zone may breach the H-He discontinuity and consequently pollute the surface with C and N. This appears to be the first mention of this evolutionary feature in the literature. This phenomenon would be 're-discovered' at the beginning of the 1990s, with Fujimoto et al. (1990) showing that the He convection zone does indeed break through, causing a H-flash. We refer to this event as the Dual Core Flash (DCF).

Meanwhile Eryurt-Ezer (1981) continued the evolution of her $3 M_{\odot}$ star onto the early AGB, finding that the shell burning phase also proceeded at a slow rate in IMS, extending the lifetime as compared to Pop II stars.

A few years later Fujimoto et al. (1984) performed semi-analytic calculations to determine if $Z = 0$ stars would pulsate on the AGB and hence possibly contribute to the early pollution of the Universe (via third dredge-up (3DUP)). They predicted that stars with mass $\lesssim 4 M_{\odot}$ would indeed develop thermal pulses on the AGB and consequently dredge up ^{12}C to their surfaces. For higher masses they predicted that thermal pulses would *not* occur – unless there had been some prior pollution of their envelopes that had brought the Z content above some critical amount ($\sim 10^{-7} \rightarrow 10^{-4}$, dependent on core mass).

Later that year Chieffi and Tornambe (1984) made a full calculation of a $5 M_{\odot}$ model, following it part of the way into the AGB phase. They found that no thermal pulses or third dredge-up (3DUP) occurred, as predicted by Fujimoto et al. (1984). They attributed this to the fact that 3α reactions occur at the bottom of the H shell in $Z = 0$ models, thus the two shells are both burning He and therefore they move outwards (in mass) at the same rate, preventing the development of an instability.

The 1980s continued to be a busy decade for primordial stellar evolution, although the later stage of evolution, namely the TP-AGB, remained unexplored, as did the core He flash in the low mass models. Eryurt-Ezer and Kiziloglu (1985) extended their work by calculating the evolution of more massive IMSs ($M = 5, 7, 9 M_{\odot}$) with $Z = 0$ to core He exhaustion and Tornambe and Chieffi (1986) explored the mass interval $2.5 > M > 8.0 M_{\odot}$ for stars of low and extremely low Z (although mainly to ascertain the nature of metal-poor Type I supernovae). In 1987 Kiziloglu and Eryurt-Ezer also calculated MS $Z = 0$ models of very low mass stars ($M = 0.2 \rightarrow 0.8 M_{\odot}$).

We give some information and the data sources for the literature review table here, in order to save space in the caption:

Details for Table 2.2: Mass is given in units of M_{\odot} (an arrow indicates a range of masses). Metallicity is given as $\log(Z/Z_{\odot})$ except when $Z = 0$ where we write 'zero'. Using $\log(Z/Z_{\odot})$ gives a rough approximation to $[\text{Fe}/\text{H}]$, which is useful for comparisons with observational studies. In column 5 we show the maximum stage of evolution that the models were evolved *through* (so it

is an inclusive designation). The ‘ \sim ’ symbol is used where the models were evolved only part of the way through the indicated phase of evolution. In the last column we show the helium mass fraction used. [Abbreviations for the evolutionary stages are: CHeB (core helium burning), DCF (dual core flash, the H-He core flash in low mass low- Z stars, also known as HEFM in the literature), SRGB (secondary RGB), DSF (dual shell flash, the H-He shell flash near the start of the AGB in low- and intermediate-mass stars, also known as HCE).]

2.3.3 DSF Discovery and DCF Modelling: 1990s to 2001

It wasn’t until the 1990s that the modelling of the most demanding of the peculiar evolutionary traits of $Z = 0$ stars was attempted – the Dual Core Flash (DCF). Although discovered almost a decade earlier (D’Antona and Mazzetelli 1982) no work had been published since on the topic. In their first paper on the subject Fujimoto et al. (1990) evolved a $1 M_{\odot}$ star through to just after the peak of the core He flash at the tip of the RGB. As reported by D’Antona and Mazzetelli (1982) they also found that the core He flash occurs much further off-centre than in more metal-rich models. This has the consequence that the resulting He convective zone breaks through the H-He discontinuity, mixing down protons into regions of very high temperature. Although their calculations did not follow the mixing in this paper, the same group modified their evolution code to include time-dependent mixing and subsequently followed the H-flash that ensued (Hollowell et al. 1990). They found that the protons were mixed down to a point where the timescale of proton capture is much shorter than that of the mixing timescale. Once the H luminosity exceeded that of the He flash luminosity the convection zone split into two – resulting in an upper H burning convective zone and a lower He burning one. Both convection zones contain ^{12}C whilst the upper one also contains CNO cycle burning products. This is of significance because they also found that the convective envelope moves inwards after the two flashes have abated and dredges up some of this polluted material to the surface. They found that the initially metal-free star now had a metallicity of $Z_{\text{cno}} \sim 0.004$ and noted that the high N abundance in a newly observed extremely metal-poor giant star (CD -38°245, Bessell and Norris 1984) may be due to the same mechanism (although their $Z = 0$ model produced too much N).

A few years later Cassisi and Castellani (1993) published a grid of calculations of very- and extremely-metal-poor models covering a large mass range ($0.7 > M > 15 M_{\odot}$, also see Table 2.2). Their models were evolved up to the end of the RGB (not including the DCF phase) for low mass stars, and through to core He exhaustion in the more massive models. They found that the value of Z remains important in the efficiency of the CNO cycles down to $Z \sim 10^{-6}$ and that all their models with $Z = 10^{-10}$ succeeded in self-producing ^{12}C before core H exhaustion, enabling the CNO cycles to operate. They also note that the maximum stellar mass at which the core He flash occurs (due to degeneracy in the core) decreases substantially with Z . At solar Z the cut-off is $\sim 2.3 M_{\odot}$ whilst at $Z = 10^{-10}$ they find it to be $\sim 1.2 M_{\odot}$. As Cassisi and Castellani mention, this implies that very low metallicity populations may be more blue in colour (we note however that also depends on the IMF). The same group (Cassisi et al. 1996) also investigated low mass stars ($0.7 > M > 1.1 M_{\odot}$) at similar metallicities. They produced isochrones from their models and also found that very few RR Lyrae variables would be expected at very low metallicity. A model of mass $0.80 M_{\odot}$ and $Z = 10^{-10}$ was also followed to the onset of thermal

Year	Author	Mass	Metallicity	Max. Evolution	Helium
1961	Ezer (1961)	1 \rightarrow 2000	zero	ZAMS	0.0
1971	Ezer and Cameron	5 \rightarrow 200	zero	MS	0.2
1972	Ezer	3.0	zero	CHeB	0.2
1974	Cary	2 \rightarrow 20	zero	ZAMS	0.0, 0.23, 0.3
1974	Wagner	0.65 \rightarrow 2.5	-6, -4, -2	RGB	0.26
1975	Castellani and Paolicchi	1 \rightarrow 100	zero	ZAMS	0.0, 0.2, 0.4
1981	Eryurt-Ezer	3.0	zero	EAGB	0.2
1982	D'Antona and Mazzetelli	0.9, 1.0	zero	RGB, \sim DCF	0.2
1983	Guenther and Demarque	0.9	zero	MS	0.2
1984	Chieffi and Tornambe	5.0	zero	\sim AGB	0.2
1985	Eryurt-Ezer and Kiziloglu	5, 7, 9	zero	CHeB	0.2
1986	Tornambe and Chieffi	2.5 \rightarrow 8.0	-6, -4, -2	EAGB	0.2
1987	Kiziloglu and Eryurt-Ezer	0.2 \rightarrow 0.8	zero	MS	0.2
1990	Fujimoto et al.	1.0	zero	\sim DCF	0.23
1990	Hollowell et al.	1.0	zero	DCF	0.23
1993	Cassisi and Castellani	0.7 \rightarrow 15	-8, -4, -2	RGB/EAGB	0.23
1996	Cassisi et al.	0.7 \rightarrow 1.1	-8, -4, -3	\sim DSF (M=0.8)	0.23
1998	Fujimoto and Iben	0.8 \rightarrow 4	zero	RGB/AGB	0.23
2000	Fujimoto et al.	0.8 \rightarrow 4	zero, -4, -2	DCF/DSF	0.23
2000	Weiss et al.	0.8 \rightarrow 1.2	zero	RGB	0.23
2001	Marigo et al.	0.7 \rightarrow 100	zero	\sim AGB (no CHeF) ^a	0.23
2001	Chieffi et al.	4 \rightarrow 8	zero	DSF, \sim AGB	0.23
2001	Schlattl et al.	0.8 \rightarrow 1.0	zero	DCF, SRGB, \sim AGB	0.23 \rightarrow 0.25
2001	Goriely and Siess	3	zero	AGB s-process ^b	0.23
2002	Siess et al.	0.8 \rightarrow 20	zero	DSF, \sim AGB	0.235
2002	Schlattl et al.	0.8	zero, -3, -2	DCF	0.23
2003	Herwig	2 & 5	zero	DSF, \sim AGB	0.23?
2004	Iwamoto et al.	1 \rightarrow 3	-2.7	DSF, \sim AGB	0.24
2004	Picardi et al.	0.8 \rightarrow 1.5	zero, -6, -5, -4	DCF, SRGB, \sim EAGB	0.23 & 0.27
2004	Weiss et al.	0.82	zero, -5	DCF, SRGB	0.23?
2004	Suda et al.	0.8 \rightarrow 4.0	zero	\sim DSF, \sim DSF, \sim AGB	0.23?
2006	Campbell (This study)	0.8 \rightarrow 3+ ^c	zero, -6, -5, -4, -3	DCF, DSF, SRGB, AGB & Yields	0.245

Table 2.2: A summary of the literature (to the best of our knowledge) for theoretical studies of low- and intermediate-mass stars of very low- and zero-metallicity. See text for details on this table.

^aThe low mass stars were not evolved through the CHeF but zero age HB branch models were constructed to enable evolution to the AGB.

^bThe s-process nucleosynthesis was done using a separate nucleosynthesis code (using a TPAGB stellar model for input physical conditions). A (parameterised) partial mixing down of protons was added to provide a ^{13}C pocket.

^cSome models with $M = 4$ & $5 M_{\odot}$ were also calculated but only part of the way through the AGB.

pulses on the AGB. The core He flash was not modelled so the DCF event was missed. Instead a ZAHB model was constructed to follow the later evolutionary stages. It was found that the He convective zone produced by the first (strong) AGB He shell flash was likely to break through the H-He discontinuity, dredging down protons to high temperatures and therefore causing a secondary (hydrogen) flash to occur. This appears to be the first report of what we refer to as a Dual Shell Flash (DSF). We use the term ‘dual’ because the event is characterised by a double peak in luminosity – one from the He flash and one from the H flash – occurring quite close together in time. They were however unable to follow the evolution further as the code did not include time-dependent mixing. They likened the event to the DCF event described in the previous section (see eg. [Hollowell et al. 1990](#)), as the He convective zone (a result of the normal TP-AGB He flash) penetrates the H-He discontinuity in both cases, with similar results. Moving back to $Z = 0$ models, [Fujimoto and Iben \(1998\)](#) brought the overall $Z = 0$ evolutionary picture into more focus. Whilst arguing that the metal deficient dwarf carbon star G77-61 (observed by [Gass et al. 1988](#)) was the result of a binary star mass transfer event from a companion population III star, they divide the peculiar evolutionary traits of $Z = 0$ stars into three distinct cases. The three cases are delineated by stellar mass:

1. $M \lesssim 1.1 M_{\odot}$: Dredge-up after the Dual Core Flash pollutes the surface with C, N and He. Stars *may* go on to experience 3DUP on the AGB, further polluting the surface.
2. $1.2 \lesssim M \lesssim 4.0 M_{\odot}$: Dredge-up after the Dual Shell Flash at the start of the TP-AGB pollutes the surface with C, N and He. Stars may go on to experience 3DUP on the AGB, further polluting the surface.
3. $M \gtrsim 4.0 M_{\odot}$: No DCF or DSF – surface remains unpolluted during entire evolution.

Note that the terminology used here (i.e. DCF and DSF) is only used in the current study.

Motivated by the growing number of observations of very metal deficient stars (eg. from the HK survey, [Beers et al. 1992](#)), the same group ([Fujimoto et al. 2000](#)) extended their investigation to models of low and very low metallicity stars. In doing this they improved on their classification scheme, taking into account the metallicity dependence of the occurrence of the DCF and DSF. In Figure 2 of their paper [Fujimoto et al. \(2000\)](#) provide a schematic diagram in the mass-metallicity plane. It can be seen in this figure that the phenomena of DCFs and DSFs continue up to (relatively) metal-rich models. Case I (in which the DCF in low mass stars leads to pollution of the surface) is however limited to a small mass range, and, in particular, very low metallicities. They argue that the stellar models can *qualitatively* explain the observed increased occurrence of C-rich extremely metal-poor stars (CEMPs), especially when taking binary mass transfer into consideration. We note that we also provide a mass-metallicity-pollution diagram in Section 9.2 on page 352, which summarises the pollution results of all our $Z = 0$ and EMP models. Our models are evolved through their entire evolution (i.e. to the end of the AGB), including detailed nucleosynthesis, so it is the results from the yields that we present in our diagram.

Motivated by the same observations [Weiss et al. \(2000\)](#) investigated how the surface of a low-mass $Z = 0$ MS or RGB star could be polluted to result in a match to the observations. They

examined two scenarios, one where the hot p-p chain reactions were taken into account, whereby extra ^{12}C may have been produced, altering the evolution, and one where the star is polluted from a nearby massive star. In the first scenario they revealed that the hot p-p chains are unimportant in these stars (the 3α reaction is very dominant in terms of producing ^{12}C). In the second scenario they found that the extra metals never diffuse down to the regions in which energy generation occurs. Interestingly Weiss et al. did *not* find that a DCF occurs in their $1 M_{\odot}$, $Z = 0$ model. This is at odds with previous studies (eg. D’Antona and Mazzetelli 1982; Hollowell et al. 1990). We note however that the same group later report that their models do experience the DCF (Schlattl et al. 2001; Weiss et al. 2004).

In 2001 Marigo et al. published the largest grid of $Z = 0$ models to date. A fine grid in mass was used, with a mass range of $0.7 M_{\odot}$ to $100 M_{\odot}$. Mass loss was not taken into account. In terms of low and intermediate mass stars the evolution was followed up till the beginning of the AGB. In two cases ($M = 2.5$ and $5.0 M_{\odot}$) the evolution was taken a short way into the TP-AGB. They found no evidence of thermal pulses in the $2.5 M_{\odot}$ model but did find well-developed thermal pulses in the $5 M_{\odot}$ model. They note that these results are at odds with the semi-analytical predictions of Fujimoto et al. (1984) for the occurrence of TPs, which predict that the $2.5 M_{\odot}$ model should have experienced TPs whereas the $5 M_{\odot}$ model should not. Marigo et al. also discuss the two critical values that are often used to define the boundary between low-, intermediate- and high-mass stars, namely M_{HeF} and M_{up} . M_{HeF} is the upper limit at which He ignites in degenerate conditions, giving rise to a core He flash. Stars of this mass and less are classified as LM stars. M_{up} is the stellar mass at which carbon ignition occurs. Stars above this mass are classified as massive stars. Between these two limits are the IM stars which ignite He quiescently and also never attain core temperatures high enough to ignite carbon. The reason we detail this here is because these values change significantly at very low and zero metallicities. Marigo et al. find (confirming previous work by Cassisi and Castellani 1993 and others) that M_{HeF} drops to $\sim 1.1 M_{\odot}$ at $Z = 0$. M_{up} on the other hand exhibits interesting behaviour as (initial) metallicity decreases – first decreasing then increasing. They note that M_{up} is primarily dependent on the mass of the H-exhausted core at the end of the MS. As metallicity first decreases (from solar) core masses increase, thereby reducing M_{up} . However, as the p-p chains become dominant in the cores of extremely low metallicity MS stars the (convective) cores become smaller again, due to the relatively low temperature dependence of the reactions. In fact, Marigo et al. find that M_{up} is much higher for $Z = 0$ stars than for stars of solar metallicity, such that $M_{\text{up}, Z=0} \sim 7.5 M_{\odot}$ (see their Figure 6). In terms of surface pollution they find that the first dredge-up in low mass stars is very shallow, only mixing up marginal amounts of He. Second dredge-up is more efficient, significantly increasing the surface He abundance in the mass range $2 \lesssim M \lesssim 8 M_{\odot}$ and also increasing the surface CNO abundance in the mass range $5 \lesssim M \lesssim 6.5 M_{\odot}$. Other polluting episodes such as the DCF, DSF and the third dredge-up on the AGB were not taken into account.

The same year Chieffi et al. (2001) published results on the AGB evolution of IM stars in the mass range $4.0 \lesssim M \lesssim 8.0 M_{\odot}$ (see also Dominguez et al. 2000). Contrary to the semi-analytical predictions of Fujimoto et al. (1984) they found that all their models *do* experience 3DUP. Some other interesting results from this study include the discovery of what we shall call ‘Hot third dredge-up’ (H3DUP, following Herwig 2003) in the more massive models, and the confirmation

of the DSF phenomenon in the less massive models (which [Chieffi et al.](#) refer to as hydrogen convective episode (HCE) H-flashes). The first phenomenon, H3DUP, was found to occur in the mass range $6.0 \lesssim M \lesssim 8.0 M_{\odot}$. When the H-rich convective envelope extended inwards protons were brought into regions of very high temperature (the temperature of the H burning shell in $Z = 0$ models is high due to the paucity of CNO catalysts). This gave rise to moderate H-flashes ($L_{HF} \sim 10^6 L_{\odot}$) at each H3DUP episode. They note that the reason that 3DUP occurs in these models in the first place is because the envelope is enriched with CNO nuclei during the second dredge-up. The second phenomenon they report appears to be what we refer to as the ‘Dual Shell Flash’ (also see [Cassisi et al. 1996](#); [Fujimoto and Iben 1998](#)). [Chieffi et al. 2001](#) appear to be the first to examine the phenomenon in detail. They find a convective feature in their lower mass models ($4.0 \lesssim M \lesssim 6.0 M_{\odot}$), which we describe here. During the early TP-AGB the H burning shell becomes convectively unstable, just after the maximum of the He shell flash. Initially this H convective episode (HCE) has no tangible effect on the evolution. However, a few TPs into the AGB they find that the HCE ingests some ^{12}C (a product of the He burning below) and subsequently a thermonuclear runaway occurs. The now C and N enriched (N is produced via the CNO cycles) material is then dredged up by the convective envelope, enriching the surface. This event is of great importance to the further evolution of the star as it is now a more ‘normal’ AGB star – the envelope has a reasonably high metallicity ($Z_{\text{env}} \sim 10^{-6}$) enabling efficient CNO shell burning (thus lower shell temperatures). In fact, [Chieffi et al. \(2001\)](#) find that these models go on to experience normal 3DUP episodes from then on. The interpulse periods also lengthen to become more ‘normal’. They also stress that the treatment of convective boundaries is very important in terms of 3DUP (and the DSF). They argue that, due to opacity discontinuities that develop in these situations, overshoot is physically plausible and thus 3DUP and other mixing events are likely to occur. In summary they find that $Z = 0$ IMS go on to experience normal TP-AGBs because of the various envelope polluting episodes that occur, and these stars are thus important sources of N and C in the early Universe.

Inspired by the theoretical predictions of 3DUP in $Z = 0$ AGB stars, [Goriely and Siess \(2001\)](#) explored the possibility of s-process nucleosynthesis in IM stars. They chose a $3 M_{\odot}$ model as a case study, using the physical profiles in a $Z = 0$ TP-AGB stellar model as input for a post-process nucleosynthesis code. By imposing a H profile just below the maximum incursion of the convective envelope during 3DUP they simulated the often postulated proton diffusion required to produce a ^{13}C pocket. They found that, despite the lack of heavy nuclei seeds for the s-process, the neutron density was sufficient to take the s-process from CNO and Ne seeds all the way to Pb and Bi. In fact they found that Pb and Bi were particularly overabundant (ie. relative to the solar distribution), such that these stars could be called ‘Pop III lead stars’.

The year 2001 was a busy one for $Z = 0$ stellar modelling. [Schlattl et al. \(2001\)](#) continued the work at the low-mass end, evolving models in the mass range ($0.8 \lesssim M \lesssim 1.0 M_{\odot}$) through the dual core flash at the tip of the RGB. Although this had been done previously ([Hollowell et al. 1990](#); [Fujimoto et al. 2000](#)) they tested the robustness of the phenomenon by varying physical parameters. Their main result was that the DCF is quite a robust phenomenon but it also appears somewhat dependent on the He content of the star (at least for $M = 1.0 M_{\odot}$). They state that the key factor is actually the degree to which the core He flash begins off-centre. The closer the ignition is to the H-He discontinuity the more likely it will be that a DCF will

occur. In terms of surface pollution from this event they find similar results to earlier studies (ie. huge amounts of C and N are dredged to the surface). They also report a new phenomenon in low-mass primordial stars – a *second* RGB (SRGB) and second core He flash. After the DCF and subsequent dredge-up of CNO and He rich material the He burning shell is virtually extinct, leaving the H shell to support the star. Thus the star again has an RGB structure, and proceeds to move up the giant branch, until a second (weaker) He core flash occurs. This time there is no associated H flash and the star subsequently moves to quiescent core He burning. Another interesting feature Schlattl et al. discovered is that the surface temperature of the star jumps discontinuously as the envelope is polluted with DCF material (in the sense that the surface becomes cooler, see their Figure 1). This is due to the sudden increase in opacity. They however note that the low temperature opacity tables they use do not properly represent the composition of the envelope, so the temperature jump may be somewhat inaccurate.

2.3.4 Latest Studies – Published During the Course of the Present Study (2002 – 2006)

In 2002 Siess et al. calculated a grid of models with $Z = 0$ and a mass range of $0.8 \lesssim M \lesssim 20 M_{\odot}$. Interestingly they found no DCF in the low mass models, at variance with most (if not all) previous studies. They confirmed the occurrence of 3DUP in the IM stars but also found it to occur in lower mass stars, such that it was operating in the mass range $1 \lesssim M \lesssim 7 M_{\odot}$. In the less massive models ($1 \lesssim M \lesssim 5 M_{\odot}$) this was due to the fact that their models experienced the same H convective episodes (ie. the DSF) as those reported by Chieffi et al. (2001), also subsequently mixing up CNO nuclei and thus allowing the star to experience a more normal TP-AGB. In their $7 M_{\odot}$ model they found that it was the 2DUP episode that enriched the envelope so much as to allow a normal TP-AGB evolution. They also note that the small amount of overshoot they used also contributed to the onset of 3DUP.

Schlattl et al. (2002) revisited the problem of explaining the C-rich extremely metal-poor halo stars (CEMPHs) which have been observed in increasing numbers in recent years. They evolved a series of $0.8 M_{\odot}$ stars through the DCF (which they refer to as Helium Flash-Induced Mixing, or HEFM). Their main conclusion was that their models (and those of other studies, eg. Fujimoto et al. 2000) produce C and N rich stars, thus qualitatively matching the results, but in quantitative terms they produce far too much C and N. In addition to this they note that the DCF/HEFM phenomenon does not occur at the metallicities of the currently observed CEMPHs. Thus they conclude that these models are not a good match to the observations.

In 2003 Herwig reported his investigation into the beginning of the AGB for $Z = 0$ and very low metallicity models of masses $2 M_{\odot}$ and $5 M_{\odot}$. He confirmed the occurrence of the HCEs at the start of the TP-AGB along with the subsequent H-flash (DSF) as protons are mixed down and C mixed up. He also found that strong H burning was occurring during 3DUP, calling this phenomenon ‘Hot Dredge-Up’. We note that this may be the same phenomenon reported by Chieffi et al. (2001), as described earlier.

The year 2004 was another busy one for $Z = 0$ stellar modelling. Iwamoto et al. (2004) continued the search for an explanation of the CEMP stars by exploring the (early) TP-AGB evolution

of intermediate mass stars ($1 > M > 3 M_{\odot}$). They confirmed the findings of earlier studies (eg. Cassisi et al. 1996; Fujimoto et al. 2000; Chieffi et al. 2001) on the occurrence of DSFs at the beginning of the TP-AGB. They also found deep 3DUP in all their models which continues to enrich the envelope with CNO nuclei after the post-DSF 3DUP (although they note that the convective mixing algorithm they use mixes one mesh point past the formal Schwarzschild boundary, enhancing the likelihood of 3DUP). A key finding was that the DSF appears to be a source for lithium enrichment in extremely metal-poor models. The Li produced during the DSF (in the H convective zone) is dredged up and enriches the envelope in all the models (except the $3 M_{\odot}$ star which does not experience the DSF). In the $2.5 M_{\odot}$ model the Li is quickly burnt by HBB but in the lower mass models it survives and probably goes on to pollute the interstellar environment via stellar wind mass loss. They also suggest that the DSF may be a source of s-process nucleosynthesis in primordial low mass stars ($M \sim 1 M_{\odot}$).

Picardi et al. (2004) also attempt to explain the observations of extremely low-metallicity C-rich stars, and in particular the star HE0107-5240, a very popular star in 2004 (the next two papers also refer to this star). HE0107-5240 was the most iron-poor star known at that stage, having a metallicity of $[\text{Fe}/\text{H}] = -5.3$ (Christlieb et al. 2002). Picardi et al. evolved low mass models ($0.8 > M > 1.5 M_{\odot}$) of zero and very low metallicity (see Table 2.2 for the Z range) through the DCF and on to the AGB. Like Schlattl et al. (2001) they also find a secondary RGB phase develops just after the DCF. Lithium is dredged up after the DCF, enriching the surface, which concurs with the findings of Iwamoto et al. (2004). By calculating a range of masses and metallicities they find that the DCF phenomenon is a robust feature, always occurring in models of $M \lesssim 0.9 M_{\odot}$ with $\log(Z) \lesssim -6$. For the same mass range they also find that even a large increase in helium content (up to $Y = 0.27$) does not prevent the occurrence of the DCF. In comparing their surface pollution results with that of CEMPH stars they find many reasons to conclude that these stars' strange abundance patterns are *not* due to the DCF event. One key reason is that, like previous studies, their models produce far too much C and N. Another is that, when confronting the theoretical model with the observations in the $\log(g), \log(T_{\text{eff}})$ plane, the (real) star appears to be on the early RGB – a long way before the DCF pollution is predicted to occur.

Weiss et al. (2004) also took up the HE0107-5240 challenge. The novelty in their study was to use ejecta from supernovae calculations to 1) pollute the surface of a $Z = 0$ model and 2) mix with Big Bang material to make a 'Pop II.5' model. As with previous authors they found that scenario 1 resulted in too much N and C being produced, as well as the $^{12}\text{C}/^{13}\text{C}$ ratio being too low compared to observations. In addition to this they find that HE0107-5240 appears to be on the RGB, well before the core He flash (or DCF) and associated envelope enrichment is expected to occur, concurring with the findings of Picardi et al. (2004). In scenario 2 some of these problems are circumvented as the DCF enrichment does not occur (due to the higher Z of the model) and the supernova material was chosen so as to match the C overabundance (and Fe abundance). The N overabundance was then obtained via first dredge-up, as CN cycling of the initial C occurs prior to this. A side effect of using SNe yields is that there is also a strong overabundance of oxygen. They find that too much O is produced for a match with HE0107-524 but also note that other CEMPs show more O enrichment. Their conclusion is that the SN plus primordial gas mixture models provide the best fit to the observations, particularly because it

is possible to find a combination of SNe to mix in order to match $[C/Fe]$ a priori.

In the same year a third group, Suda et al. (2004), also attempted to explain the surface abundances of HE0107-5240. Their pollution scenario is based on mass transfer from a binary companion. The binary system is thought to be primordial (ie. true $Z = 0$) at birth and the small amount of iron is assumed to arise from accretion (only onto the surface) from a polluted primordial gas cloud. Enrichment in the other elements arise through the mass transfer of the faster-evolving component of the binary (the primary component, which is now a white dwarf). Since the primary component of the binary is a true Pop III star it undergoes a DSF (it's mass is expected to be in the range $1.2-3.0 M_{\odot}$), which provides the large amounts of C and N needed, as well as the enhancements in O and Na. They also discuss a potential s-process signature that could be used to distinguish between Pop III and Pop II pollution material (see their Figure 6). To explore this scenario the authors calculate the evolution of a range of low and intermediate mass $Z = 0$ stars ($0.8 < M < 4.0 M_{\odot}$). As they did not include time-dependent mixing they did not evolve the stars through the DCFs and DSFs, halting the evolution at the onset of these events. Thus, in order to obtain estimates for the pollution arising from these phenomena, Suda et al. utilise the results of Hollowell et al. (1990). The key in identifying the primary component was that they noticed that the DSF event produces less C and N than the low-mass DCF event. As noted earlier, excess C and N has been a consistent problem with the low-mass Pop III pollution scenario (eg. Schlattl et al. 2002; Picardi et al. 2004). This is the main reason they predict the mass of the primary to be in the range $1.2-3.0 M_{\odot}$. They also discuss the production of O through ^{13}C burning during the DSF and also the potential to produce Na, Mg and Al (which can also be produced through later 3DUP episodes). Finally, it is interesting to note that they did not find any 3DUP in their $4 M_{\odot}$ model, in contrast to earlier studies (eg. Chieffi et al. 2001; Siess et al. 2002).

2.3.5 The Current Study In Context

One of the main aims of the current study is to examine the nucleosynthesis of primordial stars. In order to achieve this it was necessary to first modify the structural evolution code substantially (SEV code, see next two chapters) and the nucleosynthesis code to a lesser degree. The next stage was to run the calculations. Owing to the peculiar evolution of primordial stars, as evidenced by the studies described above, there were many difficult phases to evolve through. Table 2.2 gives a clear representation of where our study fits in to the further development of the field. We have calculated a grid of models with a modest range of masses ($0.85 \rightarrow 5.0 M_{\odot}$) and a wide range of metallicities (zero and $\log(Z/Z_{\odot}) \approx -6, -5, -4, -3$). Looking at Table 2.2 we can see that this grid is essentially covered by the previous studies. We note however that whilst the range has been covered it is evident that no consistent study has been performed across the range in question – it requires the addition of a few independent studies to cover the present one (especially if the stages of evolution evolved through is taken into account). This study provides a self-consistent set of models that cover all phases of evolution. In addition to this there is still a consensus lacking in some of the evolutionary traits. For example the DCF phase is found to occur in the calculations of some authors (eg. Hollowell et al. 1990; Schlattl et al. 2001) but not all (Siess et al. 2002). This in itself warrants another investigation into

the evolution of low mass $Z = 0$ stars. Furthermore, to the best of our knowledge, our models are *the first calculations of the entire AGB phase at these metallicities*. Importantly this has enabled us to calculate detailed chemical yields for these primordial stellar models, which has also never been done before (again, to the best of our knowledge). Finally we note that much work was done in the field during the period of the Author's candidature, as it has recently been (and still is) a 'hot topic' in stellar astrophysics. This is mainly due to the discovery of some extremely metal-poor Galactic halo stars, particularly the C-rich star HE0107-5240 ([Christlieb et al. 2002](#)). With the recent discovery of an even more metal-poor Halo object (HE1327-2326, [Frebel et al. 2005a](#)) and the likelihood of more discoveries in the near future, we anticipate the interest in models of these stars will continue.

Part II

METHOD

Chapter 3

Numerical Codes

“We know very little, and yet it is astonishing that we know so much, and still more astonishing that so little knowledge can give us so much power.”

– Bertrand Russell (1872-1970)

Overview

The stellar model simulations are handled in two distinct parts – the structural evolution and the nucleosynthetic evolution. The structural evolution is computed first, using the Monash version of the Mount Stromlo Stellar Structure (MSSS) code also known as ‘*EVOLN*’. For clarity I will refer to this code as the SEV code (structural evolution code) in this thesis. The SEV code includes only the nuclear reactions important for the structure and thus provides only a small amount of chemical evolution information. The second code, which is employed to calculate the detailed nucleosynthesis, is known as ‘*DPPNS45*’. The nucleosynthetic code (hereafter, NS code) uses the structural evolution information output by the SEV code necessary for calculating the chemical evolution (ie. the temperature profile, density profile, convective velocities, etc.). Thus the NS code is a post-process code. A benefit of having this two-step paradigm is that the structure need only be computed once, whereas the nucleosynthesis can be re-run many times, allowing the fast computation of models with differing reaction rates.

As discussed in the preceding chapter, very low metallicity stellar models (if not real stars!) are known to have some unique evolutionary episodes. These episodes, such as the proton ingestion episodes (PIEs) are notoriously difficult to model. Neither code was set up to handle episodes such as these. Thus I have made modifications to both codes in order to model these types of stars. The SEV code required the most changes, most notably the introduction of time dependent mixing to handle the rapid evolution during PIEs.

Both codes are described in detail in the sections below. For each code I also discuss the modifications I made during the course of my research.

3.1 Structural Evolution Code

This section briefly describes the structural evolution code as obtained by the author at the beginning of the current study. Modifications made during the course of this research are described in s3.1.3.

3.1.1 History of Development and Basic Assumptions

The Mount Stromlo Stellar Structure Program was originally developed in the late 1960s (Faulkner 1968). Initially designed to model He shell burning stages in low mass stars ($M \sim 0.9 M_{\odot}$), it has been expanded and updated numerous times such that it is now capable of modelling all phases of low to intermediate mass stars, from the pre-main sequence (PMS), through the thermally pulsing AGB phase, and on to the white dwarf (WD) cooling phase. As noted in the PhD thesis by Lattanzio (1984), descriptions of the code are widely scattered throughout the literature. To the best knowledge of the author, Lattanzio (1984) is the source with the most detail about the code. In particular it describes the difference equations used and the particular implementation of semiconvection. To provide some further key references and outline the history of the development of the code we list some landmark studies and associated code updates below:

- Thermal pulses in He shell burning stars (Faulkner and Wood 1972)
 - Neutrino losses added, opacities updated
- Hydrogen added (early 1970s. Previously only included He and C burning)
- AGB evolution of a $0.6 M_{\odot}$ star (Gingold 1974)
 - No shell-shifting methods used.
- AGB He shell flashes in stars of mass 0.8 to $3.0 M_{\odot}$ (Wood and Zarro 1981).
 - Entire stellar model now in Henyey matrix (ie. no envelope fitting).
- Third dredge-up in low mass stars (Lattanzio 1989, Frost and Lattanzio 1996).
- Hot Bottom Burning in AGB stars (Lattanzio 1992, Frost et al. 1998).

The version of this program obtained at the beginning of the current study is the Monash University version, known as ‘EVOLN’ (Lattanzio 1984; Lattanzio 1986; Frost and Lattanzio 1996). For clarity and in order to distinguish it from the nucleosynthesis code I shall refer to it as the SEV code (structural evolution code) in this thesis.

The main assumptions and approximations used in the code are:

1. Spherical symmetry (ie. no rotation or magnetic fields) \implies one spatial dimension.
2. Hydrostatic equilibrium \implies quasi-static evolution.
3. Radiation transport is treated as a diffusive process.
4. The Mixing Length Theory (MLT) is used for convection (local theory).

5. Convective zones are mixed instantaneously (ie. time-dependent mixing not included).

All these assumptions and approximations are widely used in other one-dimensional stellar codes. Indeed, the first three lead (with other physical considerations) to the standard form of the well known stellar structure equations (see eg. [Schwarzschild 1958](#); [Clayton 1983](#)). Using mass as the independent variable the equations take the form:

$$\frac{\partial r}{\partial m} = \frac{1}{4\pi r^2 \rho} \quad (3.1)$$

$$\frac{\partial P}{\partial m} = -\frac{Gm}{4\pi r^4} \quad (3.2)$$

$$\frac{\partial L}{\partial m} = \epsilon_{nuc} - \epsilon_v - \left(\frac{\partial U}{\partial t} + P \frac{\partial V}{\partial t} \right) \quad (3.3)$$

$$\frac{\partial T}{\partial m} = -\frac{GmT}{4\pi r^4 P} \nabla \quad (3.4)$$

where the variables have the usual meanings. Equation 3.1 is the mass continuity equation, equation 3.2 the equation for hydrostatic equilibrium, equation 3.3 the energy equation, and equation 3.4 the energy transport equation. Regions in a model are deemed convective based on the [Schwarzschild \(1906\)](#) criterion, such that if the radiative temperature gradient is greater than the adiabatic temperature gradient then the region is convectively unstable. The standard procedure of taking ∇ (the temperature gradient) equal to $\nabla_{radiative}$ in radiative zones is used, whilst in convective zones ∇ is calculated from the MLT.

The SEV code solves the four stellar structure equations to produce a model in hydrostatic equilibrium. The temporal advance is then based on the chemical changes brought about over a time interval Δt by nuclear reactions (and turbulent mixing). The nuclear reactions alter the mean molecular weight μ which in turn affects the density structure, and therefore the thermal structure, etc. A new hydrostatic model is calculated with the new composition profile at the time $t + \Delta t$, thus enabling us to follow the evolution through a series of ‘quasistatic’ models.

3.1.2 Overview of Numerical Method

The core of the SEV code is based on the Henyey-matrix numerical method ([Henyey et al. 1959](#); [Henyey et al. 1964](#)) which is basically a Newton-Raphson method. It uses successive iterations whereby corrections are applied to an initial guess for the structure, the new guess fed back into the matrix, then new corrections are calculated and applied, and so on. This iterative method is also known as ‘relaxation’. The code is deemed to have converged if the difference between

the current iteration's structure and the previous one's is below a certain threshold (typically $\sim 10^{-3}$). A recent description of the relaxation method can be found in Hansen and Kawaler (1994).

The change in chemical composition, which is the driving force for evolution, is derived from the rates of change of abundances due to nuclear reactions and the movement of chemical species due to convective mixing. A semi-implicit scheme is used to advance the chemical profile to the next timestep:

$$X_i^n = X_i^{n-1} + \frac{\Delta t}{2} \left[\left(\frac{dX_i}{dt} \right)^n + \left(\frac{dX_i}{dt} \right)^{n-1} \right] \quad (3.5)$$

where the X_i are the chemical species, $\Delta t = t^n - t^{n-1}$ and n and $n-1$ represent the current and previous timesteps respectively. Thus, in addition to the converged hydrostatic model, we now have a change in composition profile with which to calculate the next hydrostatic model. In this way a series of hydrostatic models form the quasistatic evolutionary sequence.

Mass is essentially the independent variable, however the SEV code has a peculiar formalism, whereby x is actually used:

$$x = \left(\frac{m_r}{M} \right)^{\frac{1}{3}}. \quad (3.6)$$

Faulkner (1968) made this choice so as to include the central point as a normal mesh point – as all derivatives using this variable are finite at the centre – and the calculations are simplified. The dependent variables in the SEV code are: L_r/L_\odot , $\ln(T)$, r/R_\odot and $\ln(P)$.

The stellar model is divided into many mass shells (the term ‘shells’ is commonly used but it should be remembered that the scheme is actually one dimensional). State variables (T , ρ , etc.) are recorded at each mesh point (some being defined between mesh points). There are typically between 500 and 3000 mesh points used, depending on the stage of evolution. The Lagrangian mesh is adaptive – the points are distributed to maintain a prescribed minimum resolution in the state variables. Thus in regions where there are steep gradients in physical properties the resolution is increased. Likewise, the timestep is constrained so as not to let the state variables (or chemical abundances) change too much between models.

3.1.3 Included Physics

Chemical Species and Nuclear Reactions

The SEV code currently follows six chemical species: ^1H , ^3He , ^4He , ^{12}C , ^{14}N and ^{16}O . These are the only isotopes considered explicitly however the rest of the isotopes involved in H, He and C burning reactions are included *implicitly*. The missing isotopes involved in the CNO cycles are included implicitly by assuming that they are always present in their equilibrium

abundances. Temperature-dependent branching ratios are used for isotopes with two possible exit channels. Only following the major isotopes simplifies and speeds up model calculations however it means that the code contains only basic nucleosynthesis – enough to properly follow the structural evolution – it lacks the detailed nucleosynthesis that is needed to confront stellar models with the detailed observations currently available. For this reason we utilise the post-processing nucleosynthesis code which is able to follow an arbitrary number of elements (this code discussed in section 3.2). The SEV code also contains one pseudo-element, called *zother*, which represents all the elements heavier than ^{16}O . The heavy products of He and C burning are added to *zother* for baryon conservation.

The code currently solves for H burning (pp chains and CNO tri-cycle), He burning (triple-alpha reaction) and C burning (which is never used in this study). Further burning stages (Ne, O, etc.) are not included, which imposes an upper limit to the mass and/or stage of evolution we are able to follow certain stars. All nuclear reaction rates are from [Caughlan and Fowler \(1988\)](#), except the rate for the $^1\text{H}(p, e^+ + \nu)^2\text{H}$ reaction which is from [Harris et al. \(1983\)](#). Although the rates used are from fairly old compilations, the aim of the SEV code is to calculate the structure only, whereas the detailed nucleosynthesis is calculated by the nucleosynthesis code which allows the accurate tracking of a large number of isotopes and is constantly updated with the latest reaction rates. We note however that recent updates to the key SEV code rates (which have not been used in the current study, but will be used for all future studies) have shown that these rates have not changed substantially from that given in the [Caughlan and Fowler \(1988\)](#) compilation.

Neutrino energy losses are included following [Beaudet et al. \(1967\)](#) for the pair neutrino process, photoneutrino process and plasma neutrino process, whilst bremsstrahlung rates are from [Festa and Ruderman \(1969\)](#). Corrections due to neutral currents are taken from [Ramadurai \(1976\)](#) (for pair, plasma, and photoneutrino processes) and [Dicus et al. \(1976\)](#) (for bremsstrahlung).

Opacity

Opacity is of particular importance to stellar modelling as it determines the heat flow through the star and thus the thermal structure, which then feeds back onto the rest of the structure and consequently the nuclear reaction rates. Here we describe the SEV code opacity regime in use at the beginning of the present study. Substantial changes were made to the opacity subroutines during the course of the current study and are described in section 4.2 on page 79.

In the SEV code opacities for each mesh point are obtained by interpolating in opacity tables. Tables of Rosseland mean opacities made available by the Lawrence Livermore National Laboratory OPAL project ([Iglesias and Rogers 1996](#)) cover the bulk of the temperature and density range of low and intermediate mass stars. We interpolate within these tables in the temperature range: $7000\text{K} < T < 5 \times 10^8\text{K}$. The OPAL tables do not include opacities for conductive material so in regions where the density is very high we use the analytical fit by [Iben \(1975\)](#) (appendix A of that paper) to the [Hubbard and Lampe \(1969\)](#) conductive opacity formulae for non-relativistic electrons and those of [Itoh et al. \(1983\)](#) and [Mitake et al. \(1984\)](#) for dense (liquid-metal) material containing relativistic electrons. Opacities for solid material are from [Raikh and Iakovlev \(1982\)](#). The subroutine that calculates these conductive opacities

was supplied by MacDonald (1992, private communication). At temperatures below 7000 K a combination of the Cox and Stewart (1970) and Huebner et al. (1977) tables are used. At very low temperatures ($T \lesssim 4000\text{K}$), such as those found in the envelopes of RGB or AGB stars, molecular opacity becomes important. As the Cox and Stewart (1970) low temperature tables do not include molecular contributions, we add in the opacity contributions from CN, CO, H₂O and TiO using the formulae suggested by Bessell et al. (1989) which are based on the molecular (and grain) opacity tables from Alexander (1975) and Alexander et al. (1983). The corrections to the formulae by Chiosi et al. (1993) are taken into account. All the opacity tables assume a scaled-solar heavy element distribution.

Turbulent Convection and Mixing

Regions in each stellar model are deemed convective based on the Schwarzschild (1906) criterion, such that if the radiative temperature gradient is greater than the adiabatic temperature gradient then the region is convectively unstable. The standard procedure of taking ∇ (the temperature gradient) equal to $\nabla_{\text{radiative}}$ in radiative zones is used. In convective zones ∇ is calculated from the MLT.

Fluid mechanics theory predicts that the onset of convection occurs when the Rayleigh number (Ra) reaches some critical value Ra_c , where Ra_c is of the order 10^3 . As conditions in stellar convective zones give rise to extremely large Rayleigh numbers ($\sim 10^{20}$, Spiegel 1971) – and also very small Prandtl numbers ($Pr \sim 10^{-9}$, where $Pr = \frac{\text{kinematic viscosity } \nu}{\text{thermal diffusivity } \kappa}$) – it is currently impossible to simulate anything even close to these conditions in the laboratory. This lack of experimental evidence necessitates either 1) a complete hydrodynamic calculation (eg. solution of the Navier-Stokes equations) or 2) a decent approximate theory of convection. The first option is very computationally demanding, especially if it is done properly in three dimensions. Some two and three dimensional hydrodynamic simulations have been calculated but they necessarily focus on small regions within a star (to make the problem tractable in a computing sense), such as the convective layer in Solar-type stars (or part thereof: Nordlund and Dravins 1990; Singh et al. 1995). A recent development is that of the DJEHUTY project (Dearborn et al. 2001) which now has a working three dimensional hydrodynamical code that can simulate an entire star (given enough computing resources). However the time it takes to evolve stars is still prohibitive in terms of a full evolutionary sequence, despite the fact that it is being run on the largest computing cluster in the world. For this reason the second option has been employed since the early days of stellar evolution. Convective approximations, mainly in the form of the widely used Mixing Length Theory (MLT; Prandtl 1925; Biermann 1951; Böhm-Vitense 1958), have allowed the modelling of convective zones in stellar models to be calculated in reasonable lengths of time. Much of the simplification of the calculations arise because the MLT is a *local* formalism, such that the properties of each convecting mass element are given solely by the conditions at its current location. Some attempts at including non-local effects in stellar modelling have been made, mainly as modifications to the MLT (eg. Shaviv and Salpeter 1973; Maeder 1976; Xiong 1985). The various incarnations of the MLT are all based on the Boussinesq approximation. One key feature of this formalism is that we have a characteristic ‘mixing length’ l which is assumed to be much shorter than other length scales in the star (eg. the pressure scale height,

H_p). However, as is well known, application of the MLT only gives reasonable results when $l \sim H_p$ (see eg. Hansen and Kawaler 1994 for a brief review). Indeed, most authors use a mixing length greater than the pressure scale height (eg. $l \sim 1.5H_p$). Despite this internal inconsistency within the (application of) MLT, and despite the wholesale assumptions used in constructing the MLT equations used in stellar model calculations, the predictive success of stellar models appears to indicate that the MLT gives a reasonable description of convection. For this reason, and for the sake of efficient computation, most authors still use the MLT (or variations thereof) and it is the formalism currently employed in the SEV code.

Another convection formalism that the author is aware of is ‘Full Spectrum of Turbulence’ (FST) (Canuto et al. 1996; Ventura et al. 2005). While still a local theory, and still based on the MLT, FST relaxes the single eddy approximation of the MLT, taking into account turbulence on all length scales. This group (Canuto, Mazzitelli, Ventura et al.) finds substantially different results when comparing with stellar models using the MLT. This serves as a further reminder that the treatment of convection is far from perfect in stellar models.

In the SEV code the mixing of chemical elements within a convective zone is assumed to happen instantaneously. This assumption is valid for most stages of stellar evolution as the convective turnover timescale is usually much shorter than the evolutionary timescale. Thus the chemical profile will be easily mixed in one timestep. However, in evolutionary stages where there are rapid changes and the timestep is consequently lowered, this assumption is not valid. This may happen during the core He flash in low mass stars or during proton ingestion episodes in zero- or very low-metallicity stars. As the current study is concerned with these cases, a time dependent mixing scheme had to be added to the SEV code (detailed in section 4 on page 49).

Finally we note that the SEV code includes the method suggested by Wood (1981) for taking into account the change in entropy due to the dredge up of heavy nuclei during the third dredge-up on the AGB. The main effect of including this physics is to slightly increase the depth of the third dredge-up.

Overshoot

Directly related to the above discussion on convection is the phenomenon of overshoot. Overshoot is defined as the extension of convection beyond the formal (eg. Schwarzschild) convective boundary. In the Schwarzschild formalism the convective boundary is defined as the first point where the actual temperature gradient ∇ is equal to the adiabatic temperature ∇_{ad} . However, a convecting parcel of gas reaching this boundary will, by definition, still have a small temperature excess ΔT , and thus a finite acceleration. As the MLT is strictly a local formalism the first point above the Schwarzschild boundary has no information about the still moving parcel below and it is designated as a radiative (non-convective) point. If a non-local scheme were used then the parcel would be followed through the Schwarzschild boundary into the stably stratified material on the other side. This subadiabatic material would then cause a deceleration of the parcel. Of course the key question here is how far the parcel will overshoot the formal boundary before finally coming to rest, as this will define the extent of the extra mixing. Non-local MLTs are often formulated in order to follow this phenomenon (eg. for convective core overshoot: Maeder 1975; Shaviv and Salpeter 1973). However, the results based on this type of method have given

varying results. Indeed, [Renzini \(1987\)](#) notes that adding non-local prescriptions to the local MLT can lead to non-physical equations and he highlights the huge variation in overshoot distances between authors (from almost zero to a few times the original Schwarzschild convective zone size). Another method to gauge the extent of overshoot is to utilise results from hydrodynamical computations. These computations are quite difficult and still require the use of many assumptions ([Freytag et al. 1996](#) provides a list). Some recent work in this area includes that by [Freytag et al. \(1996\)](#) and [Singh et al. \(1995\)](#). These groups investigate overshooting using two- and three-dimensional hydrodynamic codes respectively. [Freytag et al. \(1996\)](#) find that the vertical velocities fall off exponentially starting from within the formal convective boundaries. They also note that the concept of an overshoot *distance* is not useful (although commonly used) since their results show that the extent of overshoot is very dependent on the particular conditions at the edge of the convection zone. [Singh et al. \(1995\)](#) also find this dependence (based on their stability parameter S). Their results indicate that the overshoot distance is some fraction of H_P (the pressure scale height), which is proportional to the velocity scale height. Very recently [Herwig et al. \(2006\)](#) have performed 3D hydrodynamic simulations to mimic the convection in an AGB He shell flash. Although they do not quantify the extent of overshooting in their study, they suggest that some overshoot does occur, but at quite a minimal level due to the physical conditions. A reassuring finding in their study is that the velocities in the convective regions given by the hydrodynamic code are very similar to those obtained from the MLT. The main exception is in the exponential drop-off of velocities *before* the bottom of the convective zone (and probably continuing just beyond the formal convective boundary).

Despite the great work done to date in this field of multidimensional hydrodynamic simulations of stellar convection, it must be remembered that the field is still in its beginning stages. Many assumptions are included even in the most detailed models (as noted by the authors themselves), so the results must be used with caution. That said, the beginning of a consistent picture is starting to form, consisting of 1) there appears to be an exponential decay of velocities at the edge of convection zones and 2) the degree of overshoot seems to be very dependent on the local conditions. However it appears that we still don't really have a good quantitative handle on the extent of overshooting. Thus for now most stellar models still employ ad-hoc (although reasoned) approaches.

The method used to account for overshoot in the SEV code involves a 'search for convective neutrality' ([Lattanzio 1986](#)). The algorithm linearly extrapolates ∇_{rad}/∇_{ad} taken from the last two convective mesh points to the next point (which is radiative). If the extrapolated ratio is greater than unity (ie. $\nabla_{rad} > \nabla_{ad}$) then that point is reclassified as convective. Conversely, if the ratio is less than unity then the point remains radiative. The algorithm only allows one radiative point to be added to the convective zone each iteration. In using this procedure we ensure that the last convective point is as close to neutral buoyancy as possible. This method is applied to all convective boundaries. We note that although the method allows for core growth and (the disputed) 'core breathing pulses' during core He burning, it does not have a significant effect on the convective boundaries of flash-driven He convective zones (eg. during the TPAGB).

Finally we note that the above method for overshoot is only used in some of the stellar models in this study. During the course of the research the SEV code was modified to include a time-dependent hydrodynamically-based prescription for overshoot (see section 4 on page 49 for

details).

Semiconvection

Semiconvection in the SEV code is intimately related to overshoot. The overshoot method described above may even be classified as a method to include semiconvection, as it does bear some resemblance to the semiconvection algorithm often used in stellar codes (the [Robertson and Faulkner 1972](#) method). The Robertson and Faulkner method also searches for convective neutrality but achieves it by adjusting the abundances in a region just outside the formal convective boundary – if there exists a small convective region outside the convective core. The region between the two fully convective zones is said to be semiconvective, and a mixing procedure is used to mimic this physical process.

The method used to follow semiconvection in the SEV code relies on the previously described overshoot formalism but adds in one parameter, $\Delta q_{scvn} = \Delta m/M$ ([Lattanzio 1984](#)). Δq_{scvn} prescribes the mass spacing of the mesh points around a convective boundary. Differing values of Δq_{scvn} give rise to differing amounts of semiconvection/overshoot. In the absence of quantitative knowledge about the extent of semiconvection and overshoot (apart from inferences from some observations), Δq_{scvn} was calibrated with reference to models using the [Robertson and Faulkner \(1972\)](#) method described above.

With regards to the current study this method of following semiconvection was only used for some of the stellar models. A new formalism was introduced, as described in section 4.1.6 on page 74. The physical nature of semiconvection is also discussed in more detail in that section.

Mass loss

A particularly large uncertainty arises in the later stages of stellar evolution (in low to intermediate mass stars) when mass loss from the surface of a star becomes significant. As yet there are no theoretical/computational models developed from first principles to explain mass loss in cool stars. There is the general idea though that radiation pressure exerted on grains in the outer atmospheres of cool stars is a major factor. However currently the only method to include mass loss in stellar evolution calculations is to make use of empirical formulae. The empirical formulae are based on observations of mass loss in various types of stars. Mass loss rates are deduced by observing the Doppler shifts of circumstellar absorption lines. The formula for RGB stars by [Reimers \(1975\)](#) is still probably the most used today:

$$\dot{M}(M_{\odot}yr^{-1}) = 4 \times 10^{-13} \eta_R \frac{RL}{M} \quad (3.7)$$

where R, L and M are the star's radius, luminosity and mass in solar units. η_R is the Reimers mass loss parameter and is of order unity. As can be seen, the mass loss rate is a function of the gross physical properties of the star and thus \dot{M} evolves with the star. Although this relation was derived from observations of RGB stars it is often used for modelling AGB stars by varying

η_R . In the SEV code we use Reimers' law only on the RGB (with $\eta_R = 0.4$) as the mass loss rate towards the end of the AGB is known to be extremely strong. Indeed, a *superwind*, with $\dot{M} \sim 10^{-5} M_\odot/\text{yr}$, is needed to form planetary nebulae, which is not produced by equation 3.7. The AGB is also phenomenologically different from the RGB as AGB stars are known to pulsate. Observations show that mass loss is related to the period of pulsation. Thus for the AGB we make use of the empirical formula derived by Vassiliadis and Wood (1993) (hereafter VW93) which is based on observations of AGB stars:

$$\log(\dot{M}(M_\odot \text{yr}^{-1})) = -11.4 + 0.0125P \quad (3.8)$$

where P is the pulsation period in days. Assuming that AGB stars oscillate in their fundamental mode the period can be related to the stellar radius and mass (in solar units):

$$\log(P(\text{days})) = -2.07 + 1.94 \log R - 0.9 \log M \quad (3.9)$$

VW93 note that this equation gives superwind values of \dot{M} in stars with periods of ~ 500 days. Such a strong wind quickly enshrouds the central star in dust and it is no longer visible at optical wavelengths. This is observed in low mass populations at $P = 500$ days but the effect does not set in in higher mass populations ($M \sim 5 M_\odot$) until $P \gtrsim 750$ days. VW93 account for this by using a different mass loss formula for more massive stars (their equation (5)). In the SEV code we use a different method whereby we switch to the following relation when $P > 500$ days:

$$\dot{M}(M_\odot \text{yr}^{-1}) = \frac{L}{c v_{exp}} \quad (3.10)$$

where v_{exp} is the expansion velocity and c is the speed of light (both in km s^{-1}). This corresponds to a pure radiation-pressure-driven wind although we still include a dependence on the pulsation period by calculating the expansion velocity using equation (3) from VW93:

$$v_{exp} = -13.5 + 0.056P \quad (3.11)$$

Finally, an upper limit is set on v_{exp} ($= 15 \text{ km s}^{-1}$) to mimic the observed radiation-pressure-driven limit.

Equation of State

The equation of state (EOS) describes the interdependency of the density, temperature and pressure of a material (usually a plasma in stellar models). Depending on the physical conditions a given material will behave in different ways. For relativistic or electron-degenerate gas the SEV

code uses the fitting formulae of [Beaudet et al. \(1967\)](#). For fully-ionised gas we use the perfect gas equation (including radiation pressure). For cool outer layers where the gas is only partially ionised the Saha equation plus the method of [Baerentzen \(1965\)](#) is applied, with radiation pressure added.

As the various equations of state utilised in the SEV code are quite old, [Messenger \(2000\)](#) compared the results to a more modern EOS (provided by the OPAL project, [Rogers et al. 1996](#)). He found that the differences were so small ($< 2\%$ in pressure) that it did not warrant the factor of four increase in computation time to implement the OPAL EOS. However we note that the comparison was only performed for the parameter space in which the OPAL EOS is valid, which does not include relativistic and/or degenerate gas.

3.2 Nucleosynthesis Code

“To the extent that it is possible, it is the isotopes that keep the theorists honest.”
– David Arnett

3.2.1 Introduction

Modern abundance observations provide data for a large portion of the Elements in many stars. Since the elements have varying sources of production these observations amount to myriad constraints on stellar models (although there are sometimes large uncertainties in the observations that weaken the constraints). In addition to the constraints imposed by individual elements, the abundance *patterns* of stars also provide important constraints – and insights. Clues can be sought in these patterns for the likely stellar sites of nucleosynthesis via abundance ratios, correlations and anticorrelations. Indeed, it is always very difficult to match all the observed elements in a single star (this is also due to other complicating factors such as multiple pollution sources). Moreover, in some cases even isotopic abundances or ratios can be deduced from the observations. For example the $^{12}\text{C}/^{13}\text{C}$ ratio is routinely measured (eg. [Shetrone 2003](#)) and it is possible to deduce the $^{24}\text{Mg}:^{25}\text{Mg}:^{26}\text{Mg}$ ratios in some stars (eg. [Yong et al. 2003](#)). Knowledge of the isotopic abundances provides even more stringent constraints on the models. For example, in the globular cluster chapter of the present study (Chapter 8) we find that the elemental abundances of Mg in the globular cluster NGC 6752 are satisfactorily reproduced by the models – but the isotopic abundances show a large discrepancy relative to the observations. Thus the isotopic observations can “keep the theorists honest” – or show up problems in the models and/or reaction rates. We also note that (very accurate) determinations of isotopic ratios have been made in pre-solar grains such as those in the Murchison meteorite (see eg. [Hoppe et al. 1995](#)). These also provide constraints on the models.

With these points in mind it can be seen that the NS code, which currently has a network of 74 species and 506 reactions, is an important part of our modelling. It allows us to make detailed predictions of abundance patterns which we can confront with the observations.

3.2.2 Code Overview

As mentioned in the introduction to this chapter our nucleosynthesis code (NS code) is a post-processing code. During the calculation of the structural evolution of a stellar model (with the SEV code) the values of many structural properties are stored in a file. The NS code then uses these structural properties as a basis for calculating the detailed nucleosynthetic evolution of the model. This two step method is possible because only a few reactions (and nuclides) contribute significantly to the structural evolution of stars of low- and intermediate mass (as discussed in the SEV code section). The myriad minor nuclides and their reactions supply only negligible amounts of energy and thus do not affect the structure of the models. They do however provide interesting and complex nucleosynthesis.

The code is based on one developed by Cannon (1993) to model the extreme HBB (*rp*–*process*) occurring in Thorne-Żytkow objects (stars with degenerate neutron cores and massive H-rich envelopes). It was used for the complex nucleosynthesis and time-dependent mixing required for nuclear burning in those objects. At that stage it was attached to the Eggleton stellar evolution code. The severe HBB is the main source of energy generation in these objects so the NS code fed back physical information to the structure code. Stellar structure solutions were determined through iterations between the two codes. In this way the energy from the HBB calculated by the NS code was taken into account in the models. The code was rewritten by Lattanzio and Cannon to take input from the Monash Mount-Stromlo Stellar Structure code (ie. the SEV code). Unlike the Cannon (1993) code which used a static mesh the new NS code was written to include a moving mesh. Since all the energetically important reactions for the structure of low- and intermediate-mass stars were already included in the SEV code, there was no need for feedback between these two codes. All the (energetically) minor reactions important for nucleosynthesis could be calculated post-process. Also, since the reactions in the SEV code are a subset of those included in the NS code, and the NS code calculates the energy generation from all the reactions, it was possible to compare the energy generation given by each code as a consistency check. Finally we note that the code is written so that it is quite an easy task to expand the reaction network, and to alter/update individual nuclear reaction rates.

3.2.3 Input Physics

Inputs from the SEV Code

Not every quasi-static model that the SEV code calculates is output to the NS input file. Instead there is a set of selection criteria based on changes in the stellar properties such as the rates of change of luminosity and abundances. This reduces the time resolution during stages in which not much nucleosynthesis is occurring (but in which structural changes occurred), speeding up the nucleosynthesis calculations. Physical variables supplied to the NS code for each model include the temperature profile, density profile, abundance profiles and the velocity profile (all versus mass). This gives the NS code enough information to calculate the time dependent mixing (through the velocity profile) and the nucleosynthesis (through the temperature, density and initial abundance profiles). The total hydrogen and helium burning luminosities from the SEV code are also provided to the NS code as a consistency check.

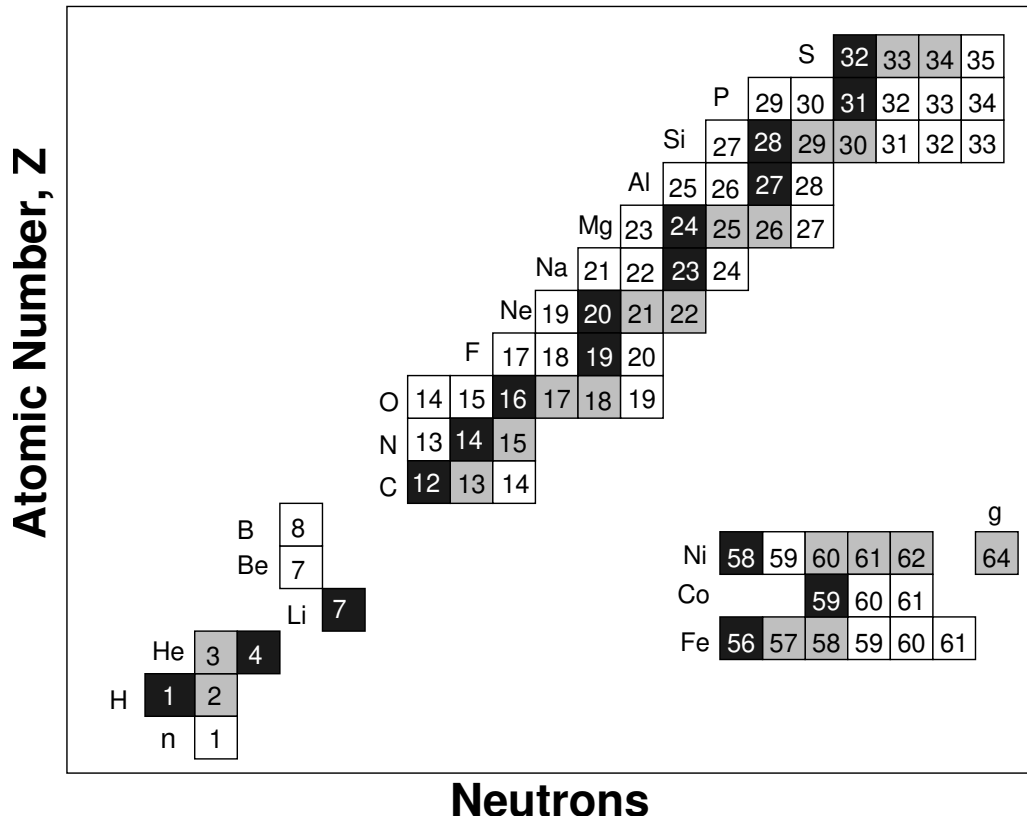


Figure 3.1: All the species included in the nuclear reaction network used for the current study (except the synthetic species used for $^{26}\text{Al}_m$, the metastable state of ^{26}Al). Dark and light grey shading indicate stable nuclides, whilst white indicates unstable nuclides.

The Nuclear Network

In Figure 3.1 we show the 74 species that are included in our nuclear network. The network is broken into two sections. The first covers all species from neutron to ^{35}S (58 species) whilst the second incorporates some iron group nuclides (Fe, Co and Ni – 14 species). Two extra ‘synthetic’ species are also included – $^{26}\text{Al}_m$ and ‘g’. $^{26}\text{Al}_m$ represents the metastable state of ^{26}Al . The g species is used to terminate the network. It is produced via a synthetic decay from ^{62}Ni which itself is produced by neutron capture on ^{61}Ni : $^{61}\text{Ni}(n,\gamma)^{62}\text{Ni} \rightarrow ^{64}\text{g}$. This species is given a mass of 64 to reflect that of the next stable species formed by neutron captures, ^{64}Ni . Following the method of [Jorissen and Arnould \(1989\)](#) the cross section for the $^{61}\text{Ni}(n,\gamma)^{62}\text{Ni}$ reaction has been artificially given as an average representing that of all the nuclides from ^{61}Ni to ^{209}Bi . In this way g keeps track of the number of neutron captures occurring beyond the end of our network. This can be used as a rough guide to estimate the further s-processing that would occur amongst the heavier elements. A similar tactic is used to account for the gap in the network between S and Fe (ie. Cl to Mn). In this case the $^{34}\text{S}(n,\gamma)^{35}\text{S}$ reaction is given an averaged cross section (see [Lugaro 2001](#) for details on the calculation of these averaged cross sections).

Nuclear Reaction Rates

Most of the reaction rates we use in the current study come from the Reaclib library ([Thielemann et al. 1987](#)). However many of the rates have been updated using various sources. These include:

$^{22}\text{Ne}(p,\gamma)^{23}\text{Na}$ (El Eid and Champagne 1995); $^{13}\text{C}(\alpha,n)^{16}\text{O}$ (Denker et al. 1995); $^{24}\text{Mg}(p,\gamma)^{25}\text{Al}$ (Powell et al. 1999); $^{25}\text{Mg}(p,\gamma)^{26}\text{Al}$ (Iliadis et al. 1996); $^{26}\text{Mg}(p,\gamma)^{27}\text{Al}$ (Iliadis et al. 1990); $^{22}\text{Ne}(\alpha,n)^{25}\text{Mg}$ and $^{22}\text{Ne}(\alpha,\gamma)^{26}\text{Mg}$ (Kaeppeler et al. 1994). We note that this set of reaction rates was compiled by Lugaro (2001) who lists all the updated rates (relative to the Thielemann et al. 1987 compilation) in her Appendix A. We refer to this combination of rates as our ‘standard’ set. There have been many new determinations of rates during the course of the current study, but they have not been used. It is this standard set that we use for all of our models – unless otherwise stated.

Time-Dependent Mixing

Time dependent mixing is important for many nucleosynthetic sites. One classic example is lithium production through HBB in AGB stars (see eg. Sackmann and Boothroyd 1992). It will also be important in our $Z = 0$ and extremely metal-poor models, since these models experience the dual core flash and dual shell flash events, which occur on rapid timescales.

The NS code receives the run of mixing velocities and mixing lengths (given by the mixing length theory of convection) versus mass from the SEV code. With this information it uses a ‘donor cell’ scheme to model time-dependent mixing throughout the star (Cannon 1993). The algorithm allows for both upward and downward moving streams/eddies. Thus any composition difference between upward moving eddies and the downward moving eddies at the same radial position in the star – which can arise if the mixing timescale is much shorter than the nuclear reaction timescales – is taken into account. The algorithm also allows for lateral mixing. Cannon (1993) notes that if the lateral mixing is very fast then the donor-cell algorithm approximates the diffusion equation (which is usually used for time-dependent mixing). In Figure 3.2 we show the mixing scheme schematically.

Other Code Details

The mesh used in the NS code is a mix of Lagrangian and non-Lagrangian points. The non-Lagrangian points are not Eulerian but follow the hydrogen and helium burning shells. The NS code reads in two structural models at a time. It then locates the H and He burning shells in each structural model, based on the H and He abundances, and places the non-Lagrangian points at key positions within the shells. An interpolation is performed between the positions of the shells in the two structural models. In this way the positions of the shells are tracked (see Figure 3.3). This allows the mesh resolution to be selectively enhanced around the burning shells. This is necessary because this is where most of the nucleosynthesis occurs. The NS code then evolves forward, using its own timesteps. When the end point of the nucleosynthetic evolution between these two structural models is reached, the next model is read in and the process repeated. A typical number of mesh points in an AGB model is ~ 200 . In some cases we have however increased this to ~ 2000 in order to resolve small radiative pockets between convection zones (eg. during Dual Flashes in $Z = 0$ models).

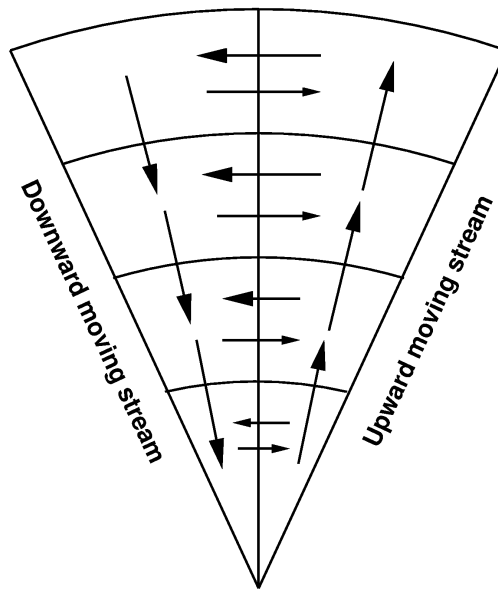


Figure 3.2: Schematic representation of the mixing algorithm used in the NS code (taken from Cannon 1993). Note that each cell is linked to three other cells. Material moves between these three cells (upwards, downwards and laterally) at rates derived from the local values of the convective velocities and mixing lengths (which are taken from the SEV code calculation).

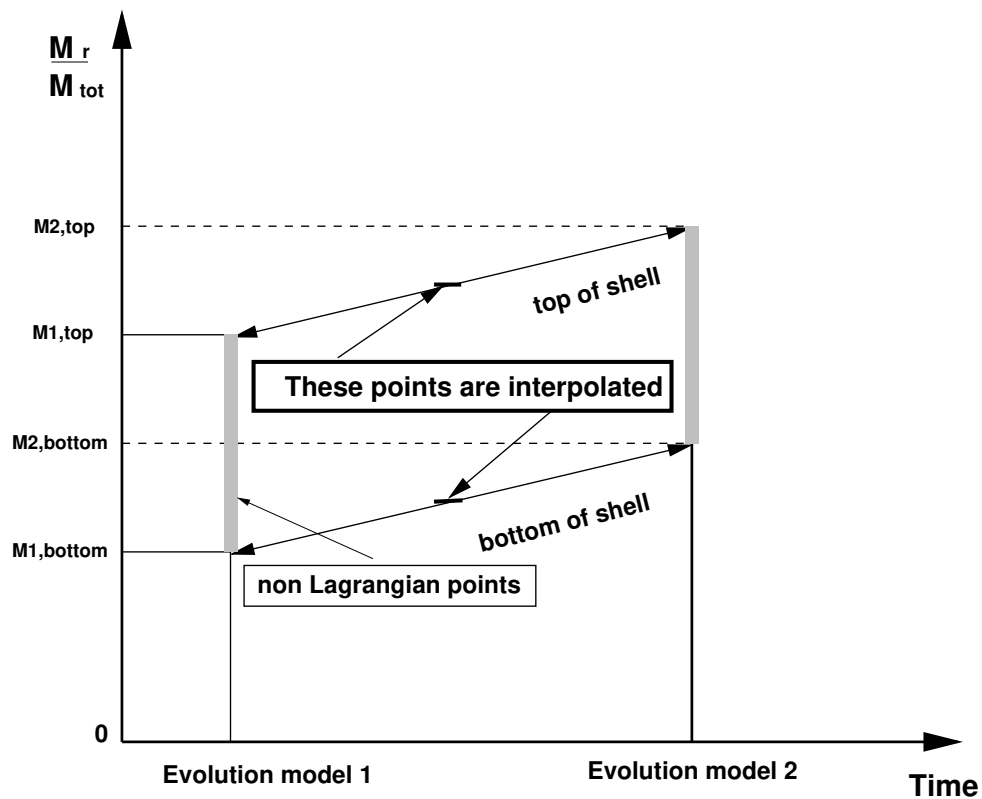


Figure 3.3: Schematic showing the location of two of the non-Lagrangian points used to follow the H and He burning shells between two structural evolution models (M_{top} and M_{bottom} , for each model). The mesh resolution is enhanced in and around these key points, to follow the rapid nucleosynthesis that occurs in the shells.

3.2.4 NS Code Modifications

As noted in the introduction to the present chapter the NS code required much less modification than the SEV code in order to enable the modelling of $Z = 0$ and extremely metal-deficient stars. There are two reasons for this. Firstly the NS code only calculates the nucleosynthetic evolution, from a given set of quasi-static structural models. Supplying it with $Z = 0$ or extremely metal-poor models has no impact on its operation, although we note that the mesh resolution needed to be increased in some of the models due to the appearance of narrow radiative zones between convective zones. Secondly the NS code already treated convective mixing in a time-dependent manner, so the conditions given by the extreme events in our new models in which the mixing and burning timescales become comparable (ie. the Dual Flash events) were already taken into account.

The only significant modification we made during the course of this study was to remove the scaled-solar assumptions for the initial abundances. This allowed the use of custom-made initial compositions such as those of our $Z = 0$ and extremely metal-poor models.

3.2.5 Yield Calculation and Synthetic Pulses

Our yields are generally given in mass fraction of each species in the total ejecta (most of them are tabulated in the appendices). Thus the yields are always positive – unlike some definitions that take into account the initial composition of the models. In the tables we also give the initial stellar mass and final mass (remnant mass), as well as the initial compositions. Using this information it is easy to convert our yields to any format.

The yields are calculated by integrating the mass of each species lost by the star over its lifetime (τ_*):

$$M_i^{tot} = \int_0^{\tau_*} X_i(t) \frac{dM}{dt} dt \quad (3.12)$$

where X_i is the mass fraction of species i . The total mass of each species lost to the ISM, M_i^{tot} , is then scaled with M_{ej} , the total mass lost by the star, to give the mass fractions.

In some cases our models failed to converge towards the end of the AGB. This is a common problem with stellar codes. Often there was very little mass left in the envelope so this was just added to the yields. However in some cases there was enough mass left that it would not have been lost in one interpulse period. In these cases we did a short synthetic evolution calculation of the remaining thermal pulses (including third dredge-up and core growth) to complete the evolution, following the method of [Karakas \(2003\)](#). Yields were then calculated including the extra mass loss. In most models the number of thermal pulses calculated in this way was $\lesssim 8$. This represents between ~ 1 and 10% of the total number of thermal pulses in most of our models. Thus the synthetic pulses generally have a minor impact on the yields.

Chapter 4

Structural Evolution Code Modifications

”It’s better to light a candle than curse the darkness.”

– Chinese Proverb

4.1 Time-Dependent Mixing

4.1.1 Motivation

As discussed in section 3.1.3, the SEV code contains the assumption that the timescale of mixing in a convection zone is much smaller than that of the evolutionary timescale. This is implemented through the instantaneous mixing approximation whereby the abundances in any convective zone are mixed to homogeneity over the whole zone. This is done each iteration after the change in composition from nuclear burning has been applied. In the majority of situations involved in the evolution of low- and intermediate-mass stars this is a valid approximation. It reduces mixing to a very simple process, speeding up calculations.

However there do exist some evolutionary episodes in which physical changes are happening at a very high rate. During these episodes the timestep is reduced markedly in order to follow the evolution accurately. In these situations the timescale of mixing over a convective region can become comparable to the timestep being used. If this happens then the instantaneous mixing approximation is not valid and the time dependence of the mixing needs to be followed. The chemical profile in a convective zone at the end of a timestep will not be uniform (as it would be with instantaneous mixing) in this case, as the convective zone will be only partially mixed. In order to model these evolutionary episodes more properly the Author decided to modify the SEV code to include time-dependent mixing. In what follows we describe the mixing paradigm used as well as the practical details of the implementation (and testing) of the new time-dependent mixing subroutine.

4.1.2 The Diffusive Mixing Paradigm

As discussed in section 3.1.3, convection in stars is in general highly turbulent. Thus mass (and heat) movement is happening on all scales simultaneously – there is a spectrum of scales,

velocities, energies involved. Unfortunately it is still not feasible to model convection from first principles. Indeed, a full mathematical description of convection remains one of the Holy Grails of physics. Solving the Navier-Stokes equations is also unfeasible for evolutionary timescales such as those of stars, as the computational demand is enormous. We are thus left with the task of *approximating* the effects of turbulent convection (and mixing) in stars.

Also discussed in section 3.1.3 is the Mixing Length Theory (MLT) of convection. The MLT is the most commonly used formalism for convection in stellar models. In practice it provides a (locally determined) velocity and mixing length for each point in a convection zone, amongst other physical quantities. Like many other authors we have chosen to retain the MLT as the convection formalism for the SEV code.

In order to simulate the *mixing* in the convective zones in a time-dependent manner we need a reasonable physical/mathematical description of turbulent mixing. Due to the random motions in turbulent convection (as opposed to the regular turnover structures in the non-turbulent regime), the problem has been likened to a diffusion process whereby random mass motions gradually smooth out the composition gradient. Indeed, diffusion can be understood in the context of kinetic theory, whereby random motions of particles of say, a gas, which has a composition gradient, will over time smooth out the gradient (eg. Giancoli 1988). This process, which is related to the second law of thermodynamics, was first quantified by Fick (1855) and is known as Fick's Law:

$$J = -D \frac{dC}{dx}. \quad (4.1)$$

Here J is the rate of transport for the quantity, say 'particles' (so units are: particles per unit area per second), D the diffusion coefficient (area² per second), C the concentration (particles per unit volume), and x the distance. It can be seen that the flux of material is dependent on its gradient in space. A steeper gradient leads to a faster rate of redistribution. In terms of the second law of thermodynamics, the material tends towards a (system-wide) maximum in entropy (disorder) – a state of equilibrium. This happens spontaneously and without any loss of energy. The natural phenomenon of diffusion/entropy-maximisation has been observed in a huge number of systems. Some simple examples include: diffusion of water into spaghetti; diffusion of perfume around a room; diffusion of He out of a balloon. Other physical processes are also well described by diffusion, such as: heat conduction, momentum diffusion and electron diffusion. The main difference in all of the different scenarios lies in the diffusion coefficient D . The diffusion coefficient contains the physical information about each particular system. For instance characteristic D s in liquids are quite different to those of gases. However, a standard result from kinetic theory arguments gives a simple form of D , relating it to the *mean free path* l_m of the moving material and its characteristic velocity v (in the direction of diffusion):

$$D = \frac{1}{3} v l_m \quad (4.2)$$

Thus, if we accept that turbulent mixing can be described as a diffusion process (ie. Fickian

transport), and if we have some information about the mean free path of convecting parcels and their velocities then we can make an order of magnitude estimation of the diffusion coefficient in stars.

Early stellar modellers first applied the concept of diffusion to the problem of semiconvection (eg. [Simpson 1971](#); [Sreenivasan and Ziebarth 1971](#)). It was needed in this regime of mixing because semiconvection is thought to cause a slow redistribution of chemical elements (see below for a discussion of semiconvection) and thus warranted the use of time-dependent mixing. Other descriptions of semiconvection had mimicked the essentially diffusive process of semiconvection by adjusting chemical profiles to achieve ‘convective neutrality’ (ie. $\nabla_{rad} = \nabla_{ad}$, eg. [Robertson and Faulkner 1972](#)). A year or so later the diffusive mixing approximation to turbulent mixing was introduced into some stellar evolution codes to calculate mixing over the entire star (eg. [Eggleton 1972](#); [Sackmann et al. 1974](#)). These authors both retained the MLT as the convection formalism. Of central importance to applying the diffusion approximation is the determination of a physically plausible diffusion coefficient. In his indomitable style, [Eggleton \(1972\)](#) chose a “naïve formula” for the turbulent mixing diffusion coefficient and stated that “...it is not necessary to have a physically correct expression in order to obtain sensible answers.”. However, he did construct his formula based on order of magnitude physical estimates. [Sackmann et al. \(1974\)](#) take a more pragmatic approach, taking the diffusion coefficient as:

$$D = v_{conv} l_{mix} \quad (4.3)$$

where v_{conv} and l_{mix} are the local convective velocity and mixing length, as calculated from the MLT. This is basically equation 4.2. As the MLT is a crude approximation to turbulent convection, this can only be taken as an order of magnitude estimate, and the factor of $\frac{1}{3}$ in equation 4.2 is irrelevant.

Equation 4.1 is actually Fick’s 1st Law, describing steady state diffusion. Fick’s 2nd Law describes the more common case of non-steady state diffusion. It is known as the standard diffusion equation:

$$\frac{dC}{dt} = \frac{\partial}{\partial x} \left(D \frac{\partial C}{\partial x} \right) \quad (4.4)$$

in the case of one spatial dimension. In the SEV code we use mass as the independent variable and assume spherical symmetry, so the diffusion equation becomes:

$$\frac{dX_i}{dt} = \frac{\partial}{\partial m_r} \left(\sigma D \frac{\partial X_i}{\partial m_r} \right) \quad (4.5)$$

where

$$\sigma = (4\pi r^2 \rho)^2 \quad (4.6)$$

and we have changed to the usual stellar notation of X_i representing each chemical species that will be transported. Equation 4.5 is the one we have applied to turbulent mixing in the SEV code. Diffusion equations have the added advantage in that there are good numerical methods to solve them. The next section describes the implementation of Equation 4.5 in the new time-dependent-mixing subroutine.

4.1.3 Choice of Implementation Method

We begin by noting that there are a few different ways in which the new mixing paradigm could be implemented in the SEV code. As the rate of nuclear burning in a star is partly tied to the local composition, and mixing alters that composition, it is sensible to say that the mixing and burning are *coupled*. Taking account of this coupling would lead to an equation for composition change:

$$\frac{dX_i}{dt} = \left(\frac{\partial X_i}{\partial t} \right)_{nuc} + \frac{\partial}{\partial m_r} \left(\sigma D \frac{\partial X_i}{\partial m_r} \right) \quad (4.7)$$

(eg. Sackmann et al. 1974) which is just Equation 4.5 with the sources and sinks from nuclear reactions summarised in the first term on the right. Furthermore, there will be (some) feedback on the structure itself if the nuclear rates are significantly altered, implying that Equation 4.7 should be coupled with the equations of stellar structure. The next question is: how does this fit in with the SEV code? The SEV code traditionally applies convective mixing after 1) calculating the (approximate) structure and 2) applying the changes in composition due to nuclear burning. This is done in a series of iterations. In this context it appears we have three possible scenarios for implementing diffusive mixing:

1. Keep the current method of mixing each convection zone each iteration, giving a ‘semi-coupled’ evolution, ie. just replace the the instantaneous mixing with Equation 4.5.
2. Apply a coupled mix and burn each iteration, so the burning and mixing are fully coupled and the chemical changes are ‘semi-coupled’ to the structure, ie. replace the current method of calculating the chemical changes due to nuclear reactions *and* the instantaneous mixing by Equation 4.7.
3. Solve Equation 4.7 for each species simultaneously with the structure equations in the Henyey matrix, ie. fully-couple structure and composition change.

At first glance, it appears that the most self-consistent method would be that of (3). However it can be argued (Wood and Lattanzio 2006, private communication) that an iterative solution (ie. method (1)) would give the same result as a fully coupled solution. Indeed, in the SEV code

and many other stellar codes, the nuclear burning and mixing are always treated in an iterative fashion. The fact that the models produced by these codes are not significantly different to fully coupled codes (also known as fully-simultaneous codes) suggests that the iterative method is equivalent to the fully-coupled method. Recent work using an updated version of the fully-coupled Cambridge University STARS code by Pols and Tout (2001) shows that this is indeed the case, at least for AGB stars. They state that their results are comparable to those from the SEV code. Wood and Lattanzio argue that all the equations would be essentially solved together with successive substitutions in the diffusion equations after each Henyey (structure) iteration. Wood also notes that convergence would probably be slower for method (1) than for an explicitly fully-coupled method, but that the iterative method may actually be more *stable* because of the slower convergence. Stability is certainly a sought-after characteristic for stellar evolution codes.

The initial decision taken by the Author was to implement method (1) and then method (3) in order to compare the results of each method directly, without the added uncertainties of comparing different codes. However, due to time constraints, only method (1) was completed in time for this thesis. Given the arguments above it seems that this should be a reasonable approach.

4.1.4 Choice of Numerical Method

Given the context just discussed above, we now describe the procedure taken to replace the instantaneous mixing procedure with Equation 4.5.

Overview and External Testing

The first step in adapting differential equations to numerical/computational work is to difference the equations. There are many methods for differencing equations, with each method having certain desirable or undesirable qualities. The methods basically fall into three groups: explicit, implicit and hybrid (a combination of explicit and implicit). Explicit methods are not usually used for stellar evolution. The reason for this is that they become unstable when using large timesteps such as those required to model stars. The approximate point at which explicit methods become unstable (giving unphysical random or periodic solutions) is given by the well-known Courant condition (Equation 4.15). The benefit of explicit methods is that they are accurate when they are stable. This contrasts with implicit methods which are unconditionally stable with any sized timestep (ie. no Courant condition) but can suffer from inaccuracies if the timestep is too large. Hybrid methods combine the explicit and implicit methods and have qualities stemming from both methods. They maintain stability for much longer timesteps than explicit methods but do have the equivalent of a Courant condition above which they are unstable. However they are more accurate (in general) than implicit methods while they are stable. The reason we describe these methods here is because we have run tests on the diffusion subroutine using a variety of differencing methods, to check for accuracy and stability. We tried three different differencing methods:

1. Our simple implicit method obtained by directly differencing Equation 4.5 (see eg. Press et al. 1992):

$$\frac{X_j^{t+1} - X_j^t}{\Delta t} = \sigma_{j+\frac{1}{2}}^2 D_{j+\frac{1}{2}} \left(\frac{X_{j+1}^{t+1} - 2X_j^{t+1} + X_{j-1}^{t+1}}{(\Delta m)^2} \right) \quad (4.8)$$

where t represents the timestep, j the mesh point and $\sigma = (4\pi\rho r^2)$. Note that Δm , ρ and D are constant in these tests. The physical values at $j + \frac{1}{2}$ are taken as averages except for D where we follow Meynet et al. (2004):

$$D_{j+\frac{1}{2}} = \frac{D_{j+1}D_j}{fD_{j+1} + (1-f)D_j} \quad (4.9)$$

which allows the smallest diffusion coefficient to dominate between mesh points. This formula for D is used in all the following methods also.

2. The implicit method described in Meynet et al. (2004) (they make an approximation to reduce the second order equation to first order) adjusted to the SEV code formalism of meshpoint numbering starting at the centre rather than the surface:

$$\begin{aligned} \frac{X_j^{t+1} - X_j^t}{\Delta t} = & -\frac{\sigma_{j-\frac{1}{2}}}{\Delta m} D_{j-\frac{1}{2}} \left(\frac{X_j^{t+1} - X_{j-1}^{t+1}}{r_j - r_{j-1}} \right) \\ & + \frac{\sigma_{j+\frac{1}{2}}}{\Delta m} D_{j+\frac{1}{2}} \left(\frac{X_{j+1}^{t+1} - X_j^{t+1}}{r_{j+1} - r_j} \right) \end{aligned} \quad (4.10)$$

3. The Crank-Nicholson method described in Meynet et al. (2004), also adjusted for the SEV code formalism.

All these methods reduce to solving a set of simultaneous linear algebraic equations. The systems of equations are all tridiagonal thus easily solved using standard methods. As an example we show the set of equations we solve for one of the implicit schemes (the modified version of the Meynet et al. scheme), rearranged ready for numerical coding:

$$\begin{aligned} X_j^t = & \left(1 + \frac{[j, j-1]}{\Delta m_j} + \frac{[j+1, j]}{\Delta m_j} \right) X_j^{t+1} \\ & - \left(\frac{[j, j-1]}{\Delta m_j} \right) X_{j-1}^{t+1} - \left(\frac{[j+1, j]}{\Delta m_j} \right) X_{j+1}^{t+1} \end{aligned} \quad (4.11)$$

where, for example:

$$[j, j-1] = \Delta t \frac{4\pi r_{j-1/2}^2 D_{j-1/2}}{r_j - r_{j-1}}.$$

Boundary conditions were taken such that the flux at the centre and surface is zero:

$$\left(\frac{\partial X_i}{\partial m} \right)_{cent} = \left(\frac{\partial X_i}{\partial m} \right)_{surf} = 0$$

which, from Equation 4.11 implies we have at the centre (where $j = 1$):

$$X_1^t = \left(1 + \frac{[2, 1]}{\Delta m_1}\right) X_1^{t+1} - \left(\frac{[2, 1]}{\Delta m_1}\right) X_2^{t+1} \quad (4.12)$$

and at the surface (where $j = jm$):

$$X_{jm}^t = \left(1 + \frac{[jm, jm - 1]}{\Delta m_{jm}}\right) X_{jm}^{t+1} - \left(\frac{[jm, jm - 1]}{\Delta m_{jm}}\right) X_{jm-1}^{t+1}. \quad (4.13)$$

To solve the matrix system we employed the subroutine from Numerical Recipes called *TRIDAG* (Press et al. 1992). The diffusive mixing subroutine is named *diffuse* (in *diffusion.f*) and is called by *abund-diffn* which is a modified version of the original SEV code subroutine *abund.f*.

In order to have some sort of reliable benchmark comparison for the above methods, we also coded an explicit method differenced in the following way:

$$\frac{X_j^{t+1} - X_j^t}{\Delta t} = \sigma_{j+\frac{1}{2}}^2 D_{j+\frac{1}{2}} \left(\frac{X_{j+1}^t - 2X_j^t + X_{j-1}^t}{(\Delta m)^2} \right) \quad (4.14)$$

which is the same as Equation 4.8 except it only uses information at the current timestep t to evaluate the values at the next timestep $t + 1$. When calculating diffusion using this method we always maintained the timestep well below that required for stability by the Courant condition:

$$\Delta t \ll \frac{(\Delta r)^2}{2D} \quad (4.15)$$

The practicality of making comparisons in this way is limited by the timesteps for the explicit method, as they are so tiny (often $< 1\text{yr}$). Here we have limited our tests to an evolutionary time interval of 3000 yr, which is not unreasonable for a single timestep in a stellar evolution calculation (depending on the evolutionary phase). We initially tested the different differencing methods outside the SEV code, by setting up an artificial chemical profile (single element) in a constant density model with uniform mass spacings Δm . The diffusion coefficient was taken as a step function with radiative (non-convective) zones on either side of a uniformly convective shell. This setup was designed to mimic a convective nuclear burning shell. Figure 4.1 displays the results of one of the tests. The main results were 1) both the implicit and Crank-Nicholson (CN) methods had significant errors and 2) the implicit methods gave quite smooth profiles (although inaccurate) whilst the CN method gave an almost random profile.

To check the dependence of accuracy on timestep we reduced the timestep for the non-explicit methods to 100 yr. Figure 4.2 shows the results of this test. Reducing the timestep by an order of magnitude and consequently taking a series of steps within the evolutionary timestep of 3000 years increased the accuracy dramatically, although the CN method still gave a non-smooth profile. Further tests revealed that the CN requires a very small timestep to return smooth results, though not as small as that needed for the explicit method.

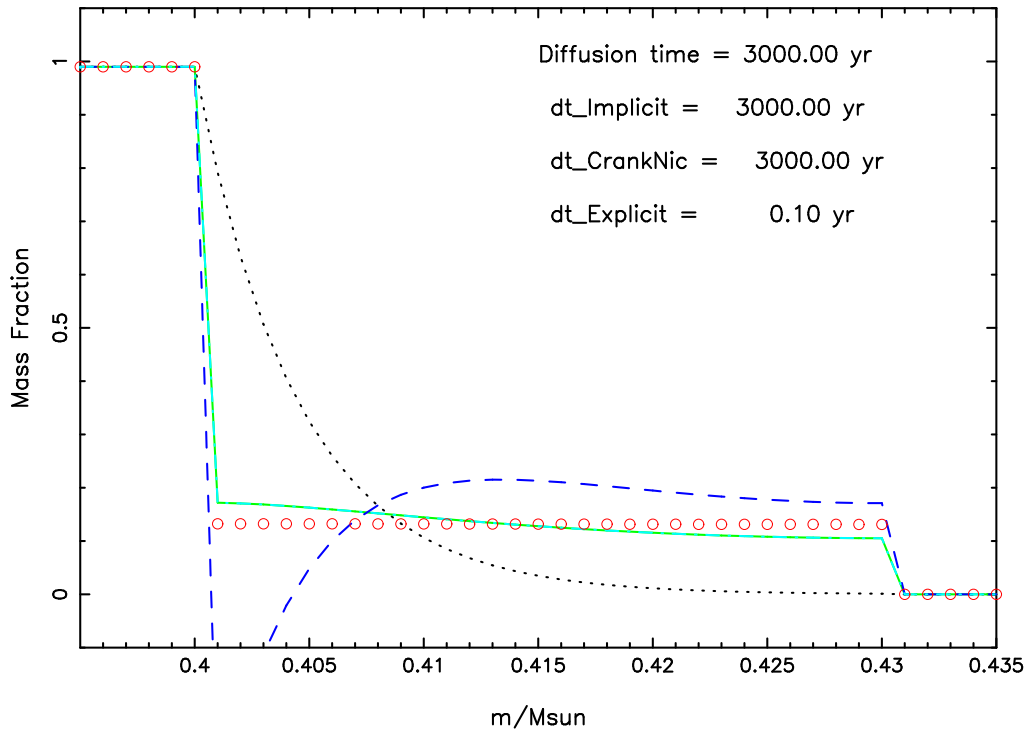


Figure 4.1: Initial testing of the diffusion subroutine (outside SEV code). The initial composition profile (dotted line, black) was designed to mimic the main product of a burning shell (eg. helium). The smoothly varying section of the initial profile resembles a build-up of composition after one timestep due to nuclear fusion. Normally this region would be homogenised by the instant mixing routine. The diffusion coefficient was taken as zero in the regions $m < 0.4$ and $m > 0.43$ to represent radiative zones around a convective shell with a moderate diffusion coefficient (one that results in the homogenisation of the region in < 3000 years, ie. as given by the explicit scheme with red circles). The simple model has $M = M_{\odot}$ and is of constant density. Resulting profiles from four differencing methods are plotted: 1) Our implicit (solid green line), 2) Meynet et al. 2004 implicit (dash-dot cyan line), 3) Crank-Nicholson (dashed blue line), and 4) Our *explicit* method (circles, red). The red circles also indicate the mesh spacing, which is the same for all cases. Note that the two implicit scheme lines overlay each other in the graph. The explicit method was given a timestep small enough to stay under the Courant condition (0.1 yr), while all the other methods had a single timestep of 3000 yr. All the diffused profiles should end up going through the red circles. It can be seen that, while all the non-explicit methods are quite inaccurate (with the given conditions), the implicit methods give smooth results whilst the hybrid Crank-Nicholson gives a result very far from the explicit solution. In fact the CN method gives ‘non-physical’ results such that the abundance profile becomes negative in one region. Note that the final profiles from both implicit methods are practically identical.

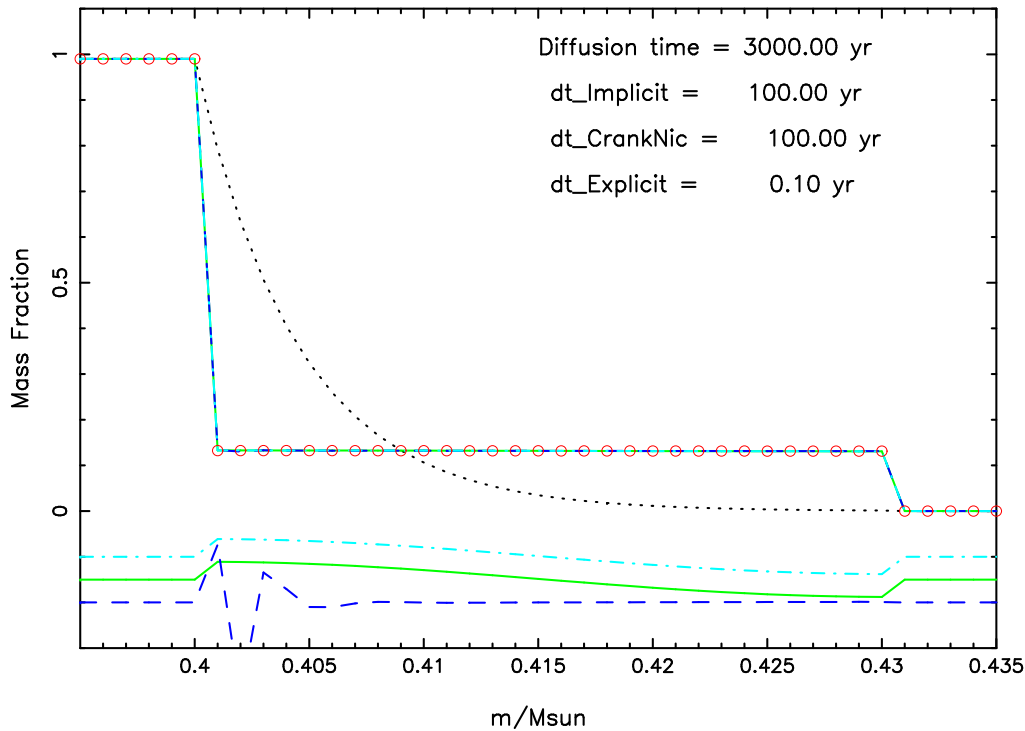


Figure 4.2: Same as Figure 4.1 except the timestep for the non-explicit methods has been reduced to 100 yr, resulting in 30 timesteps within the evolutionary timestep of 3000 yr. The three lines at the bottom are the differences between each non-explicit method and the explicit method, multiplied by 10^3 , to give an indication of error. It can be seen that all methods performed much better with the smaller timestep, as all the curves are very close to the explicit method’s solution. Again, the implicit methods give a smooth profile whilst the Crank-Nicholson is non-smooth.

Another interesting result from the testing is displayed in Figure 4.3. The plot shows the resulting composition profiles after only one sub-evolutionary timestep. Large errors can be seen in all the results, although again the implicit method results are smooth whilst the CN method results are disjointed. These results are interesting because the results by the end of the timestepping (previous plot, Figure 4.2) show very little error, despite going through this initial inaccurate stage. Comparing all three test Figures suggests that the main driver of error (in the non-explicit methods) is not the size of the timestep but the size of the composition jump – ie. how much movement of material there is during the timestep. This implies that the key issue in maintaining accuracy in the diffusion routine is to place a limit on the amount of material diffused in one timestep. This could also be achieved by limiting the amount of material burnt in an evolutionary timestep. Alternatively the evolutionary timestep could be divided into many ‘diffusion timesteps’, as the profile obtained in the case with small timesteps (Figure 4.2) was much more accurate than that when using a single large timestep (Figure 4.1).

Another important conclusion drawn from these tests was that the implicit methods are the only practical methods to include diffusion in the stellar evolution code. The reason for this is that it is totally impractical to use timesteps as small as are needed for stability by the explicit and CN methods. Although the implicit methods give somewhat inaccurate results (although stable) we believe that this is not a significant problem as there are many uncertainties in the turbulent diffusive mixing paradigm itself. For instance, the diffusion coefficient, which determines the rate of diffusion, is based on the velocities and length scales given by the MLT (Equation 4.2), which

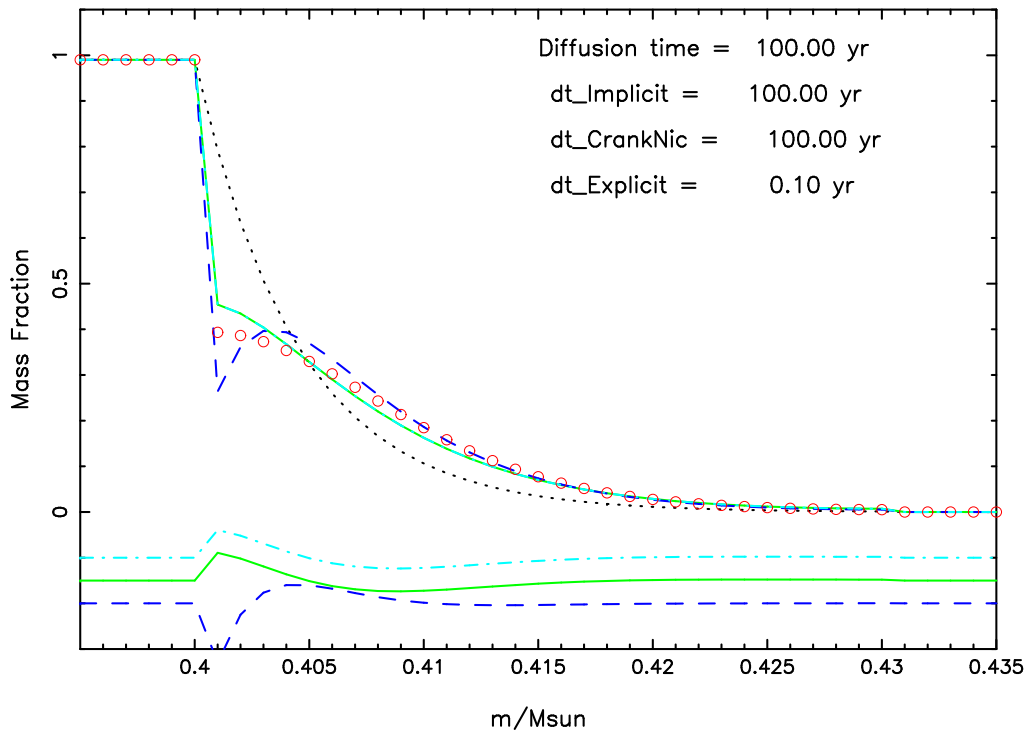


Figure 4.3: Same as Figure 4.2 except that the results for the first timestep are plotted (rather than for the final timestep). The errors have *not* been magnified. In this case the chemical profile has not had time to homogenise over the shell, resulting in an intermediate profile (ie. as given by the explicit case, red dots). It can be seen that there are substantial errors in the abundance distributions after a single timestep despite the good results seen in Figure 4.2 after completing all the timesteps. This suggests that the driving source of error is the change in profile over the timestep rather than the timestep itself, indicating that the best approach is to limit the amount of change in each timestep.

is in itself a rough approximation of convection (see section 3.1.3). Based on an investigation which mainly focused on stability (as opposed to accuracy), Meynet et al. (2004) also recently came to the conclusion that implicit finite difference methods are the best to use for diffusion in stellar modelling.

Grafting the Diffusion Routine to the SEV Code

The vast majority of the time taken in implementing turbulent diffusive mixing was spent installing the subroutine into the SEV code. Interfacing the codes proved to be more difficult than expected. However the implementation was successful in the end.

Given that the two different implicit methods give almost identical results and that they both share the same matrix solver, we decided to implement both schemes to enable comparisons within the SEV code. The instantaneous mixing routine was retained, and a switch added in the code so the operator can choose one of three mixing scenarios:

1. Instantaneous mixing all the time
2. Instantaneous mixing with a mixing timescale test that invokes the diffusion routine if needed
3. Diffusive mixing all the time

Mass conservation is a prime requirement of the diffusion routine. In order to check this we sum the mass of each chemical species before entering the diffusion routine:

$$\sum_{j=1}^{jm} \Delta m_j W_{j+\frac{1}{2}} \quad (4.16)$$

where W is the variable used for abundance in the SEV code. After the profile is diffused the same sum is calculated and compared with the original. If they differ than more than a prescribed limit (say ϵ_W) then the evolutionary timestep is reduced and the model recalculated. This is quite a stringent test as the errors are summed over *every mesh point*, although it does depend on the value taken for ϵ_W , which we have initially chosen to be 10^{-7} . Initial testing showed that the method of Meynet et al. (2004) (Equations 4.10 and 4.11) conserves mass better than the other method, so we have retained it as the default method for diffusion. Mass conservation is observed to improve as the timestep is decreased, as expected from the external testing. In the SEV code the timestepping is controlled by parameters that limit the changes of various quantities (eg. the luminosity, density, etc.). Of particular relevance to the diffusion routine is the STW parameter, which tracks the abundance changes in time and is used to limit the timestep if changes are occurring too quickly. It was found that this existing control parameter is ideal for limiting the errors in the diffusion routine, as they appear to be dependent on the degree of change in chemical profile. As a further check for the degree of mass conservation needed in practice, we also calculated the mass sums of each element before and after the nuclear burning was calculated. It was found that the errors were sometimes as high as 10^{-6} . Again this is the

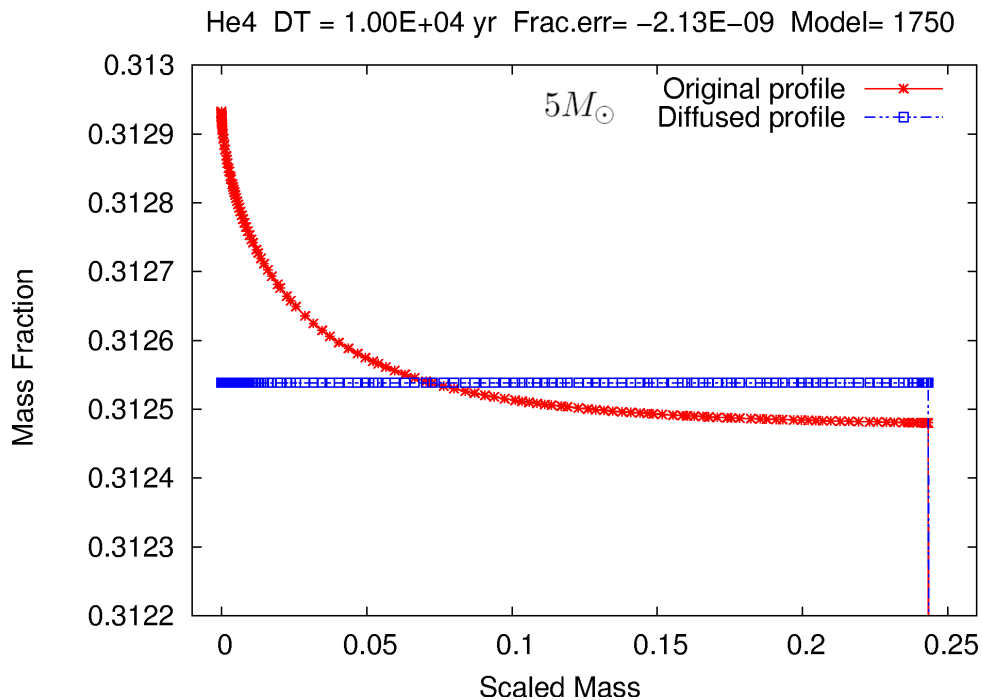


Figure 4.4: In situ testing of the diffusion routine. The stellar model has a mass of $5 M_{\odot}$ and is on the main sequence so it has a convective core and a radiative envelope (the model started with $Y = 0.25$). This particular model has a timestep of 10^4 yr. Plotted in red is the ${}^4\text{He}$ profile in the core after the nuclear burning has been calculated (during one iteration). The blue line is the ${}^4\text{He}$ profile after applying the diffusion. It can be seen that the mixing timescale is easily shorter than the evolutionary timestep as the profile is completely homogenised at the end of the timestep. Also of note is the small scale of abundance inhomogeneity before it enters the diffusion routine. This leads to the small error in the sum of Y ($\sim 10^{-9}$). The markers on each line represent the mesh points.

error summed over all points in the star. Thus we believe using $\epsilon_W = 10^{-7}$ should be of sufficient accuracy in practise.

Figure 4.4 shows the diffusive mixing subroutine in action in a real stellar model. A very simple case has been chosen here – a $5 M_{\odot}$ low metallicity star on the main sequence (MS). The ${}^4\text{He}$ profile in the core is plotted after the nuclear burn had been calculated and again after diffusion was applied. The initial profile shows that an increase of helium mass fraction of $\sim 10^{-4}$ has been produced via hydrogen burning. After the diffusion is applied the distribution is flat, indicating that the timescale of mixing is much smaller than the evolutionary timestep of 10^4 yr. Mass is conserved adequately in this example, deviating by $\sim 10^{-9}$.

The next example (Figure 4.5) is from the same star but later in its evolution. Here we choose a different type of convection zone – the convective intershell during a He flash on the AGB. In this case helium is burning at the base of the convection zone (creating the convective zone), mainly producing carbon. As can be seen, the initial abundance profile is qualitatively similar to the previous example. Despite the small timestep of $\sim 10^{-2}$ yr, the mixing timescale is again much shorter than the evolutionary timestep resulting in a flat profile. The error in this example is quite small, being $\sim 10^{-14}$ when summed over every mesh point.

Our final example is taken from one of the models calculated for this thesis. Plotted in Figure 4.6 are a series of ${}^{12}\text{C}$ abundance profiles taken during the dredge-up of the entire AGB intershell in a hyper-metal-poor star of $2 M_{\odot}$ (the model included overshoot on the AGB). In this case it

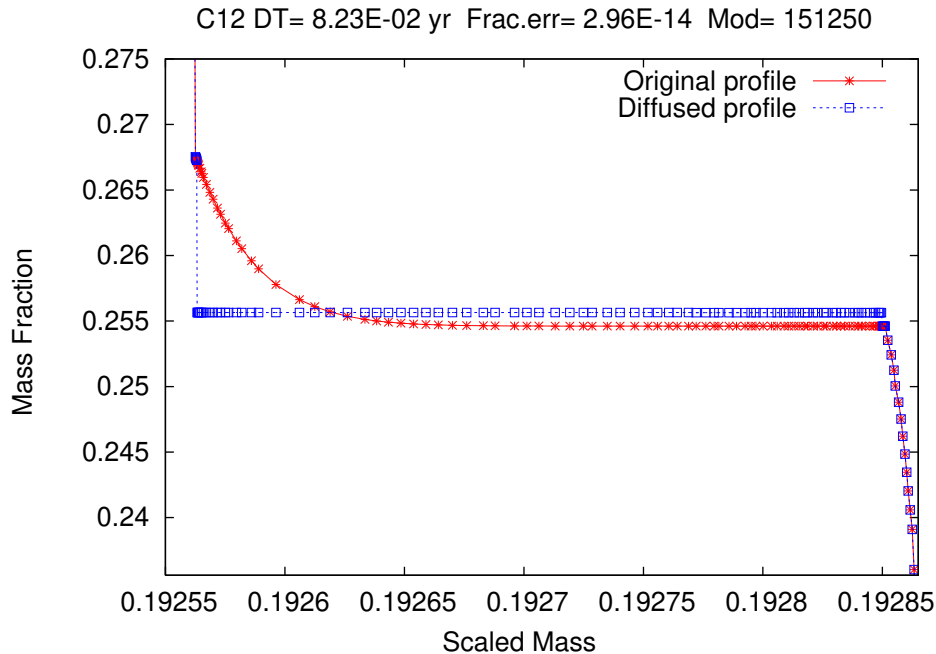


Figure 4.5: The same as Figure 4.4 but during the AGB evolution and for ^{12}C . The region plotted is the convective intershell during a He flash. Again the timescale of mixing is much smaller than the timestep ($\sim 10^{-2}$ yr), as evidenced by the flat composition profile after diffusion. The mass conservation is very good ($\sim 10^{-14}$).

can be seen that the mixing timescale is much *longer* than the evolutionary timescale, leading to incomplete mixing throughout the convective envelope. The plot shows the gradual mixing out of ^{12}C over 1000 timesteps. The chemical profiles are reminiscent of classical diffusion profiles. In this case instantaneous mixing would have been a poor approximation.

Based on the above empirical tests we conclude that the diffusion subroutine is performing well, although, as always, there are more tests that could be undertaken. In particular we believe it would be possible to use the explicit differencing method on selected stages of evolution in order to test the accuracy of the implicit method. This would be time consuming but computers are fast enough to do this test in a reasonable amount of time now. Another check that could be performed would be to improve the mass conservation of the routine. Although the routine performed very well outside the SEV code, it does not do quite as well inside the SEV code. However we currently have checks to keep the errors within reasonable bounds, as described above, and the in situ empirical tests show that the errors are not excessive in practise.

We now move on to treat two major uncertainties in stellar evolution calculations, overshoot and semiconvection – taking into consideration the new mixing paradigm.

4.1.5 Diffusive Overshoot

An overview of overshoot is given in section

3.1.3. Here we describe the implementation of a new formalism for overshoot in the SEV code.

As mentioned in section 3.1.3, there are a number of methods for including overshoot in stellar modelling. Seeing as we now have mixing being treated time-dependently, it is a natural pro-

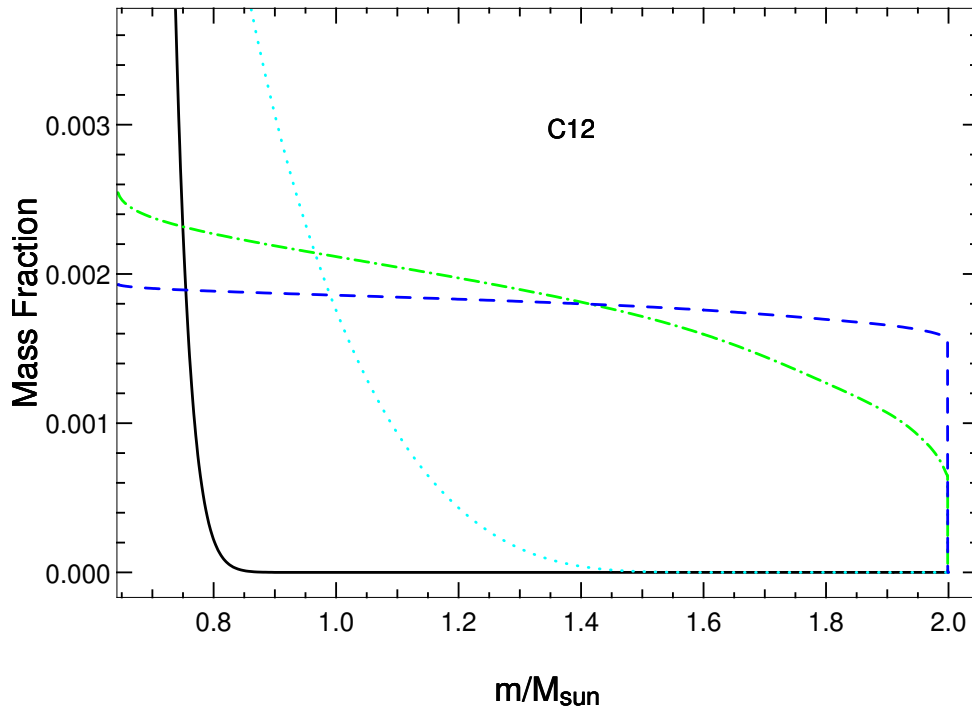


Figure 4.6: A series of ^{12}C abundance profiles taken at different timesteps. The star has a mass of $2 M_{\odot}$ and is hyper metal-poor ($[\text{Fe}/\text{H}] = -5.5$). The profiles are taken at consecutive stages during the dredge-up of the entire intershell after a very strong H-flash near the start of the AGB (overshoot was included in this model). The solid line is first in time, showing that the convective envelope initially has almost zero ^{12}C . The dashed line is the final profile plotted, whilst the other two are taken at intermediate timesteps. It can be seen that in this case the mixing timescale is much *longer* than the evolutionary timestep, as it takes many timesteps to diffuse the material out to the surface. The number of models between the first profile and the last profile is 1000, whilst the evolutionary timesteps were of the order 10^{-3} yr, so the time span represented in the figure is ~ 1 yr.

gression to treat overshoot time-dependently. Indeed, the problem is simplified in some regards as one can explicitly specify that a certain number/range of points beyond the edge of a convective zone have mixing velocities, and hence artificially create an overshoot zone. However, as mentioned earlier, the problem with overshoot is knowing how *far* to overshoot. Numerical simulations of convection (eg. Singh et al. 1995; Freytag et al. 1996) have suggested that the velocity profile reduces in an exponential fashion from the edge of a convection zone. Recently Herwig et al. (1997) implemented the parameterised results of the Freytag et al. (1996) numerical simulations into their stellar evolution code. Since then many authors have applied similar methods (eg. Goriely and Siess 2004; Ventura and D’Antona 2005a). The approach taken by Herwig et al. (1997) makes use of the local ‘velocity scale height’:

$$H_v = f_{OS} H_p \quad (4.17)$$

where H_p is the local pressure scale height and f_{OS} is a scaling factor. This is used in equation (3) in Herwig et al. (1997) to produce an expression for the exponentially reducing diffusion coefficient profile:

$$D_{OS} = D_0 e^{-\frac{2z}{H_v}} \quad (4.18)$$

where $D_0 = v_0 H_p$ is the diffusion coefficient just inside the formal convective boundary (v_0 is the corresponding velocity given by the MLT) and z is distance from the same boundary.

We chose to use Herwig’s formalism in the SEV code. Implementation was a simple procedure, as it just required the addition of a velocity profile described by Equation 4.18 onto the existing velocity profile in each convective region. The extra mixing alters the composition profile and then feeds back on the structure.

Testing the Diffusive Overshoot Routine

In Figure 4.7 we give an example of the resulting profiles when using the new diffusive mixing overshoot procedure, as compared to using a ‘hard’ Schwarzschild boundary. The stellar model used is the same as that in Figure 4.4, a MS star with a mass of $5 M_\odot$. It can be seen that the abundance profile from the run with overshoot switched on has a significantly larger core mass (increasing from ~ 0.24 to $\sim 0.28 M_\odot$, or $\sim 15\%$). Having a greater mass in the convective core leads to a longer MS lifetime as the star has more fuel to burn. It also leads to a higher core mass at the end of the MS and thus affects the later stages of evolution.

The other main difference is the smoothness of the profile on the edge of the convective zone. This is formed due to the smoothly reducing velocity profile. Without overshoot the core abundance profile has a sharp edge. The smoothness of the abundance profile is of particular interest in low mass stars towards the end of core helium burning. With a strict Schwarzschild boundary there is a growing discontinuity in the opacity at the edge of the core (due to the composition difference between the material inside and outside the core) that becomes quite large as the core helium depreciates. Just how rigid this boundary is is debatable but it seems reasonable to say that it is not perfectly impenetrable. Any mixing across the boundary (say through semiconvection)

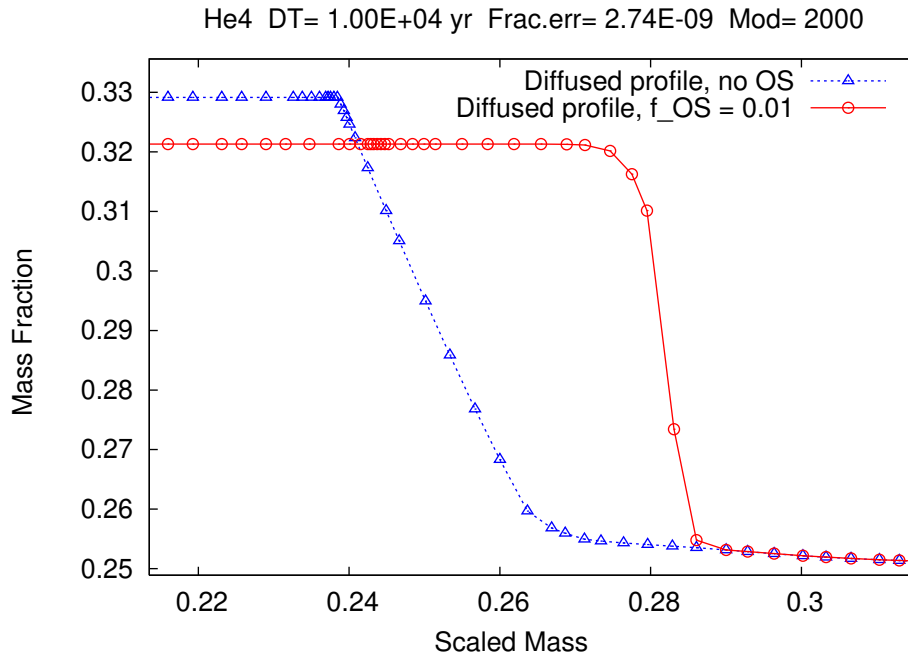


Figure 4.7: Comparison between models with and without diffusive overshoot. The region shown is the edge of the convective cores in two $5 M_{\odot}$ stars. Both stellar models were run with diffusive mixing but one had overshoot switched on a few hundred models before the timestep plotted. The two main effects of including diffusive overshoot can be seen: 1) the core is larger (an increase of $\sim 15\%$ in mass) and 2) the abundance profile at the edge of the core is smoother.

whilst the opacity discontinuity is large would cause the regions just outside the convection zone to also become convective due to an increase in opacity, thereby increasing the mass of the convective core. Through the addition of a slower velocity drop-off on the edge of the convective core, the diffusive overshoot routine naturally gives some slow mixing in the tail of the velocity profile. This leads to quite different results at the start of the He shell burning stage. Figure 4.8 shows the situation at the end of core helium burning with and without diffusive overshoot. The profiles are quite different, the first being basically a single step function as the core has not mixed out at all, and the second being a series of steps. The profile from the overshooting model results from a series of ‘core breathing pulses’ in which the core repeatedly expands due to an entrainment of extra He fuel (see eg. [Castellani et al. 1985](#); [Sweigart 1991](#); [Straniero et al. 2003](#)). The sudden expansion and contraction (in mass) leaves behind a series of steps in the composition profiles.

The difference in abundance profiles has a profound effect on the subsequent helium shell burning phase after core helium burning is completed. Figures 4.9 and 4.10 compare the subsequent (luminosity) evolution of the stars in Figure 4.8, ie. overshoot versus no overshoot. In Figure 4.9 (the model with no overshoot) it can be seen that the helium luminosity drops significantly when helium is finally exhausted in the core. Then there is a series of ‘pulsations’ of helium burning before the star settles into a stable He shell burning configuration. This phenomenon has been noted before and it was [Bono et al. \(1997\)](#) who coined the term ‘gravonuclear loops’ (GNLs) to describe it. [Bono et al. \(1997\)](#) studied gravonuclear loops in some detail and note that [Schwarzschild and Härm \(1965\)](#) found the same instability in a $1 M_{\odot}$ star. [Schwarzschild and Härm \(1965\)](#) subsequently performed an analytical analysis to see if we would expect an

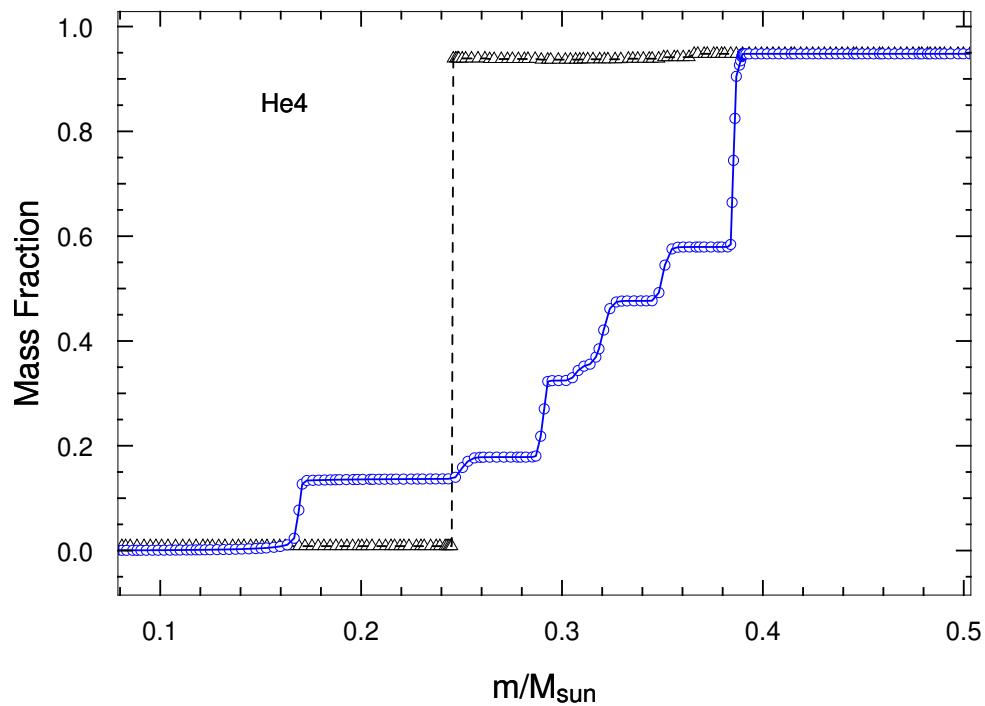


Figure 4.8: The ${}^4\text{He}$ profiles of two $1 M_{\odot}$ stars near the end of core helium burning. Both were calculated using the new diffusive mixing subroutine. One has no overshoot (dashed line, black) and one had overshoot switched on half way through core helium burning (solid line, blue). The overshoot parameter had a value: $f_{OS} = 0.01$. Markers represent the mesh points. It can be seen that the model without OS retains a very strong discontinuity in the composition profile, arising from the hard Schwarzschild boundary that did not allow any mixing. This also means that there is a discontinuity in the opacity profile, and hence the radiative gradient. The model that includes OS on the other hand has an almost step-wise composition gradient which has resulted from core breathing episodes (see text for details).

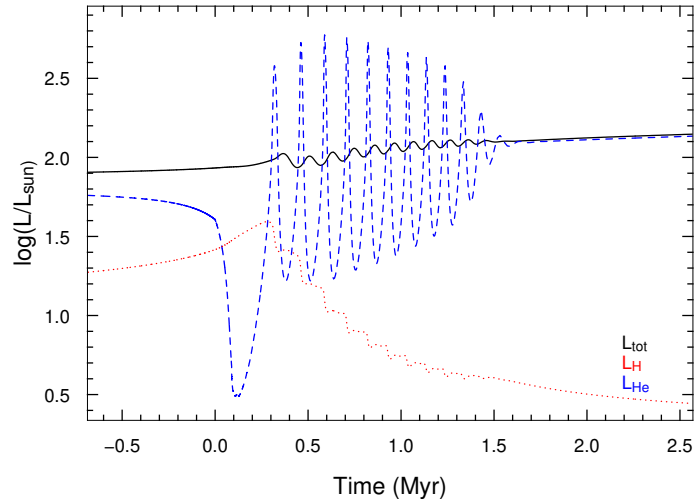


Figure 4.9: The subsequent evolution of the star in Figure 4.8 without overshoot. Plotted are the helium luminosity (dashed line), hydrogen luminosity (dotted line) and total luminosity (solid line). The zero point in time is taken (roughly) at the end of core He burning. The gravonuclear instability is clearly seen in the He luminosity evolution.

instability at this stage of evolution. They concluded that an instability should indeed arise – if the He burning shell is very thin. This differs from the conclusion of [Bono et al. \(1997\)](#) (based on super-metal-rich models with $m \sim 0.5 M_{\odot}$) who suggest that the driving factors for GNLs are 1) the opacity in the envelope (in particular the iron ‘opacity bump’ in these models, see their Appendix for details) and 2) the mass of the envelope. They also suggest that the instabilities are metallicity dependent, such that it is more common in stars with high metallicities. More recently [Sweigart et al. \(2000\)](#) performed some tests to see if the method of suppressing core breathing pulses has an impact on the occurrence of GNLs. They concluded that this was actually the prime driver for GNLs, as it determines the nature of the helium profile at the start of the shell helium burning stage. Methods that gave a thin burning shell resulted in GNLs whilst methods that had a smoother profile give a thicker He burning shell, thus avoiding the instability. This is in line with the analysis by [Schwarzschild and Härm \(1965\)](#) and is also supported by Figures 4.8 - 4.11 here. They also conclude that the effect is not dependent on metallicity or the mass of the envelope, in variance with [Bono et al. \(1997\)](#).

In Figure 4.10 we show the case in which diffusive overshoot was included. It can be seen that GNLs do not arise, due to the less abrupt He profile and resulting thicker He burning shell. In Figure 4.11 we plot both cases in the L - T_{eff} plane, in which the loops are very evident.

How Far to Overshoot?

We now return to the perennial question for any method of overshoot – how far do we extend the convective boundary beyond the formal one?

The degree of overshoot in the diffusive mixing overshoot method is governed by f_{OS} . By varying this parameter one can have as much or as little overshoot as one would like. This leads to different core masses on the MS and HB and consequently affects the later stages of stellar evolution. In order to gauge what value of f_{OS} to use as a standard we performed comparison tests between the original SEV code (which uses instant mixing and a traditional overshooting

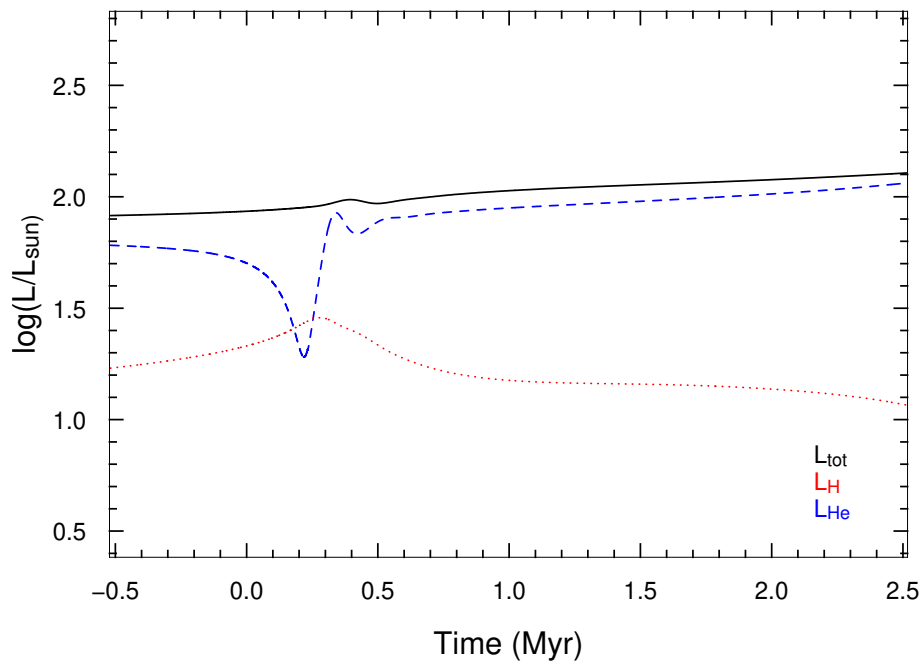


Figure 4.10: Same as Figure 4.9 but for the star with overshoot. The axes are on the same scale as Figure 4.9 to enable direct comparison. As can be seen the instability does not arise in this model, as the more gradually changing He profile leads to a thicker He burning shell (see text for more details).

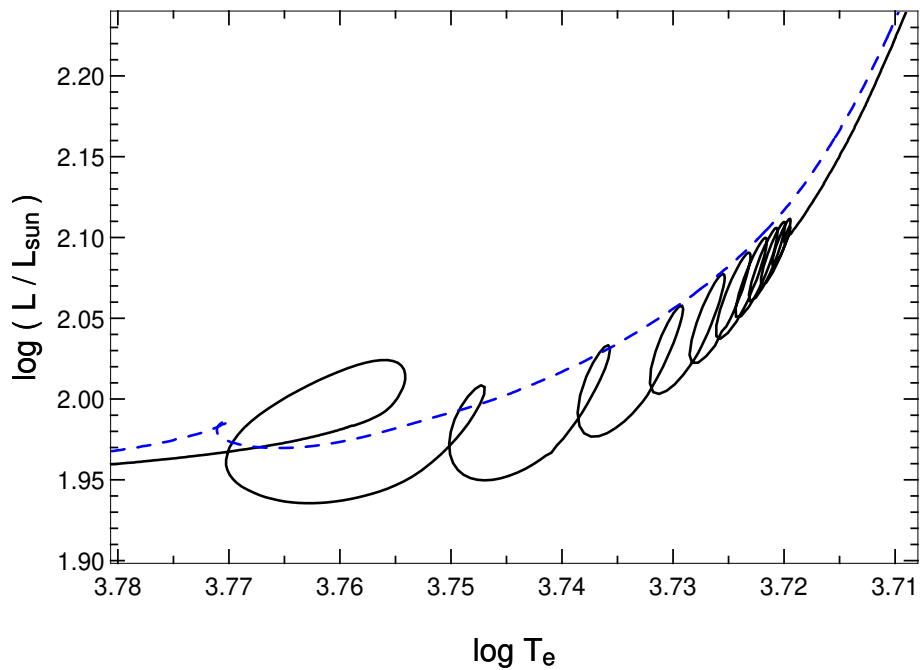


Figure 4.11: The same stars as in Figure 4.8 but showing the gravonuclear loops in the H-R plane. The dashed line is the model with diffusive overshoot (no GNLs) whilst the solid line is the model without overshoot.

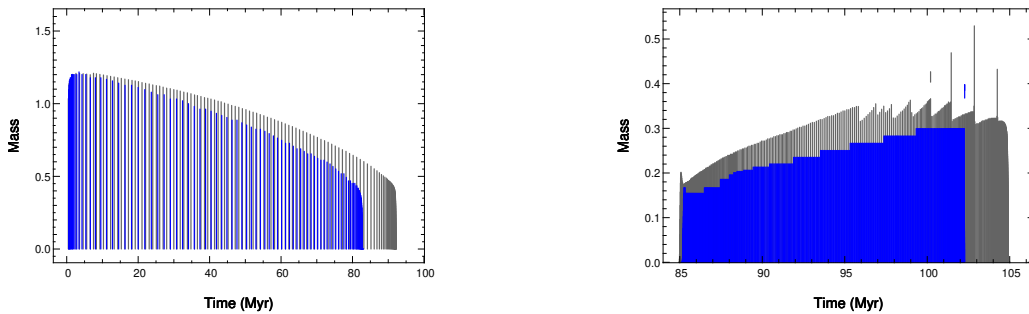


Figure 4.12: Comparison between the original SEV code and the version with diffusive mixing and overshoot (and updated opacities). The vertical lines represent convection zones (where the velocity is non-zero). The results from the original code are in blue whilst those from the modified code are in grey. Both stars have a mass of $5 M_{\odot}$. The plot on the left shows the extent of convection during the main sequence whilst the plot on the right shows convection during core helium burning. The time axis in the HB plot has been offset for clarity and the convection profiles aligned for easy comparison. Both versions of the code include overshoot but use different methods (see text for details). The diffusive overshoot parameter, f_{OS} was set at 0.01 for the diffusive mixing case. It can be seen that this is a reasonable choice on the MS, where the mass of the convective cores are fairly similar. The slight increase in the diffusive mixing case leads to a slightly longer MS lifetime. More discrepancy is noted in the HB evolution, where the lifetime of this stage is increased by $\sim 10\%$ due to a larger core throughout the HB. Significant core breathing pulses are also present in the diffusive mixing case.

method) and the modified code. A series of models with a range of values of f_{OS} used for overshoot were calculated. It was found that a value around 0.01 reproduced the core sizes and lifetimes given by the original SEV code reasonably well. To illustrate we show the results of the comparisons at two different stellar masses. Figure 4.12 shows the convection zones of a $5 M_{\odot}$ during the MS and during core helium burning. In the diffusive overshoot case we have used $f_{OS} = 0.01$ whilst we used standard overshooting in the original SEV code case (see Section 3.1.3 for the standard overshoot method). The main differences are 1) the convective cores are slightly more massive in the diffusive overshoot case (on the MS and HB) and 2) the lifetimes are both slightly longer in the diffusive overshoot case. This is indicative of the overshoot parameter f_{OS} being slightly too large to reproduce the original case exactly. Another feature is that the diffusive overshoot case exhibits some core breathing pulses, whilst the instant-mixing case does not. How significant these differences are is difficult to ascertain, as the core helium burning stage of evolution is notoriously uncertain. In order to try to gauge the significance of the differences in HB characteristics we have plotted the results from four different stellar evolution codes in Figure 4.13. This plot was generated on the *CIQuA Stellar Database* website (Ödman and Izzard 2004) which is a useful resource for code comparisons. The figure highlights the fact that the size of the convective core varies significantly between codes (from ~ 0.2 to $\sim 0.5 M_{\odot}$). Comparing this with the results from our version of the SEV code (where $m_{core} \sim 0.4 M_{\odot}$, Figure 4.12) we note that our results are well within the limits of variation. The length of the core helium burning stage also varies immensely – by a factor of two in fact – from ~ 13 to ~ 23 Myr. Again the results from the modified SEV code lie within the variation, giving a HB lifetime of ~ 20 Myr.

We continue the comparisons with Figure 4.14. Here we plot the convective regions during the core helium burning phase of two $1 M_{\odot}$ stars – one calculated with the original SEV code and one with the modified (diffusive mixing) SEV code. We don't show the MS as there is no core convective zone. We do note however that the MS lifetimes only differ by $\sim 1\%$ between the

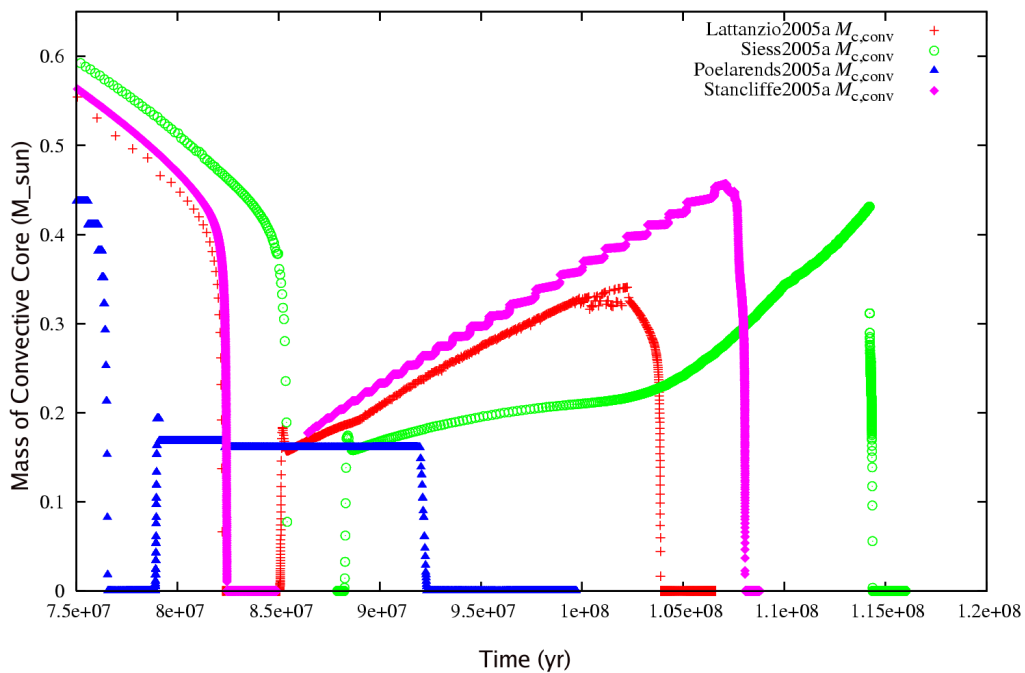


Figure 4.13: The evolution of the convective core of a $5 M_{\odot}$ star on the HB as given by four different stellar codes. This plot was generated on the *CIQuA Stellar Database* website (Ödman and Izzard 2004). It can be seen that the size of the convective core varies significantly (from ~ 0.2 to $\sim 0.5 M_{\odot}$). Comparing this with Figure 4.12 above suggests that the core mass given by the SEV code with diffusive mixing and overshoot (where $m_{core} \sim 0.4 M_{\odot}$) is reasonable. The length of the core helium burning stage also varies immensely (from ~ 13 to ~ 23 Myr). This compares well with the modified SEV code results which give a lifetime of ~ 20 Myr.

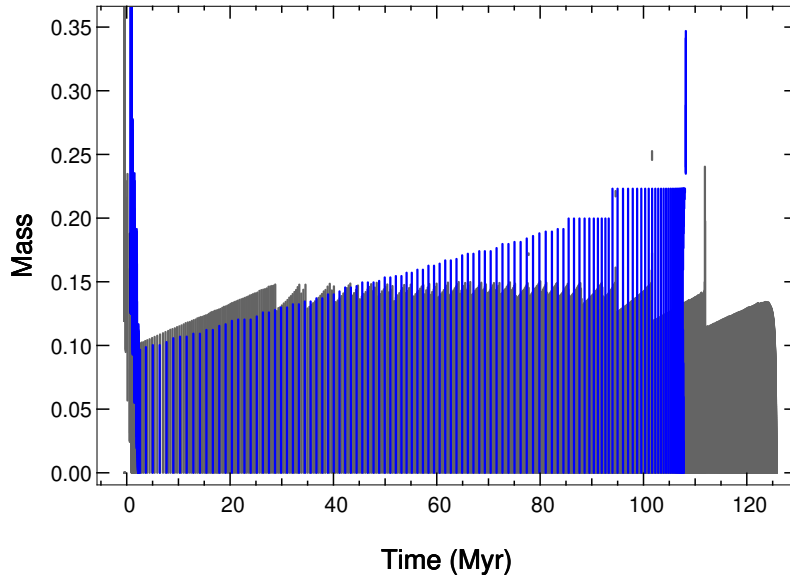


Figure 4.14: Same as Figure 4.12 except the stars have a mass of $1 M_{\odot}$. Only the helium burning stage is shown as there is no convection on the MS at this mass (the MS lifetimes only differ by $\sim 1\%$). Here we see a different effect than with the $5 M_{\odot}$ comparison – the original code gives a *larger* core mass in this case. However, the HB lifetime is again longer despite this. The same f_{OS} value of 0.01 was used.

two cases. For the diffusive mixing case we use the same f_{OS} value of 0.01. Here we see a different effect than in the $5 M_{\odot}$ comparison – the original code gives a *larger* core mass during the HB. Despite this the HB lifetime is again longer, probably due to the large core breathing pulses near core helium exhaustion. In Figure 4.15 we again try to gauge the significance of the discrepancies by comparing with other authors. A star of mass $1 M_{\odot}$ was not available in the *CIQuA* database so we compare with a $1.5 M_{\odot}$ star. We expect the HB convective core to be somewhat larger in the $1.5 M_{\odot}$ star. The core mass from the diffusive mixing version of the SEV code compares well with those found with the other codes. Interestingly, the core mass from the instant mixing version of the SEV code is somewhat larger than that obtained from the other codes. We note that one of the comparison codes in Figure 4.15 is actually another version of the SEV code (labelled Lattanzio2005). It uses instant mixing but includes updated opacities. Comparing the HB lifetimes with ours in Figure 4.14, it appears that our modified SEV code compares reasonably well with the other codes.

In conclusion, given the variability of HB lifetimes found with different stellar evolution codes evident in the plots above, it is apparent that the core helium burning stage of low and intermediate mass stars is significantly uncertain. Since the degree of core overshoot has a strong influence on HB evolution this leads us to conclude that the diffusive overshoot factor f_{OS} is also somewhat uncertain. However, we have found that a value of ~ 0.01 gives results consistent with other authors. The value should be calibrated to observations, and we leave this for future work. It must also be noted here that the degree of overshoot is not necessarily uniform throughout the evolution of a star – or even through different convection zones within a star. It most likely depends on the precise physical conditions of each convection zone (and the stable layers above or below). The simple method used for overshoot here is most likely insufficient to model overshoot from all types of convection zones, especially with a single value of f_{OS} . Again, the most promising solution to this problem is the increasing feasibility of performing multidimensional

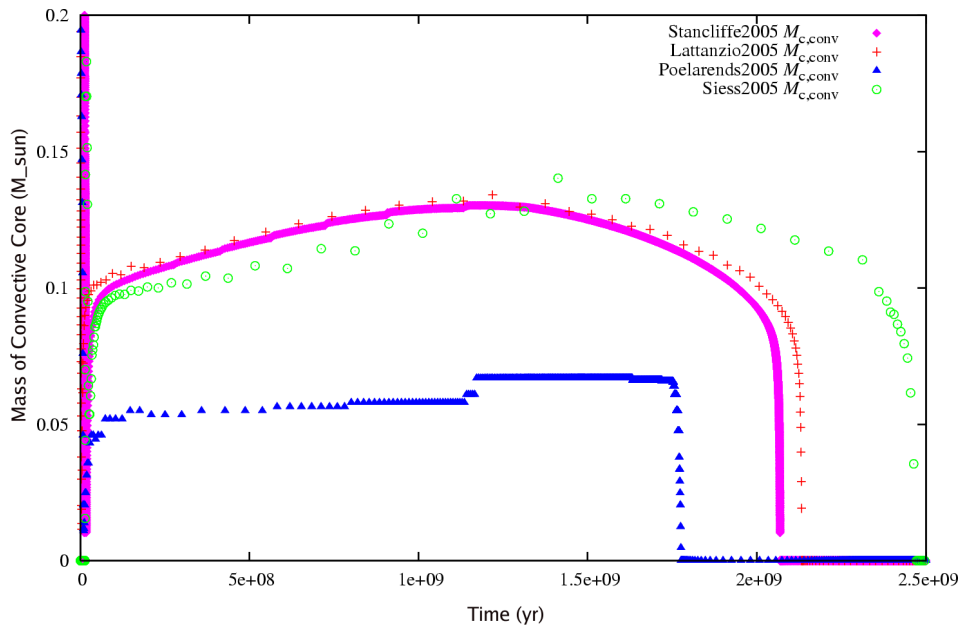


Figure 4.15: The evolution of the convective core of a $1.5 M_{\odot}$ star on the HB as given by four different stellar codes. This plot was generated on the *CIQuA Stellar Database* website (Ödman and Izzard 2004). It can be seen that the size of the convective core varies significantly (from ~ 0.07 to $\sim 0.15 M_{\odot}$). Although our comparison model has a mass of $1 M_{\odot}$, the core sizes should be similar. Comparing these models with Figure 4.14 above suggests that the core mass given by the SEV code with diffusive mixing and overshoot (where $m_{core} \sim 0.15 M_{\odot}$) is reasonable. The length of the core helium burning stage varies significantly but the Lattanzio2005 code (which is a previous version of the SEV code) results compare well with the others, suggesting that the modified SEV code should also (given the apparent uncertainties).

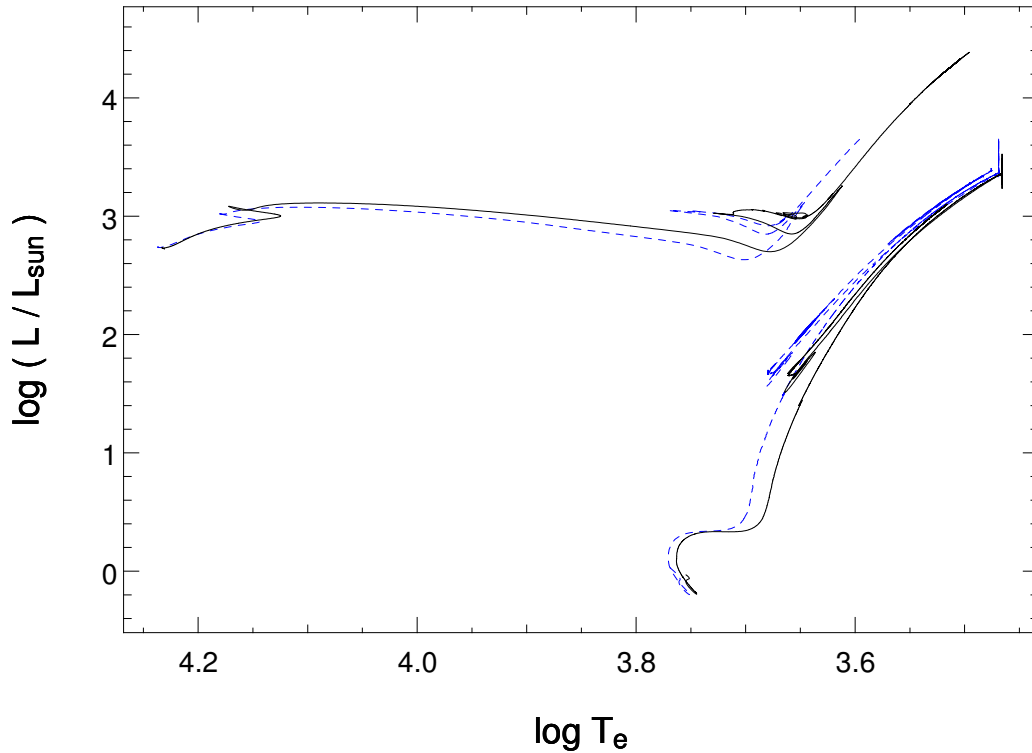


Figure 4.16: Comparison between the two pairs of stars in Figures 4.12 and 4.14. The dashed lines are the models run with the original SEV code whilst the solid are those from the SEV code with diffusive mixing (with overshoot) and updated opacities. In the $5 M_{\odot}$ case there are two differences – the new code gives slightly higher luminosities and the surface temperatures are slightly lower. The first effect is due to the larger core (see Figure 4.12) whilst the lower T_{eff} is most likely due to the updated opacities which include effects from molecules and grains at low temperatures. In the $1 M_{\odot}$ case the luminosity is practically identical but the temperature is again shifted slightly cooler. Here there is no convective core on the MS so the core masses are identical, leading to identical luminosities. Again, the cooler T_{eff} is due to the updated opacities.

hydrodynamic calculations.

Pre-AGB Comparison in the HR Diagram

As a final comparison between the original SEV code and the modified SEV code, we display in Figure 4.16 the same evolutionary runs ($M = 1 M_{\odot}$ and $5 M_{\odot}$) as discussed above, in the HR diagram. The tracks are plotted for evolution up to early AGB. In the $5 M_{\odot}$ case there are two differences – the modified SEV code gives slightly higher luminosities and the surface temperatures are slightly lower. The first effect is due to the larger core (see Figure 4.12) whilst the lower T_{eff} is most likely due to the updated opacities which include effects from molecules and grains at low temperatures (see opacity section). In the $1 M_{\odot}$ case the luminosity is practically identical but the temperature is again slightly cooler. Here there is no convective core on the MS so the core masses are identical, leading to identical luminosities. Again, the cooler T_{eff} is due to the updated opacities. We conclude that the diffusive mixing and diffusive overshoot modifications have not drastically altered the results of the code. The improved treatment of mixing will however be of much use during certain difficult stages of evolution encountered in zero- and low-metallicity stars, which is the focus of the current study.

Diffusive Overshoot on the AGB

The degree of overshoot from the convection zones during the AGB stage of evolution is at least as uncertain as that during core helium burning. During a shell helium flash there are two quite distinct types of convection zones – a He-flash-driven convective zone of small mass, and a convective envelope of large mass (until mass loss reduces the mass of the envelope). In some very recent work [Herwig et al. \(2006\)](#) attempted to gauge the extent of overshoot from a He shell flash convective zone during the AGB through multidimensional hydrodynamic modelling. Their preliminary results suggest that some mixing across the formal convective boundaries is likely to occur, but it is difficult to quantify as yet. Interestingly, [Herwig \(2005, private communication via John Lattanzio\)](#) finds that his ‘best guess’ values of f_{Os} on the AGB for his code are 0.008 at the bottom of the convective intershell and 0.130 at the bottom of the convective envelope (also see [Herwig et al. 1997](#) for more information on the calibration of f_{Os}). The first value compares well with our choice of $f_{Os} = 0.01$ derived from core helium burning comparisons. The second value seems very large to us. It does however give a significant ^{13}C pocket which leads to s-processing in Herwig’s code ([Herwig 2004](#)), which an important observational constraint in low mass AGB stars. However, Herwig also notes that a systematic calibration with observations is still needed and is yet to be carried out by anyone. As this is outside of the scope of this study we choose to retain $f_{Os} = 0.01$ for all convective zones. The fact that it lies at the lower end of Herwig’s values suggests that our overshoot may be relatively conservative in some cases. We note that there may be differences between the stellar codes so the values may not be directly comparable, but we also reiterate that the values are quite uncertain anyway.

As an example of the effect that overshoot can have during the AGB phase of evolution, we show in [Figure 4.17](#) the evolution of the core mass for two stars that had otherwise started with identical initial conditions. The difference is striking – there is virtually zero third dredge-up (3dup) in the model with no overshoot, whilst the model with overshoot has a very large amount of 3dup, with $\lambda_{3dup} > 1$ for the first ~ 25 thermal pulses. This large amount of 3dup leads to an enormous pollution of the envelope, especially in low metallicity stars. We note that the original version of the SEV code never gives $\lambda_{3dup} > 1$, even when using (the original method of) overshoot. This has consequences for envelope pollution in terms of the chemical makeup of the pollution, as more oxygen is mixed up since the PDCZ overshoots *down* into the C-O core, altering the chemical composition of the intershell, enriching it in ^{16}O . Furthermore, as the core mass is the primary factor in AGB evolution, the vastly different core masses resulting from the inclusion or non-inclusion of overshoot represent a very large uncertainty in AGB evolution.

Finally we note that we have retained the method suggested by [Wood \(1981\)](#) for taking into account the change in entropy due to the mixing up of heavy nuclei during the third dredge-up on the AGB. The main effect of including this physics is to slightly increase the depth of the third dredge-up (by about 20% in mass). We have however added a numerical switch that enables the operator to choose whether to use this routine or not. The routine only operates during 3dup on the AGB so does not effect other stages of evolution. The routine was not used in the models plotted in [Figure 4.17](#).

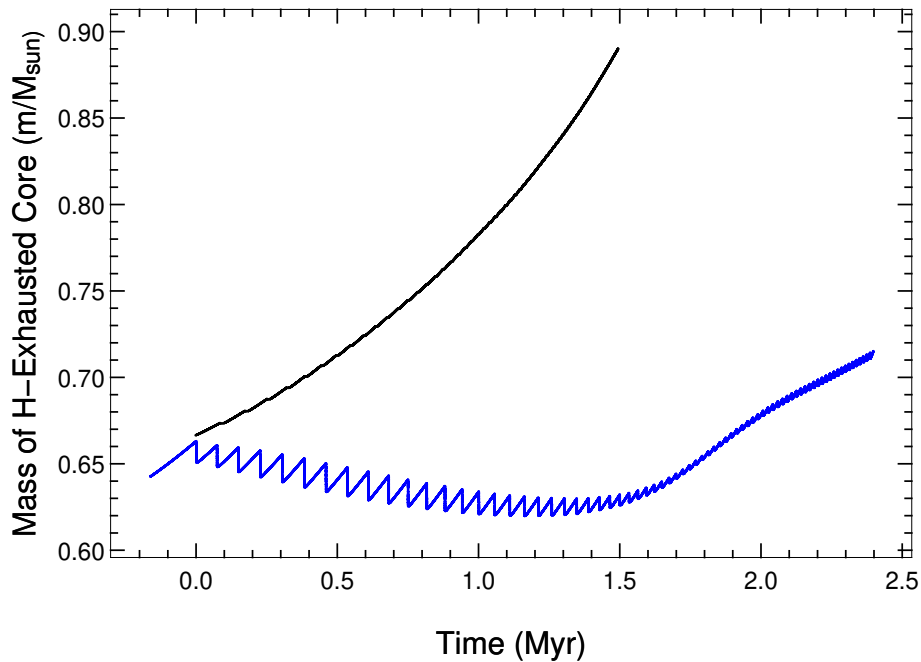


Figure 4.17: Highlighting the strong effect of including overshoot on the AGB. The time evolution of the mass of the H-exhausted core is plotted. Both stars, having a mass of $2 M_{\odot}$ and a metallicity of $[\text{Fe}/\text{H}]=-5.45$, started with the same initial conditions except for the inclusion of overshoot in one (lower curve, $f_{os} = 0.01$). An enormous difference in core mass evolution is clearly seen. The model with no overshoot (upper curve) has virtually no 3dup whilst the model with overshoot initially has $\lambda_{3dup} > 1$. As the core mass is the primary factor in AGB evolution, the vastly different core masses represent a very large uncertainty in AGB evolution.

4.1.6 Semiconvection

Another topic of perennial discussion with regards to stellar convection is semiconvection. We have previously described the method used for semiconvection in the original version of the SEV code in subsection 3.1.3. Here we briefly discuss the physical basis for semiconvection, the relevance to stars and describe our method for including it taking into account the new diffusive mixing paradigm.

It seems whenever it is deduced that partial mixing is required to circumvent apparent contradictions in the determination of convective boundaries of stars, the term semiconvection is used to describe that mixing. Thus here we view the term as meaning ‘any slow mixing process’ – ie. non-turbulent mixing.

The problems in determining convective boundaries have been present since the first studies of stellar evolution. Schwarzschild and Härm (1958) identified a problem in the MS evolution of massive stars ($M \sim 30 M_{\odot}$). In their models the convective core was found to expand on the MS (this was later found to be incorrect at this mass, but the argument still applies to other stars). The problem was that a growing discontinuity in opacity, due to the continual burning of H reducing the opacity in the core but not the envelope, leads to a contradictory situation. They noticed that since the opacity is higher just outside the convective core then this region is actually *more* unstable than the material just inside the core (since the temperature gradient depends on opacity and the other physical variables are continuous) – thus we have a contradiction – the original structure is not possible. Their solution was to assume a partial

mixing, which they called semiconvection, of the region just outside the convective core. The mixing was undertaken until convective neutrality was achieved (ie. $\nabla_{rad} = \nabla_{ad}$). This means that the convective core is still given by $\nabla_{rad} > \nabla_{ad}$ but there is a (growing) region of partially mixed material on top of the core that is just stable against normal (turbulent) convection. This leads to a different thermal structure and has significant consequences, such as the predicted ratio of red to blue supergiants ($M \sim 13$ to $30 M_{\odot}$; see eg. [Stothers and Chin 1994](#)).

A related problem occurs in low mass core helium burning stars, where a local minimum in the ratio ∇_{rad}/∇_{ad} develops in the core, again driven by opacity (see eg. [Castellani et al. 1971](#)). The [Schwarzschild and Härm \(1958\)](#) solution (and variants thereof) has been widely used for these semiconvection situations. However, the physical foundation for the occurrence of stellar semiconvection is not well defined.

The main physical arguments for semiconvection have their origin in fluid mechanics, and in particular oceanography. Early experimental work by [Turner and Stommel \(1964\)](#) showed that a stably stratified fluid which is heated from below develops an increasing number of discrete convective layers above the initial convective layer. The convection within these layers homogenises the composition, removing the stabilising gradient. The convective layers are separated by stable layers with steep composition profiles. Over time the convective layers slowly expand and merge, probably due to convective ‘scouring’ – ie. extra mixing via eddies slightly overshooting into the stable regions (see eg. [Fernando 1989](#)). The nett result of this process is that we effectively have a slow mixing process just outside the formal convective boundary – if the material is heated from below *and* there is a negative molecular weight (or density) gradient. This is reminiscent of the semiconvection situation in stellar model calculations. It is known as Double Diffusive Mixing, as theory describes the process as the competition between the diffusion of two properties – heat and chemical composition. In stars (and salt water) the timescale is far higher for heat diffusion than chemical (microscopic) diffusion and it is this that leads to the layering effect. Although this is the most cited physical analogy to stellar semiconvection (eg. [Spruit 1992](#); [Grossman and Taam 1996](#)), it still remains uncertain whether it really applies to the vastly different physical conditions found in stars (as compared to the ocean). The avenue of detailed multidimensional hydrodynamic calculations is still in its infancy due to the complexity and computational costs of the problem (for recent attempts at simulating semiconvection see eg. [Merryfield 1995](#); [Biello 2001](#)). If we do accept this mechanism for semiconvection, then we note that this type of convection is not taken into account by the Schwarzschild condition for onset of convection:

$$\nabla_{rad} \geq \nabla_{ad} \quad (4.19)$$

as it ignores the possibility of a stabilising effect from a (negative) composition gradient that gives rise to the double diffusive mixing. The [Ledoux \(1947\)](#) criterion does take this into account:

$$\nabla_{rad} \geq \nabla_{ad} + \frac{\beta}{4 - 3\beta} \nabla_{\mu} \quad (4.20)$$

where β is the ratio of gas pressure to total pressure and

$$\nabla_{\mu} = \frac{\partial \ln \mu}{\partial \ln P} \quad (4.21)$$

is the molecular weight gradient. [Kato \(1966\)](#) however argues that overstable convection – the amplifying oscillatory motion of mass elements due to thermal dissipation within a zone with a negative composition gradient – is strong enough to remove a chemical gradient just outside a convective zone. Thus they argue that the criterion for convection reduces to the Schwarzschild one and it is this, with a region just outside the core that is ‘convectively neutral’ (ie. $\nabla = \nabla_{ad}$) due to the mixing by overstable convection, that should be used for stellar modelling. Thus they agree with the [Schwarzschild and Härm \(1958\)](#) method. Other authors have however argued that there should be a slow mixing in the region between the convective boundary given by the Ledoux criterion and that given by the Schwarzschild criterion (see eg. [Langer et al. 1985](#); [Grossman and Taam 1996](#)). This is more analogous to double diffusive mixing.

There are many types of instabilities that fluids can experience (eg. Rayleigh-Taylor, Rayleigh-Bernard, Bernard-Marangoni, etc.). The manifestation of one or the other depends on the prevailing physical conditions. For example, [Turner and Stommel \(1964\)](#) list a range of physical scenarios in which various types of instabilities arise, based on salt water experiments in which the density, composition, and temperature profiles are varied. However, in stellar applications we really only need to know the (rough) timescale of mixing. [Grossman and Taam \(1996\)](#) have developed a double-diffusive extended mixing length theory for stellar evolution calculations. Their results show that there are various regimes of convection and that their derived condition for stability is almost exactly the Ledoux criterion. They present their results in a stability plane which illustrates the situation concisely. [Figure 4.18](#) is a reproduction of their figure 2, with some minor alterations. The main points which diverge from the strict Schwarzschild criterion treatment are 1) efficient convection can be reduced to semiconvection in the presence of a μ -gradient, 2) efficient convection can occur even if $\nabla - \nabla_{ad} < 0$, providing there is a positive μ -gradient, and 3) semiconvection can occur well below $\nabla - \nabla_{ad} = 0$ if there exists a sufficiently steep and positive μ -gradient. They also find that there is a dramatic change in characteristic convective velocities when crossing the Ledoux line. We have thus interpreted this in terms of three effective regimes: stable, semiconvective (ie. any slow mixing) and convective (efficient/turbulent mixing).

Given the discussion above, we have added the Ledoux criterion ([Equation 4.20](#)) to the SEV code. The criterion for deciding when a region is semiconvective that we have adopted is:

$$0 < (\nabla - \nabla_{ad}) < \nabla_L \quad (4.22)$$

where

$$\nabla_L = \frac{\beta}{4 - 3\beta} \nabla_{\mu}. \quad (4.23)$$

As we now treat mixing time-dependently throughout the entire star, it is an easy matter to also treat semiconvective regions in the same manner. This is done by applying slow mixing velocities in the region defined by [Equation 8.1](#). However, the problem of not knowing how slow to mix remains. We have initially hard-wired a fixed value velocity for semiconvection (a similar tactic

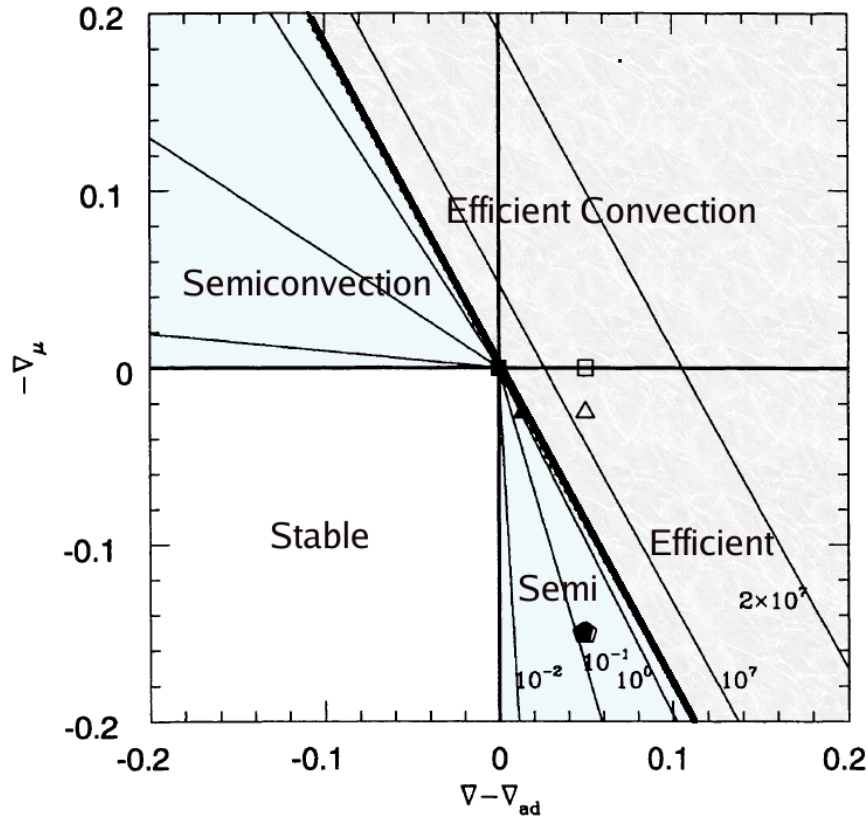


Figure 4.18: The stability diagram from Grossman and Taam (1996) (their Fig. 2). We have added some extra labelling and shading. The heavy solid line represents the Ledoux criterion, which Grossman and Taam (1996) conclude is an excellent approximation for the stability criterion given by their double-diffusive extended MLT. The thin solid lines are contours of constant convective velocity. Note that the reduction/increase in velocity is very sharp when crossing the Ledoux line. The plot shows that 1) efficient convection can be reduced to semiconvection in the presence of a μ -gradient (quadrant 4), 2) Efficient convection can occur even if $\nabla - \nabla_{ad} < 0$, providing there is a positive μ -gradient (quadrant 1), and 3) slow (\sim semiconvective) mixing can occur well below $\nabla - \nabla_{ad} = 0$ if there exists a sufficiently steep and positive μ -gradient (quadrant 1). [Figure reproduced with permission from Prof. Ronald Taam].

to that of Eggleton 1972). We note that this is insufficient and must be improved upon, but it is outside the scope of this study. We have however provided the basis for better treatment of semiconvection. One option here is to accept the velocities given by the Grossman and Taam (1996) double-diffusive MLT. We leave this for future work. Finally we note that there is now a numerical switch in the SEV code that enables one to use the Schwarzschild or Ledoux criteria at will.

4.1.7 Summary, Practicalities & Future Work

In overview, the entire convective mixing paradigm in the SEV code has been changed. The treatment is now a diffusion approximation to turbulent mixing, allowing us to follow mixing time-dependently. Overshoot and semiconvection are now also treated as diffusive mixing, through the variation of convective velocities.

We have however retained the instantaneous mixing routine (in *abund.f* – the diffusion version is in *abund-diffn.f*) and provide a numerical switch so the operator can choose which to use (the

switch is called *idiffusion*). The same switch, when given a value of 2, lets the SEV code choose when it is necessary to use time-dependent mixing or instantaneous mixing. This reduces calculation time as most evolution only requires instant mixing which is faster to calculate. It should be noted that doing this may lead to inconsistencies if different overshoot and semiconvection methods are used when switching between diffusive and instant mixing. Thus it is recommended to use one or the other during a particular run.

We have also included a switch for diffusive overshoot, so the operator can choose whether to include this or not. Related to this is another control parameter in the input file called *diffnosfac* which is the f_{OS} value for diffusive overshoot. This is a global value, used for overshooting on all convective boundaries.

Finally, there is a switch for diffusive semiconvection called *diffsemi*. This allows the operator to choose whether to use the Ledoux criterion to check for semiconvection or not (if this switch is set to ‘off’ then no form of semiconvection will be applied).

Despite all these changes there is room for improvement and we suggest the following as possible future work:

- The diffusion routine currently operates with the same timestep as that used for the structural evolution. Whilst this is reasonable (since we track the errors and the evolutionary timestep is taken to keep changes in composition minimal) it may be more efficient to use a sub-evolutionary timestep within the diffusion routine. Based on the tests carried out above this would reduce errors in the diffusion routine, removing the necessity to reduce the evolutionary timestep for the diffusion routine. The facility for this is already available in the code and would thus only require minor changes.
- Although we argue that our method of ‘burn then mix’ each iteration should give self-consistent results, it would be instructive to implement the other two methods to check, ie. 1) coupling the nuclear burning and diffusive mixing and 2) coupling the nuclear burning, diffusive mixing and structure.
- The amount diffusive overshoot should be variable depending on the physical conditions at each convective boundary. However we note to reliably quantify this requires further multidimensional fluid dynamic calculations in order to gauge the extent of overshoot under differing conditions. When the (parameterised) results from these calculations become available it will be an easy matter to implement them into the existing code.
- The diffusive semiconvection method could easily be improved to take into account Rayleigh-Taylor instabilities that arise with positive μ -gradients. At the moment we have a traditional treatment of semiconvection. The mixing velocities in the semiconvective regions should also be treated more self-consistently. This could be done by using a modified MLT (see semiconvection section above for more details).
- Given that a diffusion routine is now employed in the SEV code it should be a fairly easy task to utilise it for diffusing angular momentum also. This is the usual method for including the effects of rotation in stars. Microscopic diffusion may also be a possibility.

4.2 Opacity

The opacity setup for the original version of the SEV code is described in section 3.1.3. Here we describe the changes made over the course of the current study.

4.2.1 Low Temperature: 500 – 8000K

Low temperature opacities become important during the giant phases of low and intermediate mass stellar evolution. The temperatures can become so cool as to allow formation of molecules and grains. Therefore these particles need to be taken into account when calculating opacities. In the original version of SEV code molecular opacities were taken into account using the formulae suggested by Bessell et al. (1989) which are based on the molecular (and grain) opacity tables from Alexander (1975) and Alexander et al. (1983).

For the current version of the SEV code we have updated to the tables calculated by Ferguson et al. (2005). These tables already include molecular and grain opacity sources so the Bessell et al. (1989) formulae have been removed. The range of temperature that the tables cover is $500 < T(\text{K}) < 31,000$. We have however chosen to use them in the range $500 < T(\text{K}) < 8,000$. The main reason for this is that, although Ferguson et al. (2005) do offer to compute opacities with other compositions on request^a, the tables are not yet computable by the user online. This facility is available on the OPAL website^b and is very useful for computing opacities for arbitrary compositions. However the OPAL opacities (Iglesias and Rogers 1996) do not include very low temperatures so we retain the Ferguson et al. (2005) tables for the aforementioned low temperature range. The transition between the two sets of tables at 8000 K was chosen as this is close to the lower limit of the OPAL tables. The OPAL tables are variable in carbon and oxygen, which is needed for the change in opacity caused by increasing amounts of these elements through nuclear burning and third dredge-up – but the Ferguson et al. (2005) tables are not. The portion of the stellar model that this affects is very small however, as discussed in Appendix C.1 on page 396.

The subroutine *lowtintz* in the file *otable2005.f* now reads in the needed low temperature opacity tables from a directory below the working directory (called */optables/lowT/*) and interpolates within them (in *Z*) when the SEV code starts. The *Z* value is specified by the operator in the file *infile.list*. Thus a set of low temperature opacity tables for the requested *Z* is stored in memory and used throughout the evolution. The tables are stored in the array variable *OOP* and vary in *X*, *T*, and *R* (*R* is the OPAL variable: $R = \rho/T_6^3$, where T_6 is the temperature in MK). Interpolation in these variables is done during the evolution as needed. In regard to the initial interpolation in *Z* we have decided to use *linear* interpolation because we found that quadratic interpolation was inadequate at handling the discontinuities in the tables, giving wildly inaccurate values. Although linear interpolation can be a little inaccurate at times, it does not suffer from the huge deviations possible with ill-behaved quadratic interpolation. We reiterate that these tables are not variable in *C* and *O* and are currently only available for

^aSee the low-T opacity website at <http://www.webs.wichita.edu/physics/opacity/>

^bThe OPAL website is url is <http://www-phys.llnl.gov/Research/OPAL/new.html>

particular compositions. Some of the compositions for which the opacity tables are available (on the website) are from compilations by:

- [Seaton et al. \(1992\)](#) (including an alpha-enhanced version)
- [Grevesse and Noels \(1993\)](#)
- [Grevesse and Sauval \(1998\)](#)
- [Lodders \(2003\)](#)
- [Asplund et al. \(2005\)](#)

of which we can now use any. All of the calculations in this study have used the solar composition of [Grevesse and Noels \(1993\)](#) but [Lodders \(2003\)](#) is also available in the opacity directory for the SEV code (these were the two available at the time of installation).

4.2.2 Mid Temperature: 8000 K – 500 MK

A number of months work was spent updating the mid-range temperature opacity routines in the SEV code. The primary aims were 1) to update to the new OPAL table format, and 2) to relax all the scaled-solar composition assumptions. The old OPAL subroutine *xcotrin.f* was substantially modified to take the new OPAL format. This routine was originally written by Arnold Boothroyd (using some routines from M. J. Seaton, circa 1991). Once this was done, and the scaled solar assumptions removed, it was possible to calculate opacity tables for any composition on the OPAL website and use them with the SEV code. This version of the code was used successfully for a few months.

However, it came to the attention of the Author that Arnold Boothroyd had greatly expanded his original routine himself, and had made it available on his website^c. As this very large, detailed subroutine could actually perform both the tasks required – and much more – and it had been through much debugging, we decided to replace our new routine and install Boothroyd’s. Boothroyd’s routine is capable of accounting for opacity effects due to CNO variations (due to nuclear burning) at a particular Z value. To do this one needs an extra set of opacity tables (also available on Boothroyd’s website). Another feature is the ability to include opacities for compositions with abnormal [O/Fe]. The key feature for the current low-metallicity study is however the ability to use opacity tables of arbitrary composition generated on the OPAL website. This has been done many times now throughout the study.

The OPAL tables ([Iglesias and Rogers 1996](#)) have a temperature range of 5600 K to 501 MK and a $\log_{10}(R)$ range of -8.0 to $+1.0$. The tables are not rectangular however. The tables do not cover the higher density end at high temperatures. At high densities and temperatures conductive opacity becomes important. In these regions we retain the treatment for conductive opacities described in section 3.1.3. We have chosen the transition temperature from low temperature opacities to the OPAL opacities as 8000 K, for reasons given in the previous subsection. The transition to high temperature opacity tables is taken at the limit of the OPAL tables (501 MK).

^cBoothroyd’s website url is: <http://www.cita.utoronto.ca/~boothroyd/kappa.html>

The OPAL tables come in two types: *type 1* and *type 2* tables. Type 1 tables contain a set of 126 tables with a fixed relative metal distribution but varying X and Z. We use one of these tables for a given composition. Type 2 tables contain a set of tables (varying in number) also with a fixed relative metal distribution but varying in two chosen metals. The two chosen metals (usually C and O) increase incrementally in each table (independent of the metal distribution). Each table has constant Z and X. At each Z there are five tables varying in X. An important feature here is the variability of the two chosen metals. This allows one to take into account the change in opacity that occurs as carbon and oxygen start to dominate the composition via nuclear burning. This is important in the C-O core and when the envelopes of AGB stars become polluted with C through third dredge-up.

All the OPAL opacity tables are located in the directory `/optables/opal/` below the working directory. Tables generated on the OPAL website must be put in this directory for use, and naming conventions taken into account.

4.2.3 High Temperature: 500 MK – 2000 MK

The original version of the SEV code did not include opacities for temperatures above the OPAL limit of 500 MK. This limits the range of operation of the code, particularly at low metallicities and higher masses where temperatures can be very high. We have remedied this by adding a high temperature opacity table from Alessandro Chieffi (private communication). The table file name is `xhighTopac.tab` and is placed in the `/optables/highT/` directory below the working directory. This table has a temperature range of 400 MK to 12.5 GK. The SEV code does not include oxygen burning as yet, so structures with temperatures above ~ 2 GK can not be followed and we thus only use the range of 500 MK to 2 GK in `xhighTopac.tab`. The new subroutine `readhighT` reads in the high temperature table and stores the values in memory for interpolation when needed. The interpolation routine `HIGHTOPA` was adapted from that of A. Chieffi. The main difference is a change from cubic to quadratic interpolation. At such high temperatures there is no H or He, so the metals we have chosen to include in the opacity interpolation are C, O and Ne. Conductive opacities are included in the table already.

4.2.4 Conductive: High T and R

The method for calculating conductive opacity has not been changed (see section 3.1.3 for a description). However the routine for calculating them has been merged with the SEV code. This means that it is unnecessary to produce the file `con_opac.dat` needed for the original version of the SEV code. Everything is now done at run time. Another change is the removal of the ‘hard-wired’ scaled-solar composition assumptions. The composition is now read in from the OPAL table headers, so the conductive opacity composition automatically matches the radiative opacity composition.

4.2.5 Summary, Practicalities and Future Work

In overview, the opacity setup in the SEV code has been updated, extended and streamlined.

There is however some room for more improvement (as always!). We note a few points here:

1. There are slight discontinuities going from one set of tables/temperature regimes to the next. This may cause convergence problems (although we have not noticed a problem in practice). A remedy for this would be to interpolate between the various tables to get smoother transitions between temperature regimes.
2. It would be more consistent to have the low temperature opacity composition match the OPAL composition. This is not a problem when using scaled-solar composition (as both have tables with this composition) but it is when we compute non-scaled-solar compositions on the OPAL website, as we can't do this for the low temperature tables. However the effect may be a small one.
3. Related to 2. above is the fact that the low temperature opacities do not take into account the variability of C and O in the envelope, as no tables are provided to enable interpolation (although they could be requested). Again, the degree of effect is uncertain. (Also see the discussion in Appendix C.1 on page 396).
4. The routine that generates the conductive opacities may need updating.

Finally we note that the opacity setup is now more streamlined, as there is no need to pre-compute various opacity tables (such as the old *opalfile.dat* and *codataa*, etc.). If all that is needed is scaled solar opacities, at any Z , the only requirement on the part of the operator is to specify the Z value in the text file *infile.list*. This will normally be the case. This requires that all the opacity tables for all Z values are transported with the source code. As the full set amounts to ~ 8.5 MB (eg. the file *OPALkappa.tar.gz* from Boothroyd's website) this is not a problem with current computing resources.

If abnormal compositions are required then they can be computed on the OPAL website at <http://www-phys.llnl.gov/Research/OPAL/new.html>. The generated files must then be put in the */optables/opal/* directory.

4.3 CNO Equilibrium with He Burning at $Z = 0$

4.3.1 Motivation

A unique feature of zero metallicity stars comes about because of the complete lack of CNO catalysts. At the beginning of the MS stars of masses that would normally burn hydrogen via the CNO cycle aren't able to do so due to this lack of catalysts. Instead they burn H through the PP chains. This reaction sequence has a much lower temperature dependence than the CNO cycles (T^4 as opposed to T^{20}) which has a significant effect on the structure. Indeed, much of the star's mass can be involved in hydrogen burning. To maintain hydrostatic equilibrium the PP chains must produce enough energy and, again due to the weak temperature dependence, the central temperatures become very high. In fact, for stars of sufficient mass ($> \sim 0.9 M_{\odot}$) the core will be so hot towards the end of the MS (earlier for more massive stars) that helium

starts burning via the triple-alpha (3α) reactions – in the same location as the PP chains are operating. The resultant ^{12}C is then available for the CNO cycle, which starts immediately. The structure of the star then changes, becoming more ‘normal’ (ie. like higher metallicity stars), and a small excursion in the HR diagram ensues.

The reason we detail this here is because the original version of the SEV code did not take into account the possibility of simultaneous H and He burning in the particular situation when the CN(O) cycles are in equilibrium. Thus, in order to model $Z=0$ stars for this study, a small modification was needed in *abund.f* and *abund-diffn.f* to take the simultaneous H and He burning into account in the equilibrium calculations.

4.3.2 Equilibrium CNO Burning and Timestepping

A nuclear species is in equilibrium when its production rate is equal to its destruction rate. When the CNO cycle is operating the sum of the CNO nuclei is conserved over time. Taking both these facts into account the abundance distribution is then given by simple algebraic expressions involving the current abundances and the nuclear rates, which depend on density and temperature (see eg. Clayton 1983). As the evolution of CNO abundances is calculable via these relations, it is possible to burn more of a particular nucleus than is actually present (ie. each nuclei can react more than once in a single timestep), as we know a priori how the abundances will be distributed. The SEV code has a check to see if CN(O) equilibrium will be achieved during the current timestep and if it is the CNO abundances are scaled to the equilibrium values. In theory the abundance changes calculated explicitly through all the reactions (ie. without assuming equilibrium abundances) should give the equilibrium values. However in practice perfect equilibrium is not achieved as one nucleus inevitably gets burnt slightly faster than it is replaced (invariably ^{12}C in the CNO cycle). This effect is exacerbated on the *approach* to equilibrium as the ^{12}C will definitely not be returned through the CNO cycle fast enough, due to the $^{14}\text{N}(p, \gamma)^{15}\text{O}$ bottleneck. In both of these situations we can end up with a negative abundance and thus the timestep needs to be decreased. This has the interesting consequence that (if we don’t include equilibrium assumptions) the timestep is dependent on the metallicity of the star, since the timestepping is governed by the ^{12}C abundance during this stage of evolution. Higher metallicity stars can have much larger timesteps during CNO burning due to their increased equilibrium CNO abundances – whilst low metallicity stars need smaller timesteps. This effect is taken to the extreme with $Z = 0$ stars, which is one of the main topics in the present study. Thus we need to retain an equilibrium treatment in the SEV.

As an empirical example we computed the MS evolution a $1 M_{\odot}$ $Z = 0$ star with and without the equilibrium checks and calculations. With equilibrium the run took ~ 20 min, with timesteps of $\sim 10^5$ yr towards the end of the MS (when the 3α reactions had started). Without (CNO) equilibrium we were unable to evolve it very far into the stage in which He burning started as the timesteps were so small, being $\sim 10^{-2}$ yr. This huge difference of 10^7 in timestep suggests that it would take ~ 19 years (!) to complete the end of the MS evolution.

4.3.3 Dual Burning Modification

We now return to the problem of having 3α reactions happening concomitantly with H burning. The 3α reactions add ^{12}C to the plasma, which can then participate in the CNO cycle, increasing the sum of CNO nuclei. If there were no CNO nuclei initially present (ie. $Z=0$) then this fresh carbon initiates the CNO cycle. In addition to the ^{12}C there may also be some ^{16}O produced via $^{12}\text{C}(\alpha, \gamma)$. The method I have adopted to account for this injection of extra nuclei into the CNO cycle is to add the extra nuclei to the CNO cycle total – if the cycle is found to be in equilibrium. If it is not then all reactions are followed explicitly. The original equilibrium tests remain, as they are sufficient to determine when equilibrium is achieved, even if extra ^{12}C is being produced. As an example of the tests for equilibrium utilised in the SEV code we show the one for CN equilibrium, such that if

$$12.12 m_p X_H RC_1 \Delta t > 1.0 \quad (4.24)$$

then the cycle is in equilibrium. Here m_p is the proton mass, X_H the mass fraction of H and RC_1 the current rate of the $^{12}\text{C}(p, \gamma)^{13}\text{N}$ reaction. This essentially says that if every ^{12}C nucleus reacts more than once in the timestep Δt (via the reaction RC_1) then the whole CN cycle must be in equilibrium, and thus we can use the simple expressions for the equilibrium CNO abundances. In the original version of the SEV code all the CNO nuclei were summed into the variable V4:

$$V4 = X_C + \frac{6}{7}X_N + \frac{3}{4}X_O \quad (4.25)$$

which is a holding variable for all the CNO nuclei in terms of C . All the X_i are taken as the values from the previous timestep (ie. at the beginning of the current timestep). This is then redistributed amongst the CNO nuclei based on equilibrium assumptions. It can be seen that the CNO nuclei are thus perfectly conserved from one timestep to the next (as they should be). In order to account for the extra nuclei from the reactions involving helium we have now included the total production and destruction (from all reactions) from the current timestep into the V4 sum:

$$V4 = \left(X_C + \frac{\Delta t}{2} \frac{dX_C}{dt} \right) + \frac{6}{7} \left(X_N + \frac{\Delta t}{2} \frac{dX_N}{dt} \right) + \frac{3}{4} \left(X_O + \frac{\Delta t}{2} \frac{dX_O}{dt} \right) \quad (4.26)$$

which is then redistributed in the usual way. In this way the increase in CNO nuclei (mainly ^{12}C in practice, which then gets burnt to ^{14}N) is now followed during equilibrium. This situation (combined H and He burning) will occur whenever hydrogen burning happens at very high temperatures (starting at $\sim 80\text{MK}$), given the availability of helium and a high enough density. The four main sites we imagine this happening are:

1. During the MS of $Z = 0$ stars
2. During hot $Z = 0$ H-shell burning
3. During very hot HBB on the AGB at any metallicity

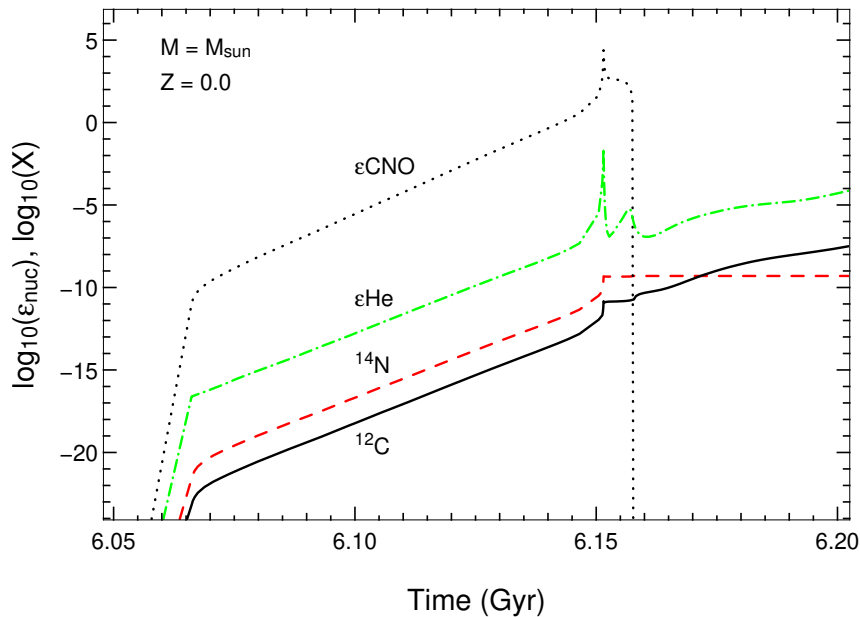


Figure 4.19: The evolution of the central ^{12}C and ^{14}N abundances, as well as the central helium and CNO energy generation. The star has $Z = 0$ and a mass of $1 M_{\odot}$. The evolution is shown from the ignition of the 3α reactions during the subgiant branch. The consequent ignition of the CNO reactions is also evident. It can be seen that the initiation of the CNO cycles occurs as soon as there is a minute amount of ^{12}C produced from the 3α reactions ($X_{\text{C}} \sim 10^{-23}$ in this case!), although the energy generation is minimal when the ^{12}C abundance very low. The ^{12}C from the 3α reactions is mostly burnt to ^{14}N by the CNO cycle. At $t \sim 6.16$ Gyr the CNO cycles cease due to the exhaustion of H at the centre.

4. During proton ingestion episodes in very low or zero metallicity stars

In the MS $Z = 0$ case the ignition of the CNO cycle due to the local production of primary CNO nuclei quickly causes the temperature to drop, bringing the 3α reactions to a virtual halt. This happens with CNO abundances of the order $\sim 10^{-10}$. As an example of this case we present in Figure 4.19 some properties of a $1 M_{\odot}$ model as given by the modified SEV code. It can be seen that the magnitude of CNO nuclei production is indeed minute. It is however enough to alter the burning regime, even giving rise to a convective core due to the extra (localised) energy release from the CNO reactions. Also of note is the negligible luminosity provided by the 3α reactions, and the rapid transmutation of the newly created C (and O) nuclei to ^{14}N .

The main aim of this modification was to enable computation of $Z = 0$ stars. We leave the discussion of the other sites of coincident equilibrium CNO and He burning till those parts of the study in which they arise.

4.4 Other Modifications

Other modifications made to the SEV code during the course of the current study include:

- Removal of all scaled-solar abundance assumptions. This allows the calculation of models with arbitrary abundance distributions. This is relevant at low metallicity as observations show that these stars often have non-solar abundance ratios (eg. alpha-enhanced Galactic globular cluster stars).

- Alteration of logical constraints that did not allow a zero value of metallicity Z .
- The addition of a treatment to handle proton ingestion episodes (PIEs) during low mass $Z = 0$ evolution. These extreme events cause convergence problems and necessitate very small timesteps. See the $Z = 0$ results section for details.
- The addition of a treatment to estimate the increase in opacity due to a ^{14}N dominated envelope during the AGB of low metallicity stars. Any dredge up of CNO nuclei is quickly burnt to ^{14}N due the high temperatures at the bottom of the convective envelope in these low- Z stars. The ratio C:N:O can become $\sim 10:100:1$ on the AGB. Since the opacity tables only include alterations due to increased C and O, the opacity in these regions would be wrong. See the $Z = 0$ results section for more details.

Part III

STELLAR MODEL RESULTS

Chapter 5

Zero Metallicity Stars: Structural Evolution

“Education is not preparation for life; education is life itself.”

– John Dewey

5.1 Background

5.1.1 Overview

The modifications to the structural evolution code (SEV code) detailed in Chapter 4 have enabled us to model metal-free primordial stars. In particular there exists a number of evolutionary features peculiar to $Z = 0$ (and extremely low metallicity) stars that require the use of time-dependent mixing. The two most important of these are the proton ingestion episodes (PIEs) that are induced by helium flash convection breaking through to hydrogen-rich regions. We refer to these events as the dual core flash (DCF) and dual shell flash (DSF). The DCF occurs at the time of the core He flash in low mass models whilst the DSF occurs during the first major He shell flash at the beginning of the TP-AGB in intermediate mass models (sometimes more than one DSF occurs). Although these events have been modelled before by other authors they are still relatively unexplored phenomena as not many studies have evolved through these difficult phases. These two events are pivotal in terms of the possible contribution of these stars to polluting the interstellar medium as they both result in considerable pollution of the envelope, which is later lost through stellar winds. The DCF and DSF are notoriously difficult to evolve though numerically and have provided a serious challenge for the author (and indeed previous authors!).

The real novelty in this study though is that we have also taken (most) of our models through to the completion of the AGB. To the best of our knowledge this is the first time this has been achieved. This allows us to make a range of interesting predictions, such as the expected white dwarf masses, the lifetimes of the various stages of evolution, and the chemical yield of primordial low- and intermediate-mass stars. We should however add a caveat here. The models suffer from the usual uncertainties such as that which derives from the use of the Mixing Length

Nuclide	Mass Fraction
^1H	0.754992
^3He	7.85×10^{-6}
^4He	0.24500
^{12}C	0.0
^{14}N	0.0
^{16}O	0.0

Table 5.1: Initial abundances used in the zero-metallicity stellar structure models, as given by Standard Big Bang Nucleosynthesis calculations by from Coc et al. (2004).

Theory of convection, the neglect of rotation, and the choice of mass-loss formalism. We discuss some of these uncertainties in the next subsection when we describe the input parameters used.

To elucidate the evolutionary features of $Z = 0$ low- and intermediate-mass models we describe two of our models in substantial detail in this Chapter. We have chosen the $0.85 M_{\odot}$ and $2.0 M_{\odot}$ models because between them they display all the peculiar evolutionary features found in our models. In particular the $0.85 M_{\odot}$ model experiences the DCF and the $2.0 M_{\odot}$ model experiences the DSF. At the end of each detailed description we provide a comparison with previous studies at similar masses. Finally, in the last section, we summarise the evolution of all our models. The models evolved are of initial mass 0.85 , 1.0 , 2.0 and $3.0 M_{\odot}$. The detailed nucleosynthesis is reported in the next chapter.

5.1.2 Physical Parameters Used & Initial Composition

Initial Composition

We have adopted a standard Big Bang nucleosynthesis (SBBN) composition for our models. A summary of Big Bang nucleosynthesis and details of our adopted initial abundances for the $Z = 0$ and extremely metal-poor models was given in Section 2.2 on page 17. For convenience we redisplay the abundances here in Table 5.1. It can be seen that all species heavier than ^4He have been set to zero, in line with SBBN.

Mass Loss

Mass loss is one of the most uncertain factors in stellar modelling. We have discussed the methods employed in the SEV code in Subsection 3.1.3 on page 41 but provide a brief discussion here also, in relation to the special case of zero metallicity.

It is generally thought that mass loss occurs via the driving force of radiation pressure. In low- and intermediate-mass (LM and IM) stars observations show that mass loss becomes important on the giant branches, and in particular at the end of the AGB. During these phases two important things occur – the luminosity increases, increasing the (potential) radiation pressure, and the envelope cools, increasing the opacity and allowing grains to form. In addition to this AGB stars pulsate, providing a further (mechanical) contribution to mass loss. The most important phase of mass loss occurs during the AGB, as this is when most of the mass of a star is lost.

In normal (metal-rich) AGB stars the main mechanism for mass loss is thought to be radiation pressure on grains. In the case of zero metallicity grains cannot form due to the lack of metals to form oxides (for example). This implies that the mass loss rate in $Z = 0$ stars should be much lower (if not zero). Although $Z = 0$ stars are more luminous than their higher metallicity counterparts, giving rise to higher radiation pressures, they also have a lower opacity, which again indicates a lower mass loss rate is warranted.

We note however that mass loss is not fully understood – there may be other mechanisms that operate at low- or zero-metallicity. In addition to this we have found that $Z = 0$ LM and IM stars experience self-enriching episodes (namely the DCF and DSF discussed above and also detailed within this chapter). This raises the metallicity of the envelope to values similar to that of the LMC (for example) in which AGB mass loss has been observed. Grains are able to form. Thus it would seem that a standard mass-loss formalism would be needed for stages of evolution occurring after the self-enriching episodes. In low-mass models ($M \lesssim 1.2 M_{\odot}$ at $Z = 0$) these episodes occur at the tip of the RGB, so that all of the RGB evolution occurs when the stars still have $Z = 0$ at the surface. However, as demonstrated in the next section which describes our $0.85 M_{\odot}$ model, the RGB phase is so short that even if some mass loss formalism is included (we use the Reimers (1975) formula on the RGB, see Section 3.1.3 on page 41) there is negligible mass lost over this phase. The rest of the star’s evolution is characterised by a relatively metal-rich envelope. In the intermediate mass case ($M \gtrsim 1.2 M_{\odot}$) we find that the models do not go through the RGB phase, so mass loss during this stage is not an issue. In addition to this these stars experience the DSF self-enrichment event at the beginning of the AGB, so that their envelopes are also (relatively) metal-rich for the key AGB mass-losing phase. This suggests that using the Vassiliadis and Wood (1993) formula for the AGB is warranted. We also note that the metallicity of a stellar model is indirectly taken into account in the Reimers’ and VW93 formulae as the bulk physical properties used in these formulae are a function of metallicity. This is because the entire structure of the models change with Z – through opacity and different nuclear burning energy sources (for example) – and thus there is a feedback on the mass loss rate. For these reasons we have decided to leave the mass loss prescriptions *as standard* in the SEV code.

Convective Boundaries and Mixing

We have employed the new diffusive mixing routine in all our models, for all phases of evolution. For details on this routine see Section 4.1 on page 49. No overshoot or semiconvection was included, such that the convective boundaries are all ‘hard’ Schwarzschild ones. This provides a good benchmark as the degree of overshoot and semiconvection is unknown, particularly at zero metallicity.

Opacity

Updated opacities, as described in Section 4.2 on page 79, were used for all models. As mentioned in Section 4.2 the low temperature tables are not variable in C and O and are currently only available for particular compositions. This should not cause a large uncertainty in the models as

the amount of mass that requires these opacity values is minuscule. We have however investigated the discrepancy in detail, and provide a separate section on this topic in the Discussion (Section C.1 on page 396). We note that most, if not all, previous studies have used non-CO-variable low temperature opacities because this is all that is presently available.

5.2 Detailed Evolution at $0.85 M_{\odot}$

5.2.1 Main Sequence to RGB Tip

In order to give some indication of the difference between primordial stars and more metal-rich stars we compare our $Z = 0$, $M = 0.85 M_{\odot}$ model with a star of the same mass but with $Z = 0.0017$. This higher metallicity model is taken from our globular cluster set of models (see Chapter 8). Figure 5.1 compares the two stars in the HR diagram. It can be seen immediately that the $Z = 0$ star is significantly hotter and more luminous than the $Z = 0.0017$ star during the MS and sub-giant branch (SGB) stages. The temperatures become comparable from the start of the RGB, but the luminosity of the $Z = 0$ star continues to be higher than the more metal-rich star. Also of note is that the $Z = 0$ model has a much shorter RGB, in the sense that the luminosity at the tip of the RGB is much lower. Thus the conditions for He flash ignition are achieved ‘earlier’ on the RGB in the $Z = 0$ model. In the same figure (Figure 5.1) we also display the CNO burning luminosities for each star. Due to the lack of CNO catalysts in the $Z = 0$ model the normal CNO-powered H-shell does not ignite until the end of the RGB, whereas CNO burning becomes significant during the SGB in the $Z = 0.0017$ model. Thus the $Z = 0$ model is supported by PP chain burning for most of its pre-He-core-flash evolution.

To further illustrate this phenomenon we present in Figure 5.2 the time evolution of the luminosities generated by the PP, CNO, and He burning reactions as well as the total luminosity for both stars. An interesting feature in Figure 5.2 is the similarity of the luminosity curves up until the end of the MS. This is as expected because stars of such low mass do not have hot enough cores to burn H via the CNO reactions on the MS (at least until the very end of the MS). Thus the lack of CNO catalysts has no effect on the MS nuclear burning regime for masses $\lesssim 0.85 M_{\odot}$. The lack of metals does however have the effect of reducing the opacity. This allows energy to escape the star more easily, leading to the star requiring an increased burning rate in order to maintain hydrostatic equilibrium. This increased burn rate gives rise to the higher luminosity, higher surface temperature and shorter MS lifetime.

The observation that CNO burning does not become important until late on the RGB in the $Z = 0$ model is explicable by the fact that these reactions can only begin when some ^{12}C is produced by the 3α reactions – which only happens as the temperature approaches ~ 60 MK. In the current model this condition is reached only towards the end of the RGB, as the density and temperature increase steadily till then (see Fig. 5.4). Indeed, the $Z = 0$ RGB structure is never dominated by the CNO cycles, unlike the $Z = 0.0017$ structure. In Figure 5.3 we show an example of CNO cycle ignition due to the local production of ^{12}C by 3α reactions (in the core of the $Z = 0$ model in this case). It can be seen that the amount of ^{12}C needed to initiate the CNO burning is very small, being of the order $X_{\text{C}} \sim 10^{-12}$ or less. Note that the ^{12}C is quickly

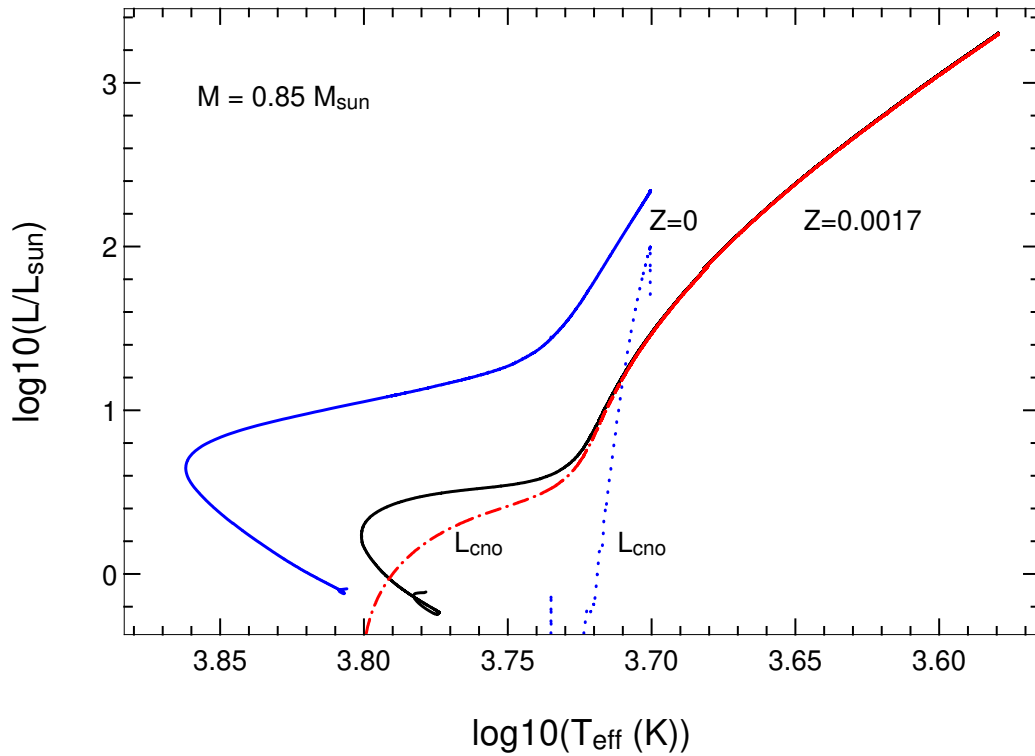


Figure 5.1: Comparison between the $M = 0.85 M_{\odot}$ primordial star ($Z = 0$) and our GC model ($Z = 0.0017$) in the HR diagram, from the MS to the tip of the RGB. The main differences are i) the $Z = 0$ star has a higher surface temperature and luminosity and ii) the $Z = 0$ star is much less luminous at the RGB tip. We also plot the luminosity from the CNO cycles for each star (dotted line for $Z = 0$ and dash-dotted for $Z = 0.0017$). It can be seen that the ignition of a CNO H-shell source is delayed in the $Z = 0$ model in until the end of the RGB, due to the lack of CNO catalysts. It thus relies on PP burning for most of its pre-He-flash evolution.

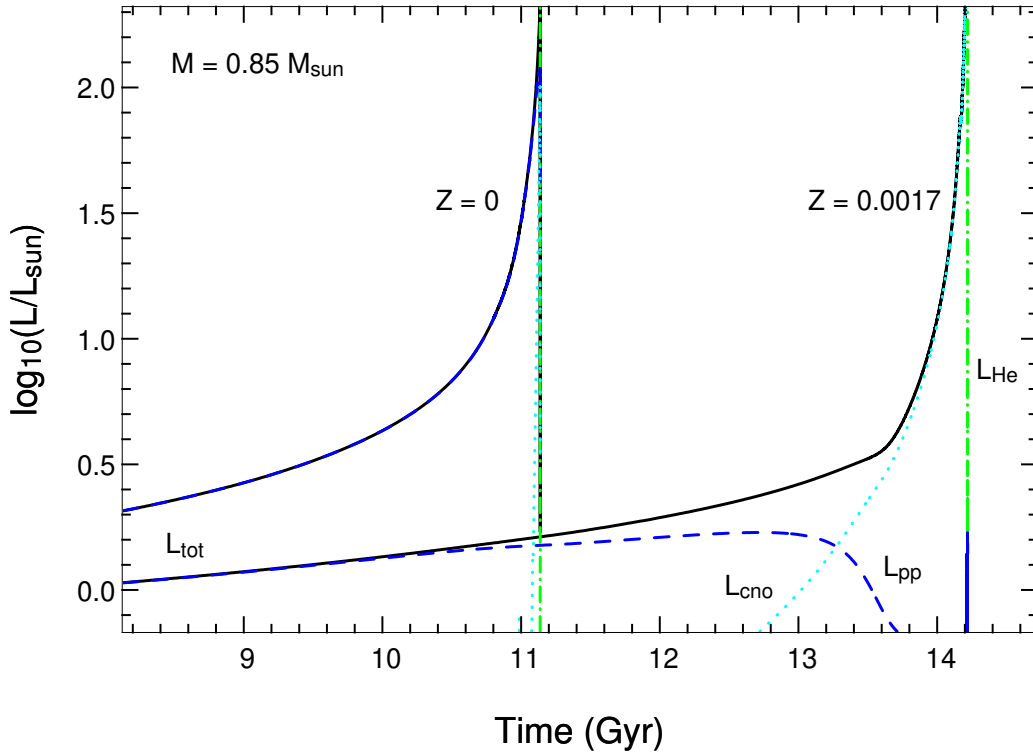


Figure 5.2: Evolution of the various luminosities over the last few Gyr of the MS and up to the core He flash. The luminosity contributions from the PP chains (dashed lines), CNO cycles (dotted lines) and He burning (dash-dotted lines) are displayed, as well as the total luminosity. Note that the PP chain luminosity overlies the total luminosity for the $Z = 0$ model, whilst the CNO luminosity only becomes significant just before the core He flash. Whilst the RGB structure in the $Z = 0.0017$ model is supported by shell CNO burning, it is supported by shell PP burning in the $Z = 0$ model. The shorter MS lifetime of the $Z = 0$ star is also evident in this plot.

burnt to ^{14}N which becomes the dominant metal species (albeit a very small amount!) until H exhaustion.

Returning to Figure 5.2 we also note the difference in MS lifetimes between the two stars. The GC model has a lifetime of ~ 11.5 Gyr whilst the $Z = 0$ model has a lifetime of ~ 10 Gyr. This has consequences in terms of the predicted observability of low mass primordial stars as 10 Gyr is significantly shorter than the age of the Universe (~ 13 Gyr, see Section # for a discussion).

In Figure 5.4 we present the run of two key central conditions – density (ρ_c) and temperature. The initial similarity of the models on the MS is also evident in this graph. However a strong deviation from ‘normal’ behaviour is also apparent. The ignition of the CNO cycle in the $Z = 0.0017$ model causes a moderation of temperature in the core (and the burning shell). This does not happen in the $Z = 0$ star until the temperature is high enough to ignite the 3α reactions.

In Figure 5.5 we compare the run of some physical parameters versus mass between the two stars during the MS phase. We have chosen models in which both have $X_H = 0.2$ in the centre for a direct comparison. It can be seen that the chemical profiles are virtually identical, as are the density profiles. The main points of difference are in the temperature and energy generation rate – both are higher in the $Z = 0$ model. Also plotted is the run of opacity, which is consistently lower in the $Z = 0$ model, as expected.

In Figure 5.6 we make the same comparison during the stage in which the models really begin

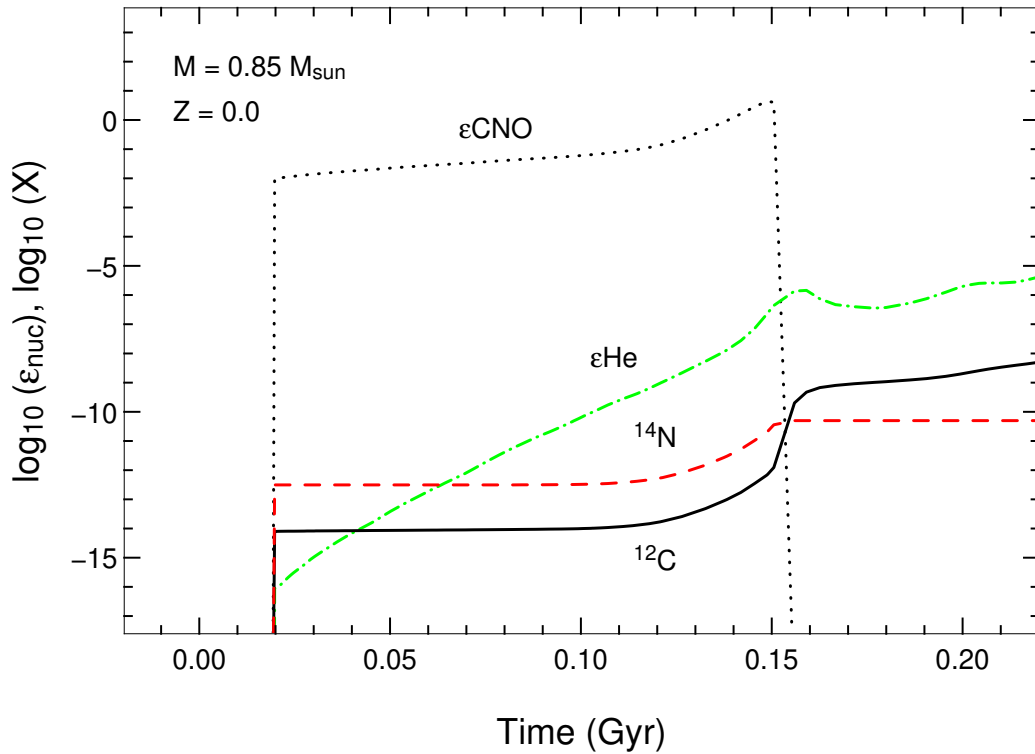


Figure 5.3: An example of CNO cycle ignition in material initially devoid of any metals. In this case it is in the centre of our $Z = 0$ model, during the RGB. Time is arbitrarily offset for clarity (zero corresponds to roughly 10.9 Gyr in Figure 5.2). It can be seen that a minute amount of He burning gives rise to a tiny amount of ^{12}C . This can then react with the protons (of which not much are left), instigating the CNO cycles. Of note is just how little ^{12}C is required, with the mass fraction being of the order 10^{-14} to 10^{-12} (note that the ^{12}C is burnt to ^{14}N very quickly). Hydrogen exhaustion occurs at $t \sim 0.16$ Gyr, at which time the CNO cycles cease and helium burning dominates. ^{14}N is static after this, but ^{12}C continues to build up due to the He fusion.

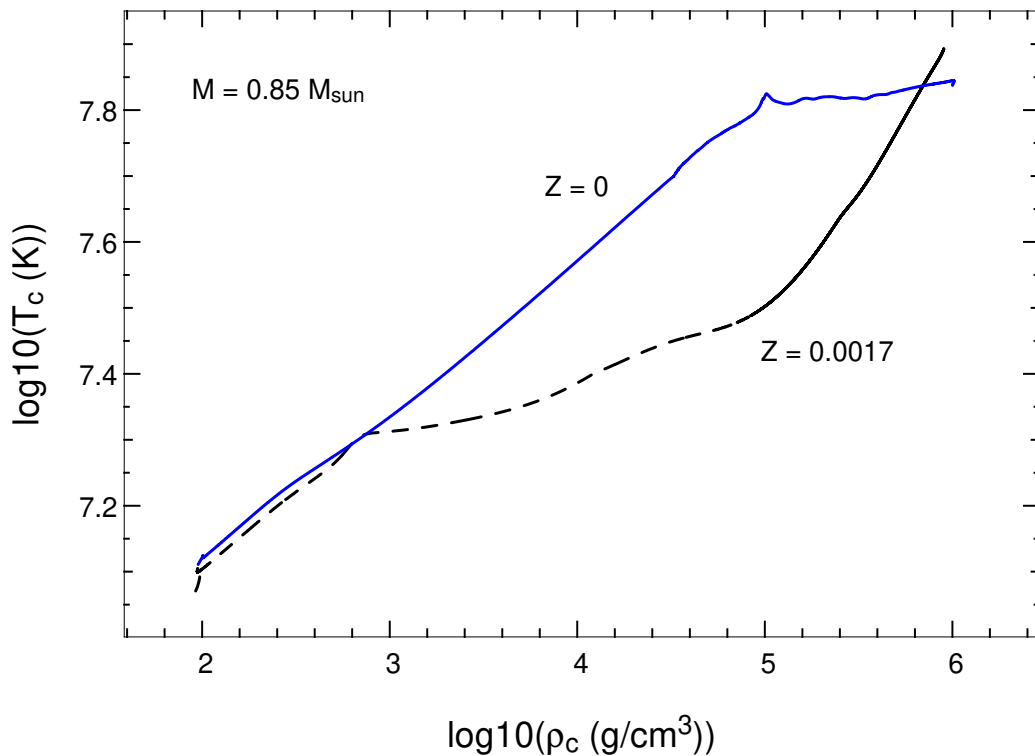


Figure 5.4: Central density versus central temperature for the $Z = 0$ and $Z = 0.0017$ stars, from the MS to the start of the core He flash.

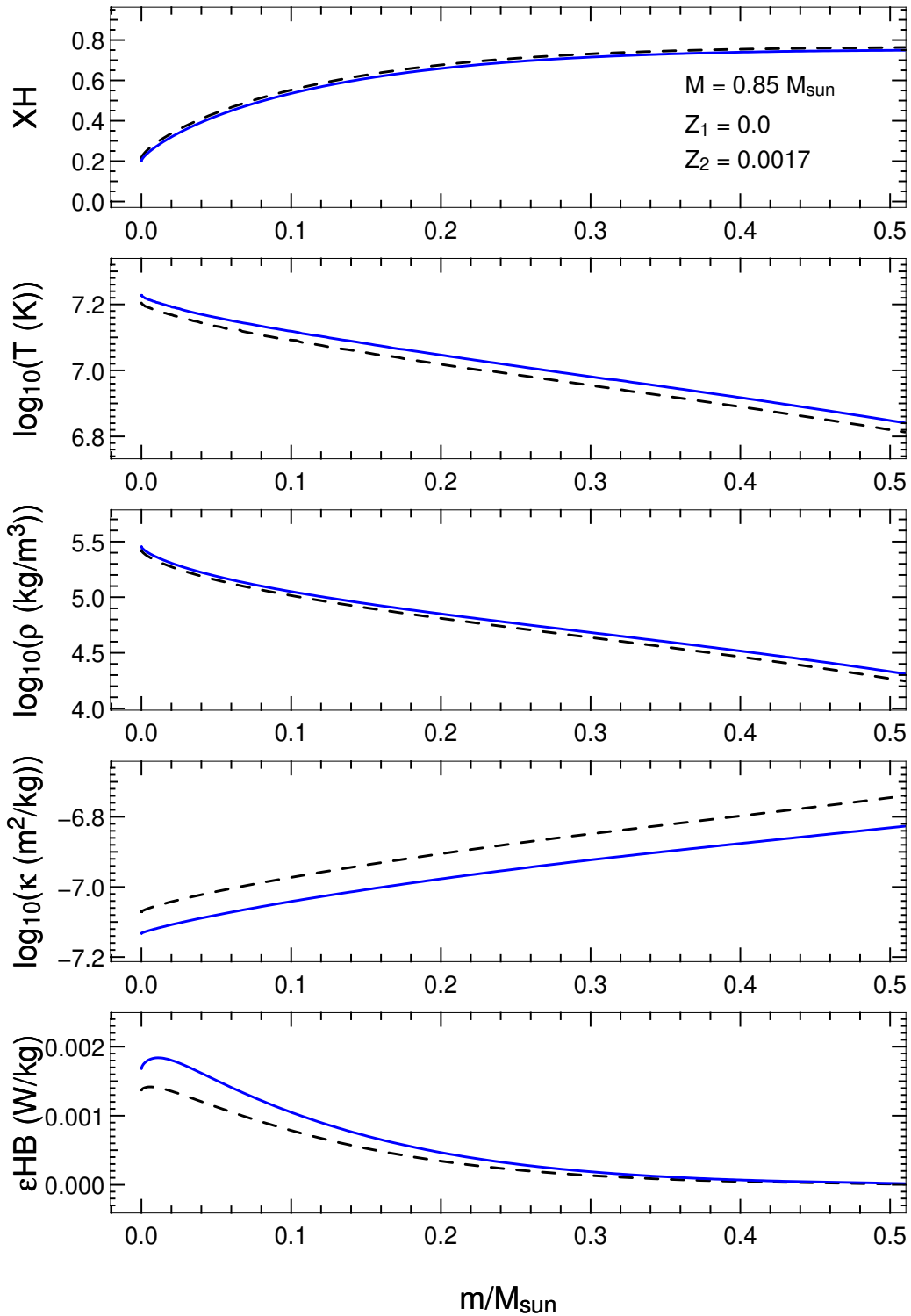


Figure 5.5: The run of physical parameters in both stars during the MS, from the centre to $m_r = 0.5 M_{\odot}$. The dashed line is the $Z = 0.0017$ model whilst the solid line is the $Z = 0$ model. From the top to bottom we have: i) the mass fraction of hydrogen (X_H), ii) temperature, iii) density, iv) opacity (κ) and v) the energy released by H burning (ϵ_{HB} , all sources). We have chosen models that have a similar chemical profile (X_H) for comparison, where the central X_H is ~ 0.2 .

to diverge — towards the end of the MS, when the $Z = 0.0017$ model switches to CNO burning. We compare models which both have central H abundances of $X_H \sim 0.01$. The chemical profile, temperature, density and opacity are all now significantly different between the models. The reason for this is clearly seen in the bottom panel, which shows that the $Z = 0.0017$ model has begun burning via the CNO cycles, whilst the $Z = 0$ star is supported only by the PP chains burning in a very thick shell.

In Figure 5.7 we move further into the evolution. Again we plot the run of physical quantities versus mass, this time for models with a H-shell burning configuration (on the RGB). The structural differences are more striking here. The $Z = 0.0017$ model is now supported by a CNO burning shell. Due to the high temperature dependence of these reactions, the burning is very localised, creating a sharp composition change as it burns outwards in mass. In contrast, the H burning shell in the $Z = 0$ model is powered solely by the PP chains, with the lower temperature dependence giving rise to a thick burning shell that has a much lower peak luminosity (see bottom panel of Figure 5.7). This also gives rise to the other smooth profiles such as the abundance and opacity profiles.

In Figure 5.8 we show the evolution of the core mass and radius (defined by $X_H < 0.05$) of both stars, as well as the evolution of the temperature of the H shell. The properties are all plotted against surface temperature. In this way we can see how the star evolves in relation to the familiar HR diagram, which is shown in the top panel. The gradual increase of the core mass due to the H-shell burning outwards in mass can be seen, as can the concurrent collapse of the core in terms of radius. This collapse takes the H shell into hotter and hotter regions, leading to increased energy generation/luminosity. In the case of the $Z = 0$ model the shell reaches temperatures hot enough to ignite helium, as discussed earlier. The core temperature of the $Z = 0$ star is quite constant during the RGB, and is also very high. We note that both stars end up with approximately the same core mass and core temperature at the tip of the RGB, indicating that these are key factors in determining the onset of the core He flash that ensues.

Despite the similar *core* masses at the end of the RGB we note that the differing evolution of the $Z = 0$ model leads to a higher *total* mass at the end of the RGB. Thus the envelope is more massive in the $Z = 0$ model at the end of the RGB. Figure 5.9 shows the time evolution of the mass loss rate and the total mass. It is clear just how short the $Z = 0$ RGB is in this diagram (more so in the bottom panel). It is however exaggerated in the top panel due to the late onset of the Reimers mass loss in this model. We note that this late onset is a consequence of the algorithm that decides when to switch on mass loss. In a ‘normal’ star H is exhausted at the end of the MS and this is when the SEV code initiates RGB mass loss. In the $Z = 0$ case however the H is *not* exhausted at the end of the MS (a little remains due to the inefficiency of the pp-chains). The mass loss thus starts at the base of the RGB when the last of the H is burnt. This delay actually has negligible effect on the mass of the star at the end of the RGB, as the mass loss rate is so low initially (see bottom panel). The difference in RGB lifetimes is quite large, being a factor of ~ 2.7 shorter in the $Z = 0$ model. The $Z = 0$ RGB lasts only 0.20 Gyr as compared to 0.54 Gyr in the $Z = 0.0017$ case. The reason for this is that the evolution of the $Z = 0$ model is cut short by the onset of the core He flash thus it never loses much mass via winds. Indeed, the total mass at the end of the RGB for the $Z = 0$ star is $0.825 M_{\odot}$ whilst that of the GC model is only $0.690 M_{\odot}$.

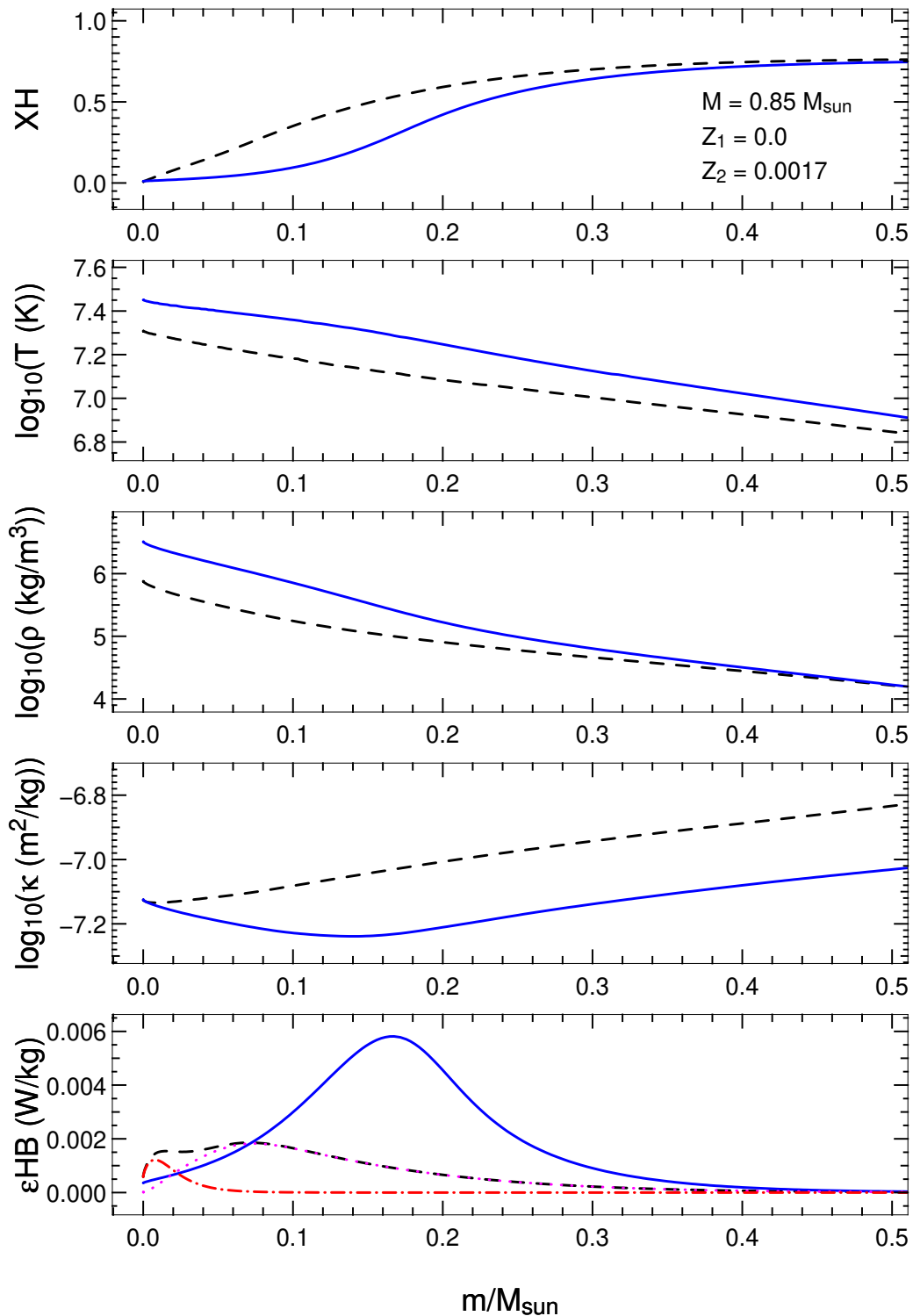


Figure 5.6: Same as Figure 5.5 but towards the end of the MS (central $X_H \sim 0.01$). Significant differences in all physical quantities are apparent. Of particular interest is the very different H burning regimes evident in the bottom panel. Here we have over-plotted the contributions from the CNO cycles (dash-dotted line, red) and the PP chains (dotted line, magenta) for the $Z = 0.0017$ star (dashed line). The energy in the $Z = 0$ model (solid line, blue) is 100% from the PP chains. Also of note is the broad spread of energy generation in the $Z = 0$ model, a consequence of the low temperature dependence of these reactions.

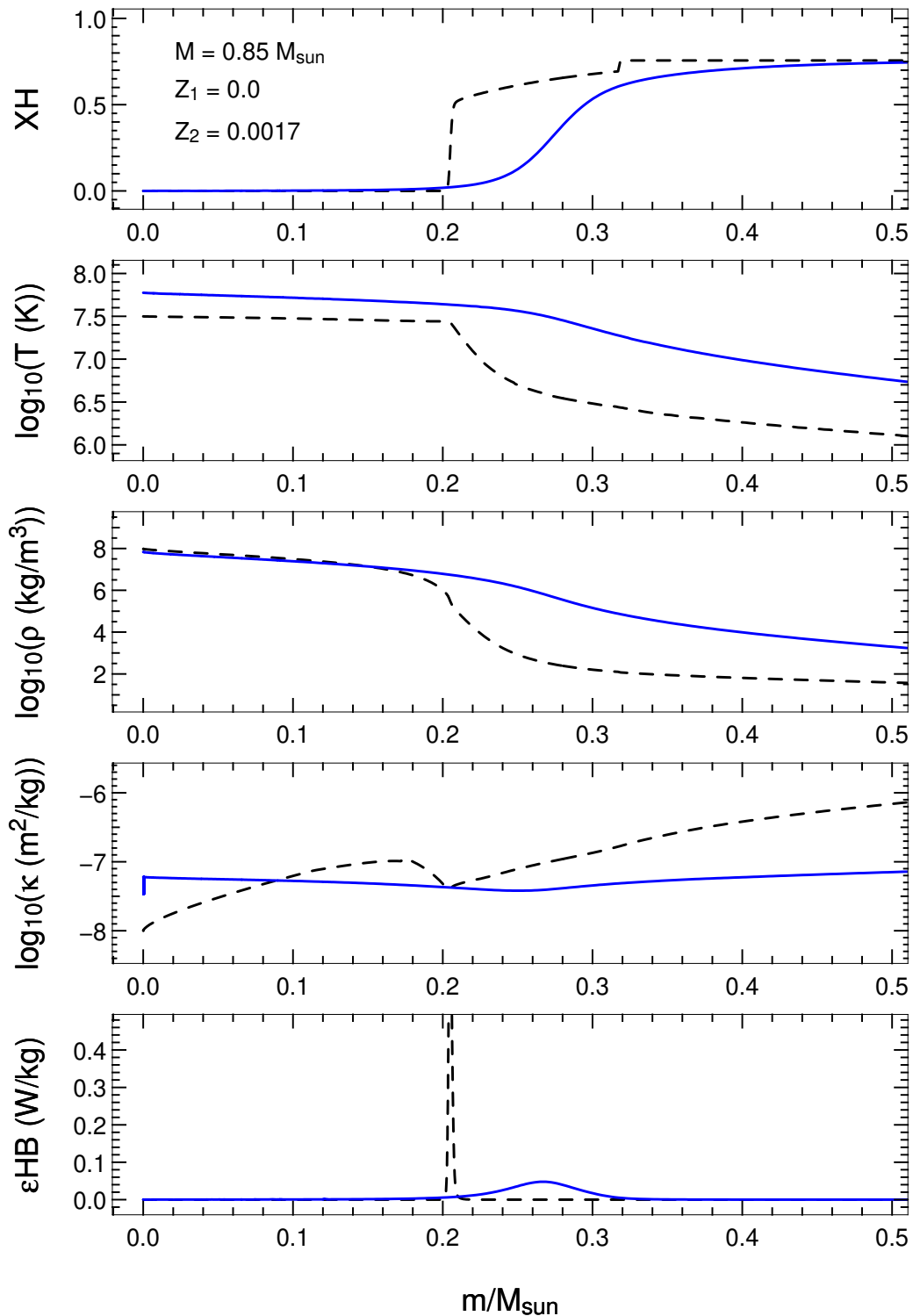


Figure 5.7: The same as Figure 5.5 except for the stars when they are on the RGB, having a shell burning configuration. Here the structures are quite different. The strong effect of having CNO cycles dominating the H burn is evident in the bottom panel. The very localised energy generation in the $Z = 0.0017$ model (dashed line) is a consequence of the strong temperature dependence of the CNO cycles. The energy generation in the shell is almost entirely from the CNO cycles. The $Z = 0$ star on the other hand, which has a PP-shell, has much smoother profiles throughout.

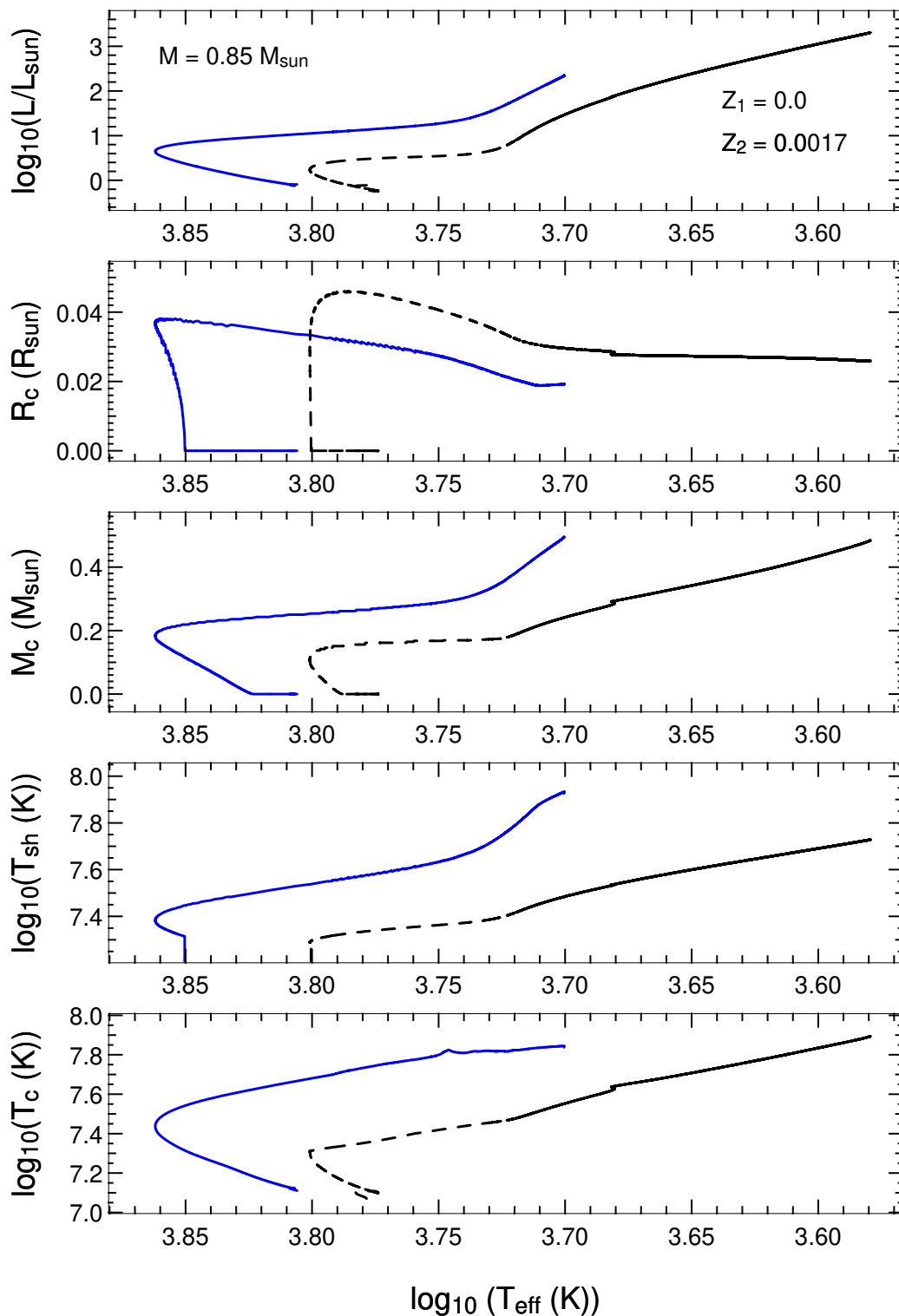


Figure 5.8: Comparison between the two stars, this time against surface temperature. The top panel is the usual HR diagram, the second shows the evolution of the H-exhausted core radius (R_c) and the third the H-exhausted core mass. The gradual core collapse at the end of the MS onwards can be seen, as can the ongoing growth of the core in terms of mass. The bottom two panels show a) the temperature at the bottom of the H-burning shell and b) the central temperature. Here it can be seen that the shell temperature in the $Z = 0$ star is very high, approaching 10^8 K. The core temperature of the $Z = 0$ star is quite constant during the RGB, and is very high. We note that both stars end up with approximately the same core mass and core temperature at the tip of the RGB.

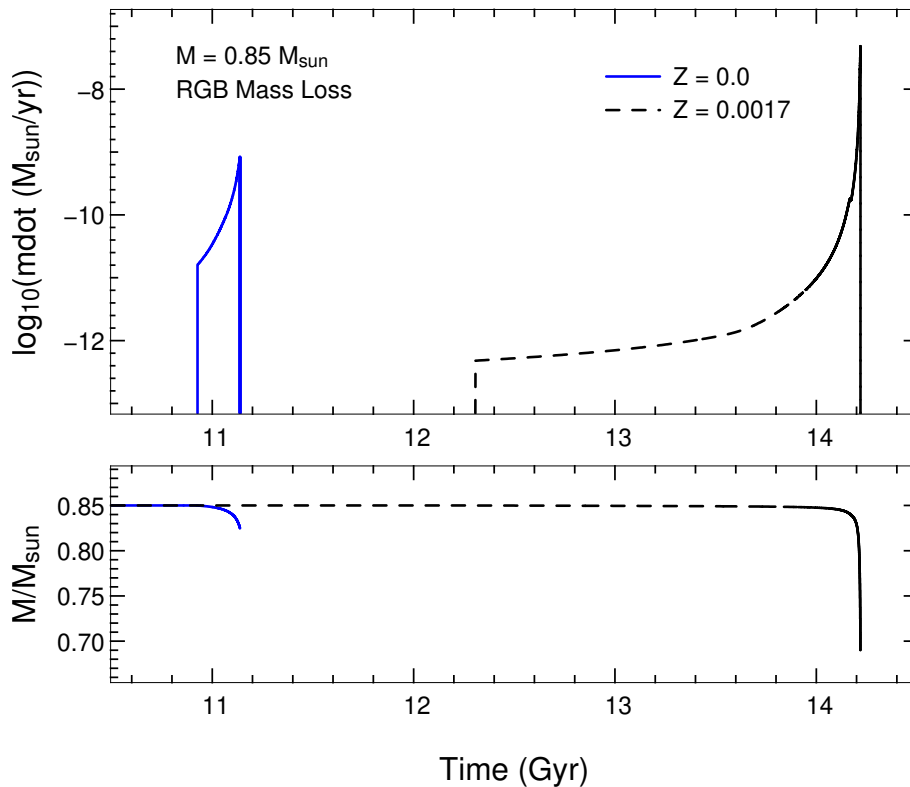


Figure 5.9: Time evolution of the mass loss rate (top) and total mass (bottom) for both the $Z = 0$ and $Z = 0.0017$ models during the RGB. The difference in time spent on the RGB is exaggerated in the top panel due to the late onset of the Reimers mass loss in the $Z = 0$ model. The $Z = 0.0017$ model actually spends ~ 0.5 Gyr on the RGB (mass loss is initiated at the MS turn-off in this model) whilst the $Z = 0$ model spends only ~ 0.2 Gyr on the RGB. This is due to the rapid evolution of the core to the conditions in which He ignites. In the bottom panel we see the direct effect of the shortened RGB – the total mass of the $Z = 0$ star is considerably higher at the end of the RGB, due to a shorter amount of time spent losing mass. We note that the late onset of the Reimers mass loss in the $Z = 0$ model has negligible effect on the mass of the star at the end of the RGB, as it is such a low rate initially (see bottom panel).

We now delve into the anatomy of the $Z = 0$ model's H-shell towards the end of the RGB, when some local ^{12}C production has allowed the CNO cycles to operate. Figure 5.10 shows the various nuclear energy generation profiles of the shell against mass. It can be seen that the CNO cycle is indeed operating, but only at the bottom of the H-shell. The top of the shell is still burning via the PP chains, and is the dominant source of energy in this model. To illustrate the cause of the CNO ignition we also plot the He burning energy release, as there is a tiny amount of 3α reactions occurring. The resultant ^{12}C profile is also plotted and it can be seen that the He burning at the top of the core/bottom of the shell is producing the minute amount of ^{12}C that is needed for the CNO cycles.

In terms of chemical pollution of the convective envelope on the RGB the first dredge-up (FDUP) event that occurs in higher metallicity stars is virtually non-existent at $Z = 0$. Although the convective envelope does make an incursion into the interior regions, the maximum depth reached (in mass) is much less than higher metallicity stars. For example, in our $Z = 0.0017$ model the envelope reaches down to a maximum depth of $m = 0.63 M_{\odot}$ whilst in the $Z = 0$ model it only reaches to $m = 0.30 M_{\odot}$. Although the H burning shell/region is much larger in the $Z = 0$ model, due to the low temperature sensitivity of the p-p chains, the convection only just touches the region of partial burning. In addition to this, as there is no CN cycling (except right at the bottom of the H shell), the only product that may be dredged up is He. The amount of He that is dredged up is totally insignificant, such that the star continues to the tip of the RGB with a pristine surface.

Finally we show in Figure 5.11 a close-up of the penultimate evolution of the hydrogen burning luminosities. It is only in the very last period before the core flash that the total CNO luminosity finally becomes comparable to that of the PP chains. The onset of the core He flash can also be seen. This interesting phase of evolution is the subject of the next subsection.

5.2.2 Dual Core Flash

It is well known that low mass stars ($M \lesssim 2M_{\odot}$, dependent on metallicity) ignite helium violently in their cores at the end of the red giant branch (see eg. Hansen and Kawaler (1994) or Böhm-Vitense (1992) for an overview). The reason that the ignition is 'violent' is because a thermal runaway occurs due to the matter being (electron-) degenerate. In degenerate matter the equation of state is quite different to that of more normal plasma – the temperature and pressure are decoupled. This means that once the temperature is high enough to ignite helium the gas will *not* expand and cool to compensate. This gives rise to a positive feedback loop in which the energy release by the nuclear reactions increase the temperature which in turn increases the rate of reactions, leading to the thermonuclear runaway. Eventually the energy released will be so large so as to remove the degeneracy (the velocity distribution of the electrons becomes Maxwellian again), and the change in equation of state then allows an expansion and cooling which ends the runaway. The reason this happens in low mass stars only is that these stars do not reach high enough temperatures in their cores to ignite helium before the core becomes degenerate. The core becomes degenerate due to the density increase during its gradual collapse, a collapse which is aided in part by energy losses from neutrino production in the core. In this subsection we look in detail at the core helium flash of our $0.85M_{\odot}$ model and find that

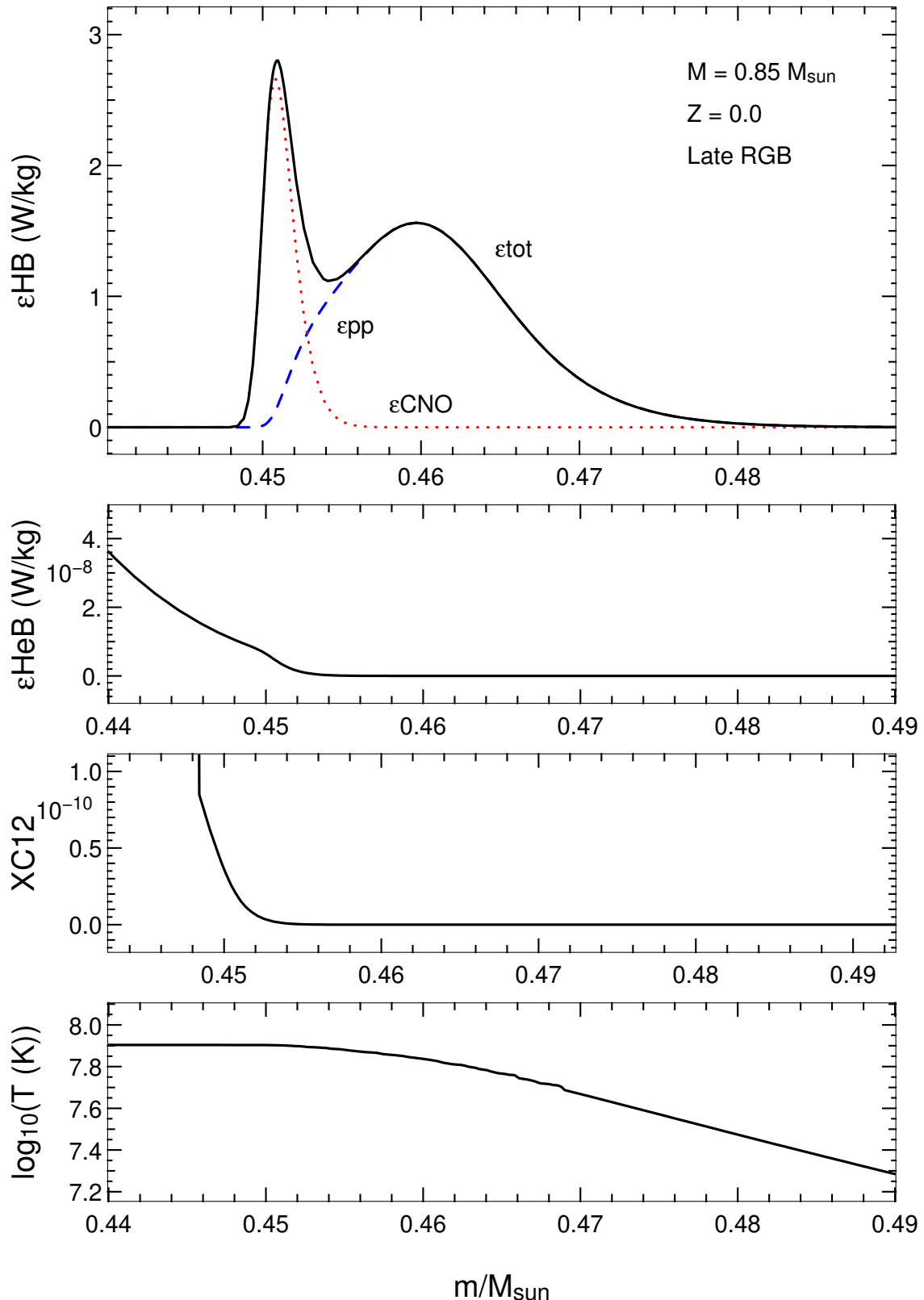


Figure 5.10: The hydrogen burning shell in the $Z = 0$ model late on the RGB. The two top panels show nuclear energy generation versus mass. The two bottom panels show the run of ^{12}C abundance and temperature, also versus mass. It can be seen in the top panel that CNO burning has started in the shell, but also that PP burning is still strong. The reason CNO burning is occurring is because there has been some He burning in the core/bottom of the H-shell (second panel), producing some ^{12}C . It is only a minute amount of He burning but produces enough catalyst for the CNO cycles. The distribution of ^{12}C (panel 3) clearly indicates where the CNO cycles can operate.

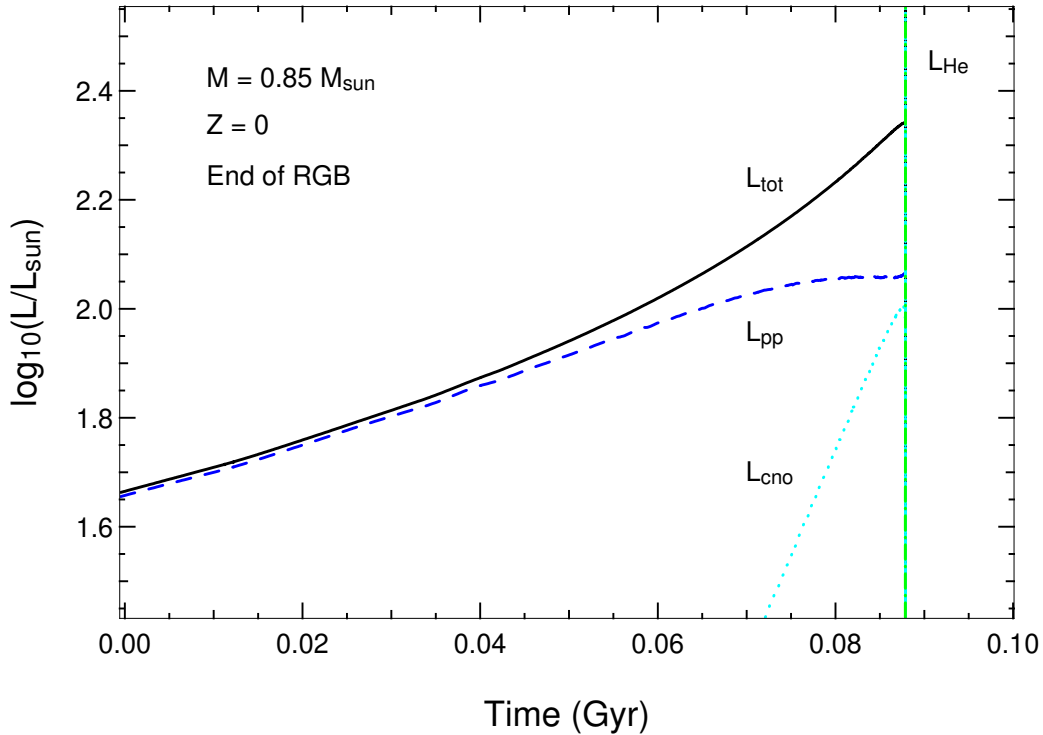


Figure 5.11: The final lead-up to the core He flash in the $Z = 0$ model. Plotted are the luminosities from the PP chains (dashed line), CNO cycles (dotted line), He burning (dash-dotted, green) and also the total luminosity of the star. Time is offset for clarity (zero corresponds to roughly 11 Gyr in Figure 5.2). It can be seen that CNO burning never dominates the energy generation in this star, as opposed to the $Z = 0.0017$ model. The onset of the core He flash is also evident (vertical line).

a second flash – a hydrogen flash – is induced by the helium flash, giving two large releases of energy within a very short time. Hence the title ‘Dual Core Flash’.

We begin by looking at the variation in helium burning luminosity with time. Figure 5.12 compares the luminosities of the $Z = 0$ model with $Z = 0.0017$ GC model. Of note here is that the flash is not a single event, there are a number of ‘mini-flashes’ after the main flash. The main flash is however of a much greater strength than the subsequent miniflashes. It can be seen that the peak luminosity of the main He flashes are approximately the same in both stars (marginally lower in the $Z = 0$ model). Also apparent is the nature of the minipulses – the $Z = 0$ model flashes are closer together in time (initially) and many more occur (8 versus 3 in the $Z = 0.0017$ model). The miniflashes are also initially stronger in the $Z = 0$ model. This probably has little consequence on the further evolution however. As mentioned in the previous subsection, the total luminosity (also displayed in Figure 5.12) at the time of He ignition (ie. the tip of the RGB) is ~ 1 dex lower in the $Z = 0$ model. This has consequences for the expected incidence of bright, low metallicity giants.

We now look at the internal characteristics of the $Z = 0$ and $Z = 0.0017$ stars just before the onset of the core He flash. Figure 5.13 shows a variety of pertinent physical characteristics – temperature, density, opacity, degree of degeneracy and energy loss from neutrino production. It can be seen that there is significant energy loss/cooling of the inner core from neutrinos. Importantly, this leads to the temperature profile (second panel) having a maximum that is offset from the centre. The energy loss cools the cores in the hot, dense regions. As the density drops off so does the cooling efficiency, leading to the higher temperature on the edge

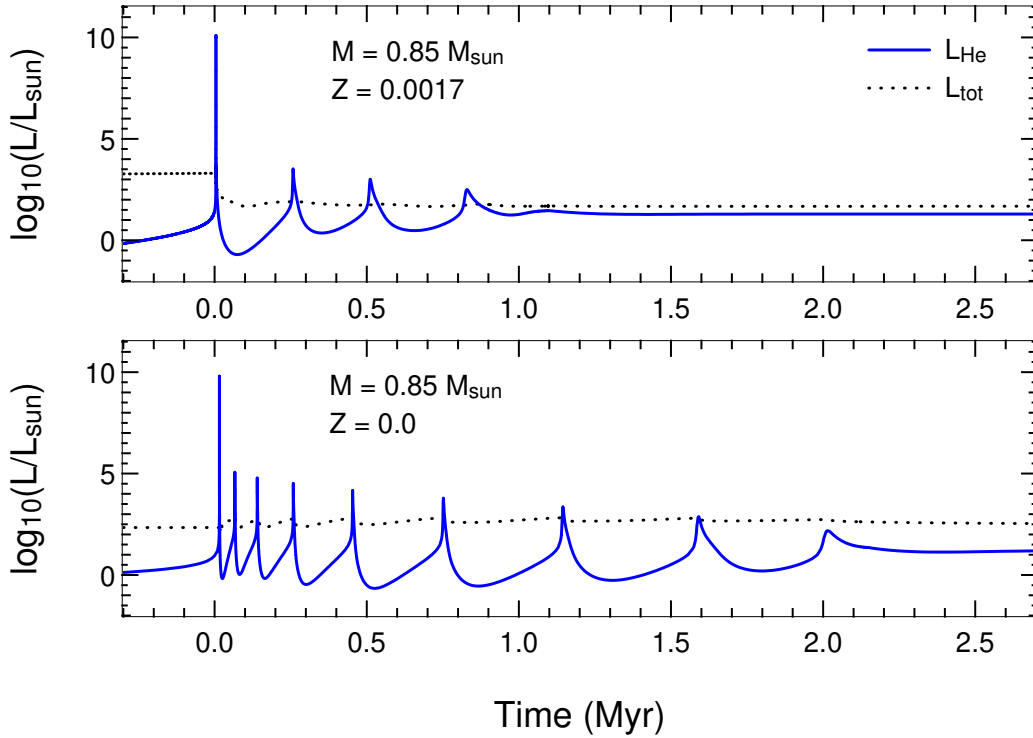


Figure 5.12: Time evolution of the helium and total luminosities in the $Z = 0$ and $Z = 0.0017$ models. Time is offset so zero coincides with the main He flash and the x-y limits are identical. It can be seen that the peak He luminosities of both flashes are approximately the same ($L_{He} \sim 10^{10}L_{\odot}$). The subsequent flashes are however stronger in the $Z = 0$ model ($L_{He} \sim 10^5$ as compared to $\sim 10^{3.5}$ for the second flashes). The $Z = 0$ flashes are also more numerous and initially closer together in time. Also of note is the lower total luminosity of the $Z = 0$ model at the onset of the He flashes.

of the cooled region. Comparing the GC star with the $Z = 0$ star we see that the $Z = 0$ star has a maximum temperature that is much more offset (located at $m \sim 0.12$ and $m \sim 0.28M_{\odot}$ respectively). Looking at the maximum temperature itself (which is approaching 10^8 K) it can be seen that this will be the location of the He ignition for the flash. The fact that the ignition happens so far out in the star will have drastic consequences for the $Z = 0$ model. Also of note is that the opacity in the $Z = 0$ star is lower than the $Z = 0.0017$ star but the degeneracy is higher.

We now move to the core helium flash itself, showing the energy generation from He burning, and the temperature, density, degeneracy and opacity profiles for both stars in Figure 5.14. The enormous energy generation from the 3α reactions is plainly visible in the first panel, being $\sim 10^6$ W/kg ($\sim 10^{10}$ ergs/sec). Also of note are the very high temperatures at which the burning is happening (panel b) – much higher than is normal for quiescent He burning. The effect of the temperature increase on the degree of degeneracy can be seen in the bottom panel – the degeneracy has been lifted in all areas above the flash location. The material below is however still degenerate, a fact that leads to the miniflashes seen in Figure 5.12. Comparing the $Z = 0$ model with the GC model it can be seen that the flash ignition has occurred in a region which is less degenerate in the $Z = 0$ model (and less dense). This gives rise to the slightly weaker flash in the $Z = 0$ model also seen in Figure 5.12.

In Figure 5.15 we display the convection zones that develop as a result of the He flashes for both models. It is immediately apparent that the convection zone is much larger (in mass) in the $Z = 0.0017$ model than in the $Z = 0$ model. Also apparent is the much larger offset from the

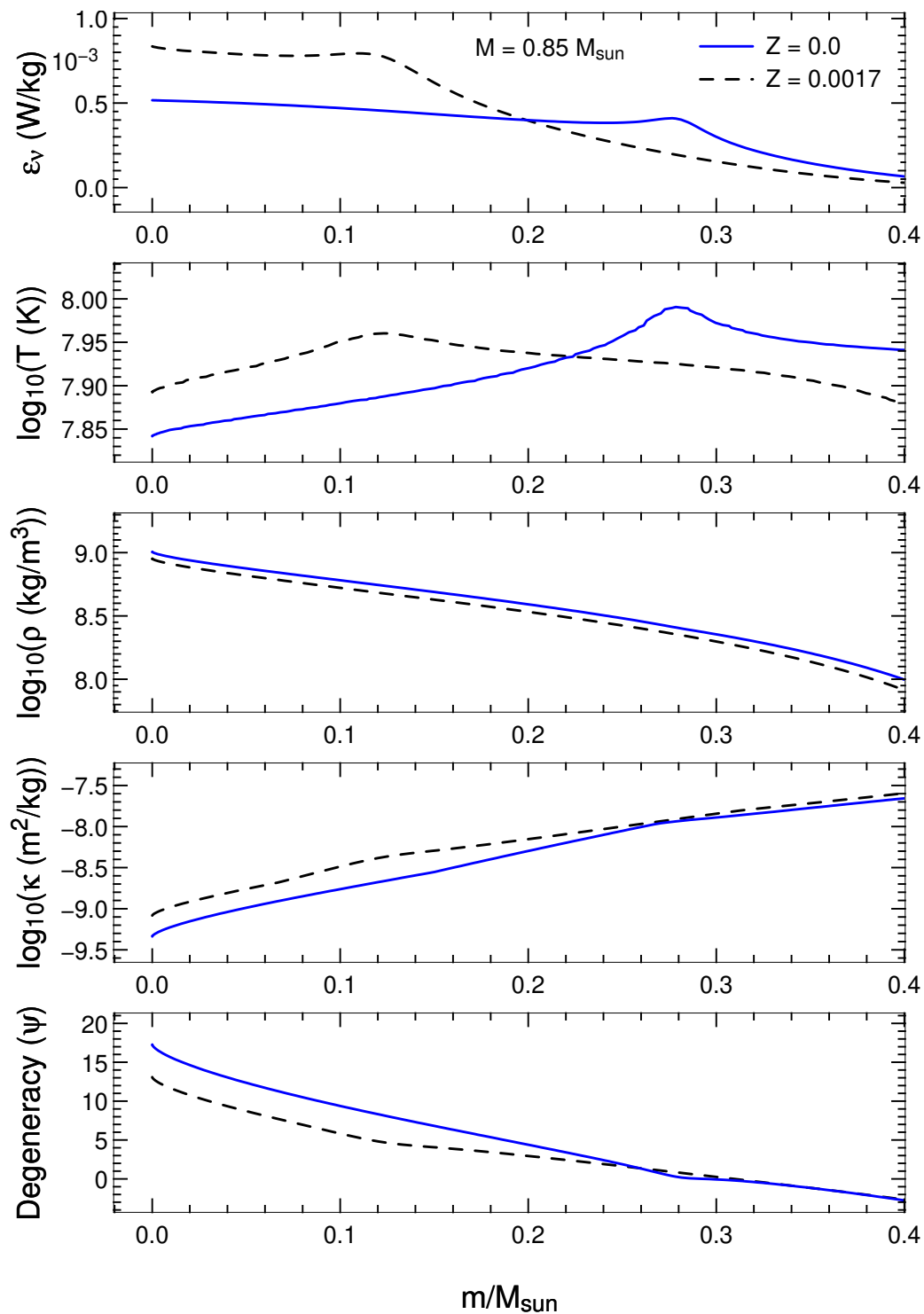


Figure 5.13: A selection of physical quantities against mass for the $Z = 0$ and $Z = 0.0017$ models. Both models are taken just before the onset of their core helium flashes (at a point where $L_{\text{He}} \sim 10^{1.5} L_{\odot}$). It can be seen that the location of the maximum temperatures for both models are significantly off-centre. The reason for this is seen in the top panel which shows the run of neutrino energy loss. The energy loss cools the cores in the hot, dense regions. As the density drops off so does the cooling efficiency, leading to the higher temperature on the edge of the cooled region. This determines the location of He ignition for the flash, which will be substantially further out (in mass) in the $Z = 0$ star. Also of note is that the opacity in the $Z = 0$ star is lower than the $Z = 0.0017$ star but the degeneracy is higher.

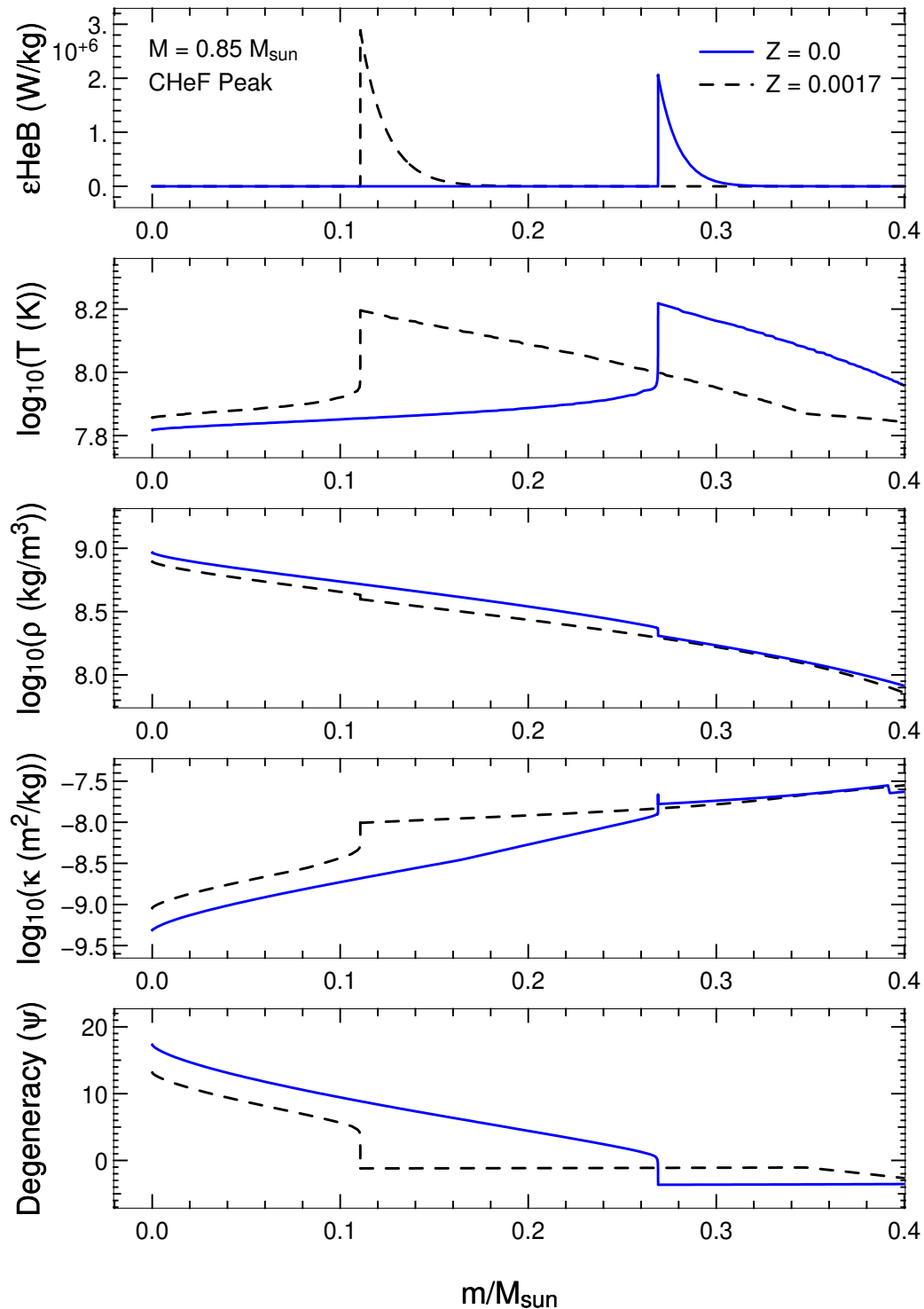


Figure 5.14: Same as Figure 5.13 except the models correspond to the peak of the He flash and the top panel displays the He energy generation rather than the neutrino energy loss. It can be seen that the ignition of helium has occurred at a mass location of $0.11M_{\odot}$ in the $Z = 0.0017$ model whereas it has occurred at $0.27M_{\odot}$ in the $Z = 0$ model. The onset of the flash has removed the degeneracy in the regions above the flash location. Also of note is the fact that the ignition has occurred in the $Z = 0$ model in a region that is less dense and less degenerate than the $Z = 0.0017$ model. The location of this model in time is marked ‘a’ in Figure 5.16.

centre. The two models are quite similar in the early stages of He ignition in terms of the extent of the He convection zone, location of the H-exhausted core (approximately at the same location as the maximum in H burning luminosity), and the timescale of convection zone expansion. However the models diverge severely as the He-flash reaches its maximum. The huge energy input drives an expansion of the He convection zone (a consequence of the large temperature gradient now imposed). In the $Z = 0.0017$ model this convection reaches almost to the H-burning shell, covering a mass of almost $0.4 M_{\odot}$ – or practically half the mass of the star. After the peak in luminosity the convection recedes. In the $Z = 0$ model the situation is quite different. As the convection zone is already so far out (in mass) in the star, the growth of the convection zone quickly reaches the H-burning shell – and indeed breaches the star’s H-He discontinuity. This mixes H down into the hot He convection zone very suddenly. Introducing these protons into such a high temperature environment leads to rapid H burning, releasing a large amount of energy (see Figure 5.16) – a second flash ensues, this time dominated by H burning. This induced H-flash – or Proton Ingestion Episode (PIE) – is a very short event. Indeed the increase in luminosity is much more sudden than that of the He flash (see Figure 5.16) although the luminosity diminishes at a similar, but still more rapid, rate. In the bottom panel of Figure 5.15 it can be seen just how close together these two flashes are in time.

In Figure 5.16 we zoom in, expanding the time axis to cover just a few years. At this time resolution we see that the H-flash actually consists of three events. In the bottom panel we plot the convection zones and the location of maximum burning for H and He. It can be seen that the peaks in the H luminosity correspond to the repetitive expansion of the He convection zone into the H-rich layers. The differing amounts of protons ingested leads to differing peak H luminosities. The differing amounts arise because 1) there is a H composition gradient left behind by the H burning shell and 2) the degree to which the convection zone expands into the H-rich layers varies. In Figure 5.17 we show the tail of the H profile, located just outside the convective zone. It can be seen that the tail is progressively ‘eaten’ by the He-H convective zone, such that each PIE entrains material that is more rich in protons than the previous PIE material. It is interesting to note that the series of three flashes compares well with the $0.80 M_{\odot} Z = 0$ model by Picardi et al. (2004), which also exhibits three H-flashes (although the later evolution of their model is different to our model). Of particular note in Figure 5.16 is the fact that the protons only mix a certain distance down into the convection zone. If the instantaneous mixing assumption were used in this case the protons would have been evenly distributed over the He convection zone after each timestep. Thus protons would have been placed in regions of extremely high temperatures ($\sim 10^{8.3}$ K, see Figure 5.18, panel 4), leading to excessively violent H-burning. With our new time-dependent mixing routine (described in Section 4.1 on page 49) the mixing velocity is taken into account, giving a more realistic situation whereby the protons are burnt during their descent into the hot He convection zone. The depth to which protons survive is dependent on the interplay between the lifetime of the protons against capture (H burning) and the timescale in which they are transported downwards (ie. the mixing velocity). It can be seen in panel two of Figure 5.16 that these factors lead to protons mixing down to a mass coordinate of $m \sim 0.44 M_{\odot}$. When the major entrainment occurs (just before line *c* in Figure 5.16) the consequent energy generation exceeds that coming from He burning (the He flash is receding by this stage). The He burning subsequently reduces significantly, causing the

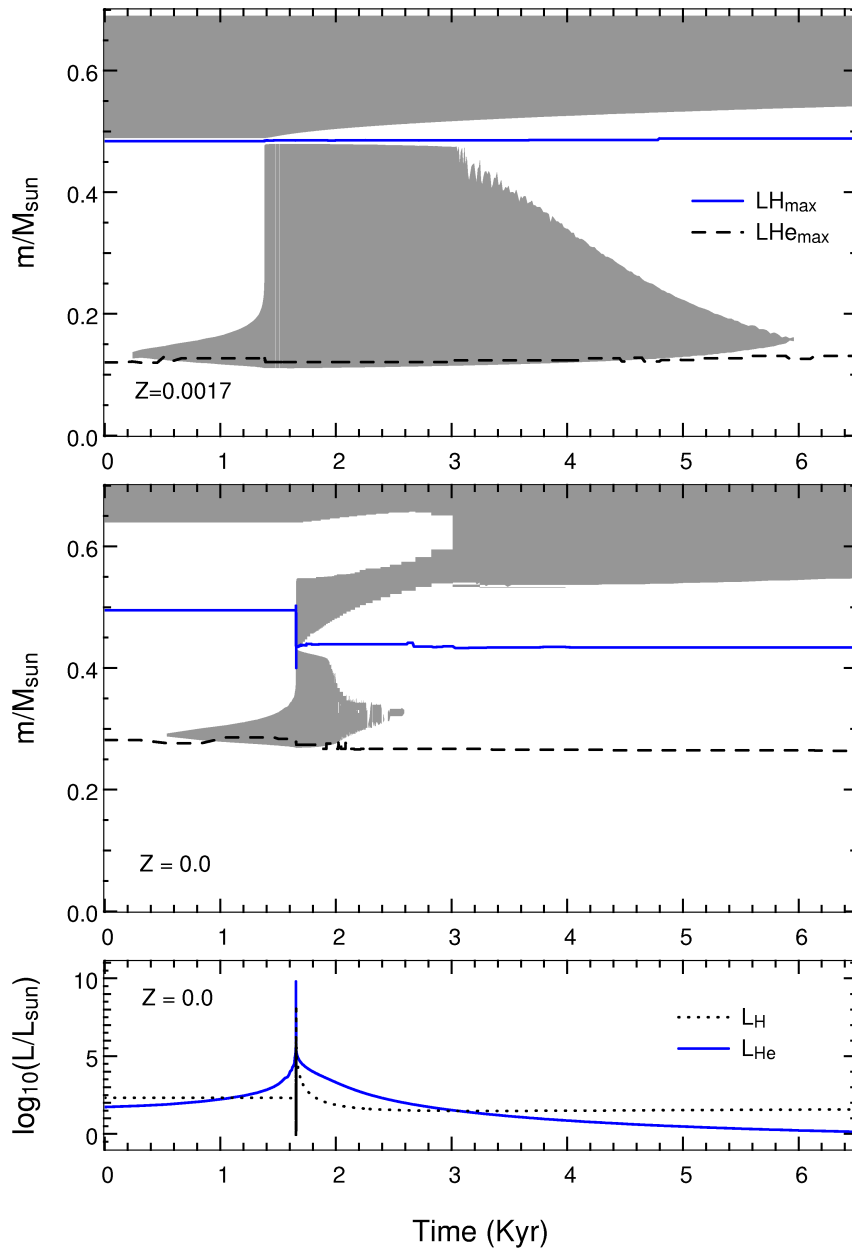


Figure 5.15: The time evolution of the convective zones (grey shading) in the $Z = 0.0017$ model (top panel) and $Z = 0$ model (second panel). The bottom panel shows the evolution of the H and He burning luminosities in the $Z = 0$ model. Note the short span of time (~ 7000 years). The axes for the top two panels are identical, so a direct comparison can be made. The duration of the He convective zone is much shorter in the $Z = 0$ model (~ 2000 yr, as compared to ~ 6000 yr in the $Z = 0.0017$ model). This is due to the off-centre ignition which induces the PIE (and consequent H-flash). The H-flash leads to a partial quenching of the He flash (see also Fig. 5.16). In addition to this there is much less He to burn in the $Z = 0$ HeCZ as it is much smaller in mass ($\sim 0.15 M_{\odot}$ compared to $\sim 0.4 M_{\odot}$). The location of the dual core flash is clearly visible in the second panel, and in luminosity in the bottom panel, at $t = 1.6$ kyr. Finally we note the suddenness of the H flash evident in the bottom panel – on this timescale the H luminosity appears to increase instantly at the start of the flash. This is in contrast to the He flash which exhibits a gradual increase in strength.

He convection zone (HeCZ) to reduce in size. We now have a distinct structure in which there are two burning shells with two associated convective regions (as well as a convective envelope). By 4 years after the peak of the He flash the energy generation from each shell is approximately equal.

To analyse this event in more detail we first look at the physical characteristics of the star during the second proton ingestion episode (PIE). The model in question is displayed in Figure 5.18 and corresponds to line *b* in Figure 5.16. The dominance of the He burning source is clear in the first panel. We note that the H burning is dominated by the CNO cycles as the He shell is abundant in ^{12}C due to the 3α reactions. In the second panel we see the extent of the convective zone and note that the peak of H burning energy generation is well inside the HeCZ. The H profile is plotted in the third panel. This is of interest in relation to time-dependent mixing as it can be seen that, although the H is in a highly convective region, it has not mixed to homogeneity, indicating that the evolutionary timestep taken is shorter than the mixing timescale in this instance. We mark the location of maximum H burning energy generation on the H abundance profile as well as the temperature profile. Hydrogen is present down to a location where the temperature is $\sim 10^{7.8}$ K. We also show the run of the degeneracy parameter ψ to highlight the fact that the H burning happens in non-degenerate conditions.

In Figure 5.19 we move to the major H-flash/PIE. In terms of time the model displayed is approximately indicated by Line *c* in Figure 5.16. Evident in both figures is the phenomenon of the development of dual convective zones. As mentioned earlier the PIE produces a huge amount of energy generation ($\sim 10^6$ W/kg). This can be seen in the top panel of Figure 5.19. This drives a new HCZ and leads to a reduction in He burning energy output and hence a shrinking of the HeCZ. As can be seen in the second panel, we now have a highly convective HCZ above a ‘less convective’ HeCZ. The third panel shows the abundance profiles. Here it can be seen that there is abundant ^{12}C in both convection zones (a product of the previous complete mixing seen in Figure 5.18) and that the HCZ has a large amount of He as well as the newly-entrained H. It can be seen in Figures 5.16 and 5.21 that the HCZ continues to expand and ingest fresh H as time goes on, before the whole convective region moves outwards in mass, leaving behind a ‘polluted’ composition profile. In the fourth panel we see that the H burning is occurring at very high temperatures of $\sim 10^{7.9}$ K. This is slightly lower than the temperature of $\sim 10^{8.0}$ K found in the $0.80 M_{\odot}$ model of Picardi et al. (2004).

We now move on to the later stages of the violent H-He burning episodes. Figure 5.21 shows the evolution following (and including) that shown in Figure 5.16. The ‘time’ axis (actually model number for clarity) covers a much larger span in this case. The behaviour of the H and He convection zones is clear in this plot, showing that there is initially one HeCZ and that a second develops as the PIE occurs. The subsequent evolution sees the two zones remaining separate, such that further dredge-up of ^{12}C and other species from the HeCZ does not occur. We note that this is in contrast with the $0.80 M_{\odot}$ model by Picardi et al. (2004) which ends up dredging up the entire HeCZ at this stage. Our results are however very similar to those of Hollowell et al. (1990) (see their Figure 9). Hollowell et al. (1990) argue that the convection splits into two separate zones due to the fact that the energy flux from the H burning region is now higher than that coming from the He burning region just below, so that a radiative zone necessarily forms just below the H burning region. In Figure 5.20 we show the run of some physical characteristics

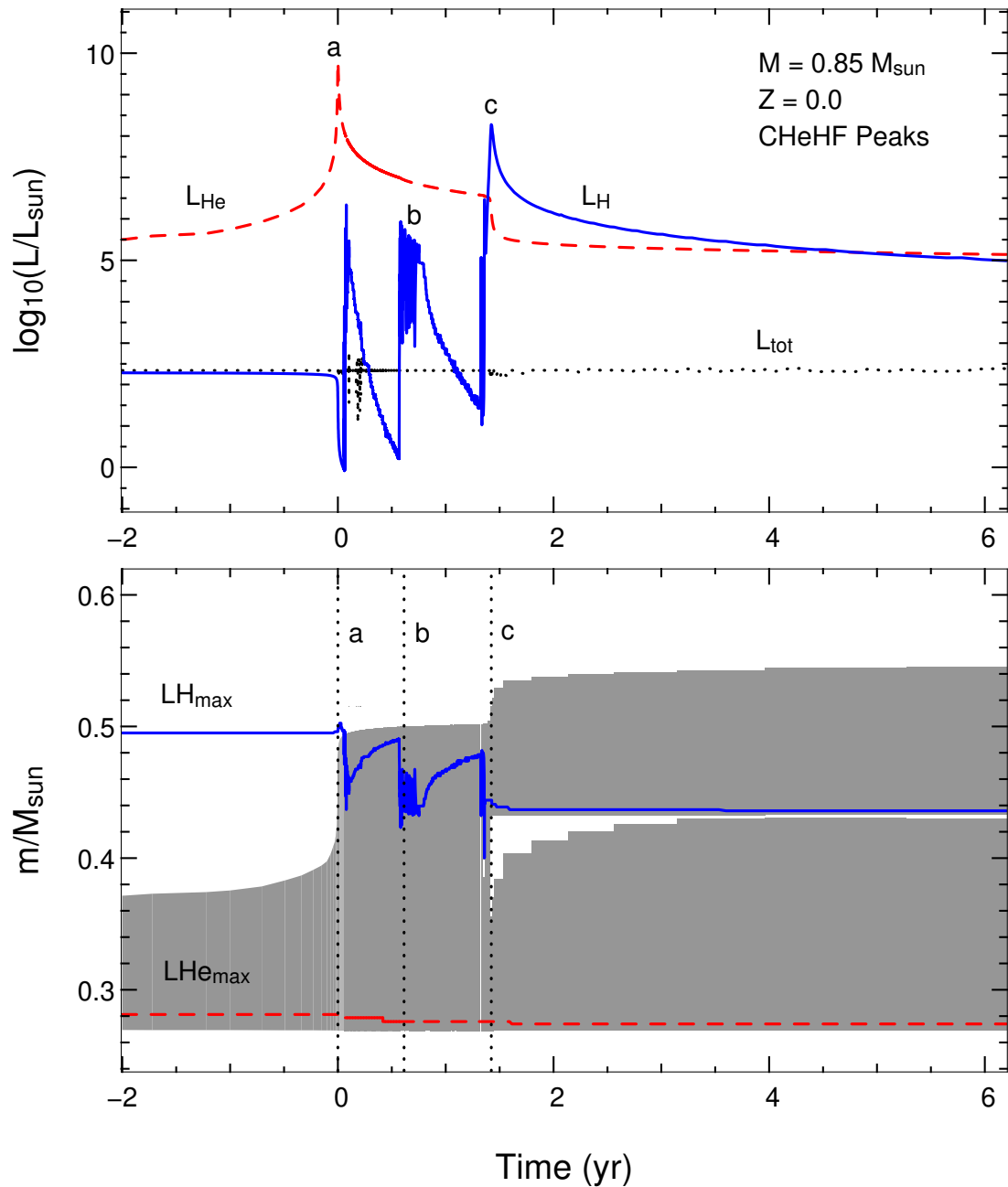


Figure 5.16: Zooming in on the dual core flash in the $Z=0$ model. Note the extremely short timescale on the x-axis. In the top panel we show the evolution of the H, He and total luminosities. In the bottom panel we show the convective zones in shaded grey (except the convective envelope which lies above this mass range) and the locations of maximum H and He burning luminosities. A series of three proton ingestion episodes (PIEs) can be seen, which give rise to the three peaks in H luminosity. It is not until a large expansion of the He-H convection zone occurs, bringing down a substantial amount of H, that the convection zone splits into two – a HCZ and a HeCZ. The H luminosity exceeds the He luminosity at this stage. These two convection zones remain separate for the rest of the evolution. The three vertical dotted lines marked *a*, *b* and *c* represent the time points at which the three models in Figures 5.14, 5.18 and 5.19 were taken. They correspond to a) the peak of the He flash, b) the second H mini-flash, and c) the main H flash.

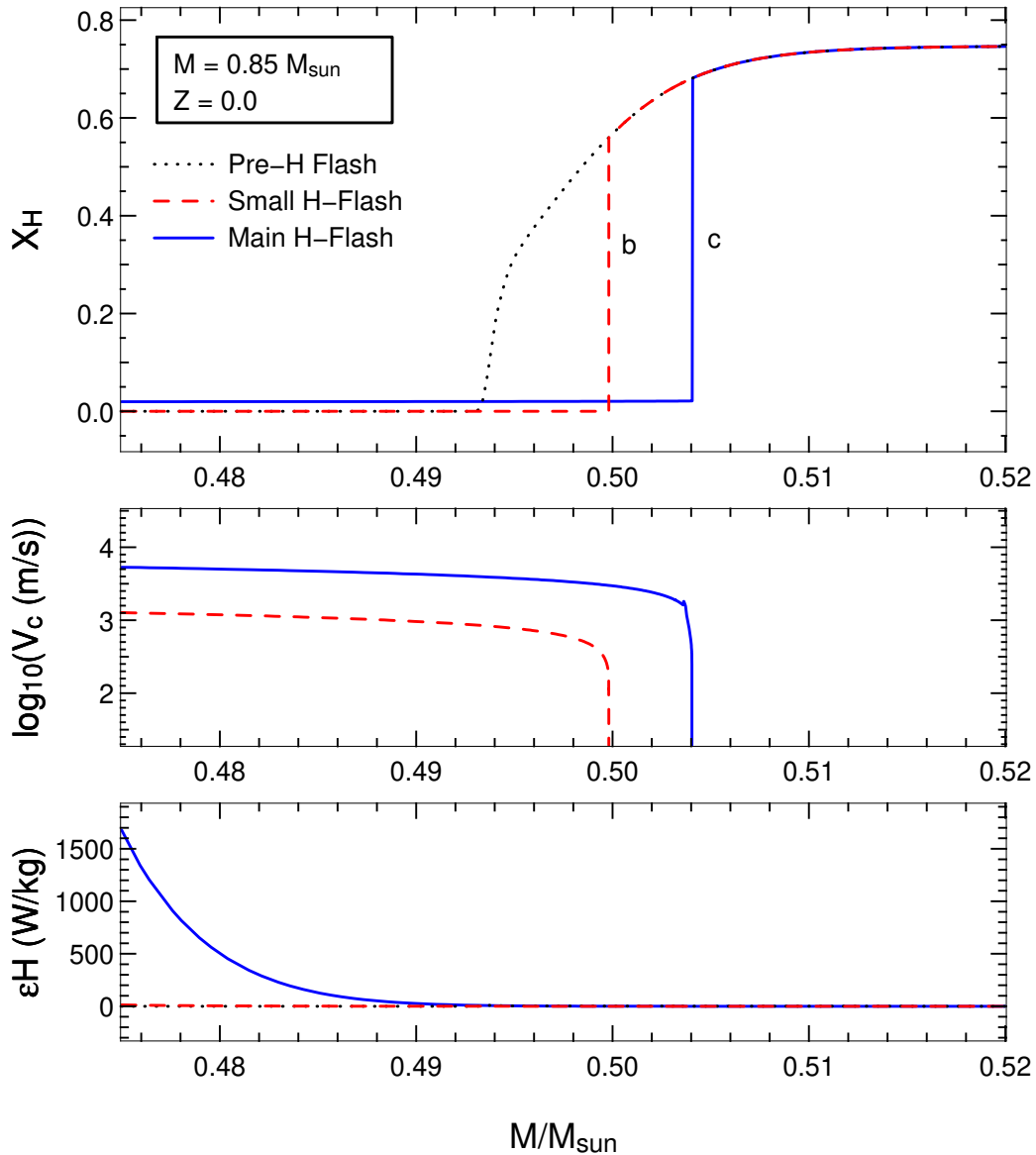


Figure 5.17: Eating the H tail. As the He-H convective zone grows it ingests more and more protons per unit mass as the depleted tail of the H profile (left behind by the H burning shell) is eroded. In the top panel we show the H profile just outside the He-H convective zone (which is identifiable through the velocity profiles in the second panel) for three different stages of evolution during the core He flash. The first model is taken just before the peak of the He flash (dotted line), before the convective zone breaches the H-He boundary. The second (dashed line) and third (solid line) models are taken during the 2nd small H-flash and the major H-flash respectively. Their labelling corresponds to points *b* and *c* in Figure 5.16. It can be seen in case *c* there is a significant amount of H in the convective shell. This is also evident in Figure 5.19.

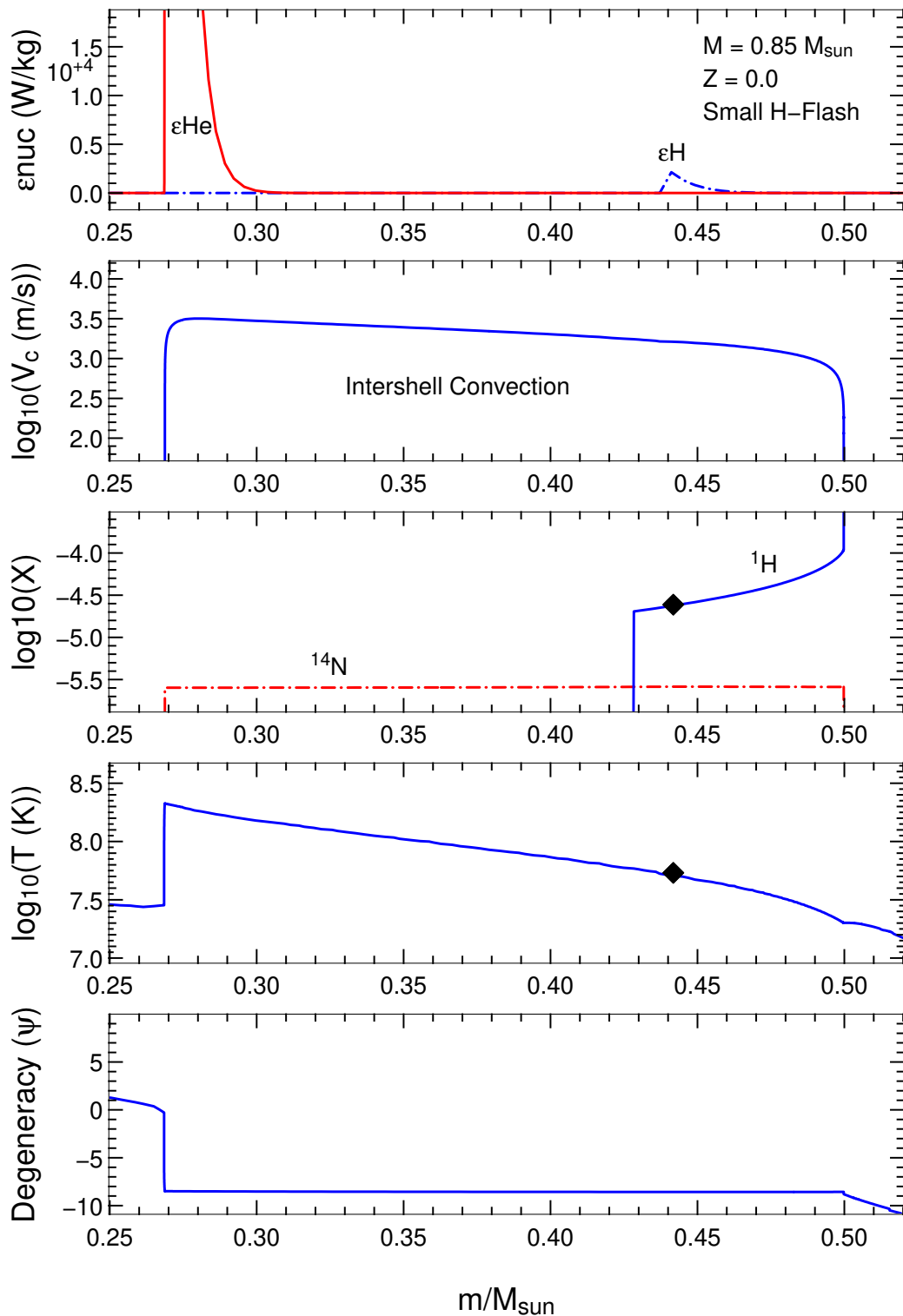


Figure 5.18: The run of some physical characteristics during the second H miniflash (the location of this model in time is marked ‘b’ in Figure 5.16). In the top panel we see that the He energy generation is still dominant. There is only a single convection zone as yet but it contains some H as well as He (panel two). The third panel shows the H abundance profile. We note that, although the H is in a convective region the profile has not been mixed homogeneously. This suggests that the evolutionary timestep is smaller than the mixing timescale and is a good example of the need for the new time dependent mixing routine. The black diamonds give the mass location of the peak energy release from H burning, which is occurring at a temperature of $10^{7.8}\text{K}$. Finally we show the run of the degeneracy parameter to highlight the fact that the H burning is happening in non-degenerate conditions.

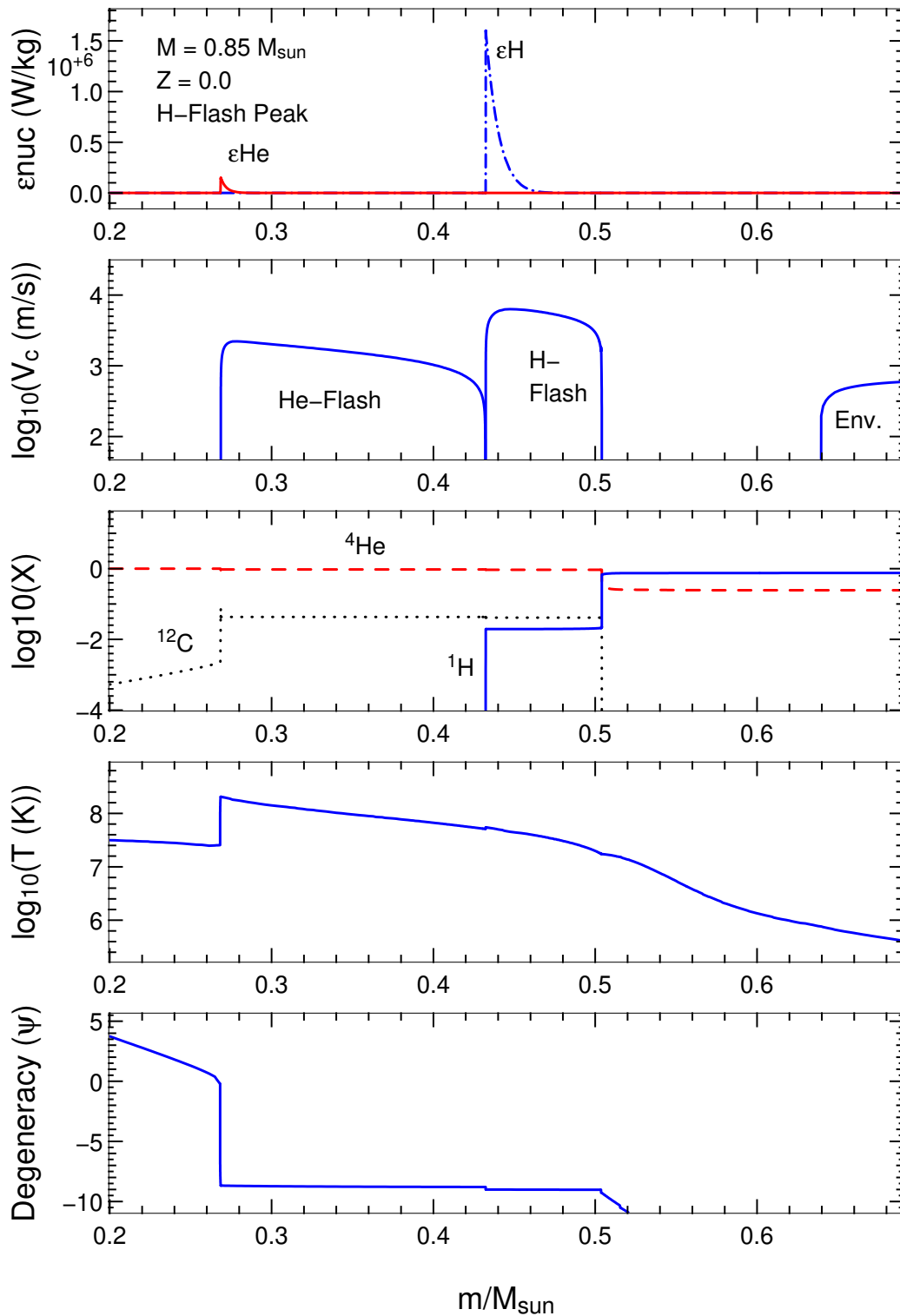


Figure 5.19: Same as Figure 5.18 except for the main H flash (the location of this model in time is marked ‘c’ in Figure 5.16). We now see the energy from H burning dominating. The development of a dual convective zone structure has also occurred (panel two). In the third panel we show the abundance profiles. It can be seen that there is a substantial amount of H in the HCZ (although it is still dominated by He). There is also a large fraction of ${}^{12}\text{C}$ present, which is allowing the CNO cycles to dominate the H energy production. The peak in H energy generation is occurring at a temperature of $10^{7.9}\text{K}$.

with mass for a model taken during the dual convection zone phase (~ 2 years after the He flash peak, see Figure 5.16). Like Hollowell et al. (1990) we show that there is a temperature inversion created by the H burning region at the bottom of the HCZ. To complement this we also show the ratio of the temperature gradients (∇_{rad}/∇_{ad}). Here we see the effect of the temperature inversion clearly, whereby the positive gradient leads to a small region that is highly stable against convection. We also find that there is a substantial region between the HeCZ and HCZ that has virtually a neutral gradient – it appears that a semiconvection zone has developed. We note however that this is soon wiped out by the subsequent re-expansion of the HeCZ.

As both flashes recede their associated convection zones reduce in mass. The convective envelope consequently cools and extends into the regions affected by the H burning and HCZ mixing, thereby dredging up some processed material and polluting the surface. We highlight this process of pollution by following the abundance evolution of total C+N+O mass fraction at one mass coordinate (second panel of 5.21). We chose a mass coordinate that reveals the composition of the HCZ as well as the convective envelope post-dredge-up. It can be seen that the material is initially devoid of any CNO but, as soon as the HCZ extends out to this point the metallicity jumps to $\sim Z_{CNO} = 0.025$ – super Solar. As time progresses and the HCZ mixes in more H, the CNO abundance is diluted somewhat. Finally the convective envelope moves in and the mass point becomes part of the envelope, showing the large dilution effect which leads to the envelope having an abundance of $Z_{CNO} = 0.004$. We thus have a star that was initially devoid of any metals now having a surface abundance of $\frac{1}{5}$ Solar, at least in terms of the lower mass elements. Also shown in Figure 5.21 are the He ‘mini-flashes’ evident in the luminosity diagram in Figure 5.12. It can be seen that some of the helium left in the core due to the off-centre nature of the (major) He flash is periodically burnt in weak flashes. We discuss this in more detail in the next subsection which deals with the core He burning stage and the early AGB.

Another interesting result at the end of the core flashes is that the GC model actually ends up with a slightly higher H-exhausted core mass. While the GC model has a core of mass $\sim 0.5 M_{\odot}$ the $Z = 0$ model has a core mass of just $\sim 0.45 M_{\odot}$. This is due to the PIE whereby H has moved deeper into the star in the $Z = 0$ case.

In summary of this Dual Core Flash (DCF) subsection we note that the main reasons that the HeCZ breaches the H-He discontinuity are (1) because the core He flash begins significantly off-centre – so the HeCZ is already relatively close to the H shell – and (2), as noted by Fujimoto et al. (1990), the entropy barrier in the hydrogen shell is very low in models of extremely-low (or $Z = 0$) models (we note that we have not explored this feature here; see eg. Iben (1977) or Schwarzschild and Härm (1967) for early discussions on entropy barriers in H-shells). Finally we note that the nett effect of the DCF phenomenon is a large pollution of the surface with CNO nuclei. This occurs ~ 3000 years after the peak of the core He flash (see Figure 5.15). We have quantified this pollution ($Z_{CNO} \sim \frac{1}{5}$ solar) here but leave the discussion of the detailed nucleosynthesis for the next chapter.

5.2.3 Secondary RGB and Core Helium Burning

We now move into the post core He-flash evolution. Both stars begin this stage with comparable core masses (the $Z = 0$ model’s is slightly lower) but the GC model has a substantially less massive

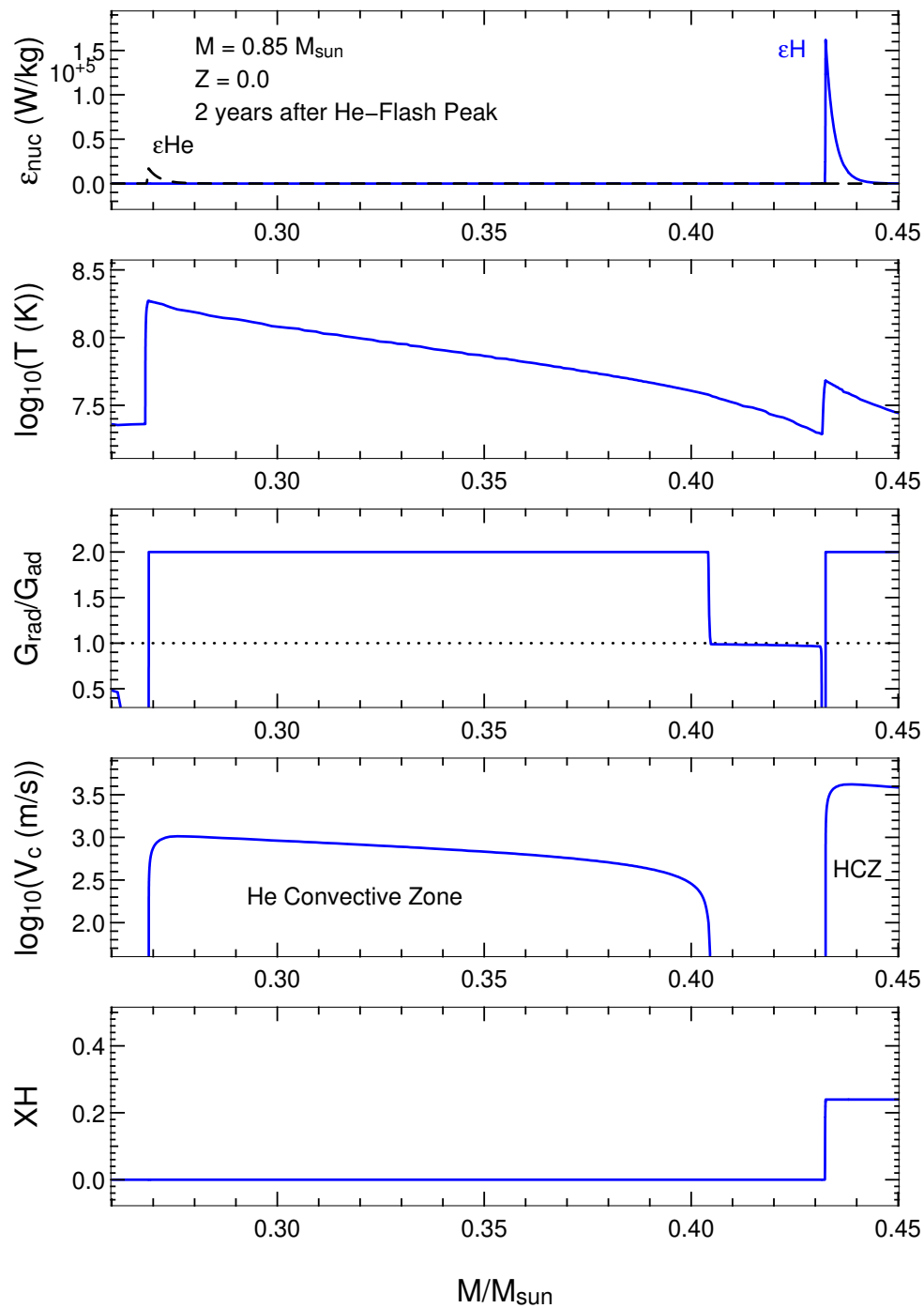


Figure 5.20: The run of various physical characteristics versus mass in the $Z = 0$ star ~ 2 years after the peak of the core He flash (which is ~ 0.5 years after the main H-flash peak – see Figure 5.16). Panel 1 (top) shows the energy generation from H and He burning. It can be seen that the H burning dominates at this stage. The consequent temperature inversions are seen in panel 2. The effect of this temperature profile can be seen in panel 3 where we show the ratio of the temperature gradients ($\nabla_{\text{rad}}/\nabla_{\text{ad}}$; note that we have set all values greater than 2 equal to 2 for clarity). The temperature inversion at the bottom of the HCZ gives rise to a small region highly stable against convection (ie. radiative), causing the continuing separation of the two convective zones. Also apparent is a substantial region between the two convective zones that is (roughly) convectively neutral. This is short-lived however as the HeCZ expands soon after this. The dotted line in panel 3 at a ratio of 1 delineates the boundary between convective and radiative regions as defined by the Schwarzschild criterion, which we are using here.

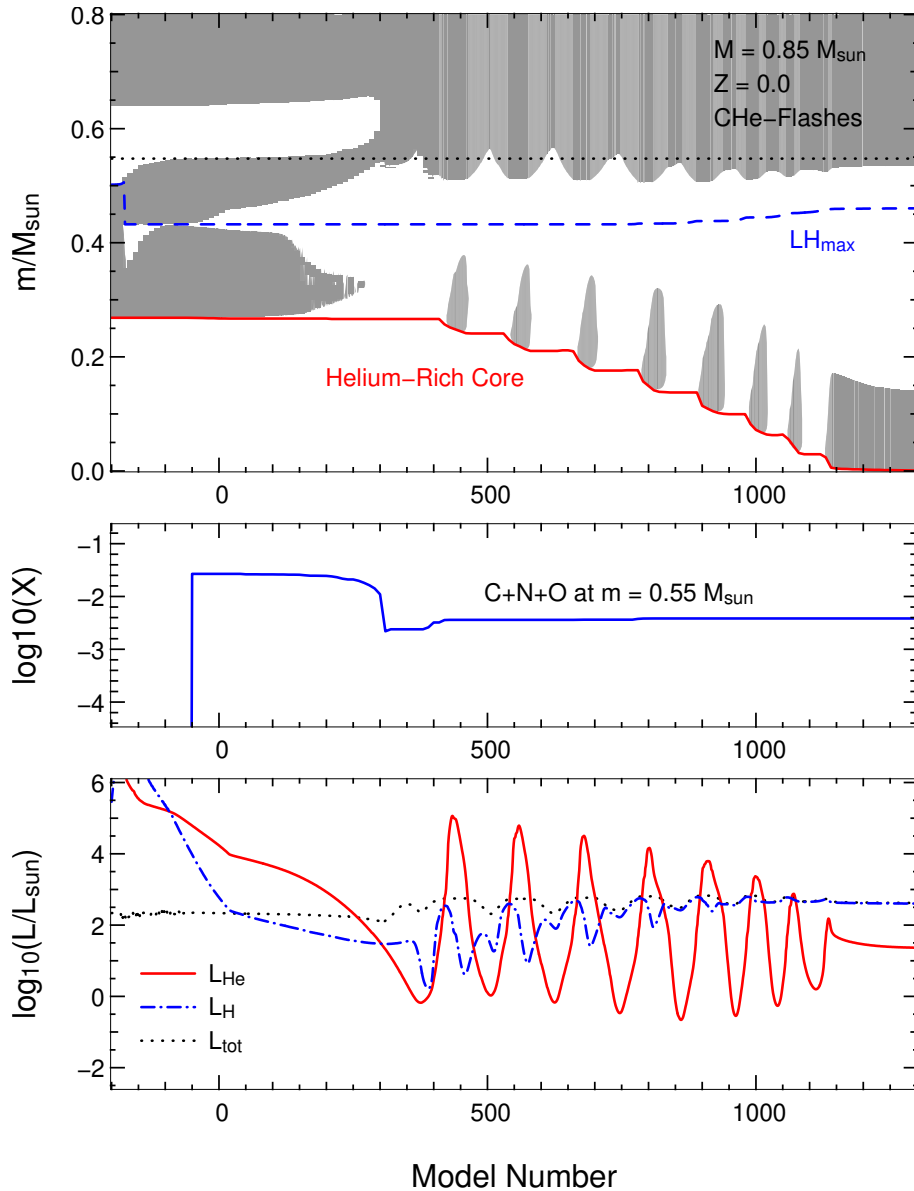


Figure 5.21: The evolution of the convective zones (top), CNO metallicity (middle) and luminosities (bottom), all against *model number*. We have chosen to plot against *model number* because it is time-like but it also spreads out the rapid changes occurring – since the SEV code timestep is mandated by the rate of change of physical properties. In the top panel we can see the PIE (marked by the inward movement of the location of maximum H burning) and the consequent splitting of the convection zones. The horizontal line at $m = 0.55 M_{\odot}$ represents the mass coordinate at which the metallicity evolution in the middle panel was taken. This mass coordinate was chosen as it initially samples the HCZ but also the convective envelope at later times. The discontinuous jump from $Z_{\text{CNO}} = 0.0$ to $Z_{\text{CNO}} = 10^{-1.6}$ is due to the movement of the HCZ out to this mass coordinate whilst the gradual reduction (starting around model 200) is due to dilution. The sudden drop at model 300 is due to the dredge up by the envelope – the CNO nuclei are now diluted over the entire envelope. The final metallicity is seen to be $Z_{\text{CNO}} = 0.004$, or $\sim \frac{1}{5}$ solar. We note that this $Z = 0$ star now has a similar surface Z_{cno} metallicity to the $0.85 M_{\odot}$ GC model. The oscillatory nature of the step-wise He burning after the dual core flash can be also seen in the luminosities (bottom panel). This is the Secondary RGB stage. The total luminosity is also oscillatory, leading to an ‘up-and-down’ motion in the HR diagram.

envelope (see previous subsection for details).

As mentioned above it can be seen in Figure 5.21 that a series of He burning flashes ensue after the main He (and H) flashes abate. These He ‘mini-flashes’ are also evident in the luminosity diagram in Figure 5.12. To elaborate on this phenomenon we show in Figure 5.22 the run of some physical characteristics against mass in a selection of three models for the $Z = 0$ star. We have chosen the models to illustrate what the effect of a minipulse has on the structure. It can be seen that the flashes occur in partially degenerate conditions. The flash has the effect of reducing the temperature and density throughout the region (see dashed lines in Figure 5.22). This causes a reduction in the He burning – but only temporarily. As can be seen in the final model (solid lines), the star heats up again (due to ongoing contraction) and He is again burnt at a high rate. As the evolution continues this will produce a new convective zone. This cycle repeats until the degeneracy in the entire core is reduced. We note that each minipulse burns only a small proportion of the local He ($\sim 5\%$ in mass, see third panel). This incomplete burning thus leaves a core that is still mainly composed of helium (^{12}C makes up most of the other 5%).

Another important feature of this stage of evolution is apparent in the HR diagram (see Figure 5.23) where we can see a significant increase in luminosity *after* the core He-H flashes. As mentioned earlier the tip of the RGB in the $Z = 0$ model is much less luminous than that of the $Z = 0.0017$ model. The fact that the luminosity increases again (by 0.4 dex above the location of the Core He-H flash) leads to a feature in the HR diagram which we refer to as the *Secondary RGB* (SRGB). This excursion to higher luminosities may have observational consequences. We note however that the time spent in this region of the HR diagram is quite brief, being ~ 2 Myr. In addition to this the star actually oscillates between this higher luminosity and the lower luminosity (due to the oscillatory nature of the He miniflashes), such that even less time is spent at the high luminosity end. Thus we would predict that not many $Z = 0$ RGB stars would be observed above a luminosity of $\sim 10^{2.4} L_{\odot}$ and below a temperature of $\sim 10^{3.7}$ K (although there is some uncertainty in the temperature due to opacity, see the discussion in Section C.1 on page 396). We also suggest that this stage of evolution could be named the *TP-RGB*, as it is characterised by a series of pulses.

In Figure 5.24 we display the mass loss history of the $Z = 0$ and $Z = 0.0017$ models during the SRGB/TP-RGB and horizontal branch (HB) stages. It can be seen that the SRGB is an important source of mass loss in the $Z = 0$ model, due to the high luminosity (here the mass loss rate is determined from the Reimers formula). The star in effect ‘catches up’ on some of the mass-losing that it missed out on during its short RGB. We note however that since this stage is also brief (~ 2 Myr) so the star still doesn’t end up losing as much mass as the GC star did on its RGB. The mass loss rate is also much higher on the HB, where it loses about twice as much mass as the GC model does during this stage (the HB lifetimes are comparable). Despite these two sources of increased mass loss the star still ends the HB substantially more massive than the GC model (0.79 versus $0.68 M_{\odot}$). This has ramifications for the AGB phase of evolution, which is discussed later.

Quiescent central He burning begins two million years after the main He-H flash. In Figure 5.25 we display the time evolution of the He convective zones and luminosities. The core He burning phase is a relatively long-lived stage of evolution, with a duration of 80 Myr. During this time

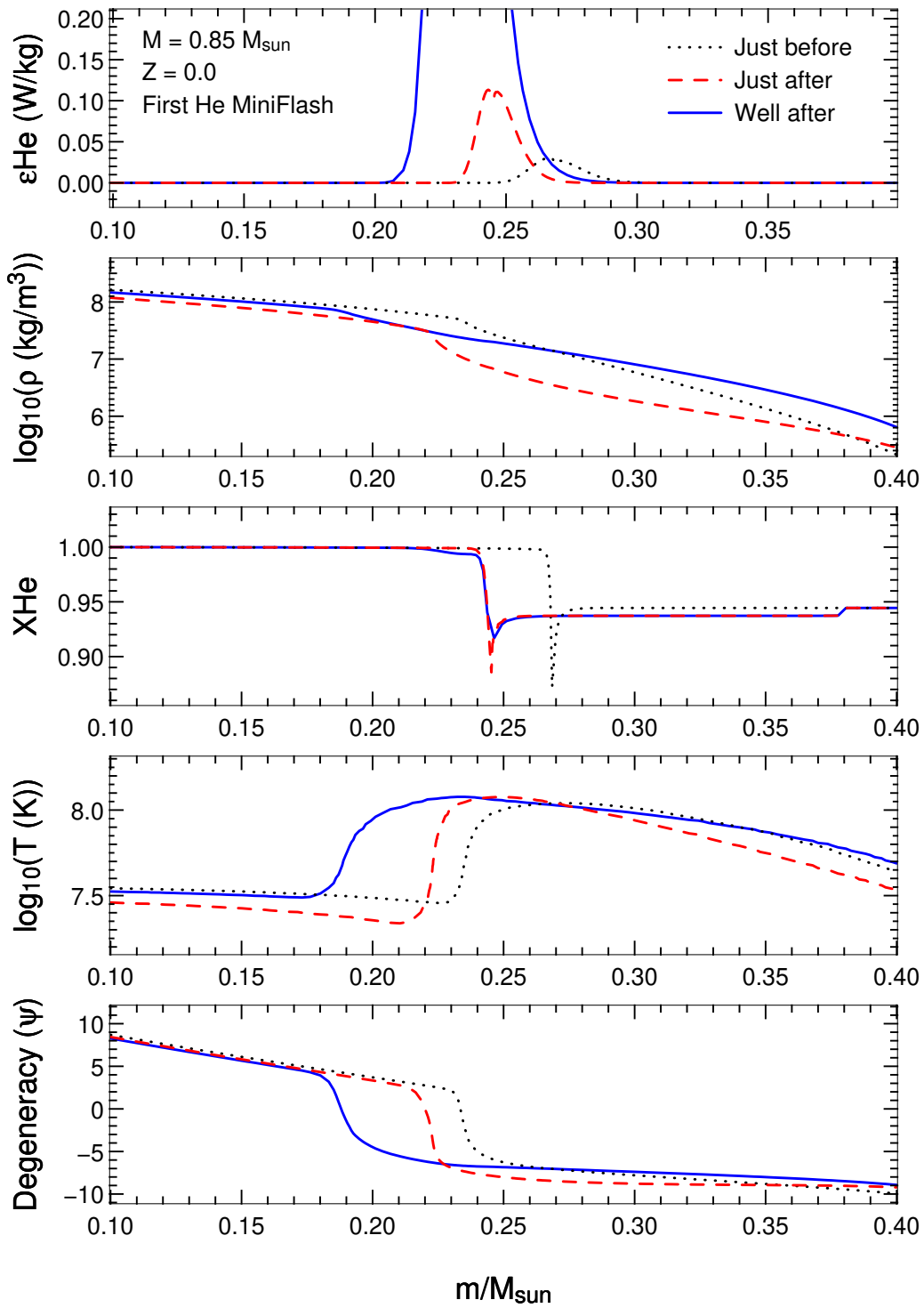


Figure 5.22: The run of some physical characteristics taken at three different times during the Secondary RGB (SRGB) evolution of the $Z = 0$ star. The dotted line represents a structure just before the onset of a He minipulse. It can be seen that the He burning is approaching regions of higher degeneracy. Indeed, the inner core is quite degenerate. Contrasting this model with the next one (taken just after the minipulse) the effect of the minipulse can be seen. The temperature in most regions has been reduced, as has the density. The degeneracy has also been removed down to a lower mass coordinate and He has been burnt in a small region. We note that the burning is incomplete - only $\sim 5\%$ of the He has been burnt (the rest is mostly ^{12}C). The next model (blue line), taken just before the onset of another miniflash, highlights the fact that the star has returned to a hotter structure, ripe for the next flash. Finally we note that He burning occurs between the minipulses, but at a low rate.

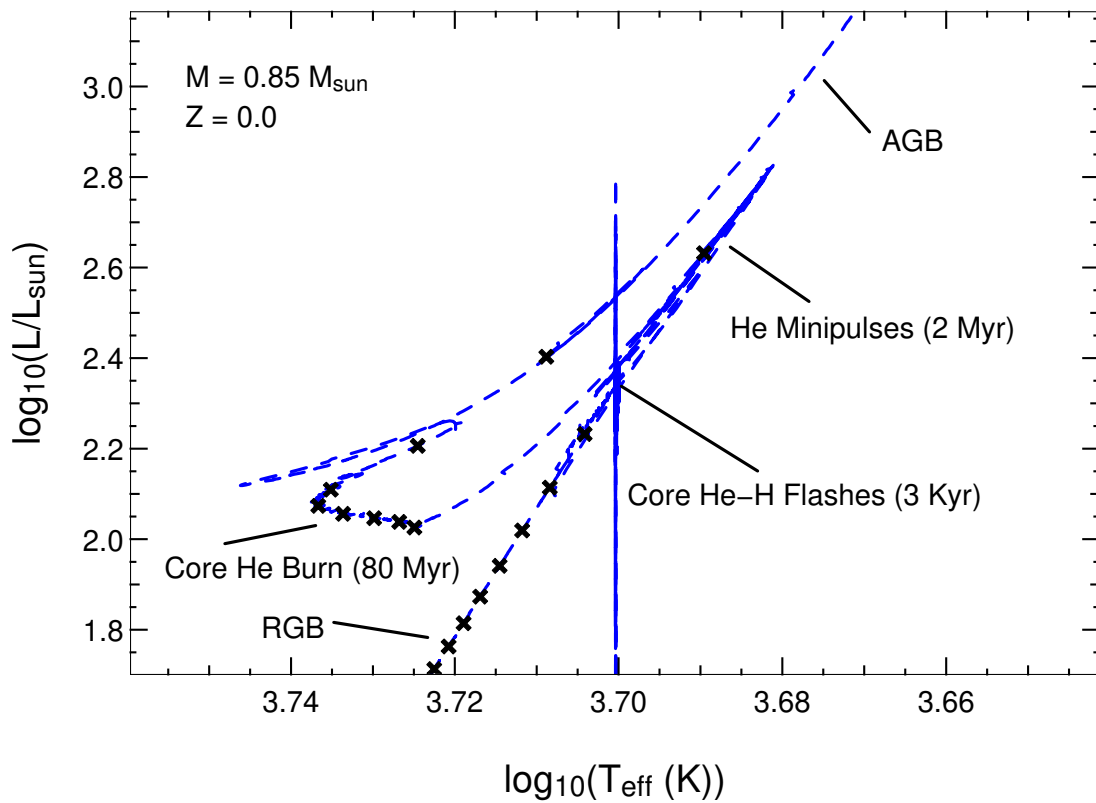


Figure 5.23: Zooming in on the HR diagram at the end of the RGB. The spike in luminosity marks the (numerically difficult) phase of the dual core flash. This occurs at a luminosity of $10^{2.4}$, quite low compared to the $Z = 0.0017$ model (see also Figure 5.12). The star does become more luminous during the He minipulse/Secondary RGB stage but this is short lived. The crosses indicate time and are placed at intervals of 10 Myr.

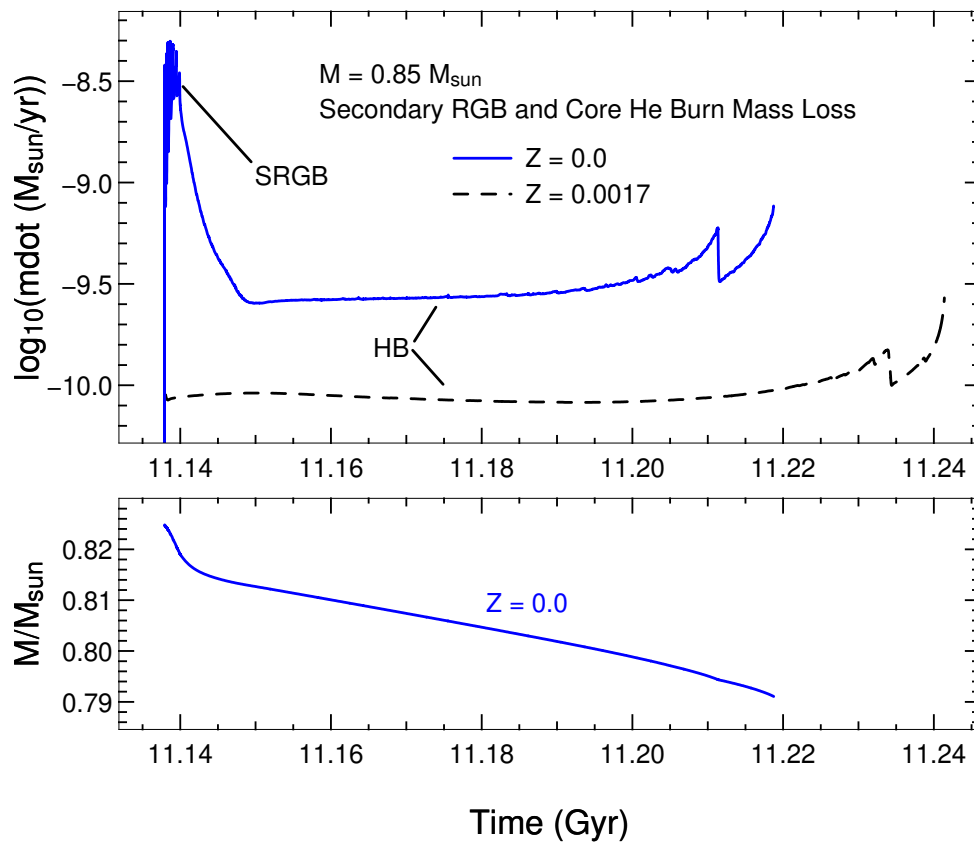


Figure 5.24: The mass loss history for the $Z = 0$ and $Z = 0.0017$ models (top panel) and the evolution of total mass for the $Z = 0$ model. In the top panel we have offset the GC time scale so that the beginning of the HB coincides with that of the $Z = 0$ model. It can be seen that the mass loss rates for the $Z = 0$ model are higher in all phases of evolution shown. Despite this the $Z = 0$ star never attains a mass as low as the GC model (which has a mass of 0.69 at the end of the RGB), it begins the AGB phase with a mass of $0.79 M_{\odot}$.

the convective core gradually grows in mass, reaching a maximum extent of $0.3 M_{\odot}$. Note that we have not applied any overshoot or semiconvection to this model (at any stage during its evolution). Despite this we find a ‘core breathing pulse’ (albeit minor) towards the end of the core burning where the convective core suddenly expands and mixes in fresh He.

During most of the quiescent core burning phase the dominant source of energy is actually the H burning shell (see panel two of Figure 5.25). It is evident from the higher luminosity in the $Z = 0$ star that the H shell is burning out in mass at a higher rate than in the $Z = 0.0017$ model. This has the important consequence that the $Z = 0$ model ends up with a substantially more massive core at the end of the HB, and hence begins the AGB with a higher core mass. Despite the GC model beginning the HB stage with a (slightly) higher core mass it ends the HB with a core mass of $0.53 M_{\odot}$ whilst the $Z = 0$ star has a core mass of $0.60 M_{\odot}$. This will also affect the the AGB evolution.

Once He is exhausted at the centre the star moves to a double shell structure, with the He burning shell then providing the bulk of the energy. This is the early AGB (EAGB) stage. Also visible towards the end of the timespan of Figure 5.25 are large luminosity variations. These are the first thermal pulses of the AGB, which are discussed in the next subsection.

5.2.4 AGB

The complete evolution of the AGB for our $M = 0.85 M_{\odot}$, $Z = 0$ star is shown in Figure 5.26. Due to the lack of third dredge-up (3DUP) the evolution on the AGB is somewhat uneventful. Indeed, the composition of the envelope only changes very minimally, due to a tiny amount of hot bottom burning (HBB) at the base of the convective envelope. It is thus the post-dual-core-flash dredge-up that has the most significant effect on the chemical yield from this star. That said, there are some interesting evolutionary characteristics of the $Z = 0$ model, which we now detail.

In terms of the thermal pulses we can see in Figure 5.26 that the interpulse period is quite short, being $\sim 10^4$ years. We provide a corresponding Figure for our $Z = 0.0017$ model for comparison (Figure 5.27). In this star the interpulse periods are of the order 10^5 yr. The conditions at the beginning of the AGB for each star are quite different also. Due to the short RGB the $Z = 0$ star did not lose much mass by the time it started the AGB, at which time it has a mass of $0.79 M_{\odot}$. On the contrary, the $Z = 0.0017$ model had a significant amount of mass loss during the RGB and starts the AGB with a mass of only $0.68 M_{\odot}$. Also of note is the difference in *core* mass between the two models. The $Z = 0$ model has a core mass of $\sim 0.60 M_{\odot}$ at the first (convective) thermal pulse whilst the $Z = 0.0017$ model has a core mass of $\sim 0.53 M_{\odot}$.

Despite the $Z = 0$ star having twice as many pulses as the GC model (30 versus 15), the entire TP-AGB evolution is considerably shorter than that of the GC model. In fact the $Z = 0$ TP-AGB phase lasts half as long – ~ 1.6 Myr as opposed to ~ 3 Myr. Also apparent in comparing Figures 5.26 and 5.27 is that the temperature at the bottom of the convective envelope is slightly higher in the $Z = 0$ model, being $\sim 10^6$ K for much of the evolution, compared to $< 10^{5.9}$ K in the GC model. This is however still too low a temperature for significant HBB.

In order to shed some light on why the $Z = 0$ star spends such a short time on the AGB compared

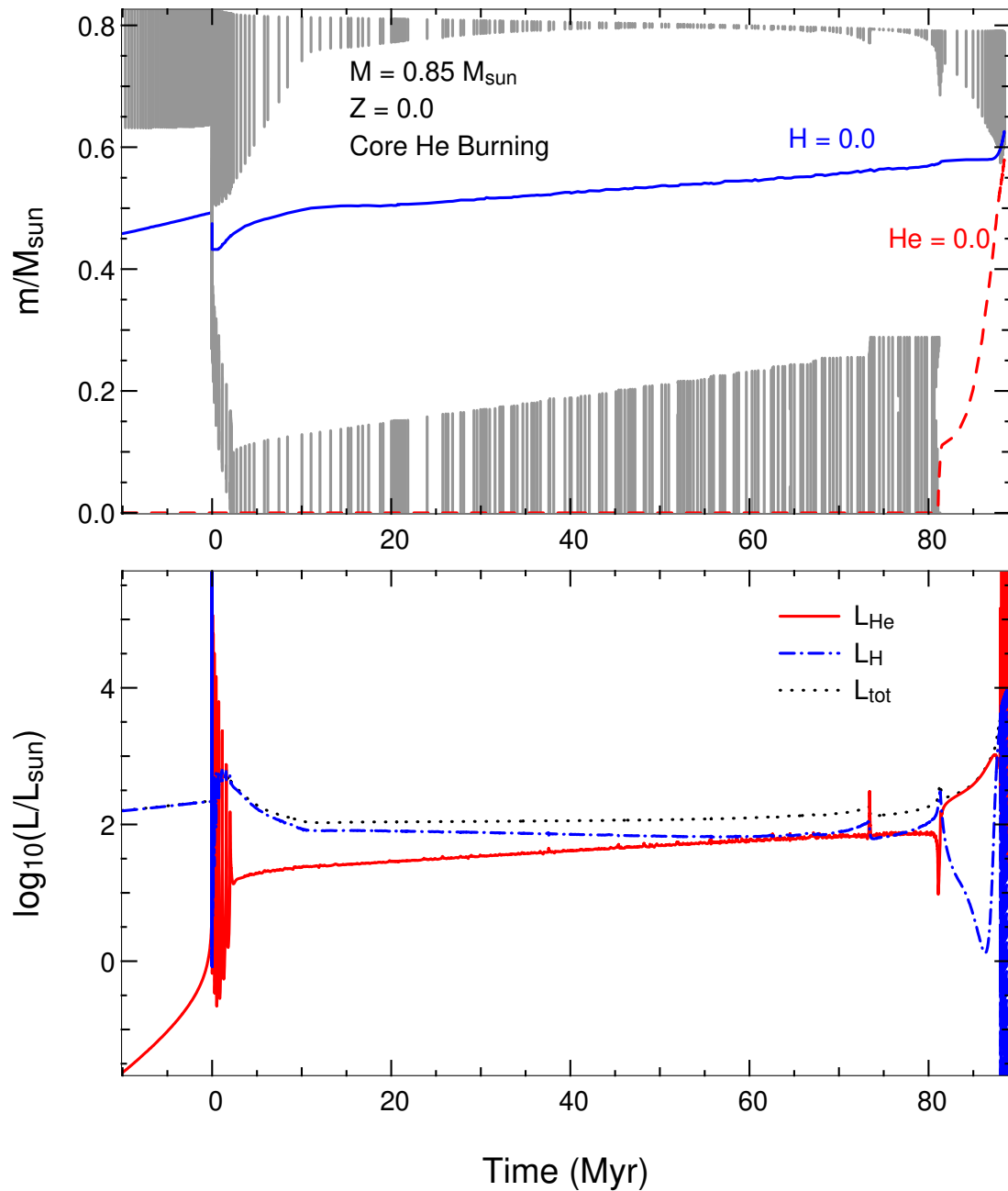


Figure 5.25: The time evolution of the convective regions (marked by individual grey lines representing every 10th model) and luminosities for the $M = 0.85 M_{\odot}$ $Z = 0$ model. The top panel also shows the evolution of the H- and He-exhausted cores (as defined by regions below the abundance = 0 lines). Time has been taken with a zero point at the dual core flash. An interesting feature is the displacement of the H burning shell during the core flash, which subsequently burns outwards with a large luminosity release. The short duration of the He minipulse/SRGB phase can be seen (~ 2 Myr in total), as well as the long quiescent core He burning phase (~ 80 Myr). There is a small core breathing pulse at $t \sim 73$ Myr accompanied by a modest peak in the He luminosity. Also of note is the fact that the H burning shell is actually the main source of energy during most of the core He burning phase. When the He is exhausted at the centre the star moves to a double shell structure, whence the He shell takes over as the main energy source. Just visible on the far right of the plots is the beginning of the thermally pulsing AGB phase.

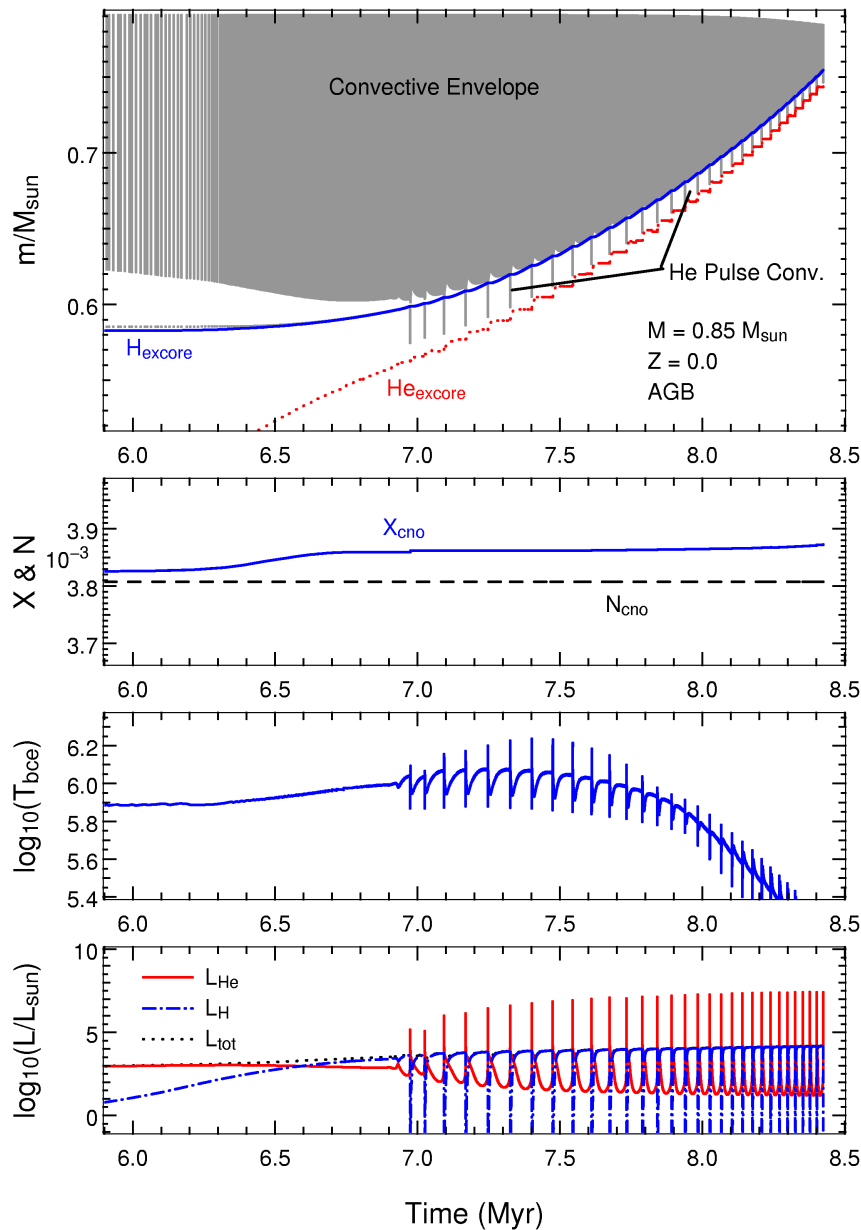


Figure 5.26: The entire EAGB and AGB evolution for the $Z = 0$ model. In the first (top) panel we show the evolution of the convective zones as well as the H- and He-exhausted cores. The rapid core growth through the AGB can be seen, as can the intershell convection zones created by the periodic shell He flashes. We note that the evolution terminates with an envelope mass of $\sim 0.03 M_{\odot}$, due to numerical difficulties. The (very short) remainder of the evolution is handled with a synthetic code (see Nucleosynthesis section for details). In the second panel we show the evolution of the surface CNO abundance (using the same method as that in Fig. 5.21) by sampling at a mass coordinate of $m = 0.77 M_{\odot}$. We plot both the mass fraction (X_{CNO}) and the number fraction (N_{CNO}). This allows us to see two things: 1) if primary CNO has been dredged up (which would cause an increase in N_{CNO} and X_{CNO}) and 2) if hot bottom burning has been active (which would cause an increase in X_{CNO} but not N_{CNO} , as the CNO cycles conserve the *number* of nuclei). It can be seen that there has been no 3DUP at all, but there has been a (very) slight conversion of ^{12}C to ^{14}N . The third panel shows the temperature at the site in which this occurs – the bottom of the convective envelope, which consistently reaches temperatures of ~ 1 million degrees. Finally, in the bottom panel we show the variation of the luminosities. Of note here is the shortness of the interpulse periods ($\sim 10^4$ yr). Indeed, the pulse frequency increases towards the end of the evolution, ending up with interpulse periods of $\sim 20,000$ yr.

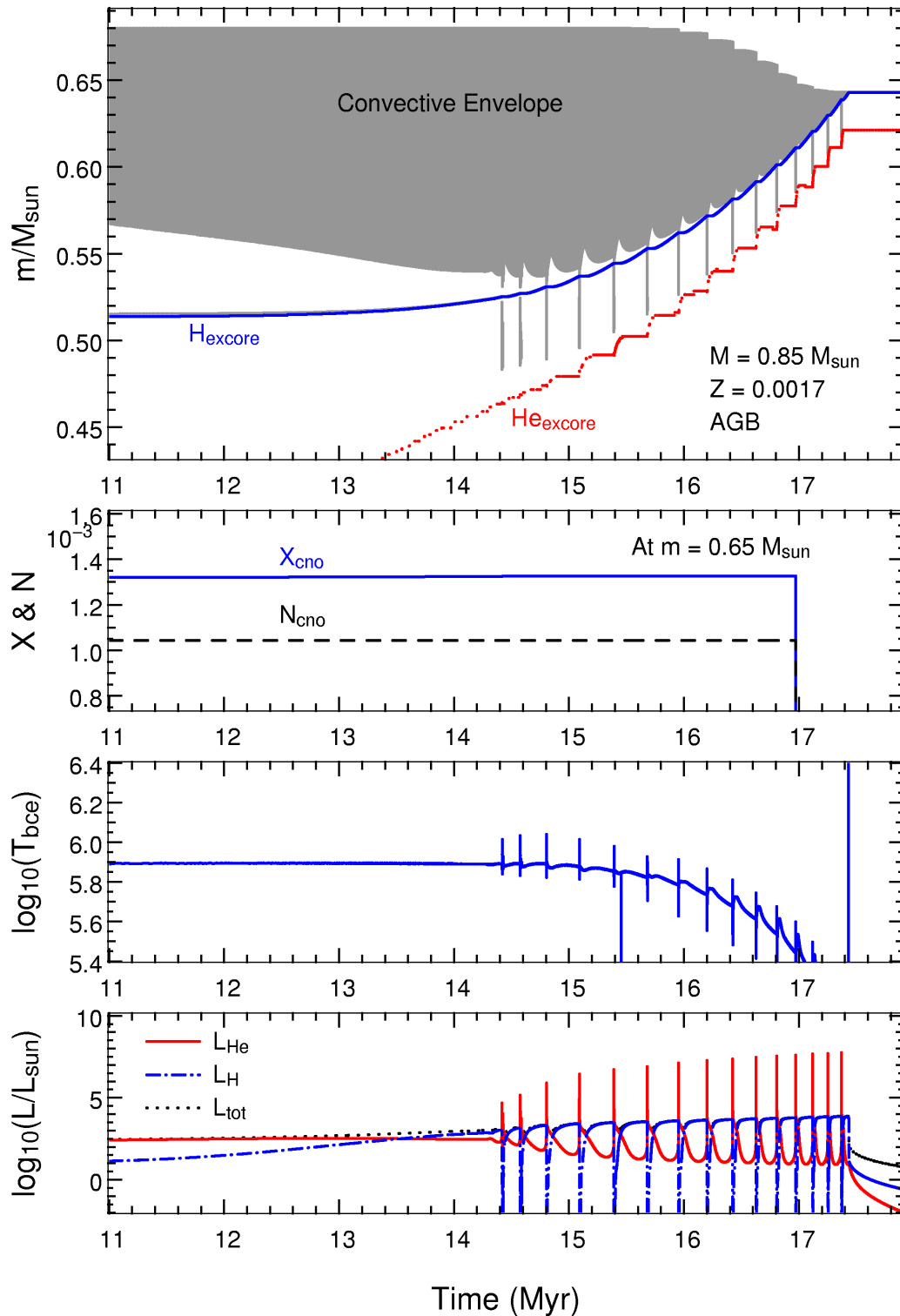


Figure 5.27: Same as Figure 5.26 except plotted for the $Z = 0.0017$ GC model for comparison purposes. Of particular note is the smaller core mass at the beginning and end of the TP-AGB in this model and also the longer time spent on the AGB. The interpulse periods are also longer in this case. Also note that the envelope abundances don't change at all, as there is not 3DUP or HBB.

to the GC star we present the mass loss histories for both stars in Figure 5.28. Firstly, the very large difference in time spent on the *RGB* between the two models is clear in these plots, as is the consequent lower total mass loss during this stage of the $Z = 0$ star evolution. The low amount of mass loss occurs even though the $Z = 0$ model begins the *RGB* with a much higher mass loss rate, due to its higher luminosity. The reason for this is that its evolution is severely truncated due to the early ignition of He in the core (ie. the onset of the dual core flash). Thus the $Z = 0$ star enters the *AGB* phase with significantly more mass, as mentioned earlier.

The difference in *AGB* evolution time is less severe than on the *RGB*, but the factor of two difference is significant. Looking at panel 1 in Figure 5.28 it is apparent that the mass loss rates are quite similar on the *AGB* – despite the much shorter interpulse periods in the $Z = 0$ model noted earlier. It therefore appears that the dominant factor determining the *AGB* lifetime is actually the amount of mass each star ‘needs’ to lose over the *AGB* phase. This is easily verified by quick (approximate) calculations of the overall *mass loss rate* on the *AGB* for the GC model:

$$\frac{\Delta m_{env}}{\Delta t_{AGB}} \approx \frac{0.04}{3} = 0.0133 M_{\odot}/Myr$$

and the $Z = 0$ model:

$$\frac{\Delta m_{env}}{\Delta t_{AGB}} \approx \frac{0.02}{1.6} = 0.0125 M_{\odot}/Myr$$

which confirm that the average mass loss rates are practically identical. So why is the *AGB* timespan so much shorter for the $Z = 0$ model? A further quick calculation of the *rate of core growth* through the *AGB* for the GC model:

$$\frac{\Delta m_{core}}{\Delta t_{AGB}} \approx \frac{0.11}{3} = 0.037 M_{\odot}/Myr$$

and the $Z = 0$ model:

$$\frac{\Delta m_{core}}{\Delta t_{AGB}} \approx \frac{0.17}{1.6} = 0.106 M_{\odot}/Myr$$

shows that the core grows much more rapidly in the $Z = 0$ model (by a factor of ~ 3). It is thus the competition between core mass growth and mass loss that determines the *AGB* lifetime.

In order to ascertain *why* the core grows so fast in the $Z = 0$ case we present in Figure 5.29 the run of some physical characteristics for structures taken during the interpulse periods of the GC and $Z = 0$ models. In particular we show the region around and including the He intershell. It can be seen that the $Z = 0$ structure is hotter and slightly more dense than the GC model. It is also supported by a H shell producing much more energy than that in the GC model (this can also be seen in Figure 5.26 and Figure 5.27). We suggest that this is the reason for the rapid core growth – the H shell is burning out at a faster rate, thereby leaving the He ‘ashes’ behind at a faster rate.

Taking the next step down the rabbit hole we suggest that there are two reasons that the H shell is so hot in the $Z = 0$ model compared to the GC model: 1) the core mass is initially higher and

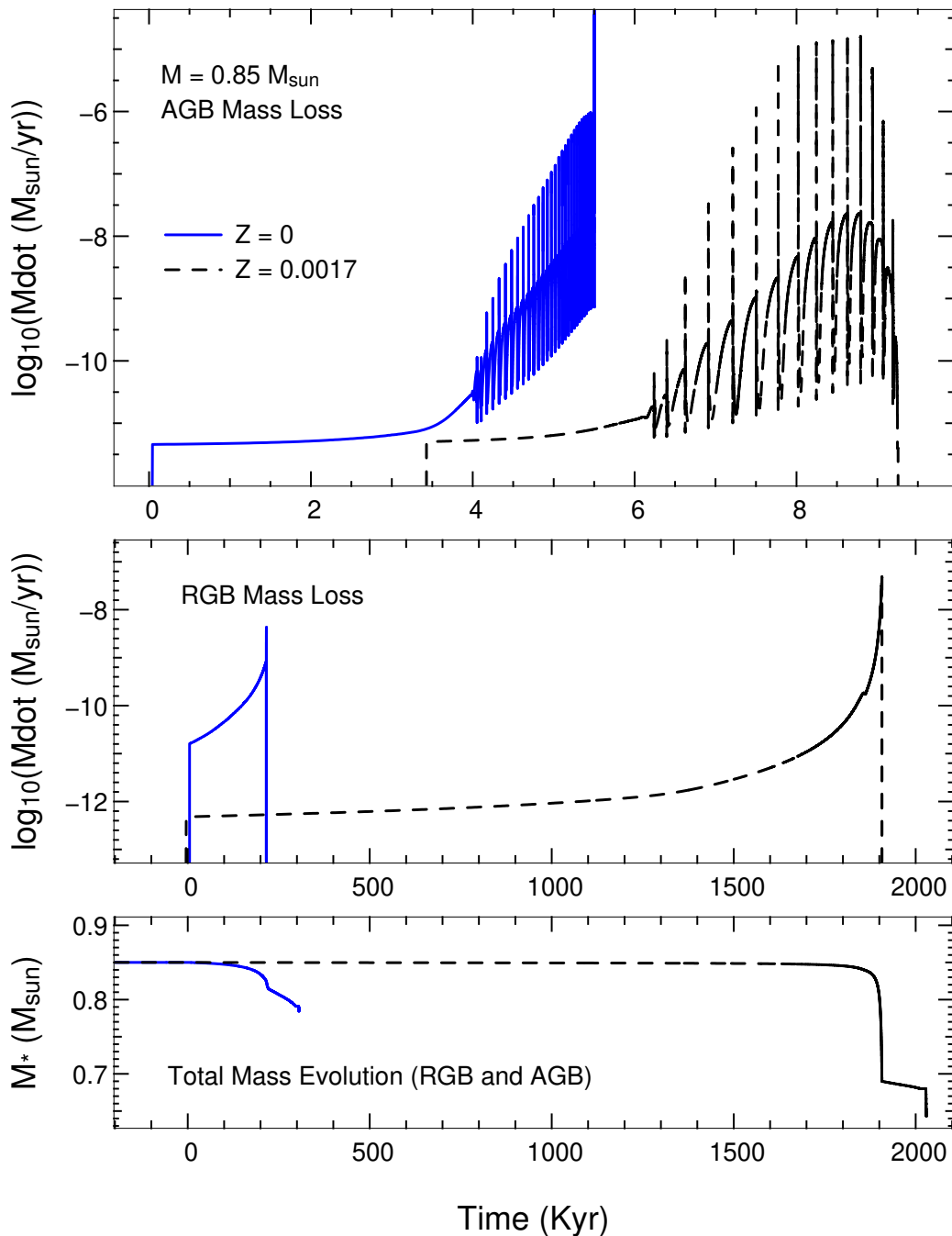


Figure 5.28: The mass loss history (top two panels) and evolution of the total mass (bottom panel) for the $Z=0$ and $Z=0.0017$ stars. The models have been shifted in time but the time scaling is identical, enabling a direct comparison. Each panel has the same amount of time shift. The top panel shows the mass loss rate during the AGB only. It is apparent that the mass loss rates are actually quite similar on the AGB, despite the much shorter overall evolutionary time. Thus it is not the mass loss rate that is causing the shorter lifetime (see text for a discussion). The middle panel shows the RGB mass loss history. This illustrates where the difference in total mass at the beginning of the AGB originated – the $Z=0$ RGB evolution is extremely short due to the early ignition of He (and H) in the core, truncating the mass loss. The bottom panel shows the evolution of the total mass of the stars. The end points represent the masses of the white dwarves produced.

2) the opacity in the envelope is (slightly) lower. Both these facts lead to higher temperatures and thus higher burning rates.

Also of interest is that the extent of the He intershell is very different between the models. The $Z = 0$ model has an intershell with a mass of $\sim 0.02 M_{\odot}$ while the $Z = 0.0017$ has one of twice this mass. This can also be seen in Figures 5.26 and 5.27 and is a characteristic feature of the evolution. We suggest that the higher temperatures in the (partly) degenerate regions in the intershell lead to an earlier ignition of He each pulse cycle, thus maintaining a smaller mass of He that defines the intershell. Thus the higher temperatures and consequent higher burning rates also give rise to the short interpulse periods in the $Z = 0$ star. We note however that it is the rate of core growth that determines the length of time the star spends on the AGB – the short interpulse period is a secondary effect.

Moving beyond the issue of rapid evolution, we present in Figure 5.30 the time evolution of a single interpulse period, bounded by two thermal pulses, from the $Z = 0$ model. At this stage (the 20th pulse) the interpulse period is 36,000 yr. It can be seen that the convective zone does not reach down very close to the He-exhausted core. It can also be seen that it does not breach the H-He discontinuity above, remaining solely a self-contained He intershell convective zone (ISCZ). About 50 years after the ISCZ recedes the convective envelope moves inwards. It never breaks through to the He (and C) rich layers however – ie. there is no 3DUP, as also indicated by panel 2 in Figure 5.26. In Figure 5.30 we also see that the peak He burning luminosity during the shell flashes reaches $\sim 10^{7.5} L_{\odot}$, which is comparable to the peaks in the GC model.

An important result from AGB evolution is the final core mass of the stars, which is the white dwarf (WD) mass. The $Z = 0$ model produces a much more massive WD, where $M_{WD} \sim 0.77 M_{\odot}$ as opposed to the $Z = 0.0017$ model which has $M_{WD} \sim 0.64 M_{\odot}$. We note that the difference in core mass between these stars at the beginning of the AGB was $0.07 M_{\odot}$, whilst the difference at the end of the AGB is $0.13 M_{\odot}$. This highlights the rapid core growth in the $Z = 0$ model.

For completeness we show in Figure 5.31 the RGB, SRGB, HB and AGB evolution of both stars in the HR diagram. We again note that there is some uncertainty in the surface temperature of the $Z = 0$ model after the post-dual-core-flash dredge-up (ie. on the secondary RGB and the AGB) due to uncertainties in the low temperature opacities (see discussion in Section C.1 for more detail).

5.2.5 Executive Summary of Peculiar Evolution

Here we give a brief summary of the peculiarities at each stage of evolution, in point form. The ‘peculiarities’ are defined relative to more metal-rich models, such as the GC model described throughout the previous discussion. In order of evolutionary phase we have:

1. MS to RGB Tip:
 - (a) The MS lifetime is substantially shorter.
 - (b) The surface temperature and luminosity are higher.
 - (c) The CNO cycle does not dominate energy production until the end of the RGB, when the star produces its own primary ^{12}C .

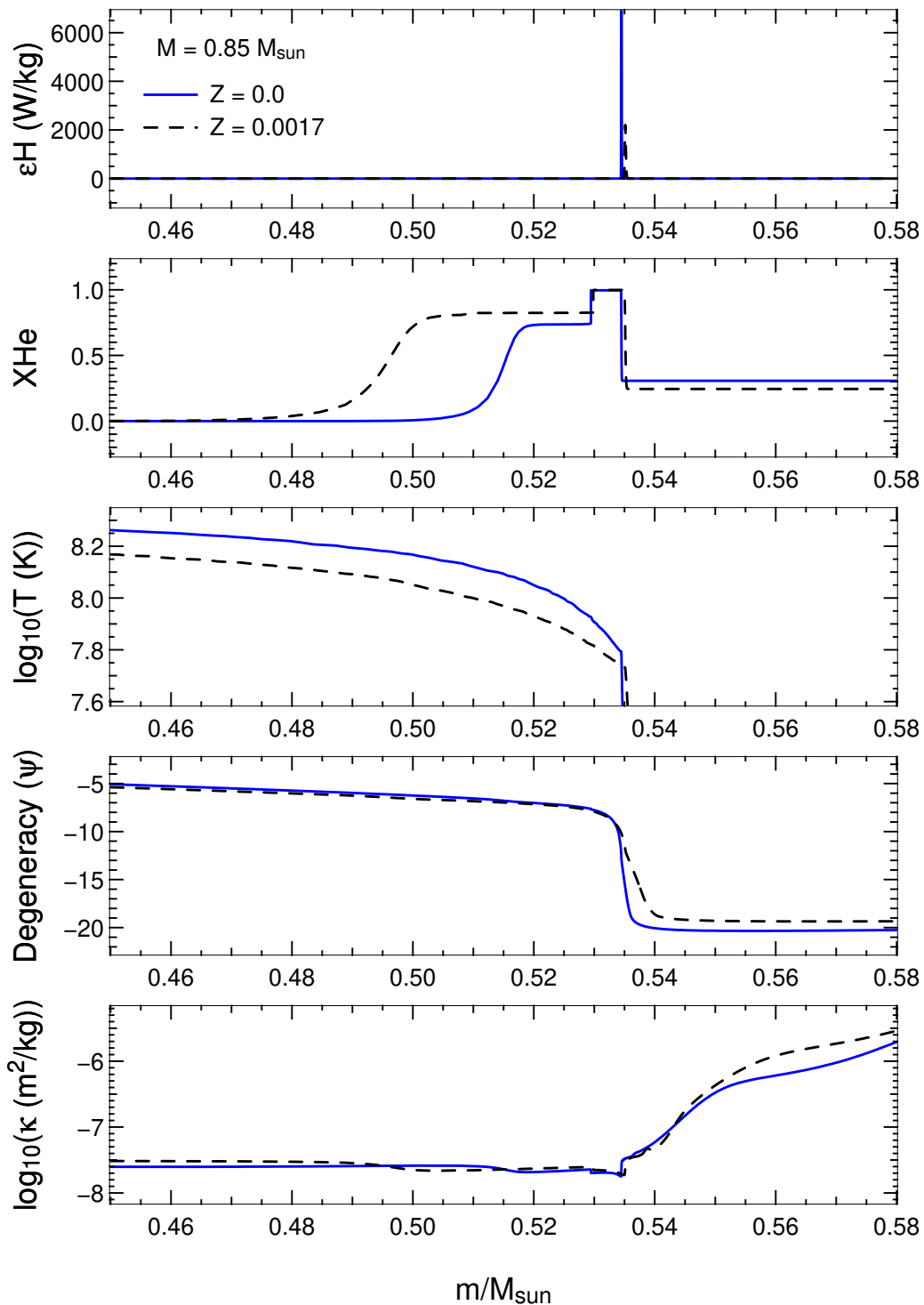


Figure 5.29: The run of various physical characteristics against mass for single AGB interpulse models from the $Z = 0$ and $Z = 0.0017$ stars. In the top panel we see that the energy release from the H burning shell is much higher in the $Z = 0$ case (the $Z = 0$ peak is outside the plotted region, at 2×10^4 W/kg). We suggest that this rapid burning leads to the shorter AGB lifetime of the $Z = 0$ star. Also of note is the higher temperature in the $Z = 0$ model and the much larger extent of the He intershell in the $Z = 0.0017$ model.

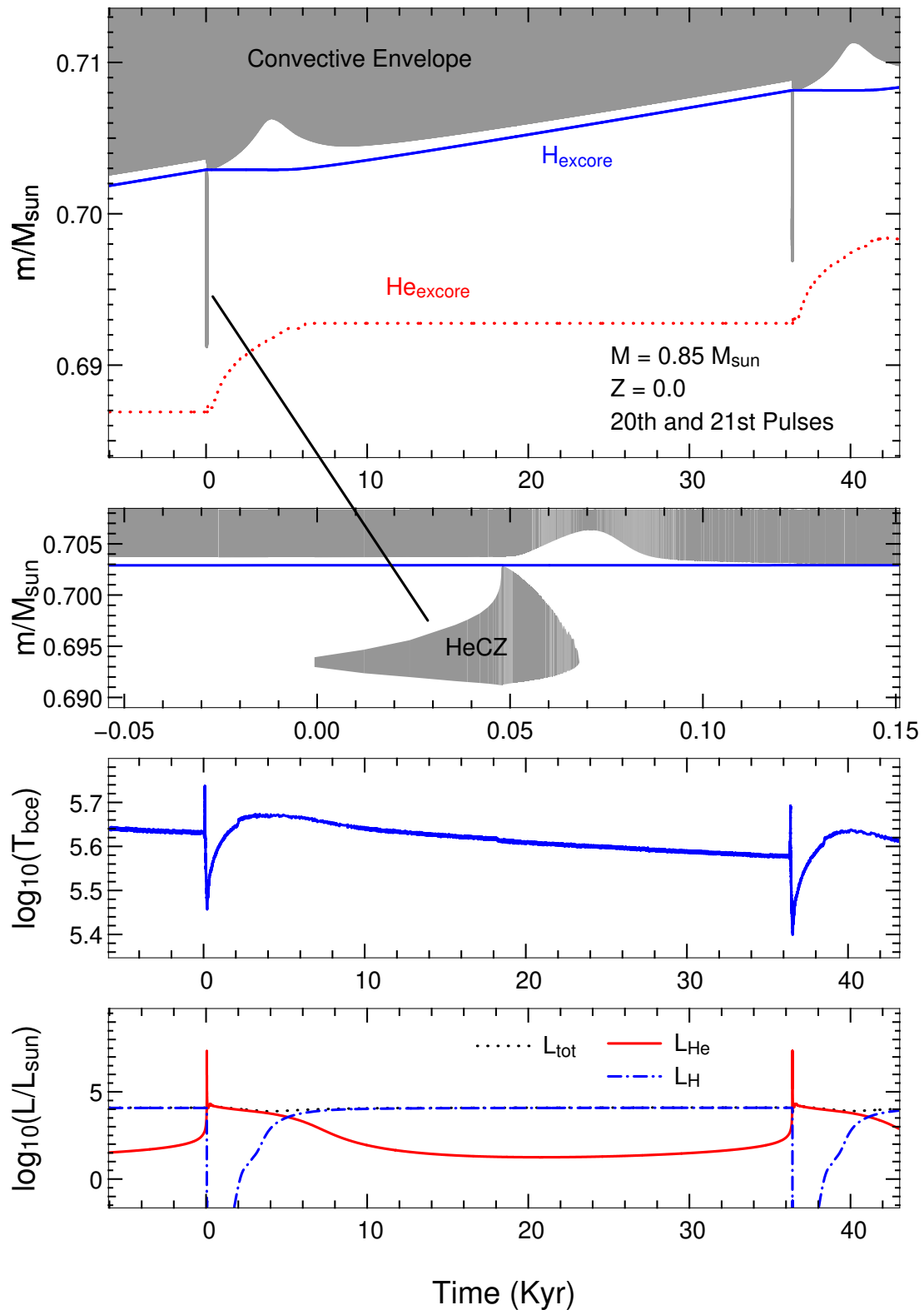


Figure 5.30: Zooming in on the evolution during one AGB pulse cycle in the $Z = 0$ model. The thermal pulses shown occur about 2/3 of the way through the TP-AGB evolution. It can be seen that the interpulse period is 36,000 years, which is short compared to the characteristic period of $\sim 10^5$ yr in the $Z = 0.0017$ model. Importantly there is no 3DUP occurring, which means that no extra heavy nuclei are added to the envelope during the AGB.

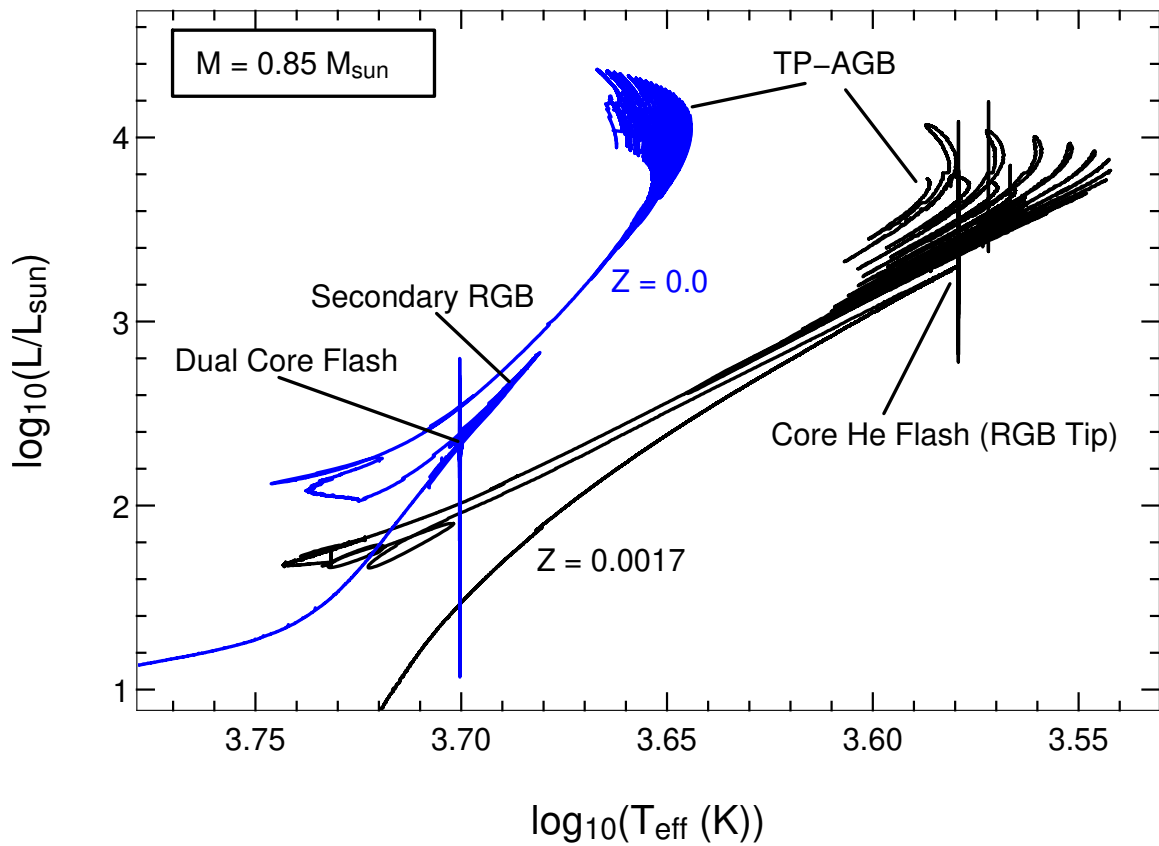


Figure 5.31: Evolution of the $Z = 0$ and $Z = 0.0017$ models in the HR diagram, from the lower RGB till the TP-AGB. The peculiar evolutionary features in the $Z = 0$ model, namely the DCF and the SRGB are marked in the diagram. The vertical lines (eg. at $\log_{10}(T_{\text{eff}}) = 3.70$ for the $Z = 0$ model) are numerical artefacts located at the core flashes.

- (d) The time spent on the RGB is very much shorter.
- (e) The luminosity at the tip of the RGB is substantially lower.
- (f) The mass of the envelope is significantly larger (but the core mass is normal) at the end of the RGB.

2. Dual Core Flash

- (a) The He core flash is much more off-centre.
- (b) The He core flash convective zone breaches the H-He discontinuity, mixing protons down to high temperatures (and ^{12}C upwards), causing a strong H-flash. We refer to this as a proton ingestion episode (PIE). The fact that it happens *during* the core He flash gives rise to the term Dual Core Flash (DCF)
- (c) An incursion of the convective envelope dredges up CNO-enriched and CNO cycle processed material, polluting the pristine surface enough to raise the Z value to $\sim 10^{-3}$.

3. Secondary RGB and Core He Burning

- (a) A sustained series of weak core He flashes provide enough luminosity to create a (thermally pulsing) Secondary RGB (SRGB), such that the surface luminosity attains values higher than the RGB tip whilst the star remains on the red side of the HR diagram.
- (b) Significant mass loss occurs on the SRGB despite its short duration but the star remains comparatively massive.
- (c) Although the quiescent core He burning phase is approximately normal in length, the H-exhausted core growth is very rapid, resulting in a more massive core at the end of He burning.

4. AGB

- (a) The time spent on the AGB is shorter by a factor of two.
- (b) The interpulse periods are much shorter, and more numerous.
- (c) The final core mass (ie. WD mass) is substantially higher, which also means less matter is lost to the interstellar environment.
- (d) Although there is no 3DUP (which is normal) the chemical yield composition will be very different from the formation material composition because it will reflect the pollution from the dual core flash dredge-up episode.

5.2.6 Comparison With Previous Work

A broad review of the literature for $Z = 0$ and very low Z stellar modelling was given in Section 2.3. Here we discuss and compare in detail our current model ($M = 0.85 M_{\odot}$, $Z = 0$, $Y = 0.245$) with similar models from the literature.

In Table 5.2 we provide a list of the relevant studies for comparison with our model. We find no studies with exactly the same mass as our star but there are a substantial number with masses close to $0.85 M_{\odot}$.

MS to RGB Tip

The study by D’Antona and Mazzetelli (1982) was the first to examine the evolution of $Z = 0$ models of mass $\lesssim 1 M_{\odot}$ past the MS. In their $0.9 M_{\odot}$ model they find the MS turnoff age to be 15 Gyr (11 Gyr for their $1 M_{\odot}$ model). In our model the MS turnoff age is 10.1 Gyr. Guenther and Demarque (1983) report an age of 14 Gyr for their $0.9 M_{\odot}$ model. Thus there is a substantial difference between the MS lifetimes when comparing with these authors. We note however that these studies are quite old, and many improvements to the input physics of stellar models has occurred since then. Unfortunately the authors that calculated the model which has the closest mass to ours ($0.82 M_{\odot}$, Schlattl et al. 2002) did not provide a MS lifetime (they were primarily interested in the DCF). They do however provide an age on the RGB of 13.7 Gyr. We have made an educated guess that the MS lifetime was approximately 12.5 Gyr. This is still some 25% greater than ours but we note that Fujimoto et al. (1990) find a MS lifetime of just 7.6 Gyr for their $0.77 M_{\odot}$ model, much shorter than our $0.85 M_{\odot}$ model. Furthermore, if we interpolate in the MS lifetimes in the grid of models by Marigo et al. (2001) we find an age for a $0.85 M_{\odot}$ star of ~ 11 Gyr, about 10% longer than our model. Thus it appears, surprisingly, that there is a degree of uncertainty in the MS lifetimes of these low-mass stars. We suggest that our value is not inconsistent with the current spread. The uncertainty in this area does however warrant an investigation, which we shall pursue as a future study.

As far as we know all authors find that there is some ^{12}C production in the core near the bottom of the RGB (earlier in higher mass stars) which leads to a minor amount of CNO burning (there is a small amount of H left in the core at this stage, due to the inefficiency of the p-p chains). We also find this occurs and it can essentially be seen in our Figure 5.1 on page 92. D’Antona and Mazzetelli (1982) reported that, although there is a minor amount of locally-produced ^{12}C in the the H burning shell on the RGB, the shell energy release only becomes dominated by the CNO cycles just before the core He flash (also evident in our Figure 5.1). D’Antona and Mazzetelli also noted that the surface luminosity at the tip of the RGB in their $1 M_{\odot}$ model is about 1 dex lower than that of a Pop II model. We also find this for our $0.85 M_{\odot}$ model. Looking at Table 5.2 (10th column, L_{RGB}) this is one feature that is reliably reproduced across all the studies.

Another finding by D’Antona and Mazzetelli (1982) was that the RGB lifetime of their $Z = 0$ model is a factor of ~ 1.7 longer than a comparable Pop II model. This is in stark contrast with the lifetimes of our models – we find that the RGB lifetime is a factor of ~ 2.8 shorter than our $Z = 0.0017$ comparison model. As the D’Antona and Mazzetelli study is quite old now we suggest that it is wise not to make quantitative comparisons in this case. The only other $Z = 0$ RGB lifetime given in Table 5.2 is that from the study by Picardi et al. (2004). They find an exceptionally short-lived RGB in their $0.8 M_{\odot}$ model (0.04 Gyr, a factor of 5 shorter than ours). We can not determine why it is so extremely short in their model. On the other hand we see that the $\log(Z/Z_{\odot}) = -8$ model by Cassisi and Castellani (1993) has a similar lifetime to our model

Authors	M_*	τ_{MS}	τ_{SGB}	τ_{RGB}	τ_{He}	m_{ign}	M_{core}	Δm_{ign}	L_{RGB}	DCF	Z_{cno}
Fujimoto et al. (1990) ^a	0.77	7.6	–	–	–	0.41	0.53	0.12	2.49	Yes	0.004
Marigo et al. (2001)	0.80	13.8	–	–	0.12	–	0.50	–	2.37	–	–
Picardi et al. (2004)	0.80	–	–	0.04	0.04	0.35	0.52	0.17	2.45	Yes	0.018
Schlattl et al. (2002)	0.82	12.5?	–	–	–	0.31	0.61	0.30	–	Yes	–
Current Study ($Z = 0$)	0.85	10.1	0.84	0.20	0.07	0.27	0.49	0.22	2.30	Yes	0.004
Current Study ($Z = 0.0017$)	0.85	11.6	2.1	0.54	0.10	0.11	0.48	0.37	3.35	–	–
D'Antona and Mazzetelli (1982)	0.90	15	–	0.6?	–	0.27	0.52	0.25	1.80	Yes	–
Guenther and Demarque (1983)	0.90	14	–	–	–	–	–	–	–	–	–
Cassisi and Castellani (1993) ^b	1.0	6.5	0.5	0.1	–	0.25	0.49	–	2.34	–	–
Weiss et al. (2000)	1.0	6.3	–	–	–	–	0.50	–	2.36	No	–
Schlattl et al. (2001)	1.0	–	–	–	–	0.15	0.48	0.33	2.31	Yes	0.013
Siess et al. (2002)	1.0	6.9	–	–	0.18	0.31	0.49	0.18	2.36	No	–

Table 5.2: Comparing our $M = 0.85 M_{\odot}$ model with similar $Z = 0$ models from the literature. Also included for further comparison is our GC model ($Z = 0.0017$) and the $1 M_{\odot}$, $\log(Z/Z_{\odot}) = -8$ model by Cassisi and Castellani (1993). The table is ordered by stellar mass. Note that we were unable to obtain many of the comparison values, as each study tends to focus on particular facets of the evolution. The table columns show M_* (stellar mass), τ_{MS} (stellar age at MS turn-off), τ_{SGB} (lifetime of shell burning stage between MSTO and start of RGB), τ_{RGB} (RGB lifetime), τ_{He} (core He burning lifetime), m_{ign} (ignition point, in mass, of core He flash), M_{core} (mass of H-exhausted core at time of core He flash ignition), L_{RGB} (luminosity at RGB tip, in L_{\odot}), Δm_{ign} (the distance, in mass, between the point of He ignition and the H-shell), DCF (whether or not the He convective zone penetrated the H-shell, or was about to, producing a dual core flash) and Z_{cno} (the C+N+O metallicity of the envelope after the DCF dredge-up). All lifetimes are in Gyr and all masses are in M_{\odot} .

^aAlso see the companion paper by Hollowell et al. (1990).

^bThis model has $\log(Z/Z_{\odot}) = -8$.

(taking the increased mass into account). It has an RGB lifetime of ~ 0.1 Gyr compared to ~ 0.2 Gyr in our model. Although this model does contain a small amount of metals, the analysis by [Cassisi and Castellani](#) shows that this star exhibits very similar evolution to our $Z = 0$ model. It is interesting to note that this model deviates by a factor ~ 1.8 or so in all the evolutionary times listed but all other values are practically identical. This suggests that the differences are mainly due to the larger mass. We conclude that our model is consistent with this study but not others, although we note that there is not much to compare with at this stage. In order to expand on this topic of RGB lifetimes we briefly look in more detail at the rapid evolution of our model. In [Table 5.2](#) we give the lifetime for the shell burning phase between the MS turnoff and the base of the RGB for our models (τ_{SGB}). In the $Z = 0$ model τ_{SGB} is shorter than the same phase in the $Z = 0.0017$ model by almost the same factor (~ 2.6) as it is for the RGB. We note that this lifetime also compares well with the value of $\tau_{\text{SGB}} = 0.5$ Gyr in the model by [Cassisi and Castellani \(1993\)](#), especially when factoring in the increased mass. As mentioned in [Section 5.2.1](#) the main difference between our $Z = 0.0017$ model and our $Z = 0$ model is that the $Z = 0$ model has its H-shell powered by the p-p chains, whilst in the $Z = 0.0017$ model the CNO cycles are always operating in the shell. This contributes to the modest difference in MS lifetime but the effect becomes stronger as the models diverge in terms of energy supply source as they turn off the MS. Whilst the $Z = 0.0017$ model switches to shell CNO burning, the $Z = 0$ model continues to burn via the p-p chains. It rapidly evolves to an RGB structure and then quickly evolves up the RGB, reaching the conditions in which the He flash ignites in a relatively short time. Thus the RGB evolution is essentially ‘cut short’. In [Figure 5.32](#) we show the time evolution of some salient physical characteristics of the models from the MS turn-off to the tip of the RGB (also see [Figure 5.8](#) on page 99). The rapid evolution of the $Z = 0$ star is clear. We can see that the rate of core mass growth is significantly higher, as is the subsequent collapse of the core. This is most likely due to the rapid, high temperature burning via the p-p chains, coupled with the increased rate of energy loss due to the low opacity. If our results are correct then this would imply that $Z = 0$ RGB stars should be relatively rare (assuming $Z = 0$ stars exist at all of course). Finally we note that this stage of evolution also requires more investigation. This is quite important in terms of potential observations, as bright (RGB) stars are more readily observable and pinning down the lifetimes would provide predictions for expected distributions. In terms of chemical pollution of the convective envelope on the RGB the first dredge-up (FDUP) event found in higher metallicity stars is virtually non-existent at $Z = 0$. As discussed in [Section 5.2.1](#) we found that the star retains its original surface composition throughout the RGB.

Dual Core Flash

Another feature reported by [D’Antona and Mazzetelli \(1982\)](#) is that the maximum temperature location just before the core He flash is very off centre in their $1 M_{\odot}$ model. Although they were unable to calculate the further evolution they suggested that the He flash occurs so off centre (at $m = 0.27 M_{\odot}$, very similar to our $0.85 M_{\odot}$ model – see [Figure 5.14](#) on page 106) that the resulting convection zone is likely to breach the H-He discontinuity, causing a proton ingestion episode (the DCF). Indeed this is what most later studies found (including the current one). We list in [Table 5.2](#) which studies have found the DCF to occur, and which have not. We also list the mass location of He-flash ignition (m_{ign} , roughly the location of the bottom of the He

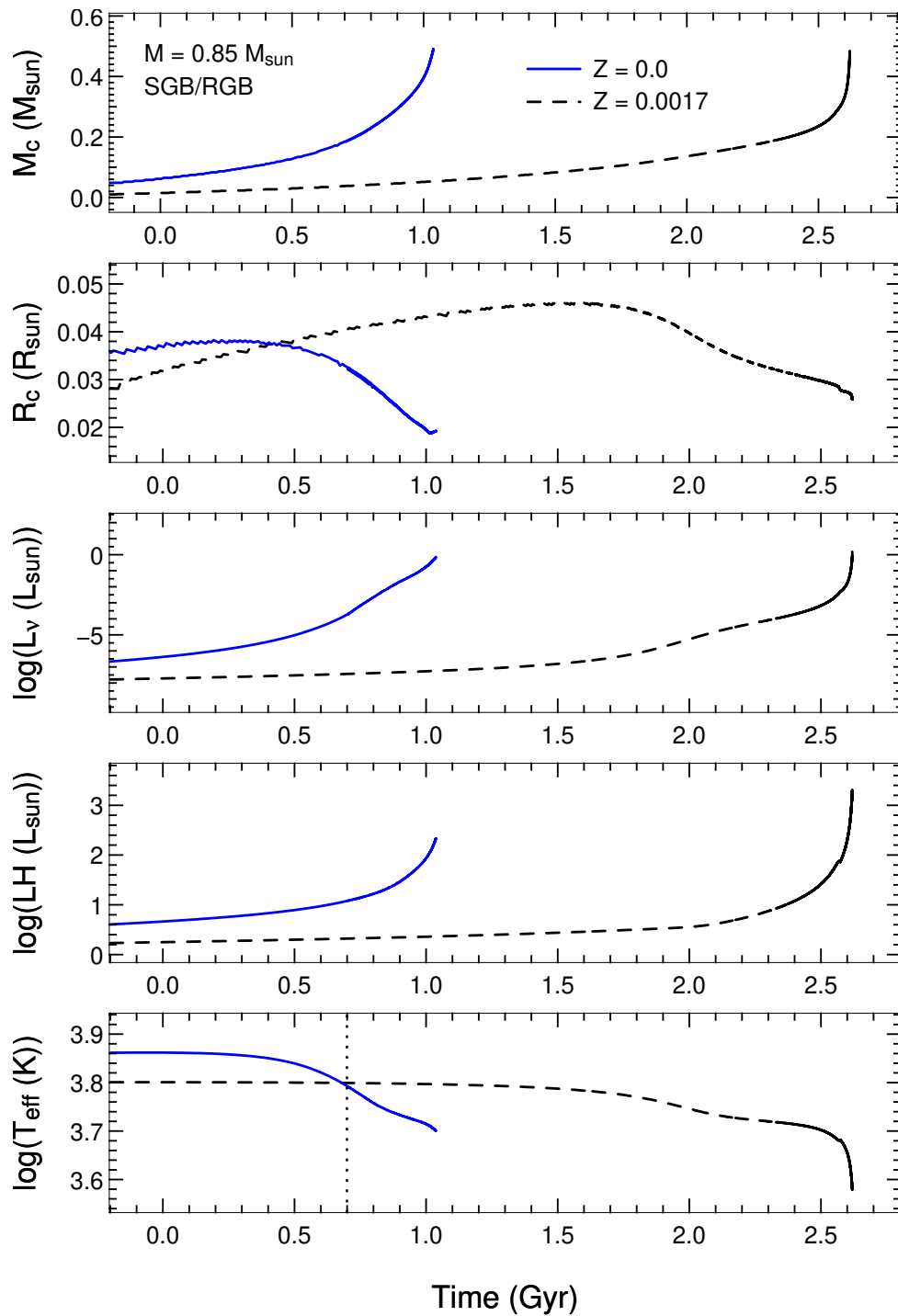


Figure 5.32: Time evolution of various physical characteristics for the $Z = 0$ and $Z = 0.0017$ models from the MS turn-off to the tip of the RGB. Both models have been offset in time to place their MS turn-off times at $t = 0$. The models can thus be directly compared in time. The vertical dotted line in the bottom panel roughly marks the time of H exhaustion in the centre (this happens to almost coincide between the two models). The rapid evolution of the $Z = 0$ model to the end of the RGB is obvious in this figure, the lifetime being a factor of ~ 2.6 shorter than the $Z = 0.0017$ model. Note that the H-exhausted core mass and radius are defined at $X_H = 0.05$.

convective zone), the mass of the H-exhausted core at ignition (M_{core}), and also the distance (in mass) between the ignition point and the H-shell (Δm_{ign}). Almost all studies in this mass range find that the DCF occurs. Actually, as the Weiss et al. (2000) group have recently found that the DCF does not occur in their models (Schlattl et al. 2001), Siess et al. (2002) are the only group that do not find it occurring (at $1 M_{\odot}$). Looking at Table 5.2 we can see that the core mass at the end of the RGB (M_{core}) is remarkably consistent between studies, the exception being the model of Schlattl et al. (2002) which has a significantly higher core mass. The location at which the He flash occurs is less consistent between studies, varying from $0.15 \rightarrow 0.41 M_{\odot}$. However, if we remove the ‘outliers’ (Schlattl et al. 2001 and Fujimoto et al. 1990 respectively), we find there is a much narrower range, centred on $\sim 0.3 M_{\odot}$. We should not remove the outliers however. Thus the large spread is probably indicative of uncertainties in the modelling. This also warrants further investigation, but is outside the scope of the present study. We note that our value of $0.27 M_{\odot}$ lies almost exactly in the centre of the range of values. In terms of the chemical pollution of the envelope due to the DCF episode (CNO enriched material is dredged up soon after the flashes recede), there appears to be a general consensus that a huge amount of pollution occurs. The Z_{cno} of the envelope becomes so high that it exceeds the observations of the C- and N-rich EMPHs. Hollowell et al. (1990) were the first to quantify this, finding that the surface N abundance in their model was ~ 2 dex higher than observed for the star CD -38.245°. Schlattl et al. (2001) find similar results, with their models exhibiting ~ 2 to 3 dex too much C and N compared to observations. They suggest that the C and N production could be reduced by an improved modelling of the strongly convective H burning region, as this is still modelled in a very simple way (1D mixing length theory) that may not be sufficiently accurate in this situation. Indeed, by reducing the mixing efficiency by a factor of $\sim 10^4$ Schlattl et al. (2002) found that the C and N pollution results were closer to the observations. There is no physical argument for altering the mixing efficiency so much. However we note that there is no reason to believe that the MLT is applicable in this situation of high temperature and strong nuclear burning – so the mixing efficiency may well be thought of as a free parameter in this case. Picardi et al. (2004) also find that C and N are over-produced. They highlight the fact that the models always predict that the $^{12}\text{C}/^{13}\text{C}$ ratio will be close to equilibrium (≈ 4) but the observations show values of ~ 50 . In addition to this, they find the C/N ratio to be ~ 1 in their models but it is ~ 50 in the CEMPHs. Another interesting result that they report is that their model produces large amounts of Li. They conclude that all the evidence points to these models *not* being the explanation for the CEMPs. Weiss et al. (2004) came to the same conclusion and also note that in an earlier investigation of theirs (Schlattl et al. 2002) that explored the robustness of the pollution predictions they found that the amount of C and N produced is quite insensitive to the model parameters. The fact that all studies have found essentially the same over-abundances despite the wide variation of the location of He ignition further substantiates this finding. In Section 5.2.2 we report that our model ends up with a surface composition having $Z_{cno} = 0.004$. This is in exact agreement of that found by Hollowell et al. (1990). The other two studies which report quantitative values for the DCF pollution of pure $Z = 0$ models find somewhat higher abundances of C and N. The models by Schlattl et al. (2001) and Picardi et al. (2004) end up with $Z_{cno} \sim 0.015$, a factor of about 4 greater than ours. We note that this higher abundance only amounts to about 0.6 dex difference when comparing with observations, thus, although it

means that their models are further from fitting observations, the overall discrepancy is about the same (ie. $\sim 1 \rightarrow 3$ dex too high). The discrepancy between models is probably a product of the evolutionary details during the DCF. In the model of [Picardi et al. \(2004\)](#) the two convective zones that are initially produced at the start of the H-flash soon merge to become one again. This naturally mixes up even more C-rich material that is later dredged up. [Hollowell et al. \(1990\)](#) find that the two convection zones remain separated, as we also find in our model (see eg. Figure 5.16 on page 110). [Schlattl et al. \(2001\)](#) also finds that they remain separated but in another model by the same group ([Schlattl et al. 2002](#)) they appear to merge. As mentioned earlier the nett result of CNO pollution is *roughly* the same across the studies so it appears that the details of the DCF evolution are not very significant. That said, the fact that there is some variation between the studies – and that one study does not even find that the DCF occurs – suggests that more work needs to be done on this phase of evolution as well. It may also affect further evolutionary stages. Finally we note that, in terms of the aims of the current study, we find that our results are reasonably consistent with the previous studies in relation to the DCF phase.

Secondary RGB and Core He Burning

[Schlattl et al. \(2001\)](#) found that, after the DCF had abated and the CNO-rich material has been dredged up, their star settled back into an ‘new-born’ RGB structure (Secondary RGB). It continued evolving up the SRGB for 50 Myr, finally ending in a second (weaker) core He flash. This second flash did not induce another H flash and the star settled into quiescent core He burning. [Picardi et al. \(2004\)](#) also find a secondary RGB in their $0.80 M_{\odot}$ model. It is however substantially different to that found by [Schlattl et al.](#) Most of the SRGB evolution in their model involves a series of weak off-centre He flashes. Each flash occurs progressively less off-centre and creates a short-lived convection zone, removing the degeneracy in the core step by step. This is essentially identical to our $0.85 M_{\odot}$ model (see Figures 5.12 on page 104 and 5.21 on page 116). They also report an SRGB lifetime of 2 Myr, which is identical to what we find. We are unsure why the model by [Schlattl et al. \(2001\)](#) is so different, having an SRGB life time an order of magnitude greater than ours.

There is only one study that we have found (see Table 5.2) that is directly comparable (and provides quantitative results) to our model in terms of the quiescent core He burning phase. Other studies either did not evolve through the DCF phase or did not find the DCF to occur. [Picardi et al. \(2004\)](#) find a core He burning lifetime of 0.04 Gyr for their $0.80 M_{\odot}$ model, which is somewhat shorter than that of our $0.85 M_{\odot}$ model which has a lifetime of 0.07 Gyr. Although we find our model increases its core mass substantially over the core He burning stage (from ~ 0.45 to $0.60 M_{\odot}$, see Section 5.2.3) the [Picardi et al.](#) model does so even more. They say the reason for this is that the Z_{cno} is very high in their model, which gives rise to very efficient CNO shell burning, thereby adding He to the core at a great rate. Their model increases its core mass from 0.49 to $0.75 M_{\odot}$ during this phase. This is an extremely large growth when compared to our $Z = 0.0017$ model which only grows from 0.49 to $0.53 M_{\odot}$. Since the Z_{cno} abundance is significantly smaller in our model it is to be expected that our He burning lifetime is somewhat longer and the core growth slower. We note that the [Picardi et al.](#) model is one of

the models which has higher envelope Z_{cno} values after the DCF, thus we expect that our core He burning lifetime would be more similar to the the study of [Hollowell et al. \(1990\)](#) who find similar pollution levels to us. If the envelope metallicity is indeed the primary reason for the difference in evolutionary timescales then this reinforces the suggestion that more work needs to be done on the DCF, as this is where the metallicity difference arises.

AGB

With regards to the AGB we find that there have not been any studies specifically dedicated to investigating this interesting phase of evolution at $Z = 0$ and $M \lesssim 1 M_{\odot}$. This is probably due to the large uncertainties that become important during this phase – mass loss and the treatment of 3DUP – and the large computational demand. The semi-analytic study by [Fujimoto et al. \(1984\)](#) predicted that at $Z = 0$ thermal pulses will only occur when the core mass is $\lesssim 0.73 M_{\odot}$. The core mass in our model is well below this limit ($0.49 M_{\odot}$) and indeed, we do find that the model experiences thermal pulses (TPs). Despite the TPs we find that 3DUP does not occur. There have been a couple of detailed modelling studies that briefly touch on the AGB. [Fujimoto and Iben \(1998\)](#) only give qualitative descriptions of their models on the AGB but report that thermal pulses do occur, and that they also find no 3DUP at these masses. [Schlattl et al. \(2001\)](#) evolve their $1 M_{\odot}$ model about 10 pulses into the AGB (they use the Reimers mass-loss formula). Although the internal regions of this model have $Z = 0$, the surface of this model has been artificially polluted, thus the pulsation characteristics are likely to be different to ours. Indeed, they find interpulse periods of ~ 0.006 Myr whereas ours are ~ 0.08 Myr (at the start of the AGB). They don't report any 3DUP. [Siess et al. \(2002\)](#) also evolve their $1 M_{\odot}$ model about 10 pulses into the AGB. They find interpulse periods about a factor of two longer than ours ($\tau_{imp} \sim 0.2$ Myr). We note however that this model does not experience the DCF, whereas ours does. The DCF can effect the TP-AGB characteristics since it dredges up so much CNO nuclei, altering the opacity. Their model did however experience the DSF which also pollutes the envelope but to a lesser extent. Interestingly [Siess et al.](#) find that their $1 M_{\odot}$ model experiences *intermittent* 3DUP. However they suggest that it is most likely a numerical resolution problem. We note that [Siess et al.](#) included some overshoot, whereas we have not. To the best of our knowledge the studies just mentioned constitute the extent of the research in to the TP-AGB phase of these stars. Based on these few studies (and the present one) it seems that thermal pulses do occur in these stars but 3DUP does not. This has implications for the chemical composition of the polluting material that will be released via winds. Without 3DUP the yield will directly reflect the pollution brought about by the DCF at the tip of the RGB. Hence the choice of mass loss prescription will have little effect on the yield composition, but will effect the amount of matter that is released and also the mass of the resulting white dwarf. We close this subsection by asserting that the evolutionary characteristics of our models are comparable to the majority of previous work. The main exception may be the AGB phase but we note that this has not been studied in detail by anyone as yet. Indeed, our models appear to be the first full TP-AGB calculations of these stars.

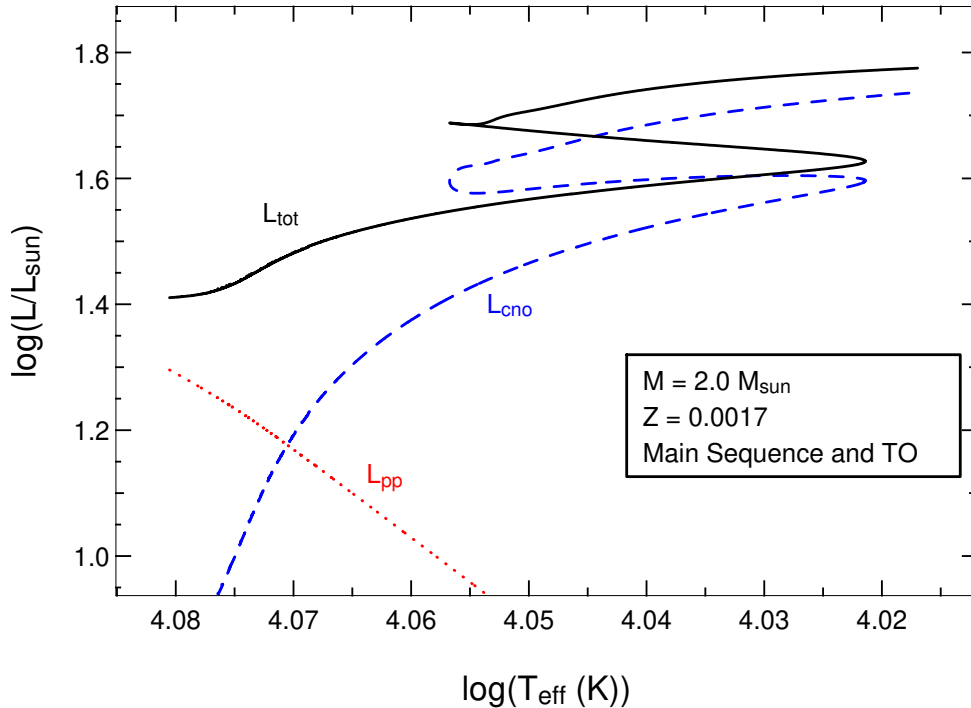


Figure 5.33: The main sequence HR diagram for our $Z = 0.0017$ model. It can be seen that the MS is dominated by CNO cycle energy generation in this ‘normal’ star.

5.3 Detailed Evolution at $2.0M_{\odot}$

5.3.1 MS and CNO Mini-Flash

The main sequence evolution of the $Z = 0$ model with $M = 0.85 M_{\odot}$ described in the previous section was not substantially different to that of a Pop II model, as Pop II stars of low mass also burn H via the p-p chains on the MS. At higher masses ($M \gtrsim 1 M_{\odot}$) Pop II MS burning starts to become dominated by the CNO cycles. This is demonstrated in Figure 5.33 where we display the various nuclear burning luminosities for a $2 M_{\odot}$ Pop II model (which we also refer to as our globular cluster (GC) model). We have calculated this model specifically for comparison with our $2 M_{\odot}$, $Z = 0$ model. It has a metallicity of $Z = 0.0017$ (scaled solar composition). All other input parameters were identical to that of the $Z = 0$ model. It can be seen in Figure 5.33 that p-p chain energy generation only dominates at the beginning of the MS in the GC model, with the CNO cycles providing most of the luminosity from then on. In fact, about half way through the MS (at $\log(T_{eff}) \sim 4.05$) 80% of the star’s total luminosity is supplied by the CNO cycles. This contrasts sharply with the $Z = 0$ model where, as can be seen in Figure 5.34, $\sim 100\%$ of the MS luminosity is provided by the p-p chains throughout the MS. As there are no CNO catalysts in the $Z = 0$ model the CNO cycles can not operate – until the star produces its own ^{12}C .

Carbon production occurred in the $M = 0.85 M_{\odot}$, $Z = 0$ model at the very bottom of the RGB, allowing the CNO cycles to burn the tiny amount of remaining hydrogen. In the $2 M_{\odot}$ model this occurs just as the star turns off the MS, when there is a small but significant amount of H still present ($X_H \sim 0.010$). Once the ^{12}C abundance reaches $\sim 10^{-12}$ there is a small thermal runaway due to the sudden increase of CNO burning efficiency. The burning is strong enough to give rise to a small convective core (see top panel in Figure 5.35) which mixes in some extra H,

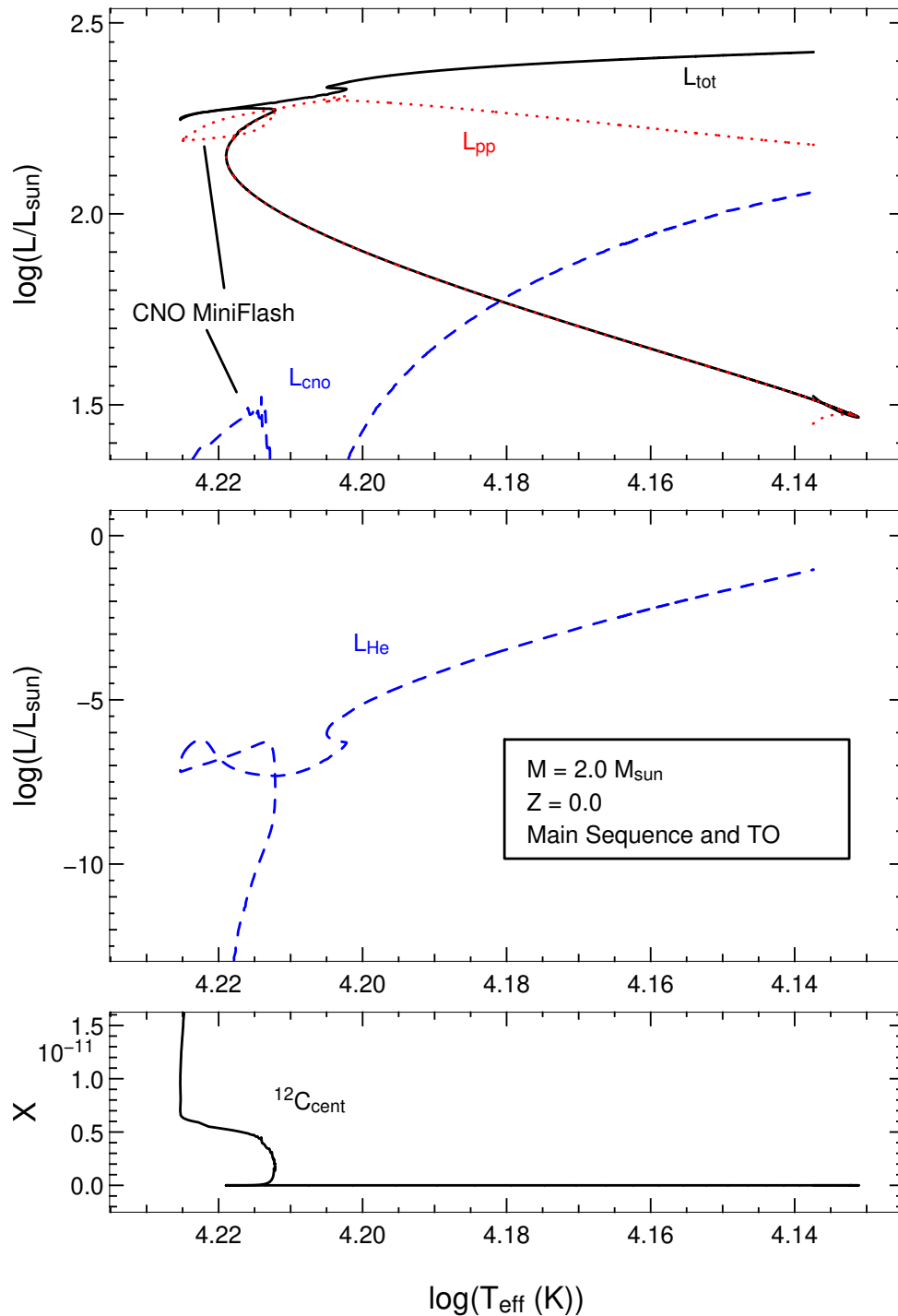


Figure 5.34: The MS HR diagram (top panel) for the $2 M_{\odot}$ $Z = 0$ model, as well as the helium burning luminosity (middle) and resultant ^{12}C production (bottom). It can be seen that the p-p chains dominate for the entire MS phase in this star, and that the star behaves more like a low-mass model as its surface temperature increases with luminosity. Also evident in the top panel is the brief CNO mini-flash, and the increasing importance of the CNO cycles as the star moves to the shell burning stage. The bottom panel indicates just how little carbon production is needed to ignite the CNO cycles.

increasing the central H abundance a little (up to $X_H \sim 0.013$). This extra fuel slightly prolongs the MS, giving rise to a CNO core burn that lasts ~ 5 Myr before the H is exhausted. We refer to the initial (minor) thermal runaway, which lasts ~ 1 Myr, as a ‘CNO Mini-Flash’. The rapid increase in CNO burning luminosity can be seen in Figures 5.34 and 5.35. We show some of the anatomy of the miniflash in Figure 5.36. This figure shows that the p-p burning has already moved off-centre, forming a thick shell, whilst the CNO burning is concentrated at the centre due to the high temperature dependence of these reaction cycles. In the $Z = 0$ HR diagram (Figure 5.34) it can be seen that the star then assumes ‘normal’ behaviour in terms of surface temperature evolution, such that the temperature decreases with luminosity. The previous evolution in the HR diagram is quite the opposite to that of the $Z = 0.0017$ model (see Figure 5.33), as the temperature *increases* with luminosity rather than decreasing. This is reminiscent of the evolution of low-mass stars which are also powered solely by the p-p chains (see Figure 5.1 on page 92). Another significant difference is that the $Z = 0$ model increases luminosity by a large amount during the MS. This is also similar to low mass p-p powered models. This will have observational consequences as the MS luminosity of the $Z = 0$ model ranges from ~ 0.5 to 1.5 dex higher than the $Z = 0.0017$ model. The $Z = 0$ model is also much bluer throughout the MS. Interestingly these differences have little effect on the MS lifetime – the $Z = 0$ lifetime is only 5% longer than that of the GC model (see Figure 5.39).

5.3.2 Core He Burning and Second Dredge-Up

In Figure 5.37 we present the further evolution in the HR diagram for the $Z = 0$ and GC models. The evolution of the $Z = 0$ model is strikingly different to that of the Pop II model. The $Z = 0$ star barely travels towards the red (on the Hertzsprung Gap) before it ignites helium in the core. The star thus avoids an RGB configuration entirely, quickly changing from core H burning to core He burning. In addition to this He ignition does not occur in a flash (as it does in the $Z = 0.0017$ model), rather the He ignites quiescently and the star settles on the HB straight away. The reason for this is illustrated in Figure 5.38, in which it can be seen that the $Z = 0$ star reaches He burning temperatures at much lower densities than the GC model. Thus the degeneracy in the core is lower, and a thermal runaway is avoided, much like a higher mass star at higher Z . Another interesting feature in Figure 5.38 is the reaction of the star to the onset of the CNO miniflash. The density reduces at (roughly) a constant temperature, due to an expansion of the core. It is interesting to note that despite all the previous differences in evolution the core He burning in both stars occurs under approximately the same central conditions (although at a slightly lower density in the $Z = 0$ case). The core He burning lifetimes are however very different. The $Z = 0.0017$ model has a lifetime of 120 Myr whilst the $Z = 0$ HB lifetime is only 30 Myr – a factor of four shorter. We note that other studies also find short-lived HBs at $Z = 0$ (see next section for comparisons with other studies).

Due to the lack of an RGB first dredge-up does not occur in this model. The ‘second’ dredge-up (2DUP) event (actually the first dredge-up event for this star) does occur in this model, but with limited consequences. In Figure 5.40 we show the evolution of the convective envelope incursion along with the evolution of the burning shells. We also show the abundance profiles of one model during the 2DUP episode. It can be seen that the convective envelope does reach down into

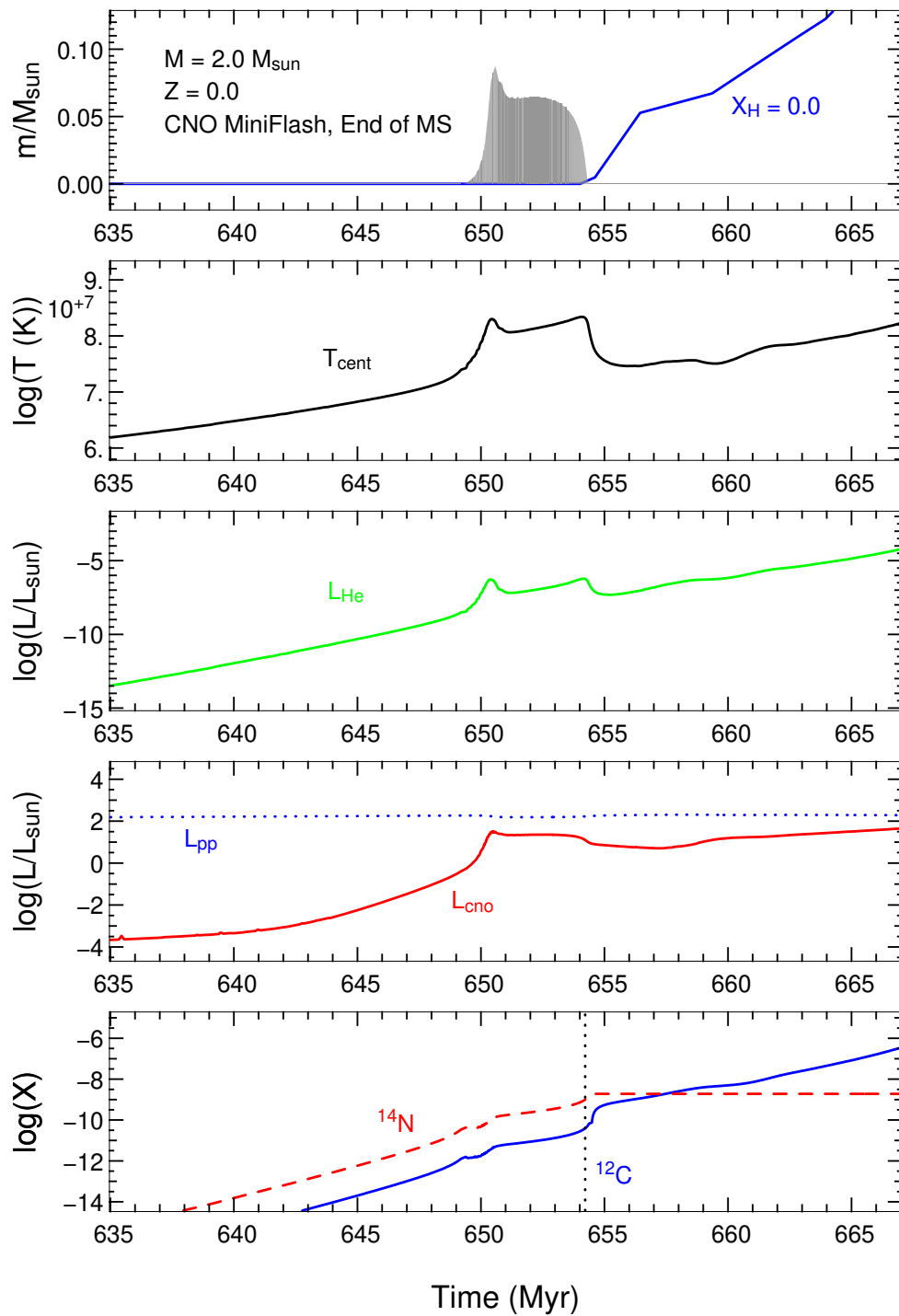


Figure 5.35: The anatomy of the CNO mini-flash in the $2 M_{\odot}$ $Z = 0$ model. The small convective core is displayed in panel 1 (grey shading). It can be seen that the miniflash lasts $\lesssim 1$ Myr and that the CNO burning core takes ~ 5 Myr to burn the remaining hydrogen ($X_H = 0.013$). In the fourth panel we can see that the CNO burning luminosity never dominates the energy production. The vertical dotted line in the bottom panel indicates the time of core H exhaustion. This event is also indicated by the fact that C stops getting cycled to N, and the C abundance continues to rise due to the increasing rate of 3α burning.

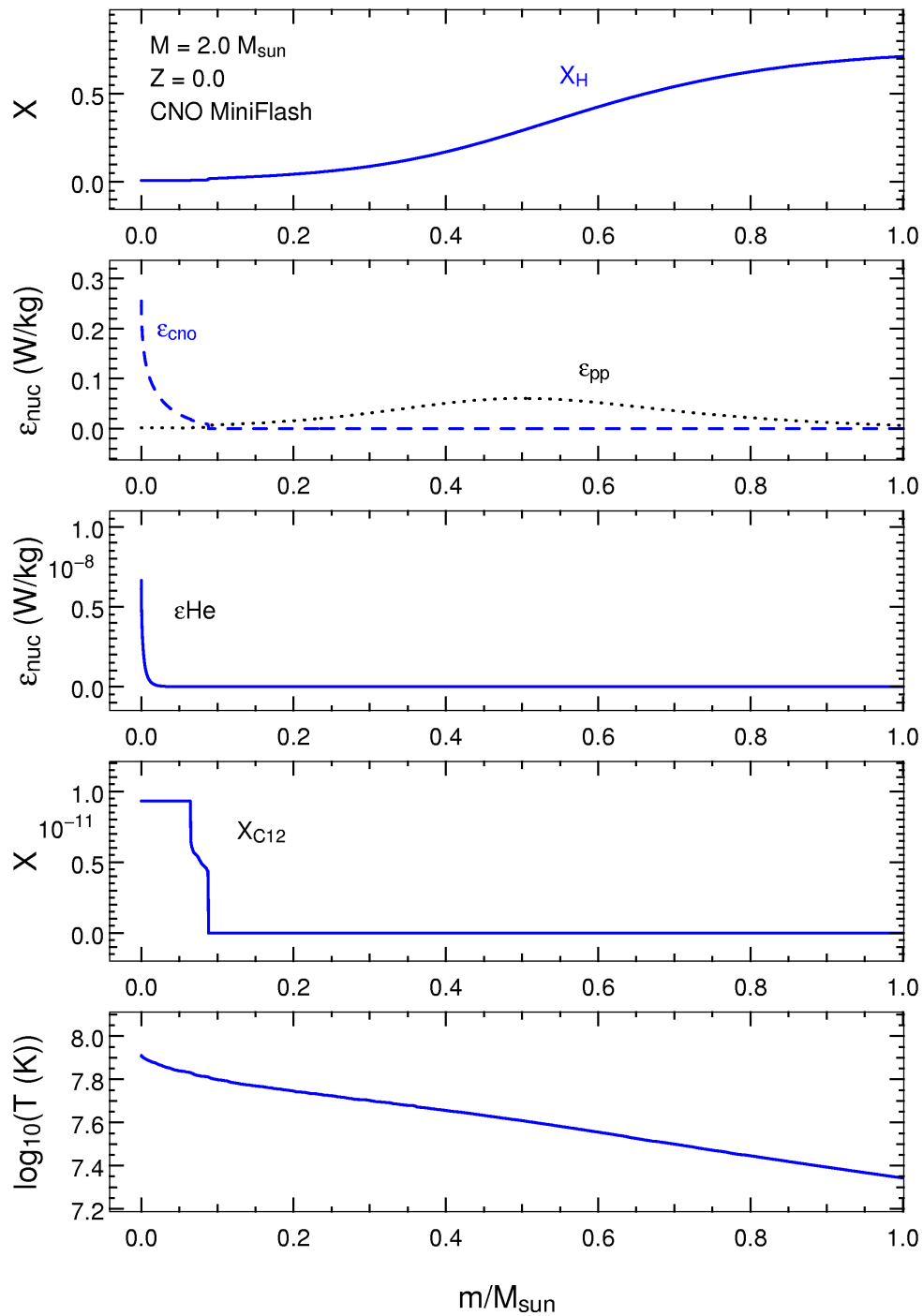


Figure 5.36: The run of some physical characteristics in a single model taken during the CNO miniflash. The top panel shows just how little H is left in the core. In the second panel we can see that the peak p-p burning has already moved off centre, and that the CNO burning is very concentrated right at the centre (due to its high temperature dependence). Also evident is the small amount of He burning (third panel) that produces the tiny amount of ^{12}C (fourth panel).

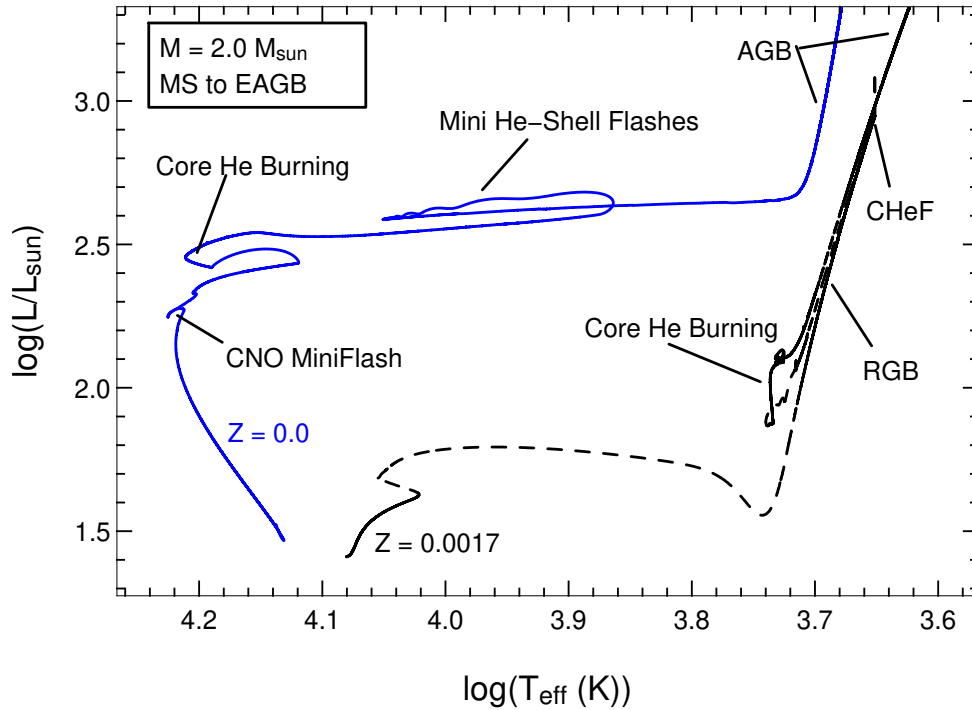


Figure 5.37: HR diagrams comparing the $Z = 0$ and $Z = 0.0017$ models. Significant differences are evident in the $Z = 0$ model, such as the large increase in luminosity during the MS, the lack of an RGB and the lack of a core He flash. Core He burning also occurs at a significantly higher luminosity in the $Z = 0$ model, and at a much higher surface temperature.

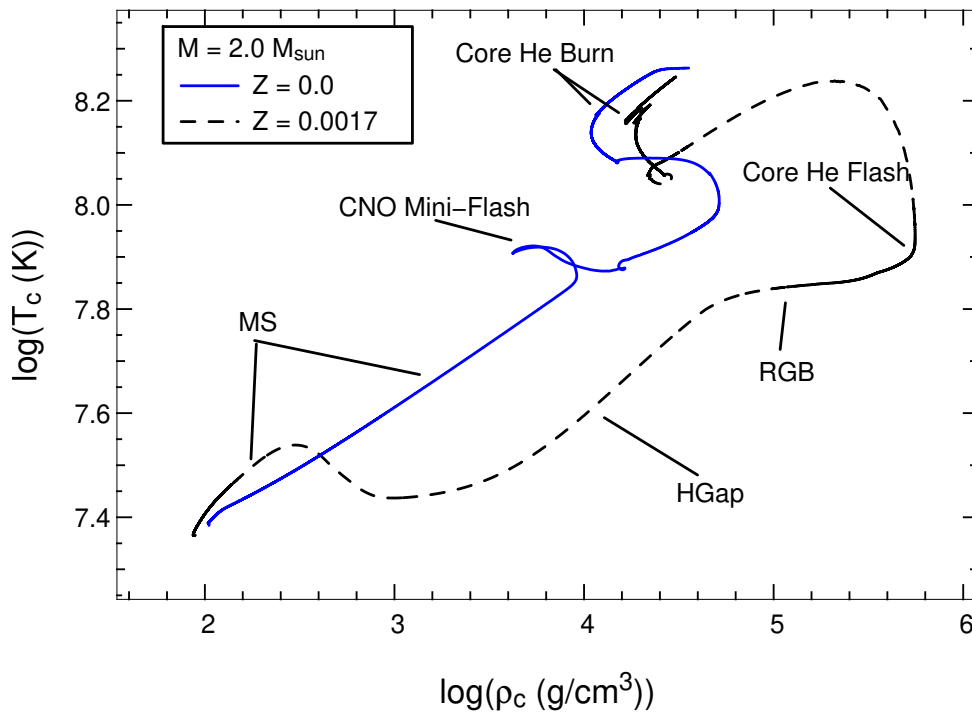


Figure 5.38: Central temperature versus central density for the $Z = 0$ and $Z = 0.0017$ $2 M_{\odot}$ models. The evolution to high temperatures and densities on the MS in the $Z = 0$ model is evident, as is the reduction in density during the CNO miniflash. Unlike the $Z = 0.0017$ model the $Z = 0$ model reaches He ignition temperatures at a lower density, thereby avoiding the core He flash due to the lower degeneracy. The $Z = 0$ model also avoids the RGB phase, practically going straight from the MS to quiescent core He burning.

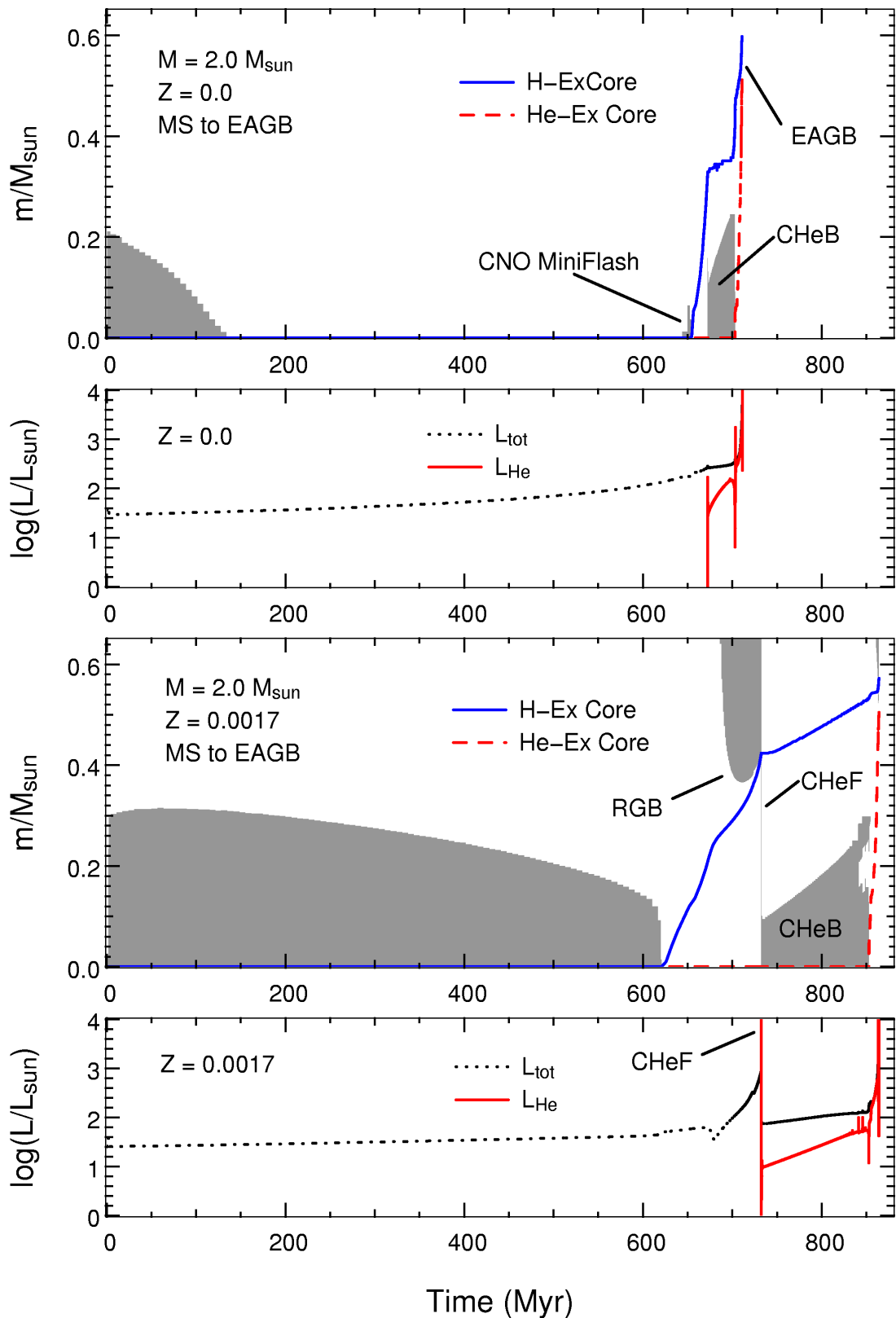


Figure 5.39: The MS and core He burning evolution in the $Z = 0$ model (top two panels) and $Z = 0.0017$ model (bottom two panels). For each pair of panels convection is shown in grey shading in the first panel and the evolution of luminosities in the second. The striking evolutionary differences in the $Z = 0$ model can be seen here – the occurrence of the CNO miniflash, the non-occurrence of an RGB phase and core He flash, and the very short-lived He burning lifetime. Interestingly both stars have quite similar H burning lifetimes, with the $Z = 0$ model lifetime (654 Myr) being slightly *longer* ($\sim 5\%$) than the $Z = 0.0017$ lifetime (623 Myr).

regions that have been subjected to partial hydrogen burning. However, as is evident from the carbon abundance profile, the burning in this region has only been via the p-p chains. It is only at the bottom of the H burning shell that carbon is being produced in situ, allowing the CNO cycles to operate. Thus the usual surface abundance increase in ^{14}N cannot occur. The surface is however polluted with a substantial amount of ^4He , raising the envelope abundance to $Y \sim 0.30$ by the end of 2DUP (the model began with $Y = 0.245$). We note that the ^3He abundance is also slightly lowered, as it has been destroyed in the regions of partial H burning. By contrast, in the $Z = 0.0017$ model most of the surface abundance changes happen at first dredge-up. The mass fraction of nitrogen increases and that of carbon decreases. The helium mass fraction after FDUP (and 2DUP) is $Y = 0.26$, much lower than that in the $Z = 0$ model (this star had the same initial He abundance as the GC model). The abundance changes during 2DUP are negligible in this star.

5.3.3 TP-AGB: Dual Shell Flashes and Third Dredge-Up

In Figure 5.41 we present the evolution of the $Z = 0$ model during the first few pulses on the TP-AGB. A series of weak pulses can be seen leading up to a major H-flash. This is the first of three consecutive H flashes. Each H shell flash is induced by a He shell flash, whereby the convective intershell breaks through the H-He discontinuity (see Figure 5.42 for a closer view of one of the DSFs). This event dredges down protons and dredges up CNO nuclei – much like the dual core flash (DCF) in lower mass $Z = 0$ models. We refer to these events as AGB dual shell flashes (DSFs), as the luminosity peaks occur at roughly the same time. A CNO-burning convective pocket forms just above the H-He discontinuity (see Figure 5.42). This processed material is later dredged up, significantly polluting the envelope. Once the envelope abundance reaches $Z_{\text{cno}} \sim 10^{-4}$ the H-flashes cease and normal He-flashes continue. The star now appears to be quite similar to a higher metallicity model – it has a CO core and a CNO-rich envelope. Indeed, it initially behaves in a more ‘normal’ (higher metallicity) fashion, with interpulse periods of the order 10^4 to 10^5 years, with no 3DUP.

However on closer inspection there are some significant differences between the $Z = 0$ and $Z = 0.0017$ models. The key difference is that the $Z = 0$ model has a substantially higher core mass at the start of the AGB. The core mass of the $Z = 0$ model at the first major He shell flash ($M_c = 0.69 M_{\odot}$) is $\sim 20\%$ larger than that of the $Z = 0.0017$ star ($M_c = 0.56 M_{\odot}$). As mentioned above the $Z = 0$ model also has a higher He abundance in the envelope. It also has no nuclei heavier than those produced by H and He burning. These differences soon lead to a divergence in AGB evolution. As shown in Figure 5.43 the $Z = 0.0017$ model experiences no 3DUP throughout its AGB evolution – the surface abundances remain the same. The $Z = 0$ model on the other hand does have 3DUP episodes. This is evident in Figure 5.44 where it can be seen that the envelope is progressively enriched by CNO nuclei, albeit in small steps. The dredge-up parameter λ is very small throughout the evolution, reaching a maximum of only ~ 0.01 . Also evident in Figure 5.44 is that the temperature at the base of the convective envelope reaches quite high temperatures ($T_{\text{bce}} \sim 7.9$ K), such that hot bottom burning (HBB) is active in this star. In the same figure it can be seen that the ^{12}C in the envelope is gradually cycled to ^{14}N . Indeed, the star’s envelope becomes dominated by ^{14}N (in terms of heavy nuclei) towards the end of the

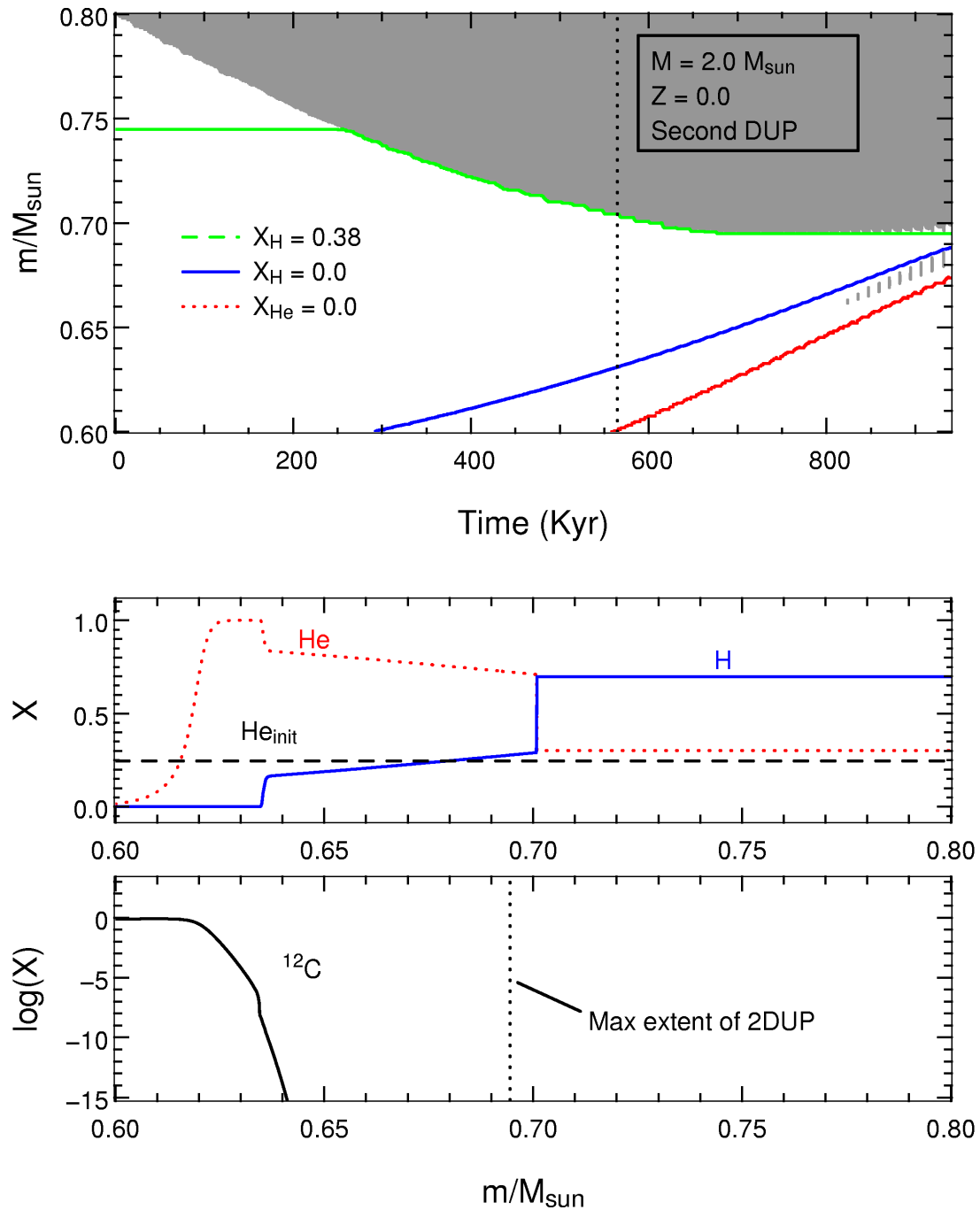


Figure 5.40: The second dredge-up episode in the $Z = 0$ model (during the EAGB). Note that the top panel shows evolution with time (which has been offset), whilst the bottom two panels show the run of abundances against *mass* for a single model. The location in time at which the single model was taken is represented by the vertical dotted line in panel 1. It can be seen that the envelope reaches down into regions that have been subjected to partial H burning. As these regions have been burnt only via the p-p chains the only species enhanced by this episode is ^4He . The bottom panel shows the lack of carbon in the region – the 3α reactions are only active right at the bottom of the H burning shell. The dashed line in the middle panel represents the initial He abundance ($Y = 0.245$). The final He abundance after 2DUP is $Y \sim 0.30$.

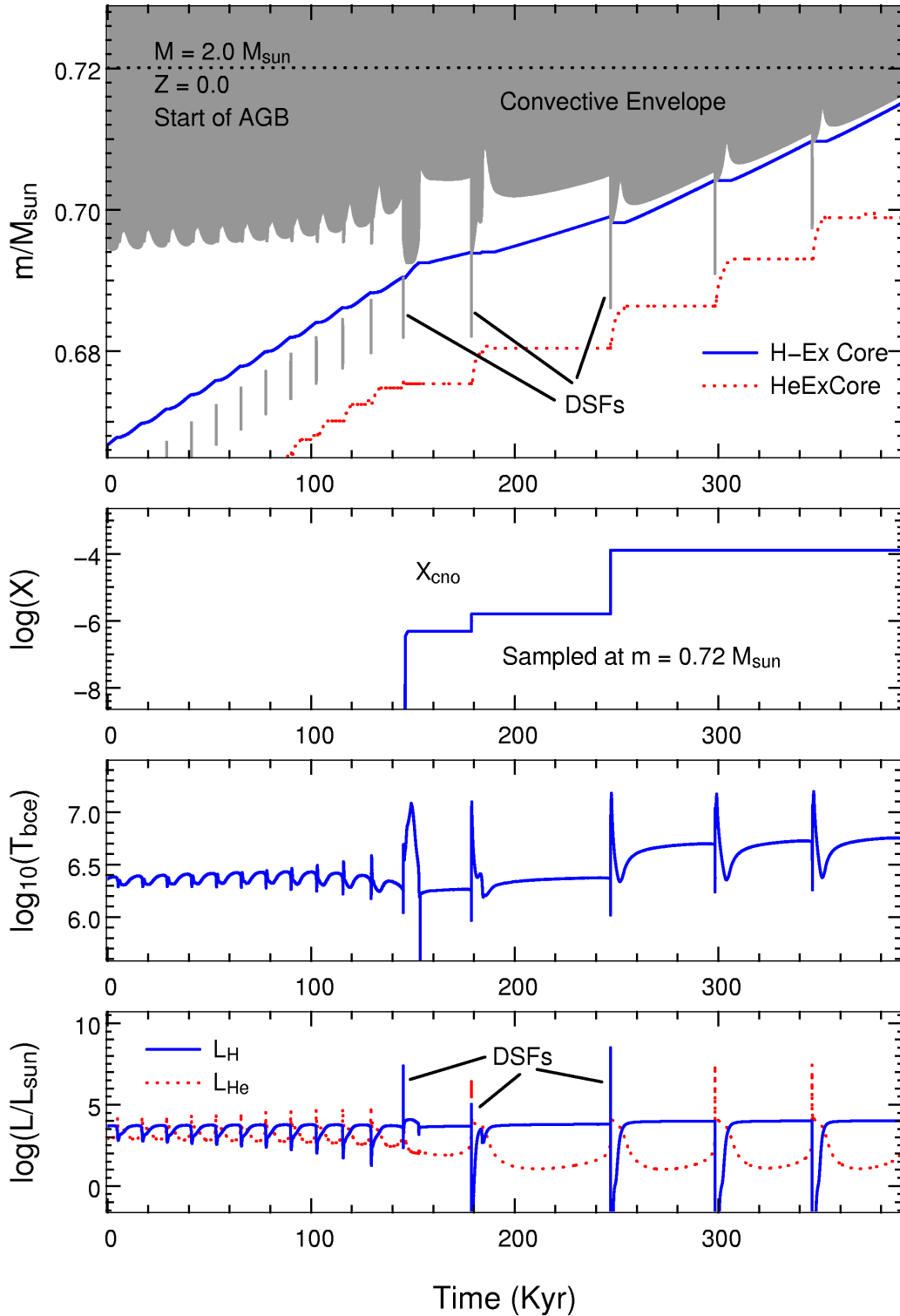


Figure 5.41: Evolution of the $Z = 0$ model during the first few pulses on the TP-AGB. A series of weak pulses can be seen leading up to a major H-flash (the first flash marked ‘DSF’). This is the first of three consecutive dual shell flashes (DSFs). The H shell flash is induced by the He shell flash, whereby the convective intershell breaks through the H-He discontinuity, consequently dredging down protons and dredging up CNO nuclei – much like the DCF in lower mass models. The CNO-processed pocket that forms just above the H-He discontinuity is later dredged up, polluting the envelope. This can be seen in the second panel which shows that the CNO abundance in the envelope increases after each DSF dredge-up episode. In the bottom panel it can be seen that the magnitude of the H flashes ranges between 10^5 and $10^{8.5} L_{\odot}$. Once the envelope abundance reaches $Z_{cno} \sim 10^{-4}$ the H-flashes cease and normal He-flashes continue (initially with no 3DUP).

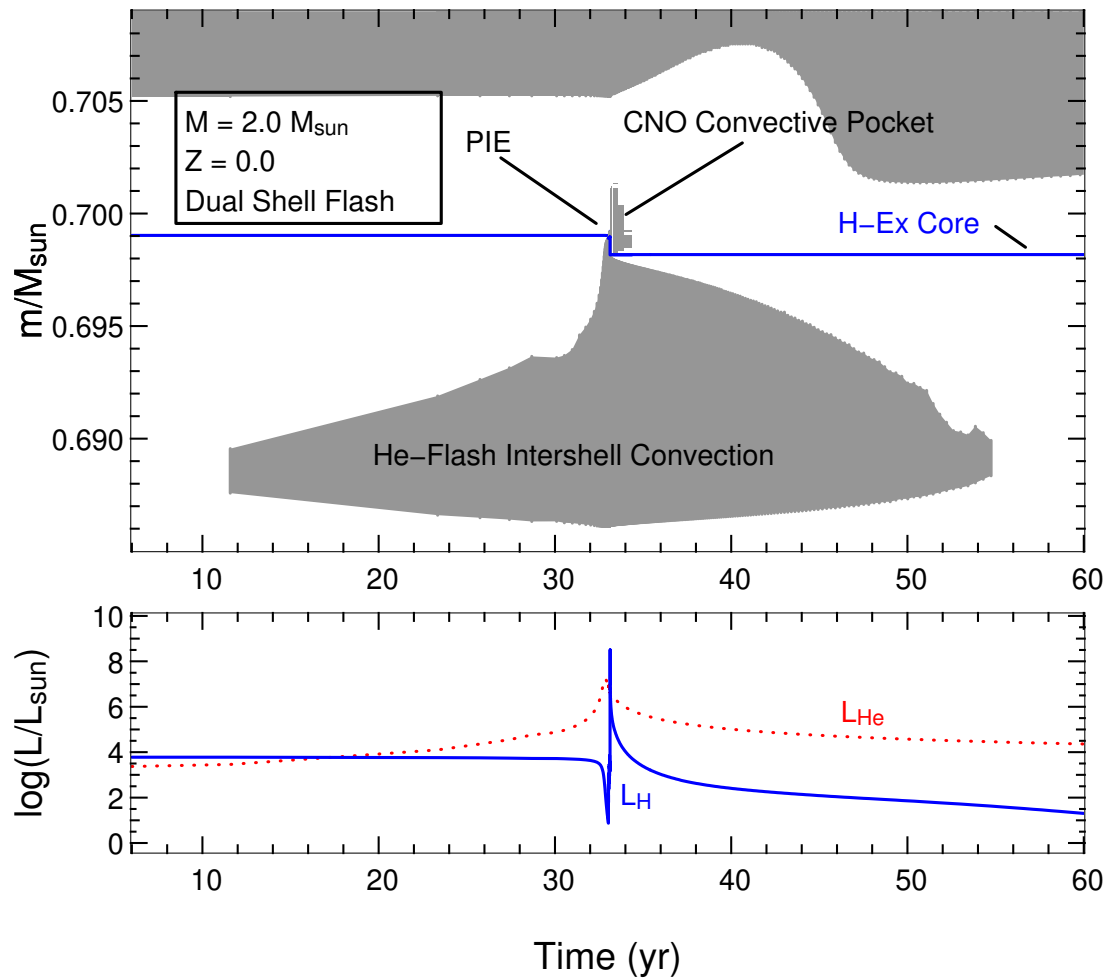


Figure 5.42: Zooming in on the evolution of the main DSF in the $Z = 0$ model (the third H-flash in Figure 5.41). The breaching of the H-He discontinuity can be seen in the top panel – protons are mixed downwards and He intershell material mixed upwards. This gives rise to an extra convection zone – a small CNO burning pocket. PIE stands for ‘proton ingestion episode’. In the bottom panel it can be seen that the H burning luminosity temporarily exceeds that of the He burning. Time has been offset for clarity.

AGB. We note that we have included an approximation to the increase in opacity due to the excess nitrogen in our $Z = 0$ models (in most studies only changes in C and O are taken into account, as the standard opacity tables only provide this option). The GC model on the other hand never attains envelope temperatures high enough for HBB (see Figure 5.43).

A feature of both models is that the interpulse period gradually decreases. This occurs as the core mass of each star increases. The core mass of the $Z = 0$ model increases at a much faster rate than that of the GC model. The bottom panel in Figure 5.45 demonstrates the increasing frequency of the pulses and also shows just how short they become in the $Z = 0$ model, reducing from $\sim 10^5$ yr to $\sim 10^3$ yr. In the top panel of the same figure it can be seen that this results in a great many pulses on the $Z = 0$ AGB – 282 in total, as compared to only 41 in the $Z = 0.0017$ model – even though the $Z = 0$ AGB lifetime is a factor of two shorter than the GC model’s (~ 1.6 Myr compared to ~ 3.5 Myr). Finally we note that the core masses at the end of the AGB (ie. the white dwarf masses) are substantially different – the $Z = 0$ WD mass ($1.1 M_{\odot}$) is $\sim 25\%$ larger than that of the $Z = 0.0017$ ($0.8 M_{\odot}$).

5.3.4 Comparison With Previous Work

In Table 5.3 we list, to the best of our knowledge, all the $Z = 0$ models of $M \sim 2.0 M_{\odot}$ in the literature. We find that there are not many key values published with which we can make comparisons. This is due to studies focusing on particular phases of evolution or focusing on describing models of other masses.

MS, CNO Mini-Flash, Core He Burning and 2DUP

Two studies give main sequence lifetimes. Marigo et al. (2001) find core H burning lasts 635 Myr in their model which compares very well with our value of 654 Myr, being only 3% shorter. Siess et al. (2002) find a MS lifetime of 742 Myr, in reasonable agreement with ours, being 12% longer. As our MS lifetime lies between those found by these two studies we suggest that it is in reasonable agreement with the literature to date, but stress that the sample is still quite small. In regards to the CNO miniflash we note that all the studies find that this phenomena occurs. As it occurs right at the end of the MS and thus involves such a small amount of H burning we suggest that it is of little observational consequence, particularly since core He burning proper begins soon after.

The same two studies that provided MS lifetimes also provide core He burning lifetimes. Here there is more variation, with Marigo et al. (2001) finding a lifetime $\sim 40\%$ longer than ours (43 Myr versus our 30 Myr) and Siess et al. (2002) finding a lifetime *more than a factor of 2 longer* than ours (68 Myr). We are unsure why the lifetime of Siess et al. (2002) is so much longer than ours and that found by Marigo et al. (2001). Such large discrepancies between studies indicates that further work is really needed in this area of $Z = 0$ intermediate mass stellar evolution, which we shall pursue as a future study.

An interesting feature of our model is the extent to which helium is enhanced in the envelope due to the second dredge-up event. We find that the He mass fraction increases from $Y = 0.245$

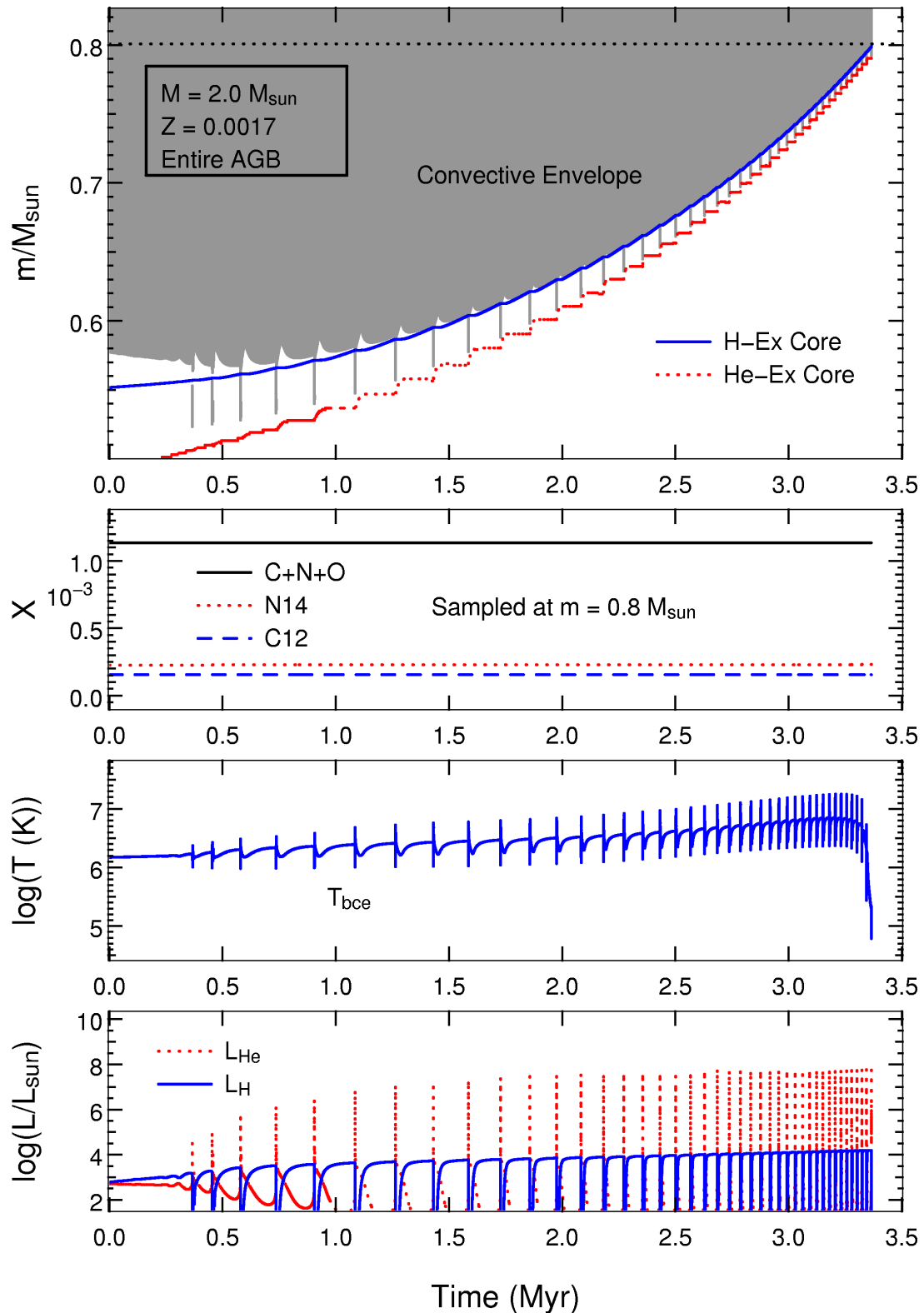


Figure 5.43: The entire AGB evolution of the $Z = 0.0017$ model. The dotted line in the top panel marks the sampling point for the abundance plot in the second panel. The model experiences 41 thermal pulses (compared to 282 in the $Z = 0$ model). As can be seen by the lack of variation in surface abundances (second panel) the star does not experience 3DUP or HBB. Time has been offset for clarity.

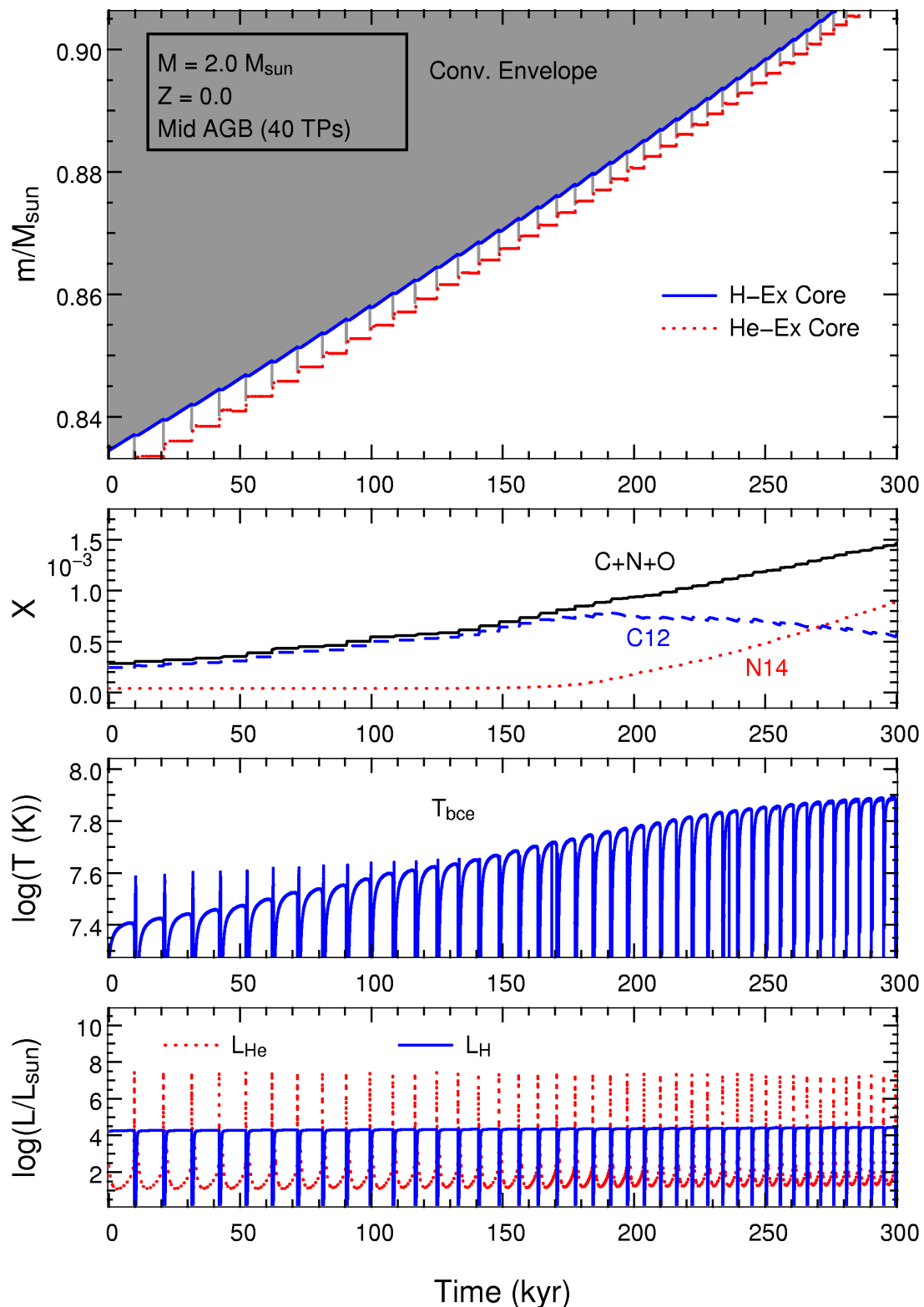


Figure 5.44: A section of the AGB evolution of the $Z = 0$ model (~ 40 pulses). The second panel shows the surface abundance evolution (sampled at $m = 1.0 M_{\odot}$). It can be seen that a small amount of 3DUP occurs during each pulse cycle ($\lambda \sim 0.01$), increasing the abundances of the CNO isotopes. The conversion of ^{12}C to ^{14}N due to HBB can also be seen towards the end of the timespan. This HBB is due to the high temperature at the bottom of the convective envelope, which is shown in panel 3. The interpulse periods are much shorter than in the $Z = 0.0017$ model. Time has been offset for clarity.

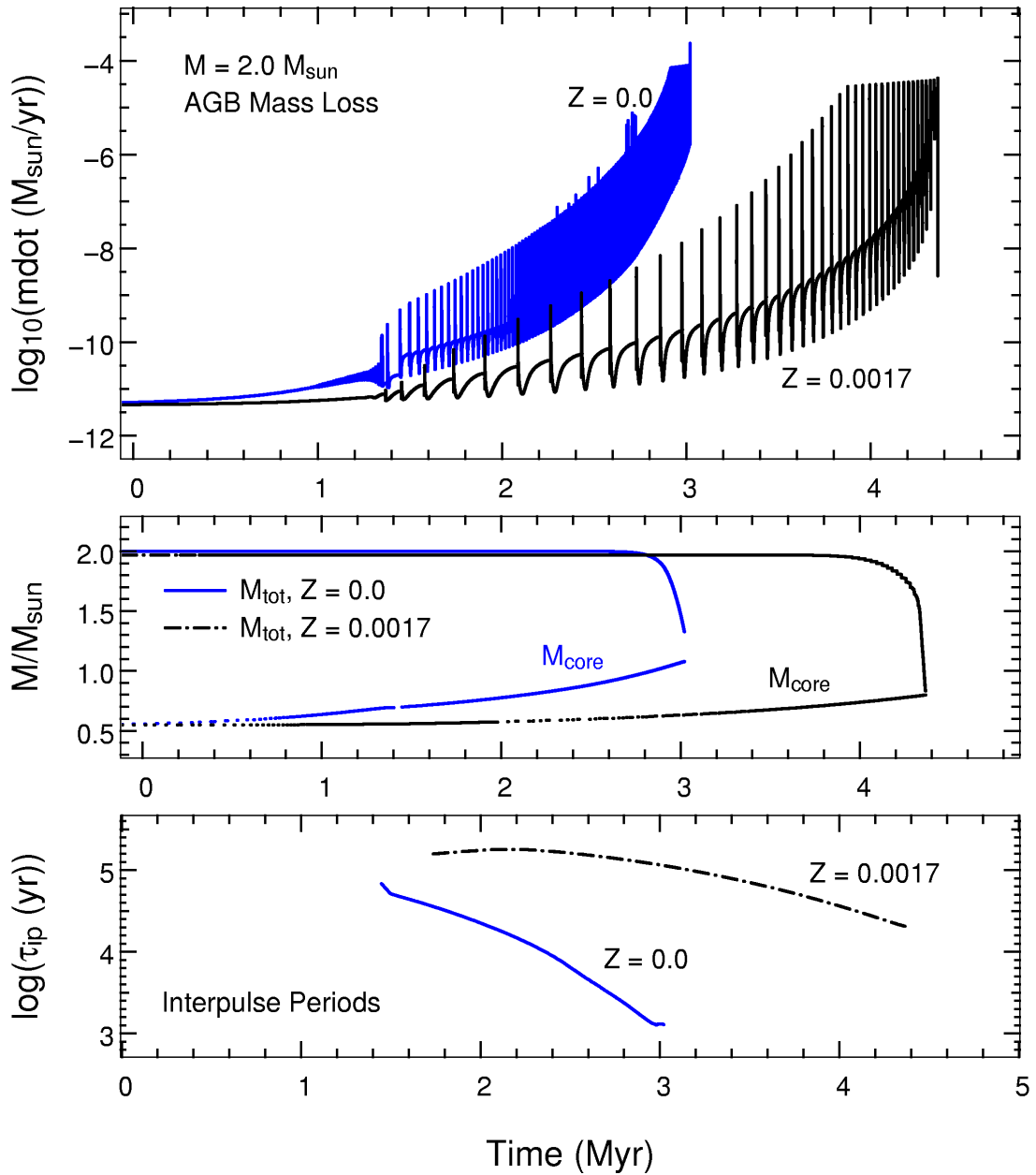


Figure 5.45: The AGB mass-loss history for both stars. It can be seen that the $Z = 0$ model quickly evolves to a higher mass loss rate than the $Z = 0.0017$ model (the luminosity and core mass is higher in this model), and that the AGB lifetime of the $Z = 0$ model is roughly half that of the GC model. In panel 2 we show the evolution of the total mass of the stars and well as the evolution of the core masses. The gap between the two $Z = 0$ curves indicates that not all the envelope was lost before the code failed to converge. The core mass in this case would not increase much more as the star has entered the superwind stage at the very end of the AGB. The bottom panel displays the evolution of the interpulse periods. It can be seen that the $Z = 0$ model has very short interpulse periods by the end of the AGB. Time has been offset for clarity.

to 0.30. [Siess et al. \(2002\)](#) find a similar increase, from $Y = 0.23$ to 0.31. The surface He abundance in the $2.0 M_{\odot}$ model of [Marigo et al. \(2001\)](#) barely increases at all (see Table 5.3) but interestingly their $2.1 M_{\odot}$ model ends up with exactly the same abundance as our model ($Y = 0.30$). This suggests that $2.0 M_{\odot}$ is near the lower limit of significant 2DUP.

AGB: Dual Shell Flash and Third Dredge-Up

Moving on to the AGB we find only one study that provides a quantitative comparison for our model. This indicates that this phase of evolution has not been well studied. Qualitatively all studies (that have evolved their models this far) appear to find the same behaviour at the beginning of the AGB. In particular they all find that a proton ingestion episode (PIE) occurs at the start of the TP-AGB due to the penetration of the shell He convective zone into the H-rich layers just above. This is the dual shell flash (DSF) phenomenon that we detailed in the previous subsection. It results in a significant pollution of the envelope, thus allowing for the (more) normal evolution of the star on the AGB. The fact that all studies have found this indicates that the phenomenon is robust (at least in 1D stellar models) since the differing input physics between stellar codes has not inhibited it. As a key indicator of the conditions for the dual shell flash we have chosen the mass of the H-exhausted core at the time of the first DSF. [Siess et al. \(2002\)](#) find that the core mass at this stage is $0.69 M_{\odot}$ – in almost perfect agreement with our value of $0.70 M_{\odot}$. We note that this is despite the large difference in He burning lifetime between our model and theirs. [Siess et al. \(2002\)](#) also calculate a number of further thermal pulses on the AGB. Examining their Figure 10 we see that the interpulse period in this early stage of the TP-AGB is $\sim 10^{4.8}$ yr. This compares well with our interpulse periods for the same stage. The model of [Siess et al. \(2002\)](#) diverges with ours soon after this though, as deep 3DUP is evident in their graph. Whilst our model has a characteristic $\lambda \sim 0.01$ their model has $\lambda \sim 0.6$ – even after only 12 pulses. The reason for this is most likely because they include a small amount of overshoot on the AGB, whilst we have not. Another difference between these two models is the number of DSFs that occur at the start of the AGB. Our model experiences three, whilst theirs has only one. We note however that their $3 M_{\odot}$ model experiences *four* DSFs. They comment that the star only stops experiencing DSFs when the envelope CNO abundance is $\sim 10^{-7}$. Finally we note that the final Z_{cno} abundance in the envelope of our model after the DSF episodes is $\sim 10^{-4}$. This compares well with that given by [Herwig \(2003\)](#) (see Table 5.3) but is 2 dex lower than that found by [Siess et al. \(2002\)](#). Although this is a large discrepancy it appears that it may be insignificant (in terms of nett envelope pollution and chemical yield), as the operation of the 3DUP soon increases the Z_{cno} abundance by more than an order of magnitude above this value. However, if the pollution of the envelope through this event is the reason that 3DUP occurs, which is probably due to the increase in opacity it causes, then the resultant pollution from the DSFs is important. We note however that it is the model of [Siess et al. \(2002\)](#) that has a much lower pollution from the DSF that has the deepest dredge-up, although we restate that they have included some overshoot so it is not an equivalent comparison. These differences, and the lack of quantitative studies of this phase of evolution (at this mass) suggest that this is another area that requires more investigation. We attempt to clarify the nature of the DSF phenomenon in the broad discussion of all our $Z = 0$ models in Section 5.4.

Authors	M_*	τ_{MS}	τ_{He}	Y_{2DUP}	DSF	$M_{c,DSF}$	$Z_{cno}(10^{-6})$	M_{WD}
Cassisi and Castellani (1993) ^a	2.3	–	–	–	–	–	–	–
Fujimoto et al. (2000)	2.0	–	–	–	Yes	–	–	–
Marigo et al. (2001)	2.0	635	43	0.23 (0.30) ^b	–	–	–	–
Siess et al. (2002)	2.0	742	68	0.31	Yes	0.69	6	–
Herwig (2003)	2.0	–	–	–	Yes	–	~ 100	–
Suda et al. (2004)	2.0	–	–	–	Yes	–	–	–
Current Study ($Z = 0$)	2.0	654	30	0.30	Yes	0.70	0.5, 2, 160^c	1.1
Current Study ($Z = 0.0017$)	2.0	623	120	0.26	No	–	–	0.8

Table 5.3: Comparing our $M = 2.0 M_{\odot}$ model with similar $Z = 0$ models from the literature. Also included for further comparison is our GC model ($Z = 0.0017$) and the $2.3 M_{\odot}$, $\log(Z/Z_{\odot}) = -8$ model by Cassisi and Castellani (1993). The table is ordered by date. Note that we were unable to obtain many of the comparison values (indicated by ‘–’), as each study tends to focus on particular facets of the evolution. The table columns show M_* (initial stellar mass), τ_{MS} (age at MS turn-off), τ_{He} (core He burning lifetime), M_{core} (mass of H-exhausted core at time of main dual shell flash), DSF (whether or not the He convective zone penetrated the H-shell, or was about to, producing a dual shell flash) and Z_{cno} (the C+N+O metallicity of the envelope after the DSF dredge-up). All lifetimes are in Myr and all masses are in M_{\odot} .

^aThis model has $\log(Z/Z_{\odot}) = -8$.

^bTheir $2.1 M_{\odot}$ model has $Y_{2DUP} = 0.30$

^cThis model experienced three DSFs.

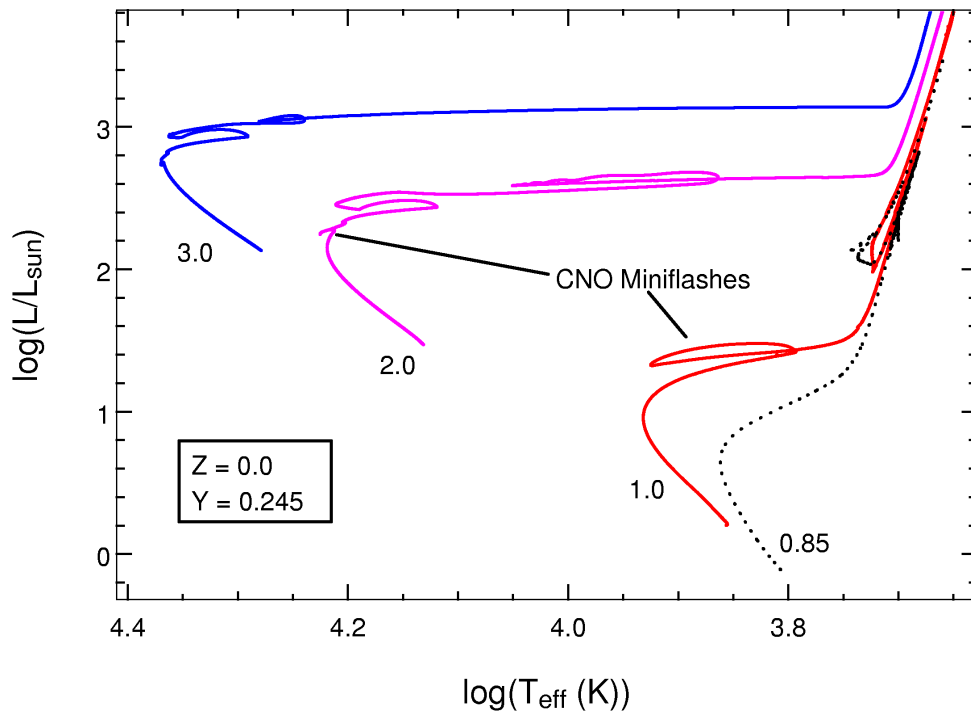


Figure 5.46: The HR diagrams for all our $Z = 0$ models. The initial mass of each is marked on the diagram (in units of M_{\odot}). Also indicated are the CNO miniflashes in two of the models. All the models experience the CNO miniflash to varying degrees. We note that the $2 M_{\odot}$ model does not experience a core He flash, unlike more metal-rich models. It is thus classed as an intermediate-mass star.

5.4 Overview and Discussion of All $Z = 0$ Models

5.4.1 $M = 0.85 M_{\odot}$ to $3.0 M_{\odot}$

Apart from the two models discussed in detail in the preceding two sections we have calculated two more models, with masses $1.0 M_{\odot}$ and $3.0 M_{\odot}$. Unfortunately we encountered convergence difficulties with the the $3.0 M_{\odot}$ model during the AGB so this model has not been taken to completion. It has however been evolved through the DSF phase and also 950 thermal pulses on the AGB so we are able to present some results for this model and thus include it in the following discussion.

In Figure 5.46 we show the evolution of all our $Z = 0$ ($Y = 0.245$) models in the HR diagram. It can be seen that there is a transition between 1 and $2 M_{\odot}$ such that stars do not reach an RGB configuration due to the early onset of quiescent core He burning. Like our $0.85 M_{\odot}$ model we find that our $1 M_{\odot}$ model also experiences a dual core flash (DCF) at the tip of the RGB. However the $2 M_{\odot}$ model does not undergo a core He flash – unlike the $Z = 0.0017$ model of the same mass, and indeed all more metal-rich models. Thus the transition between low mass and intermediate mass stars, as defined by the occurrence or non-occurrence of the core He flash, is much lower at $Z = 0$. Our work shows that the cut-off is below $2 M_{\odot}$ but above $1 M_{\odot}$, which is consistent with other studies (eg. Marigo et al. (2001) find the cut-off to be at $\sim 1.1 M_{\odot}$). We thus class the $2 M_{\odot}$ model as an intermediate-mass star.

In Table 5.4 we present the lifespans of various evolutionary stages for our models. In the previous two sections we have compared our lifetimes with all other studies available (for masses

0.85 M_{\odot} and 2.0 M_{\odot}). Here we shall compare our results primarily with the work by [Marigo et al. \(2001\)](#) as they have calculated a comprehensive grid of models. We note however that they did not calculate models for the AGB phase so not all comparisons are possible. Along with our MS and core He burning lifetimes in Table 5.4 we display the percentage differences between our lifetimes and those of [Marigo et al. \(2001\)](#). It can be seen that the MS lifetimes are in reasonable agreement, never being more than $\sim 11\%$ different than each other. This is despite the inclusion of a small amount of overshoot in the [Marigo et al.](#) models (for $M > 1.1 M_{\odot}$). We note however that overshoot should not have much effect on the MS at $Z = 0$ as the convective cores are smaller and shorter-lived, due to the dominance of the p-p chains. The core He burning lifetimes are consistently shorter in our models, by values ranging from $\sim 10 \rightarrow 64\%$. This is explicable by the fact that [Marigo et al. \(2001\)](#) have used overshoot in all models during core He burning. Taking this into account we suggest that all our models are, in general, in fair agreement with those of [Marigo et al.](#), except for the $M = 0.85 M_{\odot}$ model during core He burning. An important factor here is that [Marigo et al.](#) did not evolve their low mass stars through the core He flash/DCF. They constructed zero-age HB models to investigate the further evolution. Thus it is probably not surprising that the lifetimes are different in this case. We compared this model to other studies in an earlier section (see Table 5.2 on page 133), only finding one with which we could make a direct comparison. In this case the 0.80 M_{\odot} model of [Picardi et al. \(2004\)](#) had a considerably *shorter* core He burning lifetime than ours. We concluded that more work needs to be done in this area.

Comparisons between our other lifetimes given in Table 5.4 with the literature is not possible as studies tend not to provide these. We provide them for future studies to make comparisons with. These lifetimes are useful in terms of predicting the relative numbers of stars in a particular stage of evolution at a given time.

The details of an extra $Z = 0$ model is also given in Table 5.4. It has an initial mass of 3 M_{\odot} but a different initial helium abundance, being $Y = 0.230$ rather than 0.245. We have added this model because it did complete the AGB phase whilst the $Y = 0.245$ model did not. We have discussed the nucleosynthesis of this 3 M_{\odot} model in Section 6.4 on page 200 and thus provide some structural evolution details here (and in Table 5.5).

In Table 5.5 we have provided some more key values that characterise our $Z = 0$ models. Interesting features seen here are that the core masses of the two low mass models were identical at the time of dual core flash onset ($M_c = 0.49 M_{\odot}$) and that none of the models experienced much third dredge-up at all. A vital statistic with regards to $Z = 0$ low- and intermediate-mass stars is the degree of envelope pollution that occurs as a result of the DCF or DSF events. Table 5.5 indicates that the level of pollution from this event in the 1 M_{\odot} model is similar to that experienced by the 0.85 M_{\odot} model, such that the envelope abundance reached $Z_{cno} \sim 10^{-3}$. Interestingly the dual shell flash (DSF) event occurring in the intermediate mass models ($M = 2$ and 3 M_{\odot}) at the beginning of the AGB produced 1 to 2 dex less pollution in the envelope. As discussed earlier one of the main problems of postulating $Z \sim 0$ low mass stars as the source of pollution for the carbon-enhanced extremely metal poor halo stars (CEMPHS) is that models produce too much carbon and nitrogen, usually by about 1 to 2 dex. The result that intermediate mass stars produce less C and N suggests that these stars are better candidates for the source of the C in CEMPHS. We shall return to this topic in the main discussion of the thesis.

M_*	τ_{MS}	τ_{SGB}	τ_{RGB}	τ_{HeB}	τ_{EAGB}	τ_{AGB}
0.85	10100 (−11%)	840	200	70 (−64%)	6.8	1.5
1.0	5740 (−6%)	470	96	99 (−10%)	9	1.7
2.0	654 (+3%)	18	–	30 (−30%)	8	1.8
3.0	200 (−5%)	13	–	12 (−25%)	4.2	$\sim 2^a$
3.0 ^b	221 (+5%)	8	–	12 (−25%)	5.0	1.2

Table 5.4: Various lifetimes for all the $Z = 0$, $Y = 0.245$ models, and one $3.0 M_\odot$ model with $Y = 0.230$. All ages are in Myr and all masses are in M_\odot . M_* is the initial mass of the star. Lifetimes are: τ_{MS} (ZAMS to MS turn-off), τ_{SGB} (MS turn-off to base of RGB, or to the start of core He burning in the more massive models), τ_{RGB} (red giant branch), τ_{HeB} (core helium burning), τ_{EAGB} (from end of core He burning to first thermal pulse on AGB), and τ_{AGB} (thermally-pulsing AGB). The percentages in brackets are the differences between our lifetimes for the MS and core He burning and those of Marigo et al. (2001). A negative value implies that our lifetime is shorter.

^a This model did not fully complete the AGB.

^b This model had an initial composition for pure H and He, with $Y = 0.230$ rather than 0.245.

M_*	$M_{c,DF}$	$Z_{cno,DF}$	λ_{3dup}	N_{TP}	$Z_{cno,f}$	M_{WD}
0.85	0.49	4×10^{-3}	0.0	32	4×10^{-3}	0.77
1.0	0.49	6×10^{-3}	0.0	60	6×10^{-3}	0.83
2.0	0.70	2×10^{-4}	0.01	282	3×10^{-3}	1.08
3.0 ^a	0.78	2×10^{-5}	< 0.01	> 950	3×10^{-5}	> 1.17
3.0 ^b	0.77	2×10^{-5}	~ 0.2	390	1.2×10^{-2}	1.10

Table 5.5: Various characteristic values for the $Z = 0$, $Y = 0.245$ models, and one $3.0 M_\odot$ model with $Y = 0.230$. The column definitions are: M_* (initial stellar mass), $M_{c,DF}$ (core mass at the onset of the dual core flash or dual shell flash), $Z_{cno,DF}$ (the envelope metallicity after the dredge-up event(s) associated with the DCF/DSF episodes), λ_{3dup} (the maximum value reached for the dredge-up parameter on the AGB), N_{TP} (number of thermal pulses on the AGB), $Z_{cno,f}$ (final metallicity of the envelope), and M_{WD} (white dwarf mass). All masses are in M_\odot .

^a This model did not fully complete the AGB.

^b This model had an initial composition for pure H and He, with $Y = 0.230$ rather than 0.245.

Further surface abundance enhancements can come about by the third dredge-up (3DUP) on the TP-AGB. As we have included no overshoot at all in these models we note that our 3DUP results represent somewhat of a lower limit to the possibilities of AGB envelope enhancements. Table 5.5 highlights the zero and very weak 3DUP occurring in our models. The 3DUP parameter λ_{3dup} is only marginally above zero in the intermediate mass models (except for the $Y = 0.23$, $3 M_{\odot}$ model). Despite this the $2 M_{\odot}$ model ends up with an extra order of magnitude increase in Z (over the earlier DSF pollution) because there are so many 3DUP episodes (282 in total). Interestingly this brings the final envelope abundance of this model roughly in line with the two low mass models – all these models end the AGB with $Z \sim 10^{-3}$ (the $3 M_{\odot}$ model did not complete the AGB). Interestingly the $Y = 0.23$, $3 M_{\odot}$ model had much deeper dredge-up, with $\lambda \sim 0.2$. Although evolutionary dependencies on helium abundance are outside the scope of the present work, it is interesting to note that a lower He abundance can have such a strong effect. The high degree of surface pollution at the end of this model’s evolution is due to this increased 3DUP efficiency.

As most mass loss occurs at the end of the AGB (the superwind phase) the Z_{cno} abundances at the end of the AGB (ie. column 6 in Table 5.5) roughly represent the composition of the material returned to the interstellar medium. Detailed nucleosynthesis and associated yields from these models is the subject of the next chapter.

Finally we note the interesting result that all the models calculated here, which have started with a pristine H-He composition, experience some form of major pollution event in their lifetimes. One of the (similar) $Z = 0$ phenomena – a DCF or a DSF – always occurs. If a $Z = 0$ star undergoes a core He flash then the DCF will occur. If it doesn’t then a DSF will occur on the early TP-AGB. Both events involve some dredge-up of CN(O) nuclei from a He-rich convective shell, consequent CNO burning and then a dredge-up of this processed material by an incursion of the convective envelope. If the models are correct then this suggests that much pollution would have been caused by a population of $Z = 0$ low- and intermediate-mass stars (if such a population existed).

Chapter 6

Zero Metallicity Stars: Nucleosynthetic Evolution

“The most incomprehensible thing about our universe is that it can be comprehended.”

– Albert Einstein

6.1 Background

In contrast to the structural evolution code only minor modifications were needed to the nucleosynthesis code (NS code) in order to enable the calculation of $Z = 0$ (and very metal-poor) models. Removing the scaled-solar composition assumptions to allow arbitrary stellar chemical compositions was the main modification. Aside from this some computational problems were encountered with the dual core flash phenomenon. In particular it was found that the standard resolution of the NS code was not sufficient to follow the small radiative zones that often form after the splitting of the He convection zones in these models. If these zones were not resolved then a large degree of extra mixing would occur, leading to enrichment of the envelope inconsistent with the structural code results. The solution to this was simply to increase the resolution in the central regions during these events. This problem is discussed in more detail later in this chapter. We note that the NS code was described in detail in Section 3.2 on page 43.

6.1.1 Initial Composition

We have discussed the rationale for choosing our primordial composition earlier, in Section 2.2 on page 17. Here we re-display the abundances, in Table 6.1, for easy reference. The nucleosynthesis code handles many more species than the SEV code (see Section 3.2 for a description of this code), so all the species predicted by BBN are accounted for in the initial composition.

6.2 Detailed Nucleosynthesis at $M = 0.85 M_{\odot}$

In this section we detail the key nucleosynthetic events that occur during the evolution of the $0.85 M_{\odot}$ $Z = 0$ model. In particular we describe and quantify the events that lead to surface

Nuclide	Primordial Mass Fraction
^1H	0.754796
^2H	1.96×10^{-4}
^3He	7.85×10^{-6}
^4He	0.24500
^7Li	3.13×10^{-10}
^{12}C	0.0
^{14}N	0.0
^{16}O	0.0

Table 6.1: Initial abundances used in the zero-metallicity stellar models, as given by Standard Big Bang Nucleosynthesis calculations by [Coc et al. \(2004\)](#).

pollution and hence affect the chemical yield of the star. In this sense the defining event in this model is the dual core flash (DCF) that occurs at the tip of the RGB. Processed material from this event is dredged-up into the convective envelope, causing the surface metallicity (and helium abundance) to rise dramatically. Before this event the surface retains its primordial abundances (apart from a minor change at first dredge-up). After the DCF dredge-up the star basically retains the abundance pattern arising from this event for the rest of its evolution. The AGB phase has little effect on the surface composition (apart from some low-mass species such as ^7Li and ^3He), as there is no third dredge-up (3DUP) and only very minor hot bottom burning (HBB). We also present the chemical yield for the model.

6.2.1 First Dredge-Up

Low mass $Z = 0$ stars do evolve to an RGB configuration, although their surface temperatures are somewhat higher than Pop II stars. Their luminosities are also higher, due to hotter H-burning and lower opacity. These factors lead to a weaker first dredge-up (FDUP) episode, such that the envelope convection never reaches down into regions in which any appreciable nuclear burning has previously occurred. In Figure 6.1 we plot some of the abundance profiles at the time of maximum dredge-up. It can be seen that the only isotope that may have its surface abundance altered is ^3He , and only by a minute amount. The abundance did actually increase, but by only ~ 0.02 dex, such that chemical pollution from the FDUP is essentially non-existent in this star.

An interesting feature in Figure 6.1 is that there is a (relatively) substantial amount of ^{12}C in the core – despite the star initially having a zero abundance of C and not having reached a standard He burning phase as yet. As shown in the previous chapter there is actually a small amount of He burning just below the H burning shell (see Figure 5.10 on page 102). This feeds the bottom of the H shell with some primary ^{12}C which allows the CNO cycles to operate. This only occurs at the bottom of the H shell – the p-p chains still dominate most of the H-burning shell. As the H shell burns its way outward (in mass) it thus leaves a small trail of ^{12}C (and associated burning products) in its wake. Although this interesting abundance profile does not directly affect the chemical yield of the star, it may be significant enough to affect the nature of the He core flash burning that occurs in this region at a later time.

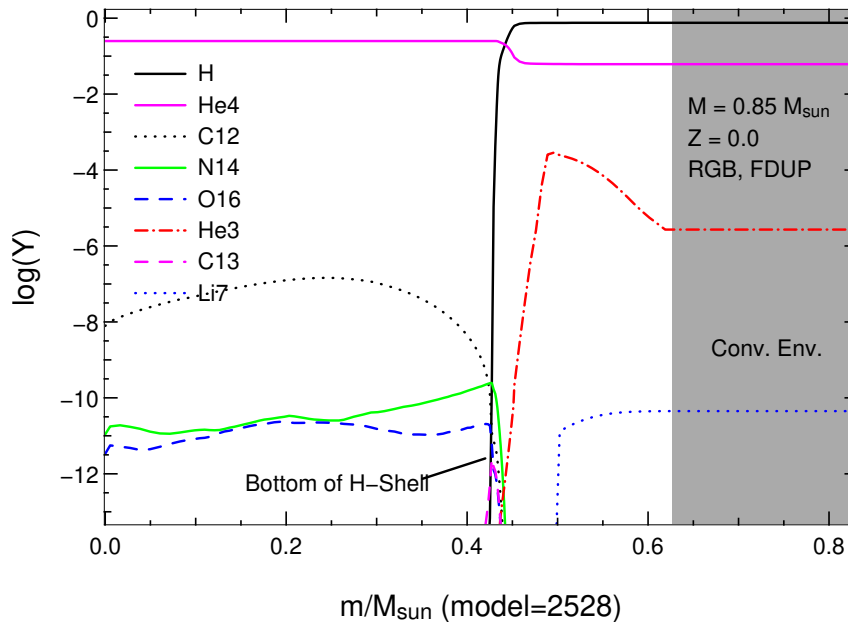


Figure 6.1: Chemical composition (log of mole fraction, Y) versus mass for the $0.85 M_{\odot}$ model at the time of maximum incursion by the envelope during FDUP. The grey shaded area represents convection.

6.2.2 Dual Core Flash

As FDUP dredges up no processed material (practically), the star retains its primordial surface composition till the end of the RGB. In fact the surface remains unpolluted even through the dual core flash phase itself. It is not until both flashes have abated and the convection moves inwards (in mass, see eg. Figure 6.3) that the envelope is polluted. Figure 6.2 demonstrates this pollution event clearly, showing that a large amount of processed material is dredged up to the surface, taking the metallicity from zero to $\sim 10^{-3}$ in a very short time. Also evident in Figure 6.2 is that, apart from some ${}^7\text{Li}$ and ${}^3\text{He}$ production on the AGB, the DCFDUP is the defining event in terms of the composition of the envelope for all future stages of evolution. The DCFDUP thus has the greatest effect on the chemical yield of this star. This figure gives a good overview of the bulk nucleosynthetic evolution (in terms of surface pollution) for a large range of chemical species and, due to the relative invariance of the composition in the later mass-losing stages of evolution, it also gives a good indication of the expected chemical yield.

As we have identified the DCF (and associated dredge-up) as the defining envelope pollution event for this star we now look into the nucleosynthesis of this phenomenon in detail, as well as some related computational aspects. We note that the structural evolution of this event has been described in Section 5.2.2 on page 101.

Figure 6.3 displays the numerical mesh that was employed in the nucleosynthesis code (NS code) during the DCF. Two key events are clear in this plot. The first is that the He convective zone splits into two as its expansion dredges down protons (this is the major H flash event). The second is that the convective envelope later extends downwards into regions that have been polluted by processed material, thereby altering the surface composition. The splitting of the convection zone initially caused some problems in the nucleosynthesis calculations due to the fact that the two resulting convection zones are divided only by a small radiative region (for some of the time). With our previous spatial resolution the two convective zones would merge,

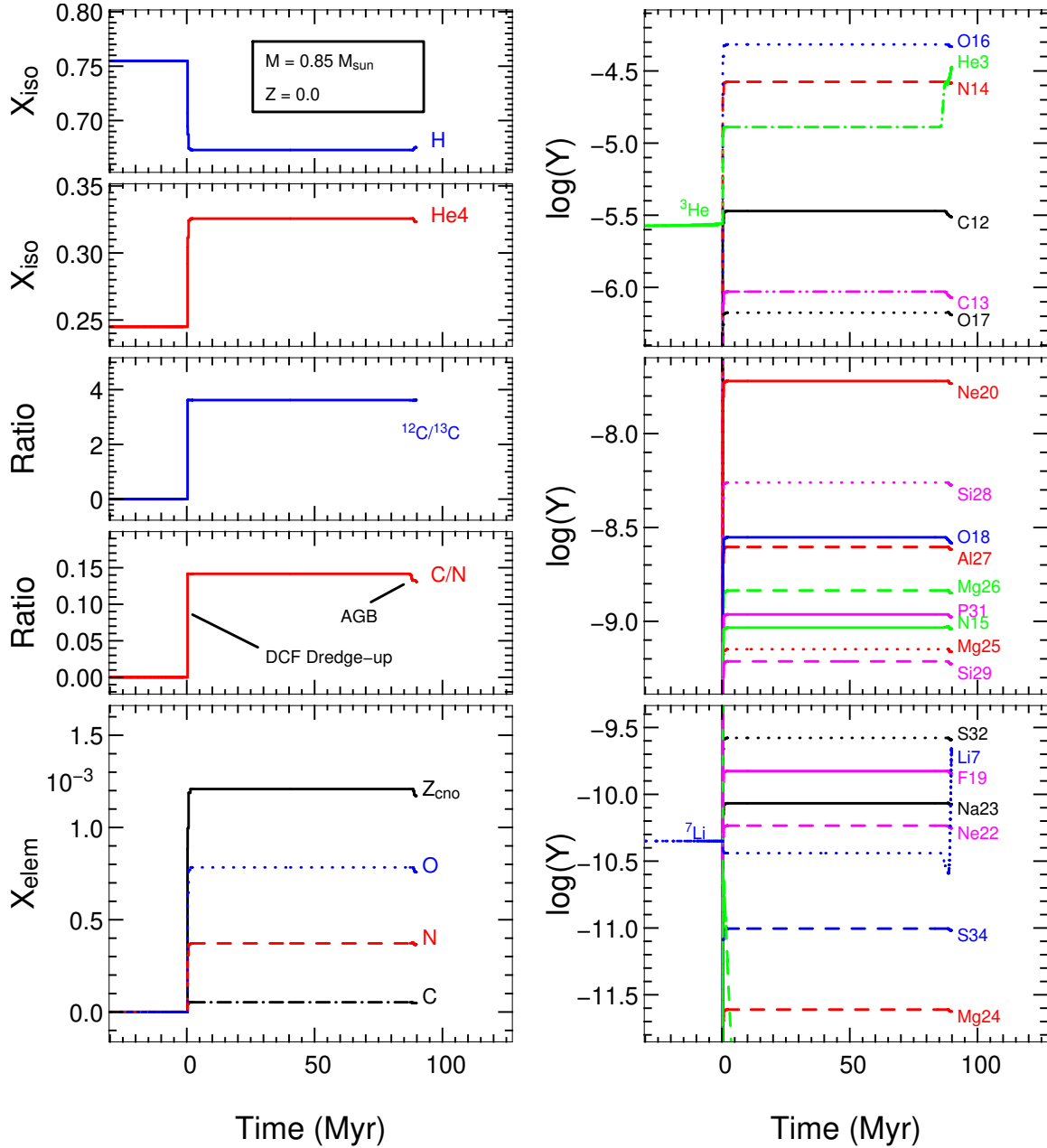


Figure 6.2: Time evolution of the surface abundances in the $M = 0.85 M_{\odot}$, $Z = 0$ model. Time has been offset so that $t = 0$ coincides with the DCF dredge-up. It can be seen that the DCF dredge-up episode is by far the main source of envelope pollution, causing a large increase in He and CNO isotopes. The $^{12}\text{C}/^{13}\text{C}$ ratio is quite low, indicating that CN burning achieved equilibrium during the DCF episode. The only species produced in significant amounts during the AGB are ^7Li and ^3He . We note that this star initially had $Z = 0$ but ends its evolution with $Z \sim \frac{1}{10}$ solar (although it is still very metal-deficient in terms of the heavier elements).

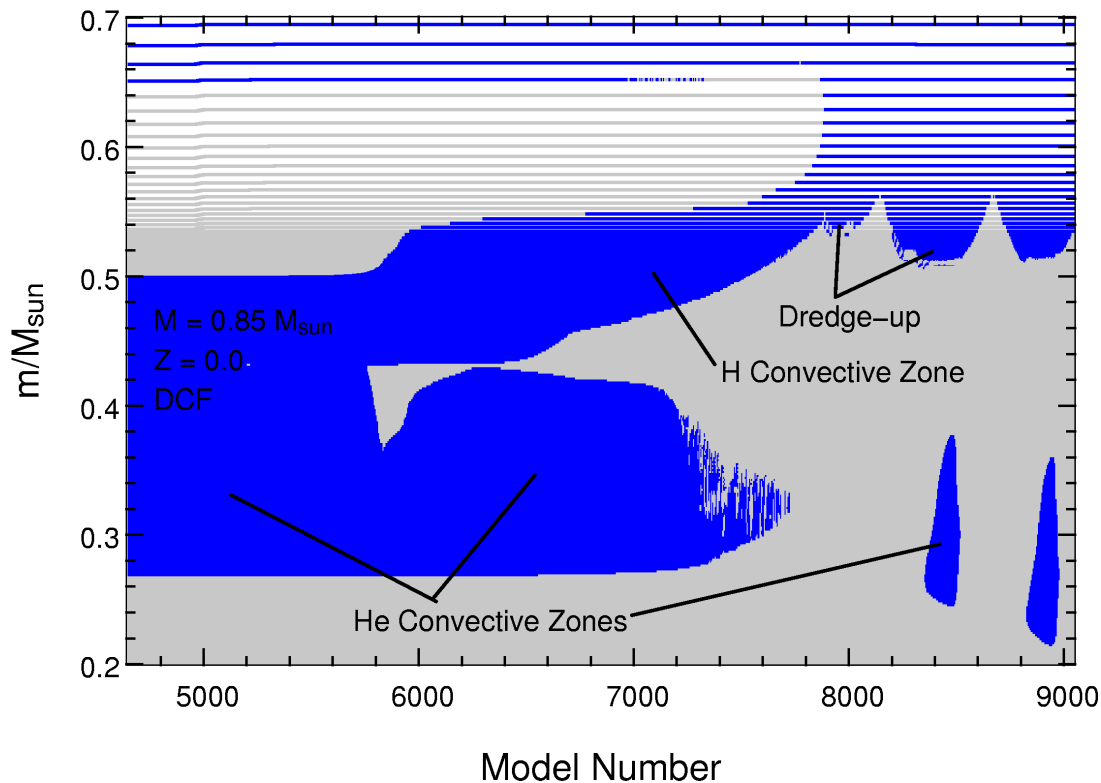


Figure 6.3: The mesh used in the nucleosynthesis code during the dual core flash phase in the $0.85 M_{\odot}$, $Z = 0$ model. Each mesh point is represented by a short horizontal line and on this wide timespan (actually model-span) they appear as long horizontal lines. Dark blue represents convective points and light grey radiative points. It can be seen that the mesh in the outer regions is much less refined than in the central regions (the resolution is so high in the core that the mesh appears as solid colour). We found it necessary to increase the resolution in the core due to the splitting convection zones in models such as this (this can be seen here at model ~ 5800). In particular the narrow radiative zones between the convective zones need to be resolved (eg. at model ~ 6200 in this case). The resolution in the outer regions is $\sim 10^{-2} M_{\odot}$, the inner regions $\sim 10^{-3} M_{\odot}$ and in the H burning shell it is as high as $\sim 10^{-9} M_{\odot}$. The two small convective zones after model 8000 are He minipulses occurring during the secondary RGB phase.

resulting in the mixing of the upper H convective zone (HCZ) with the lower He convective zone (HeCZ). Thus the HCZ would be super-enriched and the later dredge-up by the envelope would result in surface pollution inconsistent with the structural code results. Thus this phase of evolution necessitated increasing the resolution of the mesh. We found that an order of magnitude increase in resolution (in the central regions) was necessary to reliably resolve the DCF. It can be seen in Figure 6.3 that the radiative zone is now easily resolved. However, using such high resolution slowed the calculations considerably. Thus, after this demanding evolutionary phase was complete the resolution was reduced back to the standard level. We used the same method in our other models that experienced the DCF (or DSF).

In Figure 6.4 we show the evolution of the early stages of the DCF. The plot covers a timespan of only 3.5 years but elucidates the important features of the event. In particular we can see the three proton ingestion episodes (PIEs) which lead to varying intensities of H burning inside the He convective zone. The first two H flashes are not as strong as the final one because the HeCZ is ‘eating’ only into the tail of the H burning shell, where the H abundance is fairly low (see Figure 5.17 on page 111 in the structural evolution section). In these cases the energy release from H burning is not large enough to cause a splitting of the convection zone. In the third PIE

a feedback effect is instigated whereby the H burning is so strong due the influx of proton-rich material (this is the major H-flash) that the convection zone expands upwards, causing further proton ingestion. In this case there is a splitting of the He convective zone as a radiative zone develops just below the region of peak H burning energy release (there is a temperature inversion here). The energy release from the He burning shell below also reduces significantly, causing the lower convective zone to reduce in size. These two convection zones – the HCZ above and the HeCZ below – remain separated for the remainder of the evolution, as both flashes subsequently recede.

Figure 6.4 also displays the chemical evolution during this phase, as calculated using the NS code. We have sampled the composition over time at two mass coordinates, one that takes in the HCZ and one that takes in the HeCZ. This gives an insight into the nucleosynthesis that is occurring in both regions. Of most interest is the composition of the HCZ, as it is this region that is dredged up later, polluting the envelope. Looking at the chemical evolution in the HCZ we see that the metal abundances discontinuously jump from zero to $\sim 10^{-4}$ (in mole fraction Y). From then on they are quite stable (at least in this short timespan). Thus it is apparent that, in terms of bulk metallicity (ie. $Y_{cno} = Y_C + Y_N + Y_O$), there is no significant nucleosynthesis occurring in the HCZ (apart from H being burnt to He). This is due to the fact that the bulk of the nuclear burning in this region is via the CNO cycles. As the CN cycle is operating in equilibrium the relative abundances remain approximately constant. The $^{12}\text{C}/^{13}\text{C}$ ratio is also ≈ 4 , as can be seen in the surface abundance plot after the DCFDUP (Figure 6.2). This leads us to explore further down the rabbit hole, as the HCZ is not the site of the nucleosynthesis that has given it its chemical distribution. The final panel in Figure 6.4 displays the chemical evolution in the HeCZ – before and after the convection zone split occurs. Here we can see that before the HeCZ first penetrates the H-He discontinuity the chemical mix in this region is characteristic of a standard core He flash. ^{12}C is dominant due to the 3α reactions, but ^{16}O is also being produced via the $^{12}\text{C}(\alpha, \gamma)^{16}\text{O}$ reaction. As the He burning luminosity starts to reach its peak, ^{12}C is produced at a much greater rate. Not long after the He flash peak the HeCZ expands and causes a PIE. Although this is the first proton ingestion episode and thus the material dredged down is relatively proton-poor, the consequent nucleosynthesis causes a striking alteration in the chemical composition of the HeCZ. In particular ^{16}O is increased by *4 orders of magnitude* and ^{14}N by more than *6 orders of magnitude*. Conversely ^{12}C decreases by about an order of magnitude. Furthermore, not long after, many other species are produced in considerable amounts, such as ^{26}Mg , ^{22}Ne and ^{19}F . The huge variations in the CNO abundances is easily understood, such that the addition of protons into the ^{12}C -rich HeCZ causes the CN(O) cycles to operate. ^{12}C acts as an efficient sink for the protons, producing ^{14}N via the usual CN chain $^{12}\text{C}(p, \gamma)^{13}\text{N}(\beta^+)^{13}\text{C}(p, \gamma)^{14}\text{N}$. The oxygen production occurs primarily via the $^{12}\text{C}(p, \gamma)^{13}\text{N}(\beta^+)^{13}\text{C}(\alpha, n)^{16}\text{O}$ chain. This chain of reactions is so prominent because there is a large amount of He in the HeCZ. Usually the aforementioned CN chain dominates, and the CN cycle can complete, mostly producing ^{14}N and resulting in little ^{16}O production (or even ^{16}O depletion). It can also be seen in the last panel of Figure 6.4 that, as expected, the sum of C+N+O nuclei is approximately constant, as the resulting abundances of ^{14}N and ^{16}O sum to the ^{12}C deficit. Thus Z_{cno} is primarily dependent on the amount of ^{12}C produced in the HeCZ by the core He flash. So, even though the structural evolution code (SEV code) does not include the $^{13}\text{C}(\alpha, n)^{16}\text{O}$ reaction (ie. the ^{16}O production

is neglected) we note that Z_{cno} will be (practically) the same in both calculations. In terms of possibly neglecting some important energy production (or reduction) in the SEV code we also note that the energy budget in the HeCZ is easily dominated by the He burning during this first PIE.

Panel 4 of Figure 6.4 also shows that further nucleosynthesis has occurred during the first PIE. We show a few selected species to highlight this: ^{19}F , ^{22}Ne and ^{26}Mg , which are all produced in substantial amounts (considering the star began with $Z = 0$). In Figure 6.5 we show the full nucleosynthesis network used for these calculations, displayed as a nuclide chart. Overlaid on the nuclide chart are arrows indicating the nucleosynthesis occurring in the middle of the HeCZ during the initial stages of the first PIE. Although the bulk of the nucleosynthesis involves the CNO cycles (and He burning) there is much further processing via the NeNa cycle, MgAl chains, and even neutron capture reactions, all the way up to the most massive species included (note that we do not follow the production of the iron group species, which remain at zero abundance). From this figure we can elucidate the nucleosynthesis that leads to the production of the species in Figure 6.4. Indeed it can be seen that the dominant reactions include $^{13}\text{C}(\alpha, n)^{16}\text{O}$ and the CN cycle. The bulk of the ^{19}F is created through proton capture on ^{18}O (although $^{15}\text{N}(\alpha, \gamma)^{19}\text{F}$ is also operating). The ^{18}O required by this reaction is primarily produced via neutron capture on ^{14}N and subsequent α -capture on ^{14}C : $^{14}\text{N}(n, p)^{14}\text{C}(\alpha, \gamma)^{18}\text{O}$. The other main channel to ^{19}F production also involves ^{18}O , via the $^{18}\text{O}(n, \gamma)^{19}\text{O}(p, n)^{19}\text{F}$ reactions. Thus it can be seen that the substantial nucleosynthesis in the proton-polluted HeCZ arises from the combination of proton capture, α capture and neutron capture reactions. The ^{22}Ne also seen in Figure 6.4 arises through two main channels. The first also relies on ^{18}O : $^{18}\text{O}(\alpha, \gamma)^{22}\text{Ne}$. The second is via neutron captures: $^{20}\text{Ne}(n, \gamma)^{21}\text{Ne}(n, \gamma)^{22}\text{Ne}$. We note that there is a substantial abundance of neutrons available for these reactions due to the $^{13}\text{C}(\alpha, n)^{16}\text{O}$ reaction. We shall discuss the potential for s-process nucleosynthesis in the next subsection. The neutrons also lend themselves to ^{26}Mg production via $^{24}\text{Mg}(n, \gamma)^{25}\text{Mg}(n, \gamma)^{26}\text{Mg}$. This isotope of Mg is also produced through successive proton captures (the MgAl chains are operating): $^{23}\text{Na}(p, \gamma)^{24}\text{Mg}(p, \gamma)^{25}\text{Al}(\beta^+)^{25}\text{Mg}(p, \gamma)^{26}\text{Al}(\beta^+)^{26}\text{Mg}$.

It can be seen that a rich nucleosynthesis has occurred in the HeCZ before its splitting, and in particular during the three proton ingestion episodes. This abundance pattern is essentially frozen in the HCZ after the split (see Panel 3 in Figure 6.4). Consequently the surface abundances after the DCF dredge-up (see Figure 6.2) are also due to the nucleosynthesis during this stage.

As the He convective zone recedes the HCZ initially expands and then ‘moves’ outwards (in mass, see Figure 6.3). As both these changes involve mixing in pristine material from above, the dredged-up material is progressively diluted and an interesting abundance profile is left behind. This profile is displayed in Figure 6.6. The profile consists of four parts – the CNO rich zone that was the HeCZ, the region between this and the remaining HCZ, which has a varying abundance profile due to dilution, the HCZ itself, and the still unpolluted convective envelope. Also of interest is that the HCZ, soon to be dredged up, has quite a high He abundance of $X_{\text{He}} \sim 0.46$. In Figure 6.6 we also display the profiles of some other species. Of particular interest is the ^{13}C abundance which is $\sim \frac{1}{4}$ of the ^{12}C abundance, indicating that the CN cycle reached equilibrium during the earlier burn. ^{20}Ne is also displayed. Two of the main paths for its production under these conditions are: $^{16}\text{O}(n, \gamma)^{17}\text{O}(\alpha, p)^{20}\text{Ne}$ and $^{19}\text{F}(n, \gamma)^{20}\text{F}(\beta^-)^{20}\text{Ne}$.

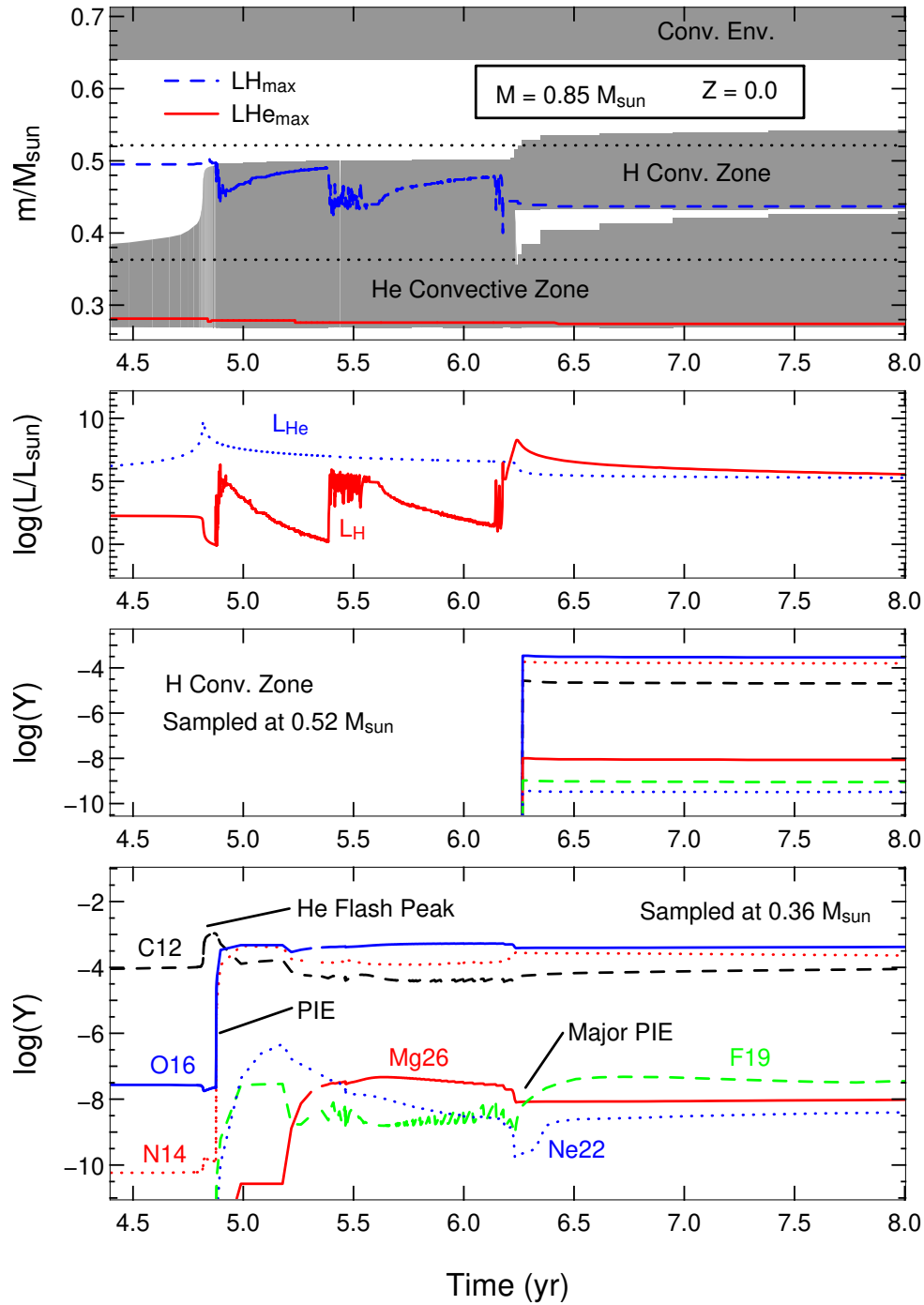


Figure 6.4: Zooming in on the evolution of convection, luminosities and abundances during the DCF. Time has been offset for clarity. In the top panel it can be seen that the convection zone does not split during the first two proton ingestion episodes (PIEs). This is because the amount of H ingested is relatively small, leading to lower H burning energy release. The two dotted lines in the top panel indicate the mass sampling points for the lower two panels which display the abundance evolution in the HCZ and HeCZ. The abundances in the HCZ are a result of the previous nucleosynthesis in the HeCZ before the split occurs – it can be seen that no significant changes are occurring in the abundance pattern in the HCZ after the convection zone splits. In the HeCZ there is a huge production of ^{16}O and ^{14}N during the first PIE which occurs primarily via the $^{12}\text{C}(p, \gamma)^{13}\text{N}(\beta^+)^{13}\text{C}(\alpha, n)^{16}\text{O}$ and $^{12}\text{C}(p, \gamma)^{13}\text{N}(\beta^+)^{13}\text{C}(p, \gamma)^{14}\text{N}$ chains respectively. It is this nucleosynthesis which later gives the envelope its abundance profile (via the post-DCF DUP). Note that the line colours in the third panel are the same as those in the bottom panel.

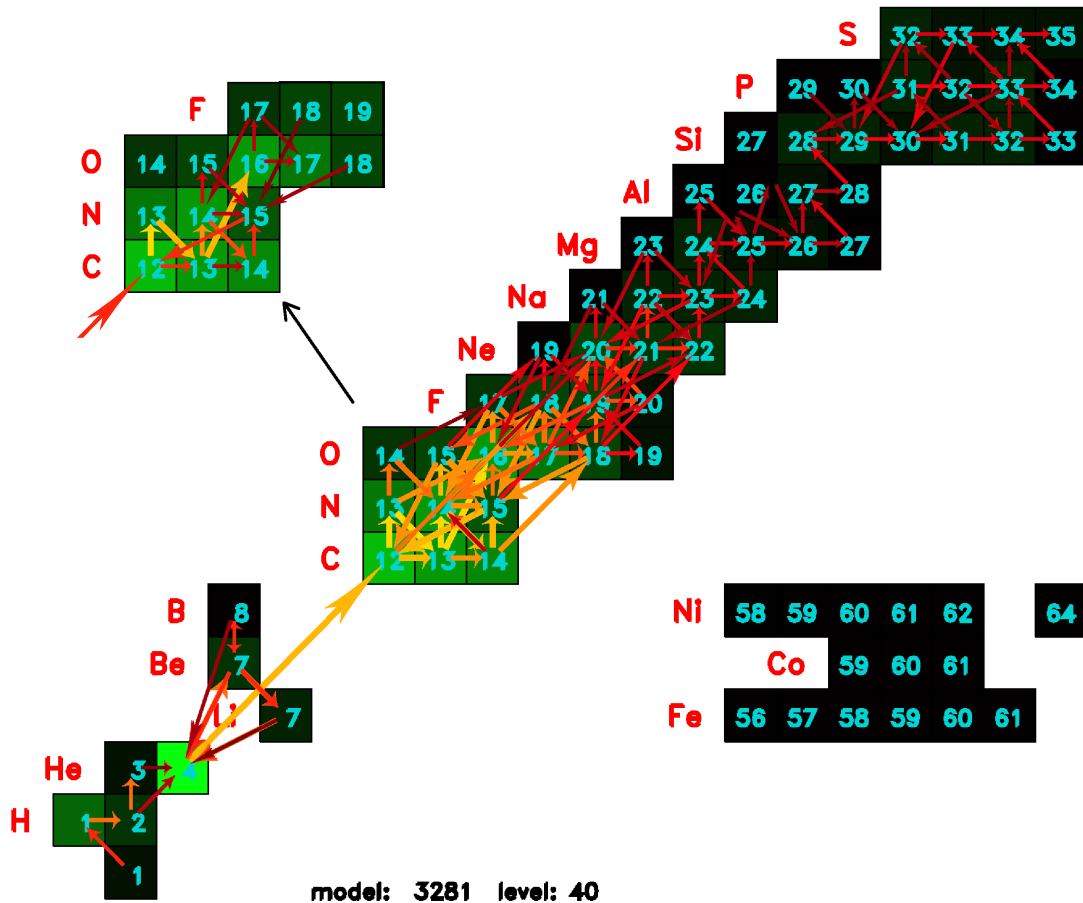


Figure 6.5: The full set of species included in our network. Arrows represent reactions that are occurring at rates greater than a lower cutoff. Yellow \rightarrow red indicates faster \rightarrow slower rates of reactions. Thicker arrows also indicate reactions happening at faster rates. The model plotted is taken during the first PIE and the ‘level’ corresponds to $m = 0.40 M_{\odot}$ which is in the middle of the HeCZ (see Figure 6.4). A second CNO(F) group (top left) is given since there are too many arrows in the main diagram to identify the reactions (due to the use of a low rate cut-off in order to display the reactions occurring amongst the heavier nuclides). It can be seen that the dominant reactions in this region are the 3α , $^{13}\text{C}(\alpha, n)^{16}\text{O}$, and also proton captures on the carbon nuclei. Neutron capture reactions can also be seen (most easily in the heavier elements), giving rise to heavy isotopes. Note that the Fe group species displayed (Ni, Fe, Co) remain at zero abundance as we did not include the species between these and ^{35}S .

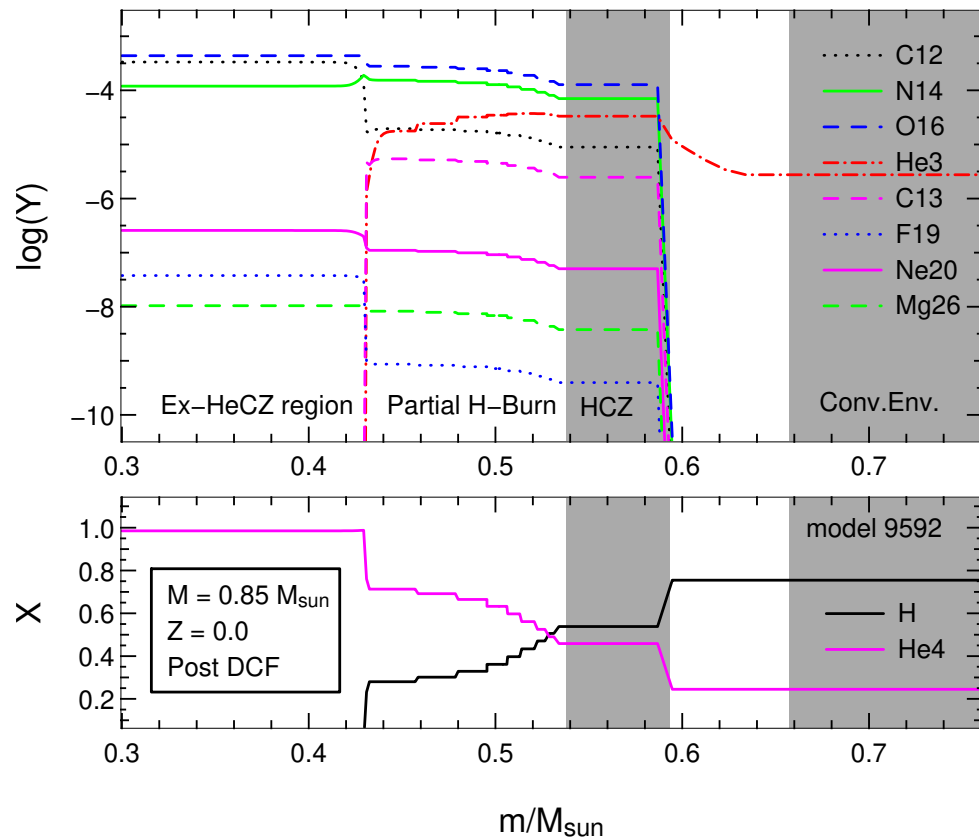


Figure 6.6: The abundance profiles after the HeCZ has subsided, just before the post-DCF dredge-up. This gives an indication of the chemical profile that the envelope will soon have. Of particular interest is the high He abundance in the HCZ, $X_{\text{He}} \sim 0.46$. A number of different regions are identified (see text for details).

Figure 6.7 shows the evolution of the convection zones, luminosities and temperature over an extended time period. It also shows the evolution of the abundances at a mass location that initially samples the HCZ but also the convective envelope at later times. The timespan takes in the DCF and post-DCF dredge-up (DCFDUP) so that the pollution of the convective envelope is evident. It can be seen that the bulk changes in composition in this region after the convection zone splits are due to dilution events rather than nucleosynthesis. After DCFDUP the star retains this chemical abundance pattern for the rest of its evolution – apart from some production of ${}^7\text{Li}$ and ${}^3\text{He}$ during the AGB, which is discussed further below.

6.2.3 Is the DCF a New s-Process Site?

In the previous subsection we discussed the nucleosynthesis occurring during the dual core flash (DCF) and in particular during the first (minor) proton ingestion episode (PIE). It was noted that one of the most active reactions at this time is ${}^{13}\text{C}(\alpha, n){}^{16}\text{O}$. This is evident in Figures 6.4 and 6.5. An enormous amount of ${}^{16}\text{O}$ is produced in a very short time, primarily at the expense of the already abundant ${}^{12}\text{C}$ (via ${}^{12}\text{C}(p, \gamma){}^{13}\text{N}(\beta^+){}^{13}\text{C}$) which itself is being produced by the core He flash 3α reactions. With such an active ${}^{13}\text{C}(\alpha, n){}^{16}\text{O}$ reaction there is a significant amount of neutrons being produced. Thus there is the potential for s-process nucleosynthesis in the proton-polluted HeCZ.

In Figure 6.8 we show the abundance profiles of two models taken during the first PIE. From these plots we can see that the HeCZ is initially dominated by ${}^{12}\text{C}$ (apart from H and He). A well known neutron sink is ${}^{14}\text{N}$. If it is present in large amounts then the ${}^{14}\text{N}(n, p){}^{14}\text{C}$ reaction will dominate over other neutron capture reactions, essentially muting the s-process. In the present case however ${}^{14}\text{N}$ is initially present only at the level of $\log(Y) \sim -10$, as compared to the ${}^{12}\text{C}$ abundance of ~ -3 . Thus other neutron capture reactions are expected to proceed. Indeed we see this in Figure 6.5 where, for example, S and P are undergoing neutron captures to produce the heavier isotopes of these elements. Unfortunately our network did not include the further reactions (or species) that lead to the production of the iron group and beyond. We note that Ni, Co and Fe are included in the network but that they remain at zero abundance because only reactions *within* this group were included. Thus we were unable to follow any s-processing that may have occurred.

Since these proton ingestion episodes are a common feature of $Z = 0$ and extremely metal-poor low-mass models, this evolutionary phase may be an important source of s-process nuclei in the early Universe. As far as we are aware this phase has not been explored as a possible s-process site before (whereas the AGB dual shell flash has; see eg. Goriely and Siess 2004). We shall definitely pursue this very interesting possibility in a future study, when we have extended the nuclear network of the NS code.

6.2.4 TP-AGB

As can be seen in Figure 6.2 the AGB has little effect on most of the species present in the envelope. This is because the third dredge-up does not operate in this model, and because the temperature at the bottom of the convective envelope is too low for any significant hot bottom

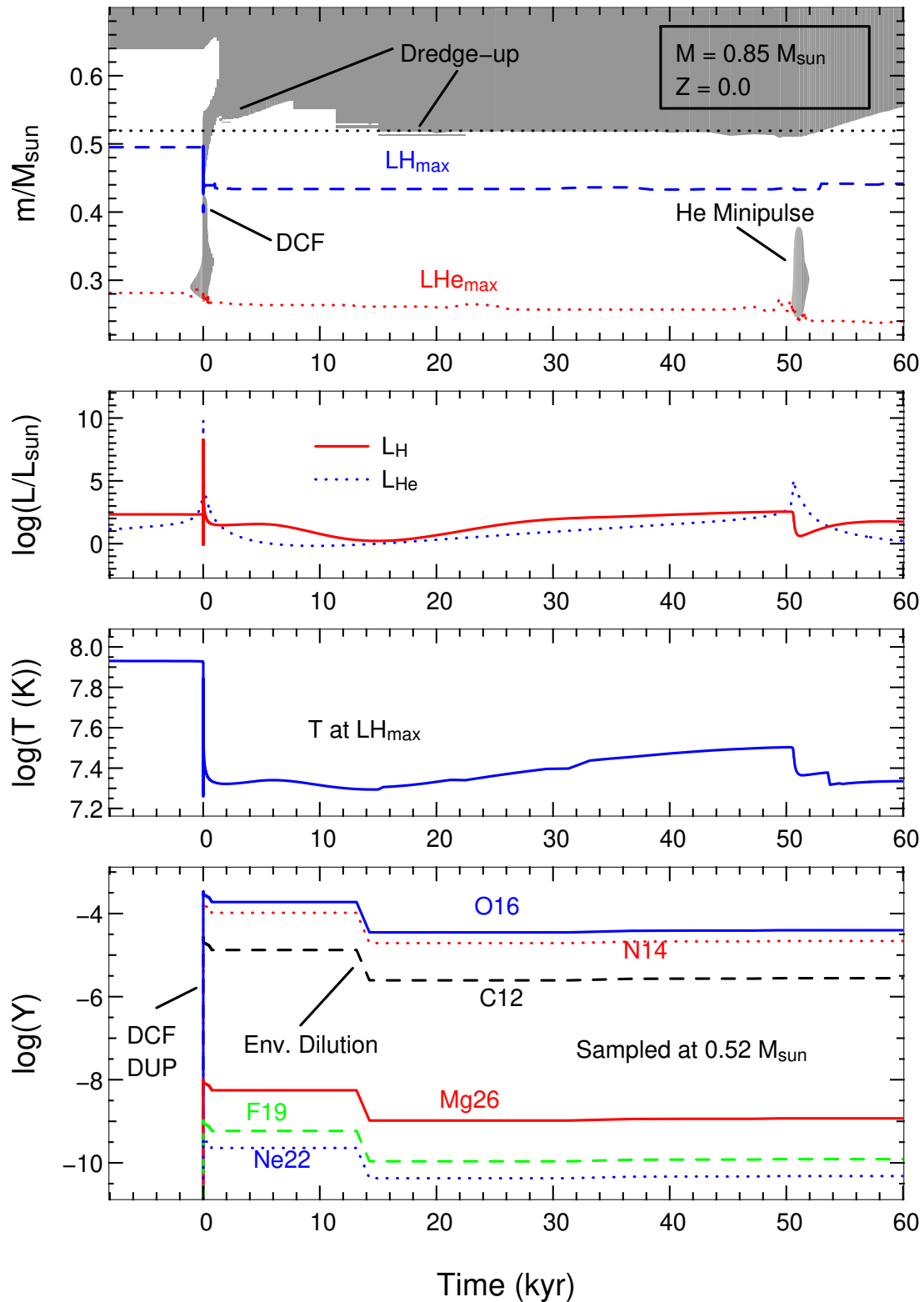


Figure 6.7: A broad view of the evolution around the DCF. The post-DCF dredge-up can be seen in the top panel. The dotted line at $m = 0.52 M_{\odot}$ in this panel indicates the sampling point for the abundance evolution in the bottom panel. It takes in the HeCZ during the DCF as well as the envelope during the DCF DUP. The dilution of the processed material throughout the envelope is evident.

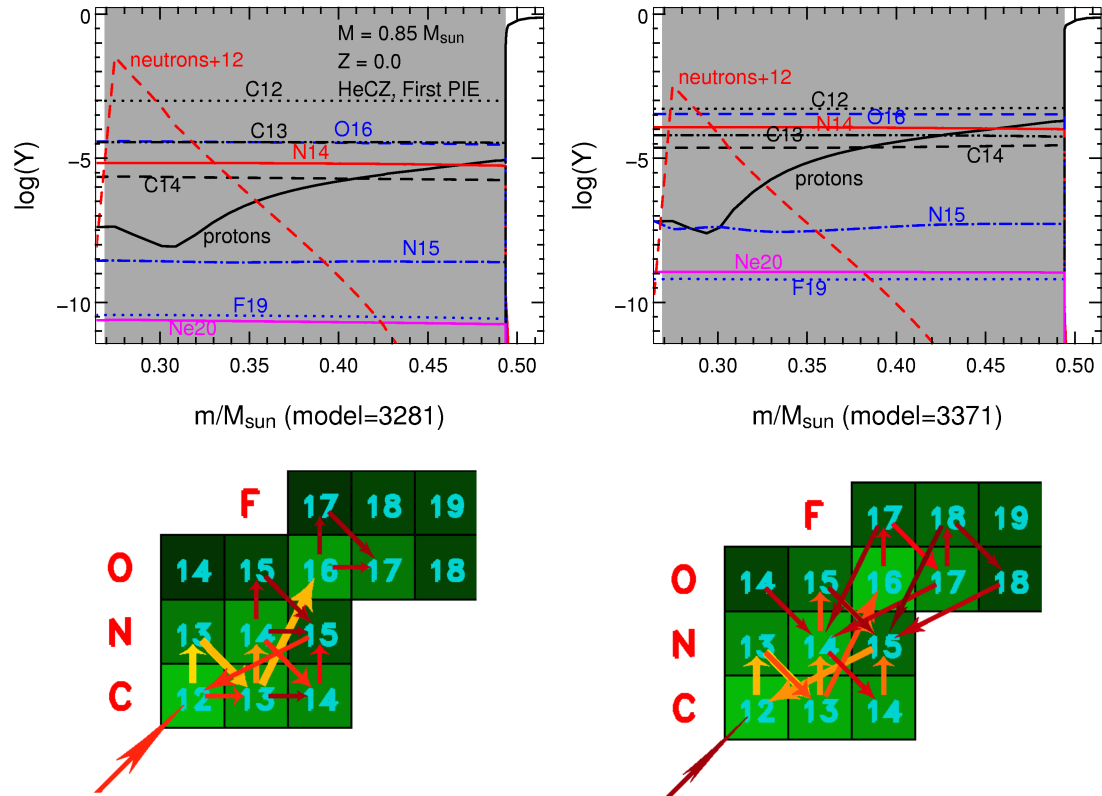


Figure 6.8: Investigating the potential for s-process nucleosynthesis during the first DCF proton ingestion episode. Two models are displayed. The first is taken at a time when the neutron abundance is near its peak and the second when the proton abundance is near its peak (they are separated in time by ~ 0.02 years). Grey shading represents convection. Below each abundance plot are corresponding rate plots (see Figure 6.5 for an explanation of this type of plot) which both sample the reactions occurring at $m = 0.28 M_{\odot}$, near the bottom of the HeCZ. The large arrow at the bottom left of each arrow plot represents the 3α reaction. Comparing the two models it can be seen that ^{16}O is produced prodigiously, increasing by ~ 1 dex, primarily via $^{13}\text{C}(\alpha, n)^{16}\text{O}$. ^{20}Ne increases by ~ 1.5 dex, mainly via a reaction that also releases neutrons: $^{17}\text{O}(\alpha, n)^{20}\text{Ne}$. The resulting neutron abundance has been offset by +12 dex. This shows that the main neutron production is towards the bottom of the HeCZ. The carbon isotopes are initially much more abundant than ^{14}N , lending themselves to strong neutron production. However ^{14}N also increases by about 1 dex over this timespan due to proton capture reactions. It then starts to become important as a neutron sink (via $^{14}\text{N}(n, p)^{14}\text{C}$), dampening the (possible) s-process nucleosynthesis. This reaction also releases protons, causing the inversion in this abundance profile at the bottom of the HeCZ.

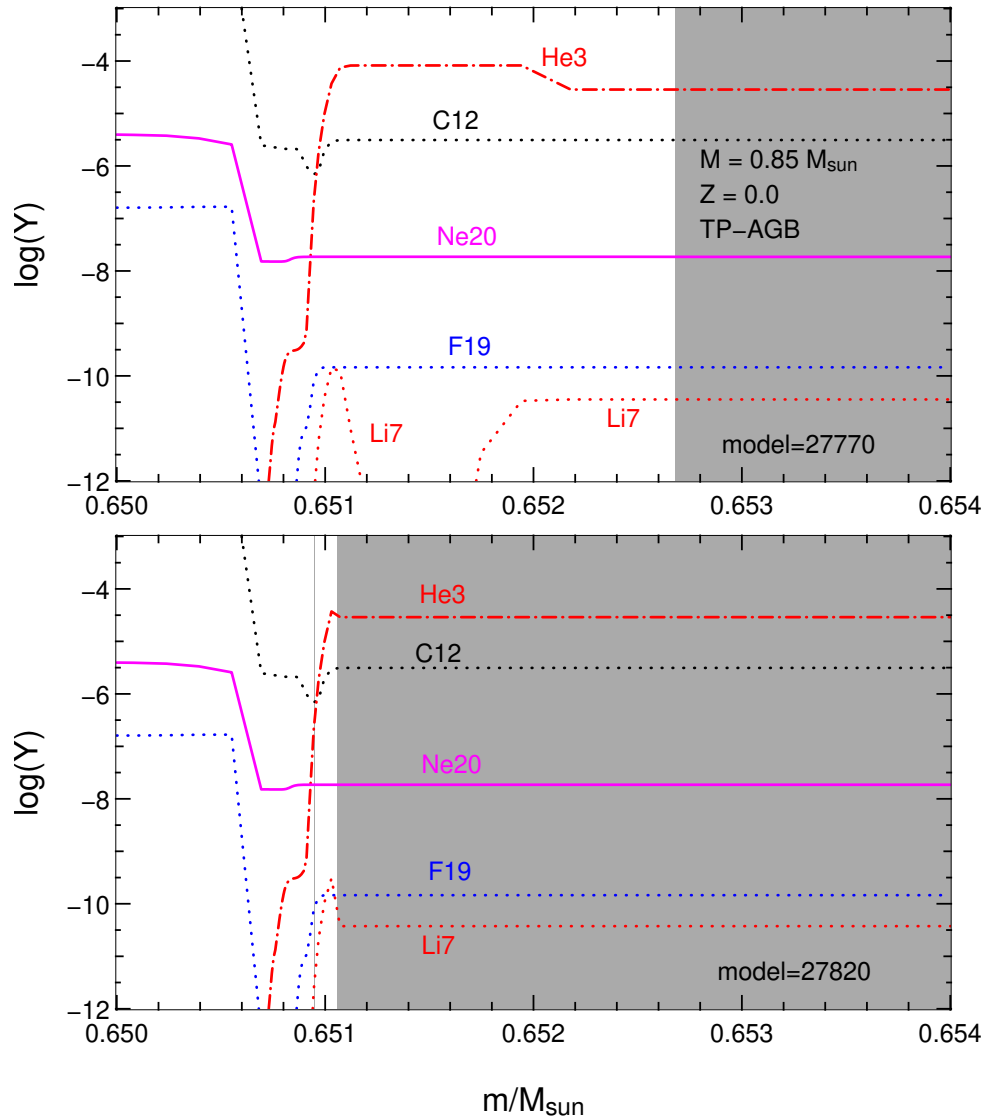


Figure 6.9: The composition profiles of two models during the AGB. The first (top) shows the abundance profiles during the interpulse period. The second (bottom) shows them just after the thermal pulse when the envelope becomes more deeply convective. This convection mixes up some material enhanced in ${}^7\text{Li}$ and ${}^3\text{He}$, which, after many pulses, gives rise to surface enrichment at the end of the AGB of ~ 0.7 and ~ 1.0 dex respectively (over the initial abundances).

burning. The only species affected are ${}^7\text{Li}$ and ${}^3\text{He}$. We display the abundance profiles of these species in Figure 6.9 where it can be seen that both are produced just above the H shell (during the interpulse period) and subsequently mixed upwards when the envelope convection moves inwards each TP cycle. By the end of the AGB ${}^7\text{Li}$ is enhanced over the initial abundance by ~ 0.7 dex and ${}^3\text{He}$ by ~ 1.0 dex.

6.2.5 Chemical Yield

The integrated output of material via stellar winds over the lifetime of this model (the chemical yield), is plotted in Figure 6.10. In total $0.074 M_{\odot}$ of material was lost via winds, leaving a WD remnant of $0.776 M_{\odot}$.

In terms of metals ${}^{16}\text{O}$ is the dominant species ejected into the ISM, with ${}^{14}\text{N}$ not far behind.

^{12}C was output at a level ~ 1 dex lower. The $^{12}\text{C}/^{13}\text{C}$ ratio is low, being ~ 3.6 , whilst ^4He is significantly enhanced, up from the primordial value of $X_{\text{He}4} = 0.245$ to 0.30. ^7Li is marginally enhanced, with an increase of ~ 0.2 dex. This is despite a large increase in Li on the AGB of ~ 0.7 dex. The reason for this difference is twofold. Firstly the ^7Li is periodically enhanced on the AGB, such that the surface abundance only reaches its peak towards the end of the AGB. As mass loss is occurring throughout the AGB the earlier winds do not have such a high Li abundance. Secondly, as seen in the structural evolution section some mass loss occurs on the RGB – when the surface of the star still has zero metallicity. Thus some of the mass lost to the ISM has a zero Li abundance, diluting the overall yield of Li. The RGB mass loss has a small but noticeable effect on the yields of all species, such that all are slightly lower than their values on the AGB (see Figure 6.2 for a comparison). The mass lost on the RGB represents $\sim 20\%$ of the mass loss via winds, whilst the other $\sim 80\%$ was lost on the AGB.

In order to place the present yield in perspective we provide a second figure (Figure 6.11) that presents the yield in relation to the Solar composition. We have used the Solar abundances from Lodders (2003). It can be seen that none of the metals are present in the ejecta at super-solar abundances. Nitrogen comes the closest, being only ~ 0.4 dex lower than the solar $[\text{N}/\text{H}]$ value. Interestingly oxygen is the second most abundant metal in relative terms, even though in absolute terms it was the most abundant. Lithium is only marginally up from the primordial value, despite its large increase on the AGB. All the other elements are $\lesssim -2$ dex lower than solar. We note that the Fe group elements are not displayed as they all remain at zero abundance due to the limitations of the network used, as mentioned in the previous subsection.

We shall discuss and compare this yield with observations in Section 7.6, after we have presented the yields for the extremely metal-poor models.

6.3 Detailed Nucleosynthesis at $M = 2.0 M_{\odot}$

In this section we detail the key nucleosynthetic events that occur during the evolution of the $Z = 0$, $2.0 M_{\odot}$ model. In particular we describe and quantify the events that lead to surface pollution and hence affect the chemical yield of the star.

Prior to the TP-AGB the only surface pollution event that this model experiences is that of second dredge-up (2DUP). The main effect of this is to mix up considerable amounts of helium, raising the He abundance from the primordial $Y = 0.245$ to $Y \sim 0.31$.

This model experiences three dual shell flashes (DSFs) at the start of the TP-AGB. These significantly pollute the envelope, raising the Z_{cno} metallicity from zero to $\sim 10^{-4}$. The DSF events are similar to the DCF event found in the $0.85 M_{\odot}$ model described in the previous section. In this case it is the AGB He flash convection zone that breaches the H-He discontinuity, dredging down protons and dredging up CNO nuclei. Convection zone splitting also occurs, due to the induced H-flash. The subsequent dredge-up by the convective envelope transports this processed material to the surface.

Unlike the $0.85 M_{\odot}$ model this model does experience third dredge-up (3DUP) that periodically increases Z_{cno} . Although the magnitude of 3DUP is quite small ($\lambda \sim 0.01$) there are so many

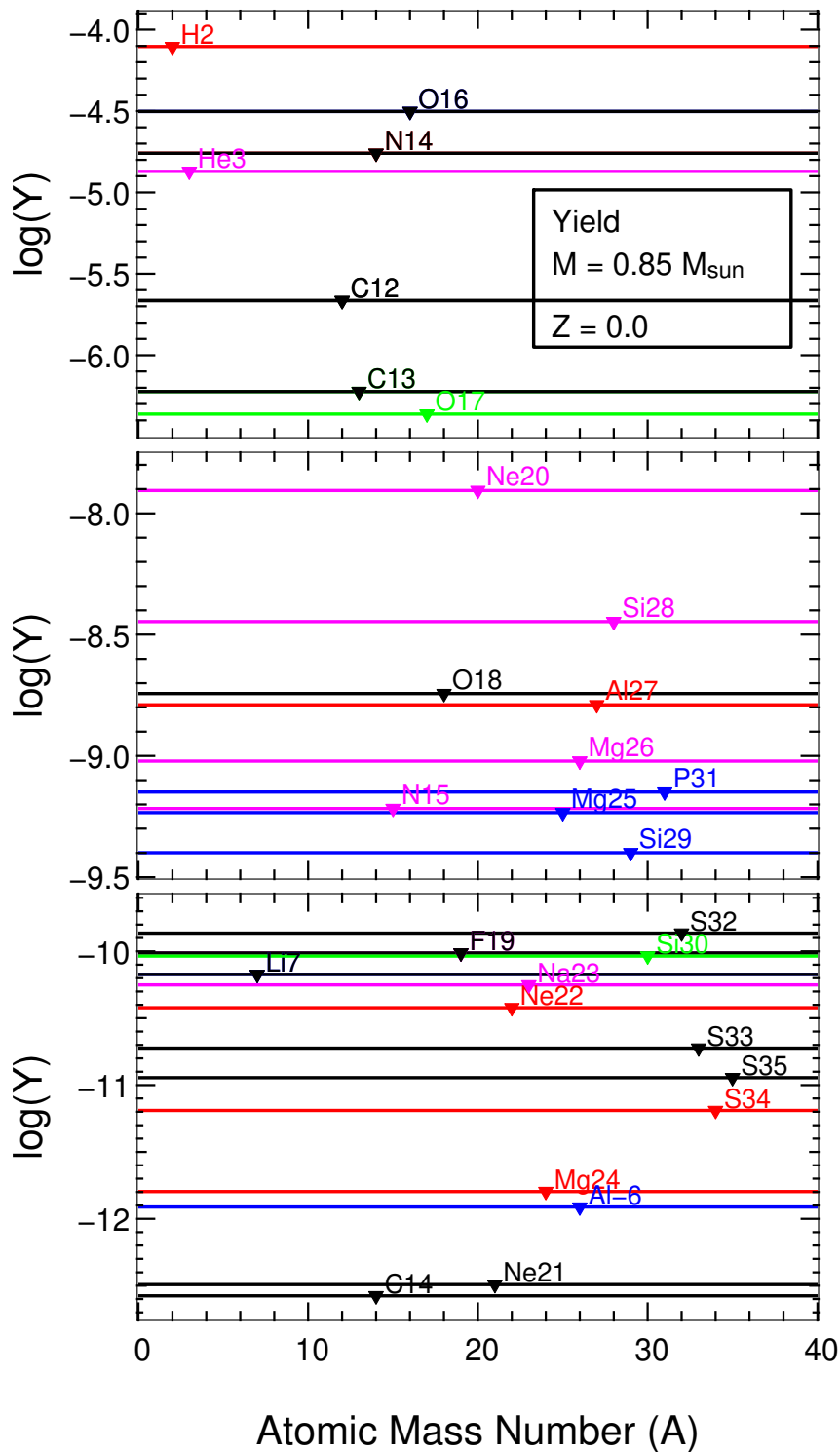


Figure 6.10: The chemical yield for the $0.85 M_{\odot}$, $Z = 0$ model. All isotopes included in the network (74 species) with an abundance greater than 10^{-13} are plotted.

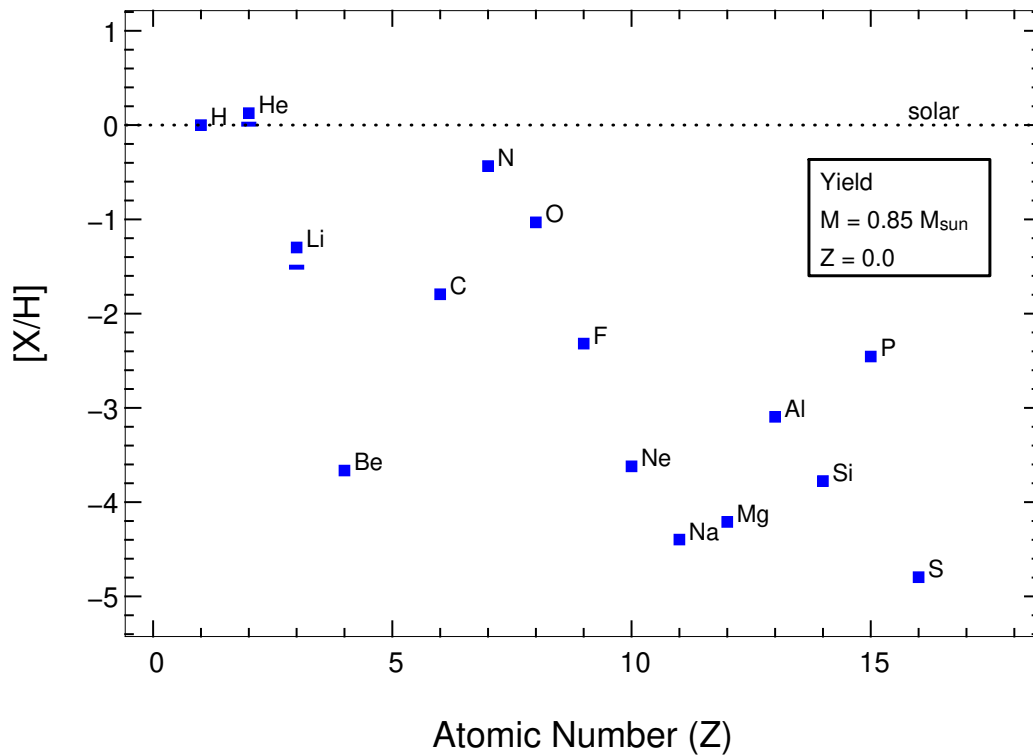


Figure 6.11: The yield for all the elements included in the network (that have abundances $[X/H] > -5$), relative to solar, for the $0.85 M_{\odot}$ model. Solar abundances are from [Lodders \(2003\)](#). Small horizontal lines indicate the initial abundance for H, He and Li (all others were zero initially). Despite oxygen being the most abundant metallic species in absolute terms (see previous figure) it is second to nitrogen when taken relative to solar. We note that Li is only marginally enhanced over the primordial abundance even though it reached relatively high abundances on the AGB (see text for a discussion).

pulses that Z_{cno} increases by an order of magnitude by the end of the AGB. This results in a chemical yield characterised by $Z_{cno} \sim 0.004$. Thus, in terms of surface pollution, 3DUP has a greater effect than the prior DSFs. We note however that the occurrence of 3DUP itself may be dependent on the occurrence of the envelope pollution arising from the DSFs, due to the increase in envelope opacity that this causes.

Also unlike the $0.85 M_{\odot}$ model this model experiences strong hot bottom burning (HBB). This envelope burning couples with the periodic dredge-up of ^{12}C , ^{16}O and ^{22}Ne (for example), and the residual pollution from the DSF episodes, to provide a rich nucleosynthetic yield.

6.3.1 Second Dredge-Up

This model does not reach an RGB configuration so first dredge-up does not occur (see structural evolution discussion in Section 5.3 on page 139). However second dredge-up (2DUP) does occur, although with limited consequences when compared to metal-rich models. The maximum incursion of the convective envelope on the EAGB is marked in Figure 6.12. Convection only reaches down into regions that have been (partially) burnt via the p-p chains, as the material here still has $Z = 0$. Nonetheless, due to the low temperature dependence of the p-p chains there has been significant production of ^4He quite far out (in mass) from the H-exhausted core. In fact much of the star has undergone some H burning (out to at least $m \sim 1.5 M_{\odot}$). Figure 6.12 also shows the abundance profiles of selected species. It can be seen that ^7Li is depleted in the interior regions above the core and that ^3He is enriched (apart from a drop-off just below the point of maximum envelope incursion). Thus, when the envelope moves inwards it is substantially polluted with ^4He and ^3He and depleted in ^7Li .

We show the time evolution of these envelope abundances in Figure 6.13. It can be seen that the ^4He abundance rises by a large amount, from the primordial value of $Y = 0.245$ to $Y \sim 0.31$. We note that this 2DUP event has the largest effect on the yield of ^4He , as the increase on the TP-AGB is less than this. It can also be seen that ^3He increases by ~ 1 dex and ^7Li decreases by ~ 0.8 dex. In terms of the chemical yield from this star this is inconsequential as both these species are almost totally destroyed by HBB on the TP-AGB.

6.3.2 Dual Shell Flashes/CNO-PIEs

A key characteristic of $Z = 0$ intermediate mass models is the occurrence of one or more dual shell flashes (DSFs) at the start of the TP-AGB. We suggest that these events may be pivotal for the further evolution of the star because they lead to pollution of the convective envelope. This pollution causes an increase in opacity consequently making third dredge-up more likely to occur. If 3DUP does occur, as it does in this model, it has a profound impact on the chemical yield of the star.

We find three DSFs to occur in this model. Each event consists of the He intershell convection zone (associated with a thermal pulse) penetrating the H-He discontinuity. This occurs near the start of the TP-AGB, when the He flash luminosity first starts to exceed $\sim 10^5 L_{\odot}$. We refer to these three DSFs as DSF1, DSF2 and DSF3. The three events are seen in context in Figure

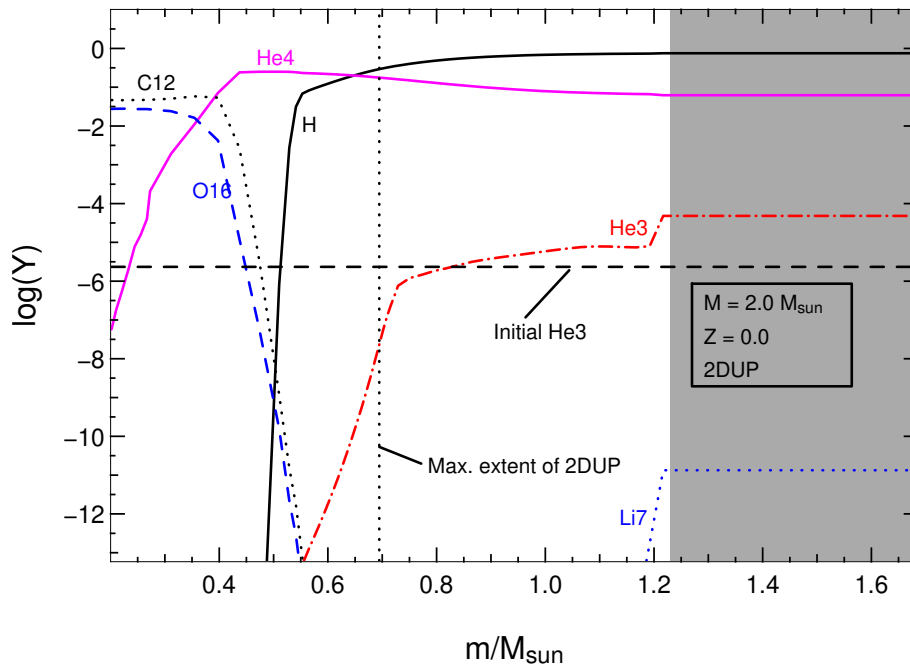


Figure 6.12: The chemical profiles of selected species in a model during second dredge-up. The deepest incursion of the convective envelope is marked by a vertical dotted line (convection is denoted by grey shading). It can be seen that ${}^4\text{He}$ will be enriched in the envelope, due to previous $Z = 0$ p-p chain burning in these regions. ${}^3\text{He}$ will also be enriched, and then slightly depleted (the original abundance is marked by the horizontal dashed line), whilst ${}^7\text{Li}$ will be depleted.

6.14. They are easily identified by the peaks in H burning luminosity occurring at the same time as the peaks of the He shell flash luminosities. Associated with each DSF is a dredge-up event, which we refer to as post-DSF dredge-up (DSFDUP). This brings up the material processed in the H convection zone (HCZ) that forms above the HeCZ during the DSF. The envelope pollution resulting from these DSFDUPs can be seen in panel 3 of Figure 6.14. The first DSF does not result in a significant pollution of the envelope ($Z_{cno} \sim 10^{-11}$) so we shall concentrate on the details of DSFs 2 and 3. DSF2 does result in substantial pollution, raising the envelope metal abundance to $Z_{cno} \sim 10^{-5}$, primarily in the form of oxygen and nitrogen. At the next thermal pulse DSF3 raises the metallicity even further, so that the envelope has a metallicity of $Z_{cno} \sim 10^{-4}$ after all the DSF episodes have completed. Interestingly the post-DSF3 DUP results in an envelope composition dominated by ${}^{16}\text{O}$ and ${}^{12}\text{C}$, where DSF2 brought up more ${}^{14}\text{N}$.

We now explore the details of the DSF episodes to ascertain what gives rise to the composition of the polluting material from each DSF.

DSF2

Figure 6.15 shows the evolution of various characteristics of dual shell flash 2. An important nucleosynthetic event occurs at the beginning of the DSF – an addition of protons into the HeCZ leads to rapid CN cycling, producing ${}^{14}\text{N}$ in an amount comparable to the abundance of ${}^{12}\text{C}$. However, before the ${}^{14}\text{N}$ abundance rises to high levels a large production of ${}^{16}\text{O}$ occurs. This happens through the activation of the ${}^{13}\text{C}(\alpha, n){}^{16}\text{O}$ reaction. Neutrons from this reaction and the ${}^{17}\text{O}(\alpha, n){}^{20}\text{Ne}$ reaction are captured by ${}^{12}\text{C}$ to produce ${}^{13}\text{C}$ (${}^{13}\text{C}$ is also produced by proton captures: ${}^{12}\text{C}(p, \gamma){}^{13}\text{N}(\beta^+){}^{13}\text{C}$ but the neutron capture channel is dominant). Thus there is a

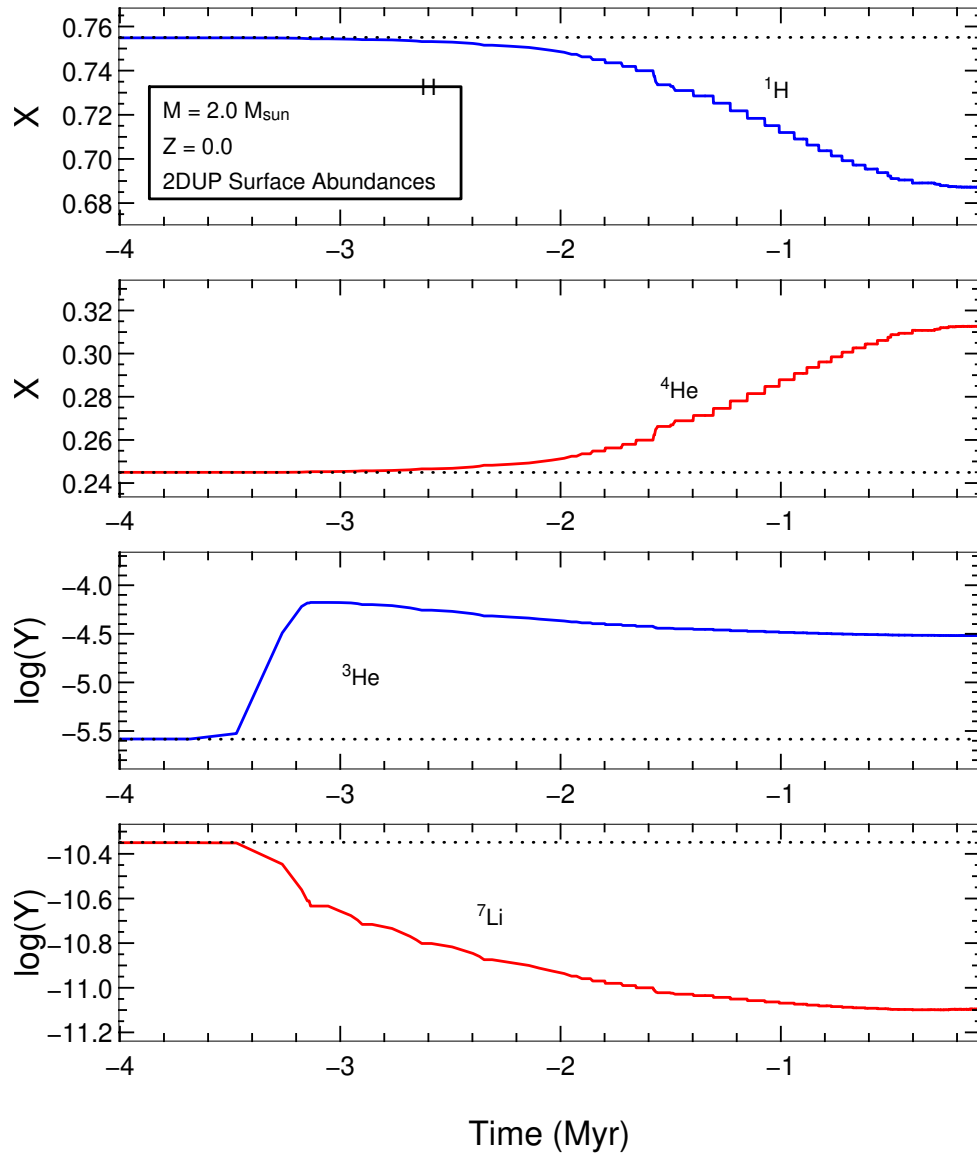


Figure 6.13: The time evolution of the surface abundances during the 2DUP event. Time has been offset for clarity. Horizontal dotted lines mark the initial abundance of each species. The main result from this event is that ^4He increases substantially, from the primordial value of $Y = 0.245$ to ~ 0.31 .

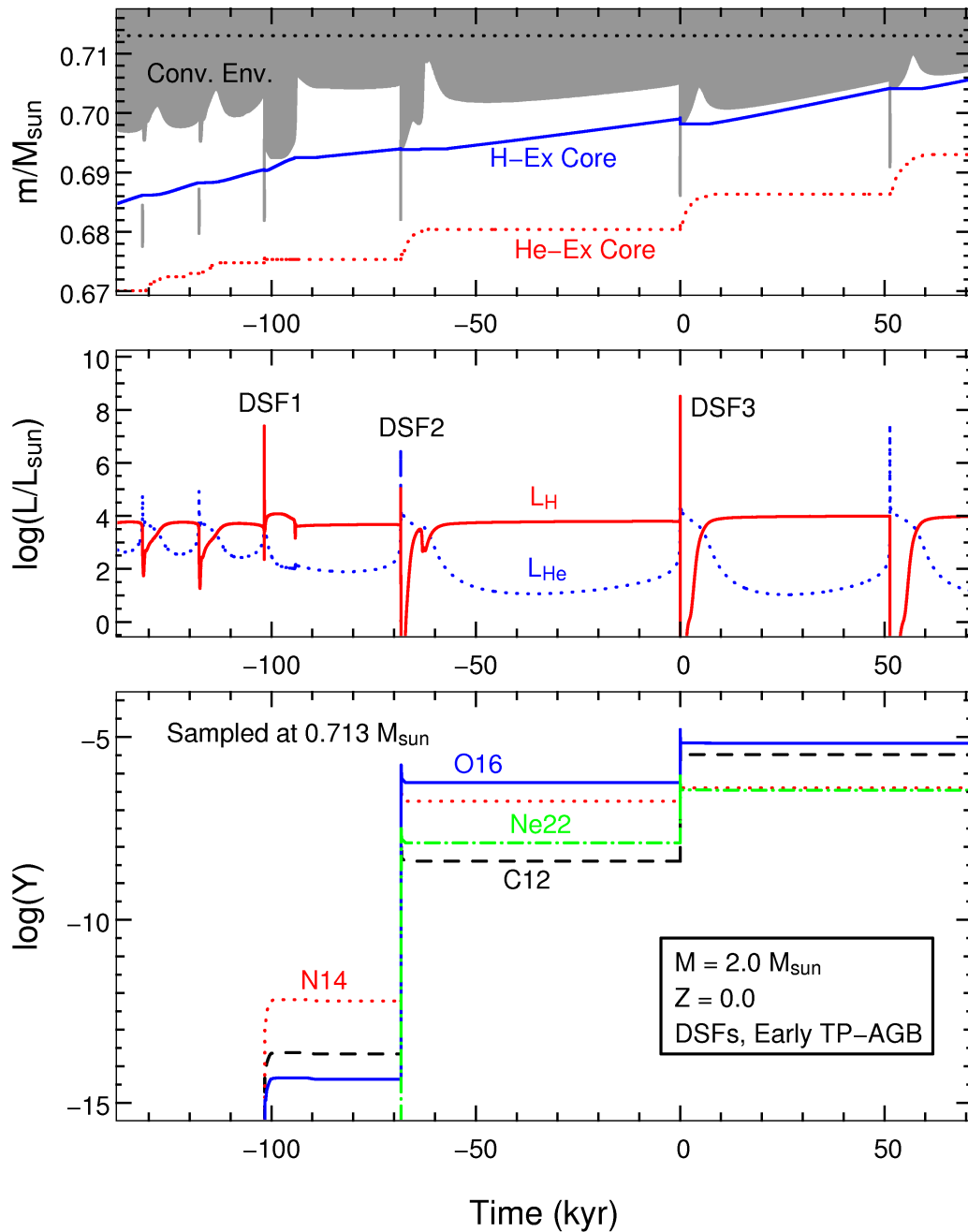


Figure 6.14: An overview of the three dual shell flashes and the resultant pollution of the envelope. Time has been offset so zero corresponds to DSF3. The DSFs are clearly marked by the peak in H luminosities which occur at the same time as the peaks of the He shell flashes. The H flashes only start to occur as the TP-AGB He flash luminosity rises above $\sim 10^5 L_{\odot}$. In the bottom panel the envelope pollution that arises due to post-DSF dredge-up of the erstwhile HCZ is shown. The dotted line in the top panel indicates the sample point for composition. DSF1 has little effect on the envelope composition whilst DSF2 raises Z_{env} to $\sim 10^{-5}$ and DSF3 to $\sim 10^{-4}$. It can also be seen that DSF2 gives rise to a ^{14}N -rich pollution whilst DSF3 does not. Interestingly both give rise to pollution in which ^{16}O is the dominant metal component.

recycling of neutrons that converts ^{12}C to ^{16}O : a C \rightarrow O channel is set up. In addition to this the $^{12}\text{C}(\alpha, \gamma)^{16}\text{O}$ reaction is still very active, so there are now two strong channels to ^{16}O production (see the rates plot for the bottom of the HeCZ in Figure 6.16). The resultant high abundance from this nucleosynthesis is important in one sense as this material is dredged up after the DSF to pollute the envelope and ^{16}O remains the dominant species in the AGB envelope until 3DUP of ^{12}C eclipses it. However, in terms of the chemical yield of this model it is relatively unimportant because most of the mass loss occurs during the HBB phase of the AGB. During HBB the ^{16}O is largely destroyed via ON cycling and other CNO nuclei become dominant.

Despite strong CN(O) cycling during the main H-flash (at $t \sim 0.25$ yr in Figure 6.15, panel 3) ^{16}O remains the dominant species in the HeCZ as there is not enough time for the ON cycle to reach equilibrium. We note that the ^{14}N from this CN burning is later converted to neon by the continuing He shell flash via $^{14}\text{N}(\alpha, \gamma)^{18}\text{F}(\beta^+ \nu)^{18}\text{O}(\alpha, \gamma)^{22}\text{Ne}$, which is the usual fate of ^{14}N in He shell flashes. However in terms of envelope pollution it is the composition of the material dredged up into the H-rich layers just above the HeCZ that is of most interest. At the time of the PIE (and indeed, because of the PIE) the abundance of ^{14}N is still quite high in the HeCZ, and the composition of the newly formed HCZ consequently reflects this. The HeCZ also has a substantial amount of ^{28}Si which is also dredged up into the HCZ. This indicates that advanced proton capture nucleosynthesis has occurred in the HeCZ. This is also evident in Figure 6.17 where we show the dominant reactions occurring in the middle of the HeCZ.

It is important to note here that, from the perspective of the H-rich layers, the PIE may also be seen as a CNO ingestion episode (or ‘CNO-PIE’), as CNO nuclei are dredged upwards at the same time as protons are mixed downwards. The addition of CNO nuclei into the H-rich layers instantly causes an H-flash that peaks at $\sim 10^5 L_{\odot}$. During the H-flash the HeCZ (temporarily) recedes. Interestingly, the burning shell *moves outwards in mass* (like a flame front) and creates a convection zone that mixes CNO nuclei further out and also mixes in fresh H fuel. This behaviour is most likely caused by the fact that the material just above the H-He discontinuity is still extremely metal-poor, such that the H shell was mainly burning via the p-p chains. The introduction of significant amounts of CNO material initiates a runaway ‘CNO flash’ as the burning switches from p-p chains to CNO cycling. After the CNO flash recedes the HeCZ reestablishes itself below.

Some of the nucleosynthesis that occurs in the HCZ is evident in panel 4 of Figure 6.15. The material dredged up from the HeCZ during the CNO-PIE is first diluted throughout the HCZ, reducing the local metallicity by ~ 1 dex (as compared to that of the HeCZ). Taking this into account it can be seen that the abundance of ^{14}N is enhanced by about 1 dex over the HeCZ value, whilst ^{12}C is depleted by ~ 1 dex. This indicates that strong CN cycling has occurred and further contributes to making the HCZ relatively ^{14}N -rich. Further proton-capture reactions occur throughout the lifetime of the HCZ, as indicated by the gradual destruction of ^{22}Ne seen in Figure 6.15, which occurs via the Ne-Na chains. Finally we note that the mass involved in this DSF is quite small (as compared to that of the next DSF), with the HCZ containing $\sim 10^{-4} M_{\odot}$ and the mass exchange between the two convective zones only amounting to only $\sim 10^{-5} M_{\odot}$, as evidenced by the size of the HCZ during the CNO-PIE (see top panel in Figure 6.15).

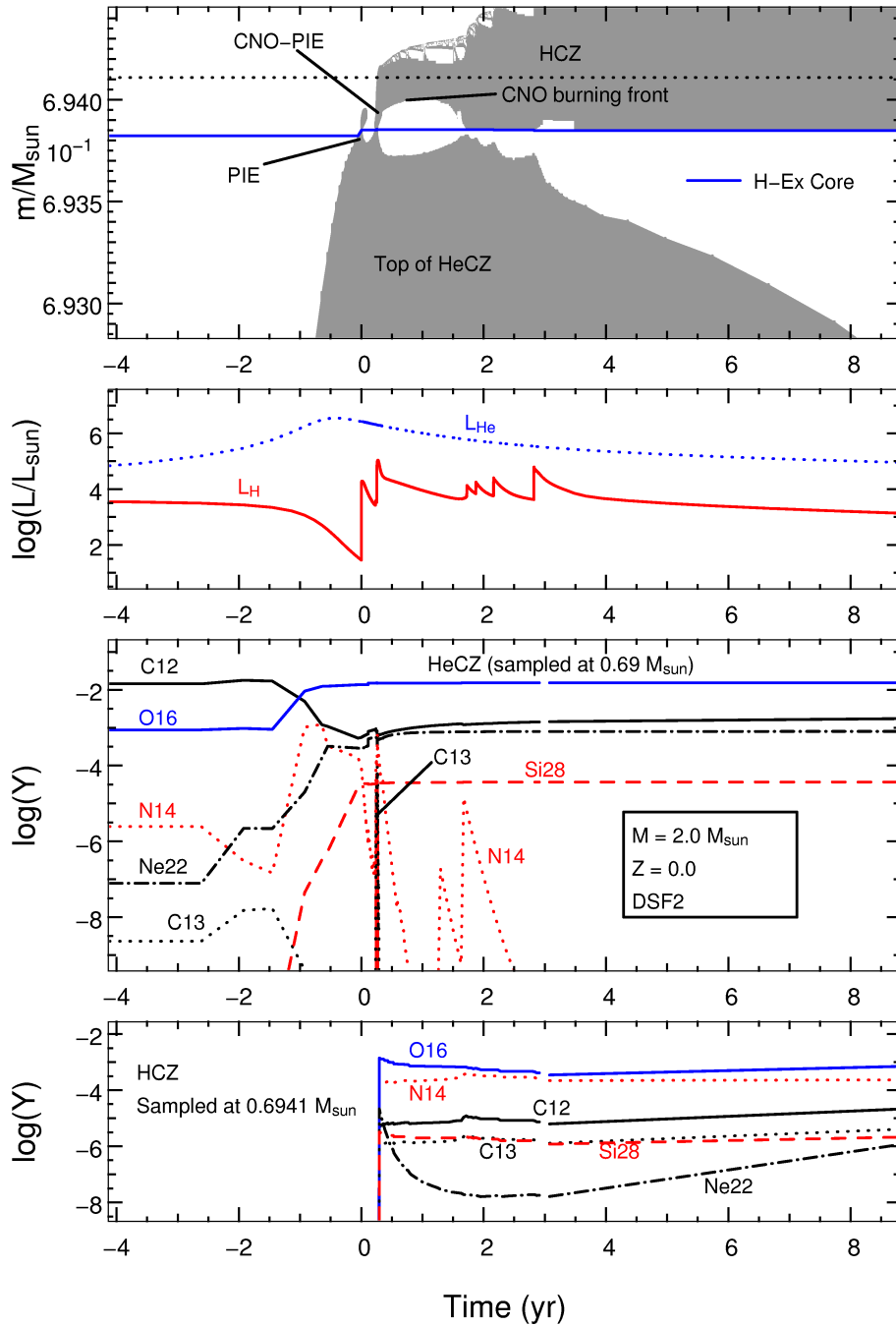


Figure 6.15: Zooming in on the evolution of DSF2. Time has been offset. The CNO H-flash is instigated by the mixing up of CNO nuclei during the ‘CNO-PIE’ (CNO proton ingestion episode). The composition of the HeCZ is shown in panel 3 and that of the HCZ in panel 4. The horizontal dotted line in the top panel indicates the sampling point for the HCZ composition. The HeCZ is sampled below the mass range of the plot, towards the bottom of the convective zone where it is more actively burning. It can be seen that, at the time of the CNO-PIE, the HeCZ is (comparatively) ^{14}N -rich. The presence of ^{28}Si indicates that advanced proton capture nucleosynthesis has occurred in the HeCZ. Some of this material is mixed up into the newly formed HCZ. As the HCZ expands the polluting material is diluted and also undergoes strong CN cycling, so that the resultant chemical profile has ^{14}N more abundant than ^{12}C . The $^{12}\text{C}/^{13}\text{C}$ is also low, being ~ 5 . The dominance of ^{16}O is the result of the $^{13}\text{C}(\alpha, n)^{16}\text{O}$ reaction. This nucleosynthesis of ^{16}O has a lasting effect as ^{16}O remains the dominant species in the AGB envelope until 3DUP of ^{12}C eclipses it (see text for details). In the bottom panel proton capture nucleosynthesis can be seen occurring in the HCZ. In particular ^{22}Ne is first destroyed then produced.

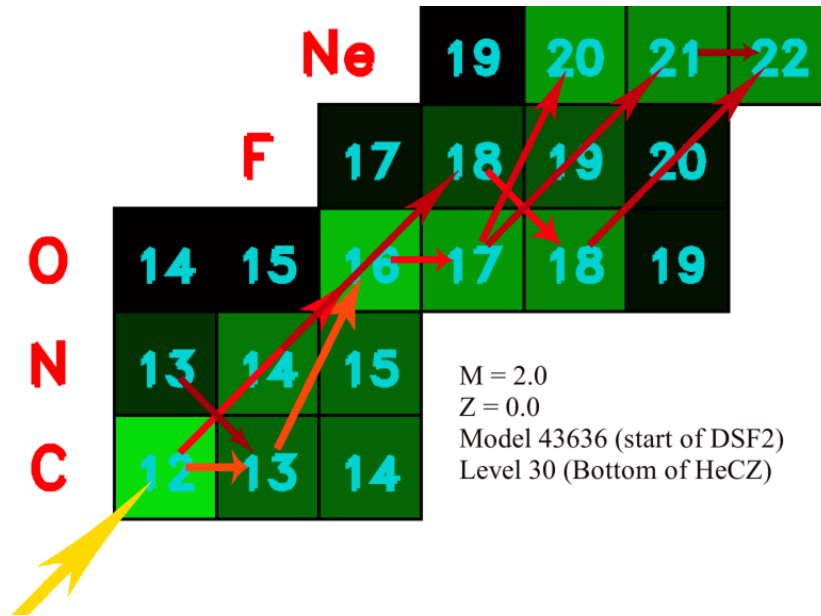


Figure 6.16: A rates plot showing the dominant reactions occurring at the bottom of the HeCZ near the start of dual shell flash 2. Lighter coloured (yellow/orange) thicker arrows indicate reactions occurring at higher rates than those represented by darker coloured (red) thinner arrows. The large yellow arrow at the bottom left represents the 3α reaction. Apparent are the two active channels cycling ^{12}C to ^{16}O , $^{12}\text{C}(n, \gamma)^{13}\text{C}(\alpha, \gamma)^{16}\text{O}$ and $^{12}\text{C}(\alpha, \gamma)^{16}\text{O}$, as well as a second neutron source, $^{16}\text{O}(n, \gamma)^{17}\text{O}(\alpha, n)^{20}\text{Ne}$.

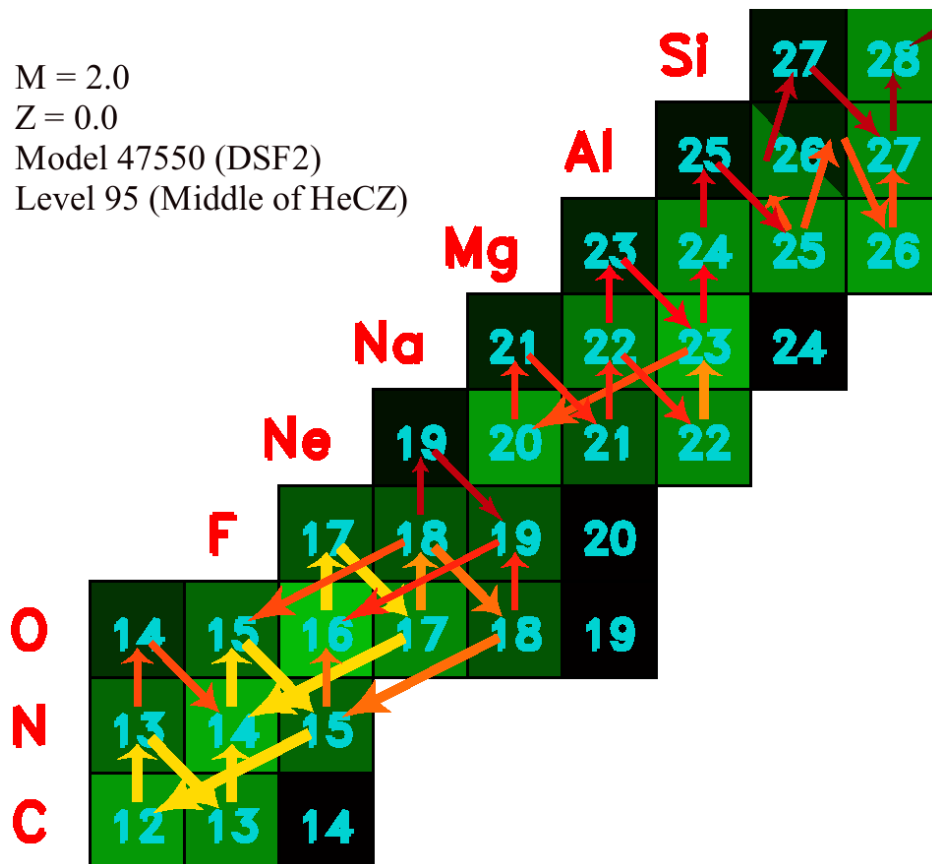


Figure 6.17: Same as Figure 6.16 except sampled further out in mass in the HeCZ, during the proton ingestion episode. Many proton capture reactions are occurring – the full CNO cycle is very active and the NeNa and MgAl chains can be seen operating. ^{28}Si is also produced.

An Error During DSF2

A peculiar feature seen in the HeCZ chemical evolution plot (panel 4 of Figure 6.15) is that the C \rightarrow O conversion, and some CN cycling, *occurs before the H-flash begins*. This implies that protons have been mixed into the HeCZ *before* it breaches the H-He discontinuity marked in the top panel of Figure 6.15. In order to ascertain how this could be possible we present in Figure 6.18 the chemical profiles of a few species at a time near the start of the He flash. It appears that the NS code has arrived at a different solution for the placement of the H shell at this point in time, as compared to the structural evolution code (SEV code). The difference between the two locations is $\sim 10^{-3} M_{\odot}$. What this means is that, when the He convection zone expands as the He flash reaches its peak, there is some H ingested into it earlier than predicted with the SEV code. This leads to the early production of ^{16}O and ^{14}N seen in Figure 6.15. We note that we have never seen such a discrepancy between the two codes before. In the $0.85 M_{\odot}$ model's dual core flash this did not occur (see Subsection 6.2.2 on page 162), and it does not occur in the next DSF of this model (DSF3). Unfortunately we have not been able to trace the error due to the time constraints on the present work. This discrepancy will however be addressed before we publish the results of this model as a journal article. It will require a close examination to find the source of the error and re-run the model. Despite this uncertainty we believe that the yield results will not be significantly affected. There are two reasons for this. Firstly, the nucleosynthesis that occurs as a result of the extra and premature proton ingestion calculated by the NS code is likely to be very similar to that of the PIE that occurs directly after (the 'real' PIE, as given by the SEV code). Looking at the dual core flash nucleosynthesis of the $0.85 M_{\odot}$ model (see Figure 6.4 on page 167), which is a very similar phenomenon, we see that the same C \rightarrow O processing occurs at the very first proton ingestion episode, such that ^{16}O becomes the dominant species at the expense of ^{12}C . We suggest that this is a robust outcome of the PIE phenomenon for DCFs and DSFs. Moreover, when the ^{16}O abundance has been raised to such high levels it is difficult for any process to reduce it, such that ^{16}O remains dominant. This brings us to our second reason. The present model soon undergoes HBB and 3DUP. 3DUP quickly increases the surface ^{12}C abundance to values much higher than ^{16}O . Meanwhile strong HBB causes ON cycling, depleting the ^{16}O dredged up in the DSF – and thus essentially erases this nucleosynthetic signature. It is 3DUP and HBB that dominate the yield of this model. Thus we believe that the yield will not be significantly altered by the error in the calculation but note again that it will nonetheless need to be addressed in future work in the interests of scientific robustness.

DSF3

Out of all the DSFs the third gives rise to the largest pollution of the envelope and thus it is the most important in terms of the chemical yield for the model. Figure 6.19 gives an overview of the DSF, showing the He and H convective zones and the evolution of the composition within these zones. As with DSF2 the composition of the HCZ after the PIE reflects the composition of the HeCZ at the time of the ingestion, aside from some modifications that occur during the PIE itself. As also seen in DSF2 the modifications are due to CN cycling: ^{14}N is strongly enhanced over the HeCZ value, and ^{12}C is slightly depleted. However, at odds with the HCZ composition

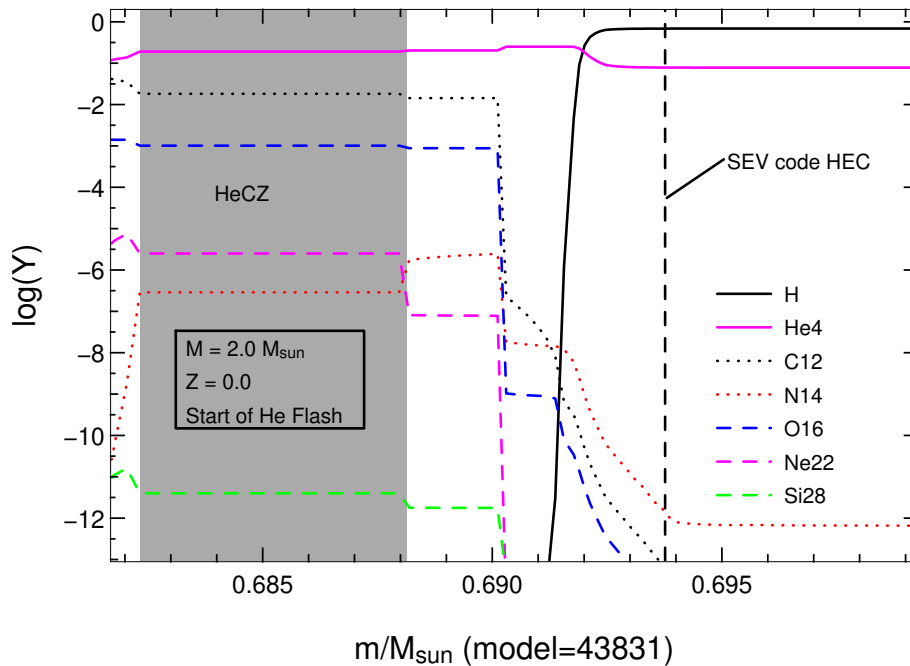


Figure 6.18: The chemical profile of some key species taken just as the He flash convection starts at the beginning of DSF2. Grey shading marks the He convective zone. The vertical dashed line marks the position of the H-exhausted core as given by the structural evolution code. As can be seen the H profile given by the NS code has placed the H-shell at a lower mass coordinate (see text for discussion). The region with high ^{12}C abundance was created by He burning in the previous He-flash. Regions with $^{14}\text{N} > ^{12}\text{C}$ indicate advanced CN cycling by the H-shell moving outwards.

in DSF2, this HCZ is still dominated by ^{16}O and ^{12}C , rather than ^{16}O and ^{14}N . The reason for this appears to be the difference in starting abundances of ^{14}N during the PIEs. In the HCZ of DSF2 we saw that there was a small PIE just before the H flash that produced a large amount of ^{14}N in the HeCZ. This high abundance was then added to via CN cycling during the H flash (in the HCZ). In the DSF3 case the ^{14}N abundance has dropped to very low levels ($Y_{N14} \sim 10^{-7}$) by the time this PIE occurs. Figure 6.20 shows that, like DSF2, there is some CN cycling during the PIE and during the rest of the H flash, but it not complete. The CN cycle does not reach equilibrium within this time and ^{12}C remains dominant. Thus the composition of the material dredged up to the envelope later is relatively ^{14}N -poor.

We suggest that the difference between the two DSFs that is expressed in the ^{14}N abundance may be due to the different environments in which each occurs. In the case of DSF2 the CNO-rich material from the HeCZ is mixed up into regions of extremely low metallicity, causing a CNO-flash as the previous burning could only occur via the p-p chains. In DSF3 the material just above the H-He discontinuity is already relatively metal-rich, so that CNO cycling is already occurring and the H flash does not occur in the same manner. In addition to this – and possibly more importantly – the strength of the He flashes are different in the two episodes. The peak He luminosity in DSF2 is $\sim 6.4 L_{\odot}$ whilst in DSF3 it is $\sim 7.3 L_{\odot}$. This leads to stronger convection in the second case, and hence to a greater breaching of the H-He discontinuity. We suggest that it is the weaker He flash that gives rise to the small proton ingestion episode just before the main H flash in the DSF2 case (this can be seen in luminosity in panel 2 of Figure 6.15), allowing some CN processing in the HeCZ prior to the main CNO-PIE. In DSF3 the PIE is more ‘assertive’ due to the stronger He flash – the HeCZ quickly breaks through the

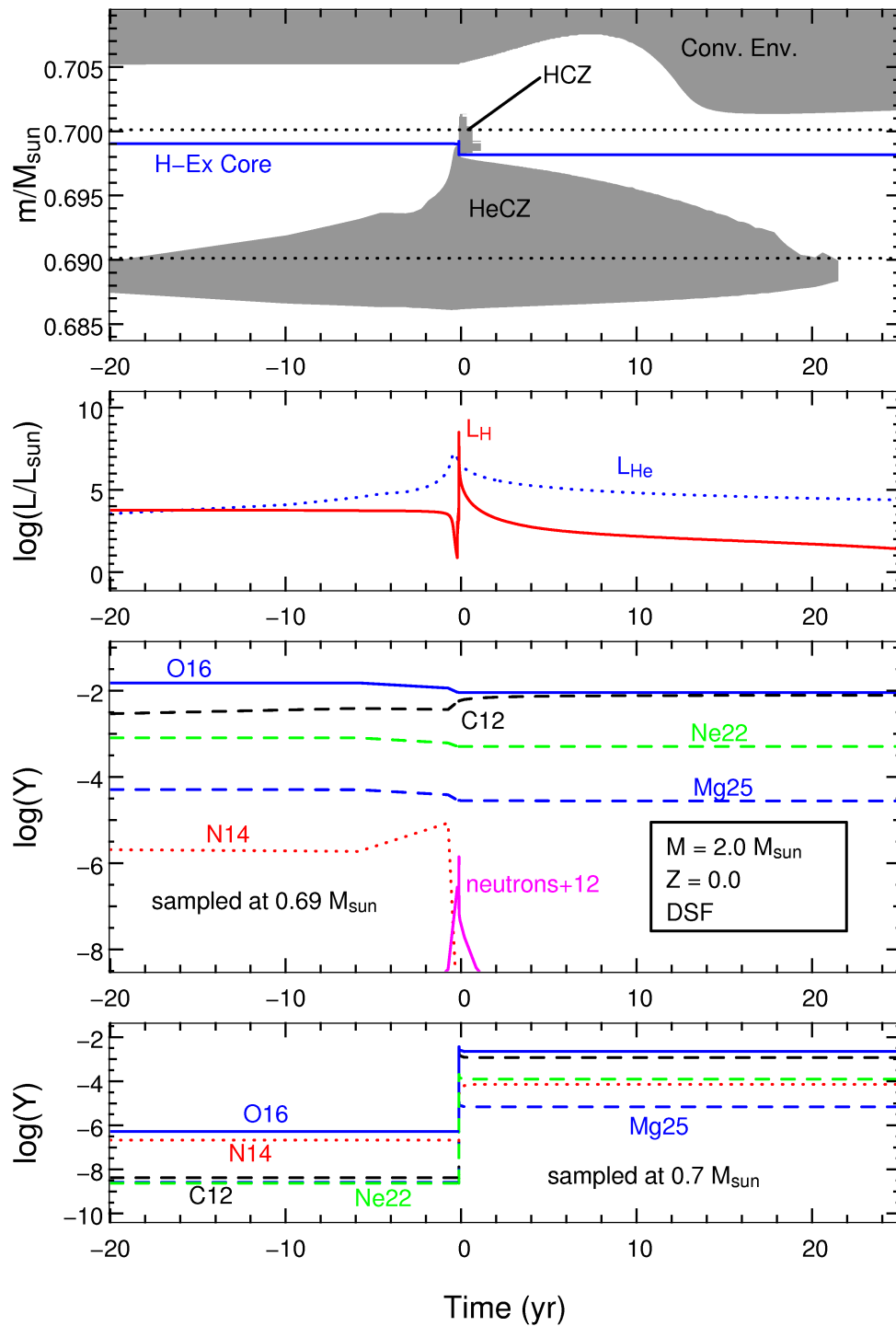


Figure 6.19: An overview of the third dual shell flash (DSF3). Time has been offset to coincide with the peak of the H flash. The two horizontal dotted lines in the top panel show the sample points for the composition of the HCZ and HeCZ shown in the bottom two panels. The extent in mass of the HCZ, and the significant movement inwards of the H burning shell, is much larger than that in DSF2. This leads to a large envelope pollution when the erstwhile HCZ is later dredged up. It can be seen that the post-PIE HCZ composition basically reflects the composition of the HeCZ apart from some CN cycling (^{14}N is enhanced and ^{12}C depleted). Also evident is a short neutron burst during the peak of the flashes, which may give rise to some s-processing.

H-He discontinuity to mix down substantial amounts of H, giving rise to an immediate strong H flash and a splitting of convection zones (although there is a very small amount of proton ingestion just before the convection zone splitting). It is interesting to note here that we have not used any form of overshoot in these models. If we were to include overshoot then we would expect even more ‘assertive’ PIEs. This may remove the small PIEs and thus any prior ^{14}N production in the HeCZs. Then ^{12}C would be more abundant than ^{14}N in the HCZ. It may also reduce the effectiveness of the C \rightarrow O conversion (due to $^{13}\text{C}(\alpha, n)^{16}\text{O}$ reactions operating in tandem with $^{12}\text{C}(\alpha, \gamma)^{16}\text{O}$), and thus reduce the oxygen content of the HCZ. Advanced proton capture nucleosynthesis may also be reduced. Thus, due to the uncertainty of the convective boundaries, there is some uncertainty in the composition of the polluting material from these events. However, as discussed in the next subsection, the ^{14}N yield from this star is primarily from hot bottom burning of ^{12}C on the TP-AGB.

In Figure 6.20 we zoom in closer on the evolution of DSF3. Here we can see that the He convective zone splits in to two, similar to the case of the dual core flash of the $0.85 M_{\odot}$ model. The mass involved in the exchange between the HeCZ and HCZ is $\sim 10^{-3} M_{\odot}$, much more than that involved in DSF2 ($\sim 10^{-5} M_{\odot}$). Also similar to the $0.85 M_{\odot}$ model these two convection zones remain separated from then on. The bottom panel in Figure 6.20 shows the chemical evolution at a particular mass coordinate that initially takes in the HeCZ and then the HCZ. ^{16}O is the dominant species in the HeCZ and thus becomes the dominant species in the HCZ after the PIE mass exchange. Apparent in Figure 6.21 is that the HeCZ primarily consists of material from the previous thermal pulse nucleosynthesis (DSF2). As detailed in the previous subsection this material underwent significant C \rightarrow O processing which gave rise to the dominance of ^{16}O .

After the third DSF abates the entire (erstwhile) HCZ is dredged up into the convective envelope (see Figure 6.20). This results in a significant increase in surface metallicity, raising it to $Z_{\text{cno}} \sim 10^{-4}$. Interestingly this means $\log(Z/Z_{\odot}) \sim -2$ such that it is comparable to the metal-poor Galactic globular cluster stars. However, in terms of the heavier elements it remains ultra metal-poor.

6.3.3 Dual Shell Flashes – Potential s-Process Sites?

We suggested in Section 6.2.3 on page 170 that the dual *core* flash of the $0.85 M_{\odot}$ model may be a good site for s-process nucleosynthesis due to the $^{13}\text{C}(\alpha, n)^{16}\text{O}$ reaction being so active during the flash. The DSF event is quite similar to the DCF as they both involve protons being introduced into a HeCZ, giving rise to interesting nucleosynthesis.

We suggest that the DSF may also be a good s-process site. In Figure 6.19 we do see a relatively large spike in the neutron abundance at the peak of the H flash ($Y_n \sim 10^{-18}$), at the mass level sampled. In Figure 6.22 we show the chemical composition of the HeCZ near the peak of the DSF. The neutron abundance is highest at the base of the HeCZ and reaches values up to $Y_n \sim 10^{-16}$. Although this is a much lower abundance than found in the $0.85 M_{\odot}$ DCF (where Y_n peaked at $\sim 10^{-13}$) we note again that, as we have not included enough species to follow the s-process, we cannot be certain how significant the resulting s-process nucleosynthesis would be. ^{13}C is only present in trace amounts ($Y_{\text{C13}} \sim 10^{-9}$) but it is more abundant than the neutron

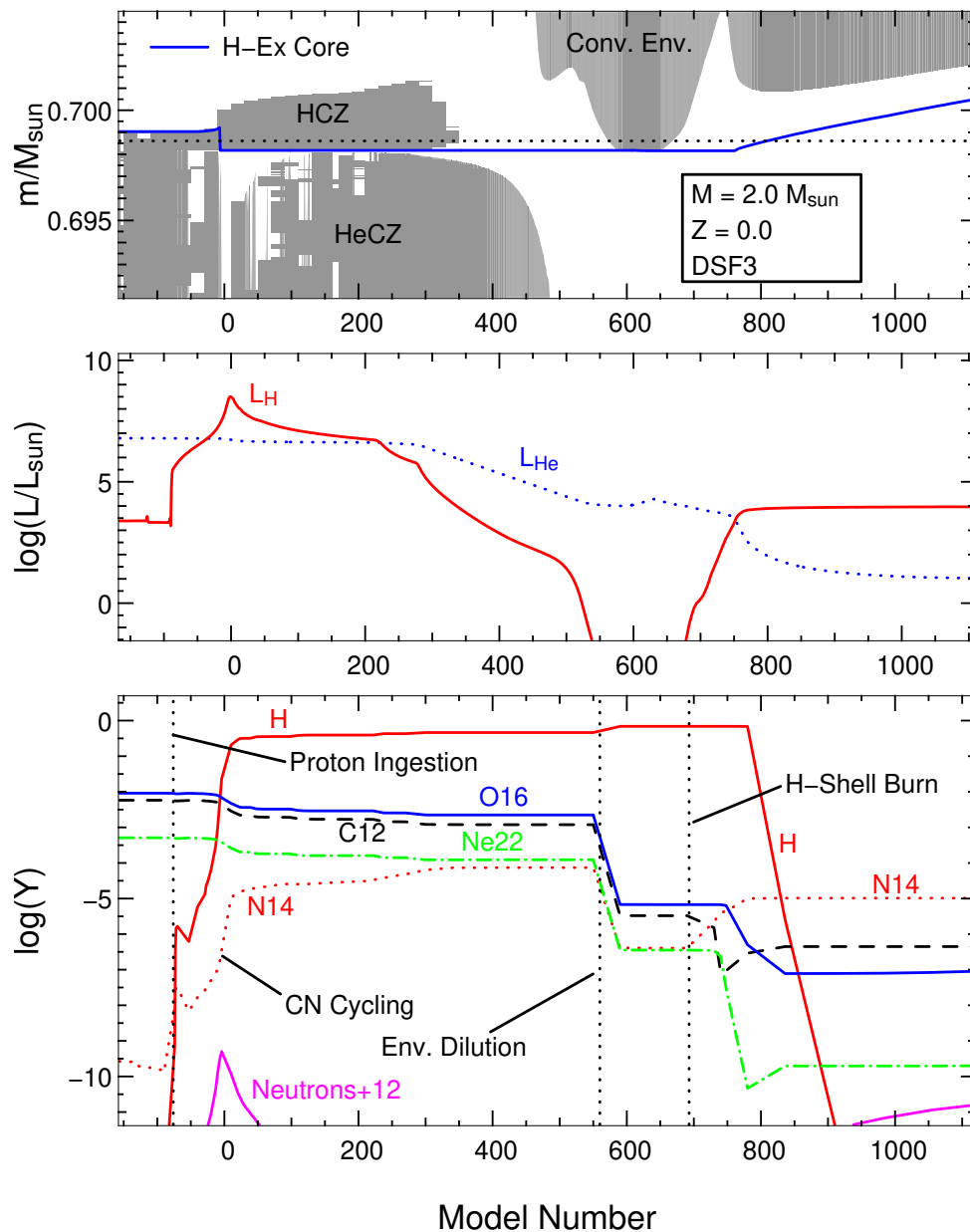


Figure 6.20: Zooming in on DSF3, the strongest and most polluting DSF. Note that the evolution is against model number rather than time. This allows us to see the rapid evolution more clearly, as the code timestepping is governed by the changes in physical quantities. The dotted line in panel 1 shows the sampling point for the composition evolution in the bottom panel. The messy part of the HeCZ (top panel, convection) occurs during the peak of the H flash and is due to the HeCZ convection essentially dying off at this time. The splitting of the convection zones is evident, as is the later dredge-up of the ex-HCZ by the convective envelope. Many regimes are marked in the bottom panel. Of particular note is the partial CN cycling during the very beginning of the PIE (before the convective zones split) and also in the HCZ after the convective zones split.

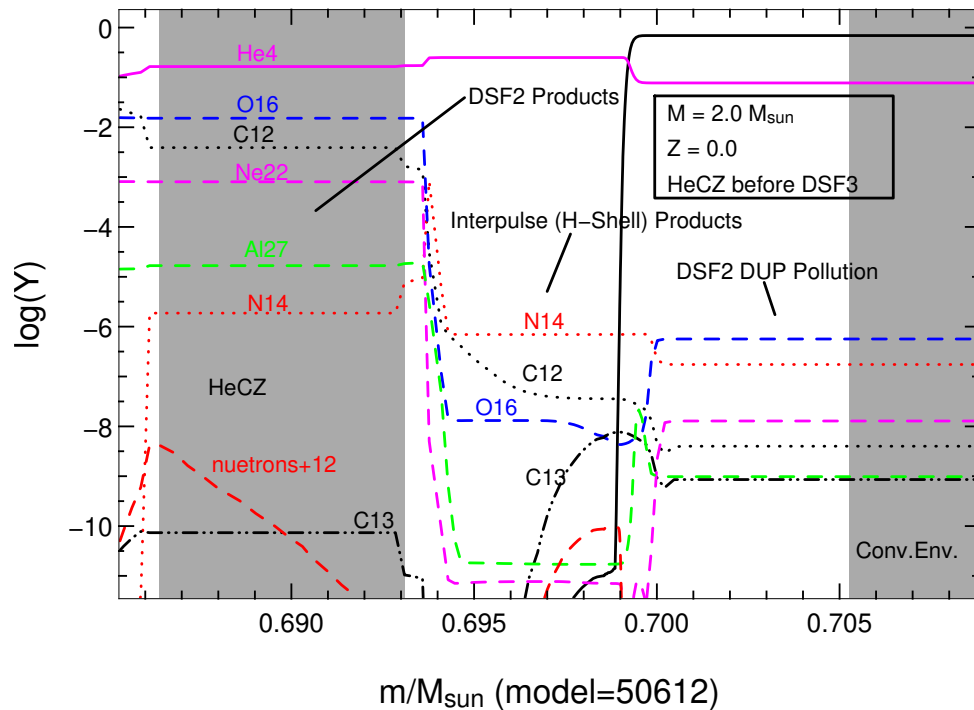


Figure 6.21: The run of abundances against mass just before the first proton ingestion episode of DSF3. As indicated in the plot the HeCZ (which is still expanding) is primarily composed of the material produced by the previous thermal pulse (DSF2). In terms of metals this material is dominated by ^{16}O (see text for details). This chemical signature is also visible in the envelope (although diluted). Between the envelope and the HeCZ we see the products of the H shell burning that occurred during the previous interpulse period, which has cycled the ^{16}O and ^{12}C to ^{14}N . Interestingly there is a ^{13}C pocket at the bottom of the H shell, where the proton abundance is $\sim 10^{-8}$. The neutron abundance is however very low ($Y_n \sim 10^{-22}$).

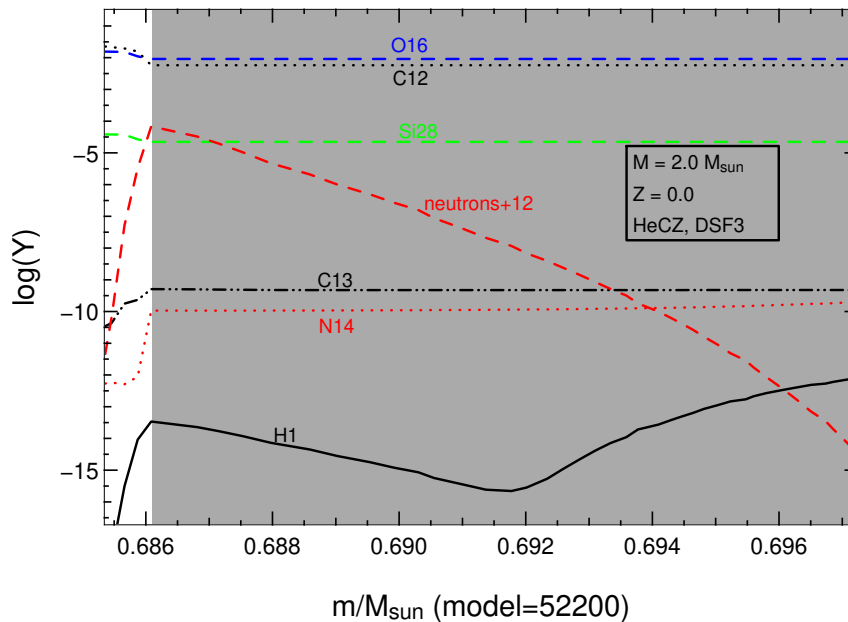


Figure 6.22: The chemical composition of the HeCZ near the peak of the core He-H flash (DSF3). Grey shading represents convection. The (relatively) large abundance of neutrons ($Y_n \sim 10^{-16}$) may give rise to some s-process nucleosynthesis.

sink ^{14}N . ^{16}O is already the most abundant metallic species. The reason for this is that both main $\text{C} \rightarrow \text{O}$ channels are operational ($^{12}\text{C}(\alpha, \gamma)^{16}\text{O}$ and $^{13}\text{C}(\alpha, n)^{16}\text{O}$), as can be seen in the rates plot in Figure 6.23. An interesting feature in this plot is that there are three competing (α, n) reactions producing neutrons; the usual ^{22}Ne and ^{13}C sources as well as the $^{17}\text{O}(\alpha, n)^{20}\text{Ne}$ reaction.

An interesting possibility from this potential nucleosynthesis is that some primary Fe may be produced via neutron captures in the DSFs. After the DSF dredge-up the surface chemical composition of the star may then appear like that of an extremely metal poor Halo star. However we suggest that the amount of Fe that would be produced would be negligible. Nonetheless this possibility should be explored properly just incase. We leave this and the other potential s-process nucleosynthesis for future work, when we have extended the reaction network.

6.3.4 TP-AGB

After the three DSF episodes have completed the star settles into a relatively normal thermally-pulsing AGB evolution. Figure 6.24 displays the surface chemical evolution of the star on the AGB, including the DSFs at the start of the AGB. Unlike the $0.85 M_{\odot}$ model this star does undergo third dredge-up (3DUP) and hot bottom burning (HBB), both of which severely modify the composition of the envelope. One thing immediately apparent in Figure 6.24 is that, in terms of bulk (Z_{cno}) metallicity, the surface pollution the star experiences during the AGB far outweighs the pollution caused by the DSFs. Thus, on the surface, it would seem that the computational effort and detailed analysis of the previous subsection was unwarranted. However we note that the DSFs are important for a couple of reasons. Firstly, it may be argued that the 3DUP that pollutes the surface on the AGB may not have occurred if the envelope had not been first polluted by the DSFs. The increase in opacity that these pollution events create allows deeper

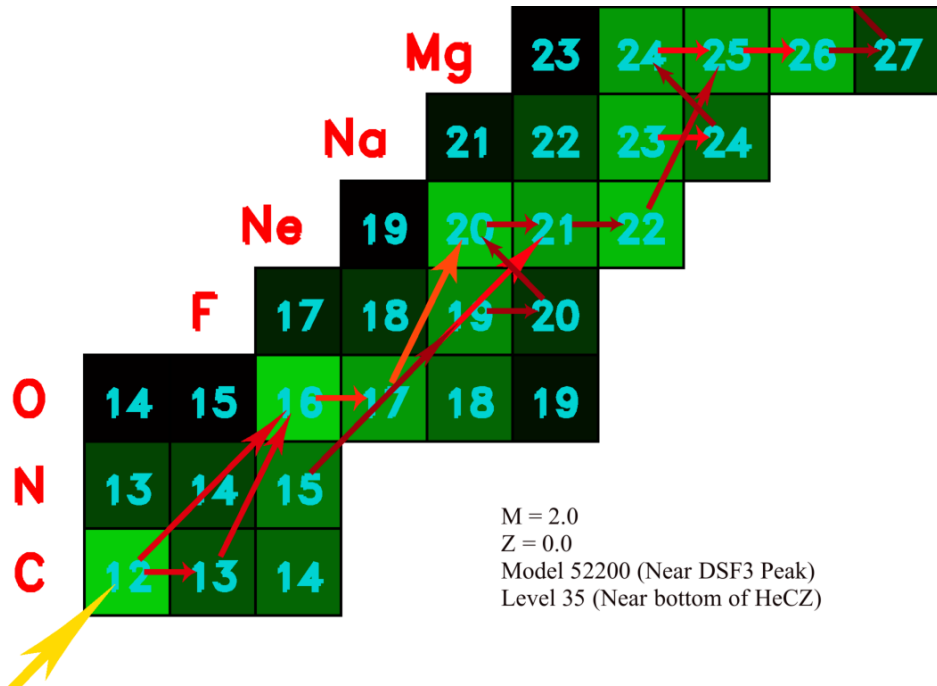


Figure 6.23: A rates plot taken during the peak of the He-H flash (DSF3). See the caption of Figure 6.16 for an explanation of this type of plot. The mass coordinate sampled is towards the bottom of the HeCZ. Interestingly there are three competing (α, n) reactions producing neutrons; the usual ^{22}Ne and ^{13}C sources as well as the $^{17}\text{O}(\alpha, n)^{20}\text{Ne}$ reaction. Neutron captures can also be seen occurring, leading to the production the heavy Mg isotopes, for example.

envelope convection, making 3DUP more likely to occur. Secondly, although 3DUP drastically increases the abundance of the CNO isotopes (which are redistributed by HBB) in the latter part of the AGB, the star retains the DSF pollution composition for about 2/3 of the time spent on the AGB. Related to this is the fact that the DSFs also provide a starting chemical distribution for the AGB, which affects the final composition of the star due to HBB acting on this material.

It is important to note here that *any* form of dredge-up from the HeCZ early on the AGB would lead to a pollution of the envelope, possibly to a similar level as that provided by the DSFs. However the nature of the DSFs gives rise to a distinct chemical distribution. This is mainly due to the proton ingestion episodes that occur at the start of the DSFs. The main chemical signature that the DSFs provide is that of ^{16}O being very prominent at the start of the AGB. This would also be the case in a model with scaled-solar composition that experienced just a few 3DUP episodes, because the initial composition is O-rich, but it would not be expected from a 3DUP event in a star with a metal-free envelope. We would expect the composition to reflect that of the HeCZ which would result in ^{12}C dominating the metals in the envelope. As shown in the previous subsection the DSF ^{16}O comes from the $^{12}\text{C}(p, \gamma)^{13}\text{N}(\beta^+ \nu)^{13}\text{C}(\alpha, n)^{16}\text{O}$ chain of reactions (and also the ongoing $^{12}\text{C}(\alpha, \gamma)^{16}\text{O}$ reaction) when protons are ingested into the HeCZ. That this chain of reactions also results in a substantial neutron production may indicate that there may be an s-process signature accompanying the ^{16}O one. As mentioned earlier we did not follow the s-process with the NS code but it will be an interesting avenue for further work.

Although the current work predicts an ^{16}O signature we should reiterate a caveat here: the DSF episode is dependent on the treatment of convective boundaries as this affects the nature of the DSFs. For example, the inclusion of overshoot would cause a larger ingestion of protons very

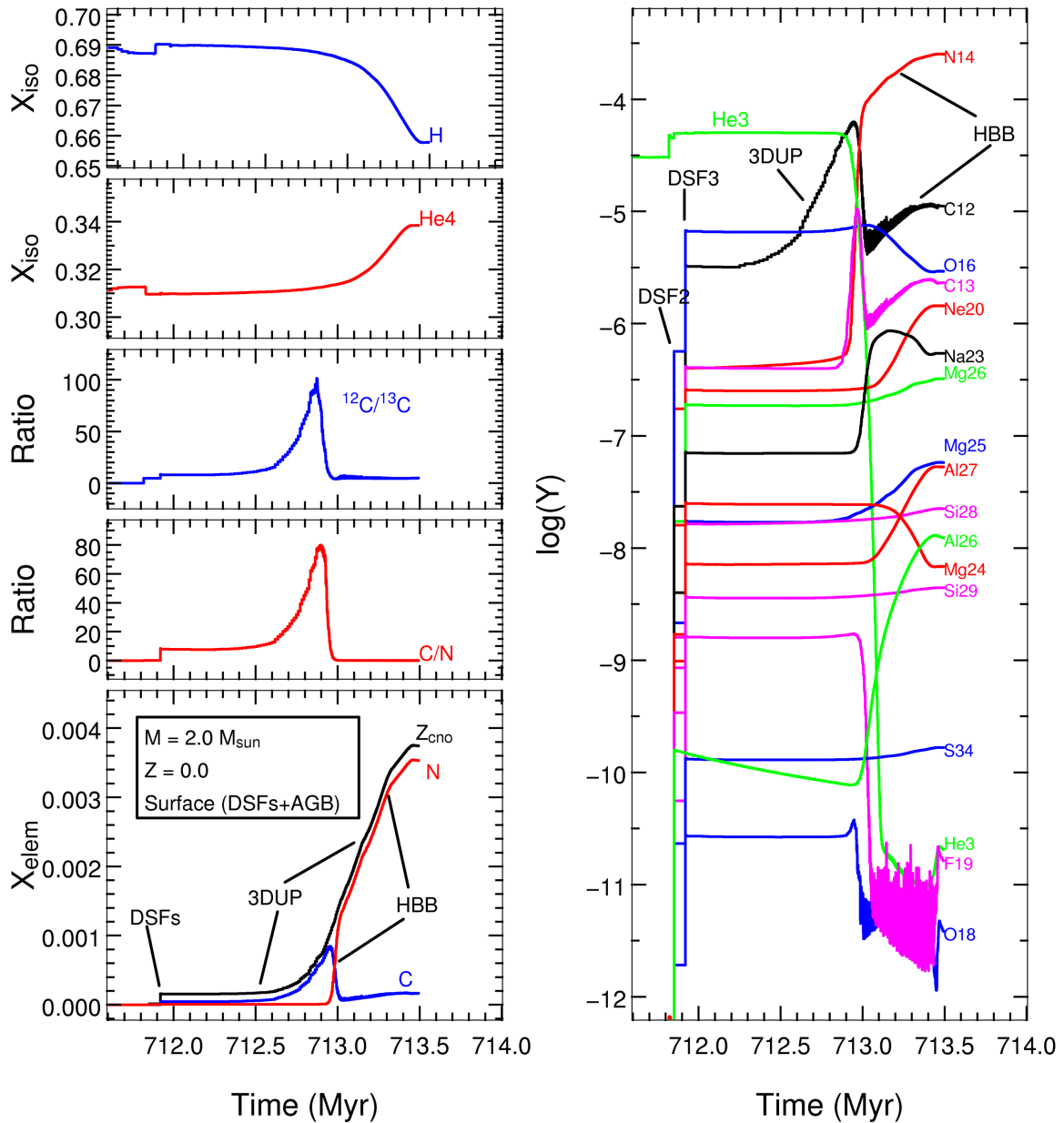


Figure 6.24: The surface chemical evolution during the DSFs and the AGB. Only selected species are shown, for clarity. In the bottom panel on the left it can be seen that the envelope pollution from the DSF episodes is swamped by the pollution from ongoing 3DUP. The onset of (significant) HBB is evident in the same panel by the strong $\text{C} \rightarrow \text{N}$ conversion. This star becomes a ‘nitrogen giant’ at this stage, as ^{14}N by far dominates the metal content of the envelope. It also dominates the yield as the majority of the mass loss occurs during this stage.

quickly, as the HeCZ expands and breaches the H-He discontinuity earlier and more abruptly. This would alter the timescale of the DSF (the extra H fuel would lead to a higher H luminosity sooner and also a quicker splitting of the convection zone). It would also alter the nucleosynthesis in the HeCZ. Thus the resultant composition of the DSF pollution is somewhat uncertain due to the uncertainty of the location of the convective boundaries. We stress that this uncertainty should be kept in mind when examining the nucleosynthetic products coming from DSFs (and DCFs).

Returning to Figure 6.24 it can be seen that the ${}^4\text{He}$ abundance rises significantly, primarily through strong HBB towards the end of the AGB. As shown in the structural evolution section for this star (Section 5.3 on page 139) the temperature at the bottom of the convective envelope reaches ~ 80 MK. Under these conditions we expect significant ON cycling and also further proton capture nucleosynthesis such as that via the Ne-Na and Mg-Al chains. Looking at the last third of the AGB in Figure 6.24 we indeed see a rich nucleosynthesis has occurred. ${}^{16}\text{O}$ is depleted by ~ 0.5 dex and proton chain products such as ${}^{23}\text{Na}$ and ${}^{27}\text{Al}$ have been enhanced by about 1 dex (over the DSF pollution levels). Before HBB sets in the ${}^{12}\text{C}/{}^{13}\text{C}$ ratio rises to very high values due to 3DUP of ${}^{12}\text{C}$. Once HBB is operating the ratio then drops down to equilibrium values (~ 3). The most striking nucleosynthetic feature is however the enormous production of ${}^{14}\text{N}$. It is so abundant that, to first order, this star can be considered a *nitrogen giant* such that N totally dominates the metal content of the envelope. The next most abundant species is ${}^{12}\text{C}$, but this is 1.5 dex less prevalent.

${}^{14}\text{N}$ production comes about via the combination of 3DUP and HBB. In Figure 6.25 we show this occurring between two thermal pulses. First, fresh ${}^{12}\text{C}$ is dredged up into the convective envelope just after the pulse, then CN cycling at the bottom of the convective envelope during the interpulse period converts it to ${}^{14}\text{N}$. Also visible is the same combination of events occurring for ${}^{22}\text{Ne}$, which is primarily burnt to ${}^{23}\text{Na}$ (note that this is before HBB is strong enough to destroy ${}^{23}\text{Na}$). It is evident in this Figure that the amount of mass dredged up is very small ($\lambda \sim 0.01$) but, as noted in the structural evolution section, the star undergoes 282 thermal pulses and thus achieves a high level of pollution despite this.

Figure 6.26 displays the dominant reactions occurring at the base of the convective envelope during the interpulse. It can clearly be seen that the C-N, O-N, Ne-Na and Mg-Al chains/cycles are all operating. In addition to this there are proton captures on ${}^{26}\text{Mg}$ and ${}^{27}\text{Al}$ causing a leakage out of the Mg-Al chains, producing ${}^{28}\text{Si}$.

We now delve into the evolution of a single thermal pulse (the 63rd for this model) and associated HeCZ, to ascertain what nucleosynthesis is occurring inside the HeCZ. This is important because it is this material that is dredged up into the envelope at each 3DUP episode. Figure 6.27 shows the evolution of the composition in the HeCZ as well as that of the luminosities and convection zones. The only species (of those displayed) which has its abundance altered significantly is ${}^{14}\text{N}$. It is quickly destroyed as the He flash gets close to its peak, ending up as ${}^{22}\text{Ne}$ via ${}^{14}\text{N}(\alpha, \gamma){}^{18}\text{F}(\beta^+ \nu){}^{18}\text{O}(\alpha, \gamma){}^{22}\text{Ne}$. Thus the abundance of ${}^{22}\text{Ne}$ is seen to increase somewhat. We note that the ${}^{14}\text{N}$ initially in the HeCZ was produced before the He flash by CN cycling in the H burning shell when it moved through this region during the previous interpulse.

Also slightly increasing in abundance during this phase are the heavy Mg isotopes ${}^{25}\text{Mg}$ and ${}^{26}\text{Mg}$,

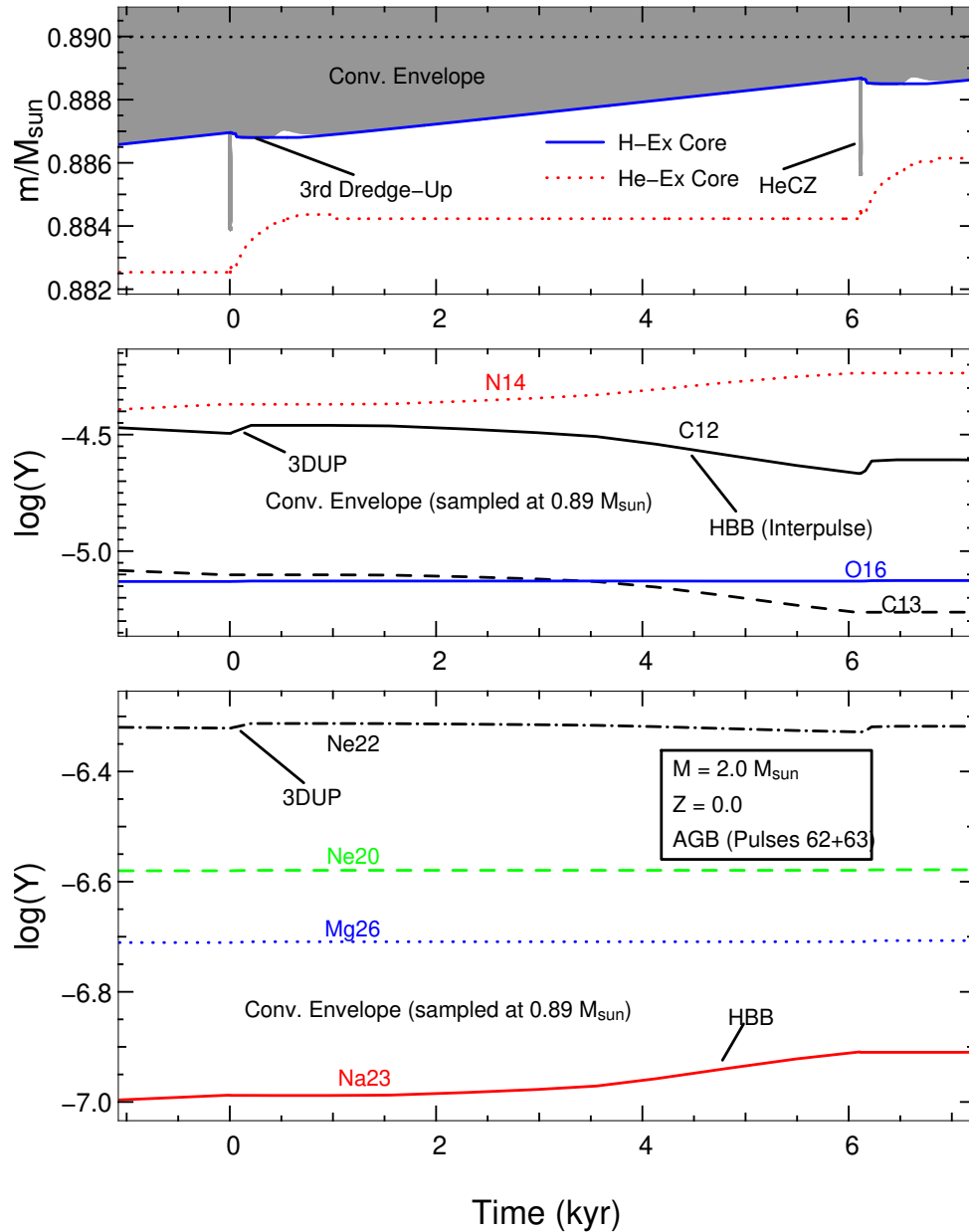


Figure 6.25: The evolution of an interpulse, just as ^{14}N is beginning to dominate the metal content of the envelope. The dredge-up of ^{12}C just after the He flashes can be seen in the second panel, as can the decrease of this species during the interpulse period. The consequent increase in ^{14}N is also evident. In the bottom panel (sampled at the same mass coordinate) a small dredge-up of ^{22}Ne can also be seen, as can its partial destruction later on. It is burnt to ^{23}Na , which can be seen increasing during the interpulse period.

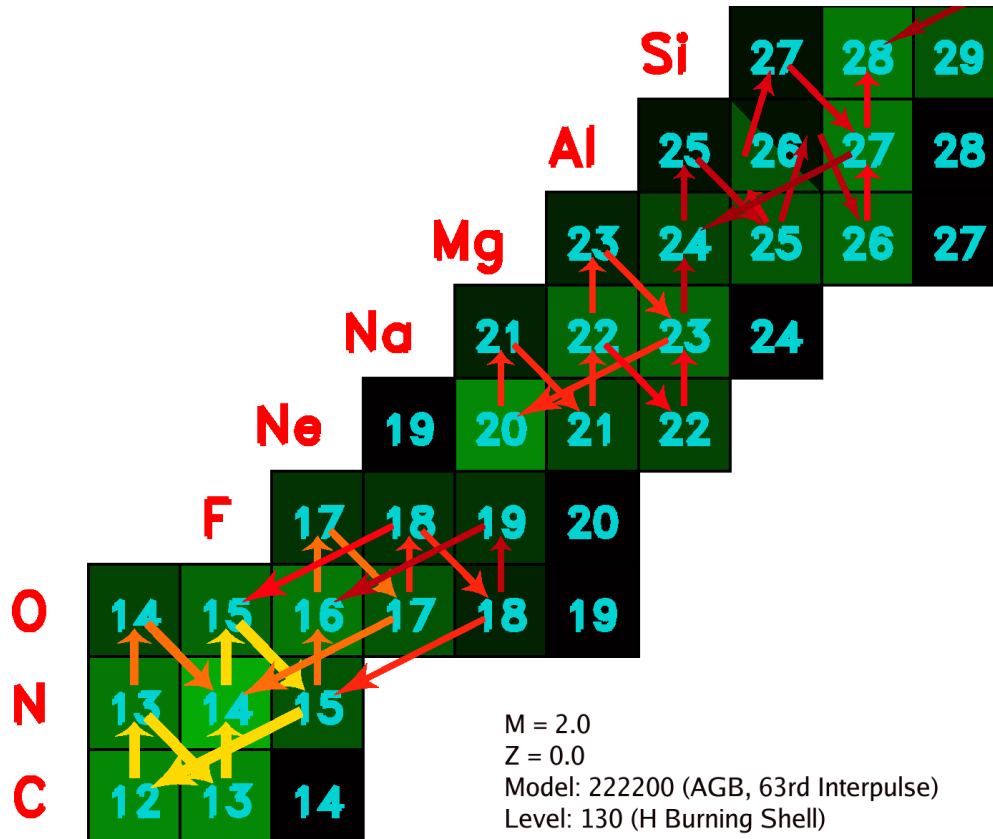


Figure 6.26: A rates plot showing the dominant reactions occurring at the base of the convective envelope during the same interpulse period as that displayed in Figure 6.25. See the caption of Figure 6.16 for an explanation of this type of plot. This is where HBB is occurring and, naturally, proton capture reactions are dominant. It can be seen that, in addition to the CN(O) cycling, the NeNa and MgAl chains/cycles are also operating. It is this nucleosynthesis that leads to the large movement of abundances during the last third of the AGB seen in Figure 6.24. As most of the mass loss also occurs during this stage it is this nucleosynthesis (combined with ongoing 3DUP) that dominates the yield of the star.

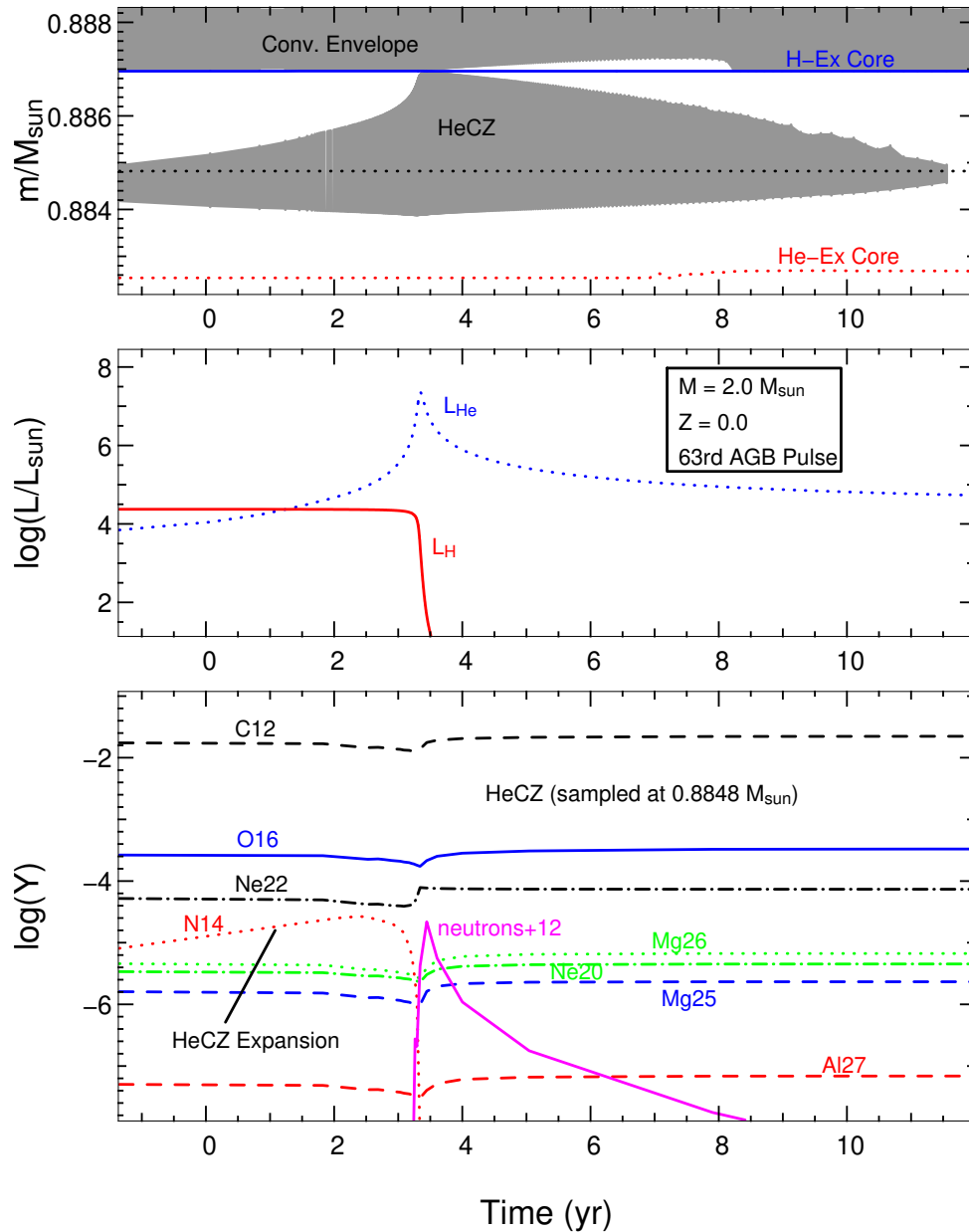


Figure 6.27: The evolution of the 63rd thermal pulse on the TP-AGB. The horizontal dotted line in the top panel shows the sample point for the composition evolution in the bottom panel. As can be seen in panel 2 there is no associated H flash – this is a normal thermal pulse. The evolution of the abundances of some selected species is shown in the bottom panel. The main nucleosynthesis happening here is the conversion of ^{14}N to ^{22}Ne via alpha captures, and the production of ^{12}C via the usual He flash reactions. Interestingly there is a (relatively) large spike in neutron abundance at the peak of the flash (see text for further details).

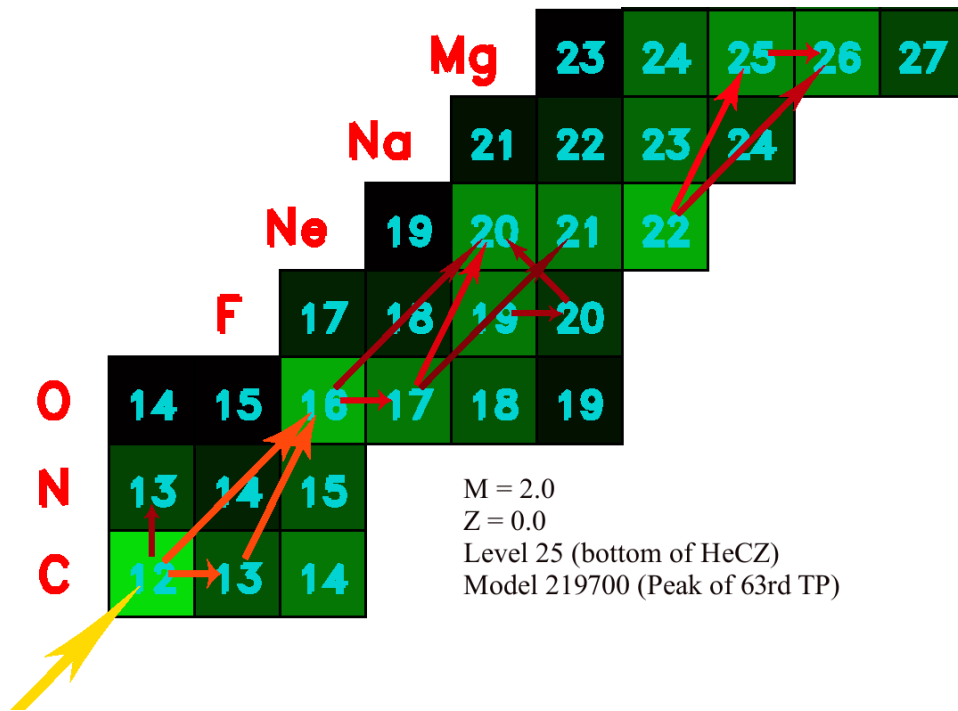


Figure 6.28: A rates plot showing the dominant reactions at the bottom of the HeCZ at the peak of the He flash of the 63rd thermal pulse. See the caption of Figure 6.16 for an explanation of this type of plot. Three key neutron producing reactions are occurring: $^{22}\text{Ne}(\alpha, n)^{25}\text{Mg}$, $^{13}\text{C}(\alpha, n)^{16}\text{O}$ and $^{17}\text{O}(\alpha, n)^{20}\text{Ne}$. This is allowing further production of ^{13}C through neutron capture on the abundant ^{12}C so that it appears that neutrons are being recycled between these two reactions: $^{12}\text{C}(n, \gamma)^{13}\text{C}(\alpha, n)^{16}\text{O}$. This neutron processing may lead to some s-process nucleosynthesis during each thermal pulse.

and ^{20}Ne . ^{25}Mg is primarily produced via the $^{22}\text{Ne}(\alpha, n)^{25}\text{Mg}$ reaction. This reaction liberates neutrons, and a neutron abundance spike can be seen in Figure 6.27 during the He flash. The neutrons are then available for capture by ^{25}Mg , which produces the ^{26}Mg . The neutrons also open up another channel for ^{20}Ne production through $^{19}\text{F}(n, \gamma)^{20}\text{F}(\beta^- \nu)^{20}\text{Ne}$. The relatively high neutron abundance during the flash may lead to significant s-process nucleosynthesis. Again, as we have not included enough species (and reactions) to follow the s-process we can only speculate on the degree of its importance here. In Figure 6.28 we show the main reactions occurring at the bottom of the HeCZ during the peak of the He flash (after ^{14}N has been depleted). The $^{22}\text{Ne}(\alpha, n)^{25}\text{Mg}$ reaction can be seen operating and, interestingly, so can the $^{13}\text{C}(\alpha, n)^{16}\text{O}$ neutron-producing reaction. This reaction is able to operate because of the production of ^{13}C via neutron capture on the abundant ^{12}C . It appears that ^{12}C is acting as an efficient neutron sink. It also appears that neutrons are being recycled between these two reactions: $^{12}\text{C}(n, \gamma)^{13}\text{C}(\alpha, n)^{16}\text{O}$. We suggest that this neutron cycle may have been triggered by the ^{22}Ne source, but note that this is difficult to ascertain. With so many free neutrons available, and with a lack of the ^{14}N neutron sink, further neutron-capture reactions are likely. We shall investigate the s-process in detail in future work with an extended nucleosynthetic network. Finally we note that s-processing here on the AGB may provide a useful nucleosynthetic signature for these stars.

6.3.5 Chemical Yield

We display the entire nucleosynthetic yield (of metals) for this model in Figure 6.29. ^{14}N is the dominant product, exceeding ^{12}C by 1.5 dex. It was primarily produced on the AGB via HBB of ^{12}C which was dredged up periodically. As seen in the previous subsection ^{12}C was the dominant metal species on the AGB just before HBB CN cycling set in (^{16}O from the DSFs was dominant before this). However, as most of the mass loss occurs towards the end of the AGB and as this model did not have any RGB mass loss, the yield reflects the composition during the late (HBB) phase of the AGB. Likewise, the $^{12}\text{C}/^{13}\text{C}$ ratio in the ejected material is low, being at a C-N cycle equilibrium level of ~ 4 . ^{20}Ne is the next most prominent species in the yield. It was produced in the HeCZ (intershell) and also through HBB. In the HeCZ the dominant reactions were alpha captures on ^{16}O and ^{17}O . It was also produced via neutron capture through the $^{19}\text{F}(n, \gamma)^{20}\text{F}(\beta^-)^{20}\text{Ne}$ chain (see Figure 6.28). This material was mixed to the surface via 3DUP. The bulk of the ^{20}Ne was however produced through HBB where proton captures destroyed much of the ^{23}Na via $^{23}\text{Na}(p, \alpha)^{20}\text{Ne}$. ^{23}Na was initially in nett production on the AGB and was more abundant than ^{20}Ne before HBB set in. It was produced by the destruction of ^{22}Ne in the Ne-Na cycle. ^{22}Ne is always abundant in the HeCZ due to the destruction of the ^{14}N left by the previous H shell burning: $^{14}\text{N}(\alpha, \gamma)^{18}\text{F}(\beta^+ \nu)^{18}\text{O}(\alpha, \gamma)^{22}\text{Ne}$. When HBB became hot enough for ^{23}Na destruction it became the main contribution to the increase in ^{20}Ne . Some leakage out of the Ne-Na cycle also occurred during HBB (see Figure 6.26), primarily through $^{23}\text{Na}(p, \gamma)^{24}\text{Mg}$. Thus the Mg-Al cycle was able to operate, resulting in the modest yield of ^{25}Mg , ^{26}Mg and ^{27}Al seen in Figure 6.29. Furthermore, HBB proton captures on these species allowed the production of more massive species. ^{28}Si was produced through $^{27}\text{Al}(p, \gamma)^{28}\text{Si}$.

^3He was almost totally destroyed during HBB, although a small amount was released in the yield as some of the mass loss occurred before it reached an extremely low abundance. ^{31}P and ^{32}S were released in small amounts ($\log(Y) \sim -8$). The main source for these two species was the DSFDUP after DSF3. Their abundances were only slightly increased during the AGB. ^{19}F was only released in trace amounts ($\log(Y) \sim -10$) due to its almost total destruction via HBB (it reached a peak abundance of $\log(Y) \sim -8$ after the DSFs). ^7Li was also mostly destroyed by HBB but it was initially produced, before the HBB temperature reached high temperatures. Its abundance reached a peak of $\log(Y) \sim -8$ before plummeting to ~ -15 . The final yield was between these two extremes, being ~ -10.2 which, coincidentally, is very close to the initial (primordial) abundance of -10.4 .

The final yield of ^4He was $X_{\text{He4}} = 0.34$, an increase of $\sim 40\%$ over the initial (primordial) value of 0.245. About 70% of this increase was a product of second DUP whilst the rest occurred via HBB of H on the AGB. This is quite a large increase (especially for a $2 M_{\odot}$ star) and represents another significant nucleosynthetic signature of this model. The He increase was at the expense of ^1H which is present in the yield at the level of $X_{\text{H}} = 0.66$, down from an initial value of 0.75, roughly a 10% decrease.

In Figure 6.30 we display the chemical yield relative to the solar composition (in elemental form rather than isotopic). This gives some perspective on the chemical makeup of the yield for this star. ^{14}N still remains dominant when scaled in this manner, being ~ 0.8 dex higher than the solar ratio. Helium is substantially super-solar and Na is just below solar (only ~ 0.2 dex lower).

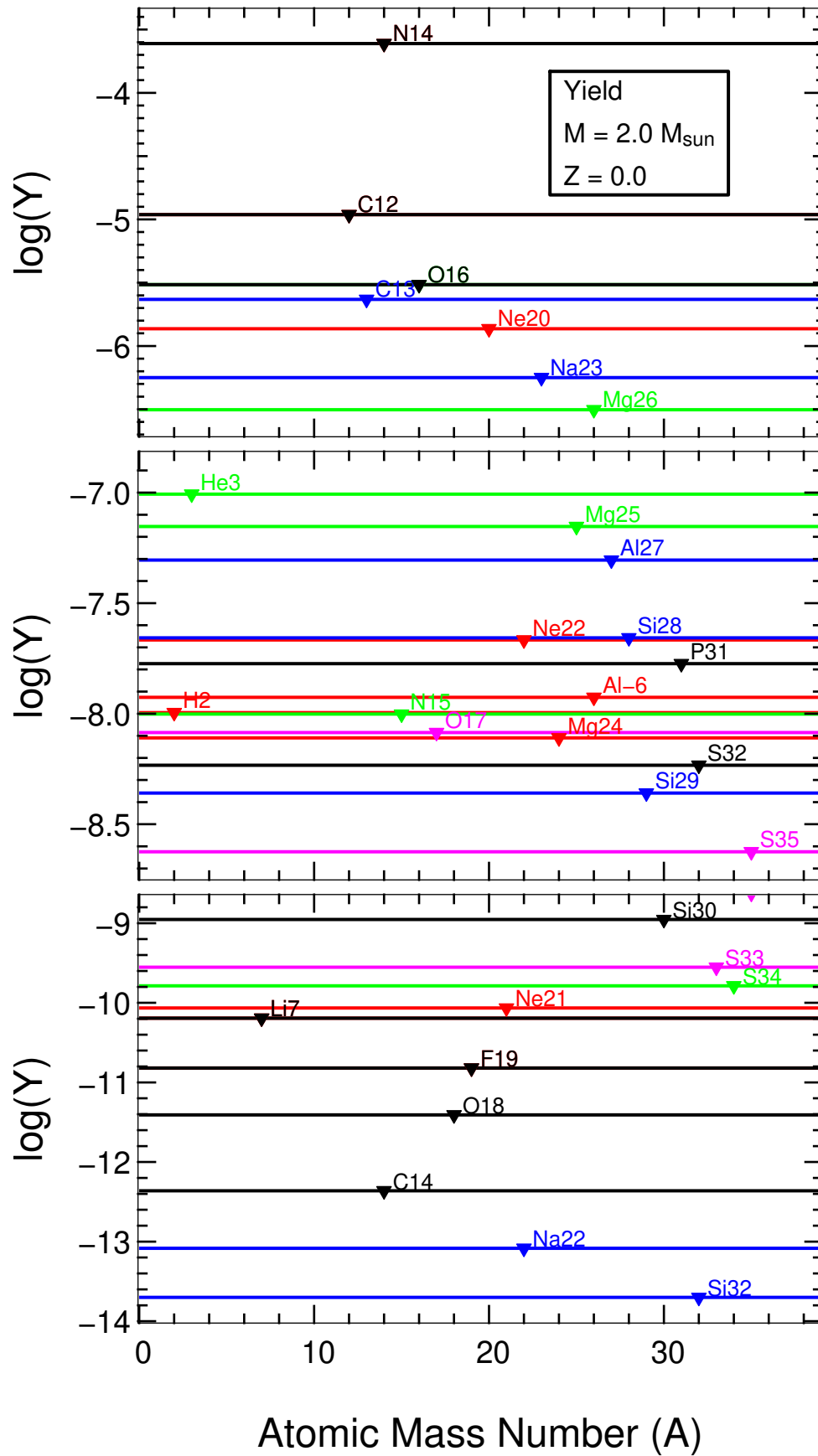


Figure 6.29: The yield of every species except ^1H and ^4He that was included in the network (which have abundances of $\log(Y) > -14$). ^{14}N is the dominant product, followed by ^{12}C , ^{16}O , ^{13}C and ^{20}Ne .

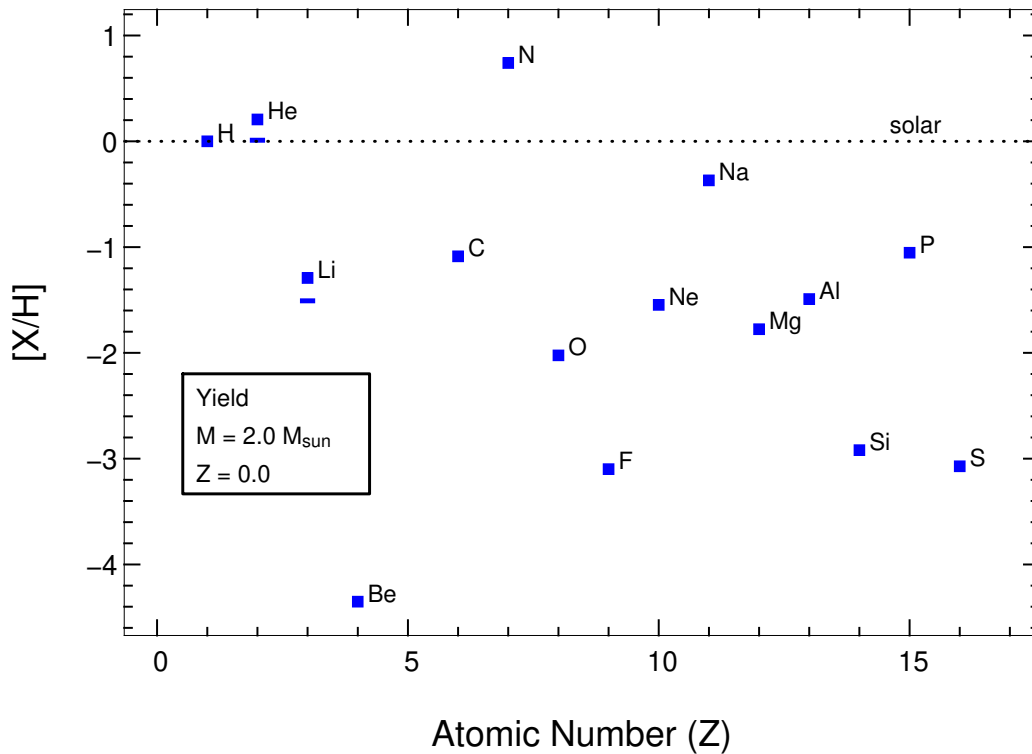


Figure 6.30: The yield for all the elements included in the network (that have abundances $[X/H] > -5$), relative to solar. Solar abundances are from [Lodders \(2003\)](#). Small horizontal lines indicate the initial abundances for H, He and Li (all others were zero initially). It can be seen that He has increased to a super-solar value. ^{14}N is very abundant compared to the solar N/H , being ~ 0.8 dex higher. The rest of the elements remain substantially sub-solar, except for Na which is only about 0.2 dex lower than the solar value. Interestingly Li remains close to its initial (primordial) value.

As mentioned earlier Li remains close to its initial primordial value. Carbon and P are the next most abundant relative to solar, being about 1 dex sub-solar. Oxygen is quite low – despite its large production during the DSFs – as it was cycled to N during the HBB phase of the AGB.

Finally we note that, if we had included reactions and species pertaining to the s-process, there may have been an additional s-process signature in the yield. This processing would have occurred during the DSFs and normal He shell flashes on the AGB (see previous subsections for more detail).

6.4 Summary of All $Z = 0$ Models and Yields

Here we *briefly* discuss the nucleosynthetic evolution of the remaining two $Z = 0$ models, which have masses of 1 and 3 M_{\odot} . We then go on to present all the yields for the four stars, in graphical and tabular form.

Some structural properties of the 1 M_{\odot} and 3 M_{\odot} models are given in Section 5.4 on page 156. The nucleosynthetic evolution of the models is discussed here in context with comparable models presented in the previous Sections. The 1 M_{\odot} experiences a dual core flash, much like the 0.85 M_{\odot} model. We thus class it as a low mass star. The 3.0 M_{\odot} does not experience a DCF but it does go through dual shell flashes and 3DUP (and HBB), much like the 2.0 M_{\odot} model just discussed in detail above. Thus we class this model as an intermediate mass star. We note that

the $3.0 M_{\odot}$ model had a slightly different starting composition to that of the other models. It was composed of a pure H-He mix, with $Y = 0.230$ (rather than 0.245). The reason we present this model instead of the $Y = 0.245$ one is because the $Y = 0.245$ model did not complete the AGB. Thus we cannot present the yield for that model. We note that the evolution of this model is quite similar to the $Y = 0.245$ model. Furthermore, as shall be discussed below, its yield closely resembles that of the $2 M_{\odot}$ model with $Y = 0.245$. This is despite the fact that it has significantly deeper third dredge-up. Similarities between the yields of the models such as this, and differences in the yields, are discussed when we present all the yields together at the end of this section.

6.4.1 Low Mass: The $1 M_{\odot}$ Model

In Figure 6.31 we show the surface evolution of the $1 M_{\odot}$ model, from just before the dual core flash to the end of the TP-AGB. It can be seen that the overall behaviour of this model is the same as that of the $0.85 M_{\odot}$ model (see Figure 6.2 on page 163). The surface retains its primordial abundance up until the DCF dredge-up, when Z_{cno} jumps to ~ 0.012 . We note that this is close to the solar metallicity. From then on the surface composition basically stays constant, reflecting the DCF DUP pollution. Only slight changes occur on the AGB as there is no 3DUP and only very minor HBB. In terms of the degree of pollution coming from the DCF episode, it is much higher in this model than in the $0.85 M_{\odot}$ model. In fact it is almost exactly one order of magnitude higher, as the $0.85 M_{\odot}$ model ended up with a surface pollution characterised by $Z_{cno} \sim 0.0012$. Regrettably we do not discuss the reasons behind this difference here, due to time and space constraints. Suffice to say that it must be due to a larger transfer of mass during the DCF. The degree of He enrichment is similar also, although slightly higher in the $1 M_{\odot}$ case ($Y = 0.33$ versus $Y = 0.30$ in the final yield). The distribution of the CNO elements is also similar, with ^{16}O and ^{14}N being the main products, followed by ^{12}C . These three species are however closer together in abundance in the $1 M_{\odot}$ model, with ^{16}O and ^{14}N being present in almost equal amounts. This also means that the C/N ratio is higher in this model than in the $0.85 M_{\odot}$ model. The $^{12}\text{C}/^{13}\text{C}$ ratio is also slightly higher in the $1 M_{\odot}$ model. Like the $0.85 M_{\odot}$ model ^{13}C and ^{17}O are the next most abundant species, having abundances of $\log(Y) \sim -4.5$ and -5.5 respectively. Interestingly the compositions diverge with regards to the less abundant species. The $1 M_{\odot}$ shows the signs of strong Ne-Na burning, manifested in the large abundances of ^{22}Ne and ^{23}Na , whilst the $0.85 M_{\odot}$ model has very low abundances of these species. This compositional difference appears to have arisen during the DCF. A further difference is seen in the Mg isotopes. In the $0.85 M_{\odot}$ model the isotopes follow the pattern: $^{26}\text{Mg} > ^{25}\text{Mg} > ^{24}\text{Mg}$ whilst in the $1 M_{\odot}$ model this pattern is reversed, such that ^{24}Mg is the most abundant isotope. Finally we note that the ^{28}Si abundance is much greater in the $0.85 M_{\odot}$ case (it is virtually non-existent in the $1 M_{\odot}$ model). Again, all these differences arise from the time of the DCF. That such different nucleosynthesis has come about in the two models, at least for the less abundant species, is very interesting. We shall explore these differences in future work, in particular exploring the dependence on overshoot.

Figure 6.32 displays the yield obtained from the $1 M_{\odot}$ model, for all species. As also seen in Figure 6.31 the yield naturally reflects the composition of the pollution from the DCF event, as

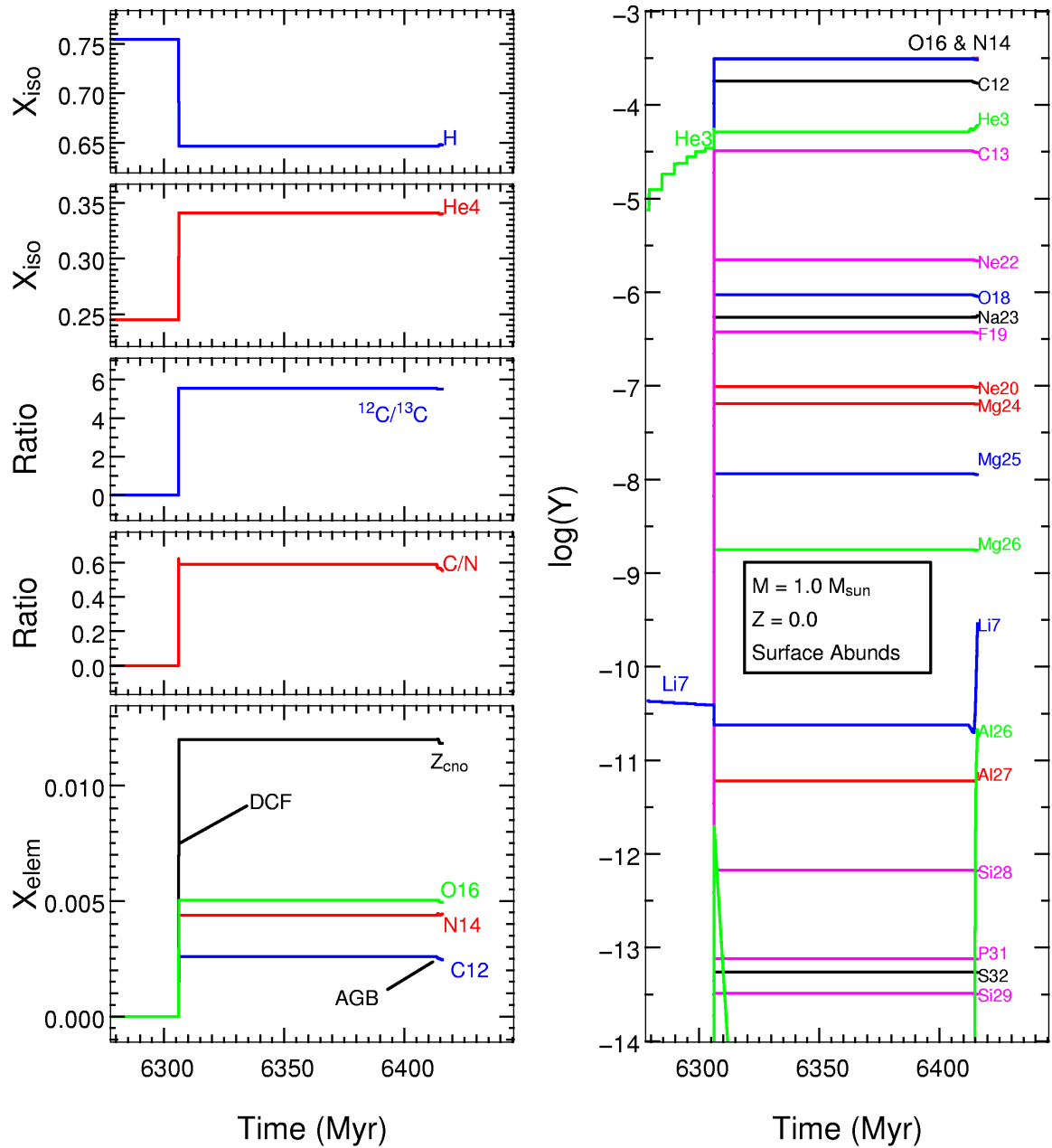


Figure 6.31: Time evolution of the surface abundances in the $1.0 M_{\odot}$, $Z = 0$ model (for selected species). It can be seen that the DCF dredge-up episode is by far the main source of envelope pollution, causing a large increase in He and CNO isotopes. The $^{12}\text{C}/^{13}\text{C}$ ratio is quite low, indicating that CN burning (almost) achieved equilibrium during the DCF episode. The only species produced in a significant amount during the AGB is ^7Li . We note that this star initially had $Z = 0$ but ends its evolution with $Z \sim$ solar (although it is still very metal-deficient in terms of the heavier elements).

no 3DUP and virtually no HBB occurred on the AGB.

6.4.2 Intermediate Mass: The $3 M_{\odot}$ Model

Figure 6.33 shows the evolution of the surface abundances for the $3.0 M_{\odot}$ model during the entire AGB phase. We note that this model had an initial composition of pure H and He, with $Y = 0.230$ rather than 0.245. This mainly affects the ${}^7\text{Li}$ abundance evolution but we note that ${}^7\text{Li}$ is easily destroyed by strong HBB on the AGB anyway. The chemical evolution of the surface is very similar to that of the $2 M_{\odot}$ model (see Figure 6.24 on page 192). The envelope is pristine up until the start of the TP-AGB, when a series of dual shell flashes occur. In the case of the $3 M_{\odot}$ model the pollution arising from its three DSFs is substantially smaller than that experienced by the $2 M_{\odot}$ model. In the $2 M_{\odot}$ model the surface Z_{cno} after the all the DSF episodes was $\sim 10^{-4}$, whereas in the $3 M_{\odot}$ model it was only $\sim 10^{-6}$. This difference appears to be immaterial however, as pollution from 3DUP soon overwhelms the DSF pollution in both cases. Furthermore, the high temperatures at the base of the convective envelope cause strong HBB, erasing most chemical signatures of the DSF episodes. In both models the dominant product is ${}^{14}\text{N}$, by a long margin (the next most abundant species is ${}^{12}\text{C}$, with an abundance ~ 1.5 dex lower). They are both ‘ ${}^{14}\text{N}$ giants’ for the HBB portion of the AGB. As discussed in the $2.0 M_{\odot}$ nucleosynthesis section ${}^{22}\text{Ne}$ is also periodically dredged up with the ${}^{12}\text{C}$. This then participates in the Ne-Na cycle/chain, producing ${}^{20}\text{Ne}$ and ${}^{23}\text{Na}$. Leakage out of this group of reactions then leads to further proton capture reactions in the the Mg-Al cycle, which gradually increases the Mg and Al abundances. ${}^{28}\text{Si}$ is also moderately produced.

The ${}^4\text{He}$ abundance is significantly increased in both models at second dredge-up and on the AGB. The increase in the abundance in the $3 M_{\odot}$ model is greater for each phase. The resultant $3 M_{\odot}$ yield has $Y = 0.41$ whilst that from the $2 M_{\odot}$ has $Y = 0.33$. In general the chemical evolution is very similar between the two models, the main difference being that the $3 M_{\odot}$ model has, in general, abundances ~ 0.5 dex lower than the $2 M_{\odot}$. This is due to the increased depth of 3DUP in this model – with λ up to 0.2 as compared to 0.01 in the $2 M_{\odot}$ model – as well as the increased number of thermal pulses. It is interesting to note that the $Y = 0.245$ $3 M_{\odot}$ model only had $\lambda \sim 0.01$, similar to the $2 M_{\odot}$ model. It thus appears that deeper 3DUP occurs with a lower helium abundance, although we note that the evolution of the $3 M_{\odot}$ $Y = 0.230$ model was not fully completed (λ may have increased later in the evolution). Another effect of the deeper 3DUP was to allow the ${}^{12}\text{C}/{}^{13}\text{C}$ ratio in the $3 M_{\odot}$ model to (temporarily) attain much higher values than in the $2 M_{\odot}$ model.

Figure 6.34 displays the yield obtained from the $3 M_{\odot}$ model, for all species. The yield reflects the processing that occurred during the TP-AGB, ie. the combination of 3DUP and HBB.

6.4.3 All $Z = 0$ Yields

Figures 6.35 to 6.38 display the chemical yield for our four models ($M = 0.85, 1.0, 2.0$ and $3.0 M_{\odot}$) in terms of elemental abundance relative to solar. We have redisplayed the figures from the 0.85 and $2.0 M_{\odot}$ sections for ease of comparison. The yields naturally split into two groups – the low mass stars (0.85 and $1.0 M_{\odot}$) and the intermediate mass stars (2.0 and $3.0 M_{\odot}$).

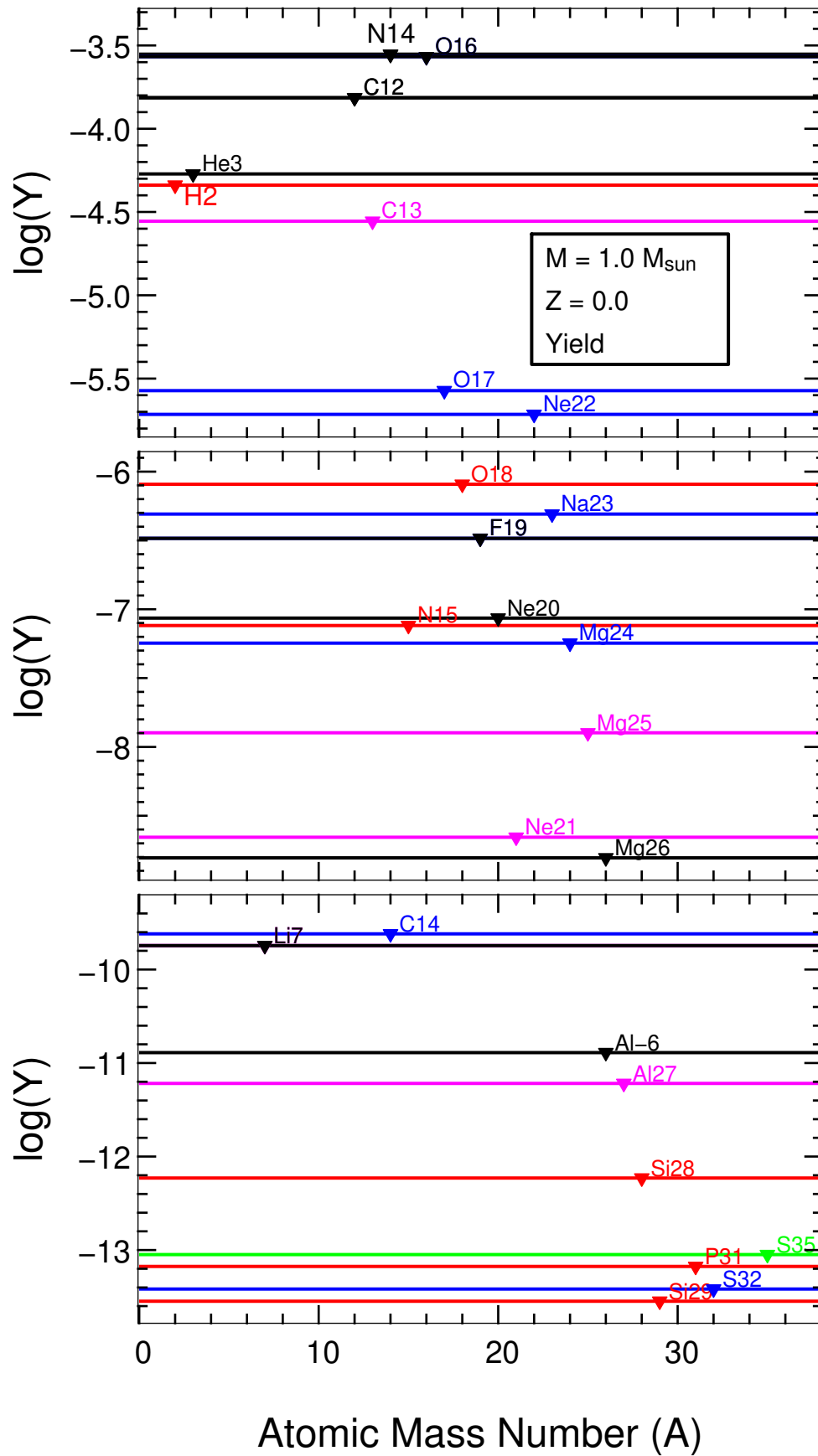


Figure 6.32: The yield from the $1 M_{\odot}$ model, in \log_{10} of mole fraction Y . All species used in the network are displayed (if their abundance is $> 10^{-14}$).

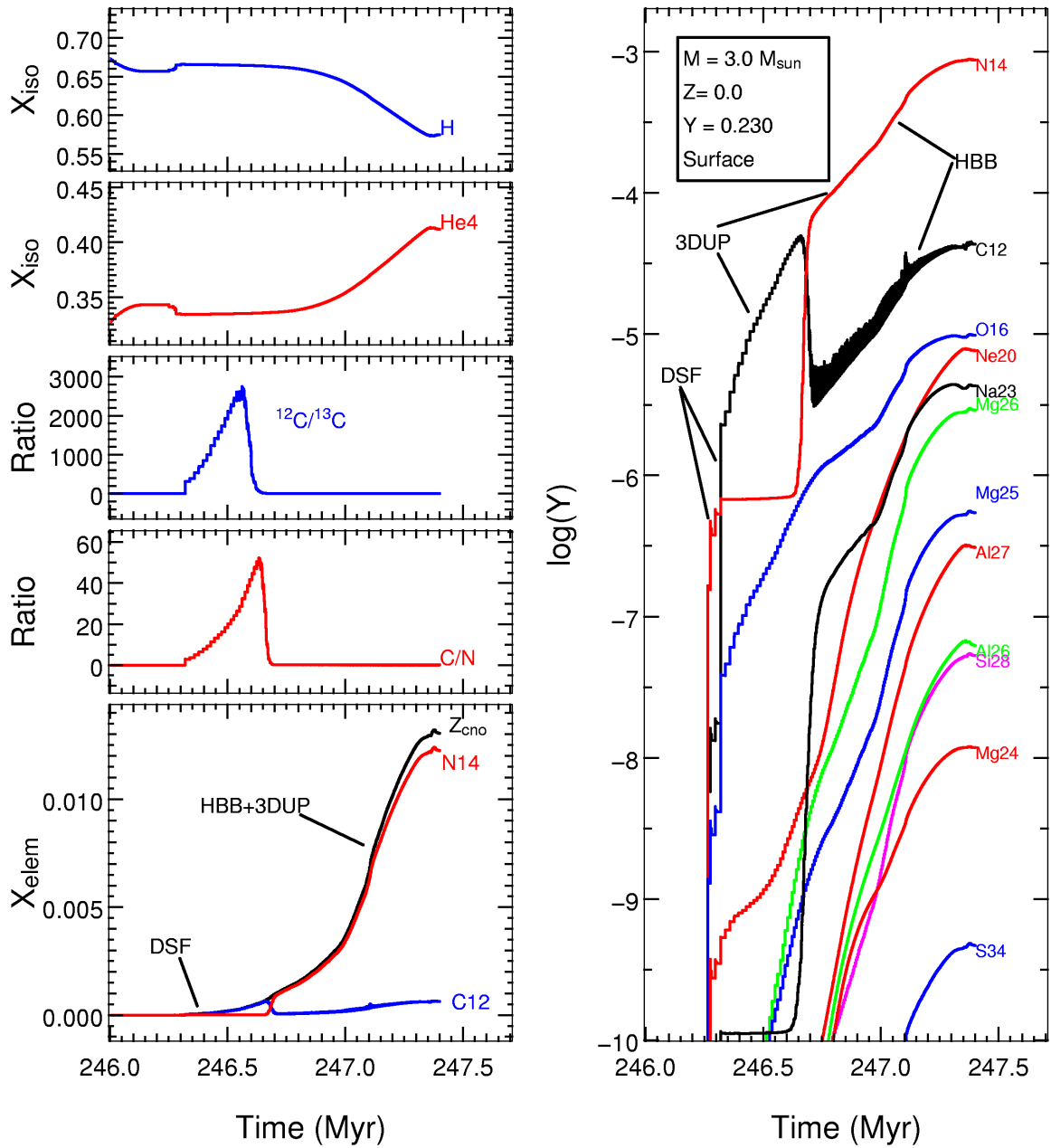


Figure 6.33: Time evolution of the surface abundances in the $3.0 M_{\odot}$, $Z = 0$ model (for selected species). The dominant contribution to surface pollution comes from the combined effects of HBB and 3DUP. As can be seen in the left-hand bottom panel the enrichment coming from the dual shell flash is insignificant compared to this. The onset of (significant) HBB is evident in the same panel by the strong $\text{C} \rightarrow \text{N}$ conversion. This star becomes a ‘nitrogen giant’ at this stage, as ^{14}N by far dominates the metal content of the envelope, just like in the $2 M_{\odot}$ model. It also dominates the yield as the majority of the mass loss occurs during this stage. Another consequence of the strong HBB is that the $^{12}\text{C}/^{13}\text{C}$ ratio is quite low. We note that this star initially had $Z = 0$ but ends its evolution with $Z_{\text{cno}} \sim \text{solar}$ (although it is still very metal-deficient in terms of the heavier elements).

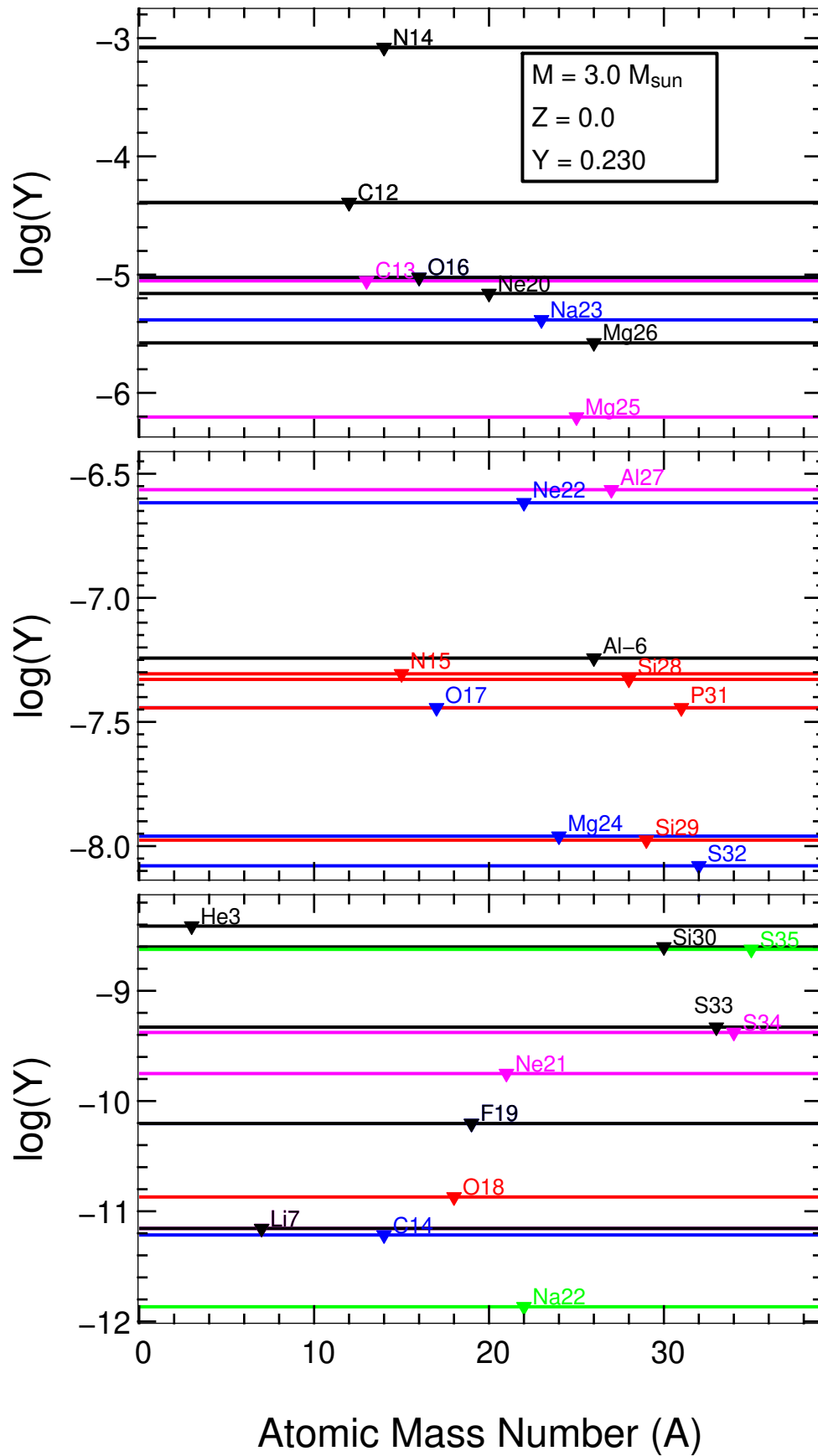


Figure 6.34: The yield from the $3 M_{\odot}$ model, in \log_{10} of mole fraction Y . All species used in the network are displayed (if their abundance is $> 10^{-14}$).

Low Mass Models

Comparing the two low mass stars similarities can be seen in the light elements. Helium is increased in both models (solely due to the DCF DUP, see eg. Figure 6.31), as is lithium. As mentioned earlier the degree of pollution from the DCF was greater in the $1 M_{\odot}$ model. This is reflected in the increased abundances of the CNO elements, such that N and O are both ~ 1 dex higher in this model. Thus the pattern of these elements is the same in both low mass stars. Carbon is substantially different however. Even accounting for the increased pollution in the $1 M_{\odot}$ model it is much more abundant in this model than the $0.85 M_{\odot}$ model. A larger divergence occurs in the heavier elements, starting from fluorine. In the $1 M_{\odot}$ model F, Ne, Na and Mg are all present in (relatively) large amounts, being a few orders of magnitude more abundant than in the $0.85 M_{\odot}$ model. Fluorine in particular is very abundant. In fact it is the most abundant species in these terms (relative to solar), being ~ 1 dex super-solar. Fluorine in the $0.85 M_{\odot}$ model is ~ 2 dex sub-solar by comparison. We note that it would be interesting to try and observe fluorine in the extremely metal-poor halo stars to give some constraints on this nucleosynthesis. Interestingly the heaviest elements (that are included in our network) are actually much more abundant in the $0.85 M_{\odot}$ model. Aluminium is ~ 3 dex higher. Silicon, P and S are present in modest amounts but virtually non-existent in the $1 M_{\odot}$ model (> 5 dex below solar). These differences are very interesting however, as mentioned earlier, we shall have to explore the detailed evolution of the $1 M_{\odot}$ model in a future study due to time and space constraints. In summary it appears that the yields for the low-mass models are similar in abundance pattern for elements lighter than F but diverge significantly for heavier elements. This must reflect the nucleosynthesis occurring in the DCF episodes, as it is this pollution that drives the surface composition and therefore yield.

Intermediate Mass Models

Moving on to the intermediate-mass model yields (Figures 6.37 and 6.38) we see that there is a striking similarity between the yield patterns of the 2.0 and $3.0 M_{\odot}$ models. All the elements expected from proton capture reactions are produced substantially: N, Ne, Na, Mg, Al, etc. There is however a difference in the degree of pollution. The $3 M_{\odot}$ model suffered somewhat more pollution than the $2 M_{\odot}$ model due to the deeper 3DUP. This is reflected in the ~ 0.5 dex increase in the yield of most species. The *lower* abundances of C and O in the $3 M_{\odot}$ model are readily understood in terms of the increased efficiency of HBB due to the higher temperatures at the base of the convective envelope in this higher mass model. The similarity between the yields of these models indicates that the yields of $Z = 0$ intermediate mass models are less uncertain than that of the low-mass models – if 3DUP and HBB occur. If 3DUP and HBB did not occur then the yields would probably reflect the pollution brought up by the dual shell flash episodes, much like the yields of the low-mass models reflect the DCF pollution. A more likely scenario is that HBB would operate on the DCF pollution, redistributing the nuclei and hence resulting in a different abundance pattern. However the occurrence of 3DUP and HBB in our models virtually erases the DSF pollution pattern, giving rise to the consistent abundance pattern between the models.

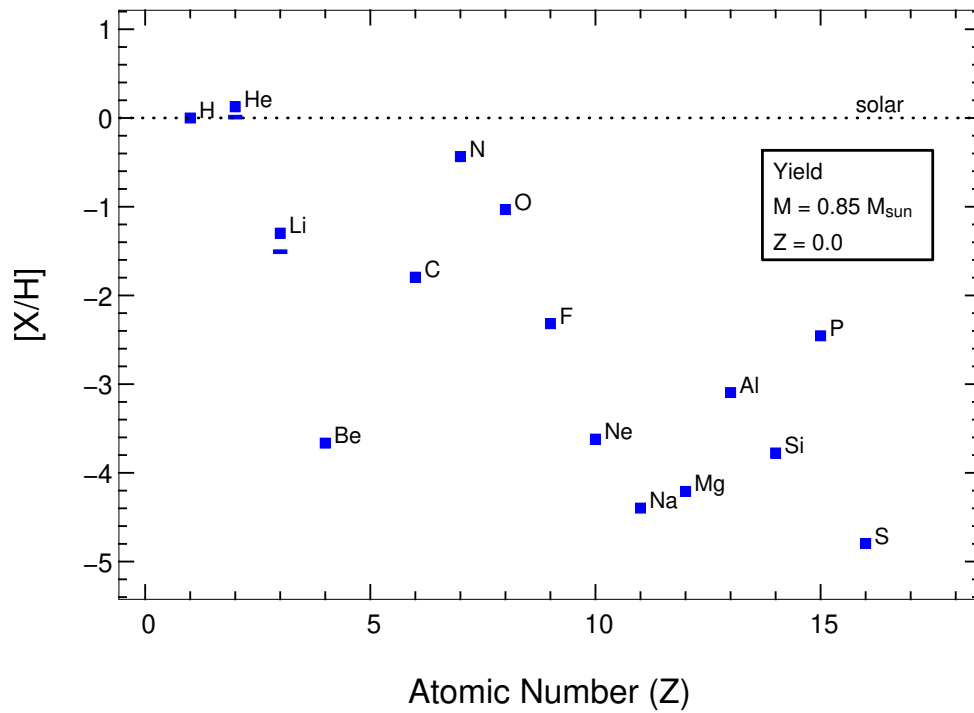


Figure 6.35: The yield for all the elements included in the network (that have abundances $[X/H] > -5$), relative to solar, for the $0.85 M_{\odot}$ model. Solar abundances are from [Lodders \(2003\)](#). Small horizontal lines indicate the initial abundance for H, He and Li (all others were zero initially). Note that the Fe group is not shown as these elements have zero yields (due to the limitations of the nuclear network – we shall expand the network in future studies).

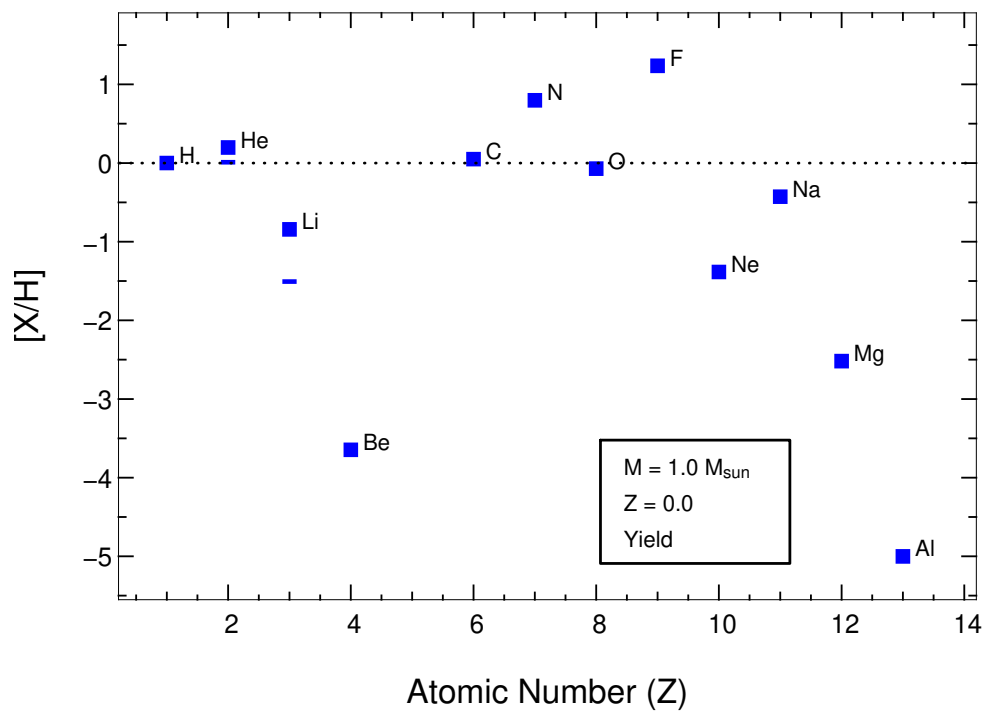


Figure 6.36: Same as Figure 6.35 but for the $1 M_{\odot}$ model.

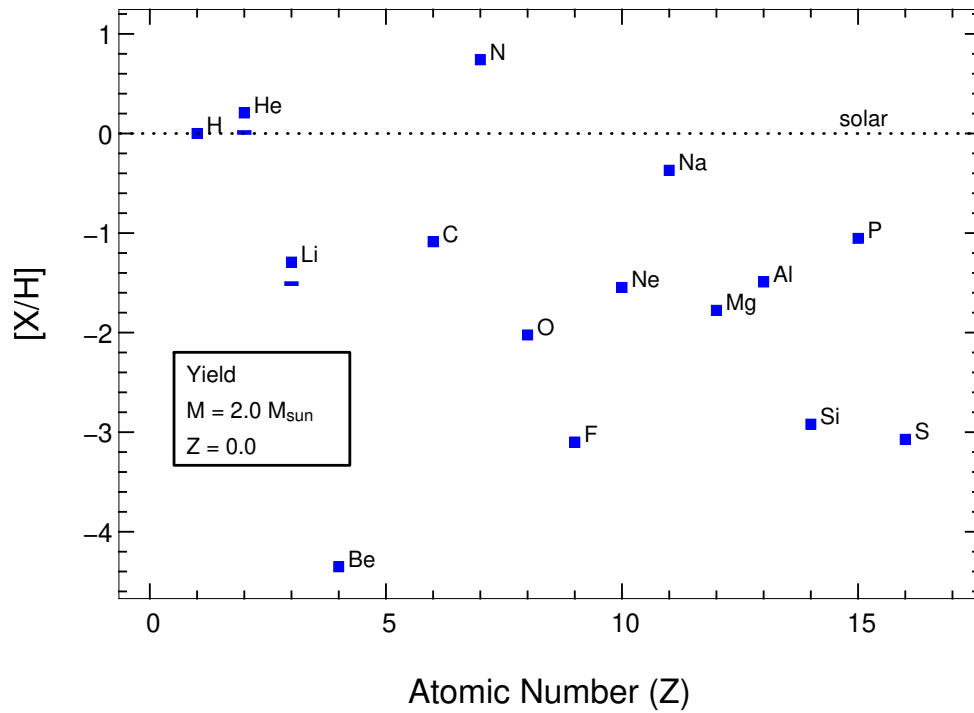


Figure 6.37: Same as Figure 6.35 but for the $2 M_{\odot}$ model.

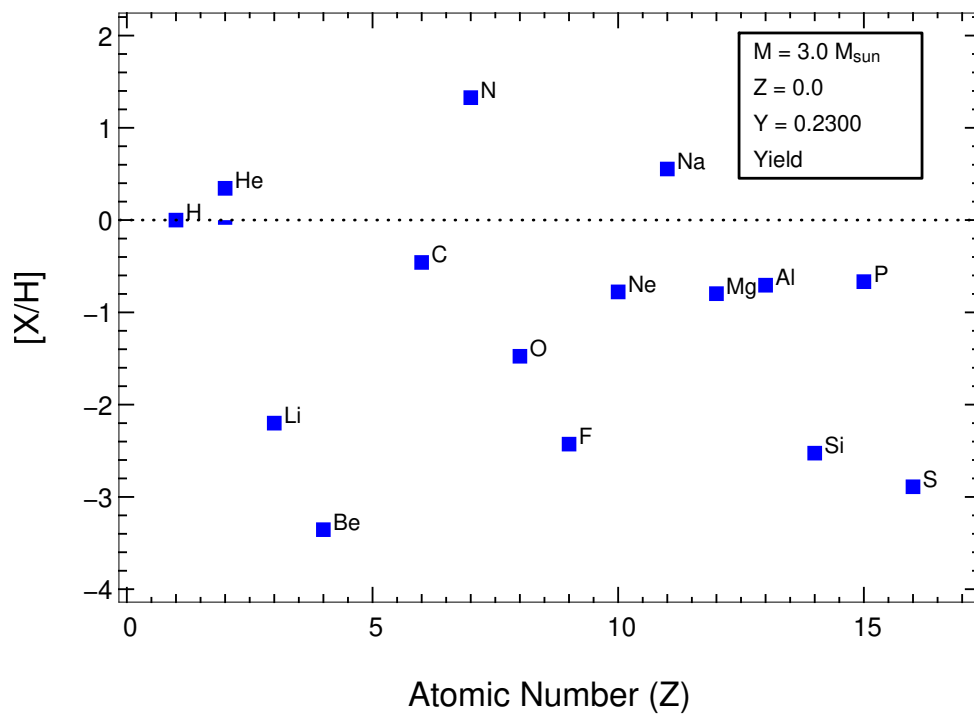


Figure 6.38: Same as Figure 6.35 but for the $3 M_{\odot}$ model. Note that this model started with a pure H-He composition, and with $Y = 0.230$ instead of 0.245.

Comparing All Models

We now compare the yields from all our $Z = 0$ models, to gain an overview of how the ejecta composition varies with mass. Figures 6.39 and 6.40 display the yields of all stars in mass fraction X . Some of the lighter, more easily burnt species follow a trend of decreasing in abundance with mass (eg. ${}^3\text{He}$, ${}^7\text{Li}$, ${}^2\text{H}$). However the abundances of most species follow a pattern of increasing with stellar mass. This is particularly evident in Figure 6.40 which displays the heavier nuclides. This is unexpected as the evolution leading to the surface pollution was quite different between the two mass ranges – the LM stars are (almost) solely polluted by the DCF event, whilst the IM stars undergo the (similar) DSF event but their surface pollution is dominated by 3DUP and HBB. The exception to this general trend is the $1 M_{\odot}$ model in which, as mentioned earlier, the heavier species are only present in very low abundances but the lower mass species are quite abundant. For example ${}^{12}\text{C}$ and ${}^{22}\text{Ne}$ are very abundant in this model but ${}^{28}\text{Si}$ is almost non-existent. As mentioned earlier we shall investigate the details of the nucleosynthetic evolution of the $1 M_{\odot}$ model as a future study.

An interesting piece of information to glean from comparing these yields would be to find a chemical signature (or signatures) that could be used to separate the LM models from the IM models. There appear to be a few possibilities. It can be seen that the LM models do not destroy the very light elements ${}^2\text{H}$ and ${}^3\text{He}$, whilst the IM stars do. In fact there is an increase above the primordial value of ${}^3\text{He}$ in the low mass stars. ${}^{16}\text{O}$ may be another tracer, as it is higher in the LM stars, but we note that there is only 0.5 dex difference between the $0.85 M_{\odot}$ model and the $3 M_{\odot}$ model. ${}^{26}\text{Mg}$ looks like the best candidate, as its abundance is ~ 3 dex lower in both the LM stars. ${}^{20}\text{Ne}$ is similar, but with only a ~ 1 dex separation.

In order to give some perspective on the yields we also present them relative to the solar abundances in Figures 6.41 and 6.42. Here we have used the usual notation:

$$[\text{Y}/\text{H}] = \log_{10} \left(\frac{N_{\text{Y}}}{N_{\text{H}}} \right)_{\text{Star}} - \log_{10} \left(\frac{N_{\text{Y}}}{N_{\text{H}}} \right)_{\odot} \quad (6.1)$$

where Y represents the particular species and N is the mole fraction. We present the yields relative to H as there is no Fe in these models. In these terms carbon is below solar in all cases except the $1 M_{\odot}$ model, in which the abundance is almost exactly solar. Nitrogen is generally super-solar, with the exception of the $0.85 M_{\odot}$ model, which is only 0.5 dex lower than solar. Oxygen is generally lower than solar, except again for the $1 M_{\odot}$ model which is \sim solar. Interestingly Na is roughly solar in all the models except for the $0.85 M_{\odot}$ model. The $1 M_{\odot}$ model has an anomalous F abundance, being ~ 1 dex super-solar, whilst in the other models' yields it is well below solar (~ 2 dex subsolar). As noted earlier observations of F in EMP halo stars could be useful for discriminating between these two cases.

Finally, in Table 6.2 we present the yields for all the $Z = 0$ models and all the species, in tabular form. The yields are given in mass fraction. We compare the yields to observations in Chapter 9.

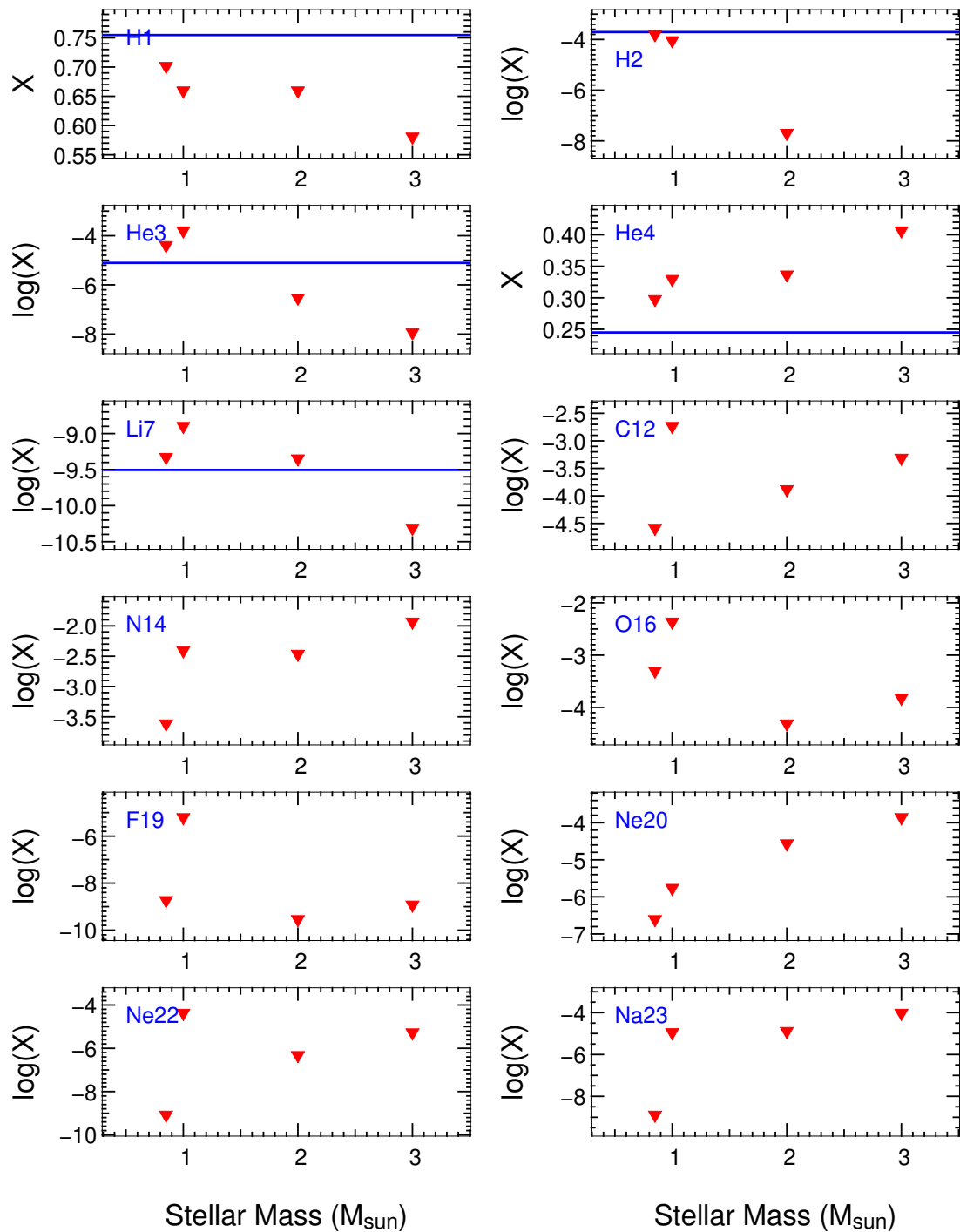


Figure 6.39: Yields of selected species against initial stellar mass, for all the $Z = 0$ models. More species are given in the next figure. Yields are given in log of mass fraction X , except for ^1H and ^4He which are given as X . The solid horizontal lines (blue) represent the initial abundances for the H, He and Li nuclides (all others were zero initially). We note that the 3 M_{\odot} model started with a pure H-He composition, with $X_{\text{He4}} = 0.230$ rather than 0.245.

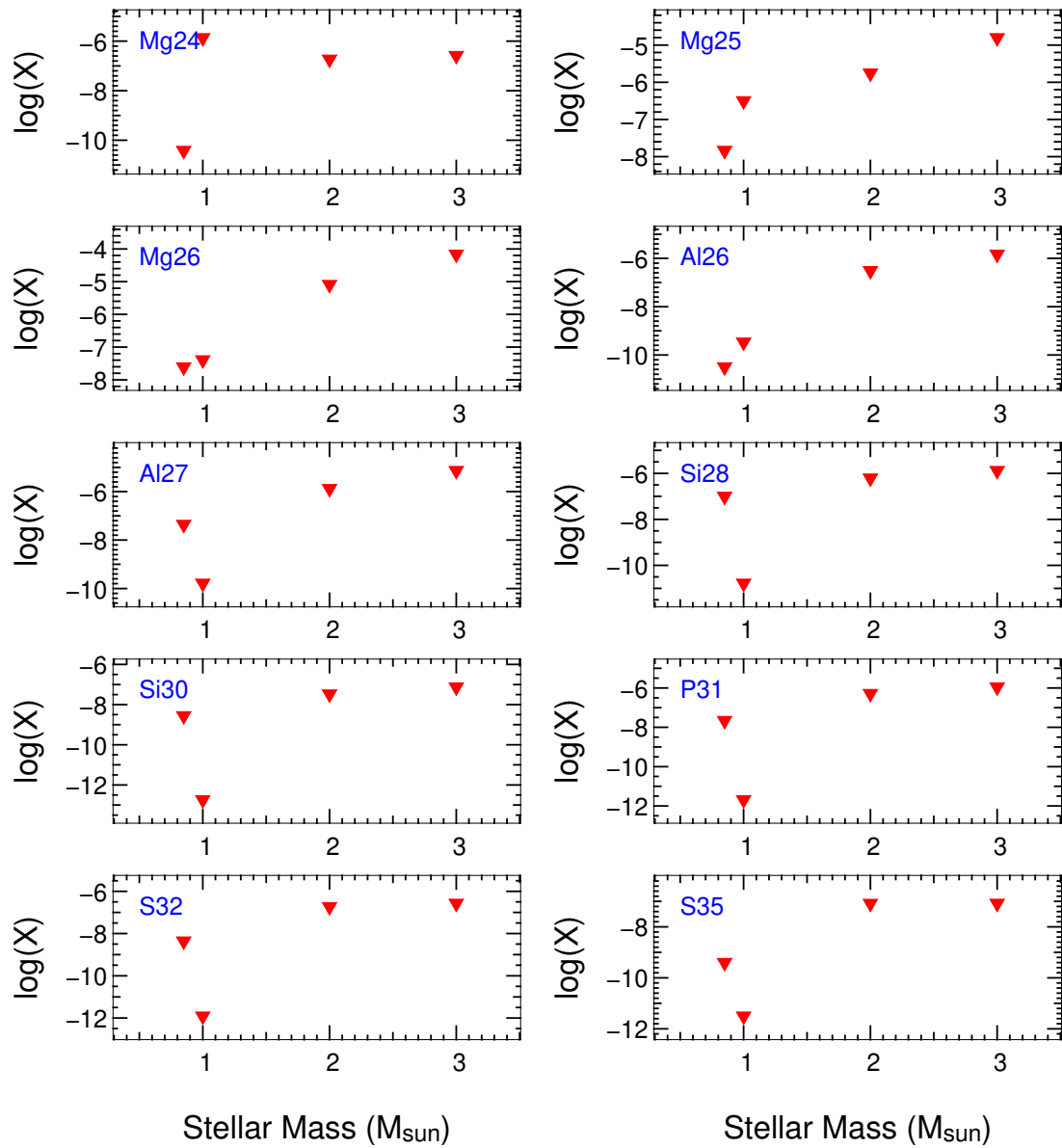


Figure 6.40: Same as Figure 6.39 except for the heavier species. Note that the Fe group is not shown as these elements have zero yields (due to the limitations of the nuclear network – we shall expand the network in future studies).

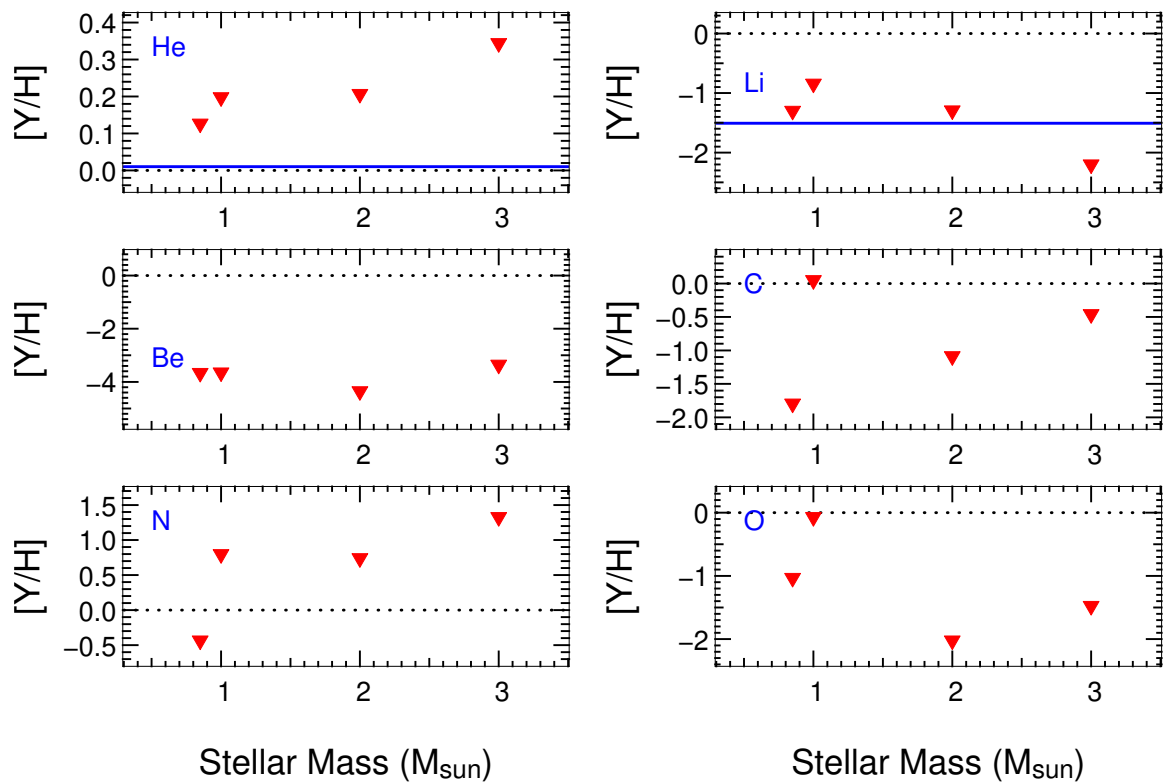


Figure 6.41: Elemental yields against initial stellar mass, for all the $Z = 0$ models. The rest of the elements are given in the next figure. Yields are given relative to solar (see Equation 6.1 for the definition of $[Y/H]$). Solar abundances are from Lodders (2003). The solid horizontal lines (blue) represent the initial abundances for He and Li (all others were zero initially). Dotted horizontal lines at $[Y/H] = 0$ indicate solar composition. We note that the $3 M_{\odot}$ model started with a pure H-He composition, with $X_{\text{He}4} = 0.230$ rather than 0.245.

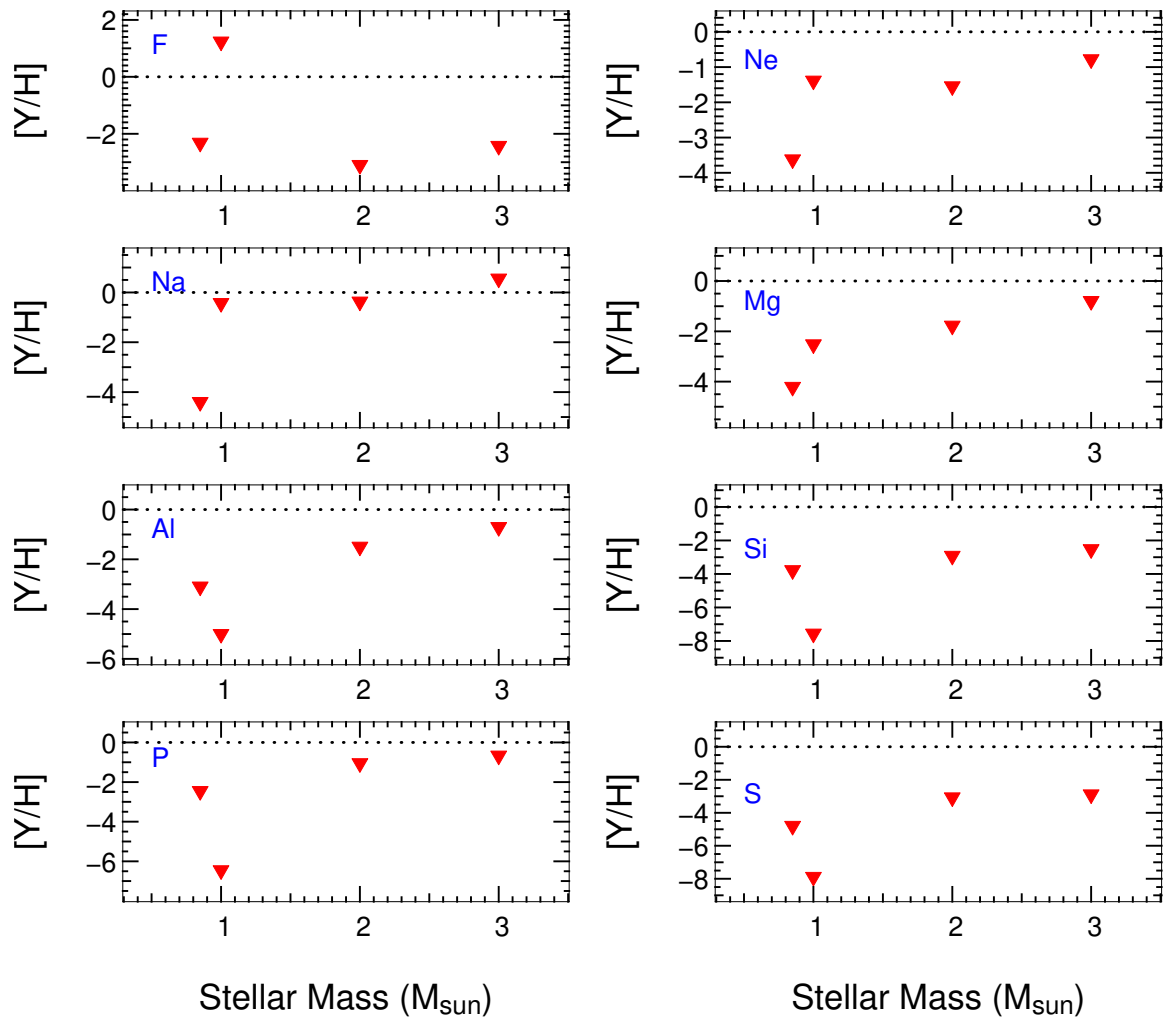


Figure 6.42: Same as Figure 6.41 except for the heavier elements. Note that the Fe group is not shown as these elements have zero yields (due to the limitations of the nuclear network – we shall expand the network in future studies).

Table 6.2: Yields and initial composition for all the $Z = 0$ models. All species in the network are listed. Abundances are in mass fraction, normalised to 1.0. The remnant masses (white dwarf masses) are in brackets below the initial stellar masses in the table header.

Nuclide	Initial Abund. ^a	0.85 M_{\odot} (0.776)	1.0 M_{\odot} (0.843)	2.0 M_{\odot} (1.080)	3.0 M_{\odot} (1.101)
h1	0.7548	0.701	0.660	0.660	0.581
h2	1.960E-04	1.57E-04	9.17E-05	2.02E-08	3.34E-18
he3	7.851E-06	4.04E-05	1.60E-04	2.95E-07	1.16E-08
he4	0.2450	0.298	0.330	0.337	0.407
li7	3.130E-10	4.70E-10	1.26E-09	4.49E-10	4.88E-11
be7	0.0	2.73E-14	2.68E-14	5.27E-15	4.61E-14
b8	0.0	1.65E-27	7.54E-27	6.34E-27	1.50E-27
c12	0.0	2.60E-05	1.84E-03	1.31E-04	4.88E-04
c13	0.0	7.78E-06	3.62E-04	3.03E-05	1.15E-04
c14	0.0	3.72E-12	3.37E-09	6.09E-12	8.53E-11
n13	0.0	0.0	0.0	0.0	0.0
n14	0.0	2.44E-04	3.92E-03	3.43E-03	1.17E-02
n15	0.0	9.10E-09	1.14E-06	1.49E-07	7.41E-07
o14	0.0	0.0	0.0	0.0	0.0
o15	0.0	0.0	0.0	0.0	0.0
o16	0.0	5.03E-04	4.33E-03	4.88E-05	1.52E-04
o17	0.0	7.40E-06	4.55E-05	1.40E-07	6.13E-07
o18	0.0	3.25E-08	1.46E-05	7.03E-11	2.42E-10
o19	0.0	0.0	0.0	0.0	0.0
f17	0.0	0.0	0.0	0.0	0.0
f18	0.0	0.0	0.0	0.0	0.0
f19	0.0	1.85E-09	6.22E-06	2.88E-10	1.19E-09
f20	0.0	0.0	0.0	0.0	0.0
ne19	0.0	0.0	0.0	0.0	0.0
ne20	0.0	2.48E-07	1.73E-06	2.74E-05	1.39E-04
ne21	0.0	6.77E-12	4.64E-08	1.81E-09	3.73E-09
ne22	0.0	8.33E-10	4.24E-05	4.74E-07	5.32E-06
na21	0.0	0.0	0.0	0.0	0.0
na22	0.0	2.30E-26	4.86E-17	1.81E-12	2.99E-11
na23	0.0	1.29E-09	1.13E-05	1.29E-05	9.54E-05
na24	0.0	0.0	0.0	0.0	0.0
mg23	0.0	0.0	0.0	0.0	0.0
mg24	0.0	3.84E-11	1.36E-06	1.86E-07	2.63E-07
mg25	0.0	1.46E-08	3.17E-07	1.76E-06	1.56E-05
mg26	0.0	2.47E-08	4.06E-08	8.16E-06	6.89E-05
mg27	0.0	0.0	0.0	0.0	0.0
al25	0.0	0.0	0.0	0.0	0.0
al-6	0.0	3.18E-11	3.36E-10	3.08E-07	1.49E-06
al*6	0.0	0.0	0.0	0.0	0.0
al27	0.0	4.39E-08	1.63E-10	1.34E-06	7.36E-06
al28	0.0	0.0	0.0	0.0	0.0
si27	0.0	0.0	0.0	0.0	0.0
si28	0.0	1.00E-07	1.65E-11	6.17E-07	1.31E-06
si29	0.0	1.16E-08	8.23E-13	1.27E-07	3.06E-07
si30	0.0	2.77E-09	1.83E-13	3.34E-08	7.49E-08
si31	0.0	0.0	0.0	0.0	0.0

Continued on next page...

^aExcept for the 3.0 M_{\odot} model which started with a pure $^1\text{H} + ^4\text{He}$ composition ($Y = 0.230$).

^bNote that there is a gap in the network between ^{35}S and ^{56}Fe , such that further nucleosynthesis is not possible with $Z = 0$ initial composition.

^cg is a synthetic species that ends the nuclear network. It gives an approximate indication of the expected yield of species heavier than ^{56}Ni . Due to the gap in the network at ^{35}S this yield will always be zero with $Z = 0$ initial composition.

Table 6.2 – continued from previous page.

Nuclide	Initial Abund.	0.85 M_{\odot} (0.776)	1.0 M_{\odot} (0.843)	2.0 M_{\odot} (1.080)	3.0 M_{\odot} (1.101)
si32	0.0	8.70E-21	7.99E-25	6.37E-13	2.20E-12
si33	0.0	0.0	0.0	0.0	0.0
p29	0.0	0.0	0.0	0.0	0.0
p30	0.0	0.0	0.0	0.0	0.0
p31	0.0	2.20E-08	2.07E-12	5.22E-07	1.12E-06
p32	0.0	3.38E-24	3.10E-28	2.47E-16	8.55E-16
p33	0.0	0.0	0.0	4.75E-24	4.23E-22
p34	0.0	0.0	0.0	0.0	0.0
s32	0.0	4.38E-09	1.22E-12	1.87E-07	2.66E-07
s33	0.0	6.24E-10	3.36E-14	9.23E-09	1.54E-08
s34	0.0	2.19E-10	1.32E-13	5.56E-09	1.42E-08
s35 ^b	0.0	3.98E-10	3.13E-12	8.31E-08	8.31E-08
fe56	0.0	0.0	0.0	0.0	0.0
fe57	0.0	0.0	0.0	0.0	0.0
fe58	0.0	0.0	0.0	0.0	0.0
fe59	0.0	0.0	0.0	0.0	0.0
fe60	0.0	0.0	0.0	0.0	0.0
fe61	0.0	0.0	0.0	0.0	0.0
co59	0.0	0.0	0.0	0.0	0.0
co60	0.0	0.0	0.0	0.0	0.0
co61	0.0	0.0	0.0	0.0	0.0
ni58	0.0	0.0	0.0	0.0	0.0
ni59	0.0	0.0	0.0	0.0	0.0
ni60	0.0	0.0	0.0	0.0	0.0
ni61	0.0	0.0	0.0	0.0	0.0
ni62	0.0	0.0	0.0	0.0	0.0
g ^c	0.0	0.0	0.0	0.0	0.0

Chapter 7

Metal Poor Halo Star Models

“If we knew what it was we were doing, it would not be called research, would it?”
–Albert Einstein

7.1 Background

7.1.1 Introduction

One of the theories put forth to explain the extremely low metallicities and strange abundance patterns observed in many Galactic Halo stars (see [Beers and Christlieb \(2005\)](#) for a recent review of the observations) is that some of them may have formed from a primordial gas cloud that had only been polluted by a few – or even one – Pop III supernovae. Such a dilution of supernova ejecta allows the iron content of a star forming from this material to be very low, and, depending on the supernova mass, may explain some of the observed abundance patterns (see eg. [Shigeyama and Tsujimoto 1998](#); [Umeda and Nomoto 2002](#); [Limongi et al. 2003](#); [Zijlstra 2004](#)). It has also often been suggested that the shocks from the first SNe may have triggered the formation of these low-mass stars in primordial gas clouds.

Another scenario utilises supernovae to provide the heavy element distribution, whilst the lighter elements are provided by the low-mass stars themselves, via some form of auto-pollution (such as the dual shell flash or dual core flash, see eg. [Fujimoto et al. 2000](#); [Schlattl et al. 2002](#); [Picardi et al. 2004](#); [Weiss et al. 2004](#)), or perhaps via mass transfer from a low- Z binary companion (see eg. [Suda et al. 2004](#)).

In this chapter we seek to explore the expected chemical signatures of low- and intermediate-mass stars that may have formed from a gas cloud polluted by a single supernova. To this end we have calculated a grid of stellar models of very low and extremely low metallicity which have an initial abundance pattern arising from the mixing of a $Z = 0$ supernova yield (as given by a theoretical calculation, see below for details) with Big Bang material.

Our modifications to the structural evolution code (SEV code) detailed in [Chapter 4](#) have enabled us to model extremely metal-deficient and metal-free stars such as these. As described in the $Z = 0$ stellar evolution chapters there exists a number of evolutionary features peculiar to $Z = 0$ and extremely low metallicity stars that require the use of time-dependent mixing. The two most

important of these are the two proton ingestion episodes (PIEs) that are induced by helium flash convection breaking through to hydrogen-rich regions. We refer to these events as the dual core flash (DCF) and dual shell flash (DSF). The DCF occurs at the time of the core He flash in low mass models whilst the DSF occurs during the first major He shell flash at the beginning of the TP-AGB in intermediate mass models (sometimes more than one DSF occurs). Although these events have been modelled before by other authors they are still relatively unexplored phenomena as not many studies have evolved through these difficult phases. These two events are pivotal as they provide considerable pollution of the envelope and could provide the source of the large amounts of C, N and O observed in the C-enhanced metal poor halo stars (CEMPHS, see eg. Aoki et al. (2007) for current observations and eg. Suda et al. 2004; Fujimoto et al. 2000; Schlattl et al. 2001 for theoretical calculations). We note that the DCF and DSF are notoriously difficult to evolve though numerically and have provided a serious challenge for the author (and indeed previous authors!).

As mentioned in the $Z = 0$ chapters the novelty in this study is that we have also taken (most) of our models through to the completion of the AGB. To the best of our knowledge this is the first time this has been achieved for stars of such low metallicity. This allows us to make a range of interesting predictions, such as the expected white dwarf masses, the lifetimes of the various stages of evolution, and the chemical yields of extremely metal poor low- and intermediate-mass stars. As also mentioned in the $Z = 0$ section we should however add a caveat here. The models suffer from the usual uncertainties such as that which derives from the use of the Mixing Length Theory of convection, the neglect of rotation, and the choice of mass-loss formalism. With this in mind we shall compare our models with observations of the Galactic Halo stars in a later chapter.

7.1.2 Brief Overview of Code Inputs

Apart from the initial composition all of the physical parameters used for the structural evolution of these models were exactly the same as those used for the $Z = 0$ models presented in the previous two chapters. We thus refer the reader to the introduction of Chapter 5 on page 88 for a detailed description of the included physics (mass loss, opacity, etc.). Some key physical inputs are however important enough to warrant a brief reiteration here.

Convective Boundaries and Mixing

We have employed the new diffusive mixing routine in all our metal-deficient models, for all phases of evolution. For details on this routine see Section 4.1 on page 49. As with the $Z = 0$ models we do not include any overshoot beyond the classical Schwarzschild boundary. Thus our models are *conservative* in terms of the amount of mixing that occurs during episodes such as the DCF, DSF and third dredge-up.

Mass Loss

Mass loss is one of the most uncertain factors in stellar modelling. We have discussed the methods employed in the SEV code in Subsection 3.1.3 on page 41 but provide a brief discussion

here also, in relation to the special case of very- and extremely-low metallicity.

First we note that the interested reader will find a more detailed discussion on mass loss in the introduction to the chapter dealing with the structural evolution of the $Z = 0$ models (in particular Section 5.1.2 on page 89). That section gives some extra background on mass loss in general, and in relation to metal-free stars.

As with $Z = 0$ stars one may expect very metal-deficient stars to be less susceptible to mass loss due to the lack of metals from which grains could form. This expectation is based on the assumption that mass loss occurs (only) through radiation pressure acting on grains. As noted in Section 5.1.2 on page 89 this may or may not be a valid assumption since, in reality, the mechanisms for mass loss are not yet properly understood. Nevertheless we shall continue our discussion with this assumption, but keep this caveat in mind.

Similar evolutionary traits are found in our metal deficient models as those found in the $Z = 0$ models. In particular almost all of our models experience self-enriching episodes (namely the DCF and DSF discussed in the previous chapters and also within this chapter). This raises the metallicity of the envelope to values similar to that of the LMC (and in some cases much higher). As AGB mass loss has been observed in the LMC it follows that grains are able to form at these metallicities (assuming this is necessary for mass loss). Thus it would seem that a standard mass-loss formalism would be needed for stages of evolution occurring after the self-enriching episodes. In the low-mass models ($M \leq 1 M_{\odot}$) these episodes occur at the tip of the RGB, so that in the subsequent evolutionary phases (HB, AGB) the star has a ‘metal-rich’ surface. Thus for these stages we suggest that it is reasonable to use the standard mass-loss formulae. In the IM mass models the main polluting event, the DSF, occurs at the start of the AGB. In these cases the envelope is enriched by a more modest amount (lower than the LMC metallicity), such that the normal mass loss prescriptions may not apply. However in all of the IM models 3DUP occurs, which, by the time the mass loss rate is significantly high, also enriches the surface by a large amount (to \sim LMC or super-LMC levels). Thus in this case also we suggest it is reasonable to use the standard mass-loss formulae. As the IM models do not in general go through the RGB phase (if they do then it is for a very brief period) it appears that the standard procedure used in the SEV code suffices for all the intermediate mass models (the [Vassiliadis and Wood \(1993\)](#) (VW93) formula for the AGB is the only one that will actually be utilised in this case).

In our low mass and lower metallicity models we find that the RGB phase is very short, as also reported for the $0.85 M_{\odot}$, $Z = 0$ model. In these cases the mass loss on the RGB is relatively small when compared to the total mass lost over the whole evolution, at least for our $1 M_{\odot}$ models (the $0.85 M_{\odot}$ models spend longer in the RGB phase). Thus, in these cases we suggest that using the standard mass-loss formulae introduces a small amount of uncertainty.

There is however one set of cases where the choice of mass loss prescriptions introduces a significant uncertainty. Unlike the $Z = 0$ and extremely metal-poor cases the RGB phases in our more metal-‘rich’ low-mass models are quite long. So long in fact that up to 90% of the mass lost from the star by the end of its evolution can be lost on the RGB (we note that we use the [Reimers \(1975\)](#) formula on the RGB, see Section 3.1.3 on page 41 for details). If this degree of mass loss is wrong then our results will be wrong. For example, since the mass lost on the RGB has the initial composition of the models, it is thus very metal-poor. This naturally has a

strong impact on the yields of these models, effectively diluting the yield from the AGB. If, in reality, the RGB mass loss should be much lower then our yields will be wrong – they should be more metal-rich. The RGB evolutionary paths of the models are also rendered uncertain as the rate of core growth would be different with a lower mass loss rate. This then has implications for the HB and RGB evolution. Thus many uncertainties arise through the unknown nature of mass-loss rates at low metallicity.

We note however that this uncertainty in the low-mass models is based on the assumption that the mass loss rate should reduce severely with metallicity, i.e. that mass loss occurs only via radiation pressure acting on grains. As mentioned above this may not be the case. Assuming for now (for the sake of argument) that this *is* the main mechanism for mass loss then one path that we could have taken, and that other studies have taken, would be to scale the mass loss rate with metallicity – such that at low metallicity the mass loss rate is lower. The question that then arises is: By what factor or function do we scale the rate? As mass loss is not yet fully understood theoretically, and there are no observations of mass loss at the very low metallicities in question, any scaling function would necessarily introduce uncertainties itself. So it appears that neither of the options – scaling the rate with Z or using the existing formulae – can be argued to minimise uncertainty in the modelling. With this in mind we have chosen the simplest option – to use the existing mass loss formalisms in the SEV code.

Finally we also note that the metallicity of a stellar model is, to some degree, indirectly taken into account in the Reimers' and VW93 formulas. This occurs because the entire structure of the models change with Z , through opacity and different nuclear burning energy sources (for example). Since the mass loss formulae utilise bulk physical properties there is thus a feedback from the composition of the star onto the mass loss rates. Some evidence for this arises during the presentation of results below, with regards to the horizontal branch and RGB mass evolution in the low mass models (Section 7.2.6).

Opacity Tables

We note that we have calculated opacity tables specifically for these metal-deficient models. This was done because the initial composition is not scaled-solar, whereas opacity tables are usually calculated for solar composition. Thus our models are self consistent inasmuch as the opacity composition matches the composition of the star. Most studies use scaled solar opacities as the differences arising in opacity are not thought to significantly affect the evolution of the models. In light of experience gained from the calculation of models for this study the Author now agrees with this approximation, at least for models with abundance profiles not too different from solar. We note however that it is now an easy task to calculate custom opacity tables for use with the SEV code by using the OPAL web service. See Section on page 79 for the web address and more details on opacity in the SEV code.

Nucleosynthesis Code Inputs

In regards to the nucleosynthesis code (NS code) only minor modifications were needed to be able to calculate the nucleosynthetic evolution of our metal-deficient models. Removing the

scaled-solar composition assumptions to allow arbitrary stellar chemical compositions was the main modification. Also, as we found many of the models experience Dual Core Flashes and Dual Shell Flashes, it was necessary to increase the resolution during these phases. This was mentioned in the $Z = 0$ chapter (see Section 6.1 on page 160 and references therein).

7.1.3 The Grid of Models

The range of mass for our small grid is:

$$M = 0.85, 1.0, 2.0, 3.0 M_{\odot}$$

and the range of metallicity:

$$[\text{Fe}/\text{H}] = -\infty, -6.5, -5.45, -4.0, -3.0$$

where we have included our $Z = 0$ models (as $-\infty$) since we shall be referring to these models in the present chapter for various comparisons. The peculiar value of $[\text{Fe}/\text{H}] = -5.45$ was chosen to match the metallicity (at least in terms of $[\text{Fe}/\text{H}]$) of the most metal poor star currently known – the Galactic Halo star HE1327-2326, (Frebel et al. 2005a).

In mass fraction of CNO nuclides the metallicities are:

$$Z_{\text{cno}} = 4 \times 10^{-9}, 4 \times 10^{-8}, 1 \times 10^{-6}, 1 \times 10^{-5}$$

which are very near the total Z value as the CNO nuclides are the dominant ‘metal’ species in the initial composition.

7.1.4 Initial Composition

The composition for these stars was arrived at by mixing the ejecta of a $20 M_{\odot}$, $Z=0$ supernova model with pristine Big Bang material. The Big Bang abundances are from the calculations by Coc et al. (2004), displayed in Table 7.1, whilst the supernova yield is from a calculation by Limongi et al. (2002, private communication) and is displayed in Table 7.2.

The variation in initial metallicity between the four sets of metal-deficient models was achieved by varying the amount of Big Bang material with which the supernova ejecta was diluted. For example, the $[\text{Fe}/\text{H}] = -4.0$ models required the supernova yield to be diluted into $1.0 \times 10^6 M_{\odot}$ of Big Bang material, whilst the $[\text{Fe}/\text{H}] = -3.0$ models required $1.0 \times 10^7 M_{\odot}$. We display the initial composition used in the SEV code calculations of the $[\text{Fe}/\text{H}] = -4.0$ set of models as an example in Table 7.3. The full composition, as used in the nucleosynthesis code (NS code), is given in Table 7.4. The abundance profiles for the other sets of models are basically scaled versions of this. Naturally the species provided by the Big Bang gas are roughly invariant between the sets of models. In particular this means that ${}^7\text{Li}$, ${}^3\text{He}$ and ${}^2\text{H}$ are always present in primordial amounts, as their abundance in the $Z = 0$ gas cloud far outweighs that produced by

Nuclide	Primordial Mass Fraction
^1H	0.754796
^2H	1.96×10^{-4}
^3He	7.85×10^{-6}
^4He	0.24500
^7Li	3.13×10^{-10}
^{12}C	0.0
^{14}N	0.0
^{16}O	0.0

Table 7.1: The chemical composition of the primordial gas cloud that the Pop III supernova pollutes. Taken from the Standard Big Bang Nucleosynthesis calculations by Coc et al. (2004). The $20 M_{\odot}$ supernova yield was diluted using this material.

Nuclide	Mass Frac.	Nuclide	Mass Frac.	Nuclide	Mass Frac.
H1	0.5453	Si29	6.84E-05	Ti50	2.98E-12
H2	3.63E-18	Si30	4.83E-05	V50	1.06E-11
He3	1.60E-06	P31	1.80E-05	V51	2.79E-07
He4	0.3506	S32	2.85E-03	Cr50	1.09E-06
Li6	1.40E-19	S33	1.35E-05	Cr52	8.55E-05
Li7	1.11E-11	S34	8.58E-05	Cr53	5.16E-06
Be9	1.99E-38	S36	5.93E-09	Cr54	1.69E-10
B10	2.06E-18	Cl35	4.27E-06	Mn55	1.55E-05
B11	1.23E-16	Cl37	1.40E-06	Fe54	1.11E-04
C12	2.26E-02	Ar36	4.64E-04	Fe56	7.86E-03
C13	2.30E-09	Ar38	2.31E-05	Fe57	2.38E-04
N14	3.93E-09	Ar40	1.29E-10	Fe58	4.84E-11
N15	2.25E-11	K39	1.12E-06	Co59	1.25E-04
O16	3.87E-02	K40	1.11E-09	Ni58	1.11E-04
O17	5.88E-10	K41	9.39E-08	Ni60	1.29E-07
O18	3.92E-09	Ca40	3.92E-04	Ni61	6.93E-10
F19	6.79E-11	Ca42	3.58E-07	Ni62	4.13E-13
Ne20	1.60E-02	Ca43	7.54E-10	Ni64	6.37E-20
Ne21	3.57E-06	Ca44	8.44E-06	Cu63	1.18E-14
Ne22	8.05E-07	Ca46	2.80E-13	Cu65	5.36E-14
Na23	2.13E-04	Ca48	1.10E-18	Zn64	8.10E-09
Mg24	7.16E-03	Sc45	3.52E-07	Zn66	7.31E-17
Mg25	7.78E-05	Ti46	1.77E-07	Zn67	1.73E-22
Mg26	8.59E-05	Ti47	4.16E-09	Zn68	1.02E-23
Al27	1.73E-04	Ti48	1.60E-05		
Si28	6.49E-03	Ti49	2.94E-07	Z_{total}	0.104

Table 7.2: The chemical composition of the $Z = 0$, $20 M_{\odot}$ supernova yield from Limongi (2002, private communication). Abundances are given in mass fraction, normalised to 1.0.

Nuclide	Initial Mass Fraction
^1H	0.75479
^3He	7.85×10^{-6}
^4He	0.24500
^{12}C	4.04×10^{-7}
^{14}N	7.03×10^{-14}
^{16}O	6.91×10^{-7}
Z_{other}	7.65×10^{-7}
Z_{total}	1.86×10^{-6}

Table 7.3: An example of the initial abundances used in the stellar structure calculations of the low and intermediate mass metal poor stars. In this case it is the composition of the $[\text{Fe}/\text{H}] = -4.0$ set of models. This composition was arrived at by diluting the $20 M_{\odot}$ yield with $1.0 \times 10^6 M_{\odot}$ of Big Bang material. Z_{other} is a synthetic species that keeps track of all nuclides heavier than ^{16}O . Mass fraction is normalised to 1.0.

the supernova. All the heavier species are present in progressively lower fractional abundances as the metallicity is lowered. As we use Fe to define the metallicity in this case the SN yield has a direct effect on the abundance pattern. The resulting composition is thus different to that given by just scaling the solar composition. The most notable difference is the lack of nitrogen, which, for example, is only present in the $[\text{Fe}/\text{H}] = -4.0$ models at the level of $\sim 10^{-14}$ (by mass), as compared to $\sim 10^{-7}$ for carbon and oxygen. This is due to the fact that it is not present in a significant amount in the yield of the $Z = 0$, $20 M_{\odot}$ supernova, nor is it synthesised in (standard) BBN. It must be noted that this lack of Nitrogen is model-dependent — some $Z = 0$ supernova models do in fact produce significant amounts of N. However we do not think that this uncertainty is of much importance, in most respects. In terms of structural evolution N is quickly produced through the CNO cycle due to the presence of C and O, and thus the (energetically important) CNO cycle operates as normal. In terms of chemical yield we have found that the initial N abundance is swamped by the pollution events occurring in these stars (eg. the DCF, DSF and/or the third dredge-up). Of course it does however affect the surface composition for early phases of evolution, before any surface pollution occurs. This may be of importance in comparing our MS models with observations of (unpolluted) dwarf Halo stars.

The other main difference that the SN+BB composition exhibits, as compared to Solar, is a modest overabundance of the alpha elements. We display some of these abundances in Table 7.5.

7.2 Structural Evolution

Here we give an overview of the evolution of all our metal-deficient models. We have also included the $Z = 0$ models of the previous chapters in most of the tables and plots, for comparison. The $Z = 0$ models provide a useful handle on the lower limit of metal-deficient stellar evolution. In particular, gradual changes in evolution can be seen as the abundance of heavy elements is increased from zero.

We follow the definition often used to distinguish between low mass (LM) and intermediate mass (IM) models, such that low mass models ignite He under degenerate conditions (in a core He

Nuclide	Mass Frac.	Nuclide	Mass Frac.	Nuclide	Mass Frac.
h1	0.7548	ne21	6.39E-11	p31	3.21E-10
h2	0.00E+00	ne22	1.44E-11	p32	0.00E+00
he3	7.85E-06	na21	0.00E+00	p33	0.00E+00
he4	0.2450	na22	0.00E+00	p34	0.00E+00
li7	3.13E-10	na23	3.81E-09	s32	5.10E-08
be7	0.00E+00	na24	0.00E+00	s33	2.41E-10
b8	0.00E+00	mg23	0.00E+00	s34	1.64E-08
c12	4.04E-07	mg24	1.28E-07	s35	0.00E+00
c13	4.12E-14	mg25	1.39E-09	fe56	1.41E-07
c14	0.00E+00	mg26	1.54E-09	fe57	4.25E-09
n13	0.00E+00	mg27	0.00E+00	fe58	8.65E-16
n14	7.03E-14	al25	0.00E+00	fe59	0.00E+00
n15	4.03E-16	al-6	0.00E+00	fe60	0.00E+00
o14	0.00E+00	al*6	0.00E+00	fe61	0.00E+00
o15	0.00E+00	al27	3.10E-09	co59	2.24E-09
o16	6.91E-07	al28	0.00E+00	co60	0.00E+00
o17	1.05E-14	si27	0.00E+00	co61	0.00E+00
o18	7.02E-14	si28	1.16E-07	ni58	1.99E-09
o19	0.00E+00	si29	1.22E-09	ni59	0.00E+00
f17	0.00E+00	si30	8.63E-10	ni60	2.31E-12
f18	0.00E+00	si31	0.00E+00	ni61	1.24E-14
f19	1.21E-15	si32	0.00E+00	ni62	7.38E-18
f20	0.00E+00	si33	0.00E+00	g	1.45E-13
ne19	0.00E+00	p29	0.00E+00		
ne20	2.87E-07	p30	0.00E+00	Z_{total}	1.86E-06

Table 7.4: An example of the initial abundances used in the nucleosynthesis calculations of the low and intermediate mass metal-deficient stars. In this case it is the composition of the $[\text{Fe}/\text{H}] = -4.0$ set of models. This composition was arrived at by diluting the $20 M_{\odot}$ yield with $1.0 \times 10^6 M_{\odot}$ of Big Bang material. ‘g’ is a synthetic species that ends the network, representing all species heavier than ^{62}Ni (see the NS code description in Section 3.2 for more details on the network). Abundances are given in mass fraction, normalised to 1.0. Starting compositions for the rest the models are given with the yields towards the end of the chapter.

Element Ratio	Abundance
[O/Fe]	0.00
[Ne/Fe]	0.36
[Mg/Fe]	0.25
[Si/Fe]	0.15
[S/Fe]	0.20

Table 7.5: Abundances of some of the alpha elements in the Pop III supernova yield, relative to Solar. Solar abundances are from [Lodders \(2003\)](#).

flash – or possibly a dual core flash) whilst IM models ignite He quiescently. In the extremely low metallicity regime of this study this means that our 2 and 3 M_{\odot} models are IM stars.

We give an overall summary of our results, and compare them to previous studies, at the end of this chapter (Section 7.5 on page 282).

7.2.1 Main Sequence to RGB Tip/Core He Ignition

Low Mass Models: 0.85 & 1.0 M_{\odot}

In Figures 7.1 and 7.2 we show the evolution of the five 0.85 M_{\odot} models and five 1.0 M_{\odot} models in the HR diagram, from ZAMS to the start of the RGB. The models have metallicities of $[\text{Fe}/\text{H}] = -6.5, -5.45, -4.0, -3.0$ and $Z = 0$. We have magnified this section of the HR diagrams to highlight the differing luminosities and surface temperatures between the models. However, also apparent is the similarity between the models during most of the MS phase. This is due to the fact that stars of higher metallicity are not hot enough to burn hydrogen efficiently via the CNO cycles, and are powered mainly by the p-p chains. Thus the paucity (or absence) of CNO catalysts in the metal-deficient models has no effect during this phase of evolution. It also appears that the opacity difference in this range of metallicity has little effect on the surface temperature during this phase either.

Differences begin to appear as the stars reach the end of the MS. The more metal-rich models begin to burn H more efficiently via the CNO cycles due to the increasing core temperatures and decreasing H abundance. The higher temperature dependence of energy generation in the CNO cycles ($\sim T^{20}$ compared to $\sim T^4$ in the p-p chains) leads to lower burning temperatures and thus lower luminosities in the more metal-rich models. Thus the MS turn-offs of the lower metallicity stars are at slightly higher temperatures and luminosities. These qualities persist as the stars change to shell burning energy sources and move off the MS, crossing the HR diagram to become red giants. The shell burning in the lower metallicity models is again dominated by the p-p chains whilst the higher metallicity models have more of a contribution from the CNO cycles (Figure 5.1 on page 92 in the $Z = 0$ chapter shows this clearly). The differences in surface temperature and luminosities is more pronounced in the 1 M_{\odot} models than the 0.85 M_{\odot} models, leading to a modest variation of MS turn-off luminosities of ~ 0.15 dex. An interesting feature in the $Z = 0$, 1 M_{\odot} model (Figure 7.2) not seen in any of the other low-mass models is the occurrence of a ‘CNO Miniflash’ during the Hertzsprung Gap evolution that leads to a loop in the HR diagram. This is similar to the CNO miniflash reported for the $Z = 0$, 2 M_{\odot} model in Section 5.3 on page 139 but it occurs earlier in this case. It indicates that a small amount of He burning has produced enough ^{12}C to allow the CNO cycles to operate, burning the small amount of H left in the core. As this carbon production does not affect the shell the further evolution is unaffected, so that the star returns to a high luminosity and temperature position after the episode.

As noted in 5.2.1 the luminosity of the $Z = 0$, 0.85 M_{\odot} model at the time of core He ignition at the top of the RGB is significantly lower than in higher metallicity models. In Figures 7.3 and 7.4 we show ‘close-ups’ of the end of the RGB in the HR diagrams for all the 0.85 and 1.0 M_{\odot} models. We again include the $Z = 0$ models for comparison. It can be seen that as the

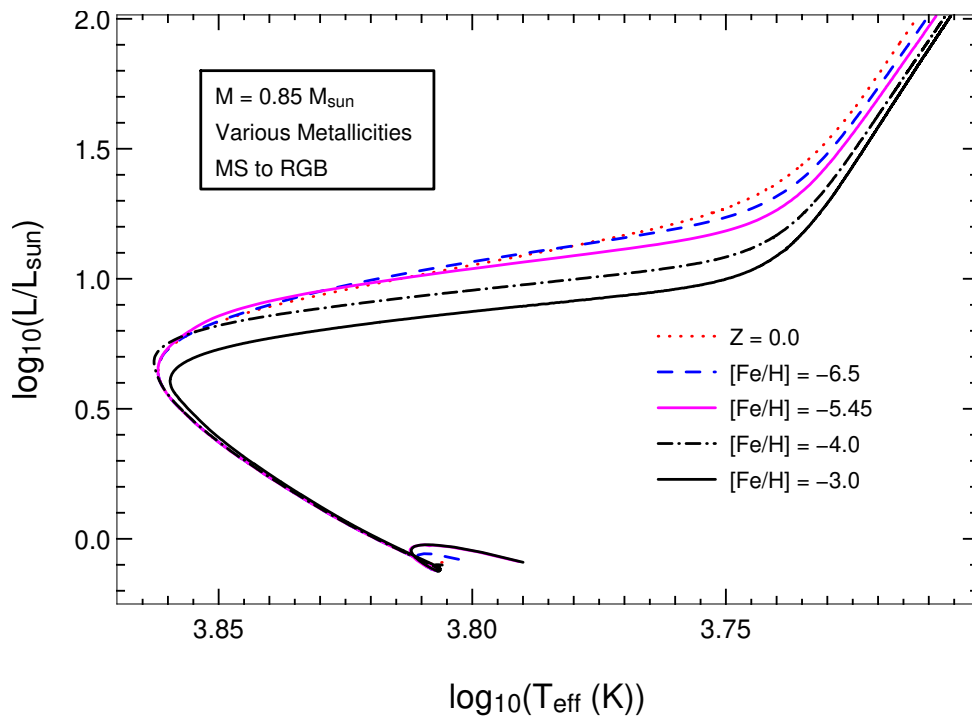


Figure 7.1: The HR diagram for all the $0.85 M_{\odot}$ low metallicity models, from ZAMS to the start of the RGB. Our $Z = 0$ model has been included for comparison.

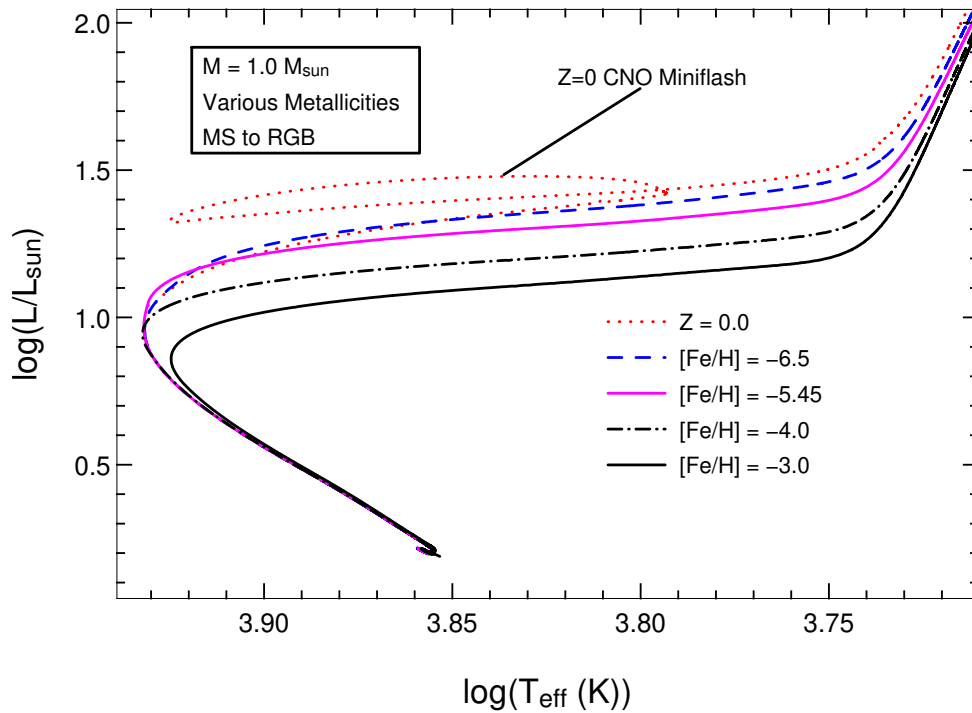


Figure 7.2: Same as Figure 7.1 but for the $1 M_{\odot}$ models.

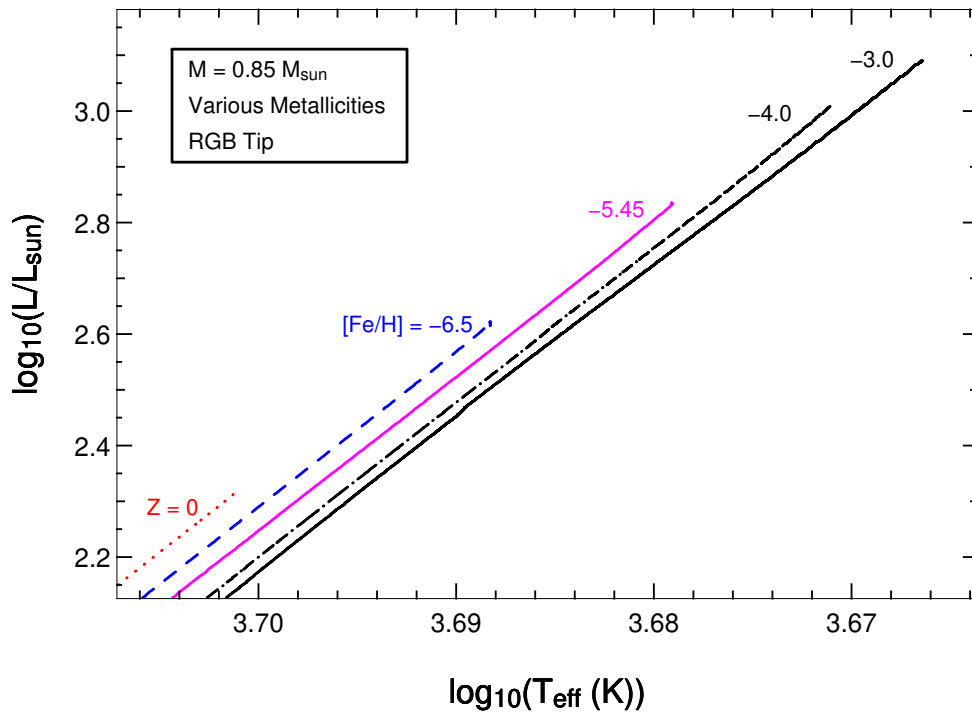


Figure 7.3: The last portion of the RGB evolution in the HR diagram for all the $0.85 M_{\odot}$ models. The curves end when He ignites degenerately in the cores. It can be seen that the luminosity at the tip of the RGB varies by ~ 0.8 dex over this metallicity range.

metallicity increases He is ignited when the stars are at higher and higher luminosities. Between the $Z = 0$ models and our most metal-rich models, with $[\text{Fe}/\text{H}] = -3.0$, there is a difference of 0.8 dex in luminosity. Interestingly the range is almost identical in the $1.0 M_{\odot}$ models as in the $0.85 M_{\odot}$ models.

Intermediate Mass Models: 2.0 & $3.0 M_{\odot}$

Figure 7.5 displays the evolution of our five $2 M_{\odot}$ models in the HR diagram, from ZAMS to core He ignition. By definition these intermediate mass stars do not ignite He degenerately, and thus do not experience a core He flash/DCF. Differences in evolution are seen to occur earlier in these models, as compared to the low mass models. In solar metallicity models the CNO cycles operate efficiently at $2 M_{\odot}$. At $Z = 0$ the CNO cycles do not contribute until the end of the MS. This CNO ignition can be seen in the HR diagram (it is labeled in Figure 7.12). A significant difference in MSTO luminosities (~ 0.4 dex) between the models can be seen in Figure 7.5, again due to the varying degrees of paucity of CNO catalysts. A more moderate variation in MSTO temperature is also present, being ~ 0.05 dex over this range of metallicity. The stepwise reduction in MSTO luminosity mirrors the reduction in metallicity. All these traits are also present in the $3 M_{\odot}$ models, as displayed in Figure 7.6. Our models thus predict a bluer and more luminous MS at lower and lower metallicities.

An additional feature in the $3 M_{\odot}$ models is the appearance of the CNO convective core ‘kink’ in the HR diagram. This is a characteristic seen at quite low masses (starting at $\sim 1.2 M_{\odot}$) at solar metallicity. It indicates that a significant convective core has formed – due to the efficient operation of the CNO cycles. The core becomes convective because the high temperature of the

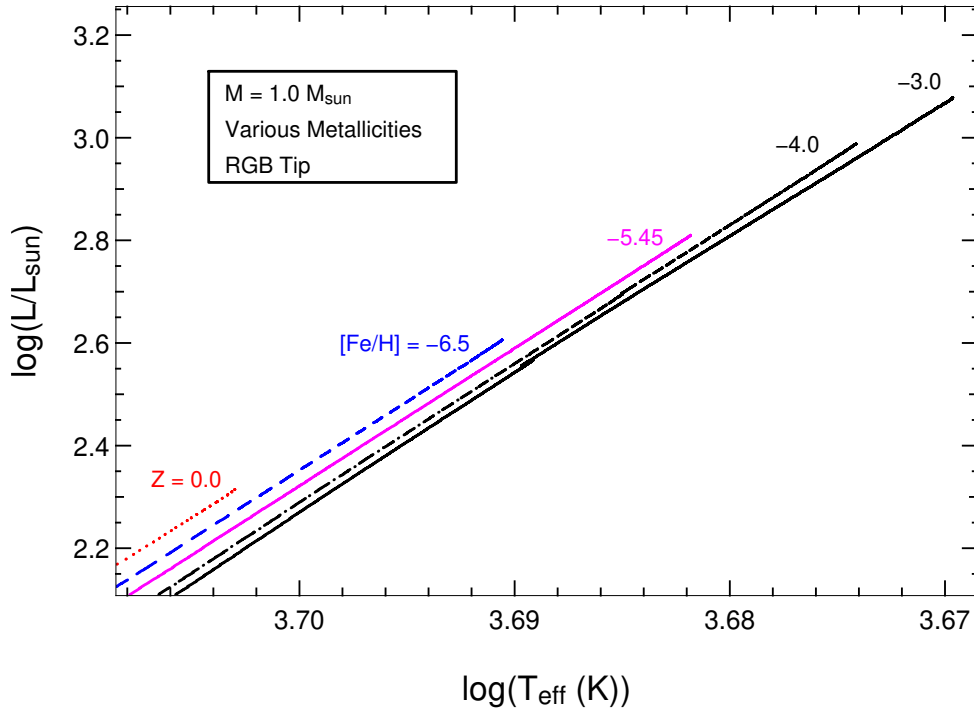


Figure 7.4: Same as Figure 7.3 but for the $1.0 M_{\odot}$ models.

CNO cycle results in a very steep temperature gradient. The kink is thus a useful indicator for our current models. Indeed, in Figure 7.5 it can be seen that a small kink is seen in the most metal-rich of our $2 M_{\odot}$ models, but not the others. This highlights the fact that the CNO cycle is not operating efficiently in the lower- Z models. In the $3 M_{\odot}$ models the two most metal-rich models show well developed kinks, indicating that, due to the higher temperatures in the cores of these more massive models, the CNO cycles are able to operate efficiently at such low metallicities. Interestingly the $[Fe/H] = -6.5$ and -5.45 models, of both masses, show perfectly smooth evolution in the HR diagram – they do not experience the $Z = 0$ CNO miniflash or the CNO convective core kink. Thus they behave more like a $1 M_{\odot}$ star at solar metallicity, although they are much hotter and much more luminous.

Also of note are the differing surface temperatures at which He is ignited in the cores. The $2 M_{\odot}$ models show a large range of core He ignition temperatures – from just after the MSTO to the (short lived) RGB in the $[Fe/H] = -3.0$ model. Out of the ten 2.0 and $3.0 M_{\odot}$ models this is the only model that reaches the RGB. The differing ignition points (in surface temperature) for He reflect the pace at which the conditions for He burning is achieved at different metallicities (ie. temperature and density). Thus all these low- Z intermediate mass models predict a lack of an RGB in colour magnitude diagrams at very low metallicity and quite low masses, as compared to solar.

7.2.2 On the Occurrence of Dual Core Flashes

By definition Dual Core Flashes (DCF) can only occur in low-mass models, as the secondary (hydrogen) flash is induced by the normal degenerate core He flash. We have found that the DCF event also occurs in some of our metal-deficient models – but not all of them.

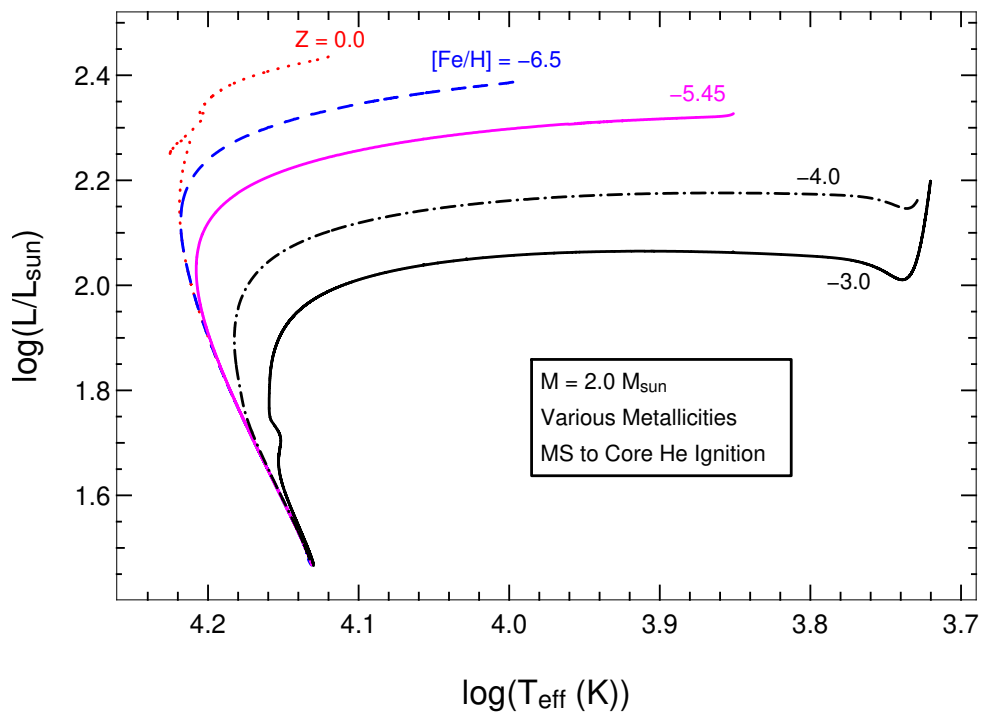


Figure 7.5: The HR diagrams for all our low metallicity $2 M_{\odot}$ models, from ZAMS to the ignition of helium in the centre. As metallicity decreases the stars ignite He earlier and earlier. Only the most metal-rich model reaches the RGB, and then only spends a brief time there.

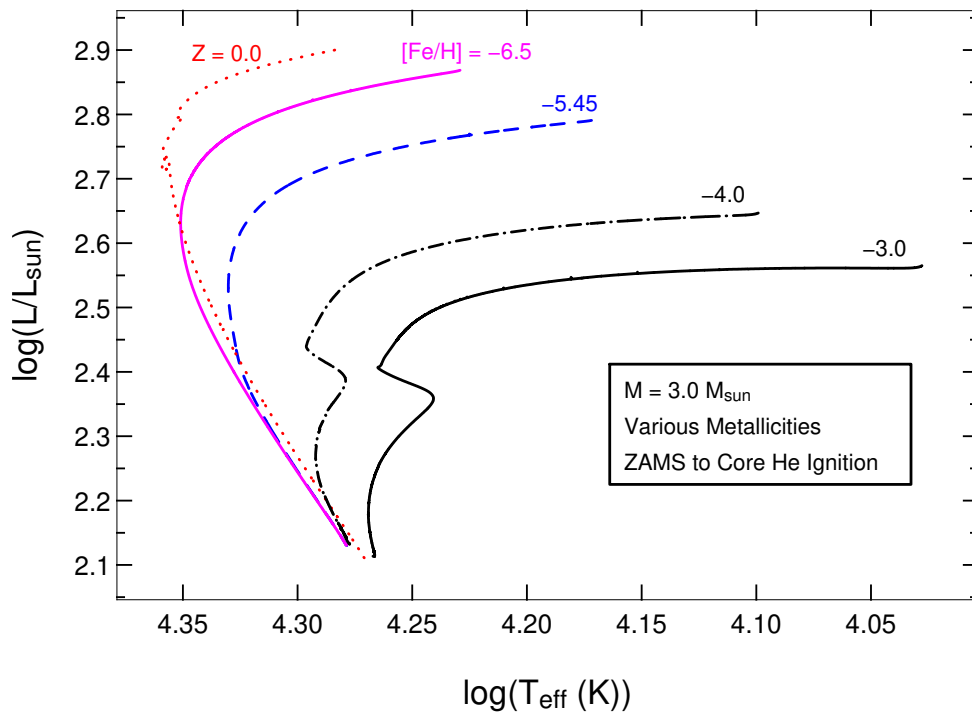


Figure 7.6: Same as Figure 7.12 but for the $3 M_{\odot}$ models. In this case none of the models become red giants as they ignite helium early and thus move back to the blue.

In Section 5.2.2 on page 101 we presented an account of the DCF that occurred in our $Z = 0$, $0.85 M_{\odot}$ model. We refer the reader to that section for a detailed description of this type of evolutionary event but reiterate the main properties here. As a guide we display some details of the DCF that occurred in one of our metal-poor models in Figure 7.7 (the $1 M_{\odot}$, $[\text{Fe}/\text{H}] = -6.5$ model). As occurred in our $Z = 0$ models He ignited a long way off centre in the metal-poor models which experienced the DCF. Helium convection zones (HeCZs) developed, as normal, due to the large energy release from the thermonuclear runaways. The extent of the convection zones increased over time, mainly outwards, again as normal. However in these cases the convection zones penetrated the H-He discontinuity. This penetration occurs for two reasons: firstly, as just mentioned, He ignites significantly off-centre, so the HeCZ is already relatively close to the H shell, and secondly, as noted by Fujimoto et al. (1990), the entropy barrier in the hydrogen shell is very low in models of extremely-low (or $Z = 0$) models. The extension of the He convection zones into H-rich layers mixed protons downwards into the He convection zones, so that H was now present in regions of very high temperature. The large energy release from the furious burning of this H then caused a creation of a secondary convection zone, the H convection zone (HCZ). Thus two (burning) convection zones now existed in the stars – a HCZ and a HeCZ. The base of the HCZ now marked the top of the H-exhausted cores, the boundaries of which had moved inwards due to the dredging down of protons. After both flashes and their associated convection zones abated the envelopes became more deeply convective, dredging up the erstwhile HCZs. As the HCZs were polluted by He burning products, which were present due to the previous He-flash burning at the locations that the HCZs formed, these post-DCF dredge-up events led to a strong pollution of the envelopes, raising their metallicities from zero to $Z_{\text{cno}} \sim 10^{-2}$. Since there was no further pollution of the envelope via third dredge-up (3DUP) on the AGB in any of these models, the pollution from these DCF events defined the chemical yield of the models.

As mentioned above we have found that the DCF event occurs in some of our metal-deficient models but not others. In column five of Table 7.6 we show which stars experienced the DCF and which did not, for all our metal deficient models (the $Z = 0$ models are also included for reference). It can be seen in this table that those models which did not experience a DCF did however go on to have a Dual Shell Flash (DSF, the topic of the next subsection). It can also be seen that the occurrence of the DCF is a strong function of the metallicity and mass of the stars. The DCF only occurs for extremely metal-deficient models, and occurs more at low masses. At $M = 0.85 M_{\odot}$ we find that only our three most metal poor models experience the DCF: the $Z = 0$, $[\text{Fe}/\text{H}] = -6.5$ and $[\text{Fe}/\text{H}] = -5.45$ ones. At $M = 1.0 M_{\odot}$ only the two most metal-poor models do: the $Z = 0$ and $[\text{Fe}/\text{H}] = -6.5$ models. The main reason for this is that the most metal-poor models ignite He a long way off centre. As metallicity increases the ignition point moves closer to the centre, making the breaching of the H-He boundary less likely (although we note that the $Z = 0$ models ignite slightly further out than the $[\text{Fe}/\text{H}] = -6.5$ models). In Table 7.6 we give the location of the ignition points for all the models. We also show the mass of the core at the time of core He ignition. Taking the difference of these two quantities gives ΔM_{ign} , the distance (in mass) that separates the ignition point from the H-He boundary (also see Figure 7.7 for a definition of the diagnostic quantities mentioned here). This value increases with metallicity, as expected, ranging from $\sim 0.2 M_{\odot}$ to $\sim 0.4 M_{\odot}$ in these models. It appears that a value less than $0.25 M_{\odot}$ leads to a DCF. Another interesting diagnostic is ΔM_c , the amount that the

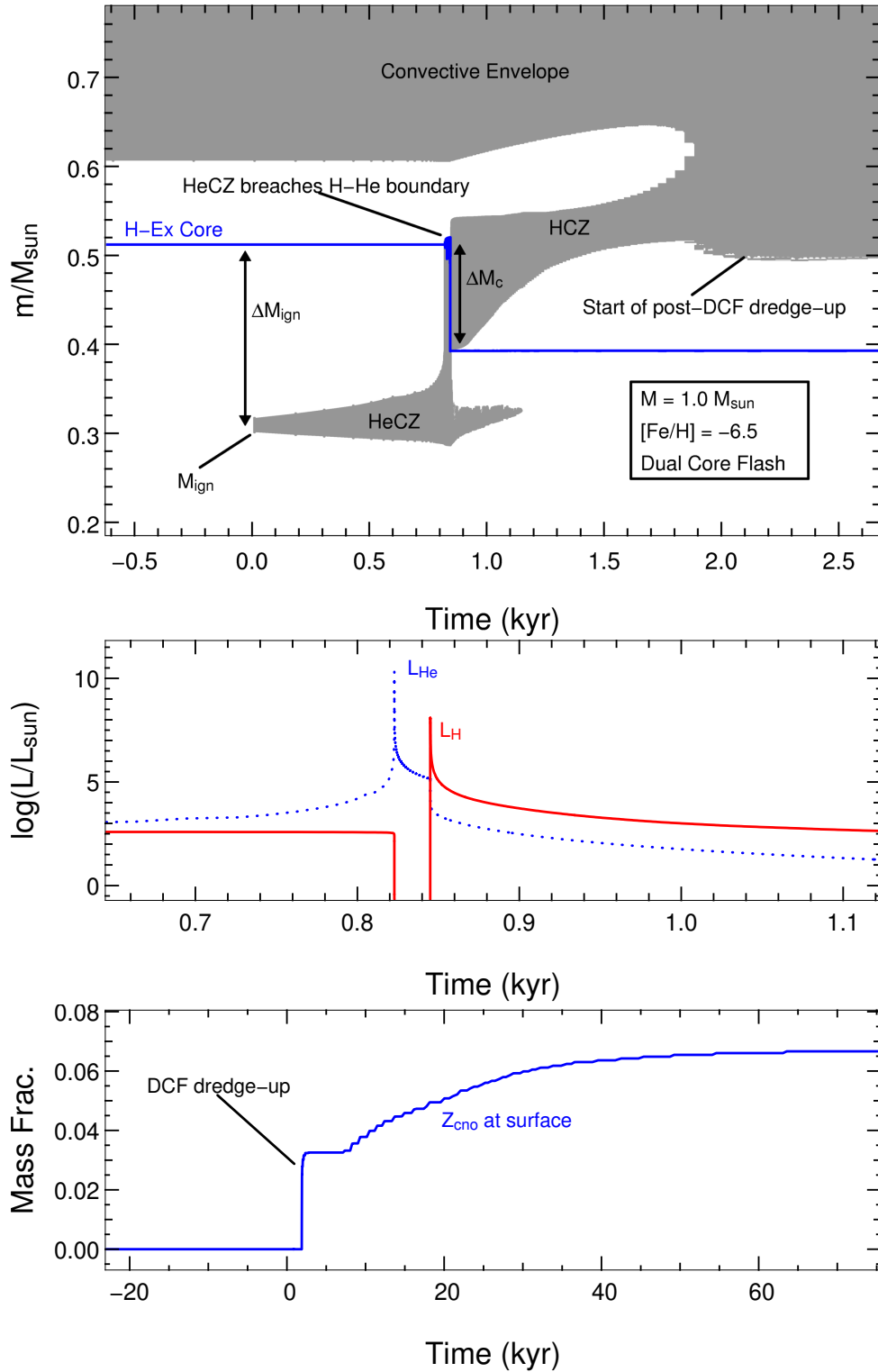


Figure 7.7: An example of one of the Dual Core Flashes that occurred in some of our low metallicity models. In this case it is the $1 M_{\odot}$ model with $[\text{Fe}/\text{H}] = -6.5$. Note that the three panels have the same time scale and have been offset by the same amount (ie. zero corresponds to the start of the He flash in all panels) – but they all cover different time-spans. The top panel shows the convective regions (grey shading) and the mass of the hydrogen-exhausted core. It also shows the definitions of some of the quantities referred to in Table 7.6. The large inward movement of the H-He boundary (H-Ex. core) due to the ingestion of protons into the HeCZ can be seen (ΔM_c). In the second panel we zoom in on the luminosity evolution. The bottom panel shows the evolution of the surface pollution arising from the DCF event, in terms of Z_{cno} , the sum the mass fractions of all the CNO isotopes.

mass of the H-exhausted core decreases by, due to the DCF. In other words it is the distance (in mass) that protons are mixed down before the secondary (hydrogen) convection zone forms. The envelope later moves inwards, usually all the way down to the new location of the H burning shell, dredging up the ex-HCZ. Thus this value ΔM_c gives a (rough) indication of the amount of pollution that occurs as a result of the DCF. Interestingly the magnitude of surface pollution from the DCFs is similar in all the models. They all end up with Z_{cno} a few times 10^{-2} , with the exception of the $0.85 M_{\odot}$, $Z = 0$ model which ends up less polluted, having $Z_{cno} \sim 10^{-3}$ at the surface. Looking more closely there is however some variation between the models, such that the resultant pollution ranges from $Z_{cno} = 1 \times 10^{-3}$ to 7×10^{-2} . This variation mostly correlates with the value of ΔM_c but in one case, the $0.85 M_{\odot}$, $[\text{Fe}/\text{H}] = -5.45$ model, the pollution is lower than expected.

7.2.3 On the Occurrence of Dual *Shell* Flashes

In 5.3.3 on page 146 we described in detail the Dual Shell Flash (DSF) event occurring near the beginning of the TP-AGB in our $2 M_{\odot}$, $Z = 0$ model. We refer the reader to that section for a detailed description of this evolutionary event but reiterate the main properties here. As a guide we display some details of the DSF that occurred in one of our metal-poor models in Figures 7.8 and 7.9 (the $2 M_{\odot}$, $[\text{Fe}/\text{H}] = -4.0$ model). The DSF is a similar event to the DCF inasmuch as it involves a helium convection zone expanding upwards and breaching the H-He interface. This proton ingestion event (PIE) also results in the creation of a second convection zone, the HCZ. Like the DCF HCZ this convection zone is polluted with He (and H) burning products, as its extent includes some of the mass that was previously part of the HeCZ (see panel 1 in Figure 7.9). Importantly this HCZ material is dredged up at a later time (when the convection has stopped), polluting the envelope. In the case of the low mass stars ($M = 0.85$ and $1 M_{\odot}$) this pollution is the main contributor to the chemical yield, as these models experience no 3DUP. Conversely, in the case of the intermediate mass models ($M = 2$ and $3 M_{\odot}$) the chemical pollution from this event is erased/swamped by the 3DUP pollution occurring later on the AGB. In Table 7.6 we display the pollution resulting from the DSF events in all the models. We also list which models do and do not experience the DSF. From this list we can see that the DSF is also very metallicity and mass dependent, like the DCF. As mentioned earlier the low mass models that do not go through the DCF always experience the DSF. At intermediate mass we see that only the most metal-poor models go through the DSF. Also, the metallicity cut-off for the DSF decreases with increasing mass – only one of our $2 M_{\odot}$ models does not experience the DSF, the $[\text{Fe}/\text{H}] = -3.0$ model – but the two most metal-rich $3 M_{\odot}$ models avoid it (the $[\text{Fe}/\text{H}] = -3.0$ and $[\text{Fe}/\text{H}] = -4.0$ models).

7.2.4 Further Evolution in the HR Diagram

In Figure 7.10 we show the full evolution of some of the $0.85 M_{\odot}$ models in the HR diagram. The MS and RGB features were discussed earlier. Of note in this diagram is the variation in the blueward excursions during the horizontal branch (HB) stage. It appears that the HB becomes redder as metallicity *decreases* – the $[\text{Fe}/\text{H}] = -3.0$ model still has a blue HB, like the (mildly)

Mass = 0.85 M _⊙							
Metallicity	M _{ign}	M _c	ΔM _{ign}	DCF/DSF	ΔM _c	LH _{max}	Z _{eno}
-3.00	0.14	0.50	0.36	Shell	0.014	8.1	1E-02
-4.00	0.21	0.52	0.31	Shell	0.004	7.7	1E-03
-5.45	0.30	0.53	0.23	Core	0.140	8.1	3E-02
-6.50	0.33	0.52	0.19	Core	0.095	7.6	6E-02
Z = 0	0.28	0.49	0.21	Core	0.056	8.3	1E-03

Mass = 1.0 M _⊙							
Metallicity	M _{ign}	M _c	ΔM _{ign}	DCF/DSF	ΔM _c	LH _{max}	Z _{eno}
-3.00	0.09	0.49	0.40	Shell	0.010	7.3	5E-03
-4.00	0.15	0.51	0.36	Shell	0.019	10.5	1E-02
-5.45	0.27	0.52	0.25	Shell	0.010	10.6	4E-03
-6.50	0.31	0.52	0.21	Core	0.120	8.2	7E-02
Z = 0	0.25	0.49	0.23	Core	0.083	8.7	1E-02

Mass = 2.0 M _⊙							
Metallicity	M _{ign}	M _c	ΔM _{ign}	DCF/DSF	ΔM _c	LH _{max}	Z _{eno}
-3.00	0.62	0.64	0.018	None	–	–	–
-4.00	0.64	0.66	0.016	Shell	4E-03	10.1	6E-04
-5.45	0.65	0.67	0.014	Shell	6E-04	8.3	2E-05
-6.50	0.67	0.69	0.012	Shell	4E-03	10.5	7E-04
Z = 0	0.69	0.70	0.011	Shell	1E-03	8.6	2E-04

Mass = 3.0 M _⊙							
Metallicity	M _{ign}	M _c	ΔM _{ign}	DCF/DSF	ΔM _c	LH _{max}	Z _{eno}
-3.00	0.798	0.804	0.006	None	–	–	–
-4.00	0.820	0.825	0.005	None	–	–	–
-5.45	0.834	0.837	0.003	Shell	9E-05	7.6	4E-08
-6.50	0.817	0.821	0.003	Shell	1E-04	7.1	8E-06
Z = 0 ^a	0.770	0.775	0.005	Shell	3E-05	8.4	8E-06

Table 7.6: Various properties pertaining to the dual core flashes (DCFs) and dual shell flashes (DSFs) for all the low metallicity models, grouped in terms of initial mass. We also redisplay the properties of the Z = 0 models for ease of comparison. All masses are in M_⊙. Metallicity is given as [Fe/H], except for Z = 0. Properties displayed are: M_{ign} (the mass coordinate at which the He flash ignites, be it a core He flash or an AGB shell flash), M_c (core mass at the onset of the flash), ΔM_{ign} (the distance, in mass, between the He flash ignition point and the H shell), ΔM_c (the distance, in mass, that the H shell moves inwards during the dual flash; this gives an indication of the degree of mass transfer between the HeCZ and the H-rich zone above), LH_{max} (log of the maximum H burning luminosity during the dual flash), and Z_{eno} (the envelope metallicity after the dredge-up event(s) associated with the DCF/DSF episodes; this excludes pollution from other episodes that occur later, such as the 3DUP).

^a This model started with a pure H-He composition, with Y = 0.230 rather than 0.245.

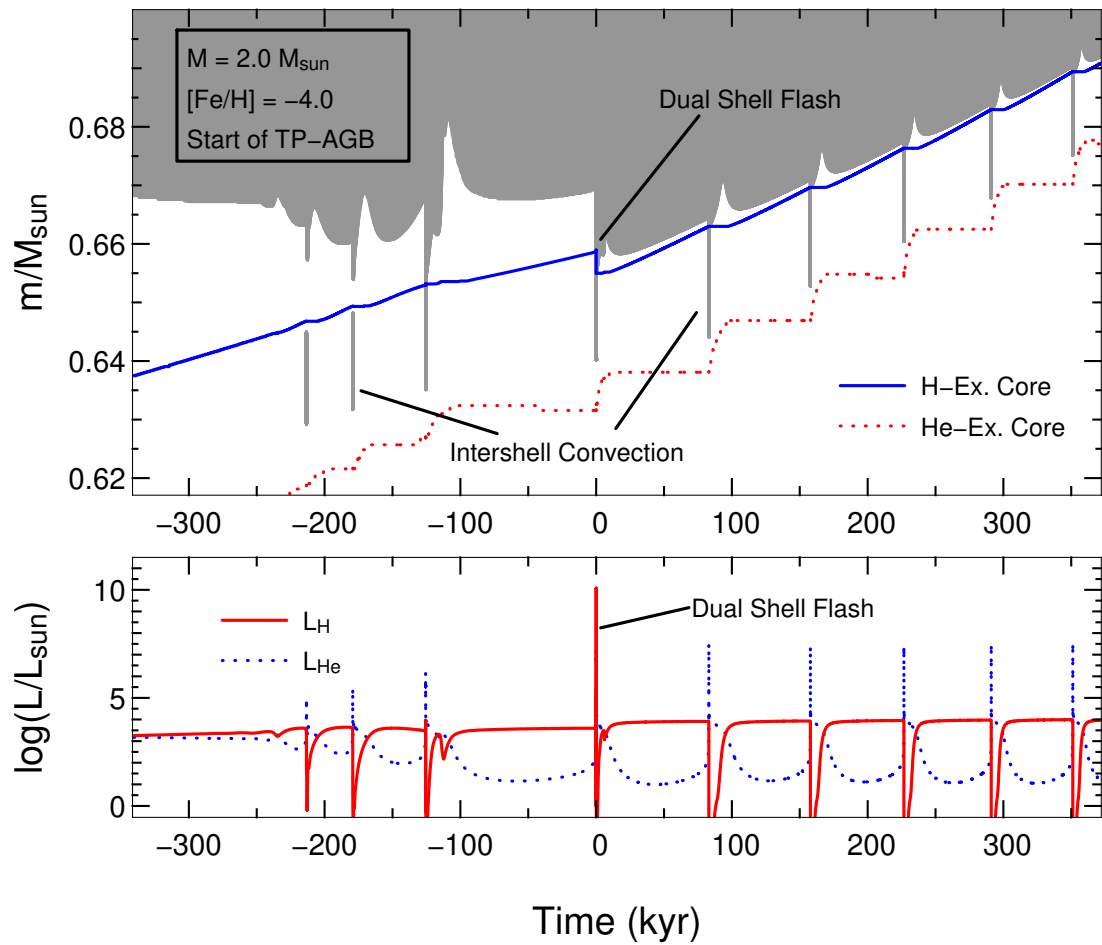


Figure 7.8: A wide-angle view of the start of the TP-AGB in the $2 M_{\odot}$ model with $[\text{Fe}/\text{H}] = -4.0$. Time is offset for clarity. This model experienced a Dual Shell Flash (DSF) at the 4th thermal pulse, as indicated in both panels. It can be seen that the hydrogen burning luminosity exceeds that of the He flash luminosity during the DSF. Figure 7.9 provides a close-up view of this event.

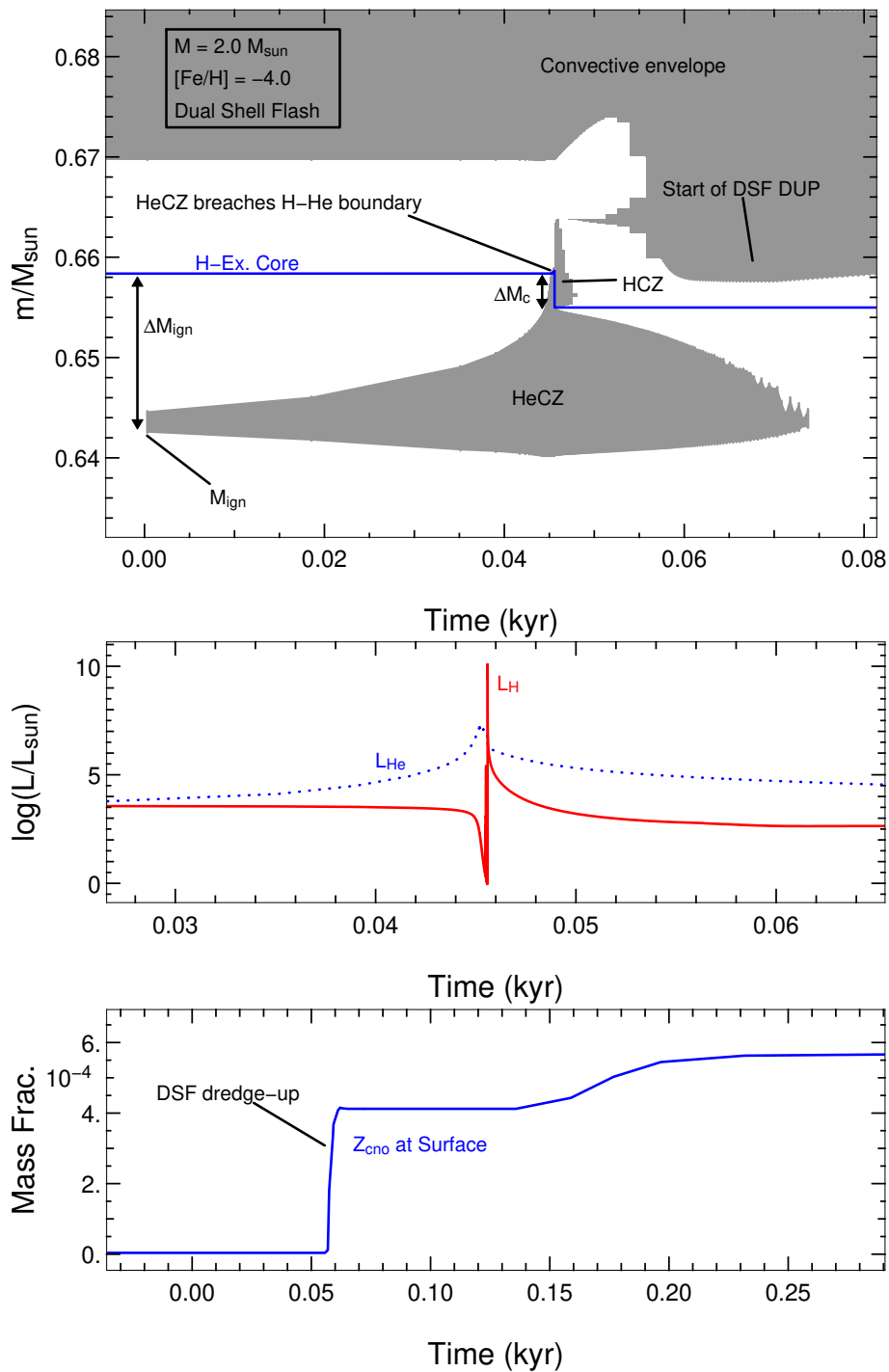


Figure 7.9: An example of one of the Dual Shell Flashes (DSFs) that occurred in some of our low metallicity models. In this case it is the $1 M_{\odot}$ model with $[\text{Fe}/\text{H}] = -4.0$. Note that the three panels have the same time scale and have been offset by the same amount (ie. zero corresponds to the start of the He flash in all panels) – but they all cover different time-spans. The top panel shows the convective regions (grey shading) and the mass of the hydrogen-exhausted core. It also shows the definitions of some of the quantities referred to in Table 7.6. The inward movement of the H-He boundary (H-Ex. core) due to the ingestion of protons into the HeCZ can be seen (ΔM_c). In the second panel we zoom in on the luminosity evolution. The bottom panel shows the evolution of the surface pollution arising from the DCF event, in terms of Z_{cno} , the sum of the mass fractions of all the CNO isotopes. The degree of pollution is much less than in the DCF case (Figure 7.7), such that Z_{cno} is 2 dex lower.

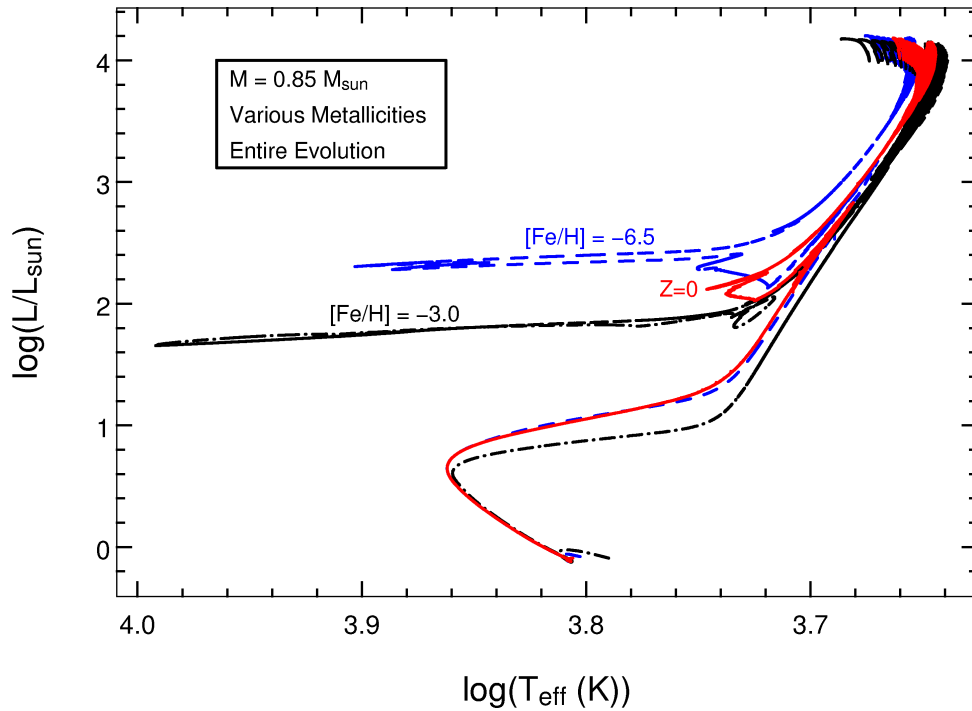


Figure 7.10: The full evolution in the HR diagram for some of the $0.85 M_{\odot}$ models.

metal-poor stars of globular clusters, but the $[\text{Fe}/\text{H}] = -6.5$ model HB is less blue. Indeed, the $Z = 0$ HB is almost like a metal-rich ‘red clump’ star, insomuch as it does not become much bluer than its RGB.

In Figure 7.11 we show the horizontal branches of all the $1 M_{\odot}$ models in the HR diagram. Here again it can be seen that the blueward excursions decrease with metallicity. However this only occurs at extremely low metallicity – the blueward excursions first increase, maximising at $[\text{Fe}/\text{H}] = -5.45$ before rapidly getting redder at $[\text{Fe}/\text{H}] = -6.5$ and $Z = 0$.

In Figure 7.12 we present the further evolution in the HR diagram of a couple of the $2.0 M_{\odot}$ models. For clarity we have plotted only the most metal-poor (the $Z = 0$ model) and our most metal-rich model ($[\text{Fe}/\text{H}] = -3.0$). All the others show intermediary behaviour, so it suffices to discuss the extreme cases here. In the $[\text{Fe}/\text{H}] = -3.0$ case it can be seen that it reaches the start of the RGB. However, before it increases its luminosity very much it ignites He in the core and consequently moves back to the blue. After completing core He burning it then returns to the red, moving up the AGB. The $Z = 0$ model on the other hand never reaches the red side of the HR diagram. It ignites He very soon after the MS turnoff and spends its core He burning lifetime as a very blue star. In fact it is as blue as its main sequence. Like the more metal-rich models it then moves to the red to become an AGB star.

Figure 7.13 displays the HR diagrams of some of the $3 M_{\odot}$ models, from ZAMS to the EAGB. As mentioned earlier none of these models reach the RGB at all. Like the more metal-poor $2 M_{\odot}$ models they ignite He in their cores whilst moving across the Hertzsprung gap (HG), thus turning back towards the blue where they spend their core He burning lifetimes. The colour of the stars during the core He burn stage is progressively bluer with metallicity. We note that this would effect the integrated light from a population of extremely metal-deficient stars.

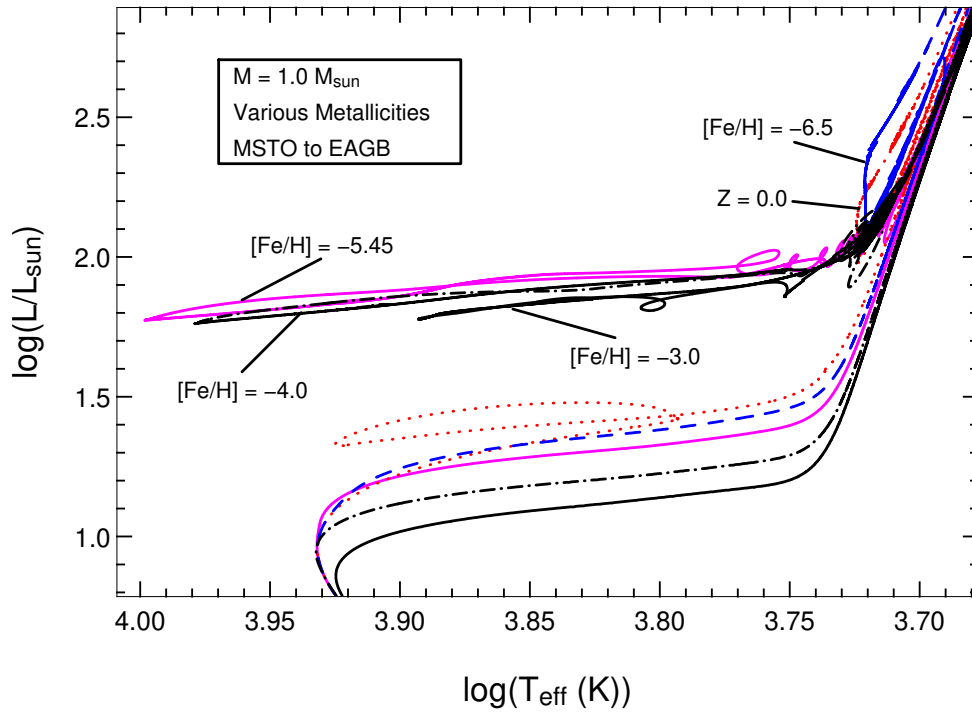


Figure 7.11: Some of the evolution in the HR diagram for all of the $1.0 M_{\odot}$ models. We note that the two most metal-deficient models have quite red horizontal branches.

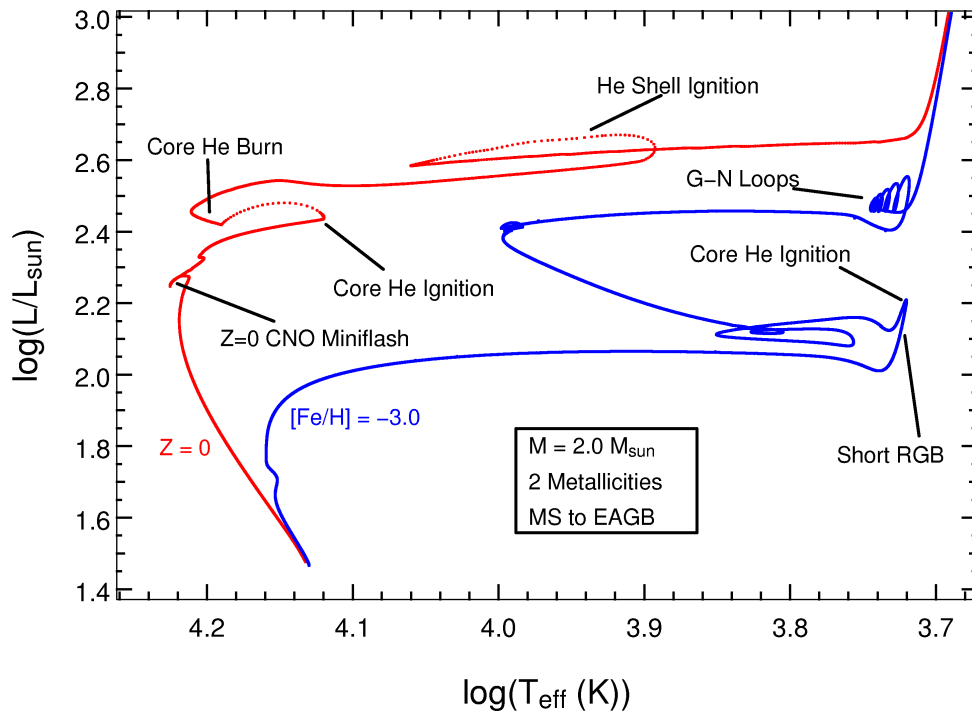


Figure 7.12: The evolution in the HR diagram for two of the $2 M_{\odot}$ models. We show only our most metal-rich and most metal-poor models for clarity. The rest of the models display intermediary evolution, gradually turning to the blue earlier and earlier (due to core He ignition) as the metallicity decreases. Also indicated is the location of the CNO ‘miniflash’ (see the $Z = 0$, $2 M_{\odot}$ structural evolution chapter for more information on this event), and some ‘gravo-nuclear loops’ in the $[\text{Fe}/\text{H}] = -3.0$ model (see Section 4.1.5 on page 61 for details on this feature).

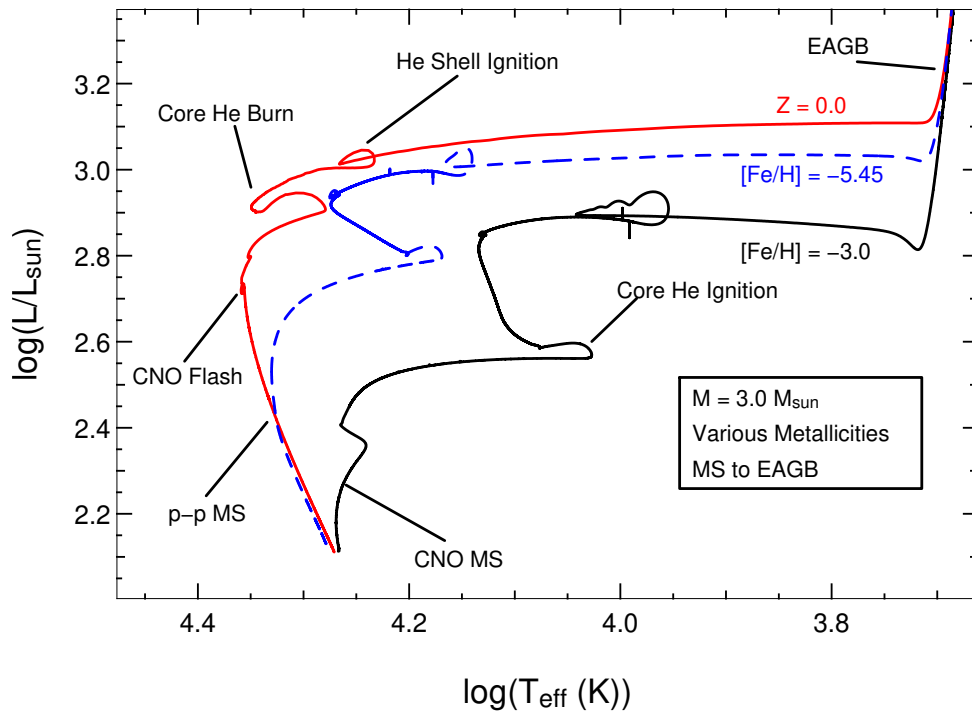


Figure 7.13: The evolution in the HR diagram of some of the $3 M_{\odot}$ models. We show only some of the models for clarity. The rest of the models display intermediary evolution, gradually turning to the blue earlier and earlier (due to core He ignition) as metallicity decreases. We note that none of the $3 M_{\odot}$ models make it to the RGB. The difference in the MS due to the competition between p-p and CNO burning is indicated (this is also discussed in Section 7.2.1), as is the location of the CNO ‘miniflash’ (see the $Z = 0$, $2 M_{\odot}$ structural evolution chapter for more information on this event).

7.2.5 TP-AGB

All stars in our grid of models go on to become thermally-pulsing AGB stars. This is the stage where they lose the most mass, and thus the composition of their surfaces during this stage has the most impact on the chemical yields. Below we begin by delineating three groups that we have identified from our grid, based on the nature of the pollution that defines the chemical composition of their AGBs. We then go on to present some details of the models. As there are so many models we have chosen two as examples, for which we give detailed figures. However we also provide selected salient quantities for the whole grid of models – in Table 7.7 (which complements Table 7.6).

DCF Dominated AGB: Low-Mass & Extremely Metal-Deficient Models

In the low mass models that experienced the dual core flash ($[\text{Fe}/\text{H}] \leq -5.45$ at $M = 0.85 M_{\odot}$ and $[\text{Fe}/\text{H}] \leq -6.5$ at $1.0 M_{\odot}$ – see Table 7.6 for a list) we found that no further pollution events occurred. This had the consequence that the AGB surface composition reflected the dual core flash (DCF) pollution for the rest of the evolution. In Table 7.7 we show the final composition of the envelope (in terms of Z_{cno}) for all the models. Indeed, it can be seen that the pollution levels in these low-mass models has not changed since that given by the DCFs. Thus the chemical yields for these models are defined by the DCF pollution event. This result was also mentioned in the $0.85 M_{\odot}$, $Z = 0$ sections.

DSF Dominated AGB: Low-Mass & Very Metal-Deficient Models

Those low-mass models that did *not* experience the DCF all went on to experience a dual shell flash at the start of the TP-AGB (see Table 7.6 for a list). The pollution from this event raised the Z_{cno} value to similar levels as that achieved by the DCF event (although somewhat lower in some cases). As the further evolution on the TP-AGB did not include any periodic 3DUP, the chemical composition of the AGB envelopes remained imprinted by the DSF event till the end of their evolution. Thus the chemical yields from these models are essentially dominated by the DSF pollution event, much like how those of the lower metallicity models are dominated by the DCF pollution.

3DUP Dominated AGB: Intermediate-Mass – All Metallicities

In the case of the intermediate mass models we found that the most metal-deficient ones did experience a DSF event at the start of the TP-AGB but the more metal-rich ones did not. The pollution that resulted from the DSF events in the IM models was however orders of magnitude less than that arising in the low mass models ($Z_{cno} \sim 10^{-6} \rightarrow 10^{-4}$ versus $\sim 10^{-3} \rightarrow 10^{-2}$). Also unlike the low mass models the IM DSF models all went on to experience many 3DUP events through their further AGB evolution. Thus the surface pollution from the DSF events was quickly ‘swamped’, such that the periodically increasing pollution from 3DUP dominated the surface composition for the majority of the AGB. Hence the chemical yield was defined by 3DUP (and HBB) rather than the DSF in these models.

In the models that did not experience a DSF event (the more metal-rich models) it was found that a similar amount of 3DUP occurred, polluting the AGB envelopes to a similar degree. Thus all of the IM mass models ended up with similar degrees of pollution, due to 3DUP.

AGB Properties

Table 7.7 gives a range of AGB properties for the entire grid of models, namely the number of thermal pulses, the average of the dredge-up parameter λ , the average length of the interpulse period, and the remnant mass (WD mass). The number of thermal pulses is seen to increase with mass, ranging from ~ 30 at $0.85 M_{\odot}$ to ~ 370 at $3.0 M_{\odot}$. This is a function of a few factors, such as the mass of the envelope that needed to be expelled, the characteristic interpulse period of each model, and the mass loss rate, which itself is dependent on luminosity and radius. The average interpulse periods for the intermediate mass models were generally of the order of 10^3 years, whilst they were longer in the low mass models, being generally around 10^4 years.

As mentioned earlier, 3DUP was absent in all our low mass models but a significant amount was found to occur in the IM models. Note that we have not included any form of overshoot so these results represent a lower limit on 3DUP. In the $2 M_{\odot}$ models the average of the dredge-up parameter λ was around 0.1, but was as low as 0.05 in a couple of models. In the $3 M_{\odot}$ models λ was higher, the average values ranging from 0.20 to 0.46. This substantial degree of 3DUP combined with the large number of thermal pulses led the envelopes of all the $3 M_{\odot}$ models to become heavily polluted, reaching $Z_{cno} \sim 10^{-2}$ (super-solar in some cases). The $2 M_{\odot}$ models

reached a lower level of pollution, characterised by $Z_{cno} \sim 10^{-3}$. As this pollution peaks towards the end of the AGB when the mass-loss rate is the highest, the chemical yield is also heavily polluted.

As examples of our metal deficient models we now detail the AGB evolution of our $1 M_{\odot}$, $[\text{Fe}/\text{H}] = -5.45$ model and $3 M_{\odot}$, $[\text{Fe}/\text{H}] = -5.45$ model.

AGB Evolution of the $1 M_{\odot}$, $[\text{Fe}/\text{H}] = -5.45$ Model

In Figure 7.14 we show most of the AGB evolution of this model. This model is representative of the low mass models that have their AGB envelope compositions dominated by the pollution from the DSF event occurring at the start of the AGB. The DSF event thus defines the chemical makeup of the yields in these cases. For an example of a case where the AGB composition is dominated by the DCF we refer the reader to the detailed description of the $0.85 M_{\odot}$, $Z = 0$ model in Section 5.2.4 on page 121.

The $1 M_{\odot}$, $[\text{Fe}/\text{H}] = -5.45$ model experienced a total of 63 thermal pulses on the AGB. However, as can be seen in panel two of Figure 7.14, only the one associated with the dual shell flash affected the composition of the envelope in any substantial way, since no 3DUP episodes occurred. The temperature at the base of the convective envelope was quite high for a star of this mass, being $\sim 10^{6.2}$ K (1.6 MK) through much of the AGB. This is high enough for minor HBB, the nucleosynthesis of which will be detailed in the next Section. The very high H burning luminosity attained during the DSF can be seen in panel 4. Figure 7.15 shows some more AGB properties of this model. The mass loss rate does not acquire very high values until the end of the AGB, when the majority of mass is lost via winds. Interestingly the yield from this star is not affected by the mass loss rate since the envelope composition is essentially set at the beginning of the AGB by the DSF event. The mass loss rate does however affect the mass of the remnant, as it puts a limit on the amount of core growth that can occur before the entire envelope is lost. The interpulse period is seen to decrease over the AGB, as normal.

AGB Evolution of the $3 M_{\odot}$, $[\text{Fe}/\text{H}] = -5.45$ Model

In Figures 7.16 and 7.17 we show some properties of the AGB evolution of our $3 M_{\odot}$, $[\text{Fe}/\text{H}] = -5.45$ model. This model is representative of all the intermediate mass models in our grid ($M = 2$ and $3 M_{\odot}$, all metallicities) since it experiences many 3DUP episodes which define the degree of chemical pollution on the AGB. The depth of 3DUP in this model can be seen for a few pulses in panel 1 of Figure 7.16, having a λ value of ~ 0.25 . This model goes through 369 pulses, and thus ends up with a highly polluted envelope, which is characterised by $Z_{cno} \sim 10^{-2}$ by the end of the evolution. We also present the evolution of the surface abundances of C, N and Z_{cno} . It can be seen that nitrogen dominates the composition of the envelope for practically all of the AGB. This is due to strong HBB driven by temperatures as high as $10^{7.95}$ K (~ 90 MK) at the base of the convective envelope. Again, as most of the mass loss occurs towards the end of the AGB (see Figure 7.17), the yield for this model will be dominated by nitrogen (after H and He of course). The 3DUP moderates the core growth in this star, as can be seen in Figure 7.17. It ends up as a WD with a mass of $1.1 M_{\odot}$. The evolution of the depth of 3DUP (λ) is plotted in

Mass = 0.85 M _⊙						
Metallicity	N _{TP}	λ _{ave}	IPP _{ave}	Z _{cno,f}	M _{WD}	N _{mods}
-3.00	40 (1)	zero	1E+05	1E-02	0.75	0.4
-4.00	35 (4)	zero	1E+05	1E-03	0.76	0.4
-5.45	18 (8)	zero	9E+03	3E-02	0.74	0.6
-6.50	27 (3)	zero	3E+04	6E-02	0.76	0.3
Z = 0	37 (6)	zero	5E+04	1E-03	0.78	0.1

Mass = 1.0 M _⊙						
Metallicity	N _{TP}	λ _{ave}	IPP _{ave}	Z _{cno,f}	M _{WD}	N _{mods}
-3.00	60 (3)	zero	7E+04	5E-03	0.85	0.8
-4.00	69 (3)	zero	7E+04	1E-02	0.85	0.8
-5.45	63 (3)	zero	8E+04	3E-03	0.87	0.5
-6.50	63 (4)	zero	2E+04	6E-02	0.85	0.7
Z = 0	65 (4)	zero	3E+04	1E-02	0.84	0.7

Mass = 2.0 M _⊙						
Metallicity	N _{TP}	λ _{ave}	IPP _{ave}	Z _{cno,f}	M _{WD}	N _{mods}
-3.00	218 (2)	0.12	1E+04	1E-02	1.04	2.1
-4.00	306 (4)	0.04	7E+03	5E-03	1.08	1.2
-5.45	257 (3)	0.12	8E+03	1E-02	1.06	1.9
-6.50	269 (3)	0.09	7E+03	8E-03	1.07	1.3
Z = 0	286 (4)	0.05	6E+03	4E-03	1.08	1.1

Mass = 3.0 M _⊙						
Metallicity	N _{TP}	λ _{ave}	IPP _{ave}	Z _{cno,f}	M _{WD}	N _{mods}
-3.00	314 (4)	0.33	4E+03	3E-02	1.07	2.5
-4.00 ^a	343	0.46	4E+03	4E-02	1.06	4.0
-5.45	369 (6)	0.26	3E+03	2E-02	1.10	2.6
-6.50	403 (7)	0.21	3E+03	1E-02	1.11	2.1
Z = 0 ^b	387 (6)	0.20	3E+03	1E-02	1.10	3.7

Table 7.7: Various properties pertaining to the AGB phase of evolution for all the low metallicity models, grouped in terms of initial mass. We also redisplay the properties of the Z = 0 models. Metallicity is given as [Fe/H], except for Z = 0. Properties displayed are: N_{TP} (number of thermal pulses; the number in brackets is how many synthetic pulses were calculated to finish the evolution once the SEV code failed to converge), λ_{ave} (the average of the dredge-up parameter over all the pulses), IPP_{ave} (average of the interpulse period over all the pulses, in years), Z_{cno,f} (the final surface metallicity in terms of the sum of the CNO nuclides), M_{WD} (mass of the white dwarf remnant, in M_⊙), and N_{mods} (the total number of models calculated for each star over its entire evolution, in units of 10⁶ models).

^a Due to a loss of data we were unable to calculate the final few thermal pulses of this model (or the yield). Here we give the number of pulses and the mass of the core at the end of the SEV code calculation.

^b This model started with a pure H-He composition, with Y = 0.230 rather than 0.245.

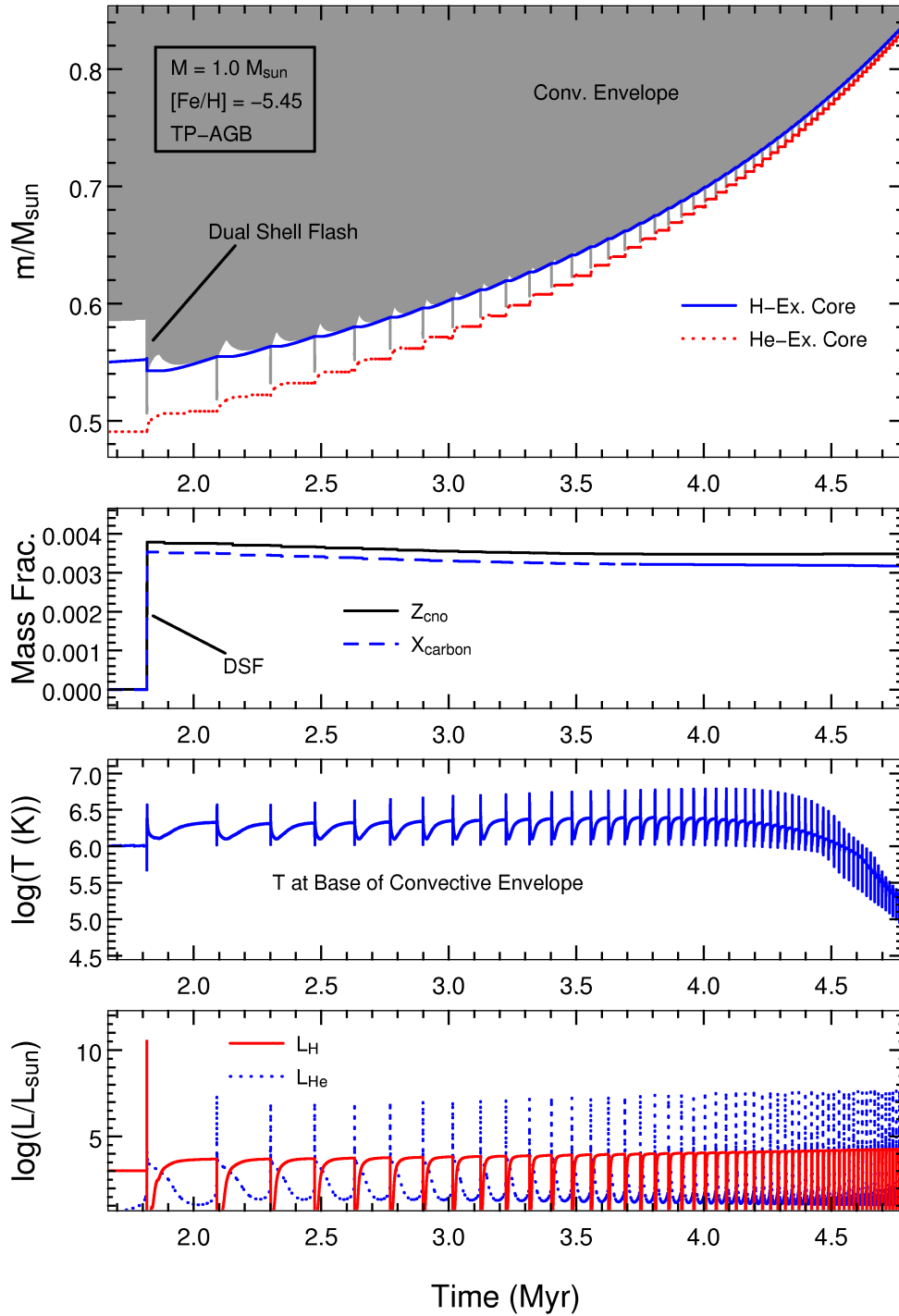


Figure 7.14: Most of the AGB evolution of the $1 M_{\odot}$, $[\text{Fe}/\text{H}] = -5.45$ model. Time has been offset. We present this model as representative of the models that have their AGB envelopes dominated by the pollution arising from the DSF event at the start of the AGB, which thus defines the chemical yield (see text for details). In the top panel the many intershell convection zones can be seen (convection is in grey shading). Indicated in the top panel is the dual shell flash that occurs near the start of the TP-AGB. This feature can also be seen as a large spike in H burning luminosity in the bottom panel. In the second panel we show the evolution of the surface abundances of carbon and Z_{cno} . Z_{cno} is seen not to increase, indicating that no 3DUP is occurring. More details of this model are presented in Figure 7.15.

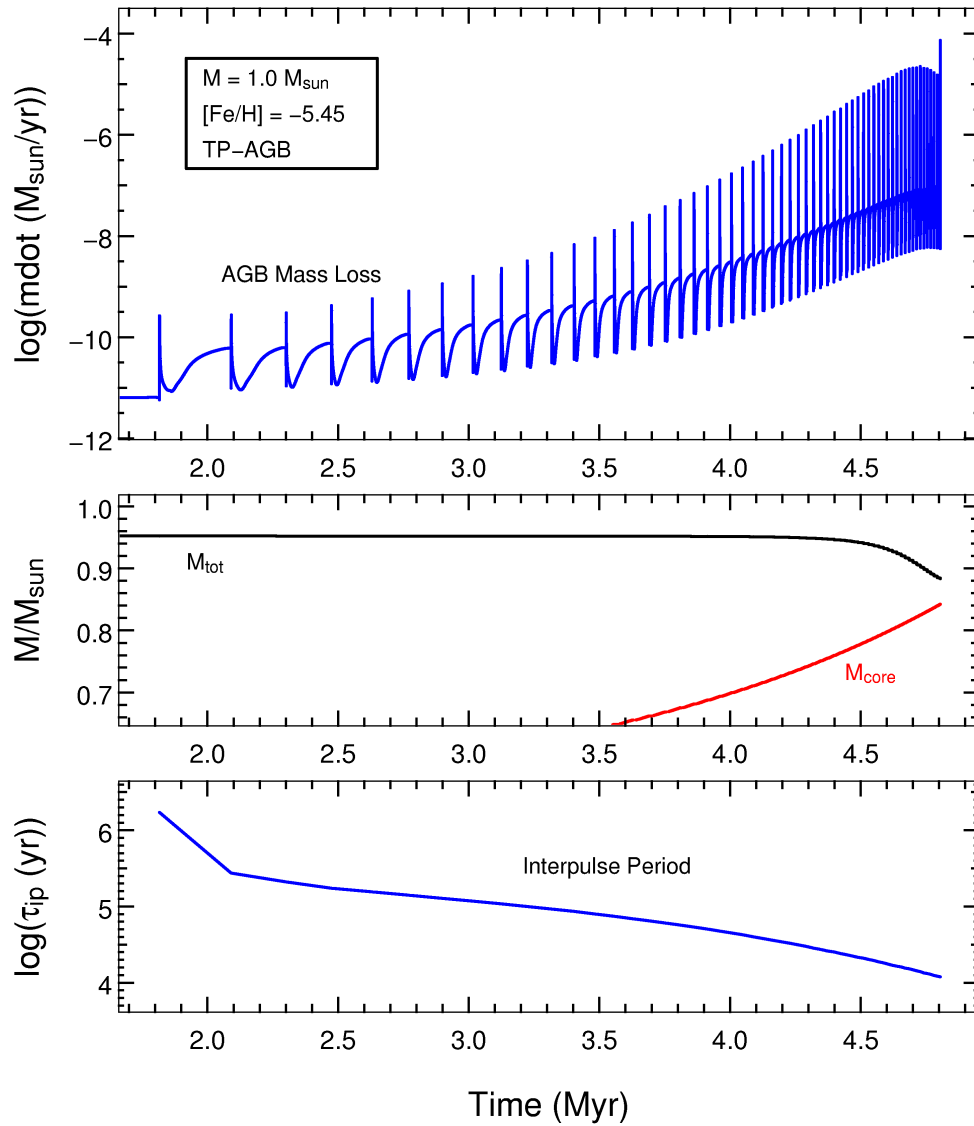


Figure 7.15: Some more properties of the AGB evolution of the $1 M_{\odot}$, $[\text{Fe}/\text{H}] = -5.45$ model. It can be seen that most of the envelope mass is lost towards the end of the AGB, and that the interpulse period decreases with the increase of the core mass. The core mass increases at a high rate due to the lack of 3DUP in this model.

the same figure. It rises to a maximum early on the TP-AGB before slowly declining to zero by the end of the evolution. The average value of λ for all the models are given in Table 7.7. For this model the average is 0.26.

Finally we note that we shall discuss the nucleosynthesis of these models in the next Section, after the subsection below which details the various lifetimes of the models.

7.2.6 Mass Loss

The mass loss formalisms used in the SEV code for these models was briefly discussed in the introduction to this chapter (Section 7.1.2 on page 218). The reduction of the total stellar mass of a couple of the models was touched on in the preceding subsections. In particular it was noted that the most rapid mass loss occurs at the end of the AGB phase, when the luminosities are highest. Indeed, in panel 2 of Figure 7.17 it can be seen that essentially all of the mass loss in the $[\text{Fe}/\text{H}] = -5.45$, $3 M_{\odot}$ occurs at the end of the AGB. This is mainly due to the fact that it does not make it to the RGB phase. In Figure 7.18 we show the evolution of the total mass for all of the $3 M_{\odot}$ models. It can be seen that all these IM mass models behave in the same way with regards to mass loss, i.e. all the mass lost from the stars occurs during the AGB phase. Thus in these models the composition of the AGB envelope wholly determines the yields. As mentioned in the introduction to the current chapter the mass loss formula used for the AGB (Vassiliadis and Wood 1993) is expected to be valid in these (initially) low- Z models since their envelopes are heavily enriched by the DSF and 3DUP episodes, especially as the AGB evolution progresses and the mass loss increases. These models are really quite similar to metal-rich models once on the AGB, as they have metal-rich envelopes and CO cores.

The situation is more complex in the low mass models. In Figure 7.19 we plot the evolution of total mass for all our $1 M_{\odot}$ models. In the figure we point out the various stages of evolution during which mass is lost. A significant fraction of the mass is lost during the RGB phase in these models. The situation is complicated by the fact that the stars turn off the RGB at earlier and earlier stages as the metallicity decreases. This was discussed above, in Section 7.2.1, where this low- Z characteristic was shown in the HR diagram. As the most rapid stage of mass loss is at the top of the RGB this has a strong effect on the mass of the star at the beginning of core He burning. This is clearly seen in Figure 7.19, where, for example, the $[\text{Fe}/\text{H}] = -3.0$ model loses $\sim 0.06 M_{\odot}$ of envelope material on the RGB whilst the $Z = 0$ model only loses $\sim 0.02 M_{\odot}$. In the more metal-rich models the mass loss on the RGB represents $\sim 40\%$ of the total mass loss from the star (the rest is lost on the AGB). This lowers to $\sim 10 \rightarrow 20\%$ at extremely low metallicity. The more mass loss there is on the RGB the more uncertain the further evolution and yields are. This is because the RGB composition is unpolluted, and thus of very low metallicity, so the mass loss rate is uncertain (see the discussion in the introduction: Section 7.1.2 on page 218). Since the RGB mass loss is greater in the more metal-rich low-mass models, this is where the most uncertainty lies.

At the lowest metallicities a second effect comes into play – there is a significant amount of mass loss on the horizontal branch (HB, core He burning phase). In fact, in the $Z = 0$ and $[\text{Fe}/\text{H}] = -6.5$ models ($1 M_{\odot}$) there is more mass lost during this phase than is lost on the RGB (50% more in the $Z = 0$ case). However the dominant source of mass loss is the AGB in

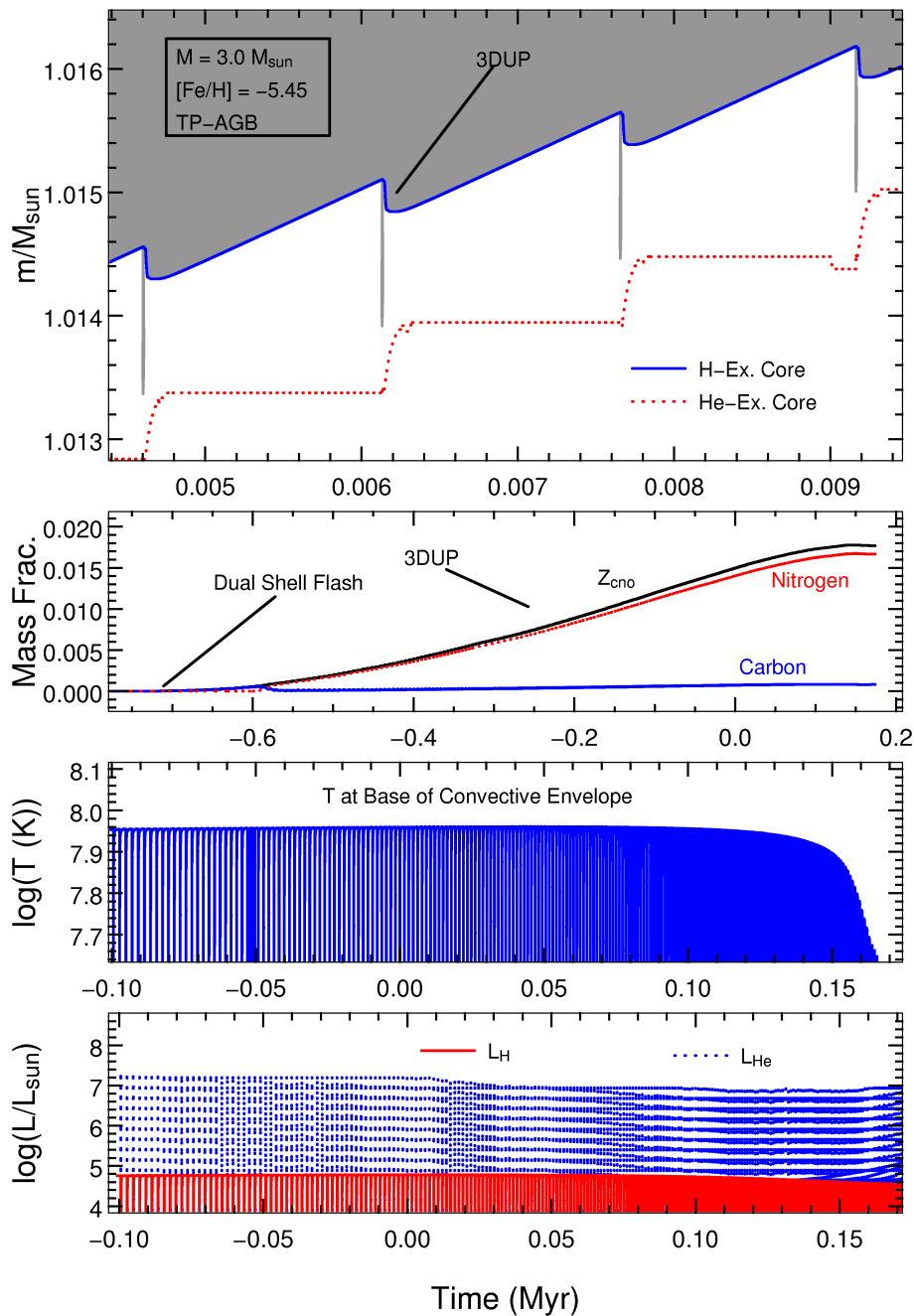


Figure 7.16: Some properties of the AGB evolution of the $3 M_{\odot}$, $[\text{Fe}/\text{H}] = -5.45$ model. Time has been offset by the same amount in all panels but note that the time span covered in each panel is different. We present this model as representative of the models that have their AGB envelopes dominated by the pollution arising from many 3DUP events during the AGB, which thus defines the chemical yield (see text for details). In the top panel a few thermal pulses can be seen (grey shading represents convection). The degree of 3DUP can be seen here. In the second panel we show the evolution of the surface abundances of carbon, nitrogen and Z_{cno} for the entire AGB. Z_{cno} is seen to increase by a very large amount due to 3DUP. The location of the DSF pollution is marked, highlighting the fact that it is dwarfed by the 3DUP pollution and thus has little effect on the yield. The composition of the AGB envelope is always dominated by nitrogen, due to the strong HBB caused by the high temperature at the base of the convective envelope ($T_{\text{bce}} \sim 10^{7.95}$), which is shown in the third panel. Note that there are so many pulses shown in the bottom two panels (~ 230) that they tend to blend together in the plot. More details of this model are presented in Figure 7.17.

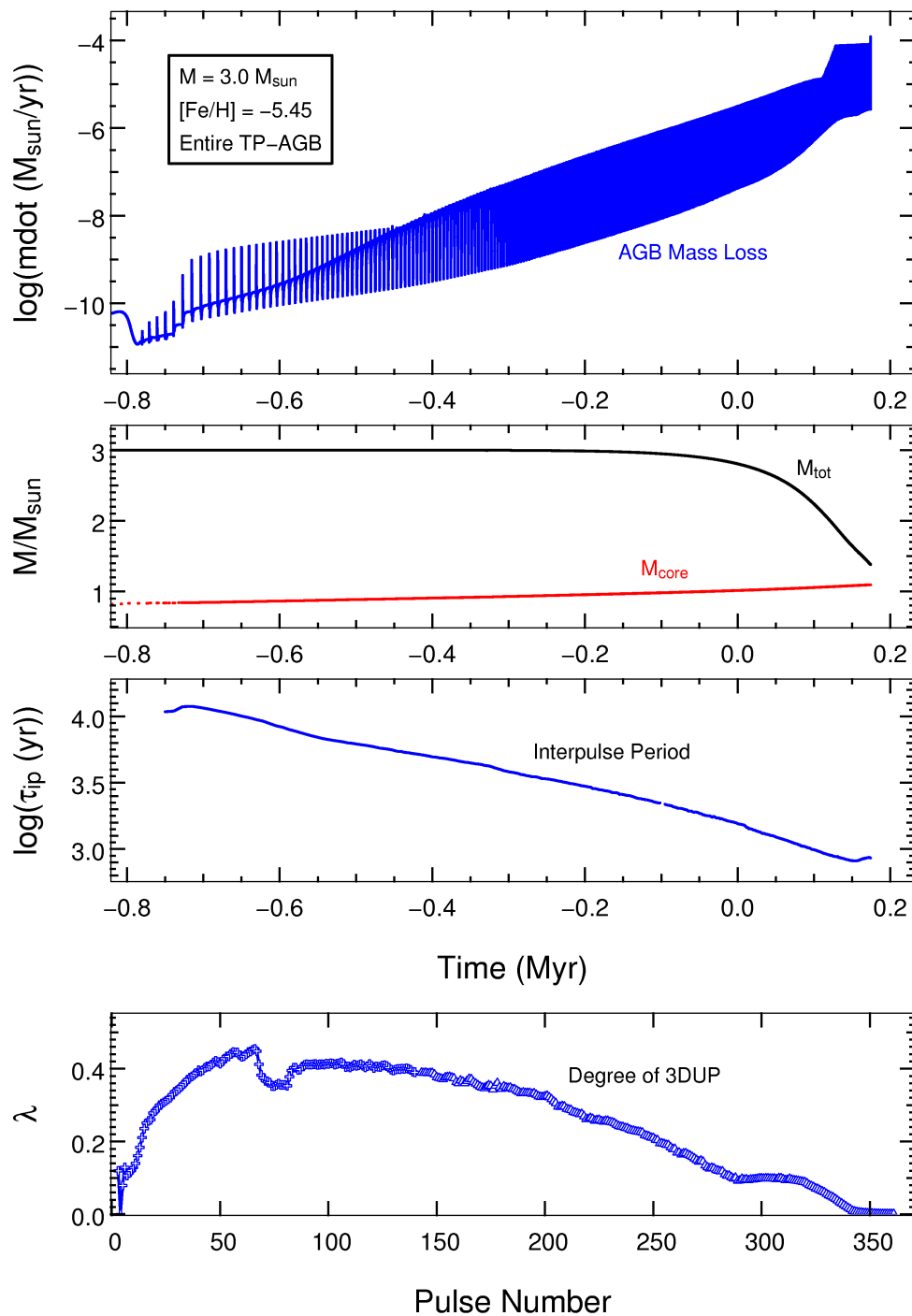


Figure 7.17: Some more properties of the AGB evolution of the $3 M_{\odot}$, $[\text{Fe}/\text{H}] = -5.45$ model. Time has been offset in the top three panels. All panels cover the entire AGB evolution. It can be seen that the mass of the star does not change significantly until half way through the AGB. Thus the chemical yield is dominated by the products of 3DUP and HBB. In the bottom panel we show the variation of the dredge-up parameter λ with pulse number. It can be seen that the depth of dredge up rises to a maximum early on the TP-AGB before slowly declining to zero by the end of the evolution.

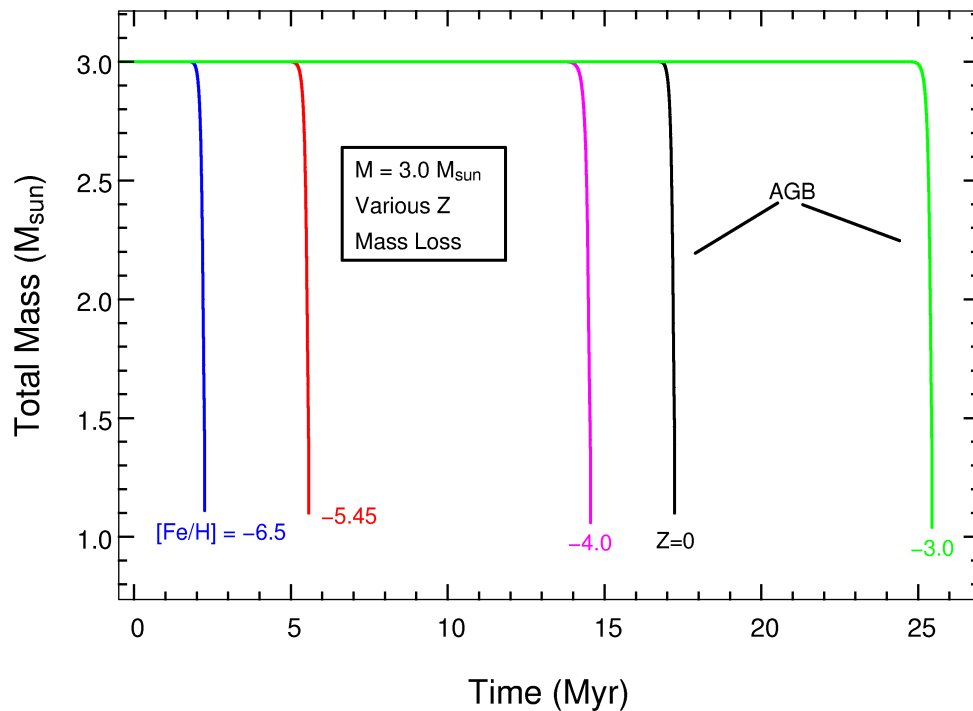


Figure 7.18: The evolution of total mass with time for all our $3 M_{\odot}$ models. Time has been offset for clarity (but by the same amount in all models). It can be seen that all the mass loss in these models occurs on the AGB. This is mainly due to the fact that these IM models do not go through the RGB phase.

these models. In the $Z = 0$ model, $\sim 70\%$ of the mass is lost during the AGB ($\sim 50\%$ in the $[\text{Fe}/\text{H}] = -6.5$ model). In the more metal-rich models the AGB mass loss represents $\sim 60\%$ of the total.

In summary, in the higher metallicity $1 M_{\odot}$ models the mass loss is generally split 40:60 on the RGB and AGB respectively, whilst in the most metal-poor models it is split 20:30:50 between the RGB, HB and AGB (roughly). The splits are more severe at lower mass, where, for example, 90% of the total mass loss in the $0.85 M_{\odot}$, $[\text{Fe}/\text{H}] = -3.0$ model occurs on the RGB (see Figure 7.20). As the mass loss occurs at different stages of evolution the yields will reflect a mix of the surface compositions from these stages. In particular, before the dual core flashes occur in the low metallicity models, and before the dual shell flashes occur in the higher metallicity models, the surface compositions reflect the initial, metal-poor compositions. Thus the mass lost on the RGB will have a diluting effect on the metal-rich yield of the AGB.

The mass loss on the HB in the extremely metal-deficient models is an interesting feature. As shown above in Figure 7.11 on page 237, the HBs of the $Z = 0$ and $[\text{Fe}/\text{H}] = -6.5$ models are substantially more luminous and very much redder than those of the other models. We suggest that this is an effect arising from the DCF pollution that occurred in these models just before their descent onto the HB. This event severely pollutes the envelopes, such that they are, from then on, much more like metal-rich models. Indeed, the change in HB morphology is much like that seen in Galactic globular clusters, where the more metal-rich populations show red HBs and the more metal-poor populations show blue HBs. It appears that this, combined with their higher luminosities, leads to a high mass-loss rate, as can be seen in the most metal-poor HB phases in Figures 7.19 and 7.20. Indeed, the mass lost on the HB in the more metal-‘rich’ models

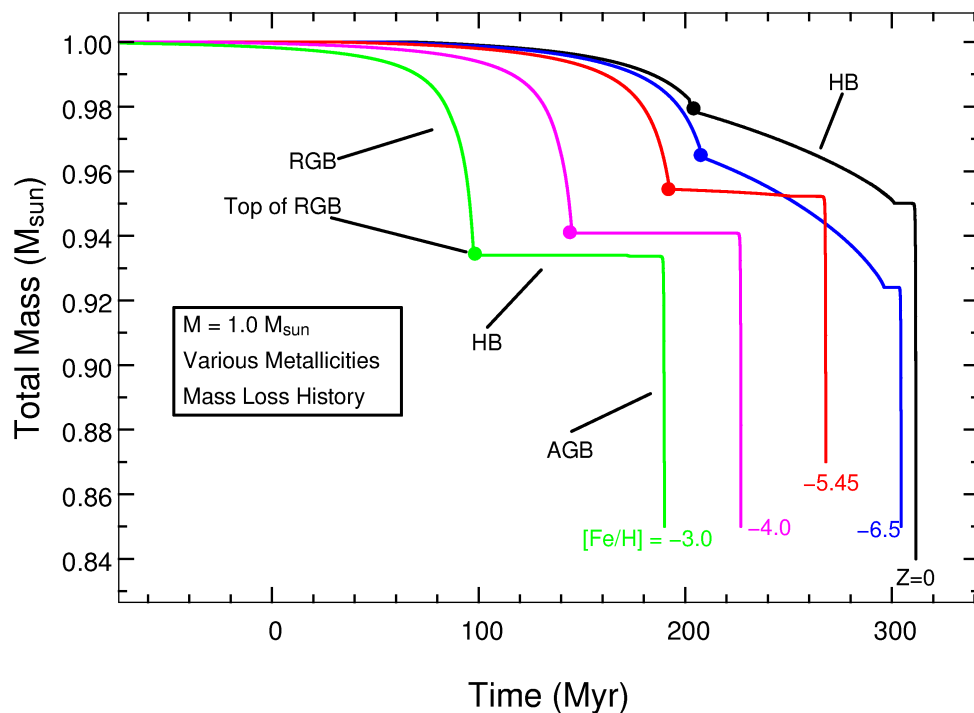


Figure 7.19: The evolution of total mass with time for all our $1 M_{\odot}$ models. Time has been offset for clarity (but by the same amount in all models). It can be seen that substantial mass loss occurs during a few different stages of evolution. In the higher metallicity models the mass loss is split 40:60 on the RGB and AGB respectively, whilst in the most metal-poor models it is split roughly 20:30:50 between the RGB, HB and AGB. The increased mass loss on the HB in the lowest metallicity models is due to the pollution arising from the DCF event that terminates the RGB. After this event their envelopes have a metallicity at least $\frac{1}{10}$ solar, whereas the (initially) higher metallicity models (with no DCF) still have very metal poor envelopes on the HB.

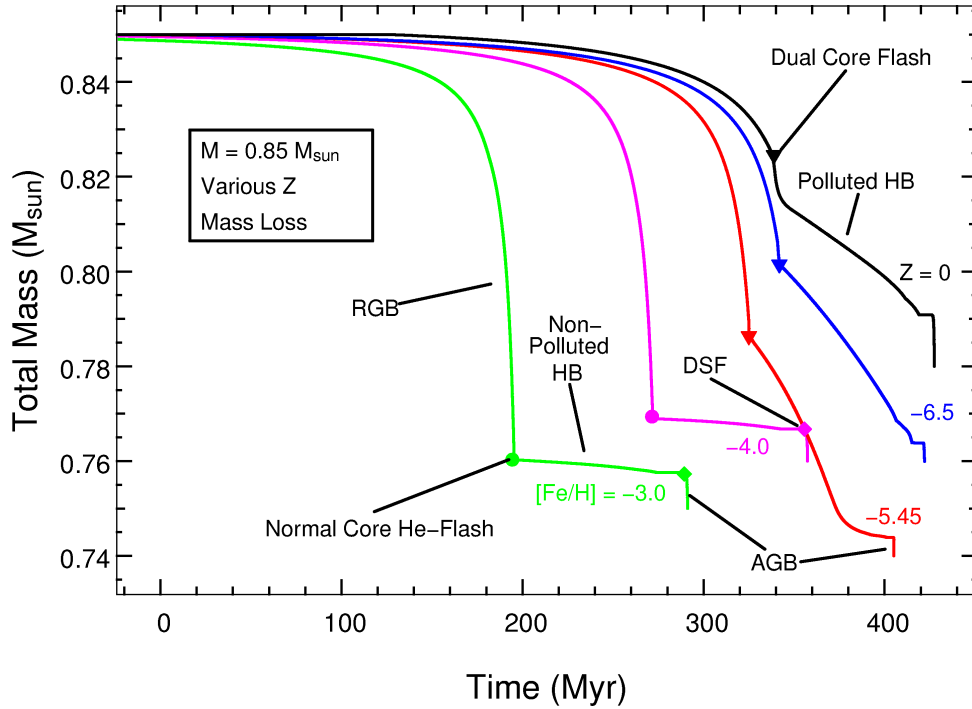


Figure 7.20: The evolution of total mass with time for all our $0.85 M_{\odot}$ models. Time has been offset for clarity (but by the same amount in all models). It can be seen that substantial mass loss occurs during a few different stages of evolution. In the higher metallicity models the mass loss is split about 90:10 on the RGB and AGB respectively, whilst in the most metal-poor models it is split roughly 55:40:5 between the RGB, HB and AGB. The increased mass loss on the HB in the lowest metallicity models is due to the pollution arising from the DCF event that terminates the RGB (marked by triangles). After this event their envelopes have a metallicity at least $\frac{1}{10}$ solar, whereas the (initially) higher metallicity models (with no DCF) still have very metal poor envelopes on the HB. Thus the initially most metal-poor models are actually the metal-rich models during this phase. The DSFs in the higher metallicity models are marked by diamonds, and normal core He flashes by small filled circles.

is much lower. Ironically this is due to the fact that by this stage the more metal-‘rich’ models are actually metal-poor compared to the models which have experienced DCF pollution (the initially metal-poor models). For example, on the HB Z_{cno} is 10^{-2} in the $[\text{Fe}/\text{H}] = -6.5$ model, whilst it remains at the initial value of 10^{-6} in the $[\text{Fe}/\text{H}] = -4.0$ model. It is interesting to see this metallicity effect on mass loss despite the fact that we have not explicitly included any metallicity dependence in the mass loss formulae.

To end this subsection we reiterate/clarify the main finding in regards to uncertainties in the modelling arising from mass-loss, as it is an important caveat to keep in mind. The main finding was that the mass loss from the RGB in some of the low-mass models – in particular the lowest mass and highest metallicity models – makes up a significant proportion of the total mass loss. This causes a problem because the envelope compositions of these models are still very metal-poor during the RGB phase, and, as the mass-loss rate is uncertain at these metallicities, an uncertainty arises in the evolution. This naturally has a strong impact on the yields of these models, effectively diluting the yield from the AGB. If, in reality, the RGB mass loss should be much lower then our yields will be wrong – they should be more metal-rich. The RGB evolutionary paths of the models are also rendered uncertain as the rate of core growth would be different with a lower mass loss rate. This then has implications for the HB and RGB evolution. Thus many uncertainties arise through the unknown nature of mass-loss rates at low

metallicity. However we note that the metallicity of a stellar model is, to some degree, indirectly taken into account in the mass loss formulae – as evidenced by the varying amounts of mass lost during the HB phases of the models discussed above.

7.2.7 Table of Lifetimes

In Table 7.8 we present the lifetimes of various stages of evolution for the whole grid of models. The MS lifetimes of the low-mass stars is essentially constant across this metallicity range, being ~ 10.1 Gyr. In the intermediate mass models ($M = 2$ and $3 M_{\odot}$) we find a variation of $\sim 20\%$ at each mass. In general the time spent on the MS increases with the decrease in metallicity. This is due to the increased dominance of p-p chain energy generation in stars that would normally be powered primarily by the CNO cycles. The lifetimes of these stars are much shorter than those of the low-mass stars (as normal), being ~ 600 Myr at $2 M_{\odot}$ and ~ 180 Myr at $3 M_{\odot}$. On the subgiant branch (SGB), which we define as the time between the MSTO and the bottom of the RGB (or He burning ignition in the more massive models), there is a moderate variation in lifetime in the low mass stars, generally seen as a decrease with an increase in metallicity. The intermediate mass models however show a very strong variation with metallicity. This is due to the fact that stars at these masses turn off the HG earlier and earlier (most do not reach the RGB at all, as mentioned earlier), as the metallicity decreases. The most extreme of these is the $3 M_{\odot}$, $Z = 0$ model which only spends 8 Myr evolving towards the red before igniting He in its core. This early turning off the HG also manifests itself in the RGB lifetimes which, naturally, are zero for most of the IM models. Only the two most metal-rich $2 M_{\odot}$ models actually spend time on the RGB – but only a few Myr. On the other hand all of the low mass models complete the full evolution of the RGB, igniting He at the top of the RGB. In an opposite trend to their SGB lifetimes the low-mass RGB lifetimes *decrease* with metallicity. At $0.85 M_{\odot}$ the lifetime ranges from 200 Myr at $Z = 0$ to 250 Myr at $[\text{Fe}/\text{H}] = -3$. At $1 M_{\odot}$ the lifetime ranges from 110 Myr at $Z = 0$ to 155 Myr at $[\text{Fe}/\text{H}] = -3$. This reflects the early termination of the RGB in the low- Z models due to earlier and earlier He ignition, as reported in an earlier section. Horizontal branch (HB) lifetimes in the low mass models appear to first decrease then increase with metallicity. The picture is clearer in the IM models, where a clear decrease of HB lifetime with metallicity can be seen. In the $2 M_{\odot}$ models it ranges from 95 Myr at $[\text{Fe}/\text{H}] = -3$ down to a short 30 Myr at $Z = 0$. In the $3 M_{\odot}$ models it ranges from 47 Myr at $[\text{Fe}/\text{H}] = -3$ down to a very short 12 Myr at $Z = 0$. AGB lifetimes are generally seen to decrease with metallicity. There is not much variation at in the IM models, with AGB lifetimes being ~ 2 Myr at $2 M_{\odot}$ and ~ 1 Myr at $3 M_{\odot}$, but a strong variation is seen at low mass. At $1 M_{\odot}$ the lifetimes range from 4.4 Myr at $[\text{Fe}/\text{H}] = -3$ down to 1.7 Myr at $Z = 0$ (although the $[\text{Fe}/\text{H}] = -6.5$ model lifetime is actually shorter). The picture is similar at $0.85 M_{\odot}$ except that there is a drastic drop from 3.8 Myr at $[\text{Fe}/\text{H}] = -4$ to 0.05 Myr at $[\text{Fe}/\text{H}] = -5.45$, before an increase at lower Z . We are unsure what are the driving factors in this case, and leave the investigation of this interesting variation in lifetimes for future work.

Mass = 0.85 M _⊙							
[Fe/H]	L_{tip}	MS (Gyr)	SGB	RGB	CHeB	AGB	Total (Gyr)
-3.00	3.1	10.0	740	250	85	4.00	11.09
-4.00	3.0	10.1	750	220	75	3.80	11.16
-5.45	2.8	10.1	820	205	75	0.05	11.21
-6.50	2.6	10.1	840	200	75	0.60	11.22
Z = 0	2.3	10.1	840	200	80	1.50	11.23

Mass = 1.0 M _⊙							
[Fe/H]	L_{tip}	MS (Gyr)	SGB	RGB	CHeB	AGB	Total (Gyr)
-3.00	3.1	5.58	470	155	74	4.35	6.29
-4.00	3.0	5.73	360	150	61	4.34	6.33
-5.45	2.8	5.73	410	131	57	3.03	6.37
-6.50	2.6	5.73	450	127	86	1.05	6.40
Z = 0	2.3	5.70	480	110	96	1.74	6.41

Mass = 2.0 M _⊙							
[Fe/H]	L_{tip}	MS	SGB	RGB	CHeB	AGB	Total
-3.00	2.2	492	140	5.7	95	2.50	745
-4.00	2.1	562	84	1.5	72	2.30	733
-5.45	–	605	58	zero	50	2.27	722
-6.50	–	625	43	zero	40	2.10	718
Z = 0	–	660	12	zero	30	2.02	713

Mass = 3.0 M _⊙							
[Fe/H]	L_{tip}	MS	SGB	RGB	CHeB	AGB	Total
-3.00	–	185	18	zero	47	1.24	255
-4.00	–	174	27	zero	38	1.19	245
-5.45	–	177	30	zero	24	0.96	236
-6.50	–	189	21	zero	17	1.04	232
Z = 0 ^a	–	222	8	zero	12	1.16	247

Table 7.8: Various lifetimes for all the low metallicity models, grouped in terms of initial mass. We redisplay the lifetimes for the Z = 0 models for ease of comparison. Also included, in the second column, are the luminosities at the tip of the RGB (L_{tip}) – if the model made it to the RGB. All ages are in Myr unless otherwise stated. Metallicity is given as [Fe/H], except for Z = 0. Lifetimes are given for: MS (ZAMS to MS turn-off), SGB (MS turn-off to base of RGB, or to the start of core He burning in the more massive models), RGB (red giant branch), CHeB (core helium burning), AGB (thermally-pulsing AGB) and Total (the entire lifetime of the star, from ZAMS to the end of the TP-AGB).

^a This model started with a pure H-He composition, with $Y = 0.230$ rather than 0.245.

7.3 Nucleosynthetic Evolution

7.3.1 Introduction

In this section we give an overview of the nucleosynthetic evolution of all our metal-deficient models. We have also included the $Z = 0$ models of the previous chapters in the discussion, as well as in the tables, for comparison. We discuss all of the key evolutionary events in separate subsections. Within those subsections we limit the discussion to some key nucleosynthetic signatures, due to time and space constraints. However, for the interested reader, we present detailed yield plots and tables in the next section and also in the appendices, from which much detailed information can be gleaned. We also give an overall summary of our results, and compare them to previous studies, at the end of this chapter (Section 7.5 on page 282).

A finding from the structural evolution section is relevant for the discussion of the nucleosynthesis in these models. In subsection 7.2.5 on page 238 we showed that our models can be divided into three distinct groups based on the source of the main contribution to AGB envelope pollution. These groups are:

1. DCF Dominated: Low-Mass & *Extremely* Metal-Deficient Models
2. DSF Dominated: Low-Mass & Very Metal-Deficient Models
3. 3DUP Dominated: Intermediate-Mass – All Metallicities

This grouping gives a good overview of the competing processes that pollute the envelopes of these metal-deficient models. Below we detail the nucleosynthetic evolution arising from these major events, as well as from other more minor events. Although we discuss all the models in the grid (20 in total) we give detailed figures of only two, in order to illustrate the various evolutionary events. The models we display both have a metallicity of $[\text{Fe}/\text{H}] = -5.45$, and masses of 1.0 and $3.0 M_{\odot}$. These cover two of the groups outlined above (groups 2 and 3). We note that this metallicity corresponds to the most metal poor star known to date (HE1327-2326, [Frebel et al. 2005a](#)) – at least in terms of $[\text{Fe}/\text{H}]$. For an example of a group 1 model we refer the reader to the detailed chapters on the $0.85 M_{\odot}$, $Z = 0$ model (Chapters 5 and 6). We do however provide tables containing key surface composition quantities for the whole grid of models – Tables 7.9 and 7.10. These complement Tables 7.6, 7.7 and 7.8 in the previous (structural evolution) section. As mentioned above we present the yields in the next section (on page 263).

7.3.2 First Dredge-Up

Apart from the two most metal-rich $2 M_{\odot}$ models, it is only the low mass models that make it to the RGB to experience first dredge-up (FDUP). Thus most of the IM models retain their initial surface composition until second dredge-up. The models that do experience FDUP all show only minor enhancements in helium. For example, in the $1 M_{\odot}$, $[\text{Fe}/\text{H}] = -5.45$ model the He abundance at the surface only changes from $Y = 0.245$ to 0.249 . This universal trait is seen in column 3 of Table 7.9.

In Table 7.10 we give the $^{12}\text{C}/^{13}\text{C}$ ratio after FDUP. We note that the initial value of this ratio is very high in all the models, due to the non-scaled-solar composition. For example, in the $[\text{Fe}/\text{H}] = -5.45$ models it is $\approx 10^7$. In some of the models the effect of FDUP on this ratio is very strong, reducing it to ~ 10 . In some models, particularly the lowest metallicity models, FDUP is less efficient, and the ratio remains super-solar after FDUP. The $Z = 0$ models are a distinct case, as there is no CN cycling above the main H burning region due to a lack of catalysts. As mentioned in Section 6.2.1 on page 161 (in regards to the $0.85 M_{\odot}$, $Z = 0$ model) the main species to be affected by the FDUP at $Z = 0$ is ^3He , as it is produced far above the main H burning shell in p-p reactions. Also due to the lack of CN-cycling the post-FDUP C/N ratio (given in Table 7.10) remains at zero (or ∞) in the $Z = 0$ models. In the metal-deficient models the C/N ratio shows a similar variation as the $^{12}\text{C}/^{13}\text{C}$ ratio does, again reflecting the degree of FDUP. The C/N ratio of the initial composition of these models is also very high, being $\sim 10^6$ in the $[\text{Fe}/\text{H}] = -5.45$ models. This is due to the paucity of N in the $20 M_{\odot}$, $Z = 0$ supernova yield. Thus it can be seen in Table 7.10 that the FDUP operates very effectively in the higher metallicity models, reducing the ratio to between ~ 5 and ~ 180 by mixing up N-enhanced material left over from CN cycling in the outer reaches of the H-burning shell. However in the more metal-poor models it can be seen that the ratio remains very high. This is mainly a reflection of the depth of FDUP. For instance, in the $0.85 M_{\odot}$, $[\text{Fe}/\text{H}] = -3$ model the maximum depth of FDUP was $0.4 M_{\odot}$ whilst it was only $0.52 M_{\odot}$ in the $0.85 M_{\odot}$, $[\text{Fe}/\text{H}] = -5.45$ model. It also reflects the reduced efficiency of the CN cycle at very low Z . Indeed, in column 7 of Table 7.10 a strong correlation between FDUP efficiency and metallicity can be seen.

The metallicity Z of the models does not change due to FDUP as the ‘polluted’ material dredged up has only undergone CN and/or p-p burning, so the catalysts have just been rearranged (ie. $\text{C} \rightarrow \text{N}$) without producing any (significant) additional number of heavy nuclei. This is why we do not display the Z_{cno} value for FDUP in Table 7.9.

In Figure 7.21 we give an example of FDUP in one of our models (the $1 M_{\odot}$, $[\text{Fe}/\text{H}] = -5.45$ model). We show the profiles of some species just as the envelope convection is extending inwards. It can be seen that a moderate amount of H burning has occurred in the region that is subsequently dredged up. The ^{14}N abundance has increased by up to 5 orders of magnitude (though we note that it is still present in very small amounts in an absolute sense), as has ^{13}C . ^{12}C and ^{16}O are scarcely affected but ^3He has increased and ^7Li has decreased. Thus, as the envelope moves inwards, it can be seen that this is the source of the decrease in the $^{12}\text{C}/^{13}\text{C}$ and C/N ratios detailed above. In the bottom panel we display the ^4He abundance, which has also increased slightly in the region of interest, leading to the slight increase in surface Y by the end of FDUP.

7.3.3 Dual Core Flashes

In our models the dual core flash (DCF) event is found to occur only in the low mass models with the lowest metallicities. In Table 7.9 we show which models go through this event, along with the surface helium and Z_{cno} abundances after the event. The DCF occurs at the time of the core He flash, at the top of the RGB. Thus the only previous envelope pollution has come from FDUP. In terms of Y and Z_{cno} FDUP has little effect in these models. Thus the values

Mass = 0.85 M _⊙								
[Fe/H]	DF	Y _{fdu}	Y _{sdu}	Y _{DF}	Y _{agb}	Z _i	Z _{DF}	Z _f
-3.00	Shell	0.25	0.26	0.28	0.28	1E-05	1E-02	1E-02
-4.00	Shell	0.25	0.25	0.27	0.27	1E-06	1E-03	1E-03
-5.45	Core	0.25	0.44	0.44	0.44	4E-08	3E-02	3E-02
-6.50	Core	0.25	0.31	0.31	0.31	4E-09	6E-02	6E-02
Z = 0	Core	0.25	0.33	0.33	0.33	zero	1E-03	1E-03

Mass = 1.0 M _⊙								
[Fe/H]	DF	Y _{fdu}	Y _{sdu}	Y _{DF}	Y _{agb}	Z _i	Z _{DF}	Z _f
-3.00	Shell	0.26	0.27	0.28	0.28	1E-05	5E-03	5E-03
-4.00	Shell	0.25	0.27	0.28	0.28	1E-06	1E-02	1E-02
-5.45	Shell	0.25	0.26	0.28	0.28	4E-08	4E-03	3E-03
-6.50	Core	0.25	0.33	0.33	0.33	4E-09	7E-02	6E-02
Z = 0	Core	0.25	0.34	0.34	0.34	zero	1E-02	1E-02

Mass = 2.0 M _⊙								
[Fe/H]	DF	Y _{fdu}	Y _{sdu}	Y _{DF}	Y _{agb}	Z _i	Z _{DF}	Z _f
-3.00	None	0.25	0.26	–	0.31	1E-05	–	1E-02
-4.00	Shell	0.25	0.27	0.27	0.30	1E-06	6E-04	5E-03
-5.45	Shell	–	0.29	0.29	0.34	4E-08	2E-05	1E-02
-6.50	Shell	–	0.30	0.30	0.34	4E-09	7E-04	8E-03
Z = 0	Shell	–	0.31	0.31	0.34	zero	2E-04	4E-03

Mass = 3.0 M _⊙								
[Fe/H]	DF	Y _{fdu}	Y _{sdu}	Y _{DF}	Y _{agb}	Z _i	Z _{DF}	Z _f
-3.00	None	–	0.26	–	0.36	1E-05	–	3E-02
-4.00 ^a	None	–	n/a	–	0.40	1E-06	–	4E-02
-5.45	Shell	–	0.30	0.30	0.39	4E-08	4E-08	2E-02
-6.50	Shell	–	0.32	0.32	0.39	4E-09	8E-06	1E-02
Z = 0 ^b	Shell	–	0.33	0.33	0.41	zero	8E-06	1E-02

Table 7.9: Various surface abundance quantities at different stages of evolution. Values for all the low metallicity models are displayed, grouped in terms of initial mass. We also show the Z = 0 models for comparison. Initial metallicity (first column) is given as [Fe/H], except for Z = 0. The second column specifies whether the model experienced a dual flash (DF) or not, be it a DCF or DSF. The abundances given are: Y_{fdu} (the mass fraction of He after the first dredge up episode), Y_{sdu} (after 2DUP), Y_{DF} (after a dual flash), Y_{agb} (at the end of the AGB), Z_i (the mass fraction of CNO nuclei initially present), Z_{DF} (after a dual flash), Z_f (at the end of the evolution/AGB). Most of the intermediate mass models did not reach the RGB so Y_{fdu} is blank in these cases.

^a Due to a loss of data we are unable to provide the Y_{sdu} value.

^b This model started with a pure H-He composition, with Y = 0.230 rather than 0.245.

Mass = 0.85 M _⊙									
[Fe/H]	DF	$\frac{^{12}\text{C}}{^{13}\text{C}}_{fd}$	$\frac{^{12}\text{C}}{^{13}\text{C}}_{sd}$	$\frac{^{12}\text{C}}{^{13}\text{C}}_{DF}$	$\frac{^{12}\text{C}}{^{13}\text{C}}_{agb}$	$\frac{\text{C}}{\text{N}}_{fd}$	$\frac{\text{C}}{\text{N}}_{sd}$	$\frac{\text{C}}{\text{N}}_{DF}$	$\frac{\text{C}}{\text{N}}_{agb}$
-3.00	S	71	34	21	21	34	1	107	44
-4.00	S	152	41	6	6	181	1	4	3
-5.45	C	2E4	6	7	7	2E6	2	7	4
-6.50	C	4E6	8	8	8	6E6	3	4	3
Z = 0	C	0	4	4	4	0	0.14	0.14	0.14

Mass = 1.0 M _⊙									
[Fe/H]	DF	$\frac{^{12}\text{C}}{^{13}\text{C}}_{fd}$	$\frac{^{12}\text{C}}{^{13}\text{C}}_{sd}$	$\frac{^{12}\text{C}}{^{13}\text{C}}_{DF}$	$\frac{^{12}\text{C}}{^{13}\text{C}}_{agb}$	$\frac{\text{C}}{\text{N}}_{fd}$	$\frac{\text{C}}{\text{N}}_{sd}$	$\frac{\text{C}}{\text{N}}_{DF}$	$\frac{\text{C}}{\text{N}}_{agb}$
-3.00	S	43	29	20	20	5	1	117	33
-4.00	S	41	25	14	14	8	1	47	25
-5.45	S	10	5	14	14	27	0.03	55	23
-6.50	C	316	10	10	10	963	4	5	4
Z = 0	C	0	6	6	6	0	0.60	0.60	0.60

Mass = 2.0 M _⊙									
[Fe/H]	DF	$\frac{^{12}\text{C}}{^{13}\text{C}}_{fd}$	$\frac{^{12}\text{C}}{^{13}\text{C}}_{sd}$	$\frac{^{12}\text{C}}{^{13}\text{C}}_{DF}$	$\frac{^{12}\text{C}}{^{13}\text{C}}_{agb}$	$\frac{\text{C}}{\text{N}}_{fd}$	$\frac{\text{C}}{\text{N}}_{sd}$	$\frac{\text{C}}{\text{N}}_{DF}$	$\frac{\text{C}}{\text{N}}_{agb}$
-3.00	N	29	26	–	5	2	1	–	0.05
-4.00	S	420	26	12	5	8E3	0.20	31	0.05
-5.45	S	–	29	5	5	–	0.50	0.04	0.05
-6.50	S	–	30	15	5	–	0.44	30	0.05
Z = 0	S	–	5	8	5	–	0.01	9	0.05

Mass = 3.0 M _⊙									
[Fe/H]	DF	$\frac{^{12}\text{C}}{^{13}\text{C}}_{fd}$	$\frac{^{12}\text{C}}{^{13}\text{C}}_{sd}$	$\frac{^{12}\text{C}}{^{13}\text{C}}_{DF}$	$\frac{^{12}\text{C}}{^{13}\text{C}}_{agb}$	$\frac{\text{C}}{\text{N}}_{fd}$	$\frac{\text{C}}{\text{N}}_{sd}$	$\frac{\text{C}}{\text{N}}_{DF}$	$\frac{\text{C}}{\text{N}}_{agb}$
-3.00	N	–	21	–	5	–	0.46	–	0.05
-4.00 ^a	N	–	n/a	–	5	–	n/a	–	0.05
-5.45	S	–	21	21	5	–	0.24	0.26	0.05
-6.50	S	–	26	81	5	–	0.23	0.51	0.05
Z = 0 ^b	S	–	5	5	5	–	0.01	0.04	0.05

Table 7.10: The $^{12}\text{C}/^{13}\text{C}$ and C/N ratios at different stages of evolution. Values for all the low metallicity models are displayed, grouped in terms of initial mass. We also show the $Z = 0$ models for comparison. Initial metallicity (first column) is given as [Fe/H], except for $Z = 0$. The second column specifies whether the model experienced a dual flash (DF) or not, be it a DCF (C), DSF (S) or neither (N). The subscripts in the table headers indicate the stage of evolution at which the values are taken: *fd* (just after the first dredge up episode), *sd* (after 2DUP), *DF* (after a dual flash), *agb* (at the end of the AGB). Most of the intermediate mass models did not reach the RGB so the FDUP entries are blank in these cases.

^a Due to a loss of data we are unable to provide the 2DUP values.

^b This model started with a pure H-He composition, with $Y = 0.230$ rather than 0.245.

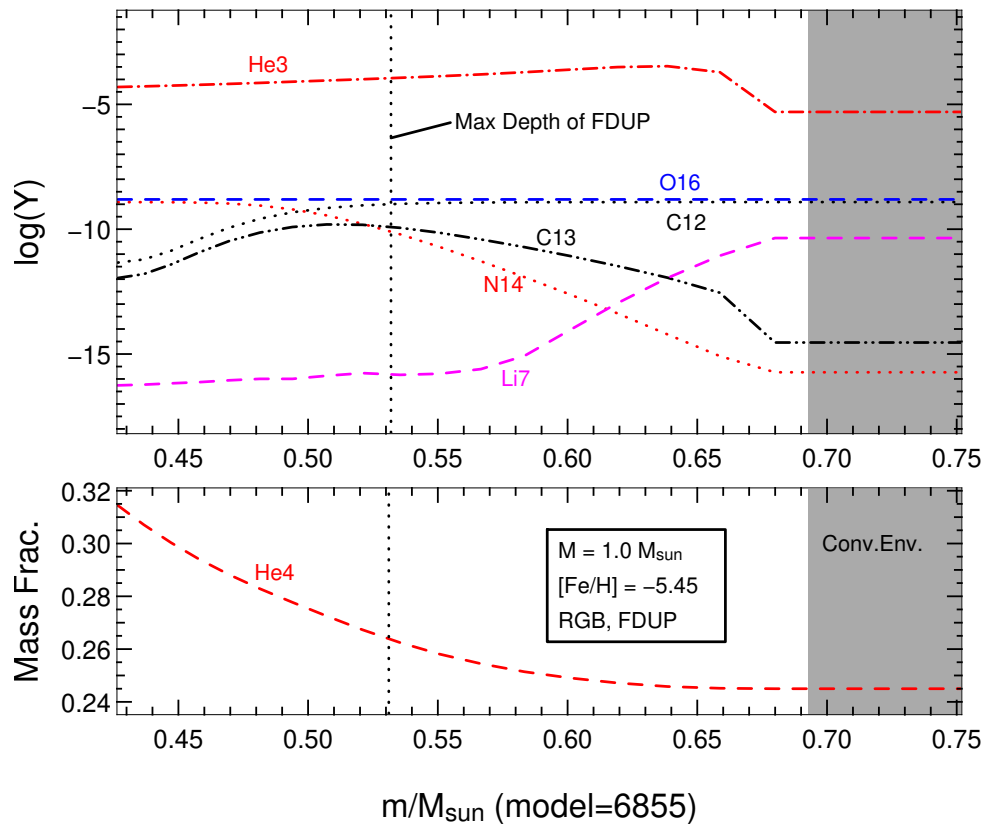


Figure 7.21: The abundance profiles of some selected species just as the envelope convection begins to deepen at FDUP (at the start of the RGB). Due to the CN cycle operating over a wide mass range it can be seen that the abundances of the CN(O) nuclides have been altered. This causes strong changes in the $^{12}\text{C}/^{13}\text{C}$ and C/N ratios. We note however that the changes occur amongst extremely small abundances of these species. Helium is slightly increased by the end of FDUP, as expected from panel 2.

for these quantities post-DCF represent the pollution resulting from this event alone. It can be seen that the abundance of He increases by a large amount. In all these models the initial Y was ~ 0.25 . After the DCFs the average value is ~ 0.35 (averaged over all the DCF models) – a 30% increase. This large increase reflects the large amount of He-rich material dredged up after the DCF (see ΔM_c in Table 7.6 on page 233, in the structural evolution section). As there is no 3DUP and no significant HBB in these models this surface He abundance is essentially retained till the end of the AGB evolution. Thus the chemical yield from these models will have a He-enriched contribution (just how strongly this affects the yields depends on the mass-loss history of each model).

In all the models which experience the DCF the $^{12}\text{C}/^{13}\text{C}$ ratio remains very high after FDUP, or, in the case of the $Z = 0$ models, it remains undefined (see Table 7.10). The story after the DCF is much different though – in all the models the ratio is then quite low, being between 4 and 10. This reflects the CN processing that has occurred in the DCF hydrogen convective zone (HCZ) and HeCZ. The CN cycle equilibrium value of the $^{12}\text{C}/^{13}\text{C}$ ratio is usually ~ 4 , so these low values show that considerable CN cycling has occurred, as expected. Unlike the FDUP event the absolute abundances of these species increases enormously, which is seen in the $Z_{cno,DF}$ values of Table 7.9.

The C/N ratios also remained high after the FDUP in these models. In the low-metallicity models the ratio dropped to much lower levels after the DCF. In both of the $Z = 0$ models the ratio, which was previously undefined due to the lack of metals, was < 1 after the DCF. Thus the surface composition contained more N than C. This may give an indication that the polluting material from the DCF event is N rich in the metal-poor models too, but it was diluted in those cases. The dominance of N is another sign of advanced CN cycling during the DCF.

As mentioned above all the models that experienced the DCF had a very large increase in surface metallicity, as defined by Z (naturally $[\text{Fe}/\text{H}]$ remains essentially unchanged). In Table 7.9 we give the initial Z_{cno} values (the sum of the mass fractions of the CNO nuclides) and also the Z_{cno} resulting from the DCFs. It can be seen that the metal abundance jumps, almost uniformly amongst the models, to $Z_{cno} \sim 10^{-2}$ (the $0.85 M_{\odot}$, $Z = 0$ model ‘only’ reaches 10^{-3}). Thus most of the DCF stars have a super-solar Z after the DCF. We note that the Z values do not change significantly between this stage of evolution and the end of the AGB, as can be seen from the final Z_{cno} values given in the same table

As second dredge-up has little effect on the surface abundances in these models (apart from a modest decrease in the C/N ratio in some of the models), and as 3DUP and HBB do not occur to any significant degree, the models essentially retain the chemical signatures from this event till the end of the AGB. Thus the metallicity and chemical profile of the yields are, to varying extents, set by the DCF events (the extent depends on the mass-loss history of each model). This also means that this contribution to the yields is directly dependent on the treatment of the DCF, and thus on the uncertainties associated with modelling this event (eg. the unknown degree of overshoot, which we have assumed to be zero). We note that this group of stars constitute our Group 1 specified in the introduction to this section – the group that we defined due to their AGB surface composition being dominated by the DCF. For a more detailed description of the nucleosynthesis of the DCF event we refer the reader to the $0.85 M_{\odot}$, $Z = 0$ model in Chapter 6.

7.3.4 Second Dredge-Up

In the models that experience the dual core flash (low mass and lower metallicities) the 2DUP has little effect on the surface He abundance. As mentioned above the He abundance arising from the DCF was quite high in all these models, and thus the 2DUP would have to bring up an enormous amount of He to alter this. The surface He abundance in these ('Group 1') models is set by the DCF for the rest of the evolution as the AGB has a negligible effect. The metallicity of these models is also unaltered by the 2DUP. Likewise the $^{12}\text{C}/^{13}\text{C}$ and C/N ratios do not change significantly (the $0.85 M_{\odot}$, $[\text{Fe}/\text{H}] = -5.45$ model is an exception, where the C/N ratio reduces from 7 to 2 after 2DUP), as they were already quite low due to the preceding DCF.

In the low-mass and intermediate-mass models that experienced the dual shell flash, 2DUP increased the surface He abundance by varying amounts. The degree of increase is mainly a function of metallicity but also of mass, with the lowest metallicity and highest mass models having the greatest increases. In the low mass models, only the most metal-rich of which went through DSFs, a typical increase was from $Y \sim 0.25$ to $Y \sim 0.27$. As mentioned below the DSF that comes after the 2DUP further increased Y , usually by a comparable amount to that gained from 2DUP. The surface abundance on the AGB in these low mass models then remained at this level of He enrichment. Thus, in these 'Group 2' models, the 2DUP is a significant contributor to the He yields, but not the only one. In the lowest metallicity intermediate-mass models the abundance reached as high as $Y \sim 0.33$ as a result of 2DUP (no FDUP occurred in these models so this increase was from the primordial value of ~ 0.25). In this group (Group 3) HBB on the AGB also increases Y in the yields. Interestingly, just like the DSF in the low-mass models (which has little effect on Y in these IM models), the HBB increases the surface He abundance by a similar amount as that gained from 2DUP. For example, in the $[\text{Fe}/\text{H}] = -5.45$, $2 M_{\odot}$ model 2DUP raised Y from 0.25 to 0.29, then HBB and 3DUP raised it to 0.34 (see Table 7.9). Thus, like in the low-mass models, the 2DUP has a significant effect on the final yield of He, but is not the only contributor.

In regards to the $^{12}\text{C}/^{13}\text{C}$ ratio in the low- and intermediate-mass models (that do not go through the DCF – ie. Groups 1 and 2), it is seen to decrease in all the models to a similar level. In the intermediate mass models the ratio ends up in the range $20 \rightarrow 30$ whilst it is slightly higher in the low mass models, being in the range $25 \rightarrow 40$. In most of the IM models there was no FDUP, thus these values were down from the (very high) primordial ones. In the LM models FDUP had already reduced the $^{12}\text{C}/^{13}\text{C}$ ratio substantially so the change was not as great. An exception here is the $1 M_{\odot}$, $[\text{Fe}/\text{H}] = -5.45$ model, which had quite a low value after FDUP ($= 10$) and thus a very low value after 2DUP ($= 5$). The $Z = 0$ IM models are a distinct case, as their $^{12}\text{C}/^{13}\text{C}$ ratios were initially zero. In this case 2DUP *increases* the ratio, universally bringing it up to 5 (the CN equilibrium value).

The C/N ratio is reduced by 2DUP in all the low- and intermediate-mass models (that do not go through the DCF – ie. Groups 1 and 2). At low mass the ratio ends up equal to 1 in all models except for the $1 M_{\odot}$, $[\text{Fe}/\text{H}] = -5.45$ model, in which it ends up very low (0.03). We note that it is this model that also has an anomalously low $^{12}\text{C}/^{13}\text{C}$ ratio after 2DUP (and FDUP). In the intermediate mass models the reduction is much stronger, always resulting in ratios less than 1. Thus all the IM models are N-rich after 2DUP (except for the $2 M_{\odot}$, $[\text{Fe}/\text{H}] = -3$ model, which

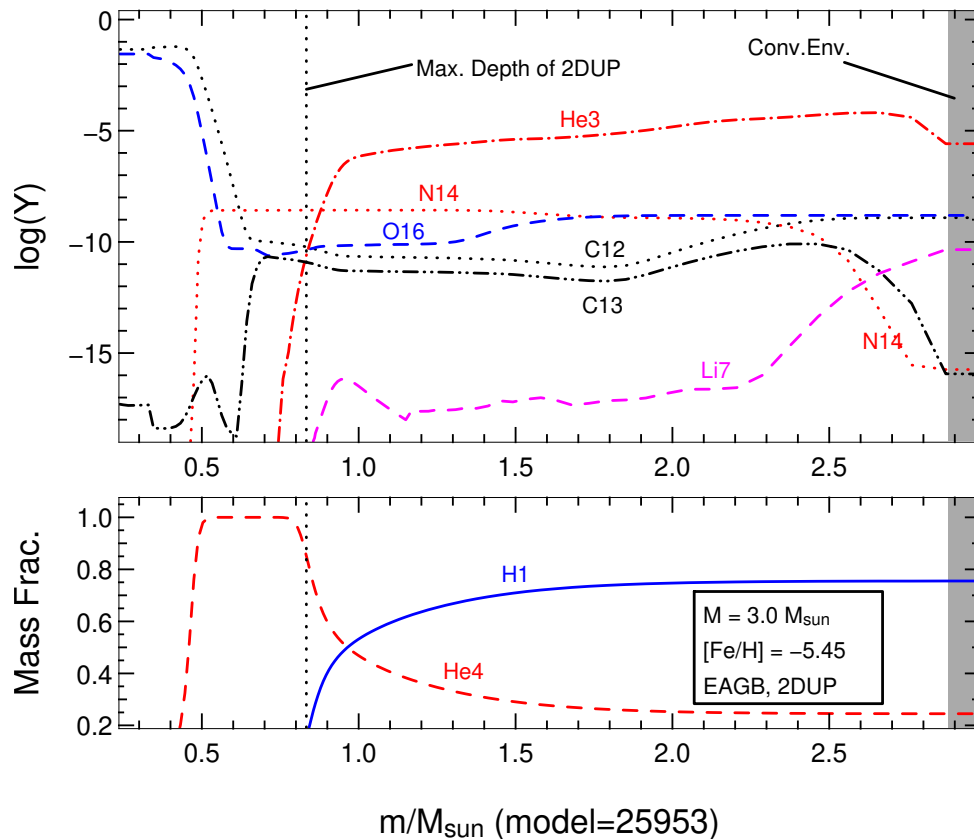


Figure 7.22: The abundance profiles of selected species against mass just as 2DUP is starting in the $3 M_{\odot}$, $[\text{Fe}/\text{H}] = -5.45$ model. The convective envelope can be seen as grey shading on the right-hand side. Interestingly a very large mass fraction of the entire star has been affected by CN(O) cycling, such that N and ^{13}C is enhanced. Indeed a large mass fraction has reached CN equilibrium. This alters the $^{12}\text{C}/^{13}\text{C}$ and C/N ratios as the material is mixed to the surface. In the bottom panel it can be seen that the He abundance will also increase, as seen in Table 7.9.

ends up with $\text{C}/\text{N} = 1$). The ratio in the majority of the models lies in the range $0.2 \rightarrow 0.5$. We note that this reduction is from the (very large) primordial value as most of these models did not experience FDUP. Again, the $Z = 0$ models represent a special case, since there was initially no C or N, so the C/N ratio *increased* to 0.01. Thus these stars are very N-rich as they begin the TP-AGB stage.

As an example of 2DUP in action we present in Figure 7.22 some composition profiles of our $3 M_{\odot}$, $[\text{Fe}/\text{H}] = -5.45$ model, just as the convective envelope starts to move in. The reason for the reduction in the $^{12}\text{C}/^{13}\text{C}$ and C/N ratios, and the increase in He abundance at the surface, can clearly be seen. Substantial CN(O) cycling has occurred above the core, in a very thick H-burning shell. Indeed, over much of the mass of the star the CN cycle has reached equilibrium (out to $\sim 2.2 M_{\odot}$, where the mass of the core is only $\sim 0.8 M_{\odot}$), such that the material in these regions is N-rich and has a $^{12}\text{C}/^{13}\text{C}$ ratio ≈ 5 . Thus, as the envelope convection deepens, the surface composition will be altered in the ways detailed above. We also note that from this diagram we expect the surface abundance of ^7Li to be significantly reduced by 2DUP as well.

7.3.5 Dual Shell Flashes

The dual shell flash (DSF) event occurs at the beginning of the AGB and is similar to the DCF insomuch as it consists of a He-flash convection zone breaching the H-He discontinuity above, thus mixing protons down and He burning products up (see Section 7.2.3 for more information on this event). More than half of the models in our grid (including the $Z = 0$ models) experience the DSF event. At low mass it appears that if the model does not go through a DCF it will always go through a DSF, such that all low-mass, very low-metallicity models experience one type of dual flash. At intermediate mass most of the models go through a DSF. The only exceptions are the most metal-rich models (the $[\text{Fe}/\text{H}] = -3$ model at $2 M_{\odot}$ and the $[\text{Fe}/\text{H}] = -3$ and -4 models at $3 M_{\odot}$, which experience no dual flashes at all (see Table 7.9).

In terms of helium the DSF has essentially no effect in the IM models. There are two reasons for this. The first is that the mass involved in the DSF is quite small, whilst the envelope mass is relatively large (see ΔM_c in Table 7.6 on page 233, in the structural evolution section). The second is that the second dredge-up in these models significantly enhances the He abundance in the envelope before the DSF, so that the DSF pollution is negligible next to this. In the low-mass models the increase in He is significant but still rather small. In general the envelope is enhanced by a similar amount as that given by 2DUP ($\Delta Y \sim 0.1 \rightarrow 0.2$, see Table 7.9). Of significance here is that the He abundance in the LM models remains at this level (there is no substantial He production on the AGB), such that the AGB contributions to the He yields are (roughly) affected equally by the DSF and 2DUP events. Thus the He yields are not highly sensitive to the treatment of the DSF at low mass, but they are affected to a moderate degree (the degree also depends on the mass-loss history of the models, as in some models a substantial amount of mass is lost during the unpolluted RGB phase). In Figure 7.23 we show an example of a low-mass model that goes through the DSF episode. The similar level of surface He pollution given by the DSF and 2DUP is clear in panel 2 of this figure. In the IM models it is HBB on the AGB that dominates the He yields. Thus the yields in these cases are essentially unaffected by the treatment of the DSF.

The surface metallicity arising from the DSF events is also more mass-dependent than metallicity-dependent. At $3 M_{\odot}$ the pollution from the DSFs only raises the envelope Z_{cno} to $\sim 10^{-6}$ whereas at $2 M_{\odot}$ it is usually raised to $\sim 10^{-4}$. At both masses 3DUP on the AGB increases Z_{cno} to $\sim 10^{-3} \rightarrow 10^{-2}$ (the average is higher at $3 M_{\odot}$), such that this pollution effect is more dominant than the DSF. At low mass we find that the reverse is true – the DSF pollution far outweighs any pollution on the AGB (which is virtually nil due to the lack of 3DUP). Interestingly the DSF pollution in the LM models raises the surface metallicity to similar levels as that given by the hundreds of 3DUP episodes in the IM models, such that Z_{cno} ends up being $\sim 10^{-3} \rightarrow 10^{-2}$ in these models as well (see Table 7.9 and an example of the time evolution of one model in Figure 7.23). Thus the AGB surface composition, and therefore a component of the yields, is set by the DSF event in the low-mass models. It is this group of models that we designated as Group 2 at the beginning of this section – low-mass models that experience the DSF and have their AGB envelope compositions dominated by this pollution event. This means that the yields from these models are partly dependent on the treatment of the DSF itself (the degree of dependence depends on the mass loss history of each model).

In Table 7.10 we also provide the $^{12}\text{C}/^{13}\text{C}$ and C/N ratios after the DSF event. The $^{12}\text{C}/^{13}\text{C}$ ratios in the low mass models had been reduced to ~ 30 in most (DSF) cases by the 2DUP. The DSF episode further reduced this ratio in most of the models, indicating that the DSF pollution material had undergone CN cycling. There was however one exception – the $[\text{Fe}/\text{H}] = -5.45$, $1 M_{\odot}$ model had a very low $^{12}\text{C}/^{13}\text{C}$ ratio after 2DUP and the DSF *increased* it to 14. Interestingly this is a similar ratio to that in the other models after their DSFs, suggesting that this may be a characteristic signature of the DSF (ie. the ratio in the DSF pollution material is moderately higher than the equilibrium value of ~ 4 , being between 6 and 21). We show the time evolution of the surface $^{12}\text{C}/^{13}\text{C}$ ratio for this model in panel 3 of Figure 7.23. In the intermediate-mass models the DF had a stronger effect on the $^{12}\text{C}/^{13}\text{C}$ ratio. In general the ratio reduced from a post-2DUP value of ~ 30 to a post-DSF value of ~ 5 . Thus the polluting material appears to have attained CN equilibrium in these stars. The one exception here is that the $[\text{Fe}/\text{H}] = -5.45$, $3 M_{\odot}$ model suffered no change in the ratio. This model appears to have had an extremely mild DSF, as the Z_{cno} value did not change significantly from the initial value either. We also note that in the $Z = 0$ models the $^{12}\text{C}/^{13}\text{C}$ ratio was already ~ 5 after the 2DUP episode. Thus the DSF kept the status quo in these cases.

The C/N ratio in the low-mass models was universally very low after 2DUP, being ≤ 1 . The DSF was also universal in its effect, raising the ratio in all the models. Despite this the final ratio was however somewhat varied between the models. In most of the models the ratio ended up between 47 and 107. The exception was the $[\text{Fe}/\text{H}] = -4$, $0.85 M_{\odot}$ model. It ended up with a ratio of only 4 (up from 1). In the intermediate mass models the C/N ratios were all initially low, being < 1 . However at these masses the DSF had the opposite effect – the ratio was *decreased* further. In fact the ratio dropped to ~ 0.04 which indicates that the DSF pollution material had reached complete CN equilibrium (this concurs with the $^{12}\text{C}/^{13}\text{C}$ ratios). Indeed, it is similar to the final AGB value attained in all the IM models after strong HBB. The one exception is again the $[\text{Fe}/\text{H}] = -5.45$, $3 M_{\odot}$ which, as mentioned above, appears to have had an extremely mild DSF, so no change in the ratio occurred.

7.3.6 TP-AGB

All of our models become thermally-pulsing AGB stars. However it is only the more massive ones that experience third dredge-up (3DUP) and significant hot bottom burning (HBB). The lack of 3DUP in the low-mass models is evident in the fact that the Z_{cno} metallicities at the end of the AGB are the same as those just after the DCF or DSF episodes. It is also evident in the unchanging $^{12}\text{C}/^{13}\text{C}$ ratios. Thus, as mentioned earlier, these models have their AGB surface composition dominated by the DCF/DSF pollution events. Interestingly there is a slight exception to this general rule. It is seen in the C/N ratios of all the low-mass, low- Z models – they all reduce (we note that at $Z = 0$ they remain constant, since they are already very low). The reason for this is seen in our example model in Figure 7.23 – ^{14}N is actually being produced on the AGB. Thus it appears that a small amount of HBB is occurring even in the low mass models (the $0.85 M_{\odot}$ models also show a reduction in the C/N ratio). The ^{14}N is produced via proton captures on the very abundant ^{12}C . ^{23}Na is also produced, via proton captures on the abundant ^{22}Ne . Interestingly both these species increase by ~ 0.3 dex on the AGB. ^7Li is

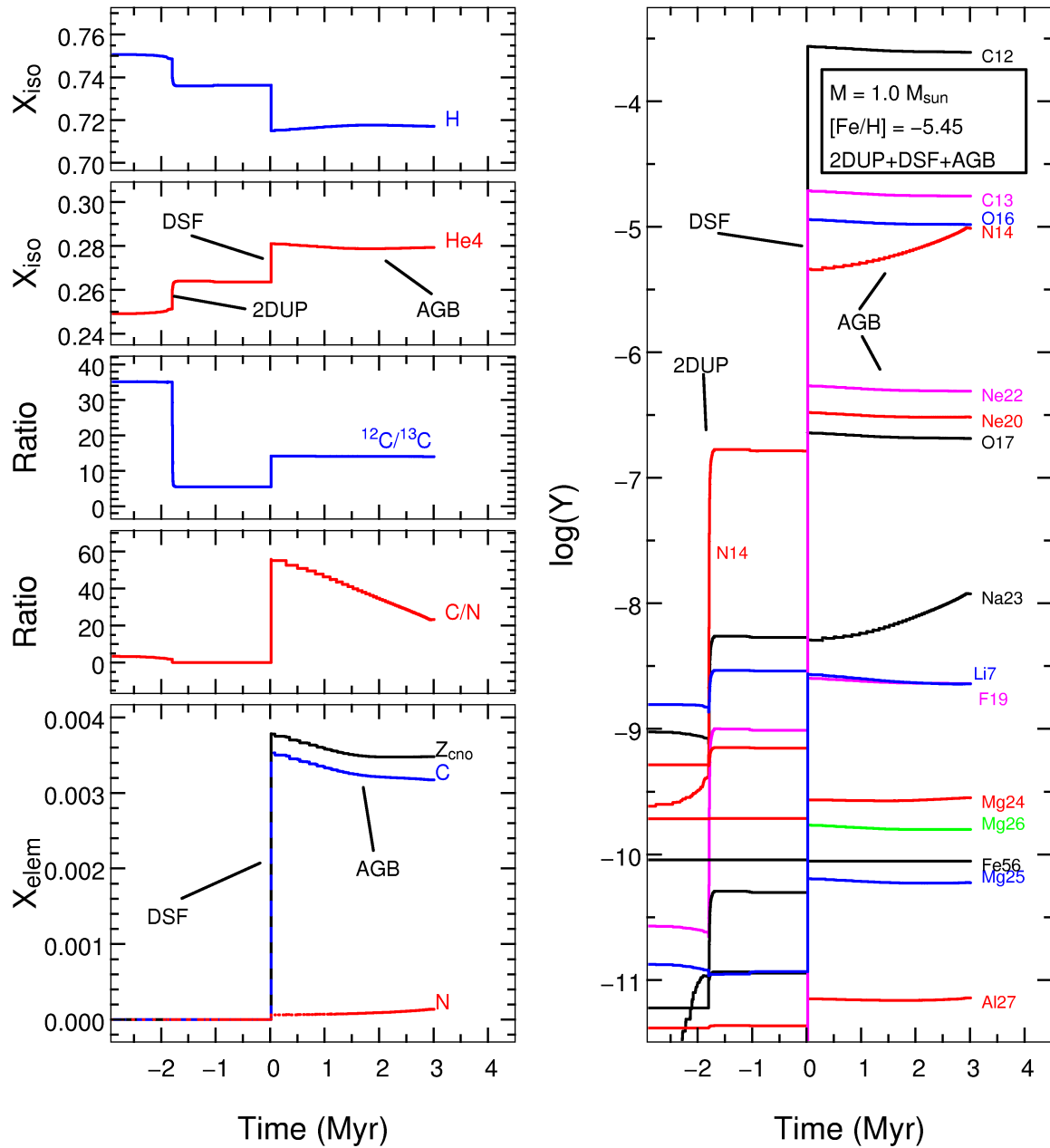


Figure 7.23: The time evolution of the surface composition of the $[\text{Fe}/\text{H}] = -5.45$, $1 M_{\odot}$ model, for selected species. This model fits into our Group 2, as its surface composition on the AGB is dominated by the DSF event. This event is clearly seen in the abrupt change in surface composition at $t = 0$ (time has been offset for clarity). In particular the metallicity of the model increases by a huge amount, from $Z_{\text{cno}} \sim 10^{-8}$ to 10^{-3} . Another interesting feature is that there is some HBB occurring on the AGB, as evidenced by the increase in ^{14}N and ^{23}Na . It is however not strong enough to significantly increase the surface He abundance (as it does in the intermediate mass models).

also (very) slightly depleted. We note however that the abundance changes occurring from this minor HBB only marginally alters the pollution given by the DCF or DSF events.

The situation in the IM models is very different. 3DUP is active in all the models, as is strong HBB. The mass fraction of He increases by a large amount, mainly due to H burning at the base of the convective envelope. Between the end of the DSF events and the end of the AGB the difference in He abundance is $\Delta Y \sim 0.03 \rightarrow 0.05$ in the $2 M_{\odot}$ models and $\sim 0.07 \rightarrow 0.09$ in the $3 M_{\odot}$ models, reflecting the higher temperatures in the more massive models. Thus the final He abundance in the most metal-poor models is ~ 0.34 at $2 M_{\odot}$ and ~ 0.39 at $3 M_{\odot}$ (see Table 7.9). Due to the many 3DUP episodes in the IM models (~ 300 on average) large amounts of He burning products get mixed into the AGB envelopes. This raises the surface metallicity in all of the models. Interestingly all the models end up with a similar level of pollution, characterised by $Z_{cno} \sim 10^{-3} \rightarrow 10^{-2}$ (the $3 M_{\odot}$ models end up slightly more metal-rich on average, at $Z_{cno} \sim 10^{-2}$). Thus the bulk level of pollution coming from the DSF events is eclipsed by the 3DUP pollution. It is these IM models, combined with the IM models that do not experience any DSF episode at all, that we designated as Group 2 at the start of this section. They are defined by the fact that their AGB surfaces are dominated by the effects of 3DUP and HBB. As an example of a member of this group we show the time evolution of the surface abundances for our $[\text{Fe}/\text{H}] = -5.45$, $3 M_{\odot}$ model in Figure 7.24. In panel 5 of this panel the relative insignificance of the DSF pollution can be clearly seen. The rich nucleosynthesis arising from the combination of 3DUP and HBB can be seen in the right-hand panel of the same figure. For most of the AGB evolution the dominant (metal) species is ^{14}N , as it is continually increased through the conversion of dredged-up ^{12}C via proton captures (ie. the CN(O) cycles). Thus it can be seen that strong HBB starts early on the TP-AGB in this model. The CN cycling naturally affects the $^{12}\text{C}/^{13}\text{C}$ and C/N ratios (see Table 7.10), causing both of them to drop to equilibrium values well before the end of the AGB. In fact *every* IM model ends the AGB with a $^{12}\text{C}/^{13}\text{C}$ ratio of 5 and a C/N ratio of 0.05, regardless of its previous pollution history (some of the models did not experience a DSF). The C/N ratio implies that N is 20 times more abundant than C, ie. ~ 1 dex. This is a robust chemical signature of these metal-deficient (and metal-free) IM models that could be compared with observations. The chemical composition of the surface during the AGB is similar in all the IM models. We thus refer the reader to the section describing the nucleosynthesis in the $Z = 0$, $2 M_{\odot}$ model in Chapter 6 on page 160 for more details of this type of model.

7.4 Yields

In this section the yields for all the models in the grid are presented, in graphical and tabular form (although some of these are actually located in the appendices for practicality). For details on the definition of Yield that we use throughout the current study we refer the reader to Section 3.2.5 on page 48. The sources of the yields for some selected species are discussed, as well as a suggested classification scheme which we use to split the yields into three chemically similar groups. We have however chosen to begin the section with a discussion on one of the major uncertainties affecting the yields of a subgroup of our models, as we believe it is important to keep this key uncertainty in mind when examining the yields given below.

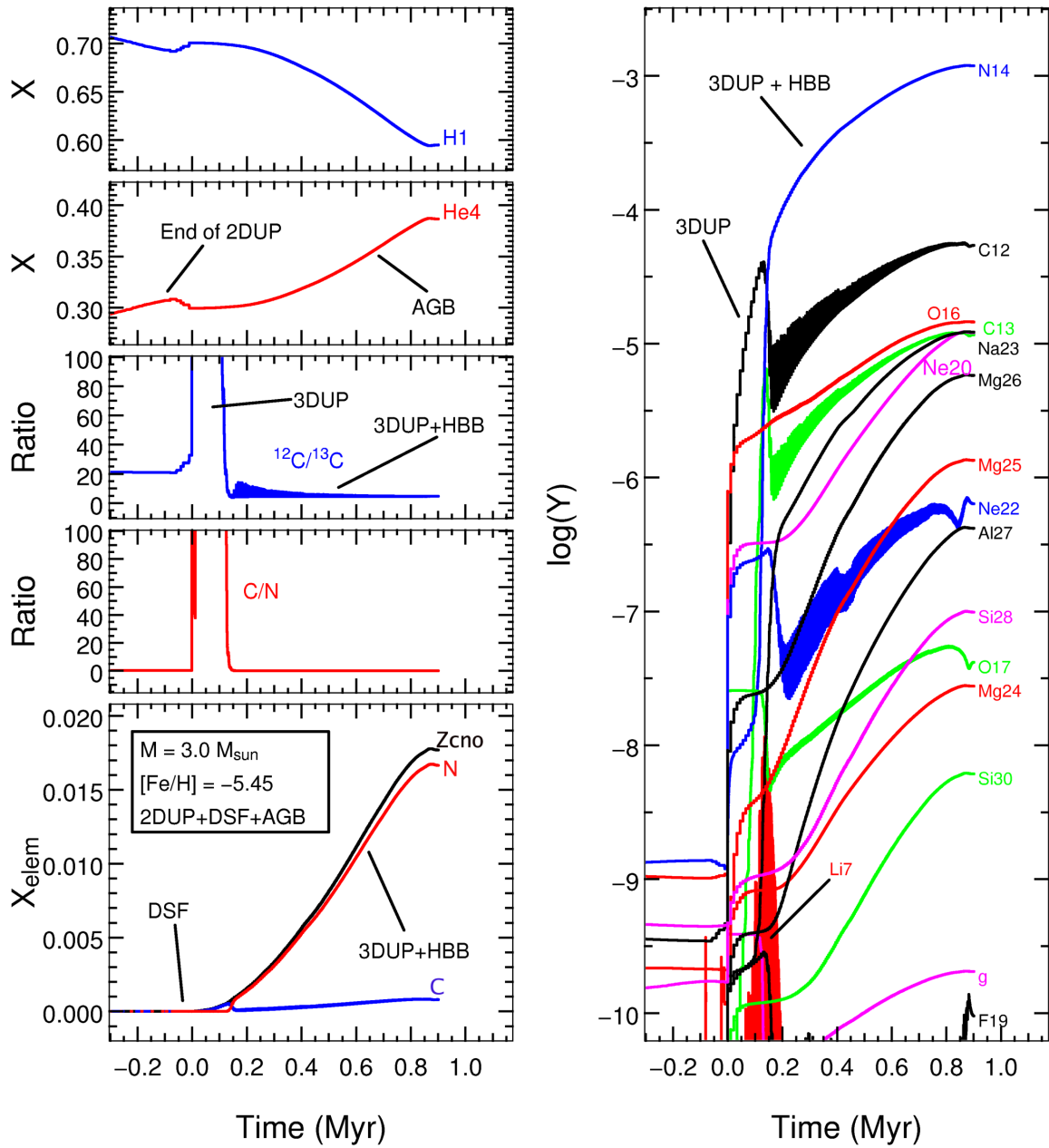


Figure 7.24: The time evolution of the surface composition of the $[\text{Fe}/\text{H}] = -5.45$, $3 M_{\odot}$ model, for selected species. This model fits into our Group 3, as its surface composition on the AGB (and thus the yield, as practically all of the mass loss occurs during the AGB in this model) is dominated by the combination of 3DUP and HBB. The relative importance of this form of pollution compared to that from the DSF event is highlighted in the bottom left-hand panel, where the metallicity is seen to increase enormously on the AGB. The metallicity of the model increases from $Z_{\text{cno}} \sim 10^{-8}$ to 10^{-2} . The rich nucleosynthesis arising from 3DUP and HBB is seen in the right-hand panel. In particular the CN cycling product ^{14}N dominates most of the AGB. The $^{12}\text{C}/^{13}\text{C}$ and C/N ratios quickly tend to equilibrium values once the (strong) HBB starts.

7.4.1 Uncertainty in the Yields of the LM, Higher-Z Models

By comparing the surface He abundances at the end of the AGB phase (Y_{agb}) in Table 7.9 with the helium yields plotted in Figure 7.25 it can be seen that the low-mass yields display lower helium abundances than their respective AGB surfaces. This is due to the fact that these models all go through the RGB stage, where they lose some mass via winds. In all cases the surface composition during the RGB is the initial one, such that Y is still equal to 0.245 (although in some cases there is a secondary RGB at which time the surface is polluted – but this is short-lived). Thus, even though the matter lost on the AGB is high in He, it is partially diluted by the He-poor material on the RGB. The degree of this dilution effect is naturally dependent on the amount of mass lost on the AGB as compared to that lost on the RGB. The relative importance of each phase of mass loss was discussed in the previous section. In particular Figures 7.18 to 7.20 display the evolution of total stellar mass with time for all of the 3, 1 and 0.85 M_{\odot} models. These figures make it clear when and to what degree mass loss occurs throughout the various stages of evolution. As stated in that section it is a complex function of mass, metallicity and the occurrence or non-occurrence of polluting events such as the DCF – not to mention the mass loss formulae themselves. However a clear conclusion was reached at the end of that discussion – a significant uncertainty arises in the low mass, higher metallicity models. The uncertainty is due to the unknown rates of mass loss at very low metallicity whilst the reason it affects this particular group of models is because they spend a significant amount of time at high luminosities on the RGB (see eg. Figure 7.3 on page 227), such that much mass is lost while the surface is still very metal-poor. Thus, in all the following discussion on yields, we need to remember that the yields from the low-mass, higher metallicity models come with a caveat. In particular we note that, if mass loss at very low metallicity is in reality much less efficient, then our yields (for these models) will be over-diluted by the material lost on the RGB. Hence we would expect that our yields would be much more metal-rich (and more helium-rich) if most of the mass was lost during the AGB phase.

With regards to the more massive and more metal-poor models, we note that they did not go through the RGB stage (or did so only for a brief time, at low luminosity), so their yields are totally dominated by the AGB mass loss, as can be seen by the close correspondence between Y_{agb} and the yields. Thus they are not affected by the uncertainty in mass-loss rates at low metallicity – the low-mass higher-metallicity caveat does not apply.

7.4.2 Grouping the Models Into Yield Types

At the beginning of Section 7.3 we defined three groups into which all the models fit. The groups were delineated by the dominant source of pollution of the AGB envelope – the DCF, the DSF or 3DUP + HBB. We referred to them as groups 1, 2 and 3, respectively. We were of the belief that this classification scheme should translate directly to a natural delineation within the yields, as much of the mass loss occurs on the AGB. However the unpolluted mass-loss on the RGB in some of the models partly undermines this categorisation because it causes a dilution of the AGB yields. Nevertheless it is apparent from the presentation of the yields below that the yields are still quite distinguishable into the three categories despite this. In the following

we also refer to Groups 1, 2, and 3 as the ‘DCF group’, the ‘DSF group’ and the ‘IM group’. The IM (intermediate mass) group is so called because all the 2 and 3 M_{\odot} models experience considerable 3DUP and HBB on the AGB, the resulting composition of which dominates the yields.

7.4.3 Some Key Properties of The Yields

To continue on from the nucleosynthesis discussion in the previous section we first present the He, Z_{cno} , C/N and $^{12}\text{C}/^{13}\text{C}$ compositions of the yields for the entire grid of models in Figures 7.25 and 7.26.

Helium

As mentioned just above, the He mass fractions in the low mass yields are quite low when compared to the composition of the envelopes of these models just after the DCF and DSF pollution episodes (see Table 7.9). The extreme case is the 0.85 M_{\odot} , $[\text{Fe}/\text{H}] = -5.45$ model. It had $Y = 0.44$ on the surface after its DCF but only $Y = 0.33$ in the yield (see Section 3.2.5 on page 48 for the definition of Yield used in the current study). This is due to the fact that it suffered considerable mass loss on the RGB, when its envelope still had the initial He-poor composition, thus the AGB (and HB) mass loss was diluted. This effect reduces with metallicity and increasing mass, as the RGB phases in the models get progressively shorter. In the most metal-rich low-mass models (the ones that did not experience a DCF, i.e. Group 2) the mass fraction of He is virtually the same as the initial one. This is partly due to the DSF and 2DUP not increasing He very much (up to $Y \sim 0.28$) but mostly due to the large amount of unpolluted mass loss on the AGB (see eg. Figure 7.20 on page 249).

The helium situation in the intermediate-mass yields is much more uniform. They all reflect the composition at the end of the AGB phase. This is due to the fact that practically all of the mass loss occurs towards the end of the AGB in these Group 3 models. In most of the IM models the He comes from two main sources – 2DUP and HBB. As noted in the nucleosynthesis section these two sources increase the helium content in the envelope by similar amounts. Interestingly the DSF, which occurs in the most metal-poor of the IM models, has little effect on the He abundance.

Metallicity

In Panel 2 of Figure 7.25 we show the metallicity in the yields, as $\log(Z_{cno})$, where Z_{cno} is the mass fraction of all the CNO nuclides combined. This gives a good overview of the degree of pollution that has made it into the yields. At intermediate masses the pollution is quite uniform – the yields are all characterised by $\log(Z_{cno}) \sim -2 \pm 0.4$. We suggest that this is due to the fact that all these models experienced a similar amount of 3DUP over the hundreds of thermal pulses. As can be seen in Table 7.9 on page 254 3DUP is the main contributor to the metal pollution of the AGB envelope (the DSF episode only raises the metallicity to a more moderate level). In the low-mass models the situation is more complex. Again the RGB dilution effect

comes into play. At the lowest metallicities Z_{cno} in the yields is not far from that reported for the end of the AGB. This is due to their short-lived RGB phases. In the more metal-rich models there is a decrease of up to an order of magnitude in Z_{cno} (from the AGB values), due to these models losing up to 90% of their mass on the unpolluted RGB.

The general result for overall metallicity is one of a huge increase over the initial abundances in all the models. There is however some variation in the degree of pollution. Ironically the (initially) highest metallicity low-mass models end up with the lowest metallicity yields, though they are still well above the initial composition. The main reason for this is that they have much more mass-loss during the RGB phase, since they spend longer at higher luminosities on the RGB. As discussed above it is these models that suffer from the most uncertainty arising from the unknown mass-loss rates at very low Z . It is interesting to note that if the mass loss rate were reduced on the RGB, then these models would have yields as metal-rich as the more metal-poor models, as the severe pollution from the DSF events at the start of the AGB raise the metallicity of their envelopes to similar levels as the DCF events do in the more metal-poor models. Thus the lines in panel 2 of Figure 7.25 would be flatter in the low mass regime. With regards to the IM yields the spread is much smaller. Unlike the low-mass yields a general trend of increasing metallicity with increasing initial metallicity can be seen, but it is not a strict rule since there are some exceptions.

$^{12}\text{C}/^{13}\text{C}$ and C/N Ratios

In Figure 7.26 it can be seen that the $^{12}\text{C}/^{13}\text{C}$ and C/N ratios follow the same pattern as Z and Y inasmuch as they are very uniform in the IM yields but have a large spread in the LM yields. The $^{12}\text{C}/^{13}\text{C}$ ratios in the IM model yields are uniformly ≈ 5 , which reflects the fact that the AGB envelopes all reached CN equilibrium due to strong HBB. The C/N ratios are also perfectly uniform, being ≈ 0.05 , for the same reason. Interestingly this means that the yields are very N-rich. Indeed, N makes up the largest part of Z in these yields.

In the low mass models we see that the (initially) lower- Z models have quite low $^{12}\text{C}/^{13}\text{C}$ ratios, being $\lesssim 10$, which is approaching equilibrium values. In these models it is the N production by the DCF event that causes the drop to such low values (the ratio in the initial composition was extremely high). Interestingly in one of the models that experienced the dual shell flash the ratio is also very low (the $0.85 M_{\odot}$, $[\text{Fe}/\text{H}] = -4$ model). This low value was a result of the DSF pollution itself. This didn't occur in the $[\text{Fe}/\text{H}] = -3$ model however, which also experienced a DSF, but which has a relatively high ratio in the yield. In fact the $0.85 M_{\odot}$, $[\text{Fe}/\text{H}] = -4$ model is an exception amongst all those that experienced DSFs, as the rest of them have moderately high $^{12}\text{C}/^{13}\text{C}$ ratios. It appears that more advanced CN processing occurred during the DSF in this model, making the chemical signature appear more like that of a DCF.

In regards to the C/N ratios in the low-mass models, they follow the same general pattern as the $^{12}\text{C}/^{13}\text{C}$ ratios – moderately high in the DSF models (i.e. more the metal-rich, Group 2 models), and quite low in the DCF models (metal-poor, Group 1 models).

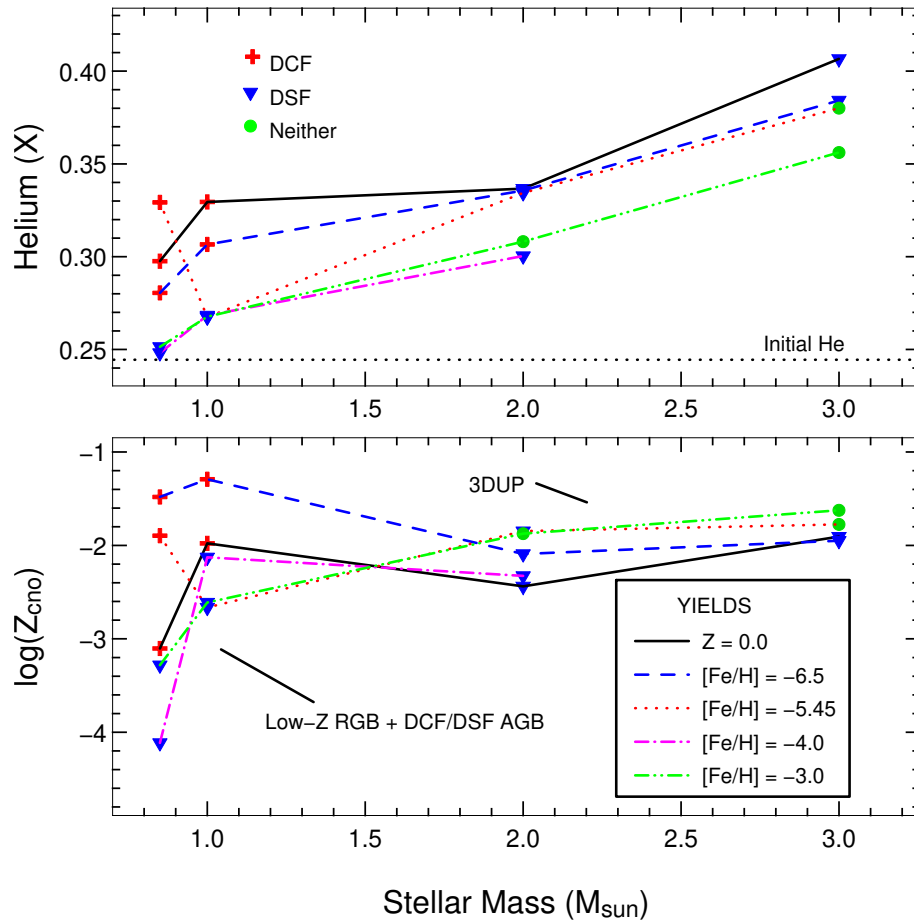


Figure 7.25: The helium yields (in mass fraction X) and metallicity yields (in Z_{cno} , the mass fraction of all of the CNO nuclides) against initial stellar mass. All models in the grid are shown, including the $Z = 0$ models. The different pollution events that occur in the models are indicated by different shaped markers, as per the key in the top panel. The metallicity key in the bottom panel applies to both panels. The main points are that He is produced more in the IM models as compared to the LM models and that all of the models have very metal-rich yields considering their extremely low initial metallicities. Note that there are no points included for the $3 M_{\odot}$, $[\text{Fe}/\text{H}] = -4.0$ model due to a loss of data.

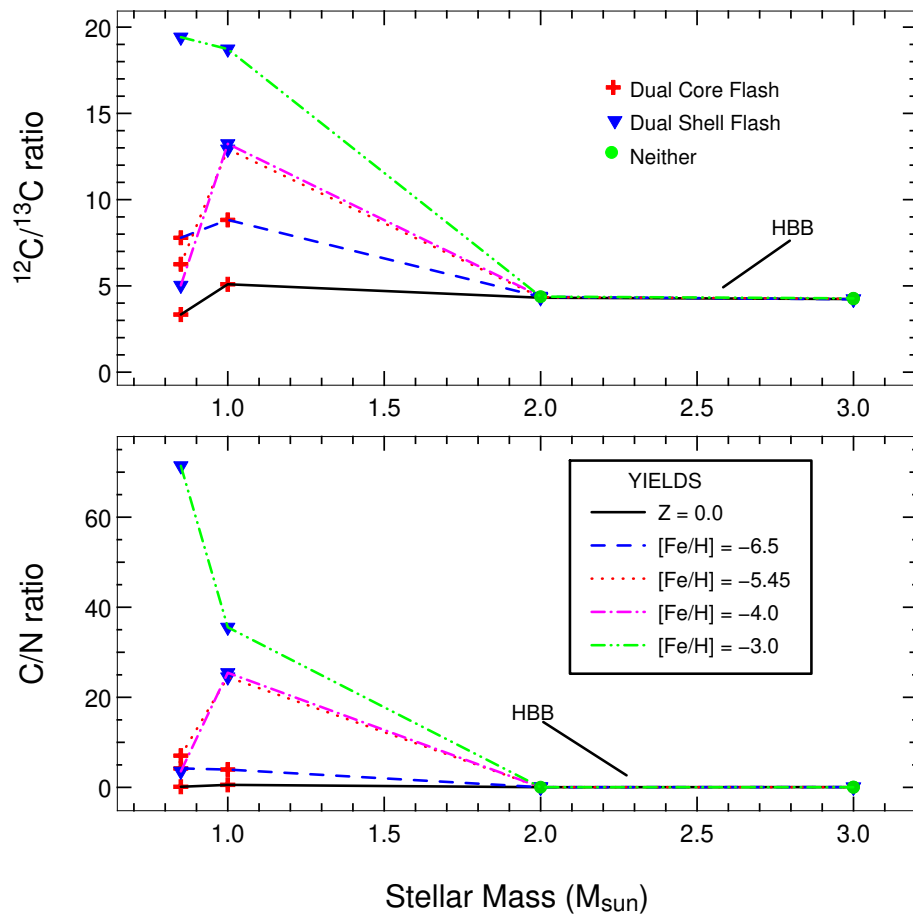


Figure 7.26: The same as Figure 7.25 but for the $^{12}\text{C}/^{13}\text{C}$ and C/N ratios in the yields. We note that the ratios in IM model yields are all at CN-equilibrium levels (due to strong HBB) whilst only the most metal-poor LM models are close to equilibrium, which is due to dual core flash pollution.

7.4.4 Elemental Yields: Helium to Phosphorus

Figures 7.27 and 7.28 show the yields of most of the elements in our network for all the $[\text{Fe}/\text{H}] = -6.5$ and $[\text{Fe}/\text{H}] = -5.45$ models, respectively. We have displayed the yields of each element versus initial stellar mass in these groups of plots. This gives a quick visual overview of how the yield of each element is dependent on mass at a constant metallicity. The rest of the figures of this type are given in Appendix A.1 on page 363.

Helium

The helium yields were discussed in detail above but we give a quick summary here, using the $[\text{Fe}/\text{H}] = -6.5$ and $[\text{Fe}/\text{H}] = -5.45$ models as examples. In the low mass models which experience the DCF (the 0.85 and $1 M_{\odot}$ models in Figure 7.27, and the $0.85 M_{\odot}$ model in Figure 7.28) the He mainly comes from the DCF pollution. It is however diluted by the unpolluted mass loss on the RGB in these models. In the low-mass model which does not experience the DCF ($1 M_{\odot}$, $[\text{Fe}/\text{H}] = -5.45$) the He comes from the combination of the 2DUP and DSF episodes, and is also partially diluted by RGB mass loss. In regards to the IM mass models the He yields are consistently high due to the combination of 2DUP and HBB. This is true whether the model goes through a DSF episode or not (the $3 M_{\odot}$ in Figure 7.28 did not experience a DSF).

Lithium

Lithium is enhanced above the primordial value in all the low-mass models of Figures 7.27 and 7.28, usually by ~ 0.5 dex. It is still below the solar value though. However in one case ($1 M_{\odot}$, $[\text{Fe}/\text{H}] = -5.45$) it has increased by 1.5 dex, to become equal to the solar abundance. Looking at Figure A.7 in the Appendix it can be seen that this is true of most of the $1 M_{\odot}$ models that experience the DSF rather than the DCF (ie. Group 2 models). By contrast the Group 2 models of $0.85 M_{\odot}$ have similar Li enrichment levels as that of the DCF (Group 1) models. The source of Li in all these low-mass models are the DCF and DSF episodes themselves. The Li production from these events is however moderated in the yields due to destruction on the AGB via (weak) HBB and also due to dilution by the unpolluted RGB mass loss. In the IM mass models Li is essentially unchanged from the primordial abundance in the $2 M_{\odot}$ model yields – which is an interesting result – but depleted in the $3 M_{\odot}$ yields. Being such a ‘fragile’ nuclide, in these relatively hot models it has a complicated history of production and destruction through the various stages of evolution. However the dominant factor is HBB on the AGB. Here it is repetitively destroyed and created. It is created via electron captures on ${}^7\text{Be}$, which itself is produced by HBB (the Cameron and Fowler 1971 mechanism, also see Sackmann and Boothroyd 1992). All the models go through Li-rich phases on the AGB, for varying lengths of time, but as evidenced by the nett destruction in the yields, the $3 M_{\odot}$ models are Li-poor for more of the time. The Li-poor portion of the $2 M_{\odot}$ winds coincidentally combine with the Li-rich portion to average to (roughly) the primordial value.

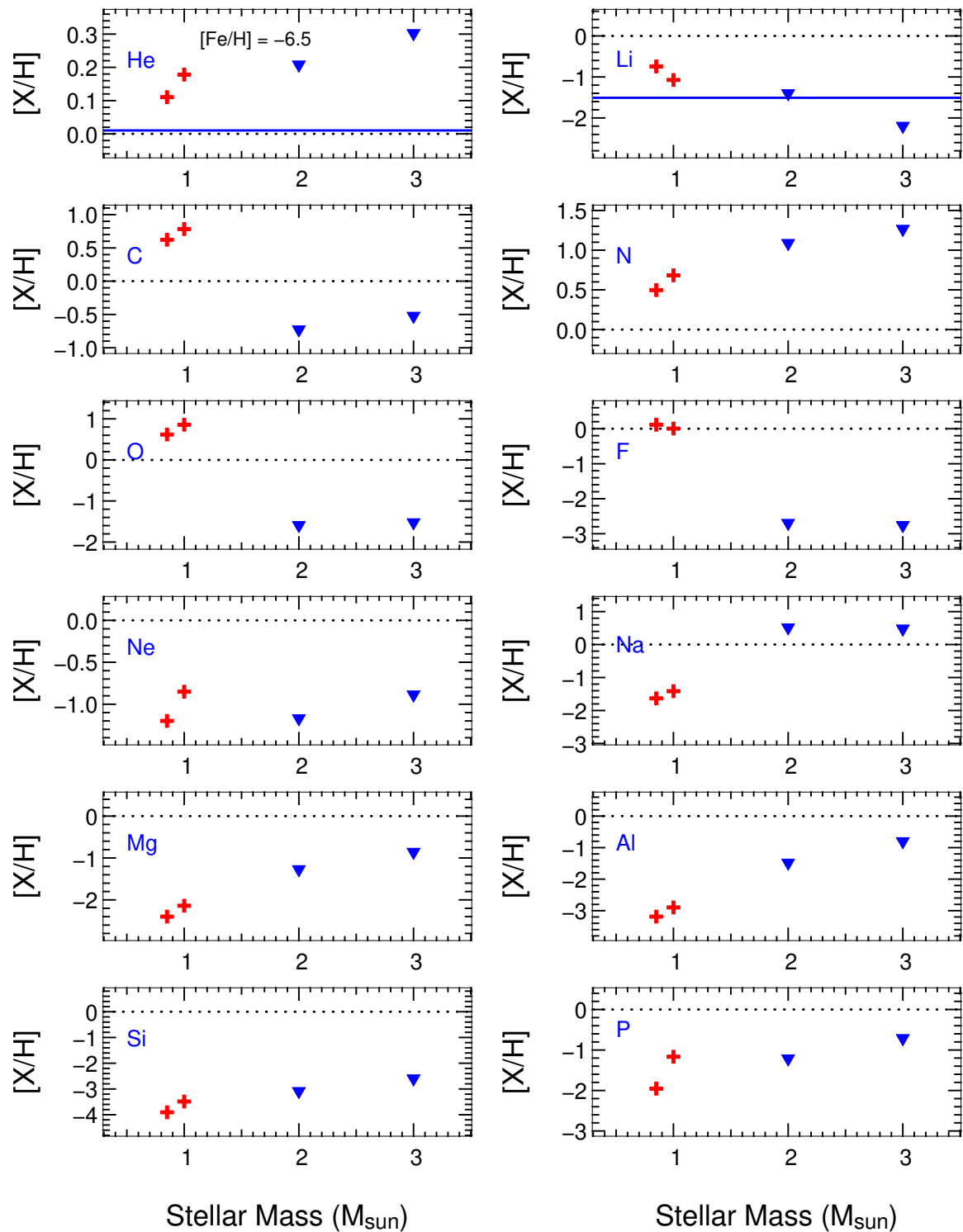


Figure 7.27: Selected elemental yields for all the $[\text{Fe}/\text{H}] = -6.5$ models, given as relative to solar against initial stellar mass. Red crosses indicate models that experienced a dual core flash (at the top of the RGB), whilst blue triangles indicate models that experienced a dual shell flash (at the beginning of the AGB). Solid horizontal lines (blue) indicate initial abundances, but are often not visible due to their relatively low values. The horizontal dotted (black) lines at $[X/H] = 0$ indicate the solar abundances (Solar abundances are from [Lodders 2003](#)). For the rest of these types of figures see Appendix A.1 on page 363.

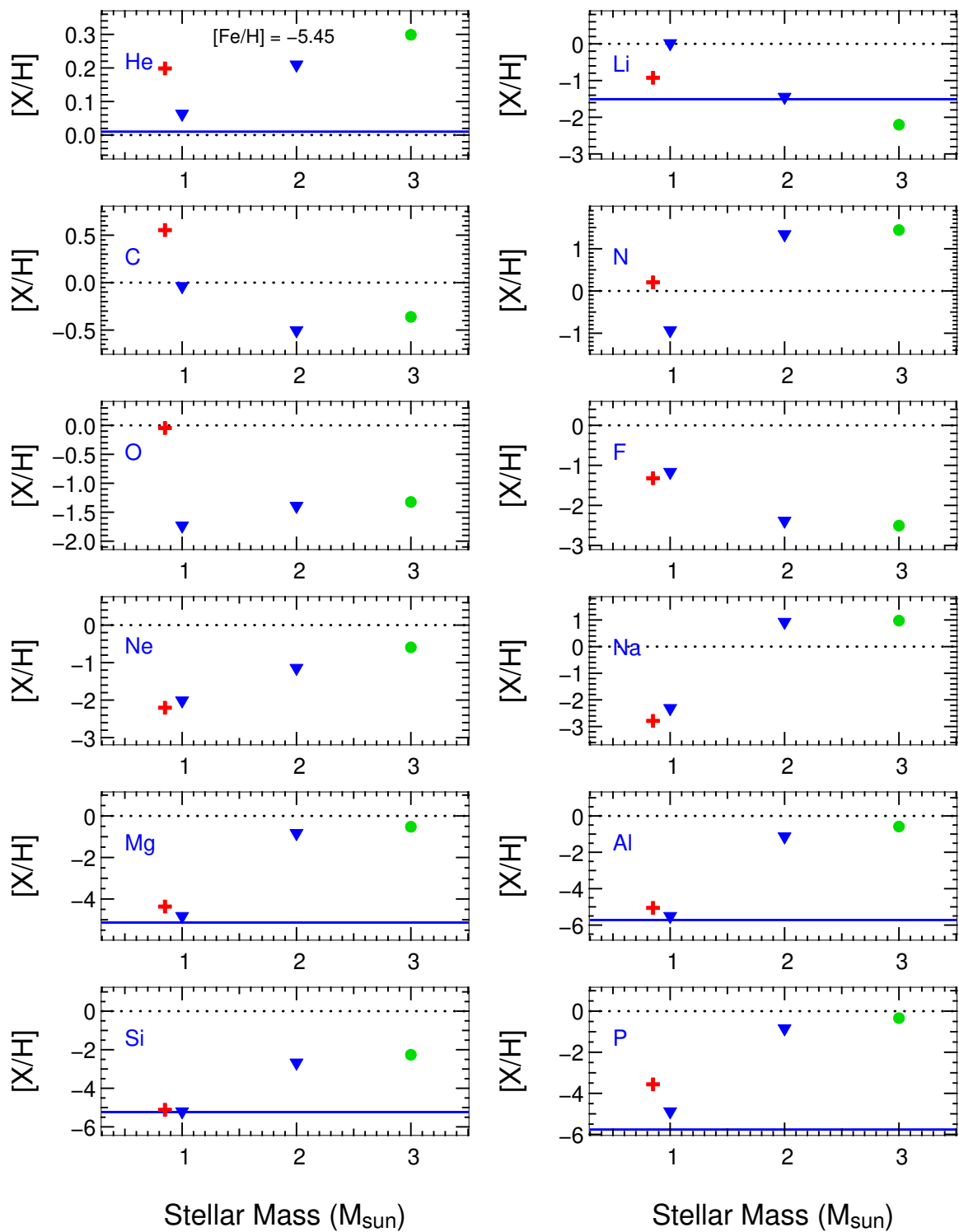


Figure 7.28: Same as Figure 7.27 but for the $[\text{Fe}/\text{H}] = -5.45$ models. Green dots indicate the model that did not experience a DCF or a DSF episode. For the rest of these types of figures see Appendix A.1 on page 363.

Carbon

In Figure 7.29 we show all the Carbon yields as $[C/Fe]$ versus $[Fe/H]$ and also as $[C/H]$ versus $[Fe/H]$. We do the same for nitrogen and oxygen in Figures 7.30 and 7.31 but only for $[X/H]$ (where X represents the elemental species). In Appendix A.2 on page 369 we give the same type of plots for most of the elements in the network up to sulphur.

It can be seen in the $[C/Fe]$ plots of Figure 7.29 that carbon is extremely enhanced – reaching values of up to ~ 9.5 dex above solar! However, looking at the $[C/H]$ plots it is apparent that this is primarily driven by the very small abundances of Fe in our metal-poor models. This highlights the fact that the abundance levels of light elements reached in the yields of these models are, in absolute terms, approaching solar or are super-solar. It also highlights the problem with using $[Fe/H]$ as a metallicity indicator. These stars still retain their original very low values of $[Fe/H]$ but their Z values are now very high. So in one sense the yields are metal-poor and in another they are metal-rich.

In terms of $[C/H]$, C is overabundant (i.e. super-solar) in the yields of all the low-mass models that experienced the DCF, except in the case of the $Z = 0$ model (which we have included artificially at $[Fe/H] = -9$). The source of the C enrichment in these models is the DCF event. In the low-mass models that don't go through the DCF (the more metal-rich models, Group 2) carbon is less enhanced, being significantly sub-solar in the $0.85 M_{\odot}$ yields and at, or slightly above, solar in the $1 M_{\odot}$ yields. The C enhancement in these cases is a result of the DSF at the start of the AGB. We note that the C yields are reduced by any time the models spend losing unpolluted matter on the RGB. Thus, in some of the models, there is an uncertainty in the C yield due to the uncertainty of the mass loss rates at low Z . In particular one would expect that the yield of C would increase with a lower mass loss rate on the RGB. This is of course true for all the elements as it is just a dilution effect. In the IM models, which do not spend much time, if any, on the RGB, the C yield is wholly determined by the combination of 3DUP and HBB on the AGB. As the temperature at the base of the convective envelope is very high (usually slightly less than 10^8 K), and due to the length of time spent on the AGB, all the IM model envelopes reach CN equilibrium. Thus the relative abundances of C and N are fixed, as mentioned above, with $N/C \sim 20$. The underlying factors in the degree of C (and N) pollution are thus the depth of 3DUP, the number of 3DUP episodes (i.e. pulses) and the mass of the envelope that is polluted. Interestingly, in Figure 7.29 it can be seen that the yields are fairly constant with metallicity but appear to increase with mass. The $2 M_{\odot}$ yields are all $\sim 0.8 \pm 0.3$ dex below solar whilst the $3 M_{\odot}$ yields are only $\sim 0.4 \pm 0.2$ dex below solar. It appears that a strong C enrichment is a robust feature of all our metal-poor models. Even though not all of them reach solar $[C/H]$ we note that they initially had very minimal abundances of this element.

Nitrogen

In Figure 7.30 it can be seen that nitrogen has also been raised from very low initial levels to abundances often super-solar. In all the low-mass models that experience the DCF the nitrogen yields are super-solar (although slightly below in the $0.85 M_{\odot}$, $Z = 0$ case). Again this is mainly due to the DCF, but 2DUP also plays a part – even in some of the $0.85 M_{\odot}$ models. Slight HBB

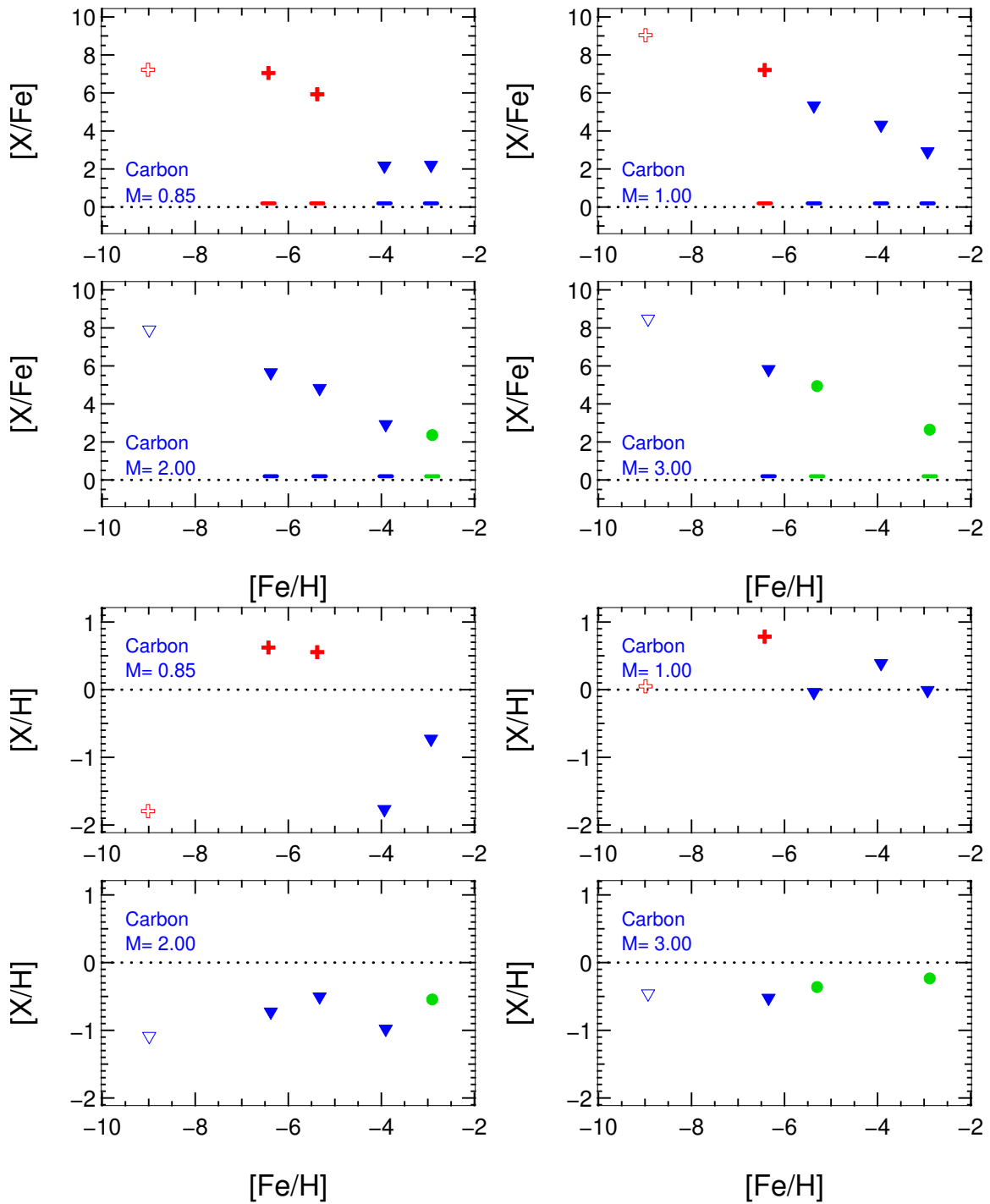


Figure 7.29: Carbon yields versus initial $[\text{Fe}/\text{H}]$ for all the models in the grid, grouped by initial mass. The $Z=0$ models have also been included for comparison (they have been given an artificial Fe abundance corresponding to $[\text{Fe}/\text{H}] = -9$ for display purposes). The top set of four plots displays the yields as $[\text{X}/\text{Fe}]$, where X is the species (i.e. carbon) whilst the bottom set displays them as $[\text{X}/\text{H}]$. Comparing the two sets highlights the fact that the extremely high $[\text{C}/\text{Fe}]$ abundances are mainly driven by the very low Fe abundances in the yields. Red crosses indicate models that experienced a dual core flash (at the top of the RGB), blue triangles models that experienced a dual shell flash (at the beginning of the AGB) and green dots indicate models that experienced neither. Short horizontal lines indicate the initial abundance for each model (which are well below the scale of the bottom panel). Note that within each group of four plots the vertical axes are identical to allow direct comparison.

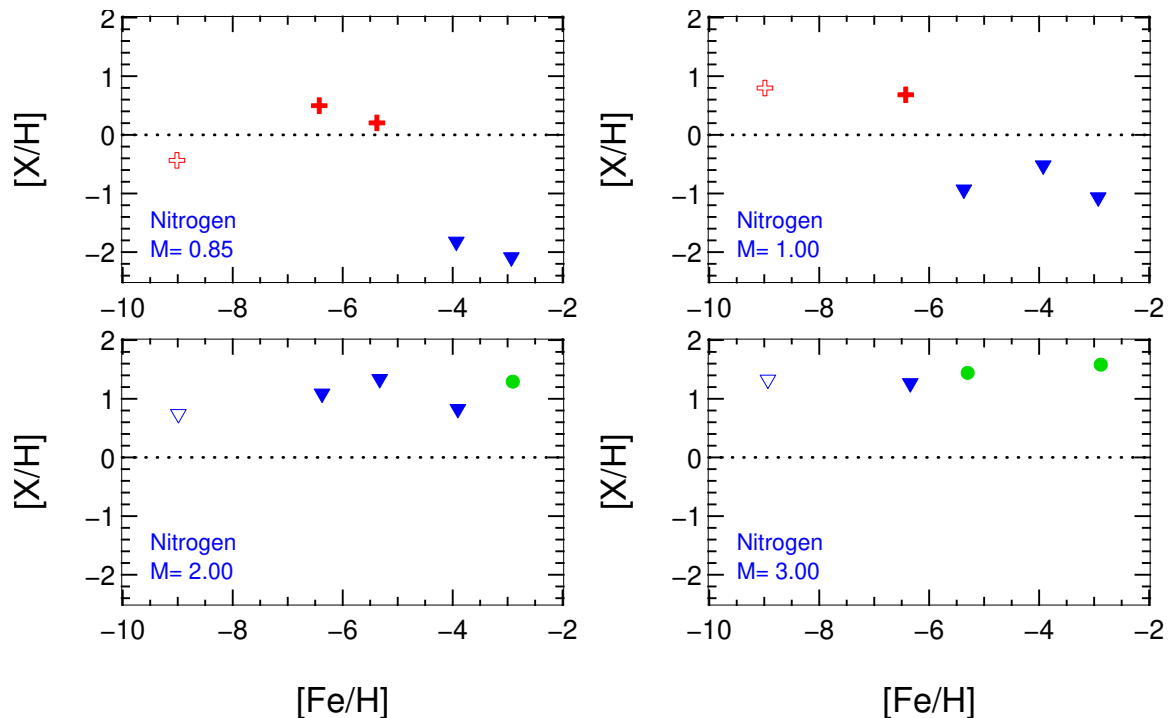


Figure 7.30: Same as Figure 7.29 except for nitrogen and only for $[N/H]$. The large amount of N in the yields of the IM models (Group 3 as described in the text) is due to the combination of 3DUP and HBB during the AGB phase. In the low mass DCF yields (red crosses, Group 1) the N comes from the DCF event whilst in the low mass DSF yields (Group 2) it comes from the DSF event.

in the $1 M_{\odot}$ models also increases N slightly, at the expense of C. The situation is uniformly different in the low-mass, higher-Z models that do not go through the DCF (i.e. Group 2). All these models show sub-solar $[N/H]$. The source of N in these models is mainly the DSF but, particularly in the $0.85 M_{\odot}$ models, it is heavily diluted in the yields due to unpolluted mass loss on the RGB. Again we note that these yields would be higher if a low mass-loss rate were used on the RGB. In regards to the IM models their N yields, like their C yields, are quite constant with metallicity, again with the $3 M_{\odot}$ yields being slightly more enhanced than the $2 M_{\odot}$ yields. The yields are all very much super-solar, with $[N/H] \sim +0.8 \rightarrow +1.6$. The source of the N here is HBB of the carbon brought up by the many 3DUP episodes. Assuming the occurrence of 3DUP and HBB are correct in our models, this is a very robust result for our IM yields. We note that we have used no form of overshoot in these models, so this may represent a lower limit to the N pollution from the low metallicity models.

Oxygen

Figure 7.31 shows the oxygen yields in terms of $[O/H]$. Again there is a strong enrichment in all the models. In the DCF models' yields $[O/H]$ is between solar and 1 dex super-solar, except again for the $0.85 M_{\odot}$, $Z = 0$ model which is 1 dex sub-solar. The main sources of the oxygen in these models are the DCF events. Due to this single event being the main source we note that this means that the yields are dependent on the treatment of this event in the structural evolution code, and thus the uncertainties therein (eg. the unknown degree of overshoot). In the DSF low-mass models (Group 2) we see that all the O yields are sub-solar, to varying degrees. The main sources of O here are the DSF events but we note that the O pollution is highly

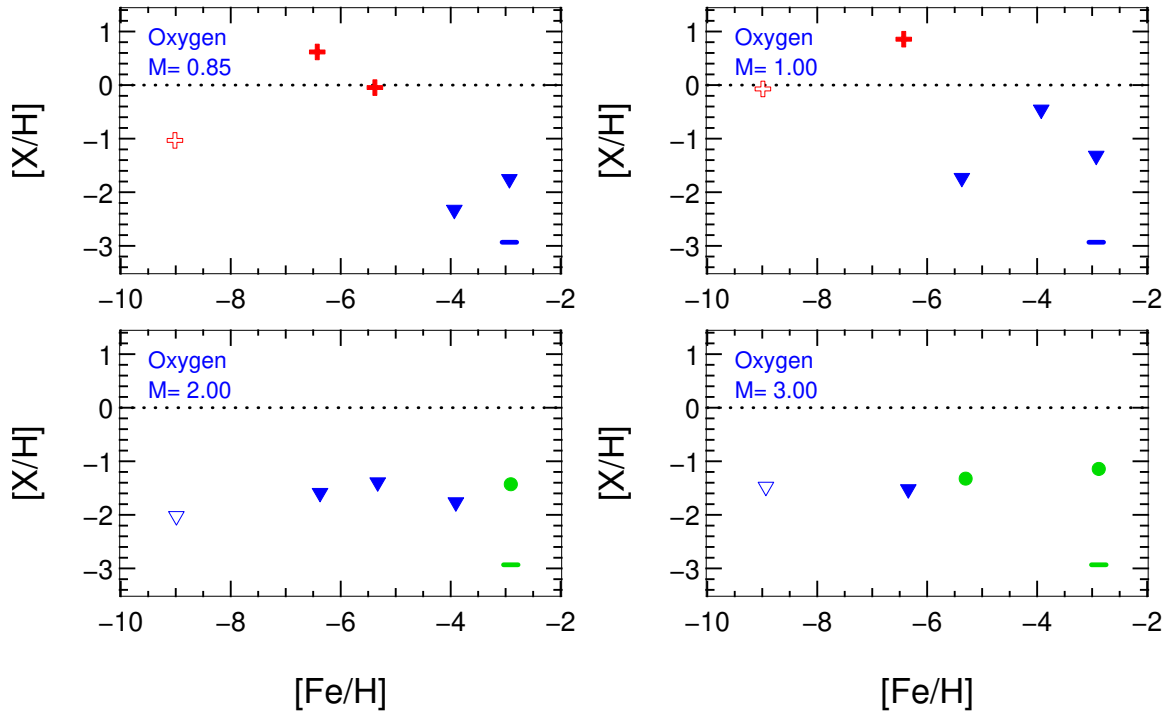


Figure 7.31: Same as Figure 7.29 except for oxygen and only for $[O/H]$. The large amount of O in the low mass DCF yields (red crosses, Group 1) comes mainly from the DCF events. In the low mass DSF models (Group 2) it comes from the DSF events whilst the O in the yields of the IM models (Group 3) arises from the combination of 3DUP and HBB during the AGB phase – 3DUP brings up the O and HBB destroys it.

diluted in some of the models, again due to the unpolluted RGB mass-loss. Thus the O yields in these models may be more of a lower limit. In the IM yields the situation is more uniform. All the $[O/H]$ yields are substantially sub-solar, being on average ~ 1.5 dex lower than solar in all the models. The source of the O enrichment in these models is primarily the AGB. The 3DUP episodes also mix up O with the C, thus repetitively enriching the envelope. The O yields from the IM models would have been higher if it were not for HBB cycling some of this O to N (even at $2 M_{\odot}$).

Fluorine

Moving back to Figures 7.27 and 7.28 it can be seen that the yields of the $[Fe/H] = -6.5$ and -5.45 DCF models are enriched in fluorine also (a plot of all the fluorine yields is available in Figure A.11 of Appendix A.2). In fact the DCF group of models is the most F-enhanced group in the grid. This is due to the production of F by the DCF event and the fact that the F is not destroyed by HBB (to a significant degree) at these low masses. In the low-mass DSF group, which does not experience 3DUP or significant HBB, the F yields are substantially lower. This is due to two factors. The first is that less F pollution occurs as a result of the DSF event, and the second is that these yields are diluted by unpolluted RGB mass loss. Again, due to HBB, the situation in the IM yields is quite uniform. The F yields in this group are all substantially sub-solar, with $[F/H]$ being $\sim -3 \rightarrow -2$. In these models F follows a similar fate to that of carbon. Its abundance first increases as it is dredged up from the intershell after each pulse (for a description of the F production process in the intershell of AGB stars see eg. [Habing and](#)

Olofsson 2003). However, when the temperature at the base of the convective envelope increases, it is destroyed by HBB (via $^{19}\text{F}(p, \alpha)^{16}\text{O}$). Hence the yield of this element is relatively low at these masses because of the extensive HBB.

Neon to Phosphorus

The main channel for neon production is $^{14}\text{N}(\alpha, \gamma)^{18}\text{F}(\beta^+, \nu)^{18}\text{O}(\alpha, \gamma)^{22}\text{Ne}$, which generally occurs in the intershell of AGB stars. Indeed, in our IM models the source of Ne in the AGB envelope is 3DUP of this intershell ^{22}Ne . With scaled-solar abundances ^{20}Ne is normally the dominant isotope of neon but in these extremely metal-poor models ^{22}Ne easily dominates as soon as some 3DUP occurs. The neon is however quickly burnt in the envelope via HBB. This is reflected in the yields, as can be seen in Figure 7.27 for example, where Ne is always sub-solar (see Appendix A for more plots). We note that if 3DUP occurred without HBB then the Ne yield would be quite high in these Group 3 models. At low mass and metallicity (the DCF group) the Ne yield is also always sub-solar in terms of $[\text{Ne}/\text{H}]$, ranging from $\sim -1 \rightarrow -4$. The source of the Ne is the DCF itself. In the low-mass models which do not experience the DCF (Group 2) the yields are similar, but in these cases the source is the DSF. As the base of the convective envelope in the low mass models is not hot enough for significant HBB the Ne in the AGB envelope survives. Thus it is apparent that the Ne production from the DCF and DSF events is relatively small. Since the main sources of the Ne from these models are the DCF and DSF, we again note that this means that the yields are dependent on the treatment of these events in the structural evolution code, and thus the uncertainties therein (eg. the unknown degree of overshoot).

As mentioned above the periodically dredged-up ^{22}Ne in the IM models is burnt to sodium in the Ne-Na cycle/chain. The main product from these reactions is ^{23}Na . Indeed Na is present in large amounts in the IM yields, always being between \sim solar and 1.5 dex super-solar. As an example of the Ne-Na cycle in action we show in Figure 7.32 the surface evolution of some salient nuclides during the AGB phase of the $2 M_{\odot}$, $[\text{Fe}/\text{H}] = -5.45$ model. The initial enrichment of the envelope with ^{22}Ne from 3DUP is seen, as is the subsequent destruction via HBB as the temperature increases. We also plot some Mg isotopes and ^{27}Al in the same figure. The yields in the IM models are enriched in Mg and Al, although not to the same extent as Na. In general the Mg yield is between \sim solar and ~ 2 dex below solar. The majority of this Mg is in the form of ^{26}Mg and comes from 3DUP of AGB intershell material. It is produced in the He intershell via alpha captures on ^{22}Ne . It can also be seen that Al is enhanced in the yields, but at an even lower level. This is apparent in all the IM yields, where $[\text{Al}/\text{H}]$ is always sub-solar, by about 0.5 to 2 dex. The Al in these yields is mainly a product of HBB destruction of ^{25}Mg via $^{25}\text{Mg}(p, \gamma)^{26}\text{Al}(p, \gamma)^{27}\text{Si}(\beta^+, \nu)^{27}\text{Al}$. The source of the ^{25}Mg seeds is the AGB intershell (via $^{22}\text{Ne}(\alpha, n)^{25}\text{Mg}$). Thus it can be seen that the Ne \rightarrow Na and Mg \rightarrow Al chains operate independently, inasmuch as the dominant source of the initial seeds, ^{22}Ne and ^{25}Mg , are both fed in from 3DUP rather than via leakage between the chains (or from other nucleosynthetic channels). Since the yields of these species all ultimately depend on the degree of 3DUP they are thus dependent on the amount of overshoot used in the modelling. Here we have used none, so the the results of our 3DUP pollution is probably a lower limit, all else being constant.

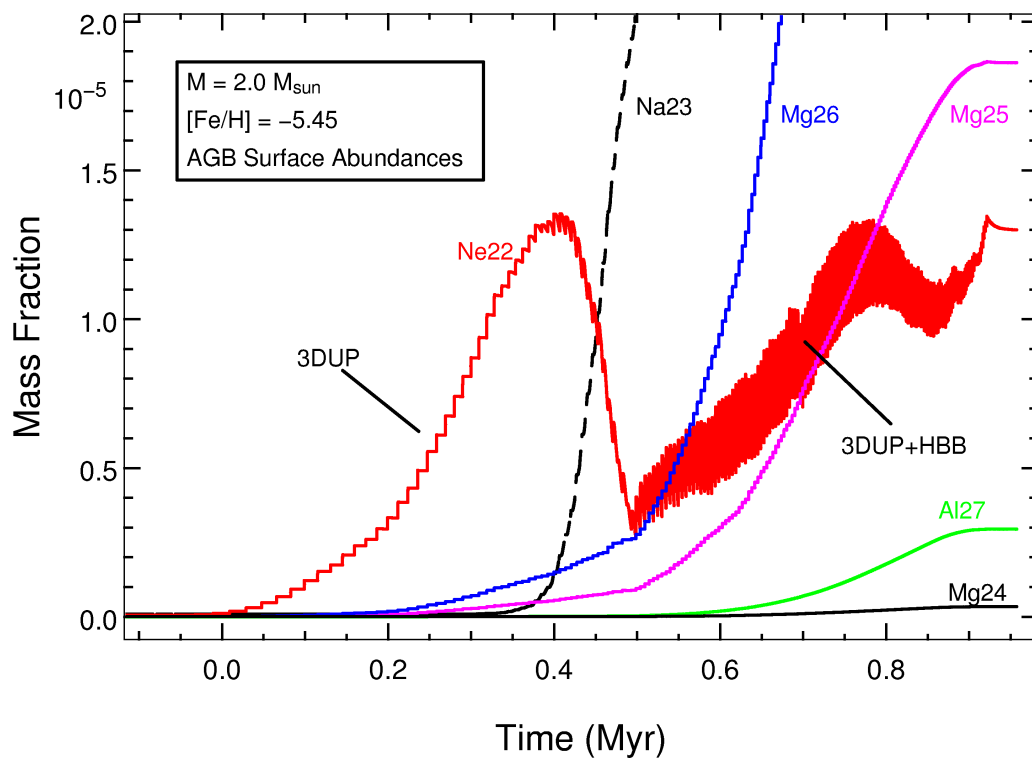


Figure 7.32: The evolution of the surface abundances for a selection of nuclides involved in the Ne-Na and Mg-Al chains/cycles during the AGB phase of the $2 M_{\odot}$, $[\text{Fe}/\text{H}] = -5.45$ model. Time has been offset. The initial enrichment of the surface with Ne due to 3DUP can be seen, as can the activation of strong HBB which transforms the repeatedly dredged-up Ne to Na. The increase in ^{26}Mg and ^{25}Mg occurs because they are dredged up at the same time as the ^{22}Ne . HBB is hot enough in this model for the Mg-Al proton capture reactions to operate, which produce ^{27}Al from the ^{25}Mg .

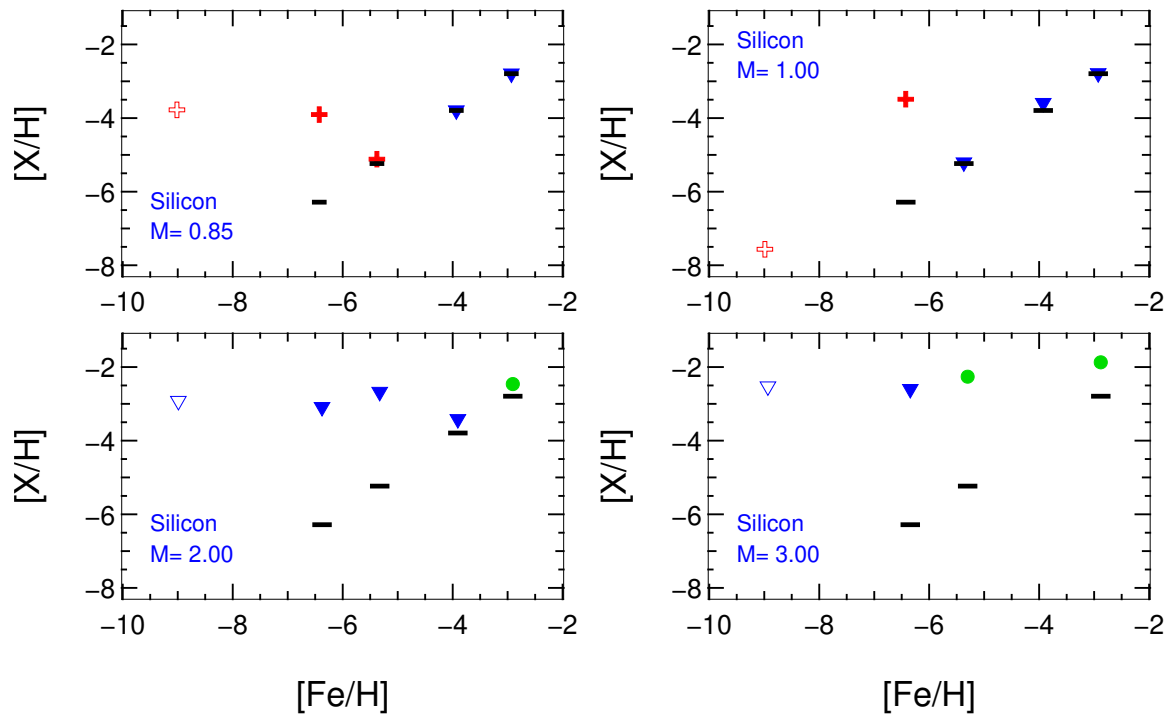


Figure 7.33: Same as Figure 7.29 except for silicon and only for $[X/H]$. It can be seen that, for most of the LM models the Si yield is practically the same as the initial abundances (shown as short horizontal lines) – except in some of the DCF models. In the IM models there is always a nett production but it is still ~ 2 to 3 dex below solar.

Returning to the low-mass models we see that the Na yields are similar to the Ne yields (relative to solar). As no significant HBB occurred in these models the source of this Na was also the DCF and DSF events. The lack of significant amounts of advanced proton- or α -capture nucleosynthesis in these models becomes increasingly apparent in the Mg and Al yields (see Appendix A for the figures). The yields for both of these elements are significantly lower than the HBB/3DUP yields of the IM models, being at least 2 dex below solar. Indeed, in roughly half of the LM models the abundances in the yields have hardly changed from the initial values. Looking at the silicon yields (Figure 7.33) this trend is continued. It is only the most metal-poor models that have any significant Si production, and this only occurs during DCFs (and not all of them). In contrast to this the IM models do all produce Si (via 3DUP), although the yields are only between ~ 3 and 2 dex sub-solar. Phosphorous is produced in large quantities relative to the lighter Si in the IM models (at least relative to solar – in absolute terms the yield is lower). In most of the yields $[P/H]$ is only ~ 1 dex sub-solar. It is mainly present in the form of ^{31}P , which is dredged up from the AGB intershell where it is produced via $^{27}\text{Al}(\alpha, \gamma)^{31}\text{P}$. At low mass it is produced to a moderate extent in the Group 1 (DCF) models (at least 1 dex below solar in the yields, usually lower) but hardly enhanced above the initial values in the Group 2 (DSF) yields.

7.4.5 Nuclidic Yield Tables by Mass Fraction

We supply the yields and initial compositions for the entire grid of models in tabular form in Appendix A.3. All species in the network are listed (except for neutrons). Abundances are given in mass fraction. The stellar remnant masses are also supplied for easy reference. Here we

present just one of the tables as a sample, the one for the $[\text{Fe}/\text{H}] = -6.5$ models (Table 7.11).

Table 7.11: Yields and initial composition for all the $[\text{Fe}/\text{H}] = -6.5$ models. All species in the network are listed except for neutrons. Abundances are in mass fraction, normalised to 1.0. The remnant masses (white dwarf masses) are in brackets below the initial stellar masses in the table header.

Nuclide	Initial [Fe/H] = -6.5	0.85 M _⊙ (0.758)	1.0 M _⊙ (0.846)	2.0 M _⊙ (1.066)	3.0 M _⊙ (1.107)
h1	0.7548	0.686	0.642	0.656	0.604
h2	0.00E+00	3.44E-19	2.08E-18	3.99E-18	3.53E-18
he3	7.85E-06	1.33E-05	1.62E-04	1.61E-07	1.72E-08
he4	0.2450	0.280	0.307	0.336	0.384
li7	3.13E-10	1.65E-09	7.22E-10	3.46E-10	5.14E-11
be7	0.00E+00	5.26E-16	7.96E-15	6.63E-14	3.71E-14
b8	0.00E+00	5.04E-26	4.00E-27	1.04E-26	5.32E-27
c12	1.30E-09	7.59E-03	1.04E-02	2.99E-04	4.38E-04
c13	1.33E-16	9.74E-04	1.18E-03	6.86E-05	1.04E-04
c14	0.00E+00	8.58E-07	2.07E-07	4.84E-11	6.76E-11
n13	0.00E+00	0.00E+00	0.00E+00	0.00E+00	0.00E+00
n14	2.27E-16	2.03E-03	2.92E-03	7.60E-03	1.06E-02
n15	1.30E-18	7.36E-06	8.92E-06	3.09E-07	7.02E-07
o14	0.00E+00	0.00E+00	0.00E+00	0.00E+00	0.00E+00
o15	0.00E+00	0.00E+00	0.00E+00	7.86E-37	0.00E+00
o16	2.23E-09	2.10E-02	3.03E-02	1.32E-04	1.42E-04
o17	3.39E-17	1.37E-03	6.21E-03	3.45E-07	5.70E-07
o18	2.26E-16	8.12E-05	1.64E-05	1.47E-10	2.30E-10
o19	0.00E+00	0.00E+00	0.00E+00	0.00E+00	0.00E+00
fl7	0.00E+00	0.00E+00	0.00E+00	1.41E-42	0.00E+00
fl8	0.00E+00	0.00E+00	0.00E+00	2.79E-34	0.00E+00
fl9	3.92E-18	4.90E-07	3.55E-07	7.24E-10	5.80E-10
f20	0.00E+00	0.00E+00	0.00E+00	0.00E+00	0.00E+00
ne19	0.00E+00	0.00E+00	0.00E+00	0.00E+00	0.00E+00
ne20	9.24E-10	3.34E-05	6.73E-05	6.12E-05	1.11E-04
ne21	2.06E-13	2.48E-06	6.69E-06	1.04E-08	2.60E-09
ne22	4.64E-14	3.14E-05	6.66E-05	5.05E-06	5.36E-06
na21	0.00E+00	0.00E+00	0.00E+00	0.00E+00	0.00E+00
na22	0.00E+00	3.24E-30	1.92E-17	4.83E-12	2.30E-11
na23	1.23E-11	7.33E-07	1.14E-06	9.86E-05	8.39E-05
na24	0.00E+00	0.00E+00	0.00E+00	6.93E-37	0.00E+00
mg23	0.00E+00	0.00E+00	0.00E+00	0.00E+00	0.00E+00
mg24	4.13E-10	4.81E-07	4.82E-07	1.89E-07	2.08E-07
mg25	4.49E-12	3.22E-07	2.44E-07	5.74E-06	1.39E-05
mg26	4.95E-12	1.68E-06	3.53E-06	2.62E-05	6.25E-05
mg27	0.00E+00	0.00E+00	0.00E+00	0.00E+00	0.00E+00
al25	0.00E+00	0.00E+00	0.00E+00	0.00E+00	0.00E+00
al-6	0.00E+00	1.66E-12	2.48E-11	4.16E-07	1.17E-06
al*6	0.00E+00	0.00E+00	0.00E+00	0.00E+00	0.00E+00
al27	1.00E-11	3.47E-08	6.31E-08	1.25E-06	6.22E-06
al28	0.00E+00	0.00E+00	0.00E+00	0.00E+00	0.00E+00
si27	0.00E+00	0.00E+00	0.00E+00	0.00E+00	0.00E+00
si28	3.75E-10	6.64E-08	1.62E-07	4.00E-07	1.16E-06
si29	3.95E-12	1.17E-08	2.77E-08	1.01E-07	2.74E-07
si30	2.78E-12	5.61E-09	1.45E-08	2.55E-08	6.90E-08
si31	0.00E+00	0.00E+00	0.00E+00	1.70E-41	0.00E+00
si32	0.00E+00	3.02E-16	2.30E-17	6.52E-12	4.98E-12
si33	0.00E+00	0.00E+00	0.00E+00	0.00E+00	0.00E+00
p29	0.00E+00	0.00E+00	0.00E+00	0.00E+00	0.00E+00
p30	0.00E+00	0.00E+00	0.00E+00	0.00E+00	0.00E+00
p31	1.04E-12	6.82E-08	3.91E-07	3.59E-07	1.05E-06
p32	0.00E+00	1.17E-19	8.91E-21	2.53E-15	1.93E-15
p33	0.00E+00	-3.08E-44	0.00E+00	1.17E-23	4.58E-22

Continued on next page...

Table 7.11 – continued from previous page

Nuclide	Initial [Fe/H] = -6.5	0.85 M _⊙ (0.758)	1.0 M _⊙ (0.846)	2.0 M _⊙ (1.066)	3.0 M _⊙ (1.107)
p34	0.00E+00	0.00E+00	0.00E+00	0.00E+00	0.00E+00
s32	1.65E-10	2.61E-08	2.05E-07	7.95E-08	2.47E-07
s33	7.78E-13	1.95E-09	2.86E-09	9.74E-09	1.63E-08
s34	5.30E-11	3.19E-09	6.39E-09	6.35E-09	1.56E-08
s35	0.00E+00	1.16E-07	6.94E-07	3.22E-08	9.27E-08
fe56	4.54E-10	4.13E-10	3.86E-10	4.42E-10	4.39E-10
fe57	1.37E-11	1.25E-11	1.17E-11	1.35E-11	1.34E-11
fe58	2.79E-18	8.97E-15	1.33E-15	4.87E-13	5.27E-13
fe59	0.00E+00	0.00E+00	0.00E+00	0.00E+00	5.86E-31
fe60	0.00E+00	5.60E-16	1.19E-16	3.35E-13	4.94E-13
fe61	0.00E+00	0.00E+00	0.00E+00	0.00E+00	0.00E+00
co59	7.22E-12	6.57E-12	6.14E-12	7.29E-12	7.24E-12
co60	0.00E+00	4.87E-20	1.04E-20	2.92E-17	4.30E-17
co61	0.00E+00	0.00E+00	0.00E+00	0.00E+00	0.00E+00
ni58	6.41E-12	5.83E-12	5.46E-12	6.24E-12	6.20E-12
ni59	0.00E+00	1.01E-18	1.93E-24	4.61E-19	1.06E-18
ni60	7.43E-15	4.18E-14	1.66E-14	1.44E-12	1.53E-12
ni61	4.00E-17	4.69E-11	7.68E-11	1.06E-11	1.40E-11
ni62	2.38E-20	2.04E-20	1.28E-20	1.99E-24	2.05E-25
g	4.67E-16	6.35E-08	3.16E-07	1.41E-09	6.38E-10

7.5 Comparison with Previous Studies

First we note that we have made detailed comparisons of our 0.85 and 2 M_⊙, Z = 0 models with those in the literature in Sections 5.2.6 (on page 131) and 5.3.4 (page 150). Given the small sets of models we have found to compare with below, and the fact that these models suffer the same ‘peculiar’ evolutionary traits as the Z = 0 models, we suggest that reading the aforementioned sections in conjunction with this one would be advantageous.

Background

In the ~ 20 years after [Wagner \(1974\)](#) calculated his grid of metal-poor models there were only two studies that explored this low-mass, low-metallicity regime again – [Tornambe and Chieffi \(1986\)](#) and [Cassisi and Castellani \(1993\)](#). This was mainly due to the paucity of observational evidence for such low metallicity stars (although we do note that much work was done on Pop III, Z = 0 modelling in the same time period). Indeed, in 1993 [Cassisi and Castellani](#) noted that there was “... a lack of metal-deficient stars found in the Galactic halo ...”. They did however note that this may be due to the restricted observational sample at the time. Observations of lower and lower metallicity (i.e. [Fe/H] < -3) halo stars started to be reported in the 80s and 90s (eg. [Bessell and Norris 1984](#); [Molaro and Castelli 1990](#)). However it was the HK survey ([Beers et al. 1985, 1992](#)) that began to discover significant numbers of halo stars with [Fe/H] < -3.0, fleshing out the low metallicity tail of the halo metallicity distribution function. More detailed follow-up observations started to reveal that there is a subclass of extremely metal-poor halo stars (EMPHs) that have large carbon (and nitrogen) overabundances (i.e. higher than solar, relative to Fe) – the CEMPs. These observations sparked a flurry of theoretical modelling in the late 90s and early 2000s. This increase in modelling can be seen in [Table 7.12](#) where we give

a summary of the literature on this particular topic of low metallicity stellar evolution at low- and intermediate-mass.

In this section we first compare our structural evolution results with those in the literature. Then we compare results from the primary low-metallicity polluting events (the dual core flash and dual shell flash) and finally provide a summary/overview of the expected polluting affects of the yields from these models. Note that we have chosen a subset of our models with which to make comparisons, partly for brevity and partly because of the fact that there are not very many models to compare with (we chose subsets that had the most overlap with the models available in the literature). We compare our results with observations of the CEMPs in the next section.

7.5.1 Low Mass Structural Evolution

We define low mass models as models that go through the degenerate core He flash (or DCF) at the top of the RGB. At $Z = 0$ the boundary is at roughly $1.2 M_{\odot}$ (Marigo et al. 2001). At very low metallicity ($[Fe/H] \sim -4$) it appears to be slightly higher, at $\sim 1.4 M_{\odot}$ (Cassisi and Castellani 1993). Our models are consistent with these values, as all of our $1 M_{\odot}$ models experience the core He flash whilst none of our $2 M_{\odot}$ models do. A finer grid of models would be required to pinpoint the transition at each metallicity.

Extremely Low Metallicity

Here we compare our 0.85 and $1.0 M_{\odot}$, $[Fe/H] = -5.45$ models with models of similar metallicity and mass from the literature. In the top panel of Table 7.13 we display a selection of evolutionary characteristics for these models. It can be seen that the intersection of our chosen comparison models and those of comparable mass and metallicity (and which give the required comparison values) from the literature is quite small. Indeed, for the $1 M_{\odot}$ case we find only one study (Wagner 1974) to compare with. In this case the luminosity at the top of the RGB and the MS lifetime agree reasonably well, considering there is more than 30 years between the studies. The RGB lifetime is however very different between the models. Our lifetime is 131 Myr whilst Wagner's is 76 Myr – almost a factor of two shorter. This may be a result of the updated physics in our model but it may also be a result of RGB lifetime definition. We define it as the length of time from the end of the Hertzsprung gap to the time of core He ignition. We note that our model experienced a dual shell flash (DSF) at the beginning of the AGB. Wagner 1974 do not report a DSF as they were probably unable to evolve through the He flash at that stage.

In the $0.85 M_{\odot}$, $[Fe/H] = -5.45$ case there are more studies to compare to. The key finding is that Picardi et al. (2004) report that a dual core flash (DCF) occurs in their $0.80 M_{\odot}$, $[Fe/H] = -6$ model, as it does in our $0.85 M_{\odot}$ model. Weiss et al. (2004) did not find this event to occur in their $0.81 M_{\odot}$, $[Fe/H] = -5.3$ model but this is expected because the initial composition of their model was heavily enriched in carbon and oxygen (eg. $[C/Fe] = 4$), giving it an increased metallicity as defined by Z_{cno} . The luminosity at the top of the RGB in the Picardi et al. (2004) model is exactly the same as ours. However their RGB lifetime is very different – it is a factor of four shorter than ours. We are unsure of the reason for this but note that the Wagner 1974 lies

Year	Author	Mass	Metallicity	Max. Evolution	Helium
1974	Wagner	0.65 → 2.5	-6, -4, -2	RGB	0.26
1986	Tornambe and Chieffi	2.5 → 8.0	-6, -4, -2	EAGB	0.2
1993	Cassisi and Castellani	0.7 → 15	-8, -4, -2	RGB/EAGB	0.23
1996	Cassisi et al.	0.7 → 1.1	-8, -4, -3	~DSF (M=0.8)	0.23
2000	Fujimoto et al.	0.8 → 4	zero, -4, -2	DCF/DSF	0.23
2004	Iwamoto et al.	1 → 3	-2.7	DSF, ~AGB	0.24
2004	Picardi et al.	0.8 → 1.5	zero, -6, -5, -4	DCF, SRGB, ~EAGB	0.23 & 0.27
2004	Weiss et al.	0.82	zero, -5	DCF, SRGB	0.23?
2006	Campbell (This study)	0.8 → 3 + ^a	zero, -6, -5, -4, -3	DCF, DSF, SRGB, AGB & Yields	0.245

Table 7.12: A summary of the literature (to the best of our knowledge) for theoretical studies of low- and intermediate-mass stars of very low metallicity. This is basically a subset of the literature review table in Section 2.3 (Table 2.2 on page 24). Mass is given in units of M_{\odot} (an arrow indicates a range of masses). Metallicity is given as $\log_{10}(Z/Z_{\odot})$ except when $Z = 0$ where we write ‘zero’. Using $\log_{10}(Z/Z_{\odot})$ gives a rough approximation to $[\text{Fe}/\text{H}]$, which is useful for comparisons with observational studies. In column 5 we show the maximum stage of evolution that the models were evolved *through* (so it is an inclusive designation). The ‘~’ symbol is used where the models were evolved only part of the way through the indicated phase of evolution. In the last column we show the helium mass fraction used. [Abbreviations for the evolutionary stages are: CHeB (core helium burning), DCF (dual core flash, the H-He core flash in low mass low-Z stars, also known as HEFM in the literature), SRGB (secondary RGB), DSF (dual shell flash, the H-He shell flash near the start of the AGB in low- and intermediate-mass stars, also known as HCE).]

^aSome models with $M = 4$ & $5 M_{\odot}$ were also calculated but only part of the way through the AGB.

Metallicity = -5.45								
Study	M_*	[Fe/H]	τ_{MS}	τ_{RGB}	L_{tip}	M_c	DF	Z_{DF}
Wagner (1974)	0.85	-6	8.2	140	2.6	-	-	-
Picardi et al. (2004)	0.80	-6	-	47	2.8	0.54	C	2E-2
Weiss et al. (2004)	0.81	-5.3	-	-	-	-	N ^a	-
<i>This study</i>	0.85	-5.5	10	205	2.8	0.53	C	3E-2
Wagner (1974)	1.0	-6	4.7	76	2.6	-	-	-
<i>This study</i>	1.0	-5.5	5.7	131	2.8	0.52	S	4E-3

Metallicity = -4.0								
Study	M_*	[Fe/H]	τ_{MS}	τ_{RGB}	L_{tip}	M_c	DF	Z_{DF}
Wagner (1974)	0.85	-4	7.9	160	2.9	-	-	-
Cassisi et al. (1996)	0.80	-4	-	-	3.1	0.53	-	-
Fujimoto et al. (2000)	0.80	-4	-	-	-	-	S	6E-3
<i>This study</i>	0.85	-4	10	220	3.0	0.52	S	1E-3
Wagner (1974)	1.0	-4	4.5	93	2.8	-	-	-
Cassisi and Castellani (1993)	1.0	-4	6.5	-	3.0	0.52	-	-
Cassisi et al. (1996)	1.0	-4	-	-	3.0	0.52	-	-
Fujimoto et al. (2000)	1.0	-4	-	-	-	-	S	-
Iwamoto et al. (2004)	1.0	-2.7	-	-	3.2	-	S	1E-2
<i>This study</i>	1.0	-4	5.7	150	3.0	0.51	S	1E-2

Table 7.13: Comparing some of our low-mass models with those in the literature. The top panel displays characteristic values for our low-mass $[\text{Fe}/\text{H}] = -5.45$ models and those with comparable mass and metallicity from the literature. The second panel does the same for our $[\text{Fe}/\text{H}] = -4$ low-mass models. Column values are: M_* (initial mass of the model), τ_{MS} (main sequence lifetime, in Gyr), τ_{RGB} (RGB lifetime, in Myr), L_{tip} (the maximum luminosity attained on the RGB, in $\log(L/L_\odot)$), M_c (mass of the H-exhausted core at the time of the core He flash), DF (which type of flash the model experienced, if any – Core, Shell or Neither) and Z_{DF} (the Z metallicity of the surface after the dual flash episode, whether it be a DCF or DSF). A dash means that the information was either not supplied in the paper or not relevant to the model.

^a This model had an initial composition with $[\text{C}/\text{Fe}] = 4$ and $[\text{O}/\text{Fe}] = 4$ so the Z-defined metallicity was actually relatively high.

between our lifetime and that of Picardi et al.. Despite this the core masses at core He ignition are all quite similar between the studies.

Very Low Metallicity

In panel 2 of Table 7.13 we show comparisons for our 0.85 and 1.0 M_\odot , $[\text{Fe}/\text{H}] = -4.0$ models. At this higher metallicity we have been more fruitful in finding comparison models. We begin with the 0.85 M_\odot comparisons. The key finding here is that Fujimoto et al. (2000) report a DSF to occur in their 0.80 M_\odot model, as we do in our model. Cassisi et al. (1996) and Wagner (1974) do not report DSFs but we note that they do not evolve through the core He flash (Cassisi et al. (1996) create a zero-age horizontal branch model for the further evolution of their 0.80 M_\odot star). The RGB tip luminosities all agree reasonably well between these models but we note that the RGB lifetime of Wagner (1974) is again substantially shorter than ours (we have found no other RGB lifetimes to compare with here).

At 1 M_\odot we find five models to compare with (although not many studies give the comparison values we use). Again, a key finding is the occurrence of DSFs in these models. This time there are two other studies that find DSFs to occur – Fujimoto et al. (2000) and Iwamoto et al. (2004). Our model also experiences a DSF. The fact that independent modellers find the same (general)

result is reassuring. The differences in surface pollution from the DCF events is discussed below. We note that our $1 M_{\odot}$, $[\text{Fe}/\text{H}] = -3.0$ model (which is not listed in the table) is actually closer in metallicity to the model of [Iwamoto et al. \(2004\)](#). This model also experiences a DSF, concurring with their findings. Finally we note that the RGB tip luminosities show a small variation between the studies ($L_{\text{tip}}/L_{\odot} = 2.8 \rightarrow 3.2$) but this is probably not significant.

7.5.2 Intermediate Mass Structural Evolution

Low and Extremely Low Metallicity

In panel 1 of Table 7.13 we show comparisons for our 2.0 and $3.0 M_{\odot}$, $[\text{Fe}/\text{H}] = -5.45$ models. Unfortunately we have not found many studies to compare with at these masses and metallicities. However an important result is that [Fujimoto et al. \(2000\)](#) also find DSFs to occur in their $[\text{Fe}/\text{H}] = -5$ intermediate mass models.

At $[\text{Fe}/\text{H}] = -4.0$ both the [Fujimoto et al. \(2000\)](#) and [Iwamoto et al. \(2004\)](#) studies find a DSF to occur in their $2 M_{\odot}$ models, which is consistent with our model. There is however some disagreement between the $3 M_{\odot}$ models. Our model and the model of [Iwamoto et al.](#) do *not* experience DSFs, whereas the model of [Fujimoto et al.](#) does. It is important to mention that the [Iwamoto et al.](#) model is significantly more metal-rich than than the other two models, having $[\text{Fe}/\text{H}] = -2.7$. Looking at our $[\text{Fe}/\text{H}] = -3.0$ model we see that it does not experience a DSF either, so the results are consistent between these two studies. The discrepancy between our $[\text{Fe}/\text{H}] = -4.0$ model and that of [Fujimoto et al.](#) remains however. Thus it appears that different modellers find (at least slightly) different metallicity limits on the occurrence of the DSF. This is not surprising as these events are dependent on the details of the treatment of convective boundaries. [Iwamoto et al.](#) have used the same minimalist approach as we have, insomuch as they do not add any overshoot to the standard Schwarzschild boundary. As far as we aware [Fujimoto et al.](#) do the same (from the code description in [Hollowell et al. 1990](#)). Of course this does not necessarily mean that all the modellers treat the numerical details of meshpoint placing in the same way. Thus there may be some form of ‘numerical diffusion’ across the Schwarzschild boundaries in all the models – which could cause the DSF to occur at slightly higher metallicities. The different results may also be due to a difference in input physics.

7.5.3 The Polluting Episodes

As this is the first study to calculate the entire AGB evolution and detailed yields for stars of such low metallicity there are no yields with which we can directly compare. However, inspired by the CEMP stars, there has been much quantitative work on the envelope pollution resulting from the dual core flash (DCF) and dual shell flash (DSF) events. We thus compare the chemical pollution results of our models at these stages of evolution with those in the literature. Some studies have evolved models a short way in to the AGB evolution, so we also discuss the occurrence (or non-occurrence) of 3DUP and HBB. We note that the comparisons of our $Z = 0$ models with those in the literature can be found in Sections 5.2.6 ($0.85 M_{\odot}$) and 5.3.4 ($2.0 M_{\odot}$).

Metallicity = -5.45					
Study	M_*	[Fe/H]	τ_{MS}	DF	Z_{DF}
Wagner (1974)	2.0	-6	545	-	-
Fujimoto et al. (2000)	2.0	-5	-	Shell	-
<i>This study</i>	2.0	-5.5	605	Shell	2E-5
Wagner (1974)	2.5	-6	289	-	-
Fujimoto et al. (2000)	3.0	-5	-	Shell	-
<i>This study</i>	3.0	-5.5	177	Shell	4E-8 ^a

Metallicity = -4.0					
Study	M_*	[Fe/H]	τ_{MS}	DF	Z_{DF}
Wagner (1974)	2.0	-4	478	-	-
Fujimoto et al. (2000)	2.0	-4	-	Shell	-
Iwamoto et al. (2004)	2.0	-2.7	-	Shell	2E-3
<i>This study</i>	2.0	-4	562	Shell	6E-4
Wagner (1974)	2.5	-4	242	-	-
Fujimoto et al. (2000)	3.0	-4	-	Shell	-
Iwamoto et al. (2004)	3.0	-2.7	-	None	-
<i>This study</i>	3.0	-4	174	None	-

Table 7.14: Comparing some of our intermediate-mass (IM) models with those in the literature. The top panel displays characteristic values for our IM $[\text{Fe}/\text{H}] = -5.45$ models and those with comparable mass and metallicity from the literature. The second panel does the same for our $[\text{Fe}/\text{H}] = -4$ IM models. Column values are: M_* (initial mass of the model), τ_{MS} (main sequence lifetime, in Gyr), DF (whether the model experienced a dual shell flash or not), and Z_{DF} (the Z metallicity of the surface after the DSF episode). A dash means that the information was either not supplied in the paper or not relevant to the model.

^a Note that this is the same as the initial composition – the DSF has practically no effect on the surface Z in this case.

Dual Core Flashes

In the $0.85 M_{\odot}$, $Z = 0$ section we showed that there was a variation in surface Z_{cno} resulting from the DCF between studies ($Z_{cno} \sim 0.015 \rightarrow 0.004$). However, despite this factor of four variation, the general result from all the studies was that the models produce $\sim 1 \rightarrow 3$ dex too much C and N, as compared to CEMP observations. Here we make further comparisons with the models in the literature, this time with regards to our low metallicity models.

In panel 1 of Table 7.15 we show the resulting pollution from some models in the literature that experience the DCF. We include $Z = 0$ models as there are not many studies at very low metallicity that give quantitative results for the pollution. All the models are naturally of low mass as the DCF only occurs in stars that go through the core He flash. Our $[Fe/H] = -5.45$, $0.85 M_{\odot}$ model agrees very well with the $0.80 M_{\odot}$ models at $[Fe/H] = -5$ and -6 by Picardi et al. (2004). In fact, our value of surface Z after the DCF (Z_{DCF}) is exactly the same as that in their $[Fe/H] = -5$ model (3×10^{-2}). Looking at the $Z = 0$ models we can see that there is not a very large amount of variation in pollution at $0.80 \rightarrow 0.85 M_{\odot}$, even when comparing to the higher metallicity models. They are all in the range $0.9 \rightarrow 3 \times 10^{-2}$, which is reassuring to see considering the results come from three independent stellar structure codes. It would seem that the ‘ballpark’ bulk pollution expected from modelling the DCF at these masses is now reasonably well constrained. The details of the pollution may be another matter – eg. degree of s-process, ratios of nuclides. We shall discuss some chemical details of the models in the next section when we compare our (and other studies’) results to observations.

In the case of our $[Fe/H] = -5.45$, $1.0 M_{\odot}$ model there is an order of magnitude less pollution arising from the DCF event than in the $0.85 M_{\odot}$ model. We have found no low- Z models to compare with (that experience the DCF) so we compare with two $Z = 0$, $1 M_{\odot}$ models. The model by Schlattl et al. (2001) has a factor of ~ 3 more pollution from the DCF than ours, which, in the context of this complex evolutionary phase, and the difference in metallicity, we consider as a reasonable agreement. The situation is better when comparing to the model of Fujimoto et al. (1990), which has exactly the same level of pollution as our $1 M_{\odot}$ model ($Z_{DCF} = 4 \times 10^{-3}$). We note that if it were not for the larger amount of pollution in the Schlattl et al. (2001) model one might say that the DCF produces more pollution at lower masses, but the number of studies is too small to make any serious conclusions on this.

In summary it appears that the pollution arising from the DCF at low mass and extremely low Z is reasonably consistent between models, being $\sim 2 \times 10^{-2}$ at $0.8 M_{\odot}$, and ranging between $4 \rightarrow 10 \times 10^{-3}$ at $1 M_{\odot}$. However we add the caveat that this conclusion is not based on a great many studies.

Dual Shell Flashes and the TP-AGB

In Table 7.15 it is apparent that there is, in general, more pollution arising from the DSF at low mass ($M = 0.8 \rightarrow 1.0 M_{\odot}$) than at intermediate mass. The Z_{DSF} value (which is defined as the surface metallicity after the DSF) ranges from $2 \times 10^{-4} \rightarrow 1 \times 10^{-2}$ in the LM models and $6 \times 10^{-6} \rightarrow 2 \times 10^{-3}$ in the IM ($2 M_{\odot}$) models. We note however that our literature sample covers

a wide range of initial metallicity which explains much of the variation, as will become clear in the model-to-model comparisons below.

We reported in Section 5.3.4 that the amount of pollution resulting from DSF episodes in the $Z = 0$ intermediate mass models is relatively small compared to that arising in low-mass models. Moreover, since these models experience 3DUP immediately after the DSF, which also brings up processed material, the polluting effect of the DSF is quickly swamped. Thus the detailed results in terms of the bulk pollution from these events are rendered insignificant. This was also recognised by Siess et al. (2002). This phenomenon is also true of all the metal-deficient $2 M_{\odot}$ models in Table 7.15 – as all studies find 3DUP to occur. We note that there may however be more subtle nucleosynthetic signatures from this event, such as that from s-processing. Putting 3DUP aside, we see that the resultant Z_{DSF} from the $2 M_{\odot}$, $[\text{Fe}/\text{H}] = -2.7$ model of Iwamoto et al. (2004) and that of our closest comparison model of $2 M_{\odot}$ and $[\text{Fe}/\text{H}] = -4$, differ by a factor of ~ 3 . We suggest that this is a reasonably close result, given the differences in initial composition. Note that our $2 M_{\odot}$, $[\text{Fe}/\text{H}] = -3$ model did *not* experience a DSF. This is an interesting difference in itself, as it shows that the line between the DSF occurring and not occurring (at a particular mass and/or metallicity) is uncertain. The only other $2 M_{\odot}$ DSF models that we have found in the literature are of zero metallicity. We compared these with our $Z = 0$ models in the $Z = 0$ chapters.

Returning to DSFs in low mass models it can be seen in Table 7.15 that the Z_{DSF} from our $0.85 M_{\odot}$, $[\text{Fe}/\text{H}] = -4$ model and that from the $0.80 M_{\odot}$ model of the same metallicity by Fujimoto et al. (2000) differ by a factor of ~ 6 . A difference of this size is quite significant when comparing to observations, as it translates to ~ 0.8 dex. Comparing our $1 M_{\odot}$, $[\text{Fe}/\text{H}] = -3$ model with the $1 M_{\odot}$, $[\text{Fe}/\text{H}] = -2.7$ model of Iwamoto et al. (2004) there is a much closer match, such that Z_{DSF} only differs by a factor of ~ 2 . A discrepancy of this size is roughly the size of the error bars in observational studies. Interestingly Iwamoto et al. (2004) report that 3DUP occurs in their model, which is absent from all our $1 M_{\odot}$ models (and the model of Fujimoto et al. 2000). However, on inspection of their Figure 5 it appears that it is very minor, at least during the beginning of the TP-AGB.

In summary we have shown that there is much variation in the results given in the literature for pollution from the DSF events. At IM this is of little importance due to the dominating effect of 3DUP on the AGB surface composition. We note however that if the DSF event leads to some form of envelope ejection (that may pollute a binary companion) then the details of the DSF are important and thus this polluting event would need to be studied more rigorously. At low mass the DSF does remain the dominant source of pollution for the rest of the AGB evolution, due to the lack of 3DUP. Although this material is usually diluted (sometimes by a very large amount) by unpolluted RGB mass loss, the details of the DCF pollution would also be important in a binary star mass-transfer scenario. At any rate it does have an impact on the yields, unlike in the IM models. Our results have been found to differ by factors of $\sim 3 \rightarrow 6$ (in Z_{DSF}) with similar models in the literature. Although the discrepancies are reasonably large they are not catastrophic when comparing to the error bars in observational studies but, in the worst cases, they are quite significant. Thus we suggest that the current state of the field is that we have a rough prediction of DSF pollution from the models, but more work needs to be done. We again add the caveat that these conclusions are based on a small number of comparison models

Dual Core Flashes				
Study	M_*	[Fe/H]	Z_{DCF}	3DUP
Fujimoto et al. (2000)	0.80	$Z = 0$	9×10^{-3}	No
Picardi et al. (2004)	0.80	$Z = 0$	2×10^{-2}	–
”	0.80	–6	2×10^{-2}	–
”	0.80	–5	3×10^{-2}	–
Fujimoto et al. (1990)	1.0	$Z = 0$	4×10^{-3}	–
Schlattl et al. (2001)	1.0	$Z = 0$	1×10^{-2}	–
<i>This study</i>	0.85	–5.5	3×10^{-2}	No
”	1.0	–5.5	4×10^{-3}	No

Dual Shell Flashes				
Study	M_*	[Fe/H]	Z_{DSF}	3DUP
Fujimoto et al. (2000)	0.8	–4	6×10^{-3}	No
Siess et al. (2002)	1.0	$Z = 0$	2×10^{-4}	–
Iwamoto et al. (2004)	1.0	–2.7	1×10^{-2}	Yes
Siess et al. (2002)	2.0	$Z = 0$	6×10^{-6}	Yes
Herwig (2003)	2.0	$Z = 0$	1×10^{-4}	Yes
Iwamoto et al. (2004)	2.0	–2.7	2×10^{-3}	Yes
<i>This study</i>	0.85	–4	1×10^{-3}	No
”	1.0	–3	5×10^{-3}	No
”	2.0	–4	6×10^{-4}	Yes

Table 7.15: Most of the dual core flashes (DCFs, top panel) and dual shell flashes (DSFs, bottom panel) reported in the literature for masses in the range $0.8 \rightarrow 2.0 M_\odot$. Only studies that have given a quantitative value for the resultant pollution (i.e. the surface metallicity after the DSF, Z_{DSF}) are included. In column two we give the initial mass of the star (M_*), in M_\odot whilst in the last column we indicate if the model experienced 3DUP during the early stages of the AGB or not. A dash indicates that the information is not given in the study (or is ambiguous).

^a This model did not experience a DSF.

available in the literature. Finally we note that a discussion and summary of the pollution effects of these models is given in Section 9.2 on page 352.

7.6 Comparison with Halo Star Observations

7.6.1 Overview

We gave a brief overview of Galactic Halo star observations in Section 2.1.2. It was noted there that the tail of the (currently known) Halo metallicity distribution function (MDF) reaches down to $[\text{Fe}/\text{H}] \sim -5.5$. Thus our grid of models, which begins at $[\text{Fe}/\text{H}] = -3.0$ and ends at $Z = 0$ has a significant overlap with the observed metallicity range but also extends well below this. This enables us to make comparisons with the current observations and also to make predictions about future, lower-metallicity discoveries – assuming stars of such low metallicity exist.

As also mentioned in Section 2.1.2 there has been two major low-metallicity halo field star

surveys: the HK survey (Beers et al. 1985; Beers et al. 1992) and the Hamburg/ESO (HES) survey (Wisotzki et al. 1996; Christlieb et al. 1999). These are the studies that have fleshed out the low-metallicity tail of the Halo MDF (see Beers and Christlieb (2005) for a review of this area). There has been a huge amount of observational work in recent years, spurred on by the discoveries of lower and lower metallicity stars such as HE 0107-5240 ($[\text{Fe}/\text{H}] = -5.3$, Christlieb et al. 2004) and HE 1327-2326 ($[\text{Fe}/\text{H}] = -5.4$, Frebel et al. 2005b). Indeed, even in just the last few months there has been quite a few publications of large data sets of abundance observations for extremely metal-poor stars (EMPs). These have been very useful for the current study. In Figure 7.34 we display the $[\text{C}/\text{H}]$ observations for a selection of these studies. The sample starts at $[\text{Fe}/\text{H}] = -1$ and ends at the aforementioned two most metal-poor stars. It is important to note that the combined sample is biased towards carbon-enhanced MP stars (CEMPs), as much interest has arisen in these objects due to their apparently very high numbers. They are often reported to represent $\sim 20\%$ of the low metallicity halo star population (eg. Beers and Christlieb 2005; Lucatello et al. 2006), although Cohen et al. (2005) report that it is somewhat lower ($\sim 9 \rightarrow 14\%$). Regardless of whether the proportion is 10% or 20% they are much more abundant than CH stars at higher metallicity ($\sim 1\%$, eg. Luck and Bond 1991) and thus represent quite a mystery. A few of the studies from which we have collected observational data focus on CEMPs in particular, so this group is over-represented in our plots. Since our model results give the chemical pollution expected from evolved stars (of low- and intermediate-mass) a large observational set that may reflect the composition of the ejecta of that generation of stars is actually very useful for comparisons. The ‘normal’ EMPs (ie. having \sim scaled-solar abundances of C) lie on the Galactic chemical evolution line (which we define as $[\text{C}/\text{Fe}] = 0$). For example, in Figure 7.34 carbon is seen to evolve with Fe in the normal EMPs. The ‘polluted’ EMPs mostly lie above this line (hence the name CEMPs). In the figures below, where we compare our models with observations of other elements, we will follow convention by identifying the CEMPs as a separate population. This will show if there are any general trends common to this group over the larger elemental parameter space. We quantitatively define extremely metal-poor carbon stars (C-EMPs = CEMPs) as those MP stars having $[\text{C}/\text{Fe}] > +0.7$. It is interesting to note that the most C-rich CEMPs have as much carbon as the Sun, meaning that they are not metal-poor in the strictest sense. Indeed their Z metallicity is roughly solar! A better term may be heavy-metal-poor, or Fe-poor. We shall however continue to follow tradition and use MP to refer to Fe-poor stars. Another interesting feature in Figure 7.34 is that there is a spread of stars between the scaled-solar $[\text{C}/\text{Fe}]$ line and the $[\text{C}/\text{H}] = 0$ line. Indeed, it looks as if there is an upper envelope at $[\text{C}/\text{H}] \sim 0$. This must reflect the maximum amount of C pollution that the low-metallicity stars can produce and will be an interesting observational feature to compare with our models.

The first comparison we make against the observations is with the surface compositions of our models just after the dual core flash (DCF) and dual shell flash (DSF) events. We have two reasons for doing this. Firstly, since these are potentially violent events, there may be an enhanced probability of mass transfer within a binary system during (or just after) these events. Secondly, if mass loss *is* a function of metallicity (as defined by Z) then these stars would lose more mass after the dual flash (DF) events as their surfaces are heavily polluted from then on. These winds could also pollute a binary companion. It has already been shown that many of the

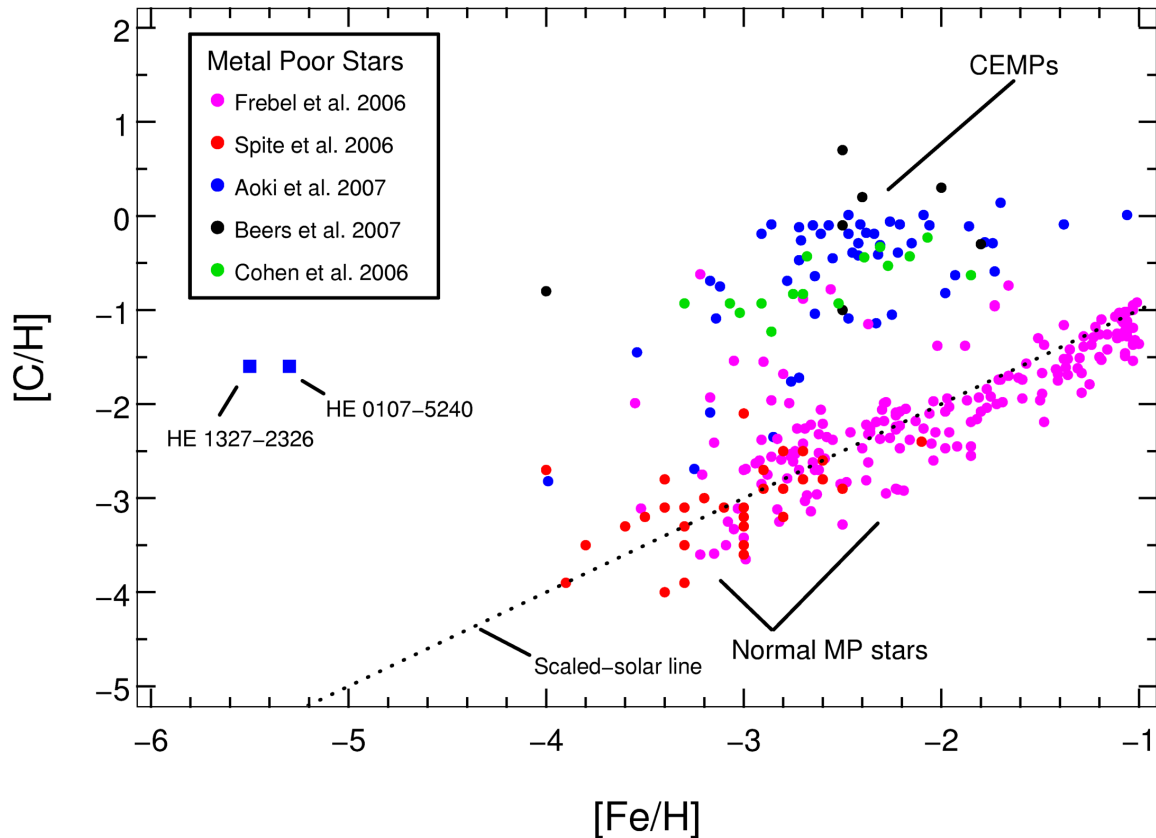


Figure 7.34: Carbon abundance observations versus $[Fe/H]$ for metal-poor stars compiled from the literature. The dotted line marks $[C/Fe] = 0.0$. The normal EMPs lie on this Galactic chemical evolution line, whilst the C-EMPs (which we define as having $[C/Fe] > +0.7$) lie above this. The two most Fe-poor stars known, HE 0107-5240 ($[Fe/H] = -5.3$, Christlieb et al. 2004) and HE 1327-2326 ($[Fe/H] = -5.4$, Frebel et al. 2005b) are labelled. We note that the most C-rich stars have similar amounts of carbon as the Sun, giving them a Z-defined metallicity that is roughly solar. Data sets are from Frebel et al. (2006b), Spite et al. (2006), Aoki et al. (2007), Beers et al. (2007), and Cohen et al. (2006).

C-EMP stars are in binary systems (in fact possibly *all* *s*-process-rich CEMP stars are binaries: [Lucatello et al. 2005](#)). Thus we believe it is important to confront the surface compositions at these stages of evolution with the observations. We note that others (eg. [Suda et al. 2004](#); [Christlieb et al. 2004](#)) also suggest a binary scenario for the formation of CEMPs. After these DF composition comparisons we then compare our *yields* with the observations.

7.6.2 Comparisons With Dual Flash Abundances

We begin with Figure 7.35 by comparing the dual flash surface abundances of carbon with the observations. In this figure our definition of CEMP stars can be seen clearly. Also indicated in the figure are the initial abundances used in the models, which are all scaled-solar for C (except the $Z = 0$ models of course). It can be seen that practically all models that experience a DF, whether it be a DCF or a DSF, have large surface C enhancements over the initial composition. An interesting bulk feature of the grid of models is that there is an upper envelope of C enhancement – just like the observations (although we don’t have many observations below $[\text{Fe}/\text{H}] < -3.5$). We have marked this envelope with a line at $[\text{C}/\text{H}] = +1.0$. We have also marked a lower envelope at $[\text{C}/\text{Fe}] = -1.0$ which probably indicates the lower limit to C and Fe pollution coming from low metallicity SNe. In terms of our models we can say little about the lower limit except that the DFs do not reduce the amount of C in the envelope so they never violate this constraint.

Looking more closely it can be seen that our higher metallicity models ($[\text{Fe}/\text{H}] = -3, -4$) of lower mass all undergo dual shell flashes. At $[\text{Fe}/\text{H}] = -4$ the $2 M_{\odot}$ model does also. This has raised the C abundances in these models to high levels ($[\text{C}/\text{Fe}] \sim 3 \rightarrow 4.5$). At $[\text{Fe}/\text{H}] = -3$ this is (roughly) consistent with the most extreme observations. The same can not be said at $[\text{Fe}/\text{H}] = -4$ but we have very little observational data to compare with here. If we extrapolated the more metal-rich observations to -4 (or interpolated up to the two most metal-poor stars) the $0.85 M_{\odot}$ and $2 M_{\odot}$ models would fit this line well. An important point to make here is that the compositions from our models really represent an *upper limit* to the level of pollution expected in a binary scenario as the material transferred would be mixed into the envelope of the secondary (possibly even if that envelope was radiative, see eg. [Stancliffe et al. 2007](#)). The material would also be diluted by any previous mass loss on the RGB (which varies with mass and metallicity in our models – see section 7.2.6 on page 244). In the case of the two $[\text{Fe}/\text{H}] \sim -5.5$ stars we see that the lowest mass models are much more C-rich (by ~ 2 dex) than the observations whilst the intermediate mass models (2 and $3 M_{\odot}$) are $\sim 2 \rightarrow 4$ dex too low. Since it is easier to dilute stellar material, the low mass models can be considered a better ‘fit’ than the IM models.

In terms of the extremely low metallicity end of the spectrum ($[\text{Fe}/\text{H}] < -6$), for which no stars have been discovered, we note that our models predict the trend of very high $[\text{C}/\text{Fe}]$ to increase. Indeed, one would expect from these results that an $[\text{Fe}/\text{H}] = -6.5$ star discovered tomorrow could have $[\text{C}/\text{Fe}] \sim 5$ or 6 – although it could be anywhere below this. It is also very interesting that the two -5.5 stars are both CEMPs. This may indicate that *all* (or most) EMP stars are C-rich. This is however speculation based on a very small sample. We would really expect to see a population at $[\text{C}/\text{Fe}] \sim 0$ also.

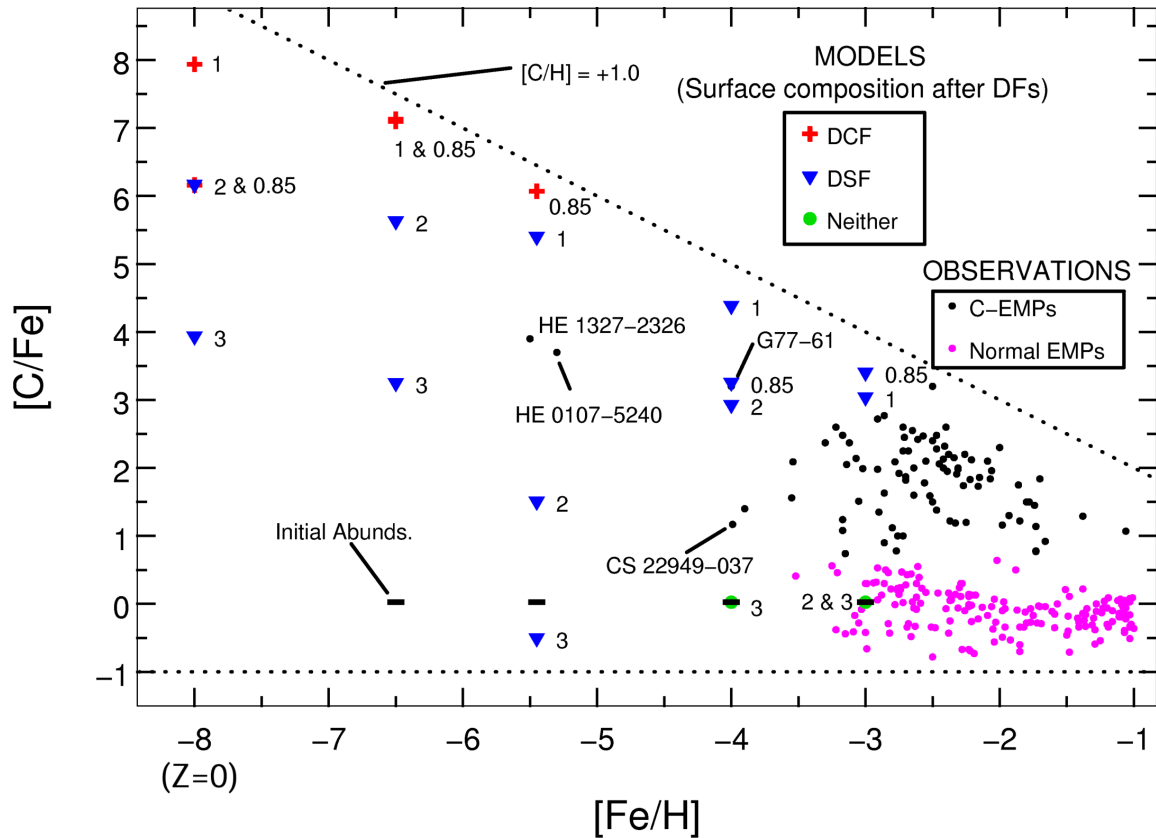


Figure 7.35: Surface $[C/Fe]$ versus $[Fe/H]$ of all our models – just after the dual flash events. We show the composition at this stage since these violent events may induce extra mass transfer in binary systems. Also shown for comparison are the observations (see Figure 7.34 for data sources). Here we have colour-coded the data into $[C/Fe]$ -rich and $[C/Fe]$ -normal, where $[C/Fe]$ -rich is defined by $[C/Fe] > +0.7$. We keep this colour coding in all the figures below. The short horizontal lines indicate the starting composition of the models (in this case they are all at $[C/Fe] = 0$, except for the $Z = 0$ models). We have plotted the $Z = 0$ models at $[Fe/H] = -8$ for comparison. The two most metal-poor stars can be seen at $[Fe/H] \sim -5.5$ (they are both C-rich). We also point out two $[Fe/H] \sim -4$ stars (G77-61 and CS 22949-037) which we discuss later. An upper envelope to the pollution in the models – and the observations – is marked by the dotted line at $[C/H] = +1.0$. A very interesting feature of the models is that the mass range that suffers surface pollution for these DF events increases with decreasing metallicity. See text for a discussion.

Another very interesting result from the models is that the mass range in which C enhancement events occur increases with decreasing metallicity. This is clearly seen when contrasting the $[Fe/H] = -3$ models with the -6.5 models. At $[Fe/H] = -3$ only the two lowest mass models (0.85 and $1 M_{\odot}$) are C-enhanced due to the DSFs, whilst at -6.5 *all* the models are. Since a significantly larger portion of the IMF is able to pollute at extremely low metallicity (assuming an IMF peaked at low mass) then we would predict that larger and larger proportions of EMP stars would be C-rich at lower and lower metallicities. This certainly seems to be the case at $[Fe/H] = -5.5$ but again there are only two observations so far. The caveat here is that this pollution arises from dual flashes – the story may be different when considering the yields. We shall return to this result in the Discussion as it is a key finding.

In Figure 7.36 we compare the surface nitrogen abundances of our models taken just after the DF events with those of the observations. First we note that the distribution of the observations is best described as a spread between an upper boundary of $[N/H] \sim +0.5$ and a lower boundary of $[N/Fe] \sim -1.0$. Ignoring the distinction between the CEMPs and normal EMPs the observations

do not break into two groups as with carbon. That said we have to note that our sample is far from perfect – we have displayed all the stars for which we have N abundances, from the full CEMP-biased sample. Despite these limitations we can safely say that most of the C-EMPs are also N-rich. Most of them lie above $[N/Fe] = 1.0$ (and even higher at lower metallicities). Conversely most of the C-normal EMPs lie below $[N/Fe] \sim 1.5$. We note that [Plez and Cohen \(2005\)](#) also mention these trends in N and/or C enhancement.

In terms of our models it can be seen that the higher metallicity low-mass models fall nicely into the spread. The higher mass models did not go through the DSF event so their N abundances are still extremely low due to the low initial abundances used. At $[Fe/H] = -4$ our DSF-polluted models appear to be in reasonable agreement with the observations. The low mass models have quite high N but dilution effects could lower this. We note that the observation sample is quite small here. Looking at the two most metal-poor objects we see that our low-mass models match the observations well. However we note that they weren't well matched by the same models in terms of carbon (we discuss abundance patterns in detail below). As seen with carbon the mass range in which our models show N overabundances from these DF events increases with decreasing metallicity. Our models thus predict that the frequency (and degree) of N-enhancements arising from these events (which may be a source of polluted material in a binary mass transfer) will increase at lower metallicities.

We make comparisons with the stellar oxygen abundances in [Figure 7.37](#). Oxygen is notoriously difficult to measure, thus there are very few observations to compare with – and these are uncertain (eg. [Israelian et al. 2004](#) give two values for each of their stars, depending on the line measured). At higher metallicities we see that there is a spread of oxygen abundances, with no discernible trend with C-richness. The DF pollution from our models is generally on the high side compared with the observations but again, these could be diluted. There is a trend in the lower metallicity stars – the O overabundances increase with decreasing metallicity (although the sample is very small). Our models also follow the same trend. The two most metal-poor stars fall between our 1 and 2 M_{\odot} models but we note that there is a very large gap of ~ 2.5 dex between the O abundances of these models (for the oxygen abundance determinations for these two stars see [Bessell et al. 2004](#) and [Frebel et al. 2006a](#)). In summary, our models do produce the large amounts of oxygen observed but often produce much more – but our observational sample from the literature is very small.

Some of the studies in our observational sample also report the $^{12}C/^{13}C$ ratio for (some of) their objects. We plot these in [Figure 7.38](#) along with the surface abundances from our models just after the DF events. The values of the ratio are also given for three of our stars that did not experience any DF events (the 2 and 3 M_{\odot} models with $[Fe/H] = -3$ and the 3 M_{\odot} model with -4). These values are taken from the surface at the start of the AGB (where the DSF would normally occur) so they reflect the ratios after second dredge-up. An interesting feature of the observations is that most of the C-EMPs have low $^{12}C/^{13}C$ ratios, whereas the normal EMPs have a range of values. We again note that our dataset is small so our categorisations may not hold with a set of observations that is more complete (we shall compare again as the data becomes available). There is one notable exception to the categorisation that most C-EMPs have low ratios – the second most metal poor star, HE 0107-5240, has a high ratio (> 50 , [Christlieb et al. 2004](#)). This contrasts strongly with the $^{12}C/^{13}C$ ratio of the most metal-poor star HE

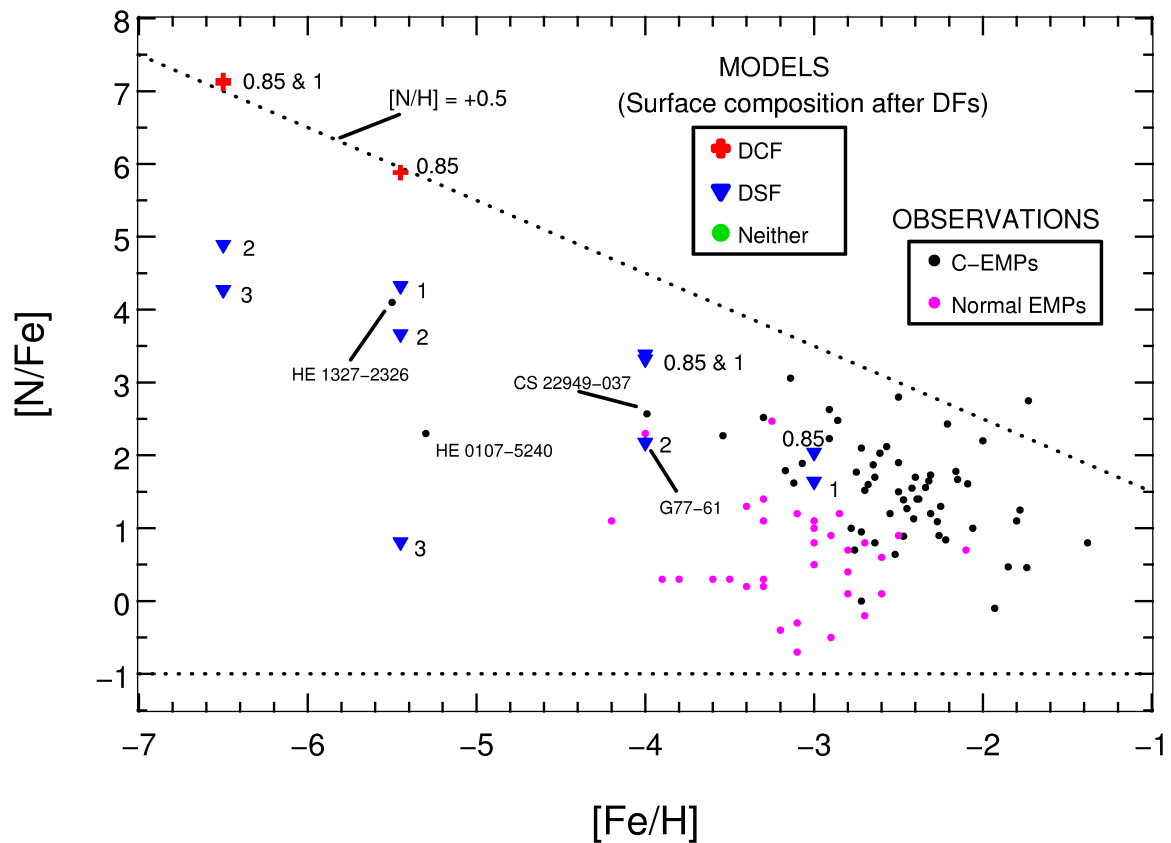


Figure 7.36: Same as Figure 7.35 but for nitrogen. Upper and lower envelopes are sketched with dotted lines. The two most metal-poor stars observed to date are indicated, as are two $[\text{Fe}/\text{H}] = -4$ stars (G77-G1 and CS22949-037). There appears to be a fairly uniform spread in N enhancement in the observations (although we note that our sample is not complete). The C-rich EMPs are, in general, more N-rich than the C-normal EMPs. Both groups show a spread. Our models are in reasonable agreement with the CEMP observations. The missing higher-mass models still have their initial N abundances at this stage, which are well below the scale of the plot. Note that we have not plotted the $Z = 0$ models in this case.

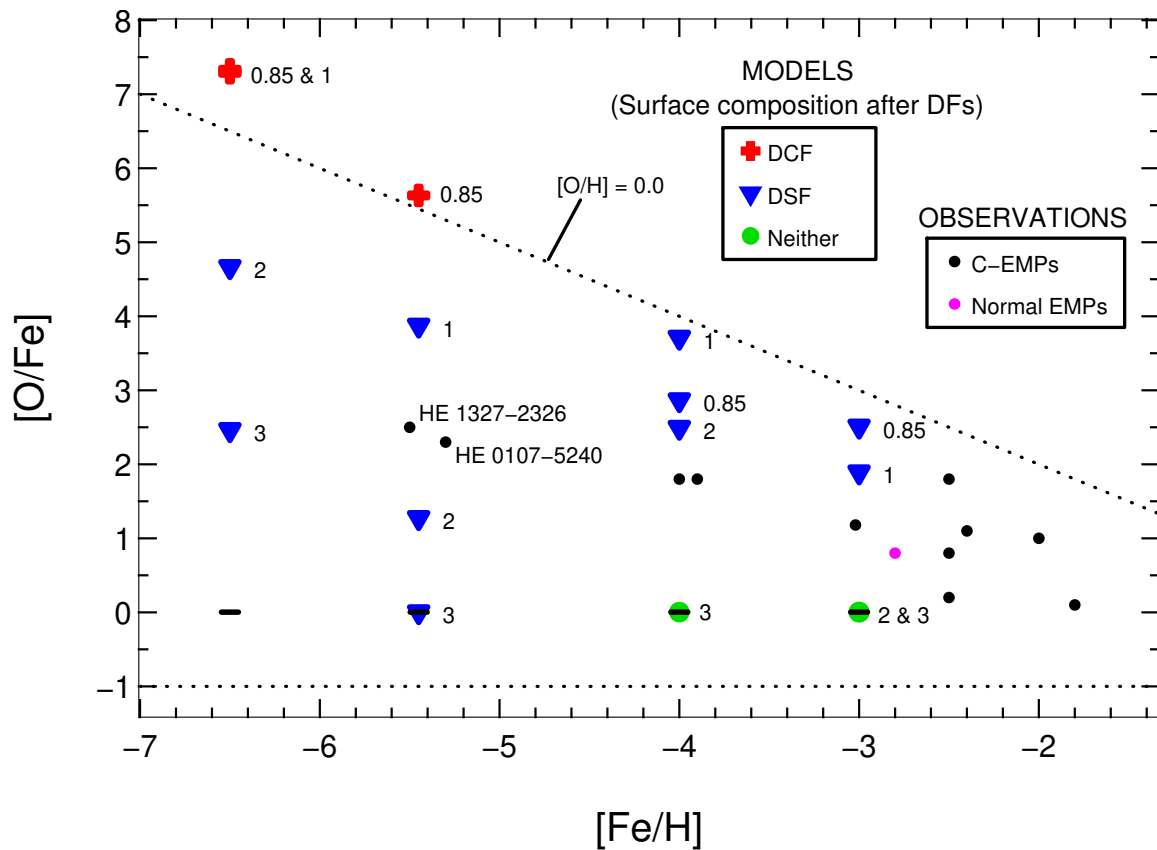


Figure 7.37: Same as Figure 7.35 but for oxygen. Very sketchy upper and lower envelopes are marked with dotted lines (there not not many observations to compare with as oxygen is difficult to measure). The two most metal-poor stars observed to date are indicated. Their oxygen abundances are from [Bessell et al. \(2004\)](#) (HE 0107-5240) and [Frebel et al. \(2006a\)](#) (HE 1327-2326). Note that we have not plotted the $Z = 0$ models in this case.

1327-2326, which is estimated at ~ 5 (Aoki et al. 2006). Note that these values are both lower limits. Picardi et al. (2004) cite the high value in HE 0107-5240 as one of the good reasons to reject the DCF scenario for explaining this star's abundances as they found that the ratio resulting from this event was low (~ 5). Indeed, as can be seen in Figure 7.38, the ratio in our $0.85 M_{\odot}$, $[\text{Fe}/\text{H}] = -5.45$ model is also close to the equilibrium value. We note that the value of > 50 is more reminiscent of a first dredge-up value. However, looking at our Table 7.10 on page 255 we see that it is only (slightly) higher metallicity models that have FDUP $^{12}\text{C}/^{13}\text{C}$ ratios of this order (although the lower metallicity models have very high values, which may also be consistent with the lower limit). It is interesting that these two most metal poor stars (of very similar metallicity) both have similar C enhancements but have such different isotopic contributions to the enhancements. This seems to imply that different C-enhancement mechanisms lead to similar levels of pollution.

It can also be seen in Figure 7.38 that the DSF events produce a range of $^{12}\text{C}/^{13}\text{C}$ ratios, although they are all low or moderately low, being $\lesssim 25$. At higher metallicities ($[\text{Fe}/\text{H}] = -3$) the ratios in our models all sit around 20. This is consistent with some of the observations but not all. In particular there is a notable lack of low $^{12}\text{C}/^{13}\text{C}$ ratios in these models. Interestingly it is the C-enhanced EMPs, which mostly have very low ratios, that are *not* matched by our models at this metallicity (at least from DSF pollution). At $[\text{Fe}/\text{H}] = -4$ our models show a spread in $^{12}\text{C}/^{13}\text{C}$ ratio, much more like the observations. There are however very few observational data points to compare with at this metallicity.

Finally, two general points can be made about the $^{12}\text{C}/^{13}\text{C}$ ratios arising from the DF pollution in our models. The first is that we find that the bulk of our models at higher metallicity ($[\text{Fe}/\text{H}] = -3, -4$) show a similar spread as the observations (although the lack of low ratios at $[\text{Fe}/\text{H}] = -3$ is a notable exception). The second is that this spread is seen to reduce with metallicity – the lower the metallicity the lower the upper envelope of the $^{12}\text{C}/^{13}\text{C}$ ratio. Indeed, at $Z = 0$ all the models show equilibrium values of ~ 5 .

7.6.3 Comparisons With Yields

Here we compare the average composition of the yields from the stellar winds with observations.

Carbon

We begin with $[\text{C}/\text{Fe}]$ in Figure 7.39. As mentioned above we have defined C-enhanced EMPs as those having $[\text{C}/\text{Fe}] > +0.7$, as shown in the figure by different coloured dots. The models are represented by coloured shapes in the same way as in the DF comparison figures above, but this time we have categorised the yields in terms of the evolutionary episodes that play key roles in the resultant yield compositions (see eg. Figure 9.1 on page 353 for an overview). In practice this just means that the IM model yields are represented by green dots (= AGB pollution) rather than blue triangles (= DSF pollution) since the 3DUP and HBB on the AGB in these models far outweigh the DSF pollution in the yields.

It can be seen in Figure 7.39 that *all* of our models contribute very C-enhanced material to the ISM. We have marked in an upper envelope line at $[\text{C}/\text{H}] = +1.0$ that is consistent with

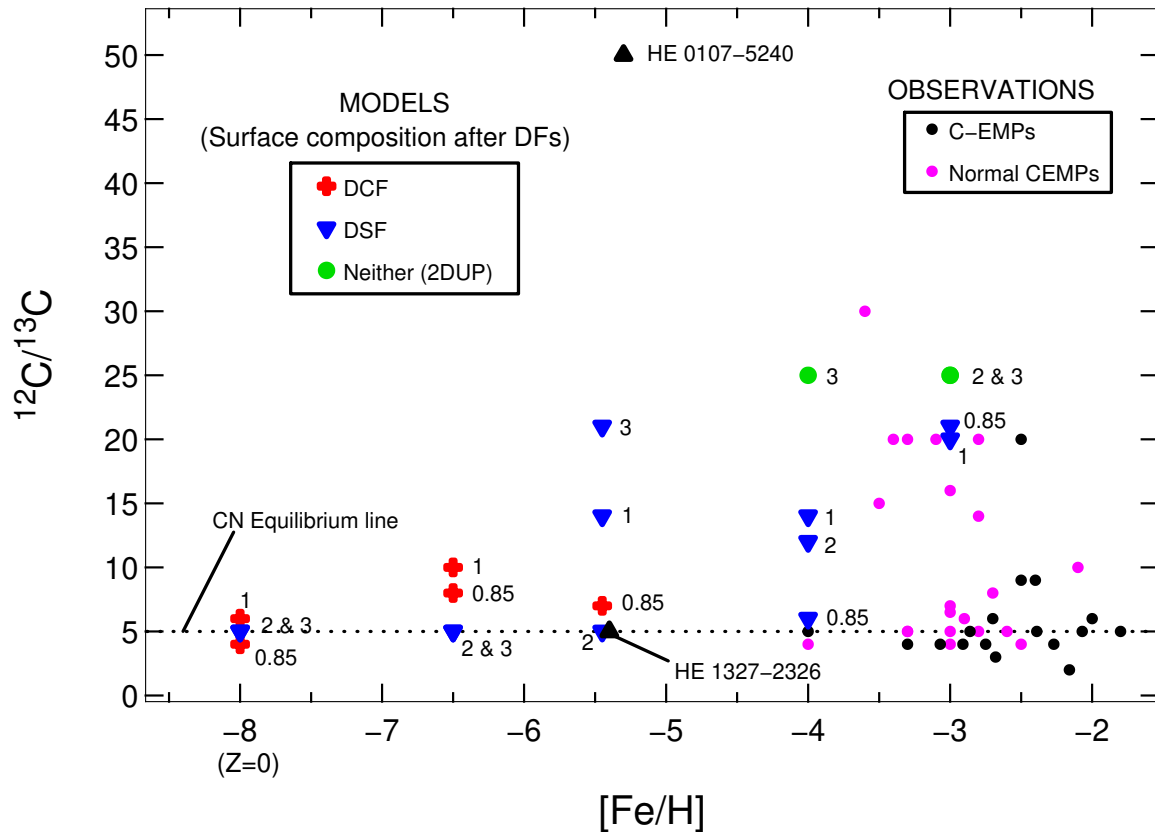


Figure 7.38: Same as Figure 7.35 except for $^{12}\text{C}/^{13}\text{C}$. We have plotted the $Z=0$ models at $[\text{Fe}/\text{H}] = -8$ for comparison. Again our observational sample does not contain many data points. Interestingly most of the C-enhanced EMPs have low $^{12}\text{C}/^{13}\text{C}$ ratios. The upper envelope of our models reduces with metallicity, such that the $^{12}\text{C}/^{13}\text{C}$ ratios of the most metal-poor models are all very low. The two most metal-poor stars are represented by upright triangles as the measurements for both these stars are lower limits. The ratios in these two stars are very different – in HE 1327-2326 it is low and HE 0107-5240 it is quite high (> 50 , Christlieb et al. 2004). Note that the green symbols (no DF episodes) give the ratios in the surface composition of these models after second dredge-up.

our models and with the observations. The trend in the models is for increasing $[C/Fe]$ with decreasing metallicity, which reflects the fact that they all lie within $2 \rightarrow 3$ dex below the $[C/H] = +1.0$ line. It is interesting to note that strong C-enhancement occurs via all of the types of polluting episodes. This is expected as the DSF, DCF and 3DUP all bring up carbon from the He burning regions. Indeed, it is the composition and the size of these He burning regions that sets an upper limit to the amount of surface pollution that can occur (dilution through the envelope also plays a part of course). It is this that sets the upper envelope in our figures. It appears that nature may also do the same!

Looking at the observations we see that *none* of the yields from our models are low enough in C to account for the normal EMPs. Thus our models predict that none of the C-normal EMPs are on the AGB – or have been polluted by stars in this phase of evolution – in the mass range of our study ($0.85 \rightarrow 3.0 M_{\odot}$). This extends to the HB in the DCF models, as in these models the surfaces become polluted at the top of the RGB. Indeed, due to the various C-enriching episodes in all our models, the lowest C abundance of *all* our yields is $[C/Fe] \sim +2$ dex (in the $0.85 M_{\odot}$, $[Fe/H] = -4$ model). This profusion of carbon matches well with the most of the observed abundances in the C-EMPs, although some dilution is needed to cover the lower $[C/Fe]$ observations. We note that our $5 M_{\odot}$ models of $[Fe/H] = -3$ and -4 also experience 3DUP (see Figure 9.1 on page 353) which means that their yields would also be C-enhanced (although possibly to a lesser extent due to their larger envelopes and smaller intershells). The lower metallicity $5 M_{\odot}$ models did not experience 3DUP so their yields would be unpolluted (SNe type 1.5 events withstanding). Thus the prediction is strengthened on widening the mass range – our models predict all yields coming from low- and intermediate-mass stars of $[Fe/H]$ at least < -3 to be C-enhanced. We note that the intermediate mass models of Karakas et al. (2002) (which have $[Fe/H] \sim -1$) and those of Herwig (2004) ($[Fe/H] = -2.3$) also show significant 3DUP. Thus the 3DUP+HBB pollution from our extremely metal-poor IM models can be seen an extension of that given by the moderately metal-poor IM models.

The situation is more intriguing at low mass. The $1 M_{\odot}$ model of Karakas et al. (2002) ($[Fe/H] \sim -1$), like our $1 M_{\odot}$ EMP models, does not show significant 3DUP – even though that study utilises a form of overshoot (we note that the Karakas et al. study uses an earlier version of same code as the current work). However, in a recent study Stancliffe et al. (2005) do find 3DUP to occur in models of mass $1 M_{\odot}$ at a metallicity of $[Fe/H] \sim -1$. The fact that they find 3DUP at such low masses (the lower limit is usually $\sim 1.5 M_{\odot}$ at solar metallicity, see eg. Straniero et al. 1996) allows them to match the low luminosity end of the carbon star luminosity function for the LMC. They also report that 3DUP is metallicity-dependent, such that their lower metallicity models experience deeper 3DUP (Karakas et al. 2002 also report a metallicity dependence, as do earlier studies). We note that they did not include any form of overshoot. Thus their code may be expected to produce 3DUP in a $1 M_{\odot}$ model at extremely low metallicity. If this were the case then this would be another avenue/mass range for CEMP pollution. Despite the fact that our models do not have 3DUP they do have very C-enhanced yields due to the DCF and DSF events. Thus we have two possible channels for C production in low mass EMP models. One way to distinguish between the pollution from these two channels is through their different chemical signatures. Low mass stars that have 3DUP are not predicted to experience HBB so N remains low whilst C is periodically enhanced. By contrast our DCF and DSF models show C

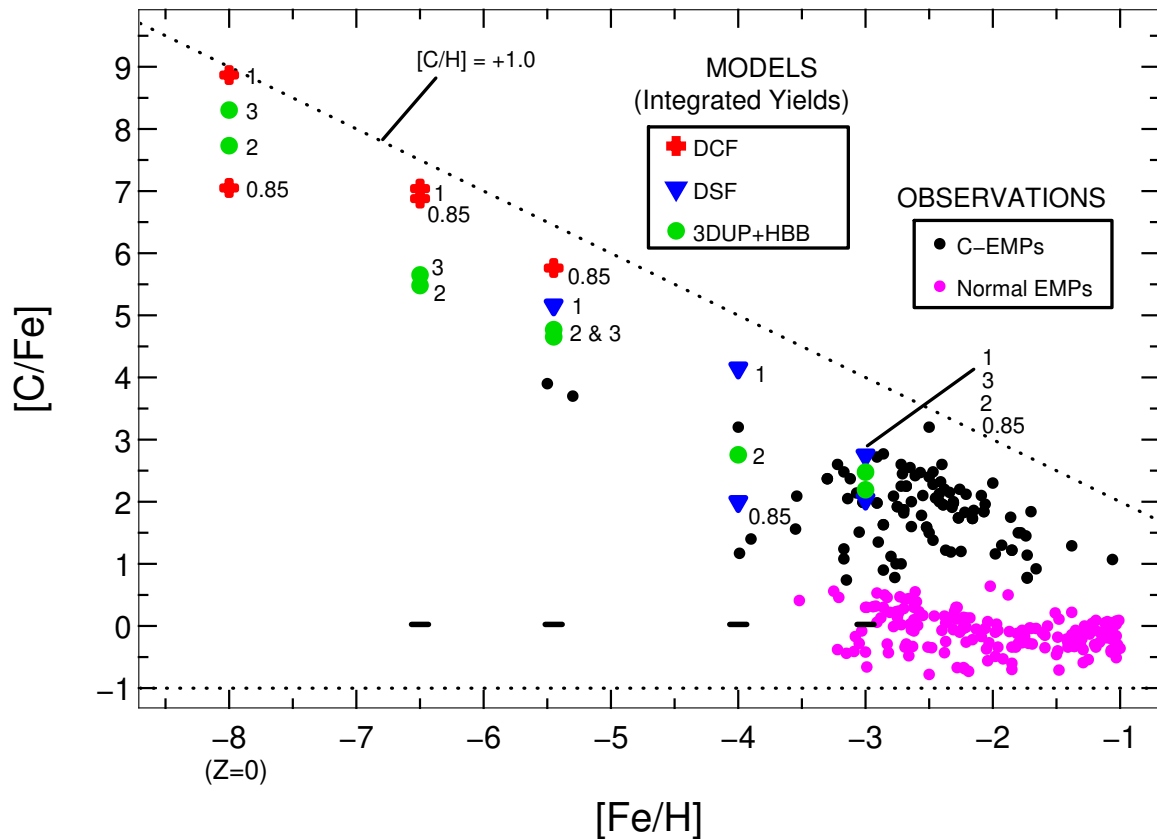


Figure 7.39: Comparing the yields from all our models with observations of EMP stars. See Figure 7.34 for the observational data sources. Here we have colour-coded the observations into [C/Fe]-rich and [C/Fe]-normal, where [C/Fe]-rich is defined by $[C/Fe] > +0.7$. We keep this colour coding in all the figures below. The short horizontal lines indicate the starting composition of the models (in this case they are all at $[C/Fe] \sim 0$, except for the $Z = 0$ models). We have plotted the $Z = 0$ models at $[Fe/H] = -8$ for comparison. The two most metal-poor stars can be seen at $[Fe/H] \sim -5.5$ (they are both C-rich). An upper envelope to the pollution of the models – and the observations – is marked by the dotted line at $[C/H] = +1.0$. The yields from our models are colour- and shape-coded to highlight the different episodes that produced the bulk of the pollution in each yield.

and N enhanced at the same time. Interestingly this dual enhancement appears to be required by the observations, which we discuss below (see Figure 7.42). Related to this are the $^{12}\text{C}/^{13}\text{C}$ ratios – they would be high in the 3DUP case due to repetitive dredge-up of ^{12}C but are low in the DCF and DSF models because of CN cycling (they are lowest in the DCF models).

Another interesting possibility is that DFs and 3DUP could occur at low mass (which may be possible in our models by using overshoot). In this case the models would again be C and N rich. This is because the N from the DSF and DCF events has no way of being depleted in the H-rich envelopes. Since 3DUP appears to enrich the yields with C to a similar degree as the DF events, the C enhancement would probably not increase significantly in this scenario over our present DF-only results. The $^{12}\text{C}/^{13}\text{C}$ ratios may however increase but we are uncertain how significant this would be. Clearly this scenario requires further modelling – the combination of DFs with 3DUP may well provide a better match to the observations. We shall pursue this avenue at a later date and will return to this important topic in the Discussion chapter.

$^{12}\text{C}/^{13}\text{C}$ Ratio

Moving back to the yield-observation comparisons we present in Figure 7.40 the $^{12}\text{C}/^{13}\text{C}$ ratios in the yields of all our models. In most cases the ratios are basically the same as those reported earlier for the DF surface compositions. The only changes have been brought about by HBB in the IM models. All the 2 and 3 M_{\odot} models now have low ratios, reflecting the substantial CN cycling that occurred in their AGB envelopes. The pattern of reducing spread in the $^{12}\text{C}/^{13}\text{C}$ ratio with reducing metallicity remains in the low-mass yields. As mentioned above *all* the models have CN equilibrium values at $Z = 0$ (the $Z = 0$ models are included at $[\text{Fe}/\text{H}] = -8$ in the figure). Most of the carbon-enhanced EMPs have low ratios. From the perspective of our models this means that they could have been polluted by AGB HBB material or DCF material (or possibly DSF material in some cases). The observations of the C-normal EMPs reveal a spread in $^{12}\text{C}/^{13}\text{C}$ ratio. This may reflect stars at different stages of evolution (eg. deep mixing in RGB stars can reduce the ratio – see Spite et al. 2006 for some observational evidence), or inhomogeneous formation material. HE 0107-5240 is again an outlier. It has a lower limit to its ratio of 50, well outside the range of our models. In terms of an AGB mass transfer scenario we suggest that it could have such a high ratio if the matter was transferred from an IM star during its early TP-AGB phase – when some 3DUP of ^{12}C had occurred but HBB had not set in (see Christlieb et al. 2004 for a detailed discussion on possible sources of the abundance pattern of this star).

Nitrogen

In Figure 7.41 we display $[\text{N}/\text{Fe}]$ against $[\text{Fe}/\text{H}]$ for the observations and our model yields. First we note that our N sample is small and also biased. That said, it can be seen that the C-enhanced EMPs are also N-enhanced (in general). Some of the C-normal stars are also N-enhanced but, in general, not as much as the CEMPs. The two populations appear to each have a large spread in N, which overlaps between the populations. Looking at our model yields we see that they are all enhanced in N. The lowest abundance is $[\text{N}/\text{Fe}] \sim +1.0$, in the 0.85 M_{\odot} , $[\text{Fe}/\text{H}] = -3$ model. Thus *all* our yields are enhanced in C *and* N. The yields that are dominated by 3DUP+HBB contain very large amounts of N. In fact all of these yields lie above the rough upper envelope we have inscribed for the observations in Figure 7.41 at $[\text{N}/\text{H}] = +0.5$. The large amount of N production is a robust prediction of the models that have 3DUP and HBB. This N excess may indicate that dredge-up is not as deep in real stars, since this would reduce the C seeds for the N production. We note that this may not actually be a problem in a binary scenario due to (probable) dilution effects. Another interesting feature of the model yields is that the DSF models all produce much less nitrogen (whilst still having large amounts of C). These yields lie right in amongst the observations, at least at higher metallicities. Looking at the two most metal-poor stars we see that HE 1327-2326 is not far from the lower envelope of our models (~ 0.2 dex from our 1 M_{\odot} model). However HE 0107-5240 is well below the envelope. This star has very high C but not so high N (although it is enhanced in both). Our EMP models produce too much N to explain this star.

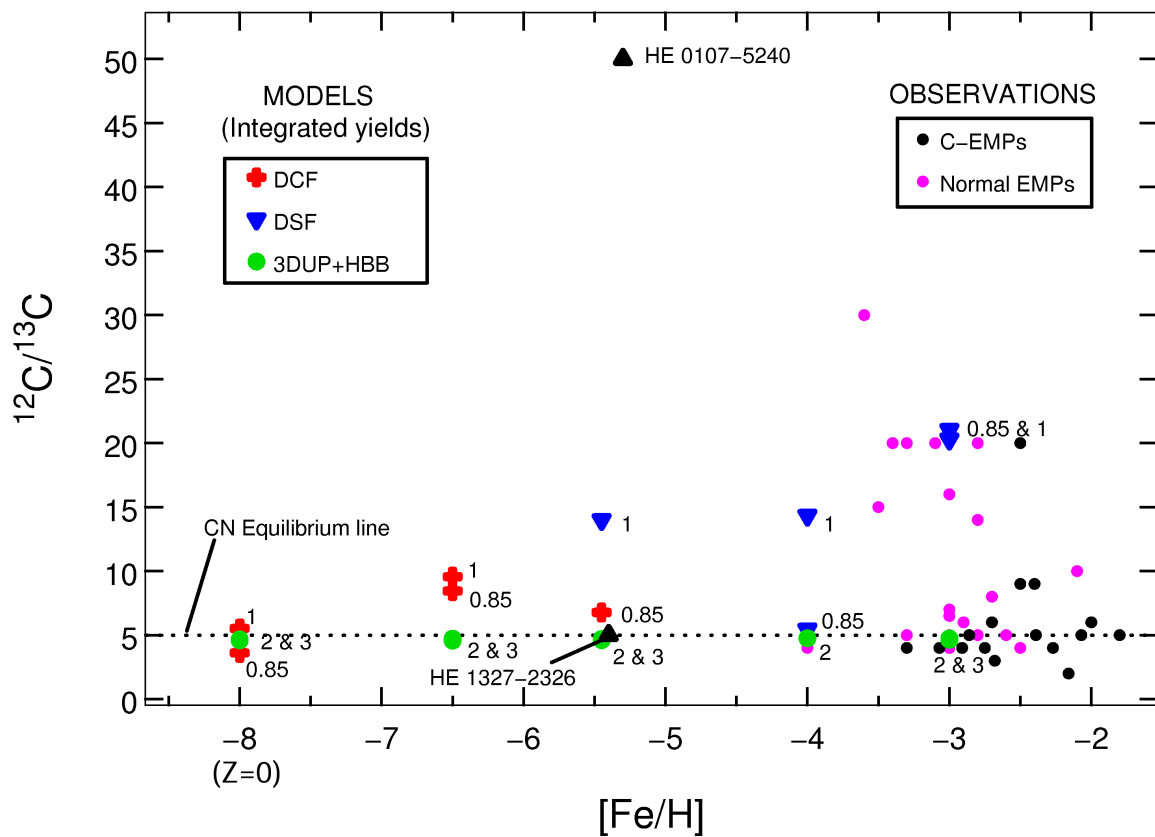


Figure 7.40: Comparing the $^{12}\text{C}/^{13}\text{C}$ ratios in our models with those from observations. We have plotted the $Z = 0$ models at $[\text{Fe}/\text{H}] = -8$ for comparison. See Figure 7.34 for the observational data sources (note that only some have reported $^{12}\text{C}/^{13}\text{C}$ ratios). C-EMPs and normal EMPs are defined in Figure 7.39, as are the symbols used for the yields. The dotted line at $^{12}\text{C}/^{13}\text{C} = 5$ indicates (roughly) the equilibrium value from the CN cycle. All the HBB models end up on this line. An interesting feature here is that most of the C-EMPs have low ratios, whilst the normal EMPs show a spread.

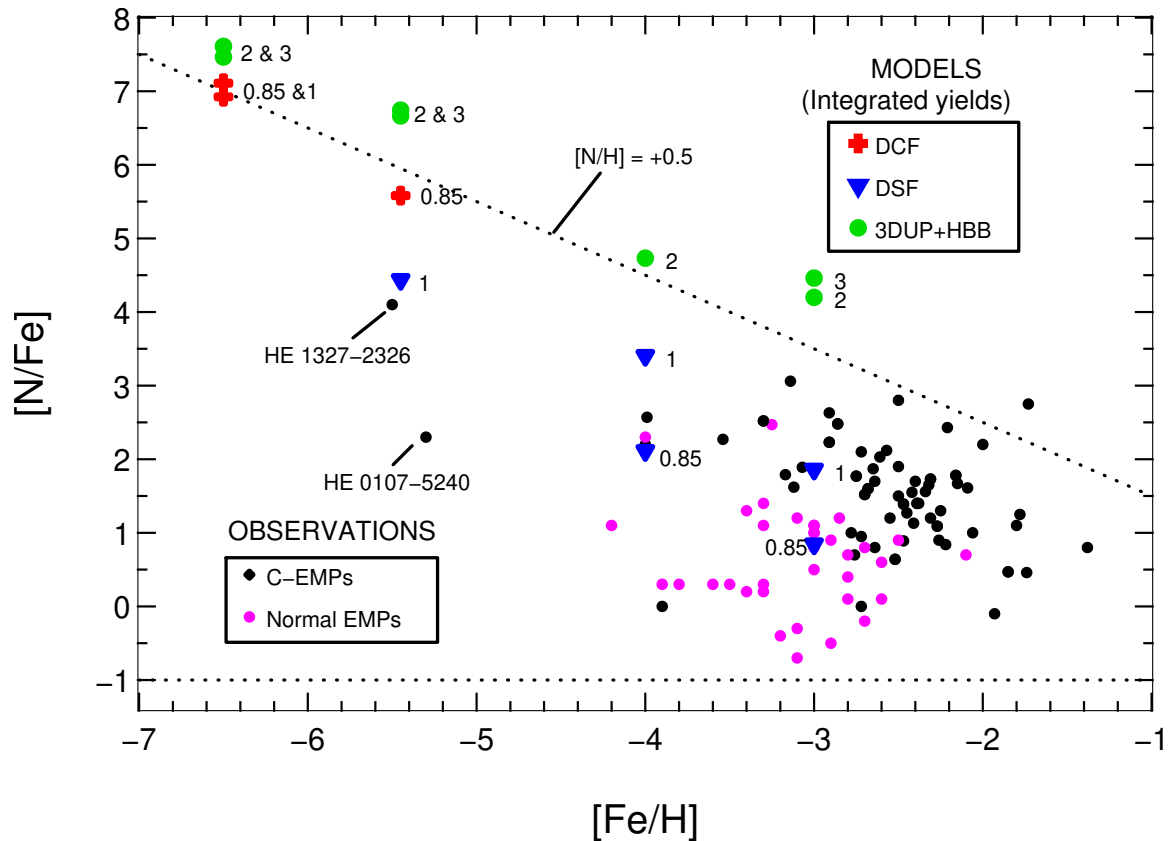


Figure 7.41: Comparing the $[N/Fe]$ ratios in the yields of our models with those of the observations. See Figure 7.34 for the observational data sources. C-EMPs and normal EMPs are defined in Figure 7.39, as are the symbols used for the yields. All the HBB models (2 and 3 M_{\odot}) produce enormous amounts of nitrogen, whilst the DSF models produce less (although still substantial amounts). The observations show that C-EMPs are generally more N-rich than normal CEMPs, but there is an overlap in the distributions. We have sketched in upper and lower envelopes for the observations (dotted lines). Note that we have not plotted the $Z = 0$ models in this case.

C/N Ratio

This brings us to our next figure where we show the C:N ratios for model yields and observations, relative to solar (Figure 7.42). HE 0107-5240 is seen to be on the upper envelope of the observations in this parameter space. The normal EMPs appear to occupy the whole range between $[C/N] = -2.0 \rightarrow +1.0$. This is in contrast to the C-EMPs which are mainly found in the range $-0.5 \rightarrow +1.5$. This shows that C dominates over N in the CEMPs, even though they are rich in both (there are exceptions though). The spread probably reflects differing degrees of C \rightarrow N processing in the polluting material, whether the material be supplied internally or externally. Looking at the models the most robust prediction is the very low $[C/N]$ values in the 3DUP+HBB yields – they all have $[C/N] \sim -2.0$. This reflects the fact that CN equilibrium was achieved in the AGB envelopes, such that $C/N \approx 0.05$ (ie. $N/C \sim 20$). Interestingly this also appears to be the lower envelope for the observations. All of the yields for our other models fall above the $C/N = 1$ line. Thus – like the observations – C is always dominant over N in the yields. There is a bit of a trend with metallicity in the yields, insomuch as the lower the metallicity of the model, the lower the value of the upper envelope. All the yields are however either at or above the solar ratio, again similar to the observations.

Oxygen

In Figure 7.43 we compare the observations of oxygen with our model yields. As mentioned earlier oxygen is difficult to measure so there are not many observations to compare with. This is evident in our literature sample. The trend in the observations is one of increasing O enhancement with decreasing metallicity (although the sample is small). There is however a spread at the higher metallicities. The spread is partially covered by our yields at $[Fe/H] = -3$ but the lowest values are not matched. Interestingly there are a couple of C-EMPs that have approximately solar $[O/Fe]$, where we might expect the C-normal stars to lie (we only have one C-normal star with an O abundance unfortunately). At $[Fe/H] \sim -4$ our $0.85 M_{\odot}$ DSF model and our $2 M_{\odot}$ 3DUP+HBB model both have similar O abundances to the two stars for which we have measurements. On the other hand our models at $[Fe/H] = -5.5$ all overproduce O relative to the two most metal-poor stars, by at least ~ 1 dex. Again this could be remedied by invoking dilution of the yields. In the figure we also sketch a rough upper envelope for O enhancement from our models (note that the $Z = 0$ models have exaggerated O since we have artificially chosen an Fe abundance for plotting purposes). This limit is also consistent with the observations. Finally we note that more observations of oxygen are really needed to constrain the models.

Sodium

We now move onwards to sodium, which we show in Figure 7.44. Most of the observational data we have for Na is for the C-EMPs. The observations show a large spread at $[Fe/H] \sim -3$, ranging from $[Na/Fe] \sim 0.5$ dex below solar to ~ 2.5 dex super-solar. Our models at this metallicity show an even larger spread, from solar to ~ 4 dex super-solar. This is mainly driven by the huge amounts of Na from the 2 and $3 M_{\odot}$ models, which is a product of HBB of Ne dredged

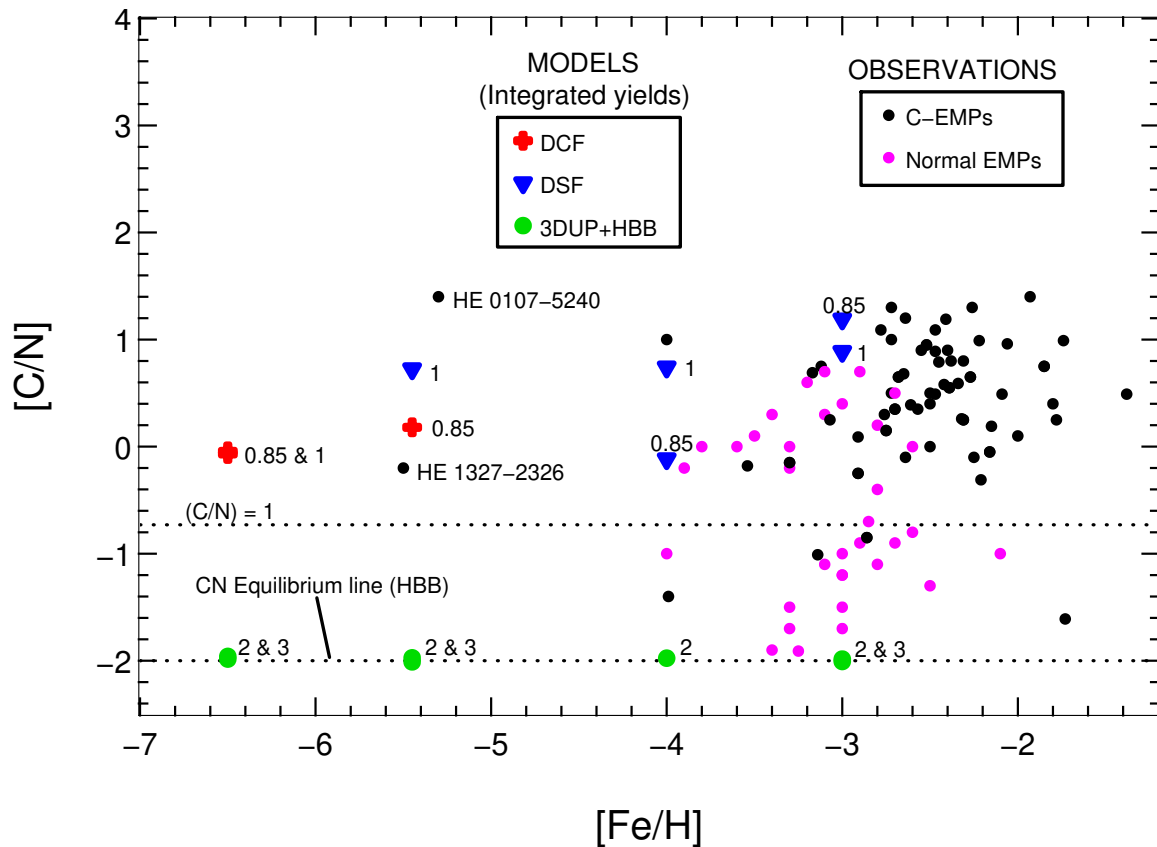


Figure 7.42: Comparing the $[C/N]$ ratios in the yields of our models with those of the observations. See Figure 7.34 for the observational data sources. C-EMPs and normal EMPs are defined in Figure 7.39, as are the symbols used for the yields. We have marked in the CN equilibrium line (for HBB) at $[C/N] = -2$ (ie. $C/N = 0.05$). All the HBB models fall on this line. We have also marked in a dotted line at $[C/N] \sim -0.8$ which is where $C/N \sim 1$, so that C dominates N above this line. An interesting feature of the observations is that most of the CEMPs lie above the $C/N = 1$ line whilst the normal CEMPs show a spread. Thus the CEMPs are rich in C *and* N but have more C. There are however a few stars that show strong C enhancements and have $N > C$. The yields of our models are consistent with the spread of the observations. However HE 0107-5240 lies significantly above out models of comparable metallicity. Note that we have not plotted the $Z = 0$ models in this case.

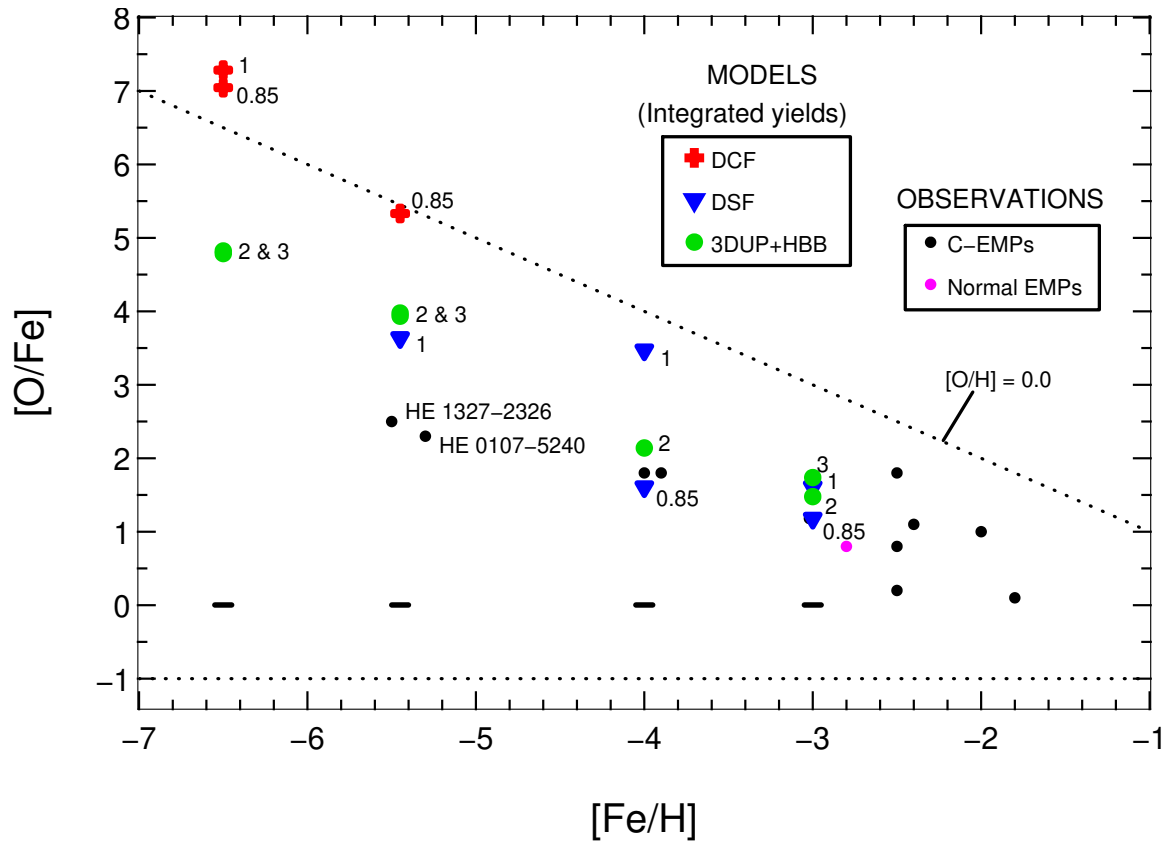


Figure 7.43: Comparing the $[O/Fe]$ ratios in the yields of our models with those of the observations. See Figure 7.34 for the observational data sources. C-EMPs and normal EMPs are defined in Figure 7.39, as are the symbols used for the yields. Very sketchy upper and lower envelopes are marked with dotted lines (there not not many observations to compare with as oxygen is difficult to measure). The two most metal-poor stars observed to date are indicated. Their oxygen abundances are from Bessell et al. (2004) (HE 0107-5240) and Frebel et al. (2006a) (HE 1327-2326). It can be seen that all models produce large oxygen enhancements, but the DCF events produce the most. The yields from HBB and DSF models match the observations well at the higher metallicities but are ~ 1 dex higher than those of HE 0107-5240 and HE 1327-2326 at $[Fe/H] \sim -5.5$. Note that we have not plotted the $Z = 0$ models in this case.

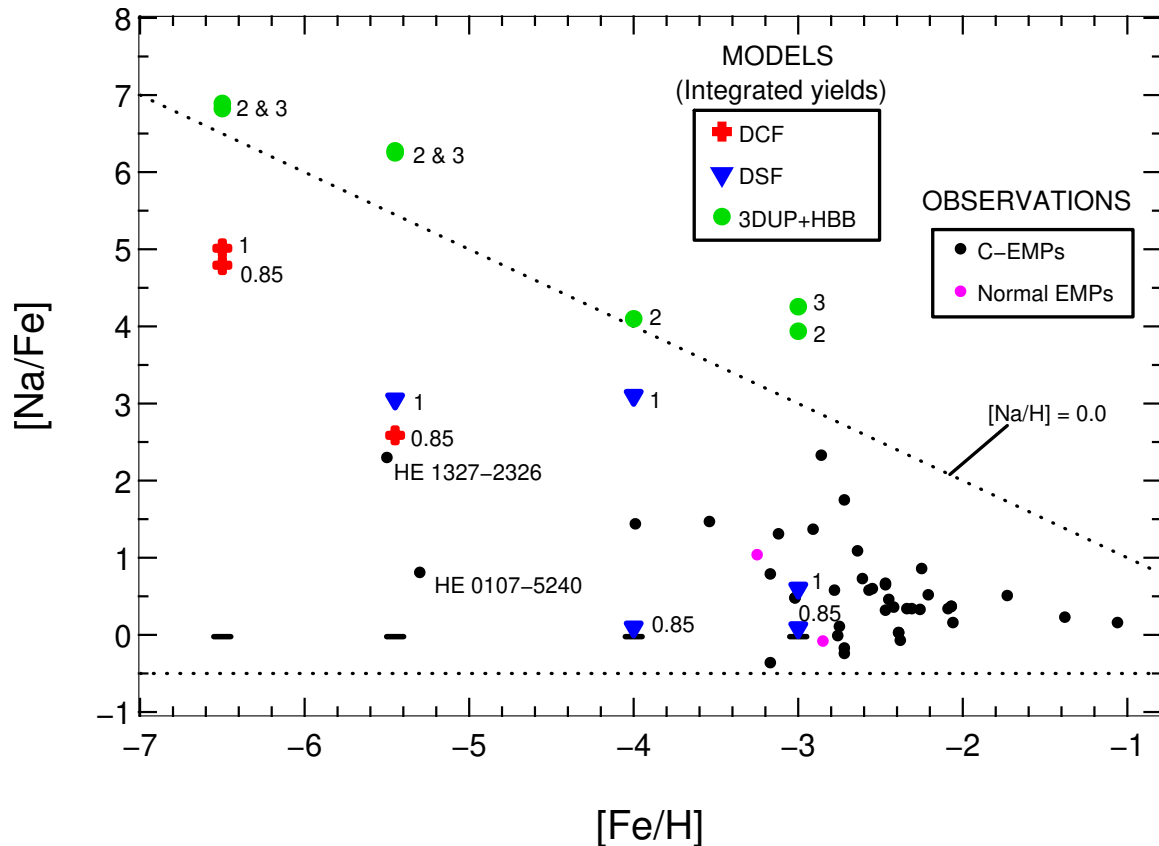


Figure 7.44: Comparing the $[\text{Na}/\text{Fe}]$ ratios in the yields of our models with those of the observations. See Figure 7.34 for the observational data sources. C-EMPs and normal EMPs are defined in Figure 7.39, as are the symbols used for the yields. Upper and lower envelopes are sketched with dotted lines at $[\text{Na}/\text{H}] = 0.0$ and $[\text{Na}/\text{Fe}] = -0.5$. The observations show a wide spread in Na amongst the C-EMPs and it can be seen that our HBB models produce enormous amounts of Na. Note that we have not plotted the $Z = 0$ models in this case.

up from the intershells. These very large overabundances continue at lower metallicities and are reminiscent of the huge N overabundances – which have the same source (with C as the seed). Thus Na is another argument for less 3DUP in the models. This may be consistent with C as well, but this is less clear. If not, then these results may imply that HBB is too efficient in our models. Looking at the two most metal-poor stars we see that HE 1327-2326 is very close to our $0.85 M_{\odot}$ yield at $[\text{Na}/\text{Fe}] \sim 2.5$, but HE 0107-5240 again defies the models, having a relatively low Na abundance. Interestingly all of our models produce Na enhancements at $[\text{Fe}/\text{H}] = -6.5$ and $Z = 0$.

7.6.4 Comparisons with Individual EMP Halo Stars

Stars With $[\text{Fe}/\text{H}] \approx -4.0$

In our sample from the literature we have about 10 stars which have $[\text{Fe}/\text{H}] \sim -4$. However there are only a couple for which we have C, N, O, Na and Mg abundances. In Figure 7.45 we plot the abundances of these two stars along with the abundances of the yields from all our $[\text{Fe}/\text{H}] = -4.0$ models. It is thus a raw, direct comparison (ie. no scaling of Fe). The abundances for the C-EMP star G77-61 are from Plez and Cohen (2005) and those for CS 22949-037 (also

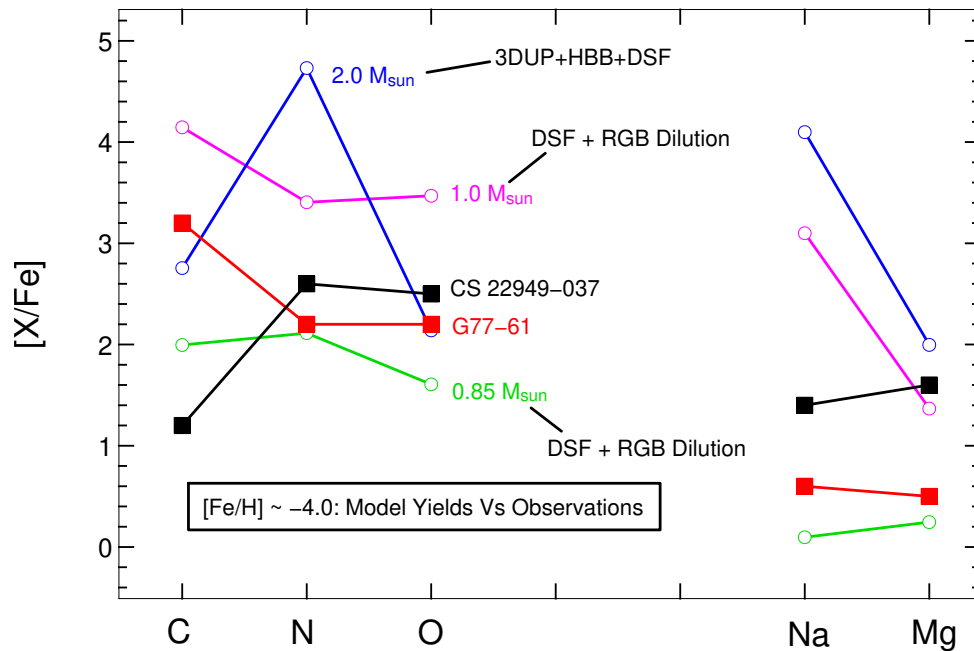


Figure 7.45: Comparing the abundance pattern in our $[\text{Fe}/\text{H}] = -4.0$ yields with observations of stars with the same metallicity. See text for sources of the abundance determinations in these stars. The clear 3DUP+HBB signature of high C and O combined with very enhanced N can be seen in the $2 M_{\odot}$ model (note that we do not display the $3 M_{\odot}$ yield due to a loss of data, but it would be very similar to the $2 M_{\odot}$ one). The AGB yields of both the 0.85 and $1 M_{\odot}$ have been diluted by varying amounts of unpolluted mass loss on the RGB. See text for a discussion.

a C-EMP) are from [Israelian et al. \(2004\)](#) and [Spite et al. \(2006\)](#). In the figure we indicate which were the dominant sources of pollution in the yields for each model. At this metallicity we have representatives from only two of the three pollution groups – the DSF and 3DUP+HBB groups. This is because the DCF only occurs in models of lower metallicity. The clear signature of HBB can be seen in the $2 M_{\odot}$ yield – N is very abundant, being ~ 2 dex above C in the same model. Oxygen is overabundant but still less abundant than C and N. The large Na production from the combination of HBB and 3DUP can be seen, as can a ~ 2 dex overabundance of Mg (from 3DUP). The DSF yields show variation. The $0.85 M_{\odot}$ model shows roughly a 2 dex lower enhancement in C, N and O than the $1 M_{\odot}$ model. Nitrogen is more dominant in the $0.85 M_{\odot}$ yield (relative to its C and O). With regards to Na and Mg the two yields diverge – Na is much more prevalent in the $1 M_{\odot}$ model (~ 3 dex higher) whilst Mg is only ~ 1 dex higher. The ~ 2 dex gap in the CNO group yield between these models is partly due to the dilution of the yields by unpolluted RGB mass loss (see Figures 7.20 and 7.19 on page 248 in the structural evolution section), and partly due to the greater surface enrichment from the DSF event in the $1 M_{\odot}$ model. The difference in abundance *patterns* is due to the differences in the dual shell flashes. The gas in the $1 M_{\odot}$ model achieved more advanced proton burning on top of the dredged up He intershell material, whilst the $0.85 M_{\odot}$ yield shows more signs of CN cycling.

Looking at the abundance patterns in the two $[\text{Fe}/\text{H}] = -4$ stars in Figure 7.45 we see that they have similar N and O abundances. Their C abundances are however very different. G77-61 has ~ 2 dex more C than CS 22949-037. On the other hand CS 22949-037 is more enhanced in Na and Mg, with both being about 1 dex higher in this star. The abundance pattern of CS 22949-037 is closest to that of the HBB model ($2 M_{\odot}$) except for the fact that its oxygen abundance is

similar to its N abundance, whereas in the HBB model O is much lower than N. Thus it appears that the CS 22949-037 material has undergone CN cycling but not ON cycling. This would be the case in a star with less efficient HBB. Deep mixing could also do this but the large CNO abundances would need to be explained as no dredge-up occurs on the RGB. This may be a candidate for a scenario in which a low mass star with DSF+3DUP and only weak HBB gets its CNO enhancements from the DSF and then cycles C to N whilst O remains high from the DSF. The moderate enhancements in Mg and Na would come from the 3DUP+HBB also. Again, it will be interesting to calculate some models at these metallicities with 3DUP via the inclusion of overshoot, which we leave as a future project. Moving now to G77-61 we see that there is a very nice match to its CNO abundance pattern in the $1 M_{\odot}$ yield, albeit offset upwards by ~ 1.5 dex. The model yield and the star both have high C overabundances while N and O about 1 dex lower than C. Magnesium is similarly offset upwards. Sodium is however ~ 2.5 dex higher in the model. Interestingly the Na-Mg pattern is very similar to the HBB Na-Mg pattern. We discuss this interesting (partial) match in terms of the DSF abundance patterns below.

Comparing With the Dual Flash Abundances: The G77-61 Case

In Figure 7.46 we make a comparison between the surface compositions of our 1 and $2 M_{\odot}$ models taken just after the dual shell flash events and the observed composition of the star G77-61. This star is a cool carbon-rich dwarf (also identified as a carbon star, due to the presence of strong C-based molecular bands). Since it is a dwarf it can not have gained its surface abundances via autopollution. The binary mass transfer hypothesis (from a low or IM companion) has always been the most favoured scenario for explaining its abundance pattern (eg. Dahn et al. 1977; Plez and Cohen 2005). Dearborn et al. (1986) found that it indeed had a binary companion. By comparing the abundance pattern of this star with our DSF surface compositions we are sampling the early TP-AGB stage as a candidate for the mass transfer hypothesis. As mentioned earlier we suggest that the DSF (and DCF) events may lead to enhanced mass loss since they are (at least) mildly violent events. In addition to this the surfaces of these models are not enhanced in carbon until this stage, so any mass transfer before this would not have a significant effect on the surface composition of the secondary star. Moreover, the pollution may also enhance the stellar winds due to grain formation, again increasing the mass transfer rate.

Looking now at our models in Figure 7.46 we see that both models (1 and $2 M_{\odot}$, $[\text{Fe}/\text{H}] = -4.0$) show a very similar abundance pattern to that of G77-61 at this stage of their evolution. In the case of the $1 M_{\odot}$ model this abundance pattern is retained for the rest of its evolution, as it experiences no 3DUP. This is evident in the yields shown in Figure 7.45. In this case the yield is diluted by unpolluted RGB mass loss, so the abundances are scaled down. This could be an explanation for the G77-61 abundance pattern, especially if there were more dilution. However, looking at Na and Mg we see that the ratio of these two elements is very different to that in G77-61. These two elements have similar overabundances in G77-61 (~ 0.5 dex above solar) but in the models Na is ~ 1.5 dex higher than Mg. This excess Na problem is reminiscent of the globular cluster abundance problem, where standard AGB models produce too much Na (see next chapter). We note that this may be a product of poorly constrained reaction rates (Illiadis and Lattanzio 2007, private communication) and we shall pursue this uncertainty as a

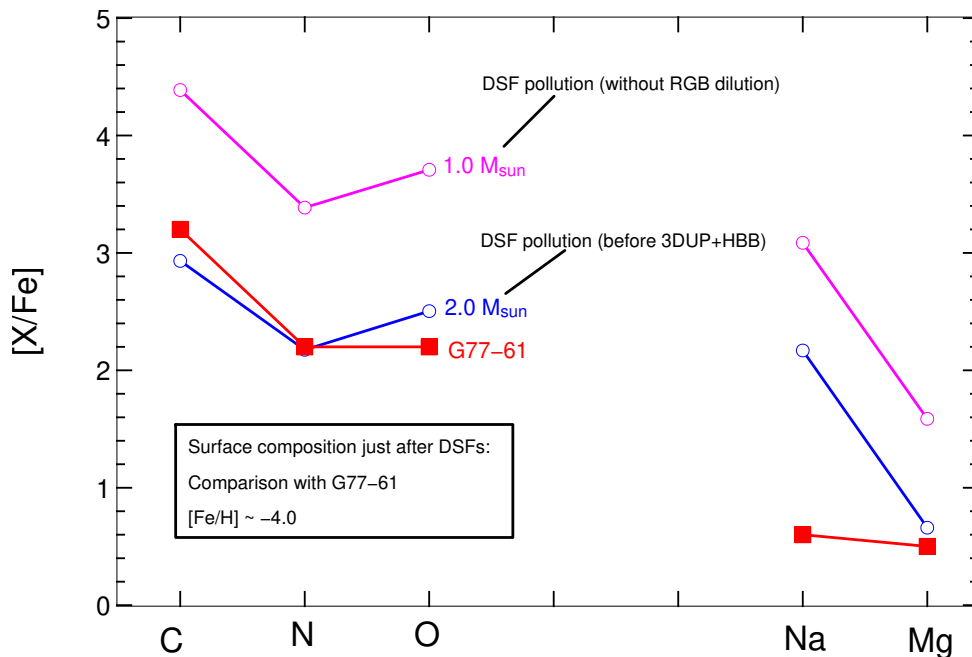


Figure 7.46: Comparing the abundance patterns in our $[\text{Fe}/\text{H}] = -4.0$ models taken just after the DSF events with the C-EMP dwarf star G77-61. See text for sources of the abundance determinations of this star. By contrasting the chemical signature of this event with that of the integrated yields (Figure 7.45) it can be seen how strongly the 3DUP+HBB affects the yields (eg. in the $2 M_{\odot}$ model). Interestingly the DSF CNO signature matches fairly well with G77-61, particularly if observational uncertainties are considered (usually $\sim \pm 0.3$ dex or so). The only problem with the match is that the models produce by far too much Na.

future study. Looking now at the $2.0 M_{\odot}$ DSF surface composition it can be seen that there is a good match with the CNO pattern – and absolute abundances – of G77-61. Taking into account abundance determination uncertainties (which can vary between studies by $\sim \pm 0.3$ dex or more), it is a very good match. We reiterate that no scaling has been performed on these compositions. There is however the same problem with excess sodium (the Mg matches very well though). An important point here is that the $2 M_{\odot}$ model goes on to experience 3DUP soon after the DSF event. This means that this abundance pattern is not maintained for very long, as C will quickly increase. Once HBB sets in this C is burnt to N and the classic HBB abundance pattern will emerge (see the yield pattern for this model in Figure 7.45), which is very different to that of G77-61. One way to circumvent this problem would be to postulate that the DSF gives rise to an envelope ejection (or partial envelope ejection). In this way the companion star, G77-61, would accrete matter with the DSF pattern. This is however very speculative – fluid dynamics simulations are really needed to test if the DSF event can do this.

Stars With $[\text{Fe}/\text{H}] \approx -5.5$: Comparisons with Yields & DF Abundances

This metallicity represents the lower boundary of all observations made of the Universe by humanity to date. No objects with metallicities lower than the halo stars HE 0107-5240 ($[\text{Fe}/\text{H}] = -5.3$, Christlieb et al. 2002) and HE 1327-2326 ($[\text{Fe}/\text{H}] = -5.4$, Frebel et al. 2005b) have been discovered – yet. There are of course projects underway to better sample the Halo (eg. GAIA, SEGUE), which may reveal stars as metal poor as our models :)

A fact that has raised considerable interest is that both of these stars are very C-rich. This

implies that the *majority* of stars at such low metallicities should be C-rich. However the sample is of course very small.

HE 1327-2326 has been identified as either a dwarf or a subgiant (Aoki et al. 2006), whilst HE 0107-5240 is probably an RGB star (Christlieb et al. 2004). Thus HE 1327-2326 should not have altered its own abundance pattern, but HE 0107-5240 may have (eg. via deep mixing or FDUP).

In Figure 7.47 we show the abundances of C, N, O, Na and Mg in the yields of all our $[\text{Fe}/\text{H}] = -5.45$ models. We also do the same for the observations of the two stars. The abundance pattern of HE 1327-2326 is different to all the stars we have looked at so far. It has high C and N but low(er) oxygen, unlike either of the $[\text{Fe}/\text{H}] = -4$ stars and HE 0107-5240. It is interesting to note that amongst our four comparison stars we have three different patterns in CNO! This suggests that there are many paths to becoming a C-rich EMP, possibly combined with many paths to altering the abundance patterns post-pollution. This naturally makes attempts to decipher pollution scenarios quite difficult. On the other hand the abundance pattern of HE 0107-5240 is very similar to that of the $[\text{Fe}/\text{H}] = -4$ star G77-61. We noted in the previous subsection that this pattern was matched by the DSF patterns of our 1 and 2 M_{\odot} models – except for Na. Looking at the patterns in our $[\text{Fe}/\text{H}] = -5.45$ yields we see that none of them match very well with the HE 0107-5240 pattern, although the 1 M_{\odot} model comes reasonably close. These yields are however averaged over the lifetime of the stars. In Figure 7.48 we plot the patterns of the 0.85 and 1 M_{\odot} surface compositions just after the DCF (0.85 M_{\odot}) and DSF (1 M_{\odot}) events. Here it can be seen that, at this stage of evolution, the 1 M_{\odot} does provide a reasonable match to the pattern of HE 0107-5240. The reason for this improved match is due to the fact that the 1 M_{\odot} model undergoes (slight) HBB on the AGB that converts some of the C to N, thus altering the pattern. It is not a perfect match though. If we scale the yield down (via some form of dilution with unpolluted material) then we see that C, N, O and Na would all match fairly well – but Mg would be underabundant. We suggest that the extra Mg needed could be supplied by some 3DUP. Since N is relatively low compared to C, it would need to be a low mass AGB star that supplies the pollution, without HBB.

Moving back to Figure 7.47 we can see the strong HBB pattern in the 2 and 3 M_{\odot} yields. This pattern appears to be the best match for the pattern of HE 1327-2326. However carbon is a bit high relative to N in this star for CN equilibrium. This may indicate that the pollution material underwent only partial CN cycling. This would be the case before HBB fully sets in near the start of the AGB in an IM star, or for a lower mass star that does not undergo very hot HBB. Since this star is a dwarf it should not have altered its CNO composition itself (as deep-mixing RGB stars can). In Figure 7.49 we compare the abundance pattern of HE 1327-2326 with the surface composition of our IM models just after their DSF events. In the 3 M_{\odot} case the DSF had very little effect on the surface composition (the abundance ratios are all \sim solar which are the initial abundances, except for N which was initially very sub-solar). The increased N and decreased C at the surface in this model is mainly due 2DUP. The 2 M_{\odot} model on the other hand has a HBB-like surface composition. The magnitude of the surface pollution is also similar to that of HE 1327-2326. However C and O in this model are much less abundant than in HE 1327-2326. The operation of 3DUP after the DSF could remedy this by dredging up these two elements whilst N remains constant. We have indicated this in the diagram. This raises a significant issue in relation to these sorts of comparisons. The time *evolution* of the surface

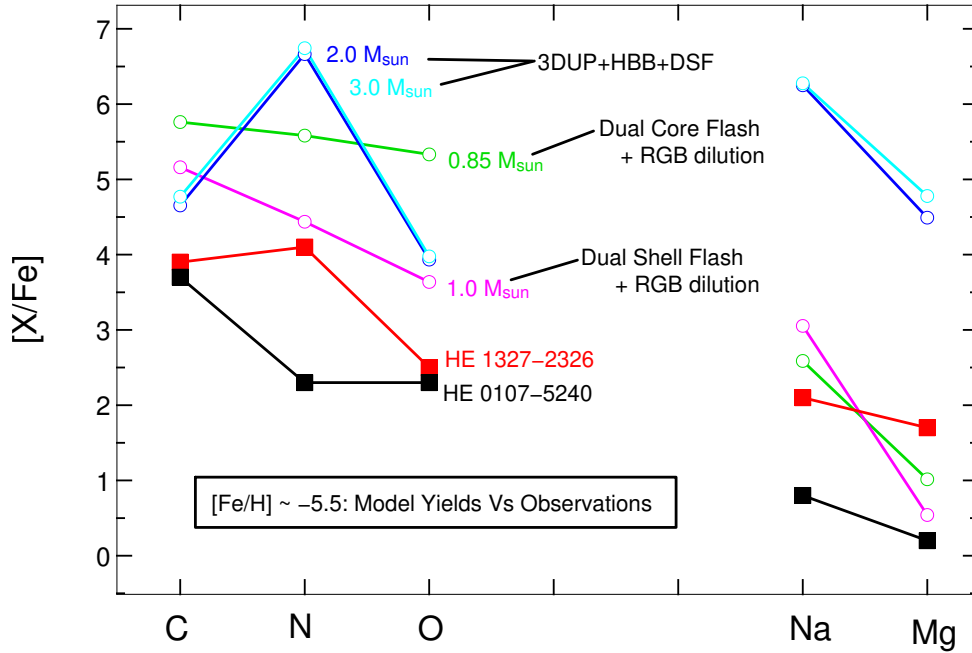


Figure 7.47: Comparing the abundance pattern in our $[Fe/H] = -5.45$ yields with observations of stars with the same metallicity. The abundance determinations in these stars are from Aoki et al. (2006) (HE 1327-2326) and Christlieb et al. (2004) (HE 0107-5240). The clear 3DUP+HBB signature of high C and O combined with very enhanced N can be seen in the 2 and 3 M_{\odot} models. The AGB yields of both the 0.85 and 1 M_{\odot} have been diluted by varying amounts of unpolluted mass loss on the RGB. It can be seen that the HBB models are the closest match to the pattern of HE 1327-2326, although there is not so much N in this star. These models produce far too much Na and Mg. See text for a discussion.

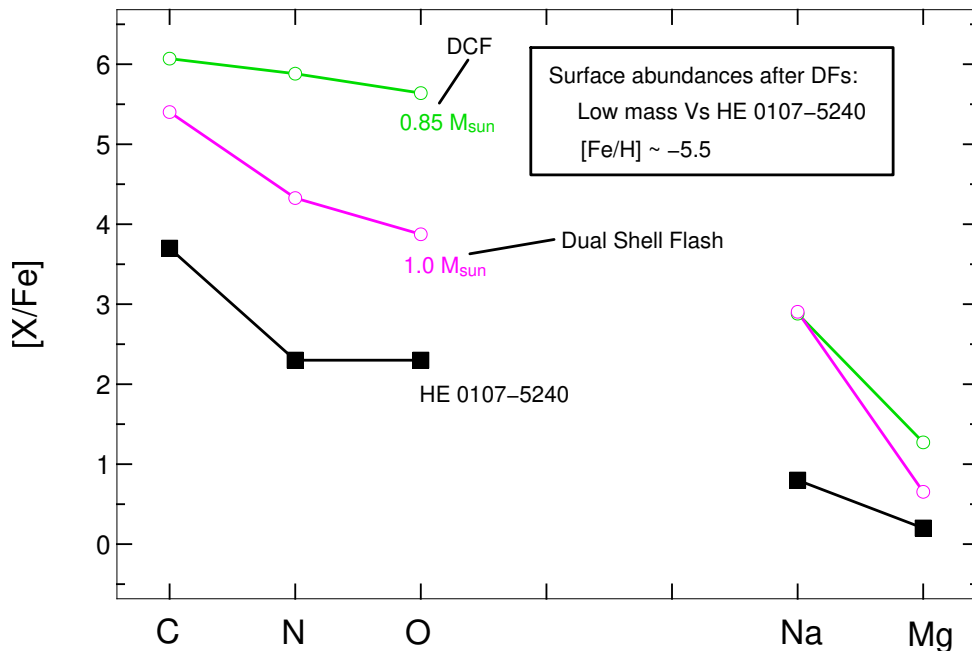


Figure 7.48: Comparing the abundance patterns in our low-mass $[Fe/H] = -5.45$ models at times just after the DSF and DCF events with the RGB CEMP HE 0107-5240. This star has a similar abundance pattern to that of the more metal-rich star G77-61. Contrasting these abundances with those of the yields (Figure 7.47) it can be seen that this material was slightly diluted by unpolluted RGB mass loss, and that slight HBB CN processing occurred in the 1 M_{\odot} model. The pattern of the 1 M_{\odot} matches well with the observations – apart from the fact that a scaled down version (through dilution) would have too much Mg.

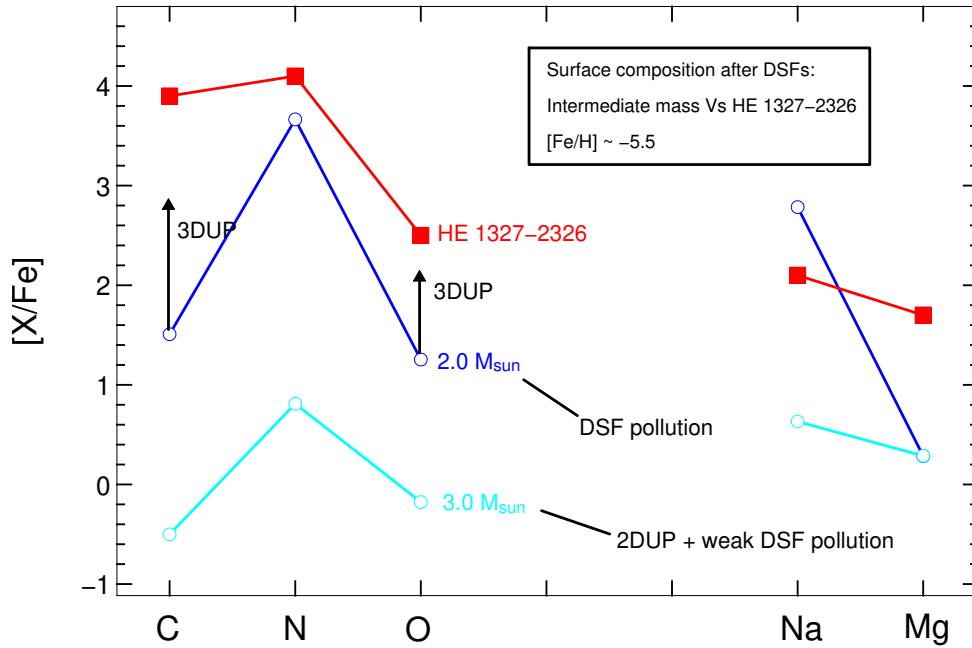


Figure 7.49: Comparing the abundance patterns in our intermediate-mass $[\text{Fe}/\text{H}] = -5.45$ models at times just after the DSF events with the CEMP dwarf (or subgiant) star HE 1327-2326. By contrasting these abundances with those of the yields (Figure 7.47) it can be seen that 3DUP+HBB increased the abundances of all these elements by a few orders of magnitude. Interestingly the pattern from the DSFs in these intermediate-mass models is similar to that from HBB (and different from the DF patterns of the low-mass models). The $2 M_{\odot}$ model has a similar amount of N as the star, but has lower C and O. We suggest that a few 3DUP episodes would increase the C and O whilst keeping N constant (before HBB sets in), as indicated by the vertical arrows, making a better fit. Na and Mg may still be a problem though. We note that the $3 M_{\odot}$ model abundance pattern has mainly come about via 2DUP, as the DSF pollution was very weak.

abundances may be a better way to make comparisons. Weighting would need to be applied due to the different timescales of the different evolutionary stages. We shall attempt these types of comparisons in our future publications, due to time and space constraints here, although we note that we have partly included this dimension by comparing with the DSF surface abundances as well as the yields. Returning to the $2 M_{\odot}$ model we see that the abundances of Na and Mg are poor matches for those of HE 1327-2326. Na is again too high whereas Mg is too low. Although Mg increases through 3DUP in this model, so does Na, so the problem remains.

7.6.5 Summary

In summary we find that our yields only offer partial fits to the abundance patterns at extremely low metallicities – none of the models match any of the stars’ patterns across the five elements considered. We note however that the time evolution of the surface composition of the models is not taken into account in these types of comparisons – these stars may have been polluted by binary companions at any stage of the companion’s evolution. To further complicate matters their gas may have been polluted by more than one star. The fact that our sample of four stars has three distinct abundance patterns shows that the formation of the patterns in Nature is indeed complex. We highlight this by comparing all of the observed patterns (from our four comparison stars) in Figure 7.50. It can be seen that the patterns of G77-61 and HE 0107-5240 are almost identical (especially so when considering the uncertainties in the observations)

– despite the order of magnitude difference in Fe abundance between them. We note however that one of the stars, CS 22949-037, is an odd one. Unlike almost all of the other CEMPs in our large sample it has a C/N ratio less than 1 – such that it is C-rich but N-richer (see Figure 7.42 for C/N ratios in the observations). The other three stars in Figure 7.50 are ‘normal CEMPs’, having $C/N > 1$.

On the bright side of our comparisons we recall a few key indicators that our models do reproduce:

1. All our models produce large C overabundances in their yields, as observed in the CEMPs.
2. All models produce large N overabundances, as observed in most of the CEMPs.
3. Many of our models show low $^{12}\text{C}/^{13}\text{C}$ ratios, as seen in most CEMPs.
4. All our models, except for the HBB ones, have $C/N > 1$ – as seen in most CEMPs.
5. All our models produce oxygen overabundances, as seen in most CEMPs.
6. The yields show a spread in Na, as seen amongst the CEMPs.
7. Some of the DSF CNO abundance patterns match those of some of the most metal-poor CEMPs.

Problems arise when we attempt to match all these – and the extended abundance patterns – simultaneously (and quantitatively). Clearly there is much work to be done here in attempting to decipher the pollution scenarios. Some major uncertainties that need to be explored include the nuclear reaction rates and the degree of overshoot in the models. We shall continue to pursue this complex task in future studies – it is quite a challenge! One first step will be to compile all the observational data to determine if there are some common abundance patterns that dominate the CEMPs.

Finally we note that there are other pollution scenarios in the literature that attempt to explain the abundance patterns of these stars apart from the binary mass transfer and autopollution scenarios mentioned in the current study. In particular massive stars ($M \gtrsim 10 M_{\odot}$) are often invoked to explain the abundance patterns of the heavier elements (eg. [Chieffi and Limongi 2002](#)). Indeed these stars are needed in the low- and intermediate-mass scenarios as the LM and IM stars cannot produce many of the heavy elements (s-process elements withstanding). [Chieffi and Limongi \(2002\)](#) showed that standard SNe models in the mass range $15 \rightarrow 80 M_{\odot}$ can not explain *all* the patterns in the observations, but they do match a significant number of them. However [Umeda and Nomoto \(2003\)](#) showed it may be possible for all the elements to come from SNe – including the large CNO excesses – by assuming the low-energy SN ‘mixing and fallback’ scenario in their models. They match the abundance pattern of one of the stars considered here, HE 0107-4240, but note that by varying the nature of the explosion they should be able to explain stars with other abundance patterns. In this scenario low- and intermediate-mass stars are not required.

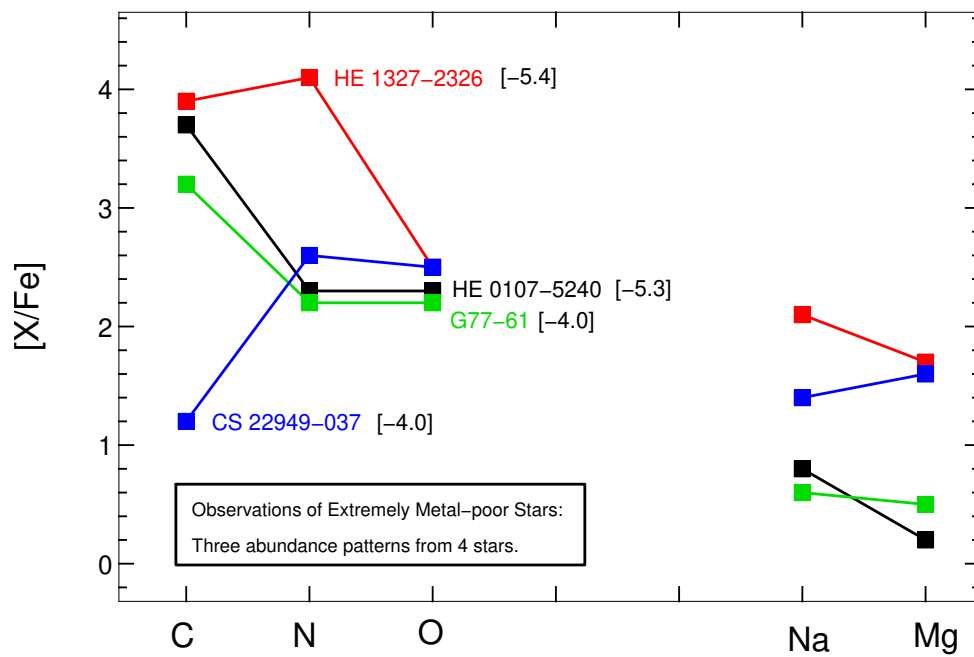


Figure 7.50: Highlighting the complex nature of the abundance patterns at extremely low metallicity. It can be seen that in our sample of four stars there are no less than three distinct abundance patterns. The (similar) patterns of G77-61 and HE 0107-5240 are reasonably well matched by the abundance patterns of some of our DSF models (at the time of the DSFs) – except for Na, which is overproduced. We note that CS 22949-037 is an odd CEMP since it has $C/N < 1$, whereas most CEMPs do not.

Chapter 8

Galactic Globular Cluster Stars

“The activist movements of the past 40 years have had a significant civilizing effect.”
– Noam Chomsky

8.1 Introduction

8.1.1 The GC Abundance Anomalies Mystery

Most Galactic globular clusters (GCs) have a very uniform distribution of heavy elements. This indicates that the cluster gas was well mixed when the stars formed. However, in contrast to the Fe group, it has been known since the early 1970s that there is a large spread in Carbon and Nitrogen in many GCs (eg. [Bell and Dickens 1974](#); [Da Costa and Cottrell 1980](#)).

The first ‘anticorrelation’ was found 25 years ago – C is low when N is high. This observation is explicable in terms of the CN cycle, where ^{12}C is burnt to ^{14}N . It has also been found that the C abundance decreases with luminosity on the red giant branch (RGB) in many GCs. This is known as the C-L anticorrelation and is also observed in halo field stars (see eg. figures 4 and 5 in [Smith 2002](#)). This is thought to be the result of Deep Mixing – extra mixing of the convective envelope into the top of the H-shell, allowing C-N cycling to alter the composition of the surface. Another effect of C-N cycling is the reduction of the $^{12}\text{C}/^{13}\text{C}$ ratio (it approaches an equilibrium value of ~ 4). This has been observed in GCs and in the field (see eg. figure 2 in [Shetrone 2003](#)).

GCs also show other abundance features. The most famous of these is the O-Na anticorrelation: O decreases with increased Na. This is readily explained by hot(ter) hydrogen burning, where the O-N and Ne-Na chains are operating – the ON cycling reduces O, whilst the Ne-Na chain increases Na (at $T \sim 45$ million K). *Where* this occurs is still a mystery. The notable thing about this abundance trend is that it only occurs in GCs – *it is not seen in field halo stars* (see [Gratton et al. 2000](#) for a comparison of M13 stars and fields stars of similar metallicity).

There also appears to be a Mg-Al anticorrelation in some GCs (eg. NGC 6752, [Grundahl et al. 2002](#)). This can also be explained through high-temperature ($T \sim 65$ million K) proton capture nucleosynthesis, via the MgAl chain (Mg depleted, Al enhanced). Again the site for this is uncertain and it *is not seen in field stars*. Furthermore, the light elements show various

(anti)correlations amongst themselves (see eg. Figure 9 in Kraft et al. 1997 for O, Na, Mg, and Al in M13). All these (anti)correlations point to hydrogen burning – the CN, ON, MgAl, NeNa cycles/chains – at various temperatures. The most popular theory for the site of this burning is at the base of the convective envelope in AGB stars - where hot bottom burning (HBB, first proposed as a possible site by Cottrell and Da Costa 1981) occurs. HBB provides the proton-capture nucleosynthesis needed, and at low metallicities (like those of GCs) HBB occurs at higher temperatures. Qualitatively it seems to fit the observations– although some deep mixing is required also, to explain the C-L anticorrelation. We note that another possible site for the abundance anomalies has recently gained increased popularity – that of rotating massive stars (see eg. Maeder and Meynet 2006).

8.1.2 GC Stellar Models: The Grids and Input Physics

The Grids of Models

During the course of the current study we have investigated whether the AGB GC pollution scenario also fits *quantitatively*. To this end we have calculated a few small grids of models to emulate a generation of stars in NGC 6752 ($[\text{Fe}/\text{H}] = -1.4$) which may have given rise to the abundance patterns – either via supplying the material for star formation of the current generation, or by supplying the material for accretion by the current generation. The reason we have calculated more than one grid of models is so we can investigate the uncertainties in the model predictions. We have calculated four sets of models, although not all sets contain the full mass range:

1. The Standard set ($M = 1.25, 2.5, 3.5, 5.0, 6.5 M_{\odot}$) – using our standard mass loss formalism on the AGB (VW93) and our standard reaction rates.
2. Mass loss variation set ($M = 2.5 \text{ \& } 5.0 M_{\odot}$) – using Reimers’ mass loss on the AGB and our standard reaction rates.
3. Reaction rate variation set ($M = 2.5 \text{ \& } 5.0 M_{\odot}$) – using the NACRE compilation for some important reactions, whilst using the standard mass-loss rate on the AGB (VW93).
4. No 3DUP set ($M = 2.5, 3.5, 5.0, 6.5 M_{\odot}$) – standard mass loss and rates but 3DUP inhibited.

Initial Composition

All the sets of models we calculated using the same initial composition. This composition was arrived at through a chemical evolution model in which the gas was enriched by a population of $Z = 0$ stars. The IMF used was top-heavy, so most of the pollution was from massive Pop. III stars (see Section 8.3 for more details). In order to match the metallicity of NGC 6752 ($[\text{Fe}/\text{H}] = -1.4$) the mostly supernova material was mixed with pristine Big Bang material. We list the initial composition in each yield table for each set of models in Appendix B. The key differences between this composition and the Solar composition is that N is very underabundant

and the α elements are enhanced. This is a direct result of the $Z = 0$ supernovae yields used in the chemical evolution model.

Input Physics

Since the models were computed using the non-scaled-solar composition mentioned above, it was necessary to remove all scaled-solar assumptions from the codes. In addition to this we calculated opacity tables specifically for this composition on the OPAL website – so that the opacity would be consistent with the stellar composition (rather than scaled-solar).

The version of the SEV code that we used for the first three sets of models listed above did not have time-dependent mixing (as this had not been completed yet). It did however have all the opacity updates (see Chapter 4 for details). The version of the SEV code used for the fourth set of models, the ones with no 3DUP, was the same as that used for our $Z = 0$ and halo star models. Thus it included all the modifications reported in Chapter 4. In particular it contained time-dependent mixing and the option of using the Ledoux criterion for convective boundaries. For our standard mass-loss rates and reaction rates see Chapter 3.

In the nucleosynthesis code (NS code) most of our reaction rates come from the Reaclib library (Thielemann et al. 1987). However many of the important rates involving the Mg and Al isotopes have been updated using various sources. These include: $^{24}\text{Mg}(p, \gamma)^{25}\text{Al}$ (Powell et al. 1999); $^{25}\text{Mg}(p, \gamma)^{26}\text{Al}$ (Iliadis et al. 1996); $^{26}\text{Mg}(p, \gamma)^{27}\text{Al}$ (Iliadis et al. 1990); $^{22}\text{Ne}(\alpha, n)^{25}\text{Mg}$ and $^{22}\text{Ne}(\alpha, \gamma)^{26}\text{Mg}$ (Kaeppeler et al. 1994). We refer to this combination of rates as our ‘standard’ set, and it is this set that we use for all of our models, unless otherwise stated. See Section 3.2 for further details on the NS code.

8.2 Models of NGC 6752 Stars

We have calculated three different sets of models for this part of our globular cluster study. The first is a ‘standard’ set whilst the other two were designed to test the sensitivity of the results to two of the major uncertainties in the model calculations – reaction rates and mass-loss.

8.2.1 The Standard Set

Input Physics

Some of the key input physics used in the structural evolution code (SEV code) for this ‘Standard’ set of models are:

- Reimers (1975) mass loss formula on the RGB.
- Vassiliadis and Wood (1993) mass loss formula on the AGB.
- Instantaneous mixing (see Chapter 3).
- Updated opacities which also match the non-scaled solar composition (see Section 4.2).

Convective boundaries were treated using the Schwarzschild criterion plus the standard SEV code overshoot method described in Section 3.1.3 on page 39.

In the NS code we have used the standard set of reaction rates, as described in the introduction to this chapter (also see Section 3.2 for further details on the NS code).

Results

Here we briefly describe a couple of representative models from our standard set. We shall provide more detail of the evolution of all our models in a forthcoming paper. These models follow quite normal evolutionary paths – unlike the $Z = 0$ and EMP models presented in the previous chapters (they experience no dual flash events). For reference we note that the version of the code used for these models is similar to that used in the studies by Karakas and Lattanzio (2003) and Karakas et al. (2002) – apart from some opacity updates in our version. The third dredge-up (3DUP) results are similar to that found by Karakas et al. (2002). In particular our $Z = 0.0017$ ($[\text{Fe}/\text{H}] = -1.4$) GC models have very similar λ values to their $Z = 0.004$ models. To highlight this we show in Figure 8.1 some of the AGB evolution in our $3.5 M_{\odot}$ model. It can be seen that $\lambda \approx 0.98$, which is the same as that found by Karakas et al. (2002) in their $3.5 M_{\odot}$ model. This model experiences ~ 18 thermal pulses before leaving the AGB. The temperature at the base of the convective envelope does not become high enough for significant HBB ($T_{bce} \lesssim 25$ MK). In Figures 8.2 and 8.3 we show some of the surface abundance evolution from the NS code for this model, during the AGB phase. The effect of 3DUP of intershell material on the surface abundances can be seen in the periodic jumps in ^{12}C and ^{22}Ne . The heavy Mg isotopes are also enhanced by 3DUP, increasing by ~ 3 dex at the surface over the lifetime of the AGB (Figure 8.3). A slight increase in ^{14}N can be seen but this is mainly due to 2DUP. Oxygen, ^{24}Mg and ^{23}Na are all barely affected on the AGB in this model.

Moving to a higher mass model we see that the temperature at the bottom of the convective envelope is much higher – reaching ~ 90 MK in the $5 M_{\odot}$ model (see panel 2 of Figure 8.4). This gives rise to strong HBB after only ~ 5 thermal pulses into the AGB (this model experiences ~ 80 TPs in total). This can be seen clearly in the ^{12}C and ^{14}N surface abundance evolution in Figure 8.5. Once the temperature is high enough $\text{C} \rightarrow \text{N}$ cycling converts the dredged-up ^{12}C to ^{14}N very quickly. It can also be seen that some $\text{O} \rightarrow \text{N}$ cycling is occurring, as the ^{16}O abundance decreases towards the end of the AGB – despite the fact that it is being dredged up with the carbon. Thus there is full CNO cycling occurring in the envelope of this model. In the context of the GC abundance anomalies this is good, since oxygen is seen to be depleted in some stars (by up to ~ 1 dex in NGC 6752). Na is seen to anticorrelate with oxygen in many GCs. In Figure 8.6 we can see that the abundance of ^{23}Na indeed increases with evolution along the AGB. Thus an anticorrelation is present in our (higher-mass) models. The increase in Na mainly comes from the HBB destruction of ^{22}Ne , which is dredged up from the intershell. It can be seen in Figure 8.6 that ^{22}Ne and ^{23}Na play similar roles to ^{12}C and ^{14}N , respectively. ^{22}Ne increases through 3DUP initially because T_{bce} is too low for Ne-Na cycling, but as the temperature increases most of it ends up in the form of ^{23}Na . Hence the abundance of ^{23}Na increases enormously, just like that of ^{14}N . In terms of the Mg-Al anticorrelation in NGC 6752 we can see in the same figure that ^{27}Al is increased by ~ 0.5 dex over the AGB phase. However the heavy Mg isotopes are

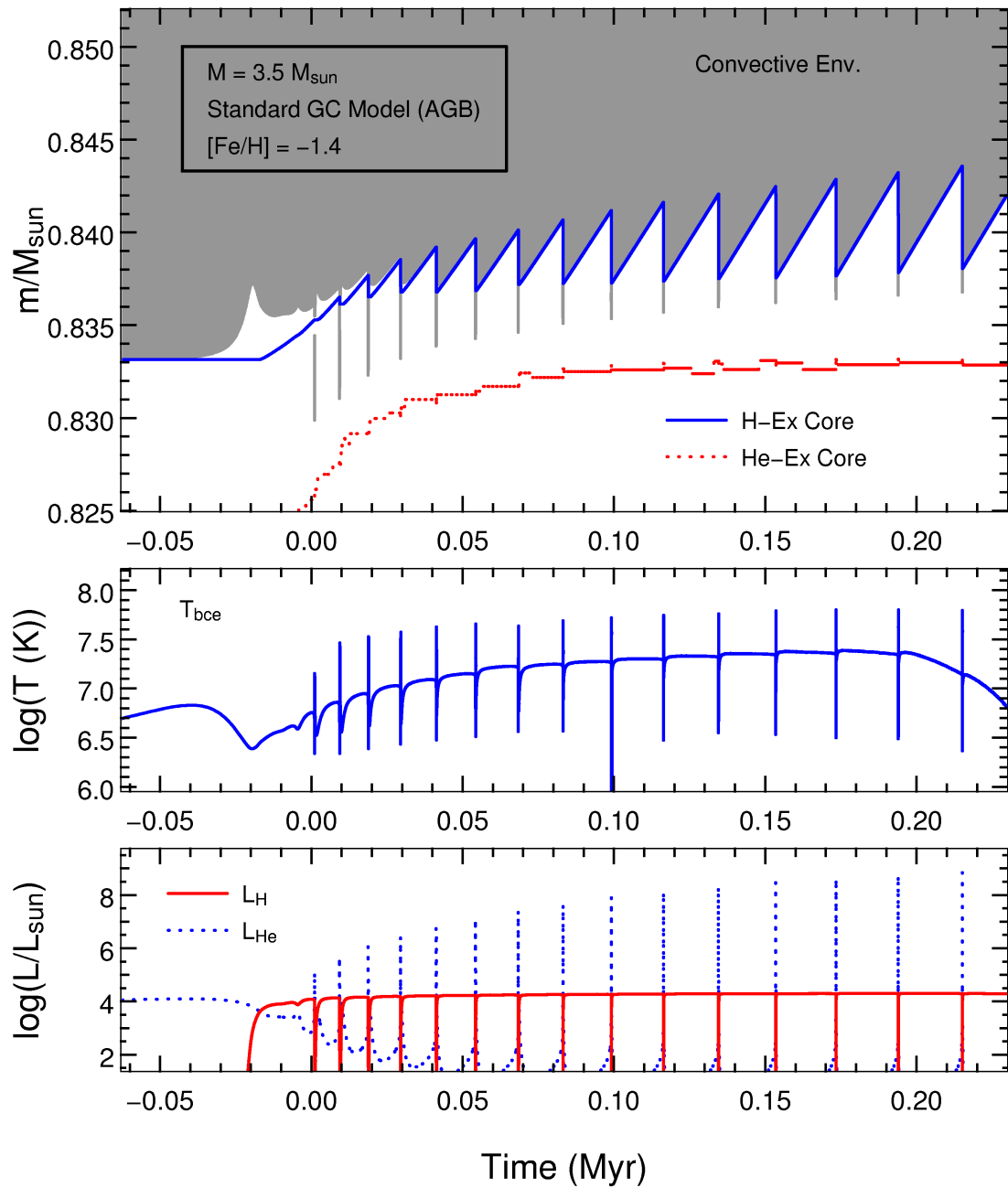


Figure 8.1: Most of the AGB evolution of our standard GC model of $3.5 M_{\odot}$. Time has been offset. It can be seen in the top panel that this model experiences deep 3DUP, with $\lambda \sim 0.98$. The temperature at the base of the convective envelope (second panel) is only high enough for minor HBB, so this model becomes a carbon star during the AGB.

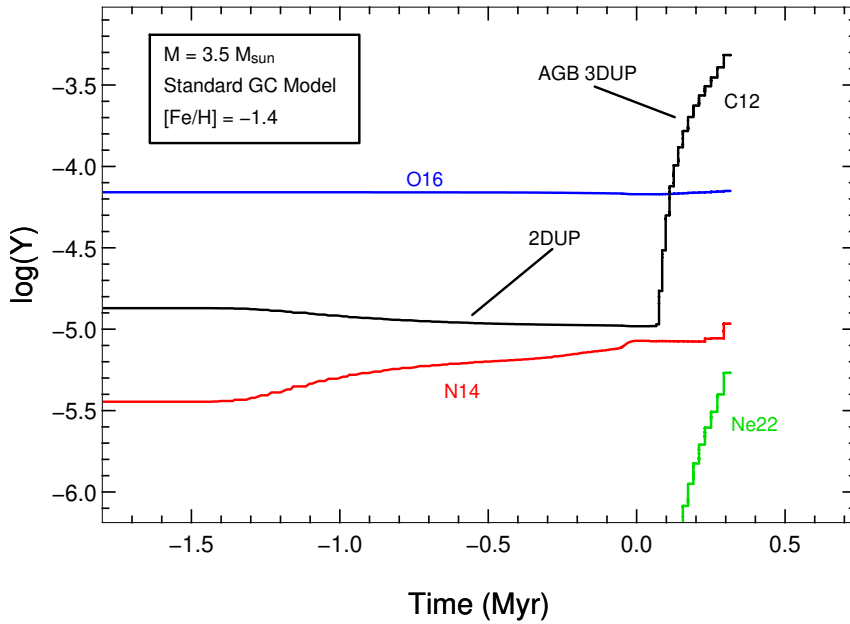


Figure 8.2: The surface abundance evolution of some of the CNO isotopes and ^{22}Ne in our standard GC model of $3.5 M_{\odot}$. Time has been offset. Included in the timeframe is the 2DUP phase where ^{14}N -rich material is dredged up into the envelope. The stepwise increase in ^{12}C and ^{22}Ne is due to 3DUP of intershell material. The temperature at the base of the convective envelope is only high enough for minor HBB, as can be seen in the constancy of ^{16}O and ^{14}N during the AGB.

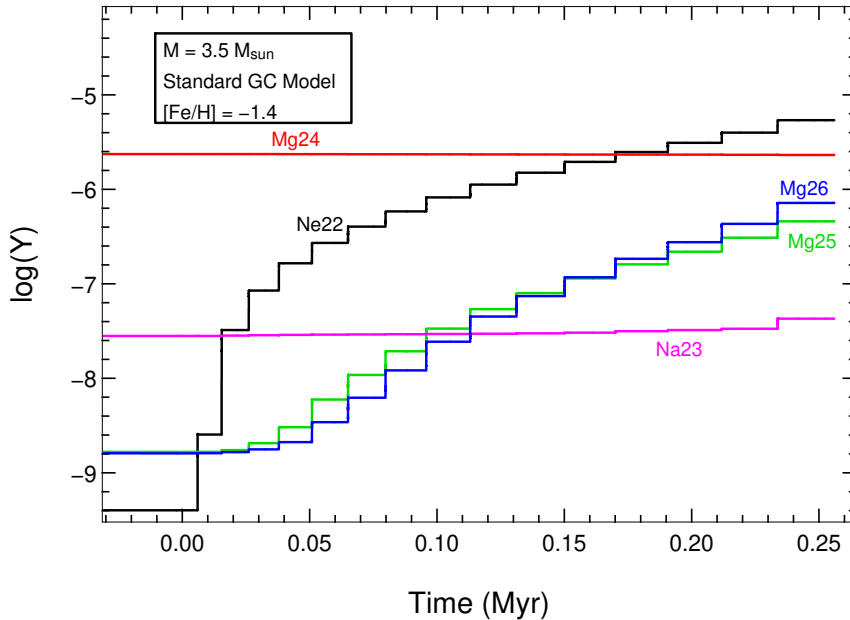


Figure 8.3: The surface abundance evolution of some of the Mg isotopes, ^{22}Ne and ^{23}Na in our standard GC model of $3.5 M_{\odot}$. Time has been offset. The stepwise increase in the Mg isotopes is due to 3DUP of intershell material. It can be seen that ^{23}Na only increases very marginally. No significant Na-O anticorrelation is present in this model.

also produced in large amounts (^{24}Mg is depleted slightly). Thus our models show a *positive* correlation between Mg and Al – which is not present in the observations.

Figure 8.7 shows the yields for all the stars in our standard-model grid. We show the yields for each element (relative to solar) against the initial mass of each model. This gives a clear idea of the mass dependence of the yields. Starting at the lower masses it can be seen that C is between ~ 1 and 2 dex super-solar in the yields. In general it is more prevalent in the lower mass yields ($M \leq 3.5 M_{\odot}$), due to the fact that deep dredge-up occurs in these models and there is no HBB to destroy it. The higher-mass model yields have on average less C but they are still enhanced by ~ 1 dex above solar (and ~ 0.7 dex above the initial composition). N is enhanced in all the models. In the low mass models it is first and 2DUP that does this. N is more abundant at higher masses due to HBB CN(O) cycling. Oxygen follows a clear pattern with initial stellar mass. In the lower mass models it is unchanged, whilst the higher mass models burn it via the ON cycle during HBB. It can be seen that the higher the mass the more O is depleted, due to the increasing T_{bce} . Interestingly oxygen ends up at the solar abundance (relative to Fe) in the $6.5 M_{\odot}$ model. Na is produced mainly in the higher mass models due to HBB of dredged-up ^{22}Ne (the $2.5 M_{\odot}$ is an exception at low mass, it has produced a significant amount of Na, but less than the higher mass models). Magnesium and Al do not start increasing over the initial abundance until $M \sim 3.5 M_{\odot}$. In the 5 and $6.5 M_{\odot}$ model yields it is enhanced by ~ 1 dex. As mentioned above this tandem increase is the opposite to that seen in the NGC 6752 stars. Finally we note that phosphorous is very enhanced in most of the yields, peaking at ~ 3 dex above the initial composition in the $5 M_{\odot}$ model.

8.2.2 Models Varying Mass-Loss Rates and Reaction Rates

Overview

In order to estimate the sensitivity of our results to two of the major uncertainties in the model calculations, we calculated two sets of comparison models in which we altered:

1. Some of the reaction rates used in the NS code.
2. The mass-loss formula used during the AGB phase in the SEV code.

Two representative models were calculated for each set, with masses of 2.5 and $5.0 M_{\odot}$. In the first comparison set we altered the rates used for the Mg-Al, Ne-Na chains/cycles and that for the $^{22}\text{Ne} + \alpha$ reactions. The standard rates were replaced with those from the NACRE compilation (Angulo et al. 1999). In the second comparison set we altered the mass loss formula on the AGB from that of Vassiliadis and Wood (1993) to that from Reimers (1975) (with $\eta_{AGB} = 3.5$).

Results

In Figure 8.8 we show the yields from the three sets of models – the two sets just described above, plus the standard set. The elements pertaining to the Na-O and Mg-Al anticorrelations in NGC 6752 are displayed. It can be seen that altering the reaction rates had very little effect

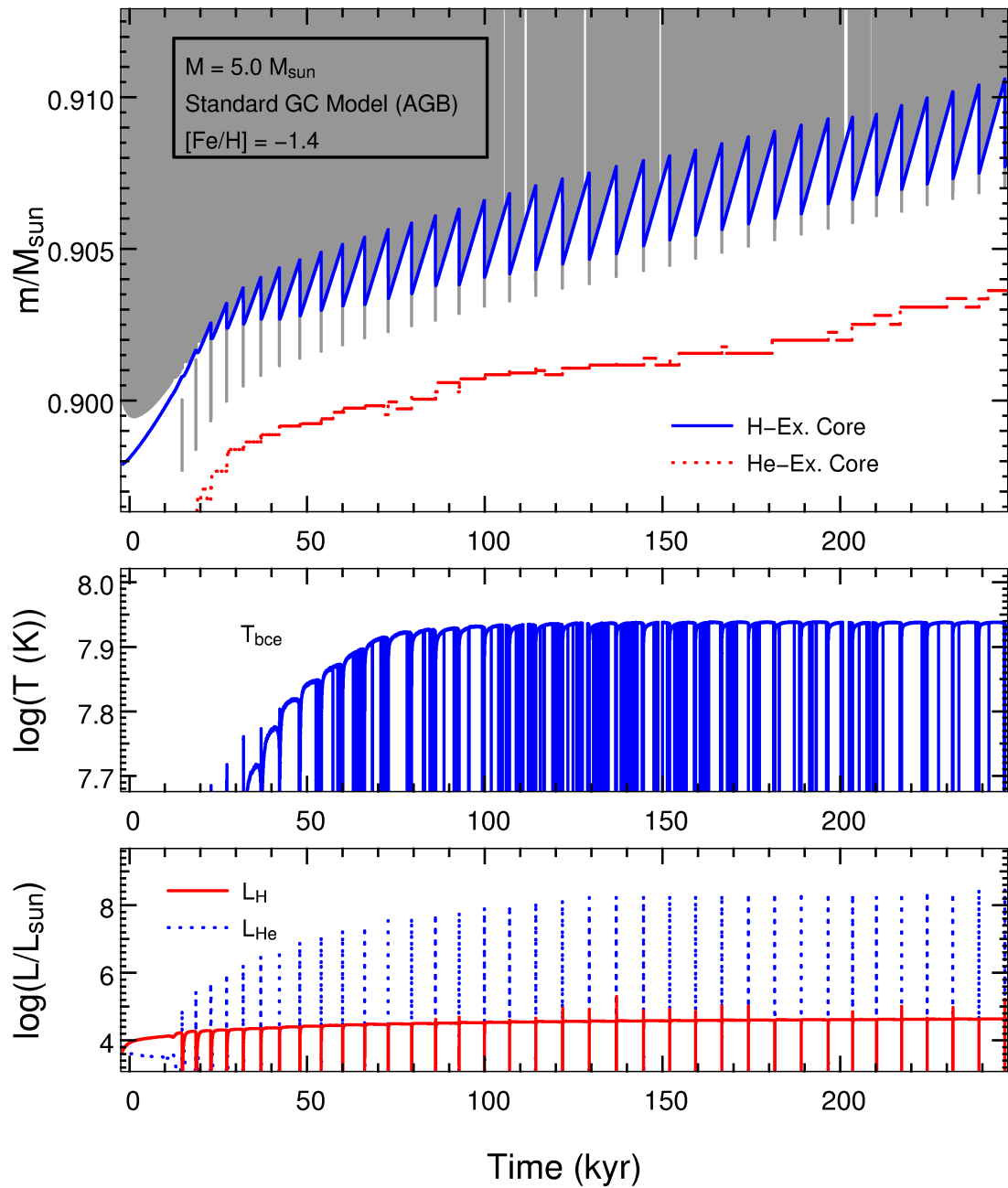


Figure 8.4: About half of the AGB evolution of our standard GC model of $5.0 M_{\odot}$ (this model experiences ~ 80 thermal pulses in total). Time has been offset. It can be seen in the top panel that this model experiences deep 3DUP, with $\lambda \sim 0.9$. The temperature at the base of the convective envelope (second panel) approaches 10^8 K – so strong HBB occurs.

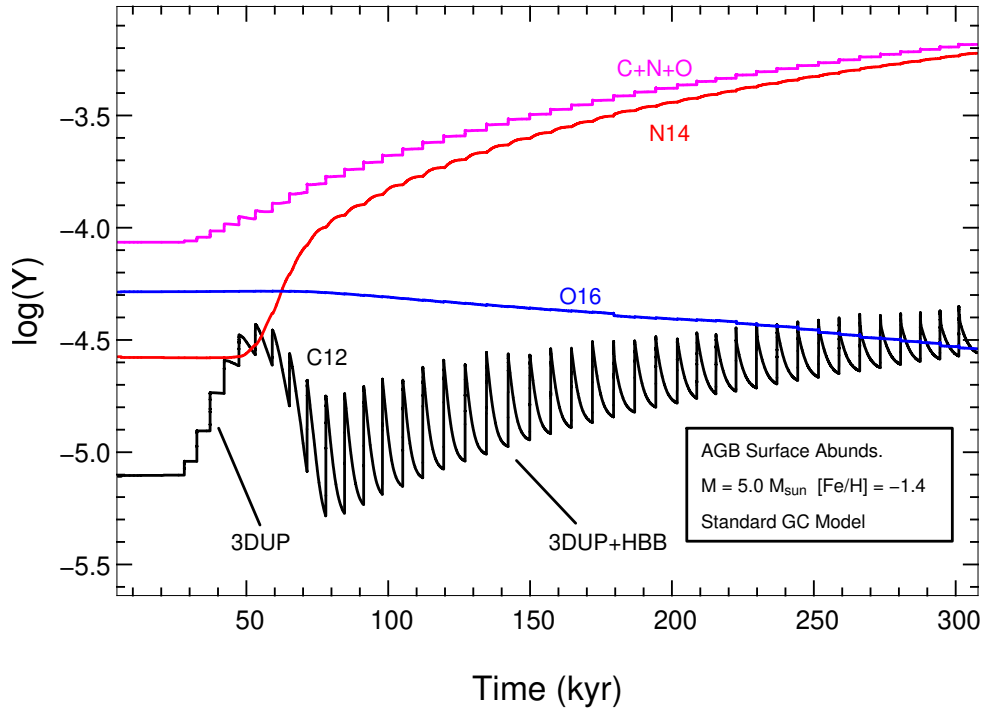


Figure 8.5: The surface abundance evolution of some of the CNO isotopes and the sum of C+N+O in our standard GC model of $5.0 M_{\odot}$. Time has been offset. An initial increase in ^{12}C and can be seen at the start of the AGB before the temperature at the bottom of the convective envelope increases and HBB sets in. Then the ^{12}C is converted to ^{14}N which increases substantially. ^{16}O is also seen to reduce, indicating that O \rightarrow N cycling is operating as well.

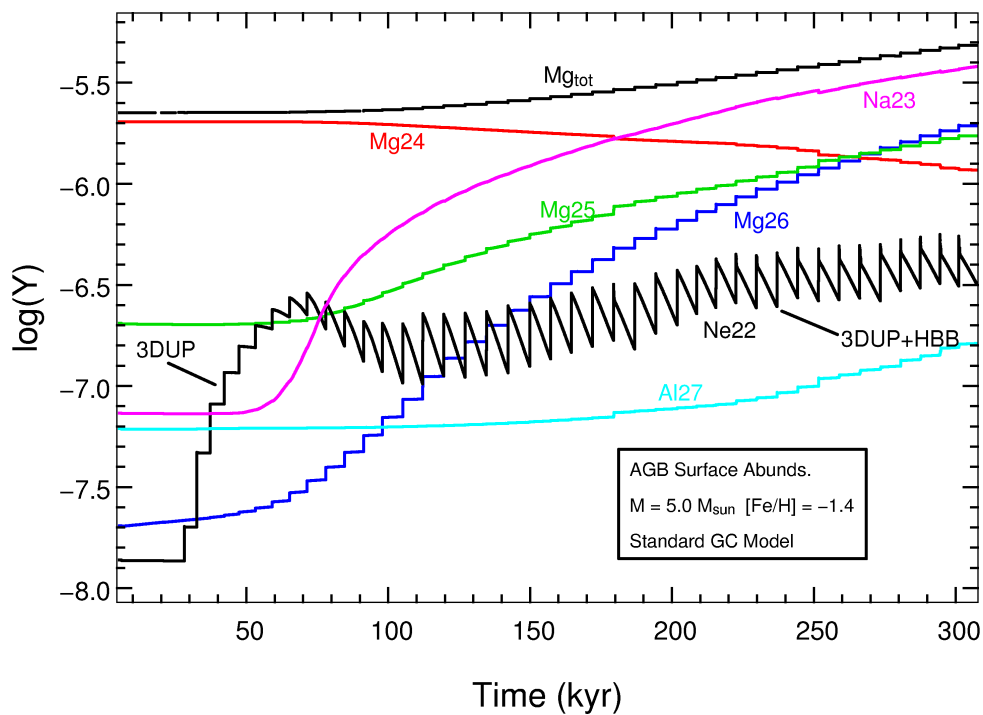


Figure 8.6: The surface abundance evolution of some of the Mg isotopes, ^{22}Ne and ^{23}Na in our standard GC model of $5.0 M_{\odot}$. Also plotted is the sum of the Mg isotopes (Mg_{tot}). Time has been offset. Here we can see the HBB of ^{22}Ne to ^{23}Na (when the temperature increases at $t \sim 70$ kyr), as well as the dredge-up of the heavy Mg isotopes and the HBB destruction of ^{24}Mg . This model shows a nett increase in Mg and Al.

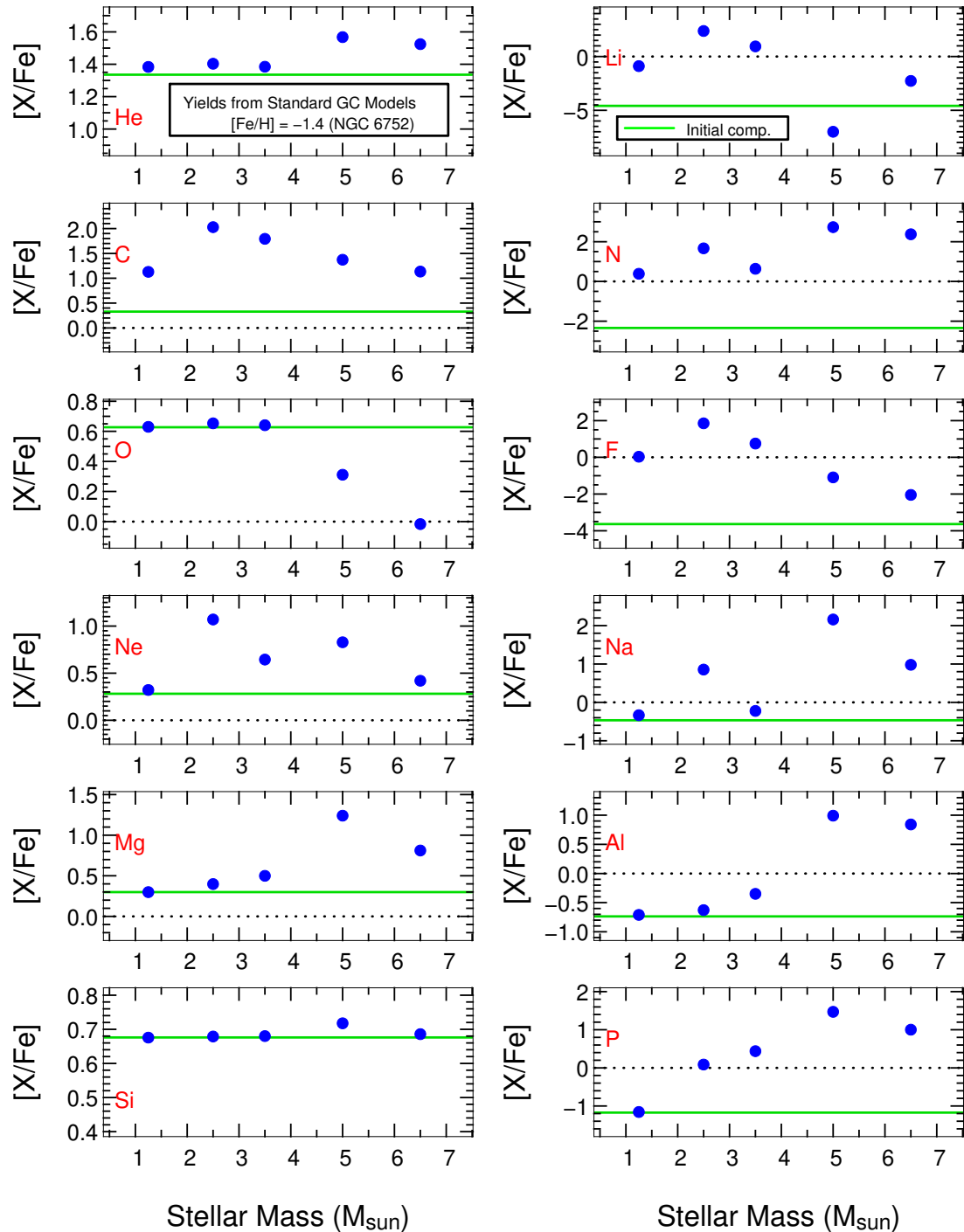


Figure 8.7: The yields of all the standard GC models, relative to solar, for a selection of elements. The green horizontal lines show the initial composition of the models.

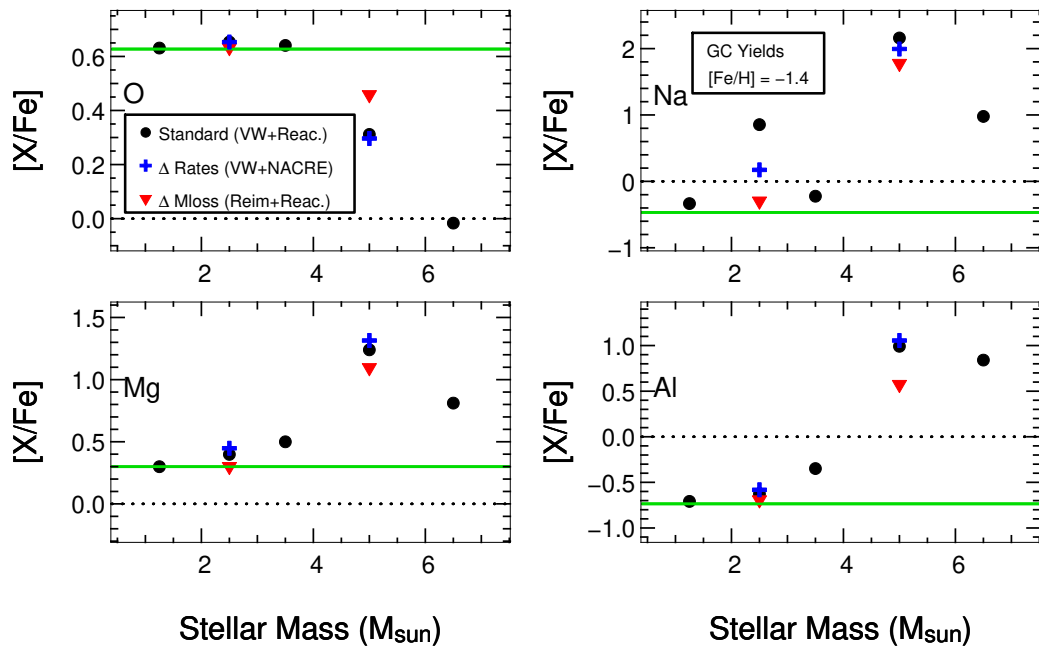


Figure 8.8: Comparing the standard yields (black circles) with those from the models that used the Reimers’ mass loss formula on the AGB instead of VW93 (red triangles) and those from the models that used the NACRE rates for the Ne-Na and Mg-Al cycles/chains (blue crosses). It can be seen that altering the mass loss rate had the most effect on the yields.

on the final yields. The only exception is the Na production in the $2.5 M_{\odot}$ model, which was lowered. However, even in this case, it is the mass-loss formula for the AGB that had the greatest impact on the yields. Sodium yields are significantly higher with the [Vassiliadis and Wood \(1993\)](#) (VW93) mass-loss formula, owing to the increased number of third dredge-up episodes that progressively increase the Na abundance at the surface, and to the fact that much of the convective envelope is lost during the final few thermal pulses (the ‘superwind’ phase) – when the surface abundance of Na is at its highest. Since mass-loss is more evenly spread through the AGB phase when using the [Reimers \(1975\)](#) formula, more material is lost earlier on in the AGB phase, prior to the high envelope abundance of Na. Looking at oxygen we see that the use of Reimers’ mass-loss reduces the oxygen destruction. This is because depletion of ^{16}O in the envelopes is due to HBB, which operates for a shorter time in models with Reimers mass-loss (due to the faster initial mass-loss rate as compared to VW93).

In summary it appears that the mass loss uncertainties are more important than the reaction rate uncertainties – at least in the case of these particular elements. We however add a caveat that further alterations of reaction rates may alter this conclusion. For example the large uncertainty in the $^{26}\text{Mg}(p,\gamma)^{27}\text{Al}$ reaction rate may allow more production of ^{27}Al , at the expense of ^{26}Mg ([Arnould et al. 1999](#)). This would probably not effect the broad outcome of the models – that Mg production is correlated with Al and that Na is anticorrelated with O – but it is worth testing. We will pursue this in a future study.

8.3 GC Chemical Evolution with AGB Yields

8.3.1 Abstract

Here we make a brief report on our test of the popular theory that the observed abundance anomalies in the Galactic globular cluster NGC 6752 are due to ‘internal pollution’ from intermediate mass asymptotic giant branch stars. For a more detailed report we refer the reader to the main article by [Fenner et al. \(2004\)](#), of which I am the second author. In the test we used a chemical evolution model to track the composition of the intracluster medium over time. Custom-made stellar evolution models were calculated using an earlier version of the SEV code (with updated opacities but no time-dependent mixing) and the nucleosynthesis was calculated with the current version of the NS code (these models were just presented in Section 8.2). Yields from these calculations were used as feedback in the chemical evolution model. A novelty of this study is that the stellar evolution of the second generation stars was calculated using the appropriate composition (not scaled-solar), as given by the chemical evolution model itself. By tracing the chemical evolution of the intracluster gas we were able to test the internal pollution scenario, in which the Na- and Al-enhanced ejecta from intermediate mass AGB stars is either accreted onto the surfaces of other stars, or goes toward forming new stars.

We found that our model *cannot* account for the Na-O *or* Mg-Al anticorrelations. In addition, we found that the sum of $C + N + O$ should vary by up to an order of magnitude (between stars with varying levels of anomalies) if the pollution is coming from AGB stars. However, the sum is observed to be (roughly) constant in globular clusters for which this has been measured. Thus the results of our model do not compare well with observational data — the qualitative theory is not supported by this quantitative study.

8.3.2 The Pollution Model

As heavy elements are primarily produced by massive stars, the observations of GCs suggest that there was a generation of massive stars which polluted the pristine protocluster gas, followed by a later release of lighter elements, presumably from lower mass stars. In our model we assume a two stage star formation/pollution history, similar to that used in the dynamical evolution study by [Parmentier et al. \(1999\)](#). We now describe those two stages.

Stage 1: Initial Pollution by ‘Generation A’ (Pop. III) Stars

The initial mass distribution used to model the first stars that pollute the primordial gas was based on the work of [Nakamura and Umemura \(2001\)](#). They predict a bimodal initial mass function (IMF) for a $Z=0$ population. In addition to being bimodal, it is also ‘top-heavy’, favouring massive star formation.

Stellar yields were taken as input for the chemical evolution (CE) model. The yields of [Umeda and Nomoto \(2002\)](#) were used for the $150 \rightarrow 270 M_{\odot}$ range, [Chieffi and Limongi \(2002\)](#) for the $13 \rightarrow 80 M_{\odot}$ range, and [Karakas \(2003, private communication\)](#) for the intermediate mass stars

(nb: these were $Z = 0.0001$ models rather than $Z = 0$ models but they played a negligible role in polluting the early cluster due to the top-heavy IMF).

Star formation occurred in a single burst, with newly synthesised elements returned on timescales prescribed by mass dependent lifetimes (Guesten and Mezger 1982). In this way the cluster gas was brought up to $[\text{Fe}/\text{H}] = -1.4$ (the yields were diluted with pristine Big Bang material), which is the current value (see e.g. Gratton et al. 2001). The next generation of stars formed from this polluted gas.

Stage 2: Pollution by ‘Generation B’ Stars

Stage 2 in the model sees a population of stars forming from a mix of the ejecta of the $Z = 0$ stars (from stage 1) and Big Bang material. A standard IMF (Kroupa et al. 1993) was adopted for Generation B. However, it was assumed that the GC only retained the ejecta from stars with mass $< 7 M_{\odot}$ – the winds and ejecta from SNe are assumed to have escaped the system due to their high velocities. Thus only the yields from intermediate mass stars impact upon the chemical evolution from then on. Yields from a specifically calculated grid of models were used as self-consistent feedback in the CE model (the models from Section 8.2 of the current study).

8.3.3 Generation B AGB Stars

The Fiducial Set of Models

This generation of stars has a unique chemical composition given by the first stage of pollution - they lack nitrogen, are α -enhanced, and are of low metallicity. The models were computed using the exact (non-scaled-solar) composition that resulted from the evolution of the chemical pollution model described above. This required removing all scaled-solar assumptions from the codes and computing new opacity tables specifically for these stars. For this ‘fiducial/standard’ set of models, the Reimers (1975) mass-loss law was used during the RGB and the Vassiliadis and Wood (1993) law during the AGB (see Section 8.2 for more details on these models).

The Effects of Switching Reaction Rate Compilations & Mass Loss Rates

To estimate the sensitivity of the GCCE model to the various prescriptions used in the stellar model calculations, some experiments were run in which the following were altered: 1) the reaction rates for the NeNa chain, MgAl chain and Ne22 + α reactions and 2) the mass-loss formula used for the AGB evolution. Reaction rates and mass-loss are two of the key uncertainties in the stellar models (these models were presented in Section 8.2). It was found that altering the mass-loss formula on the AGB had a greater impact on the stellar yields than changing reaction rate compilations. The effects of these changes are further diluted when the yields are integrated in the CE model.

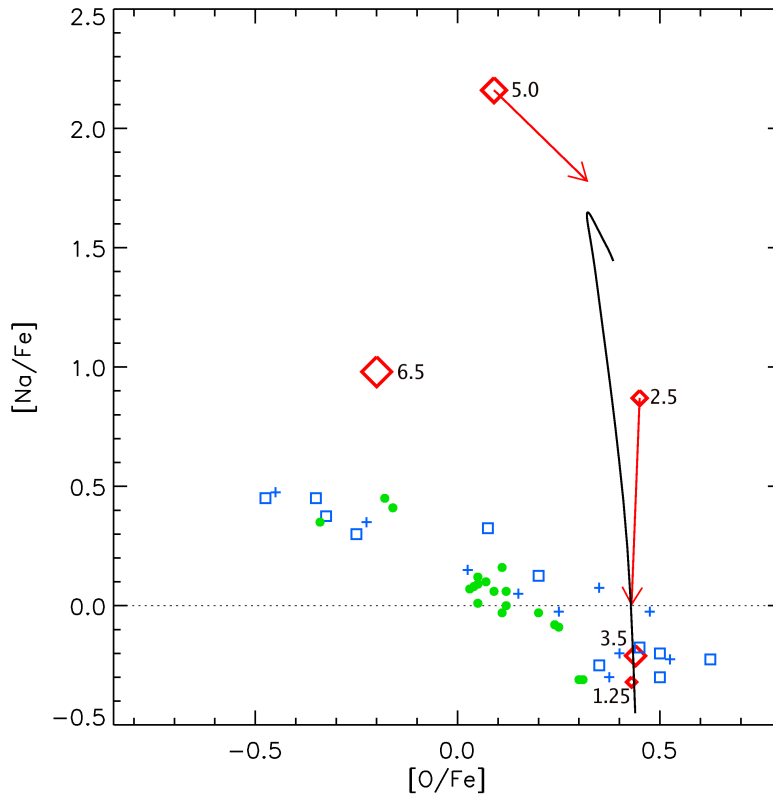


Figure 8.9: The O-Na anticorrelation in NGC 6752. The solid line is the predicted trend given by tracking the chemical evolution of the intracluster medium in the CE model. Blue and green symbols are the observational data (from Grundahl et al. 2002 and Yong et al. 2003 respectively), while the diamonds are the AGB yields (initial stellar masses are marked, in M_{\odot}). The red arrows indicate the change due to the use of Reimers' mass-loss law on the AGB (instead of VW93). Note that oxygen is shifted ~ 0.2 dex compared to our yields plots in Section 8.2 due to the use of a different Solar oxygen abundance (to keep in line with that used for plotting the observations). [Figure courtesy of Yeshe Fenner, Harvard University, USA. Also see Fenner et al. (2004).]

8.3.4 Results

Figure 8.9 compares the GCCE model results with observational data for the O-Na anticorrelation. As can be seen, the predicted variations in Na and O do *not* match the observations. The spread in Na is easily achieved (actually too much is produced), but the oxygen is not depleted enough. Although O is significantly depleted in the 5.0 and 6.5 M_{\odot} stellar models, through HBB on the AGB, these stars are not very numerous in a standard IMF. Biasing the IMF towards higher mass AGB stars may allow the matching of the Na-O anticorrelation but the Mg-Al anticorrelation would still be a problem. This anticorrelation is not matched by the model either (see Figure 8.10). The increase in Al is achieved (although offset), but the Mg *also* increases – which the opposite to the observations (which show Mg decreasing as Al increases).

In addition to these problems, we note that HBB AGB stars are known to produce primary C (which arrives at the surface via 3DUP). Indeed, AGB stars are predicted to enhance the abundance of C by about an order of magnitude. This alters the sum of C+N+O in the polluting material (which CNO cycling alone does not do). Therefore, if it is these stars supplying the material for the GC pollution, we would expect a variation in the sum of C+N+O from star to

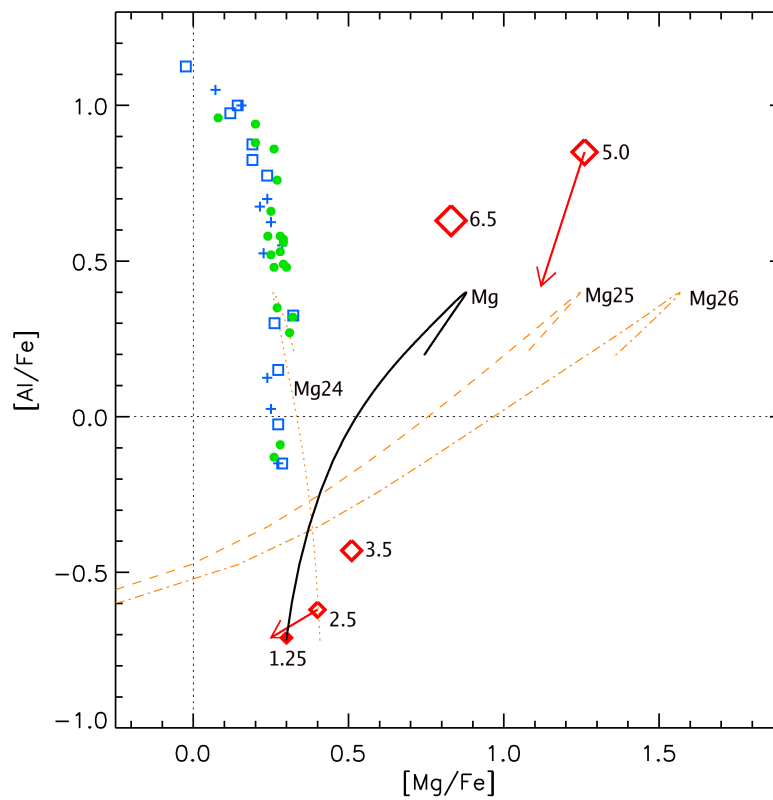


Figure 8.10: Same as Figure 8.9 except for the Mg-Al anticorrelation in NGC 6752. Chemical evolution tracks are shown for the Mg isotopes as well as total Mg. It can be seen that the CE model predicts a *positive* correlation rather than an anticorrelation between these elements. [Figure courtesy of Yeshe Fenner, Harvard University, USA. Also see Fenner et al. (2004).]

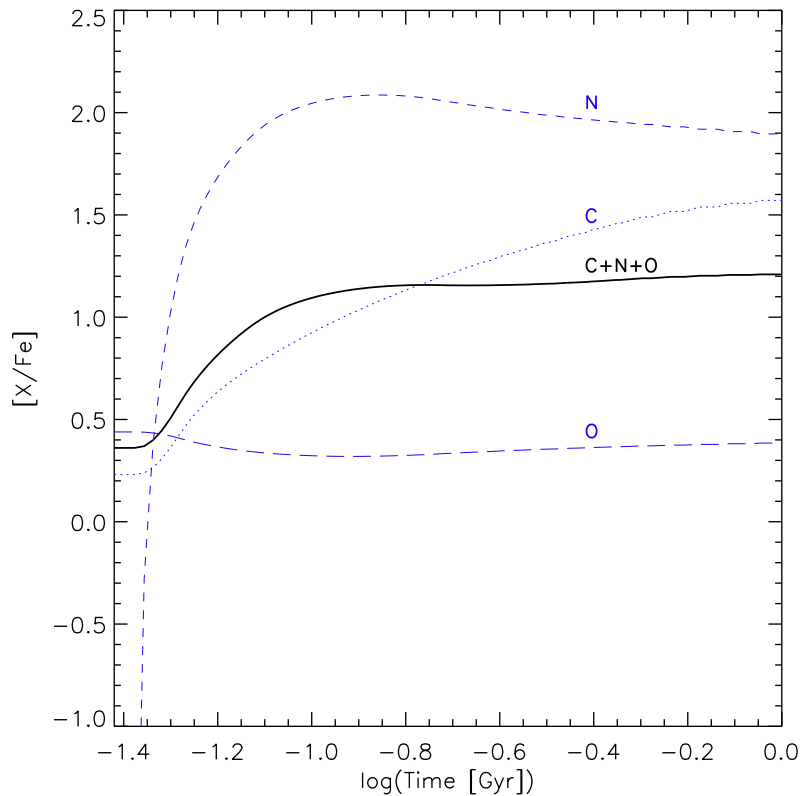


Figure 8.11: The time evolution of C, N, O and the sum C+N+O in the chemical evolution model. It can be seen that the model predicts a ~ 1 dex variation in C+N+O – which is not observed. [Figure courtesy of Yeshe Fenner, Harvard University, USA. Also see [Fenner et al. \(2004\)](#).]

star, depending on the amount of polluting material each has received. The CE model results in Figure 8.11 support this prediction.

However, C+N+O has been observed to be (at least roughly) constant in all clusters measured so far (eg. in M4, [Ivans et al. 1999](#); M13, [Smith et al. 1996](#); and M92, [Pilachowski 1988](#)). Thus, unless GC AGB stars do not undergo 3DUP, this is a strong argument against AGB pollution causing the anomalies.

8.3.5 Summary

Using detailed nucleosynthetic yields we have computed the chemical evolution of the intracluster medium in the globular cluster NGC 6752. Abundance spreads in Na and Al were found, however too much Na was produced, while the Al was offset from the observations. The O-Na and Mg-Al anticorrelations were not matched. In particular, neither O nor Mg are sufficiently depleted to account for the observations. Altering the IMF to favour more massive AGB stars may allow the matching of the Na-O anticorrelation but the Mg-Al anticorrelation would still be a problem. Furthermore, stars bearing the imprint of AGB ejecta are predicted to be strongly enhanced in CNO nuclei (ie. the sum of C+N+O), also in conflict with the observational data. Thus, although the second generation intermediate-mass AGB stars do show the hot hydrogen burning (via HBB) that is required to explain the observations, this quantitative study suggests that HBB in AGB stars may *not* be the site. Altering the mass-loss prescriptions and reaction

rate compilations in the stellar models does not alter this conclusion. We note however that the single stellar models of Ventura and D’Antona (2005b) do come close to matching the abundance anomalies. This is due to their use and development of an alternative theory of convection, which alters the evolution of their models significantly (see eg. Ventura and D’Antona 2005a for details). It would be interesting to see a chemical evolution study using their models, to see if the (partial) match is maintained when convolving with an IMF.

8.4 Models of NGC 6752 Stars *Without 3DUP*

8.4.1 Motivation

Current standard models of intermediate-mass AGB stars with third dredge-up (3DUP) do not reproduce the observed C-N, O-Na or Mg-Al inverse-correlations observed in most GCs. This is supported by the models presented earlier in this chapter (also see Fenner et al. 2004). We note however that the models of Ventura and D’Antona (2005b) do come close, due to their use and development of an alternative theory of convection, which alters the evolution of their models significantly (see eg. Ventura and D’Antona 2005a for details). In the standard models the combination of hot bottom burning (HBB) and 3DUP during AGB evolution does predict enhancements of nitrogen, sodium and aluminium, and a reduction in oxygen – all of which are needed to explain the observations – however they also predict an increase of carbon and magnesium, giving positive C-N and Mg-Al correlations which is in direct violation of the observations. In addition to this the models do not *quantitatively* account for the large degree of O depletion and tend to over-produce Na, thus falling short of the mark with the O-Na inverse-correlation as well (e.g., Denissenkov et al. 1997; Denissenkov and Herwig 2003; Ventura et al. 2004). Furthermore, the standard AGB models produce ejecta with an overall increase in CNO nuclei of ~ 1 to 3 dex (mainly due to the dredge-up of carbon), whilst observations show that the sum of CNO nuclei is virtually constant, varying by a factor of only two or so at most (e.g., Pilachowski 1988; Smith et al. 1996; Ivans et al. 1999). These discrepancies are based on confronting single stellar models with observations. Taking the evolution of an entire cluster of stars into account – in particular convolving with an IMF – presents further problems as the stars with the prerequisite hot hydrogen burning are few in number when using a standard IMF (e.g., Fenner et al. 2004), whilst these stars need to contribute an amount of polluting material that is a large fraction of the GC mass. Despite all these discrepancies it should be stressed that the AGB pollution scenario should not be dismissed outright just yet, as the models are well known to have many serious uncertainties (eg. the treatment of convection, overshoot, mass loss and the uncertainties in reaction rates). For example the non-standard models of Ventura and D’Antona (2005b), which use a different convection model, can reproduce most of the abundance anomalies, although some overshooting and the adoption of a high mass-loss rate is required. In addition to the uncertainties in the input physics of all stellar models, numerical details can also significantly affect the results. For example, time-stepping during diffusive mixing can cause changes in the stellar structure, hence altering the temperature at the bottom of the convective envelope, and thus the resulting nucleosynthesis and yields (Siess, private communication). Attempts have been made to reconcile the (standard) models with the

observations but have universally ended with a need to ‘tweak’ the relative effects of HBB and 3DUP to an unpalatable degree (e.g., [Denissenkov and Herwig 2003](#); also suggested by [Fenner et al. 2004](#)).

With the results of these stellar modelling studies in mind we have chosen to investigate the limiting case – by calculating yields for AGB models that do not experience any 3DUP. Thus, in models that are hot enough (ie. massive enough), we will see pure HBB as the primary source of the abundance patterns in the yields. By decoupling HBB from 3DUP we hope to shed light on the relative importance of these two processes in shaping the yields, particularly in relation to the Na-O and Mg-Al anticorrelations. In addition to this most of the evidence points to (possibly pure) hot hydrogen burning as the source of the abundance anomalies – which HBB in AGB stars provides.

8.4.2 Inhibiting 3DUP

Although ‘turning off’ 3DUP in our models is ad-hoc, it was surprisingly easy to achieve. By adding an extra physical condition for the determination of convective boundaries – the molecular weight gradient – via implementing the [Ledoux \(1947\)](#) criterion rather than the Schwarzschild criterion we found that no dredge-up at all occurred in our models.

In Section 4.1.6 on page 74 we discussed the SEV code modifications with regards to semiconvection and the addition of the Ledoux criterion. For ease of reference we repeat some details of the changes here.

Given the discussion in Section 4.1.6, we decided to add the Ledoux criterion (Equation 4.20 on page 75) to the SEV code as an alternative option for simulating semiconvection. Our adopted criterion for deciding when a region is semiconvective was:

$$0 < (\nabla - \nabla_{ad}) < \nabla_L \quad (8.1)$$

where

$$\nabla_L = \frac{\beta}{4 - 3\beta} \nabla_\mu. \quad (8.2)$$

The definitions of the rest of the variables are available in Section 4.1.6 on page 74. Since we now treat mixing time-dependently throughout the entire star, it was an easy matter to also treat semiconvective regions in the same manner. This was done by applying slow mixing velocities in the region defined by Equation 8.1. In Section 4.1.6 we pointed out that there is the problem of not knowing how slow/fast to mix. We initially hard-wired a fixed value velocity for semiconvection (a similar tactic to that of [Eggleton 1972](#)). In order to inhibit 3DUP in this case we have chosen a mixing velocity of zero – such that the convective boundary is now a ‘hard’ Ledoux one (we have used no overshoot either). As mentioned above, this was sufficient to inhibit 3DUP totally – in models of all masses considered here.

8.4.3 The Grid of Models

We have calculated four no-3DUP models, with masses 2.5, 3.5, 5.0, 6.5 M_{\odot} . This covers most of the masses of our standard models presented in Section 8.2, so direct comparisons can be made. The initial composition is identical to the standard models.

Input Physics

The version of the SEV code used for these models was the same one used for our $Z = 0$ and EMP models in chapters 5 and 7. In particular it had the updates for time dependent mixing, opacities, diffusive overshoot and choice of convective boundary criteria. As mentioned above 3DUP was inhibited by using the Ledoux criterion for convective boundaries in these models. A couple of other key inputs of note are:

1. Time dependent mixing was always used.
2. No overshoot was used.
3. Scaled-solar opacities were used.

We believe that using time-dependent mixing rather than instantaneous mixing (as used in the standard models) should not have effected the results significantly. Particularly since no very rapid events like the dual flashes of the $Z = 0$ models occur in these models. The use of scaled-solar opacities rather than opacities with the exact composition (as used in the standard models) also has little effect. The suppression of 3DUP is by far the major factor affecting the results of these models. The non-use of overshoot helps with this suppression.

In regards to the nucleosynthesis we used the same nuclear reaction rates as those used in the standard models in Section 8.2. As mentioned there altering the rates had little effect on the yields.

8.4.4 Results

AGB Surface Abundance Evolution

In Figure 8.12 we show the surface abundance evolution of the main CNO isotopes in the 5 M_{\odot} model. In contrast to the standard 5 M_{\odot} model (see Figure 8.5 on page 325) it can be seen that there is no initial enrichment of the surface in ^{12}C . This is of course due to the total lack of 3DUP. However the decrease in ^{12}C is seen once T_{bce} increases and HBB sets in. The corresponding increase in ^{14}N is also seen, just as in the standard case. The increase in the no-3DUP case is however much less than in the standard case. Interestingly ^{14}N continues to increase throughout the AGB in the no-3DUP case also, despite the lack of fresh C for CN processing. This is due to significant O \rightarrow N cycling, as can be seen in Figure 8.12. The difference between the final N abundances is very different though. In the standard model ^{14}N increases by ~ 1.5 dex over the abundance at the start of the AGB phase, whilst in the no-3DUP model it only increases by ~ 0.7 dex. Naturally the reason for this is the lack of fresh C and O nuclei to be cycled to

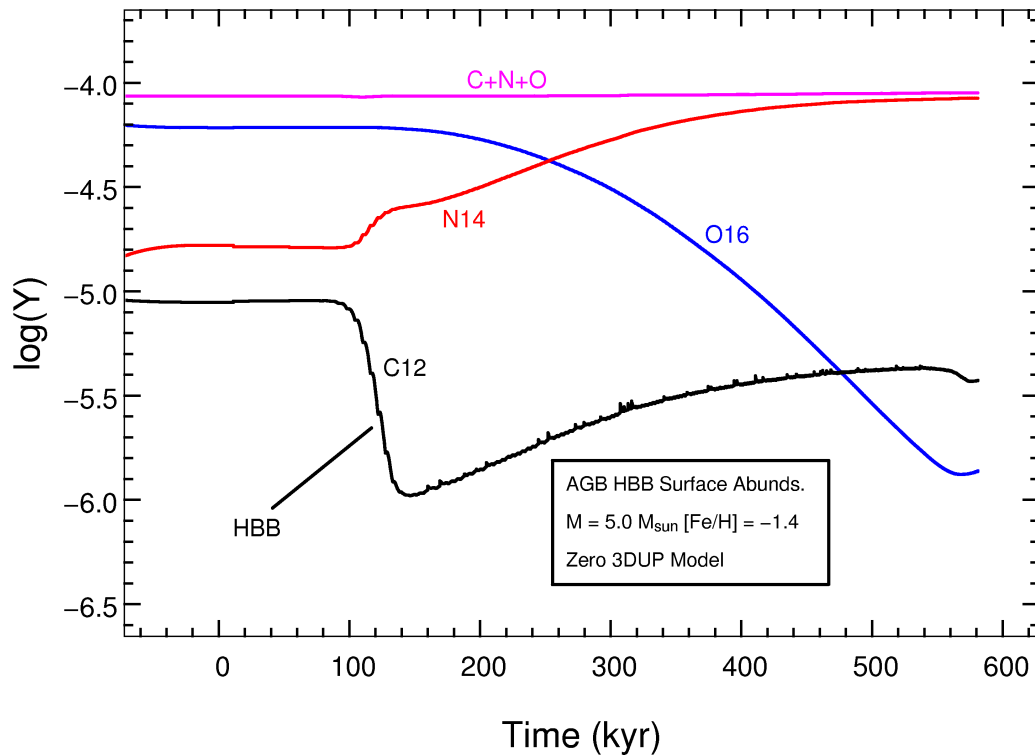


Figure 8.12: Surface abundance evolution of some of the CNO nuclides in the $5.0 M_{\odot}$ no-3DUP model during the AGB. Time has been offset. Also plotted is the sum of C+N+O which can be seen to stay constant despite large changes in its constituents. This is due to the fact that the CNO cycles conserve the number of CNO nuclei.

N in the no-3DUP model. Indeed, it can be seen that the sum of C+N+O is constant in the no-3DUP case, whilst it increases by ~ 1 dex in the standard case. Thus this model satisfies this key observational constraint where the standard model did not. Furthermore, it can be seen that ^{16}O is heavily depleted (by ~ 1.7 dex) in the no-3DUP model. In the standard model is only depleted by ~ 0.3 dex. The reason for this difference is also the lack of 3DUP. In the standard case HBB does deplete oxygen but it is also periodically replenished by 3DUP, so the decrease is moderated. Thus the no-3DUP model satisfies another constraint in the observations of NGC 6572 which show the most extreme stars having O depleted by ~ 1 dex. Moreover, C is seen to be strongly reduced whilst N is enhanced, also matching the observations (the standard models show N *and* C enhancement).

In Figure 8.13 we show the surface abundance evolution of some key isotopes involved in the Ne-Na and Mg-Al cycles/chains. Starting with Ne we see that ^{22}Ne is initially enhanced at the beginning of the AGB. This comes about through the destruction of ^{21}Ne . As the temperature increases ^{22}Ne is itself destroyed, cycling through to ^{23}Na . Likewise, as the temperature increases further, ^{23}Na is cycled through to ^{20}Ne . ^{20}Ne is very abundant ($\log(Y) \sim -5.3$) compared to the other Ne isotopes so its abundance is scarcely enhanced by this addition. Some leakage occurs out of the Ne-Na cycle through $^{23}\text{Na}(p, \gamma)^{24}\text{Mg}$ but this has little effect as ^{24}Mg is (initially) so abundant. The rearrangement of the Mg isotopes is clearly seen in Figure 8.13. ^{24}Mg is almost totally destroyed, mainly ending up as ^{25}Mg via $^{24}\text{Mg}(p, \gamma)^{25}\text{Al}(\beta^+)^{25}\text{Mg}$. Also enhanced by proton captures is ^{26}Mg , at the expense of ^{25}Mg and ^{27}Al at the expense of ^{26}Mg . Leakage out of the Mg-Al cycle causes a slight increase in ^{28}Si but this is minor due to its (relatively) large

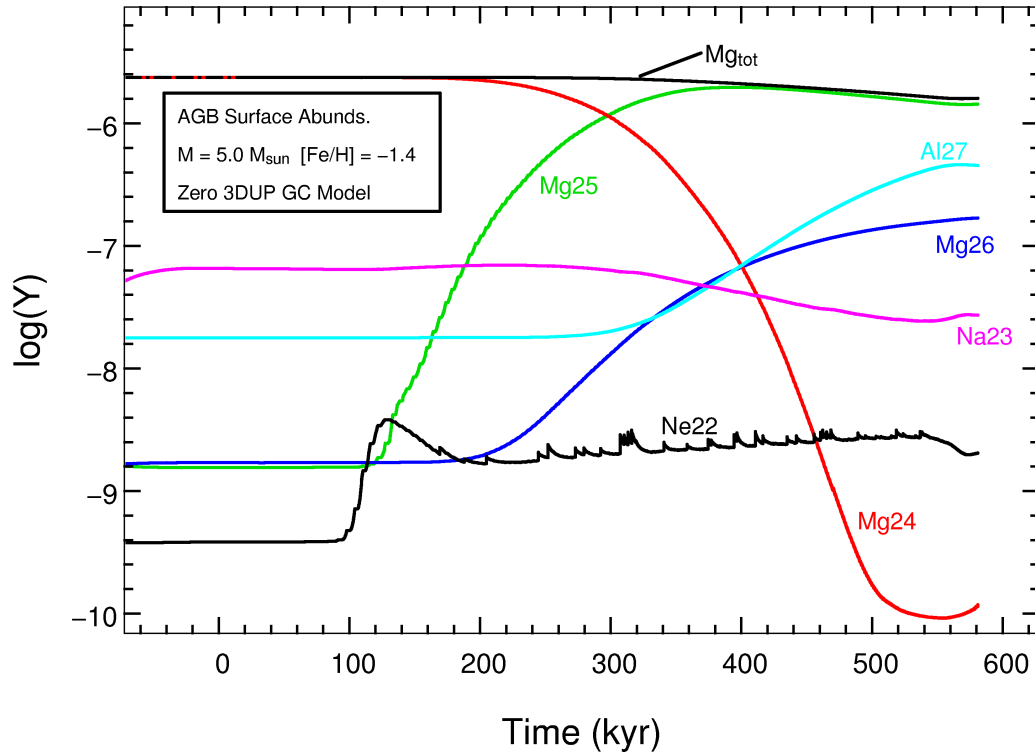


Figure 8.13: Surface abundance evolution of some of the Mg, Al, Ne and Na nuclides in the $5.0 M_{\odot}$ no-3DUP model during the AGB. Time has been offset. Also plotted is Mg_{tot} , the sum of the Mg isotopes. This is seen to reduce slightly towards the end of the AGB. It can be seen that the Mg isotope ratios are very non-solar by the end of the AGB.

initial abundance. It does however cause a small but significant decrease in the total abundance of the Mg isotopes. Thus the elemental Mg abundance reduces, as seen in NGC 6752 stars. Add to this the increase of ^{27}Al and we see that this model shows a Mg-Al anticorrelation, which is again good news for comparing with GCs. This contrasts with the situation in the standard models (see Figure 8.6 on page 325 for the standard $5.0 M_{\odot}$ surface abundance evolution). In that case we saw that the total Mg abundance *increased* by about ~ 0.5 dex, due to the fresh injection of heavy Mg isotopes from each 3DUP episode. Also present in that model is a very large increase in ^{23}Na , due to HBB of dredged-up ^{22}Ne . In the no-3DUP case we see that ^{23}Na actually suffers a net *decrease* (although small) over the AGB lifetime. Given the decrease in oxygen this means Na and O are positively correlated – in contradiction to the observations.

Yields

In Figure 8.14 we present the yields of most of the elements in the network for all our no-3DUP models. Also plotted in this figure are all the yields for the standard set of GC models. This enables a quick comparison that reveals the key role 3DUP plays in the production of many elements. Conversely it also reveals which elements are primarily a product of HBB.

It can be seen that carbon is drastically reduced in the yields of all the no-3DUP models, as compared to the standard models. In fact all the no-3DUP yields show a net decrease in C from the initial abundance. This is due to first dredge-up and 2DUP in the lower mass models. An added factor in the higher mass models is HBB which cycles much of the C to N. Due to

the lack of 3DUP in all the models C can never increase after these events. Nitrogen on the other hand is increased in all the models, as it is in the standard models. In the higher mass models it is however much less enhanced, since there is no 3DUP to provide the C seeds for C \rightarrow N conversion. Indeed, its abundance is limited by the initial C (and O) abundance since the only way it can increase is via CN(O) cycling, which conserves the sum of C+N+O nuclei.

Oxygen exhibits the same pattern as that in the standard models – it decreases with initial stellar mass. The difference here is that O is more severely depleted in the no-3DUP models. As mentioned earlier this is due to the lack of O replenishment by 3DUP that moderates the O reduction. Interestingly fluorine is seen to have a strong dependence on 3DUP – it is consistently lower in the no-3DUP models. The same applies to Ne (as expected). In fact Ne does not change from its initial abundance at all. As mentioned above Na comes from the destruction of ^{22}Ne from 3DUP, so this element is also not enhanced in the no-3DUP yields. Mg shows the opposite trend to that in the standard models – it decreases slightly with initial stellar mass. Interestingly aluminium is present in the yields of the two sets of models in practically the same amounts. Thus it is, in this case, primarily produced by HBB rather than 3DUP. The yields are similar because there is more than enough ^{24}Mg and ^{25}Mg available (Mg is much more abundant than Al initially) for its production via $^{24}\text{Mg}(\text{p},\gamma)^{25}\text{Al}(\beta^+)^{25}\text{Mg}(\text{p},\gamma)^{26}\text{Al}(\beta^+)^{26}\text{Mg}(\text{p},\gamma)^{27}\text{Al}$ or via $^{24}\text{Mg}(\text{p},\gamma)^{25}\text{Al}(\beta^+)^{25}\text{Mg}(\text{p},\gamma)^{26}\text{Al}(\text{p},\gamma)^{27}\text{Si}(\beta^+)^{27}\text{Al}$ in both sets of models.

8.4.5 Discussion

A salient result from our new stellar models is that oxygen is now heavily depleted in the more massive models. Also of importance is the fact that there is now an opposite trend for Mg (in the same stars) – it is depleted instead of produced, whilst Al is still enhanced. Furthermore, the C is depleted whilst the N yield remains quite high. All of these features (except the increase in Al) derive from the lack of 3DUP, as O is now not periodically replenished, C cannot increase and fresh fuel for the MgAl cycle is not available. The lack of 3DUP also allows the sum of CNO nuclei to remain constant, as fresh CNO is not added to the envelope and the CNO burning cycles (occurring at the base of the convective envelope) conserve the number of CNO nuclei. All these features indicate that a better fit to the observations is expected (IMF withstanding). To clearly demonstrate the situation with respect to O-Na and Mg-Al we re-plot these elements together in Figure 8.15. The effect of removing 3DUP is beneficial (in relation to matching the anticorrelations) in all cases – except for sodium. Sodium is observed to be enhanced in some NGC 6752 stars by ~ 1 dex, however in the no-3DUP yields it is barely enhanced at all ($\lesssim 0.2$ dex). In the $6.5 M_{\odot}$ case it is even depleted slightly. Thus, although we can reproduce a large O reduction needed, our no-3DUP models cannot reproduce the Na-O anticorrelation!

At the high masses (ie. temperatures) required to deplete O and Mg via the MgAl and ON cycles, Na is not produced enough, or rather it is destroyed too much by proton captures, resulting in the low yields. Moving to lower masses (temperatures) improves the Na situation (slightly) but prevents O and Mg from being depleted. Interestingly this is the identical problem that Ventura and D’Antona (2005b) have with their best-fit (for the Na-O inverse-correlation) model. Denissenkov and Herwig (2003) also report this problem. We note that the models of Ventura and D’Antona (2005b) are quite independent as they use a different treatment for convection.

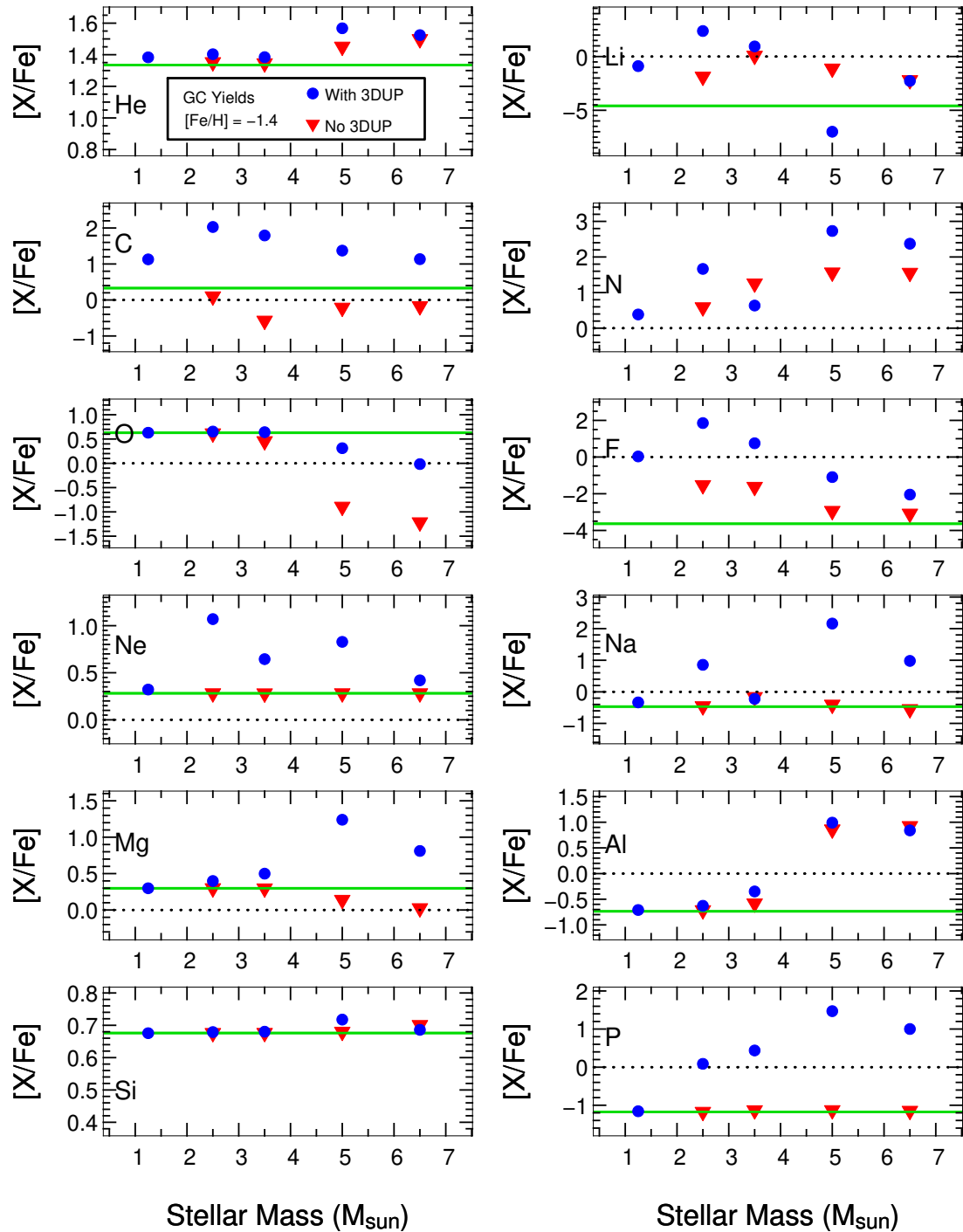


Figure 8.14: Yields of most of the elements in the nuclear network. The yields from the no-3DUP models are shown as red triangles whilst those from the standard models are shown as blue circles. The initial composition of each element is marked by a green horizontal line in each graph.

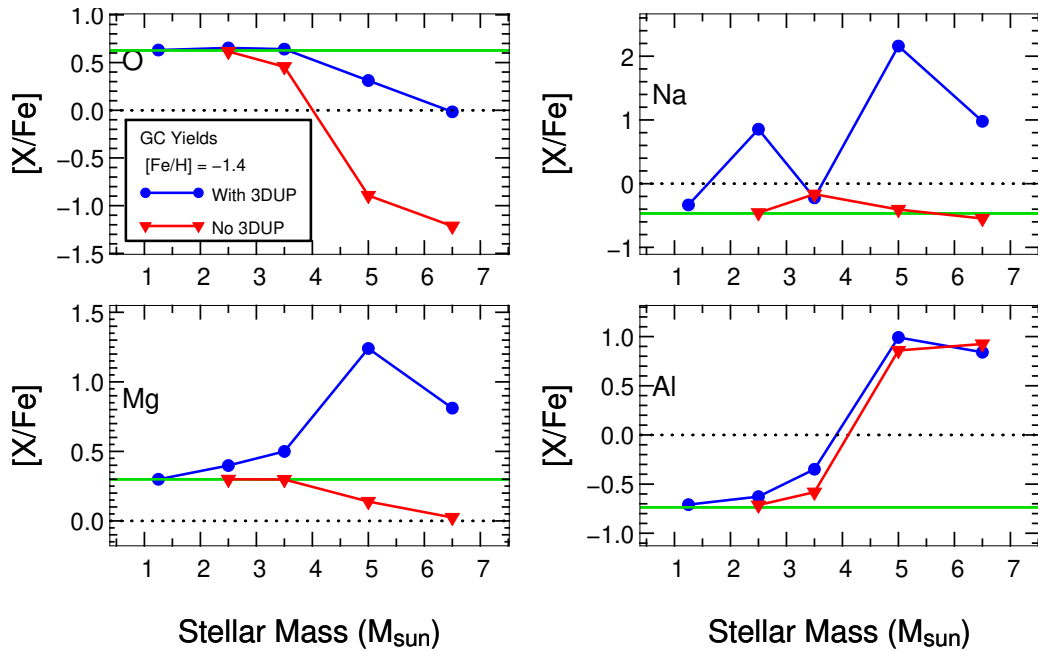


Figure 8.15: Comparing the Na, O, Mg and Al yields from the standard models (blue circles) and the no-3DUP models (red triangles). In terms of the Na-O and Mg-Al anticorrelations in NGC 6752 it can be seen that the lack of 3DUP (1) increases the O destruction, (2) causes a Mg destruction (3) retains the Al production but (4) removes the Na production. Thus these models are a better fit to the observations but problems remain.

In a recent and very timely study [Ventura and D’Antona \(2006\)](#) have investigated this problem in detail, finding that their stellar model requires either the addition of some overshooting or a reduction of the $^{23}\text{Na}(p,\alpha)^{20}\text{Ne}$ reaction rate in order to produce the required Na yield whilst maintaining the O destruction. The [Ventura and D’Antona \(2005b, 2006\)](#) models, like our more ad-hoc models, otherwise match the abundance anomalies fairly well. We highlight this by plotting some of these no-3DUP yields against the observations in [Figures 8.16](#) and [8.17](#). It can be seen in [Figure 8.16](#) that the magnitude of Mg destruction is very similar to that seen in the NGC 6752 stars. The magnitude of increase in Al is also a very good match (the absolute values of Al are easily shifted upwards by using an initial composition that matches the lower-Al observations). Thus it appears that the no-3DUP yields provide a good match to the Mg-Al anticorrelation. However a serious problem actually remains. [Yong et al. \(2003\)](#) have been able to deduce the ratios of the Mg isotopes in the stars of this cluster. They find that the ‘unpolluted’ stars (ie. low Al, low Na stars) show a roughly solar ratio of $^{24}\text{Mg}:^{25}\text{Mg}:^{26}\text{Mg}$ ($\sim 80:10:10$; see eg. [Boyer et al. 1971](#) for the solar ratio), whilst the polluted stars show a ratio of $\sim 60:10:30$. Thus there appears to have been an increase in ^{26}Mg , probably at the expense of ^{24}Mg , whilst ^{25}Mg is constant (in a relative sense – the sum of the absolute abundances has reduced in these stars). Turning to the surface abundance evolution of our models ([Figures 8.6](#) and [8.13](#)) we see at a glance that the Mg isotopic ratios are *extremely* different to those observed! ^{24}Mg is heavily depleted in all the no-3DUP models that produce Al (higher masses), whilst ^{25}Mg is dominant. The ratio in the $5 M_{\odot}$ model *yield* is $\sim 0.1:10:1$, which compares very poorly with the observed ratio. Interestingly the situation is better in the yield from our standard model (of $5 M_{\odot}$). It has a ratio of $\sim 2:10:26$. This model does however still show a huge depletion of ^{24}Mg which is not seen in the observations – not to mention the fact that the standard models have other

problems in explaining the anticorrelations. We are thus in a dire situation with respect to the Mg isotopes, despite having a good fit to the Mg-Al (elemental) anticorrelation. How this can be remedied is a difficult question. A partial solution may be found in using the observed ratios in the unpolluted stars in the initial composition of models. We note however that this would be scaled-solar, which is what most studies usually use anyway. Reaction rate uncertainties are also another avenue to explore. We shall pursue this tantalising mystery in our future work.

In Figure 8.17 we compare the no-3DUP yields with the Na-O anticorrelation observations in NGC 6752. As mentioned earlier oxygen is efficiently depleted in the higher mass models, and much more than in the standard models. In fact our models display O deficiencies much greater than that observed in the stars (up to ~ -1.7 dex in the models versus ~ -1 dex in the observations). This effect may be reduced by dilution effects but we note that the discrepancy is significant. The most serious problem lies however in Na. As discussed above it is barely produced at all – especially in the O-depleted models where it is most needed to match the observations.

8.4.6 Conclusion

In summary we have used these ad-hoc models to investigate the interplay between 3DUP and HBB and the effects they have on the predictions of (anti)correlations from stellar model yields, in the context of the GC abundance anomalies problem. We have found that the yields from the no-3DUP models match the Mg-Al anticorrelation in NGC 6752 well, and also have oxygen significantly depleted, as needed (although too much in some cases). However Na is not produced enough (even depleted in some cases). This is in direct contradiction with the observations. Furthermore, the Mg isotope ratios are very different to those of the observations. In particular ^{24}Mg is always heavily depleted by HBB whilst it is still relatively abundant in the polluted star observations. This occurs at the same temperatures that are needed to produce the Al enhancements and oxygen depletions, making the solution to this problem seemingly impossible to resolve in the AGB HBB scenario (or possibly any pure hydrogen-burning site). Thus, although we appear to have a better fit to the observations with the no-3DUP models, there remains some serious discrepancies. We shall continue with this fascinating (and frustrating) problem in our future studies – one of which is a globular cluster observing project described in the next section.

Finally we note that these models may actually simulate the effects of a previously ignored population of stars, the Super-AGB stars ($8 M_{\odot} \lesssim M \lesssim 11 M_{\odot}$). We may expect the sort of pollution as produced by our no-3DUP models to come from these stars since they are expected to either have either zero or very little 3DUP. Even if they do have 3DUP characterised by a large λ value the pollution visited on their envelopes would be quite small due to their small intershells and massive envelopes (Siess and Doherty, 2007, private communication). They would also probably suffer strong HBB – much like our no-3DUP models (for more information on SAGB stars see eg. [Ritossa et al. 1996](#); [Poelarends et al. 2006](#); [García-Berro et al. 2006](#))

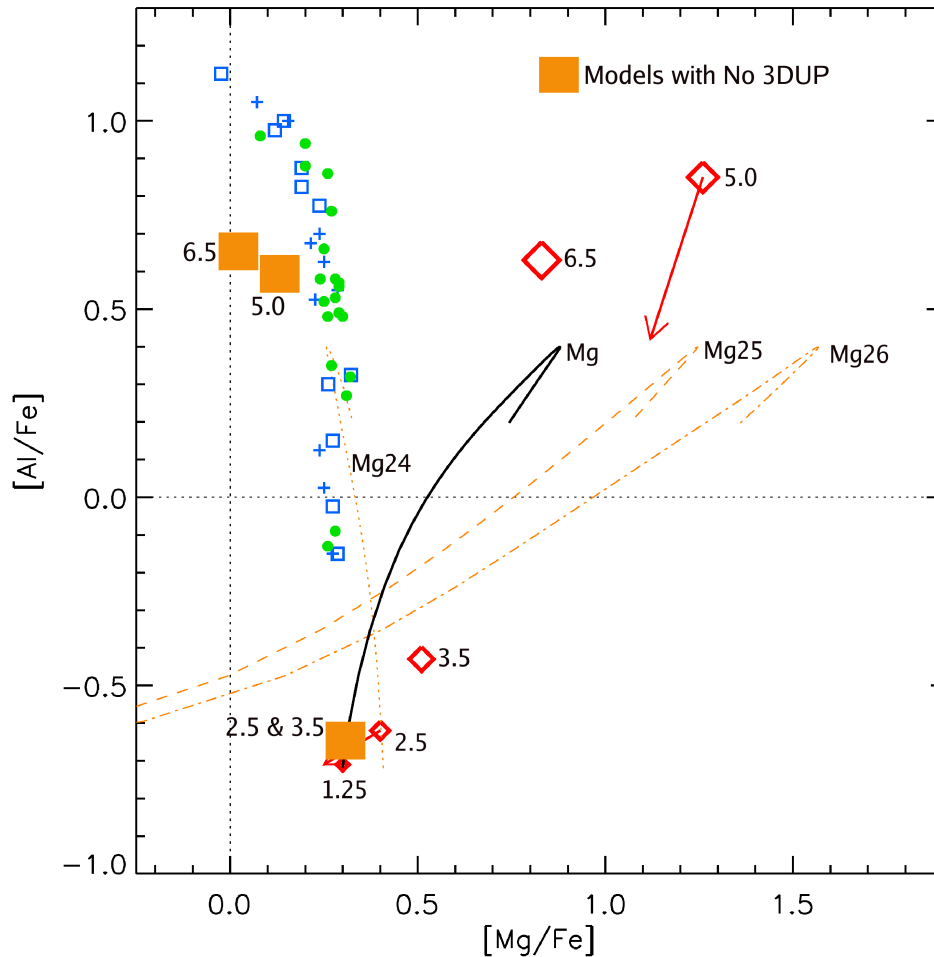


Figure 8.16: The Mg-Al anticorrelation in NGC 6752. Same as Figure 8.10 on page 331 but with our no-3DUP model yields over-plotted (large orange filled squares). Blue and green symbols are the observational data (from Grundahl et al. 2002 and Yong et al. 2003 respectively), while the diamonds are the AGB yields (initial stellar masses are marked, in M_{\odot}). The red arrows indicate the change due to the use of Reimers' mass-loss law on the AGB (instead of VW93). The solid line is the predicted trend given by tracking the chemical evolution of the intracluster medium in the CE model. Chemical evolution tracks are shown for the Mg isotopes as well as total Mg (broken orange lines). It can be seen that, apart from an offset downwards in Al, the no-3DUP yields match well with this anticorrelation. The Al offset would be easily remedied by adopting the Al abundance of the unpolluted stars as the initial composition in the stellar models. We note however that the Mg isotope results from the no-3DUP models are even a worse match than that of the standard models (see text for a discussion).

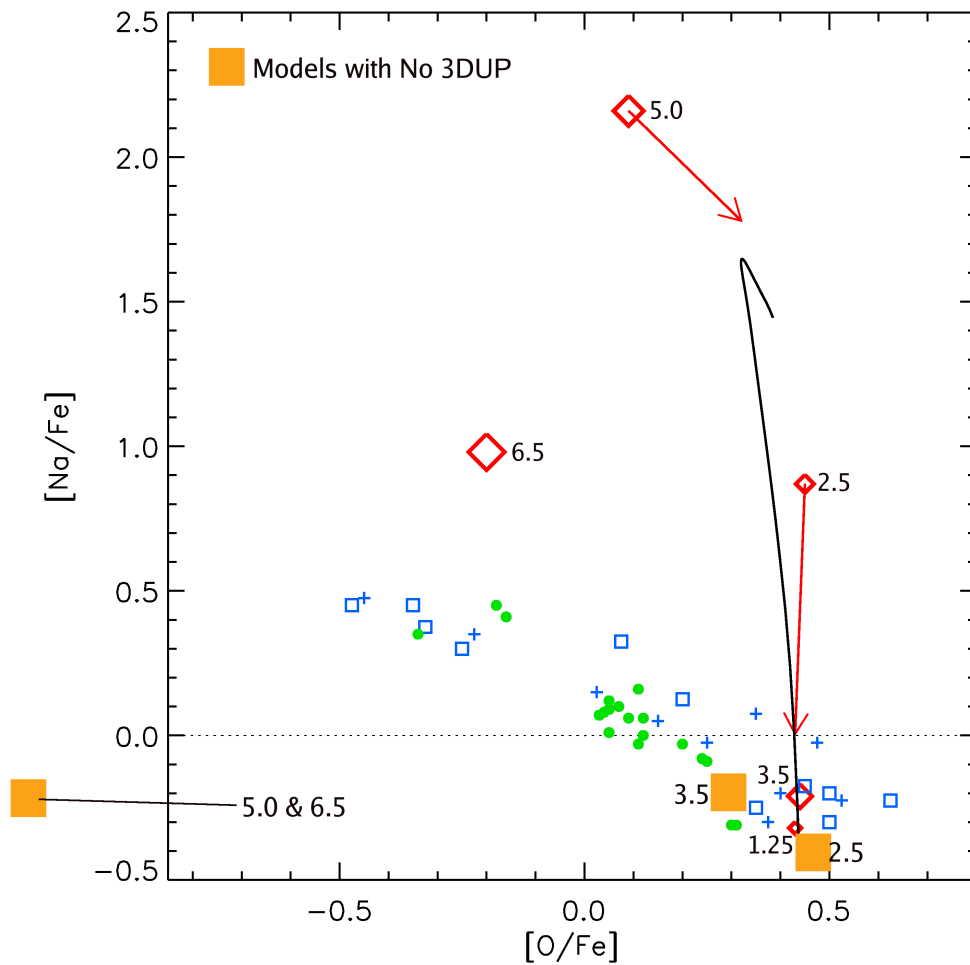


Figure 8.17: Same as Figure 8.16 except for the Na-O anticorrelation in NGC 6752. It can be seen that not enough Na is present in the yields of the higher mass models to match the observations. The dilemma is that it is these models that provide the strong O depletion needed in the ‘polluted’ stars. Note that the oxygen yields of the 5 and 6.5 M_{\odot} models are off the scale of this figure. They should be located at $[O/Fe] \approx -1.2$ and -1.4 respectively. Thus they show more O depletion than the most polluted GC stars. The $[O/Fe]$ values of the yields are shifted ~ -0.2 dex compared to our yield plots due to the use of a different Solar oxygen abundance (to keep in line with that used for plotting the observations).

8.5 Cyanogen in GC AGB Stars: Observing Project

8.5.1 Abstract

On reading an old paper about galactic globular cluster abundance observations (of NGC 6752) we came across an intriguing result. [Norris et al. \(1981\)](#) found that there was a distinct lack of cyanogen-strong (CN-strong) stars in their sample of AGB stars, as compared to their sample of RGB stars (which had roughly equal numbers of CN-normal and CN-strong stars). Further reading revealed that similar features have been discovered in the AGB populations of other clusters. Recently, [Snedden et al. \(2000\)](#) followed up on this possibility (and considered other proton-capture products) by compiling the existing data at the time and came to a similar conclusion for two more clusters. Unfortunately all of these studies suffer from low AGB star counts so the conclusions are not necessarily robust — larger, statistically significant, sample sizes are needed.

In this section we outline the results of a literature search for relevant CN observations and describe our observing proposal to test the suggestion that there are substantial abundance pattern differences between the AGB and RGB in galactic globular clusters. The literature search revealed that the AGB star counts for all studies (which are not, in general, studies about AGB stars in particular) are low, usually being $\lesssim 10$. The search also revealed that the picture may not be consistent between clusters. Although most clusters appear to have CN-weak AGBs, at least two seem to have CN-strong AGBs (M5 and 47 Tuc). To further complicate the picture, clusters often appear to have a combination of both CN-strong and CN-weak stars on their AGBs – although one population tends to dominate. Again, all these assertions are however based on small sample sizes. We aim to increase the sample sizes by *an order of magnitude* using existing high quality photometry in which the AGB and RGB can be reliably separated. For the observations we will use a wide-field, low- to mid-resolution multi-object spectroscope to obtain data not only on the AGB but also on the horizontal branches and first giant branches of a sample of clusters. With the new information we hope to ascertain whether significant abundance differences really exist.

8.5.2 Introduction

We are attempting to perform a conclusive test of the suggestion put forward by [Norris et al. \(1981\)](#), which has been touched upon by many authors since and recently explored by [Snedden et al. \(2000\)](#), that there are differences in cyanogen abundance distributions between the first and second giant branches in galactic globular clusters.

Although galactic globular clusters (GCs) are chemically homogeneous with respect to Fe and most other heavy elements (see eg. [Kraft et al. 1992](#)), it has long been known that they show inhomogeneities in many lighter elements (eg. C, N, O, Mg, Al). These inhomogeneities are considered anomalous because they are not seen in halo field stars of similar metallicity (see eg. [Gratton et al. 2000](#)).

One of the first inhomogeneities discovered was that of the molecule Cyanogen (CN, often used as a proxy for nitrogen). A picture of ‘CN-bimodality’ emerged in the early 1980s whereby

there appears to be two distinct chemical populations of stars in most, if not all, GCs. One population is known as ‘CN-strong’, the other ‘CN-weak’ (the CN-weak population might be more informatively called ‘CN-normal’ – as these stars show CN abundances similar to the Halo field stars). Originally, observations of CN were mainly made in stars on the giant branches but more recently there have been observations on the main sequence (MS) and sub-giant branch (SGB) of some clusters (eg. Cannon et al. 1998). These observations show that there is little difference in the bimodal CN pattern on the MS and SGB as compared with the giants — indicating a primordial origin for the differing populations. Figure 6 in Cannon et al. (1998) exemplifies this situation.

Due to the paucity of asymptotic giant branch (AGB) stars in GCs (a result of their short lifetimes) there have been very few systematic observational studies of the CN anomaly on the AGB in globular clusters (Mallia 1978 is one that the Authors are aware of). What little that has been done has been an aside in more general papers (eg. Norris et al. 1981; Briley et al. 1993; Ivans et al. 1999). However these studies have hinted at a tantalising characteristic: most (observed) GCs show a lack of CN-strong stars on the AGB. If this is true then it is in stark contrast to the red giant branch (RGB) and earlier phases of evolution, where the ratio of CN-Strong to CN-Weak stars is roughly unity in many clusters.

This *possible* discrepancy was noted by Norris et al. 1981 in their paper about abundances in giant stars in NGC 6752. They state that “The behaviour of the CN bands in the AGB stars is... quite difficult to understand... not one of the stars studied here has enhanced CN... yet on the [first] giant branch there are more CN strong stars than CN weak ones.” (also see Figure 3 in that paper). More recently Sneden et al. (2000) presented a conference paper on this exact topic. Compiling the contemporaneous preexisting data in the literature they discussed the relative amounts of CN in AGB and RGB stars in the GCs NGC 6752 (data from Norris et al. 1981), M13 (data from Suntzeff 1981) and M4 (data from Norris et al. 1981; Suntzeff and Smith 1991). They also discuss Na abundance variations in M13 (data from Pilachowski et al. 1996b; Pilachowski et al. 1996a). Their conclusion for the CN variations was that the clusters in question all showed significantly less CN on the AGB as compared to the RGB. However the data compiled only contained about 10 AGB stars per cluster. In their closing remarks they suggest observations with larger sample sizes are needed — which may be done using wide-field multi-object spectroscopes. This is exactly the conclusion the present authors also came to, inspiring a presentation at the Eighth Torino Workshop on Nucleosynthesis AGB Stars held at the Universidad de Granada, Spain, in 2006.

8.5.3 Literature Search Results and the Observing Proposal

We conducted a literature search (which may not be complete) to ascertain what work had already been done in terms on CN on the AGB in galactic globular clusters. The results are displayed in Table 8.1. The main result from this search was that the available number of AGB star observations are not statistically significant enough to come to any real conclusion about the nature of the CN abundance distributions. This has mainly been due to technological constraints. However, the data that does exist shows that there appears to be a strong trend towards CN-weak asymptotic giant branches. The picture is not so simple though, as two clusters

Cluster	No. AGB Stars	AGB CN	Reference
M3	8	weak	Suntzeff (1981)
M4	11	weak	Ivans et al. (1999)
M5	8	strong	Smith and Norris (1993)
M13	12	weak	Suntzeff (1981)
M15	2	weak	Lee (2000)
M55	10	weak	Briley et al. (1993)
NGC 6752	12	weak	Smith and Norris (1993)
47 Tuc	14	strong	Mallia (1978)

Table 8.1: Results of the literature search for CN abundances in GC AGB stars. Note that ‘weak’ or ‘strong’ means that there is a very significant majority of that class of star in each case.

in Table 8.1 actually have CN-strong AGBs. In addition to this, most clusters have some stars of the opposite class on their AGBs – the classifications given in Table 8.1 (usually) refer to strong majorities in each cluster, rather than totally homogeneous populations.

A vital part in being able to observe significant numbers of AGB stars is having photometry good enough to separate the AGB from the RGB. Photometric observations have now reached such high accuracy that it is becoming feasible to separate the AGB and RGB populations reliably. In addition to this, wide-field multi-object spectroscopes are now available. During our literature search we came across some very high-quality photometric studies. For example, the study of M5 done by Sandquist and Bolte (2004). Their set of observations is complete out to 8-10 arc min. They also tabulate all their stars according to evolutionary status – and find 105 AGB stars! This represents a sample size increase of *one order of magnitude*. In Figure 8.18 we plot some of the observations from Sandquist and Bolte (2004) in a colour-magnitude diagram. A clear separation between the AGB and RGB can be seen. Further to this we found colour magnitude diagrams for two more GC candidates that have the required accuracy (and high AGB star counts). Thus our current study involves three GCs, one of which appears to have a majority of CN-strong stars on its AGB (M5) which makes it an important outlier that may cause problems for some explanations of the (possible) phenomenon.

Fortuitously, observations of CN bands require only low- to mid-resolution spectroscopes. This combines well with the fact that a large sample is required, which is easily achievable with multi-object spectroscopes which also tend to have lower resolutions. We show a sample fibre setup for the 2dF multi-object spectrograph on the Anglo Australian Telescope in Figure 8.19 (note that this instrument has now been superseded, but similar instruments are available). Our proposal also includes some (red) HB stars, as this may let us know which stars reach the HB only, and which stars proceed to the second giant branch. RGB stars will be used as control stars as they are very well studied already – and have similar temperatures and luminosities to the AGB stars. Depending on the quality of the final data we will also attempt to derive abundances for aluminium and CH (a proxy for carbon).

8.5.4 Discussion

Assuming for the purpose of discussion that the lack of CN-normal AGB stars is real, then this is actually the opposite to what we would expect based on observations at the tip of the RGB.

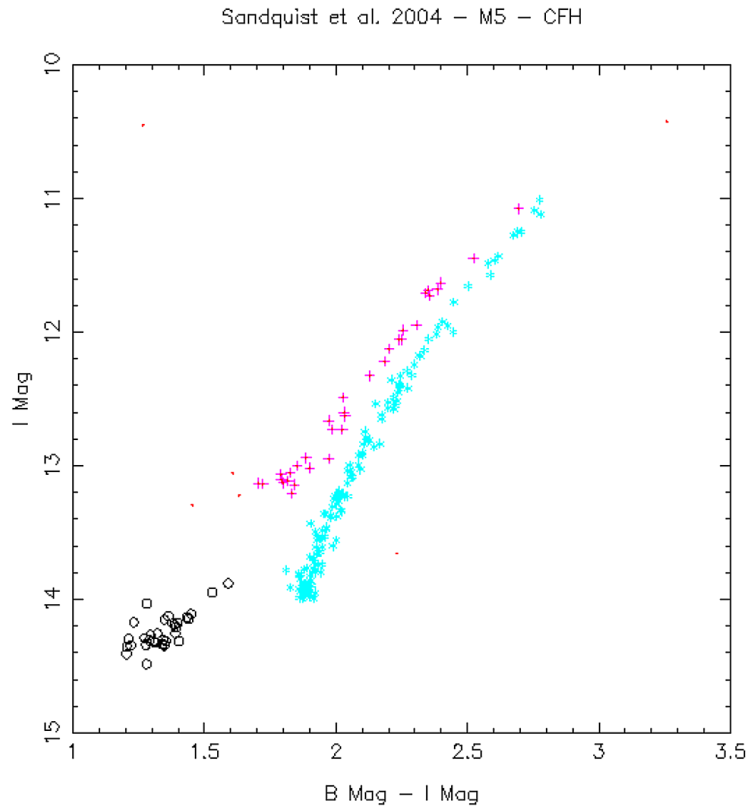


Figure 8.18: An example of AGB star identification in a CMD. Data is from Sandquist and Bolte (2004). Crosses, stars and open circles represent AGB, RGB and HB stars respectively.

These stars, which are the precursors to the AGB stars (via the HB), actually tend to become *more* N-dominated due to ‘extra mixing’ (the results of extra mixing are routinely observed in Halo field RGB stars as well GC RGB stars – see eg. Shetrone 2003). Thus we would predict an *increase* in the number of CN-strong AGB stars over the RGB mean – rather than a decrease.

Norris et al. (1981) proposed two possible explanations to explain the (apparent) lack of CN-strong stars on the AGB:

1. The two populations in NGC 6752 have different He abundances (they suggest $\Delta Y \sim 0.05$). This may have come about through a merger of two proto-cluster clouds with differing chemical histories or through successive generations of stars (ie. self-pollution). The He-rich material would also be N-rich. The He-rich stars would then evolve to populate the blue end of the HB – and not ascend the AGB – leaving only CN-normal stars to evolve to the AGB.
2. Mixing in about half of the RGB stars pollutes their surfaces (increasing N) and also increases mass-loss rates, again leading to two separate mass groups on the HB. As before, the CN-strong, low mass group does not ascend the AGB.

A constraint on the first explanation (for NGC 6752) is that about *half the mass of the cluster* must be polluted, as the number of CN-strong and CN-normal stars is roughly equal. As Norris et al. state, this is not a serious problem for the merger scenario, as the merging clouds/proto-clusters may very well have had similar masses. However, due to the constancy of Fe group

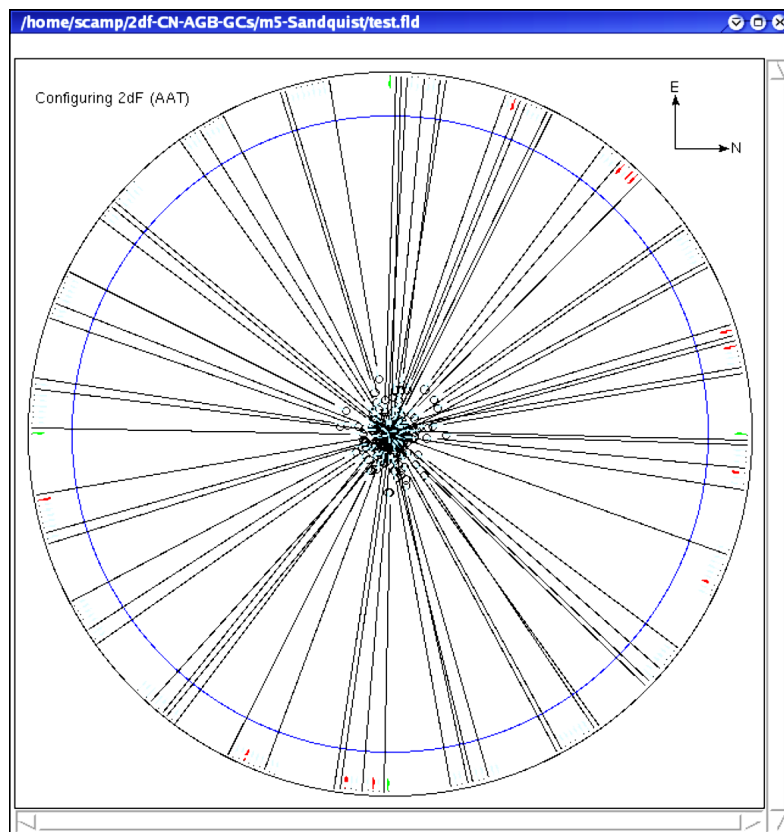


Figure 8.19: One of our 2dF plate setups for the M5 sample from [Sandquist and Bolte \(2004\)](#). Lines represent optical fibres whilst open circles represent the mini-prism placements for the stars. Note that most of the objects are concentrated in the centre. This is due to the fact that we need to sample the dense regions of the cluster to get reasonable numbers of AGB stars, and that the 2dF instrument has such a large field of view.

elements, the chemical histories of the two clouds/proto-clusters would have to have been identical with respect to these heavy elements. This is more difficult to explain since we require a differing chemical histories for the light elements.

The self-pollution scenario, whereby a second generation of stars pollutes the cluster at an early epoch, also needs to satisfy these two constraints. Fenner et al. (2004) have recently explored this scenario. To maintain the heavy element abundances whilst increasing N (and other elements) they assume that the cluster does not retain the ejecta from the second generation supernovae but does retain the material from the less energetic winds from intermediate mass AGB stars. Qualitatively AGB stars have a perfect site for the hydrogen burning needed to produce many of the abundance anomalies in GCs – the bottom of the convective envelope (so-called ‘hot-bottom burning’). However, the theoretical study of Fenner et al. (2004) suggests that there are actually serious problems for the scenario as the AGB stars not only produce the N needed but also produce primary carbon (which is dredged up to the surface). This also alters the sum of C+N+O significantly which is observed to be (roughly) constant in GCs. Constraints from other hydrogen burning products also cause this model to fail.

In light of recent observations on the MS and SGBs of some clusters, the second explanation by Norris et al. may require some clarification. As N appears to have a preformation source (as evidenced by MS observations), the extra mixing is not required (although it does still exist). However, the general suggestion that the differing compositions may affect mass-loss rates and lead to different mass populations on the HB may be a valid one.

An important point visible in Table 8.1 is that it appears that there may be variation between the clusters themselves – some asymptotic giant branches seem to be CN-strong as opposed to the majority which appear to be CN-normal. In addition, the fact that most clusters have a *mix* of CN-strong and CN-normal AGB stars (although usually strongly dominated by one population), rather than a homogeneous set, suggests that there may be a continuum of CN-strong to CN-normal ratios. Theories such as those of Norris et al. (1981) will have to account for these points also if the conclusions from observations to date are proven correct. Of course, the low sample sizes may be artificially complicating the issue.

If there really are substantial abundance differences between the RGB and AGB then this may also reveal other clues to the GC abundance anomaly problems (ie. those of the heavier p-capture products - see Sneden et al. 2000 for a discussion), and the second parameter problem.

Our study seeks to clarify the understanding of abundance differences between the various stages of evolution by very significantly increasing the amount of information available about the asymptotic branch.

Finally we note that the AGB stars in question are generally *early* AGB stars – they are not thermally pulsing. However, this should have no impact on the testing for abundance differences as they are not expected to reduce their surface abundance of nitrogen. Indeed, third dredge-up on top of preformation pollution and deep mixing would make the issue even more complex.

Part IV

CONCLUSION

Chapter 9

Summary of $Z = 0$ and EMP Models

“Science is facts; just as houses are made of stone, so is science made of facts; but a pile of stones is not a house, and a collection of facts is not necessarily science.”

– Jules Henri Poincaré (1854-1912)

9.1 Peculiar Evolution

A large part of this study has centred on the peculiar evolutionary traits found in $Z = 0$ and extremely metal-poor (EMP) stellar models. In Section 5.2 we gave a detailed report on the evolutionary properties of our $0.85 M_{\odot}$, $Z = 0$ model, whilst in Section 5.3 we did the same for our $2.0 M_{\odot}$, $Z = 0$ model. We note that in Section 5.2.5 on page 127 we gave a concise summary (‘executive summary’) of the interesting evolution of our $0.85 M_{\odot}$, $Z = 0$ model that may be useful as a quick reference. Two of the key peculiar evolutionary events found in these models are present in many of our $Z = 0$ and EMP stars. We refer to these events as the ‘Dual Core Flash’ (DCF) and ‘Dual Shell Flash’ (DSF). The term dual is used because these events are characterised by a twin peak in luminosity. They occur during – and are induced by – the normally occurring helium flashes (which also occur in higher-metallicity models). We note that other authors have used (many) different names for these events. The He flashes lead to a breaching of the H-He interface above the He-burning region. This brings down protons into the hot He burning regions, causing a secondary (but often stronger) hydrogen flash. The difference between a DCF and a DSF is that the DCF happens during the core He flash in low-mass models of $Z = 0$ and extremely low metallicity, whilst the DSF happens during the first few thermal pulses (i.e. He shell flashes) in intermediate-mass models of $Z = 0$ and extremely low metallicity. As just mentioned both events involve the same phenomenon – a He flash inducing a mixing between the H-rich zones and the He-burning zones. Thus we have given a general term to the H-flash portion of these events – proton ingestion episodes (PIEs). We note that, whilst protons are dredged down and lead to the secondary H-flash, He burning products are also mixed upwards. This has significant consequences for the $Z = 0$ models as it leads to an ignition of the CNO cycles where there was only p-p chain burning occurring (due to a lack of CNO catalysts). However the main consequence of both the upward and downward mixing is that polluted material is then located above the He burning region, and this is dredged up to

pollute the surface at a later stage (the pollution arising from this is summarised in the next section).

Although the DF events appear to be ubiquitous in the stellar models of all studies there is some variation in the details of exactly which masses and metallicities they occur at, and also how much pollution arises from them. This is most likely due to the different input physics and numerical schemes used between the studies. A key factor is the degree of overshoot used. We used none in our models but the inclusion of overshoot would most likely increase the frequency of occurrence of these events, widening the metallicity range in which they occur. If the increase in the proportion of CEMP stars at low $[\text{Fe}/\text{H}]$ is due to these DF events (as conjectured below) then the observations may be able to constrain the models. Indeed, the upper metallicity limit may already be visible in the observations. We shall investigate this in the near future.

9.2 Chemical Pollution

9.2.1 Mass-Metallicity Pollution Diagram

[Fujimoto et al. \(2000\)](#) appear to have been the first to provide a clear overview of the expected polluting effects from low- and intermediate-mass very metal-deficient models. In their Figure 2 they sketch the various regimes of pollution episodes in the mass-metallicity plane. The current study is the first to evolve stars of such low metallicity through to the end of the AGB, and thus to produce yields from detailed calculations. In Section 7.3 we categorised our models into three groups, based on the source of pollution for their AGB envelopes. Using these three groups we now also provide an overview of expected pollution in the mass-metallicity plane, which we summarise graphically in Figure 9.1. Note that we describe all our categories in the caption of this figure. In the figure we have added a fourth group, based on some higher-mass models for which we have calculated a large portion of the structural evolution (hundreds of pulses on the AGB). Although we have not fully completed these calculations we are confident that the yields from these models will not be affected by any significant pollution events (unlike the lower-mass cases). These models, which have the same metallicity range as our other models, but are of mass $5 M_{\odot}$ (there is also one of mass $4 M_{\odot}$ with $Z = 0$), experience no third dredge-up at all. As they do not experience the DSF event either their yields will be unpolluted – i.e. practically the same as their initial compositions. The only pollution event that slightly alters the yield compositions is 2DUP, but this is (relatively) minor. We note however that the core masses in these models are all approaching the Chandrasekhar mass and thus they may end up as type $I_{\frac{1}{2}}$ supernovae, as described by [Iben and Renzini \(1983\)](#). This would then cause the yields to be polluted with SN products and our ‘no pollution’ (Group 4) categorisation would need to be revised. The evolution to supernovae type $I_{\frac{1}{2}}$ is however strongly dependent on the mass loss rates used. We shall pursue this interesting avenue of low metallicity stellar evolution as a future study (we note that some recent work has been done on this topic, see eg. [Gil-Pons et al. 2006](#)).

Comparing our ‘pollution diagram’ (Figure 9.1) with the diagram of [Fujimoto et al. \(2000\)](#) (Figure 2 of that paper) we note that our results are very similar. They have similar boundaries for the different dominant polluting events, and they also delineate four groups that match with

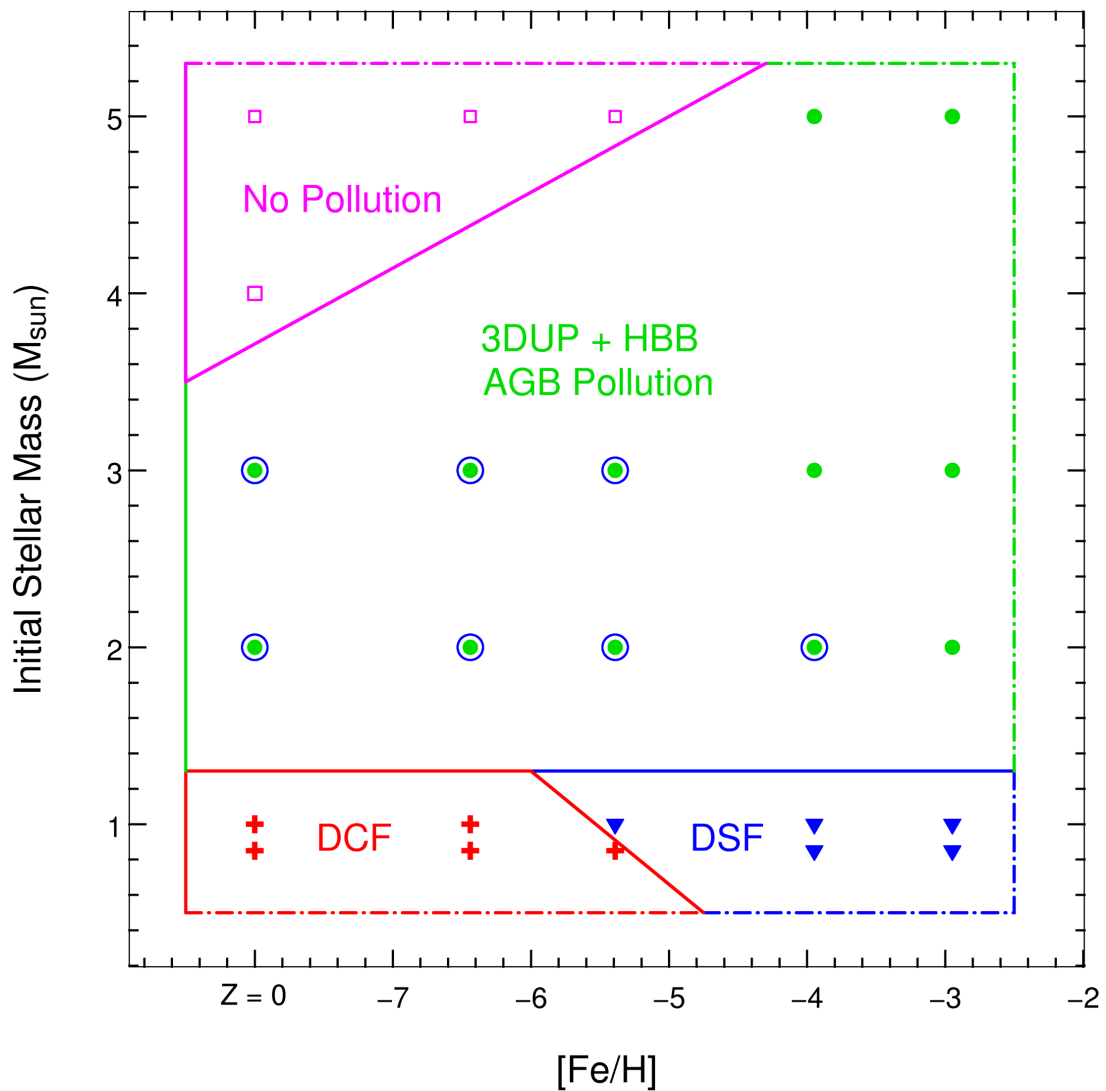


Figure 9.1: Mass-metallicity diagram summarising the dominant sources of pollution in the yields. Each symbol represents one of our detailed stellar models. Note that we have only calculated detailed nucleosynthesis for the models in the mass range $0.85 \rightarrow 3.0 M_{\odot}$, but we have calculated a sufficient amount of the AGB evolution of the 4 and $5 M_{\odot}$ models to be quite certain of the nature of the yields (type 1.5 supernovae events withstanding). We identify four categories into which we group the chemical outputs from our models: *DCF* (pollution primarily from the dual core flash event = Group 1), *DSF* (primarily from the dual shell flash event = Group 2), *AGB* (from third dredge-up and hot-bottom burning on the AGB = Group 3) and *No Pollution* (no major events pollute the AGB envelope, thus no enhancements in the yields = Group 4). The open circles (blue) around the filled circles (green) indicate intermediate mass models that experienced DSFs. Pollution from 3DUP (and HBB) easily dominates the pollution from the DSF events at IM mass so the yields of these models fall into the AGB group. The dash-dotted lines represent the fact that these categorisations may extend out to higher metallicities and/or higher/lower masses. As we have included our $Z = 0$ models (artificially at $[\text{Fe}/\text{H}] = -8$, as marked on the x-axis) the low metallicity boundary is known, and therefore represented by solid lines. We note, for the interested reader, that Fujimoto et al. (2000) also provide a mass-metallicity sketch for their low-metallicity study.

ours (their extra group, Case IV, is outside our metallicity range). The main point of difference is that our boundary for the AGB-DSF models (green filled circles with blue haloes in Figure 9.1) is at a lower metallicity than theirs. Our diagram also shows a mass dependency in addition to the metallicity dependency for the pollution events. Finally we note that one dimension is not elucidated by these types of pollution diagrams – the degree of dilution that some of the yields suffer through unpolluted RGB mass-loss. Naturally this effect is only relevant at low masses, but we have found it to be very significant in some of the models (see Section 7.4.1). This adds some (further) uncertainty to the pollution diagram. The RGB mass-loss dilution is however not important in the case of a binary mass-transfer event just after (or during) a DCF or DSF event.

9.2.2 Extra Channels for Producing CEMPs

As noted above, the dual flash (DF) events have strong consequences for the surface composition of many of our models. The surfaces of the models are polluted after the flashes recede – the convective envelope extends inwards in mass and dredges up polluted material that was left behind just above the He shell. This material has been through He burning *and* H burning. Thus it is dominated by the three main products of these types of burning – carbon, oxygen and nitrogen (in terms of metals). The magnitude of the surface pollution is usually very large: $Z=0$ and EMP models often end up with super-solar metallicity in terms of Z (they do of course remain EMP in terms of $[\text{Fe}/\text{H}]$).

In Figure 9.2 we give an overview of the four pollution groups discussed in the previous subsection, in terms of evolutionary status. We do this by indicating in HR diagrams at which stages of evolution the models have polluted surfaces. The most notable result visible from this perspective is that the low mass models ($M \lesssim 1.3 M_{\odot}$) have their AGB surfaces polluted by the DF events only. Our models do not show 3DUP at these masses and metallicities so this remains the dominant source of pollution throughout the AGB evolution. If it is correct that 3DUP does not occur in stars of this mass and metallicity then *these DF events represent a serious increase in C production at extremely low metallicities*, since models without the DF events would release no polluted matter (and DFs do not occur at higher metallicities). *Thus the model results predict that the proportion of stars that are C-enhanced should be higher at extremely low metallicity.* Moreover, our models predict that *the proportion of CEMPs should continue to increase at lower and lower metallicities.* This is due to the fact the mass range in which the DF events occur increases with decreasing metallicity – i.e. the carbon-enriching DF events become more common with decreasing metallicity. The increase in the proportion of CEMPs would be compounded through the binary star population (via mass transfer events) since some of the primary stars would have undergone DFs. Furthermore, as these events are quite violent, one might expect that enhanced mass-loss would occur during these phases – possibly even envelope ejection. This is something that needs to be explored properly with fluid dynamics simulations. If this were the case then this would *again* increase the proportion of CEMPs in EMP populations, since the secondary components in binaries would be preferentially polluted by material from these events.

Another salient result visible in Figure 9.2 is that the models which experience the DCF at the

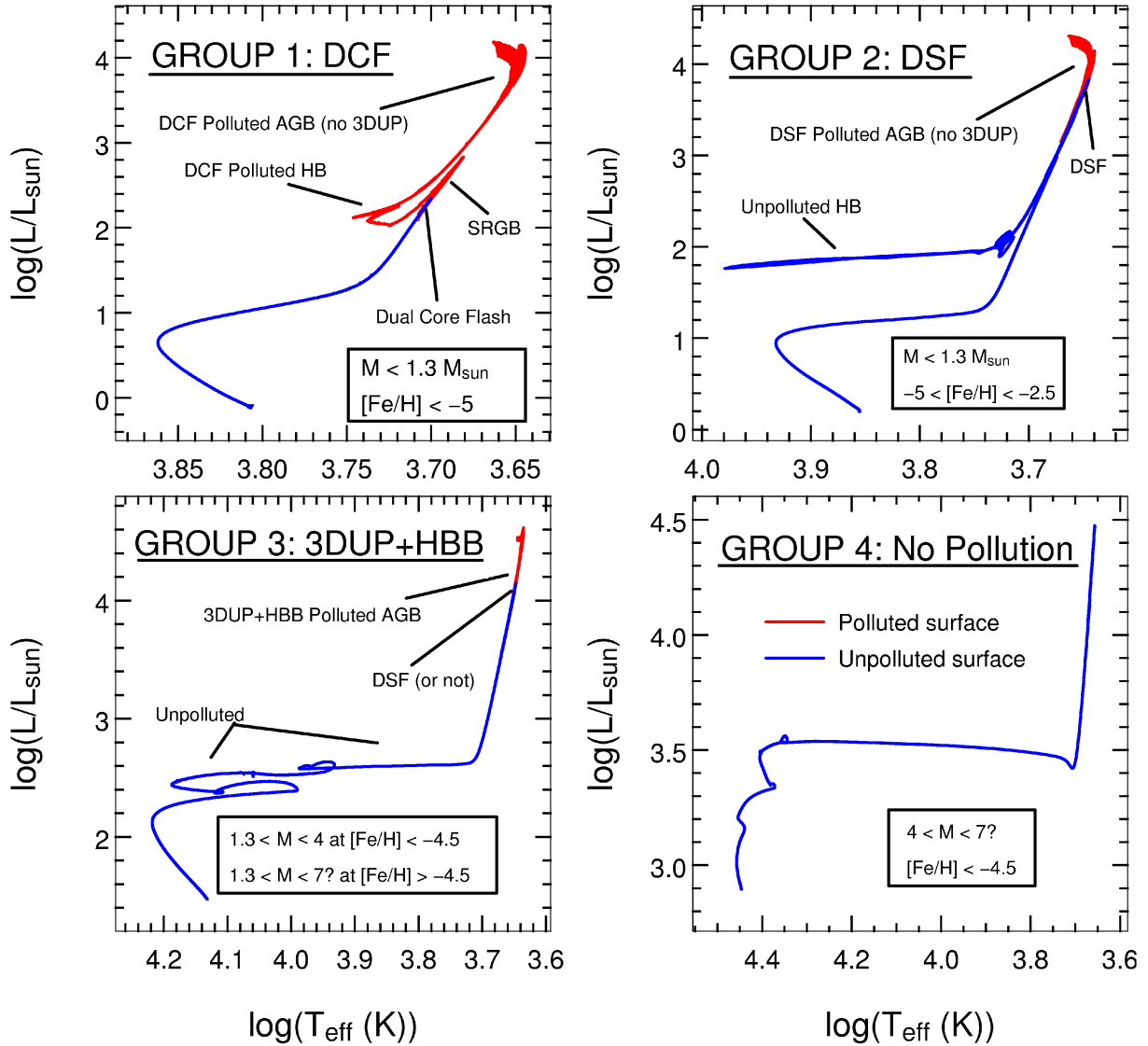


Figure 9.2: An evolutionary perspective on the four pollution groups. Displayed in each HR diagram is a representative example from our grid of models for each pollution group (see Figure 9.1 for the definitions of the groups). Red lines indicate phases of the evolution in which the surface is strongly polluted with CNO nuclides (from the DCF, DSF or 3DUP events). Blue lines indicate that the surface still retains the initial metal-poor composition. Evolutionary stages and pollution sources are marked, as are the mass and metallicity ranges of each group. Question marks indicate unknown upper boundaries (due to the limited mass range of the current study). Two key features are (1) the DCF group has a polluted HB and (2) both the DCF and DSF groups, which are of low mass, have polluted surfaces during the AGB despite the lack of 3DUP. These features mean that our models predict a greater proportion of C-rich stars at extremely low metallicity, as these events do not occur at higher metallicities.

top of the RGB have polluted surfaces for a significant portion of their lifetimes. This is because their surfaces are already polluted during the HB phase (and secondary RGB phase, but this is quite short-lived like the AGB). Interestingly our models predict that, at ultra low metallicities ($[\text{Fe}/\text{H}] \lesssim -5$), *all low-mass stars in the HB phase should have polluted surfaces*. In terms of the binary mass transfer scenario this is of particular importance. Since these stars are polluted for a longer portion of their evolution it is more likely that companions would accrete polluted material. Thus we have *another* CEMP formation channel.

It will be very interesting to see if future observations of ultra-metal-poor halo stars show such high proportions of CEMPs, as forecast by the models.

Finally, as mentioned above, our higher mass models ($M \gtrsim 4 M_{\odot}$) of extremely low metallicity do not undergo DF or 3DUP events, so their surfaces remain unpolluted. We note that this should have little (direct) observational consequence in regards to halo observations as these stars have short lifetimes. Interestingly it also means that secondary stars in binary systems with these stars would not be (significantly) polluted upon mass transfer. Thus we have one *less* way of creating a CEMP star at extremely low metallicities (since higher metallicity stars in this mass range *do* experience 3DUP).

Simultaneous Enhancement of C and N

As mentioned above our models have very C-enhanced yields due to the DCF and DSF events. Another way to produce C enrichment is via 3DUP. Most studies find that 3DUP efficiency increases at low metallicity (eg. Karakas et al. 2002; Stancliffe et al. 2005). Stancliffe et al. (2005) even find 3DUP to occur in $1 M_{\odot}$ models of LMC metallicity. If 3DUP were to occur in low-mass ($M \lesssim 1 M_{\odot}$) EMP stars then this would be another avenue for CEMP pollution (we note however that, like our models, the $[\text{Fe}/\text{H}] = -2.7$, $1 M_{\odot}$ model of Iwamoto et al. (2004) does *not* experience 3DUP). This would again lead to an increase in the proportion of C-rich stars at extremely low metallicities since models of higher metallicity generally do not experience 3DUP. Thus it appears that there may be two possible channels for C production in low mass EMP models. One way to distinguish between these two channels is through their different chemical signatures. Since low mass stars that have 3DUP are not predicted to experience HBB their surface abundance of N remains low whilst C is periodically enhanced. By contrast our ***DCF and DSF models show C and N enhanced at the same time***. Interestingly this dual enhancement appears to be required by the observations, which we discussed in Section 7.6 on page 290.

Another interesting possibility discussed in Section 7.6 is that DFs *and* 3DUP could occur in low mass EMP stars (which may be possible in our models by using overshoot). In this case the models *would again be C and N rich*. This is because the N from the DSF and DCF events has no way of being depleted in the H-rich envelopes at such low masses. Since 3DUP appears to enrich the yields with C to a similar degree as the DF events, the overall C enhancement would probably not increase significantly in this scenario over our present DF-only results. The $^{12}\text{C}/^{13}\text{C}$ ratios may however increase but we are uncertain how significant this would be. Clearly this scenario requires further modelling – the combination of DFs with 3DUP may well provide a better match to the observations. We shall pursue this avenue in future work.

CEMP Abundance Patterns

Finally we note that in Section 7.6.5 on page 314 we gave a summary of all the comparisons we made between our models and the EMP halo star observations. It was found there that many features of the CEMPs could be explained by our models that experience the DCF and DSF episodes (some of which have just been discussed above). However our comparison with the extended abundance *patterns* of a few of the most metal-poor objects known (which are, interestingly, all CEMPs) showed that *our models fail to fully explain these abundance patterns*. There were however some abundance patterns amongst the (small sample of) CEMPs that showed strong similarities with our models. We also noted that there are uncertainties in our models that may account for the remaining differences in some cases. A useful continuation for this line of study would be to collate all the observed abundance patterns of CEMPs to see if there are any consistent groups of patterns. We shall pursue this in our future work as well.

Chapter 10

Concluding Remarks

“Doing a PhD is a strange state of being.”

– Lisa J. Pinter

10.1 Reflecting on the Journey

In the current study we have investigated a wide range of stellar modelling at low metallicities. We began by modifying the structural evolution code (SEV code) to enable it to compute the evolution of $Z = 0$ and extremely metal-poor models. The main change we made to the code was to alter the mixing paradigm. We removed the assumption of instantaneous mixing and replaced it with a time-dependent formalism (Chapter 4). The formalism chosen was that of ‘diffusive mixing’. This change was necessary due to the peculiar evolutionary events that these model stars experience. During the ‘Dual Flash’ events the evolution proceeds so rapidly that the evolutionary timesteps become comparable to the convective turnover timescales – so the assumption of instantaneous mixing no longer holds. Other changes were also made to the SEV code to facilitate the modelling of these types of stars. These included increasing the temperature range in which the SEV code could operate (eg. via adding high-temperature opacity tables) and allowing arbitrary compositions to be used (eg. by removing scaled-solar assumptions). We note that these changes have also brought the code closer to being able to model other types of stars as well – such as ‘Super AGB’ stars (eg. [Doherty and Lattanzio 2006](#)).

With the SEV code armed with the new capabilities we embarked on a few different investigations within the fascinating world of low-metallicity stellar evolution.

The first challenge (chronologically) was that given by the Galactic globular cluster abundance anomalies mystery (Chapter 8). This notorious problem has been around for at least 30 years – and has defied explanation to the current day. In our early work on the subject we decided to quantitatively investigate the oft-cited qualitative explanation of the abundance anomalies – that the source of pollution is AGB stars. We calculated a small grid of models (Chapter 8) of which the initial composition was taken from a chemical evolution model by [Fenner et al. \(2004\)](#). The yields from our (second generation) stellar models were then fed back into the chemical evolution model. We found that the qualitative theory was not supported by our quantitative study. The reasons for this turned out to be fundamental problems, such as the strong increases in

C+N+O and magnesium, which are both due to third dredge-up (3DUP). Only very significant changes in the AGB models could remedy the situation. One such change is the alteration of the convective mixing model (Ventura and D'Antona 2005b). As a diagnostic tool we then calculated some models without 3DUP. The inhibition of 3DUP had been made possible due to the inclusion of the Ledoux criterion for convection in our time-dependent mixing scheme. These models (Section 8.4) proved to be a much better match to the observations, but still fell short in some comparisons. We note that these models have recently been utilised in a chemical evolution model that uses a different paradigm for the source of the polluting gas that formed the abundance anomalies. In this case the gas is theorised to come from an external source, namely the original host of the GC – a low-mass dwarf galaxy (Bekki et al. 2007). To complete our foray into the GC problem we began an investigation into an interesting GC observation first noted by Norris et al. (1981) – that there appears to be differences in the numbers of cyanogen-strong stars on the AGB as compared to the RGB in NGC 6752. Our literature search (Section 8.5) appeared to support this conjecture for most GCs, but the samples were all very small (including that for NGC 6752). We therefore put together an observing proposal – that should increase the sample sizes by an order of magnitude – to investigate the situation. This work is still underway.

The next challenge was to return to the originally proposed topic of the thesis – modelling $Z = 0$ stars. With the time-dependent mixing routine in place this was now possible. These models did however present some difficult problems due to the severe nature of the dual flash events. Code convergence was often an issue. Much time and effort was spent in getting these models to work. Nevertheless it was a worthwhile experience as it forced the author to *really* get to know the SEV code. It is often the case that we learn the most when things do *not* go smoothly. When we did finally get the code to handle the $Z = 0$ stars, we were inspired, in a momentary lapse of reason, to explore the whole parameter space of low- and intermediate-mass extremely metal-poor stellar evolution. Spurred on by the fact that there were some very interesting observations at these extreme metallicities, and by the fact that no one had quantitatively explored the pollution arising from these models through full computation of AGB structure, nucleosynthesis and yield calculations, we embarked on a large modelling crusade. The grid of models we calculated amounted to 30 stars, of which about 20 were successfully completed and presented in Chapter 7. Here we need to acknowledge the support of the Australian Partnership of Advanced Computing (APAC) who were very helpful, particularly in increasing our quota of CPU hours, of which we used ~ 15000 for this grid of models (see Figures C.5 and C.6 on page 401). These models, although certainly full of uncertainties, represent the most comprehensive investigation into EMP evolution and nucleosynthesis to date. In comparing our results to observations we found some broad agreements but note that some of the details do not match well (see Section 7.6). Although naturally also full of uncertainties, we have provided the yields from all of our models in the appendices. These will be of use to chemical evolution studies of the early Universe. Indeed, they are the only yields at these masses and metallicities of which the author is aware.

10.2 Future Work

Throughout the current study we have noted many areas that require more work. We list some of them here, with references to the parts of the study in which we noted them:

- Main sequence lifetimes of low-mass $Z = 0$ models vary between studies (Section 5.2.6 on page 131).
- Core helium burning in intermediate-mass $Z = 0$ models vary widely between studies (Section 5.3.4 on page 150).
- Investigate the effects of mass loss on the yields of EMP and $Z = 0$ models (Section 7.2.6 on page 244).
- Possible s-processing during the Dual Core Flash of low-mass $Z = 0$ and EMP models (Section 6.2.3 on page 170).
- Possible s-processing during the Dual Shell Flash events (6.3.3 on page 187).
- Determine the reason that the $1 M_{\odot}$ and $0.85 M_{\odot}$, $Z = 0$ models have a different abundance pattern amongst the heavier proton-capture elements (Section 6.4 on page 200).
- Investigate the potential for supernova type 1.5 events in the 4 and $5 M_{\odot}$ models (9.2 on page 352).
- Investigate the effect of the combination of 3DUP + dual flash polluting episodes in low-mass models via the inclusion of overshoot (Section 7.6.4 on page 308).
- Make comparisons with observations including the time evolution of the abundances (Section 7.6.4 on page 308).
- Collate abundance patterns of CEMPs to determine whether there are any consistent pollution patterns amongst them (Section 7.6.5 on page 314).
- Try (more) alternative rates in relation to the Na-O and Mg-Al anticorrelations in GCs (Section 8.2 on page 319).
- Investigate how the Mg isotopic ratios could be so different between the models and the observations of GCs (Section 8.4 on page 333).
- Investigate the implications of the surface opacity uncertainty described in Section C.1 on page 396.

It can be seen from this (non-exhaustive) list that many uncertainties and unknowns remain in this field of low- and intermediate-mass metal-poor stellar evolution – and thus that there is much work that still needs to be done. We shall certainly not be lost for things to do!

Part V

APPENDICES

Appendix A

Yields: Metal-Deficient and $Z = 0$ Models

This appendix holds all the yields for all the EMP and $Z = 0$ models. It is divided into three sections.

The first section gives the yields in elemental form (i.e. the sum of all nuclides of each element) relative to solar, against initial stellar mass. One plot is given for each metallicity (5 plots in total).

The second section gives the yields in elemental form relative to solar, against the initial $[\text{Fe}/\text{H}]$ of the models. This gives an idea of how the yields vary with metallicity. They are presented in graphical form (13 plots).

The third section gives the yields for every species in the nuclear network (except neutrons), in mass fraction. These are presented in tabular form (5 tables).

A.1 Plots: Elemental Yields Versus Initial Mass

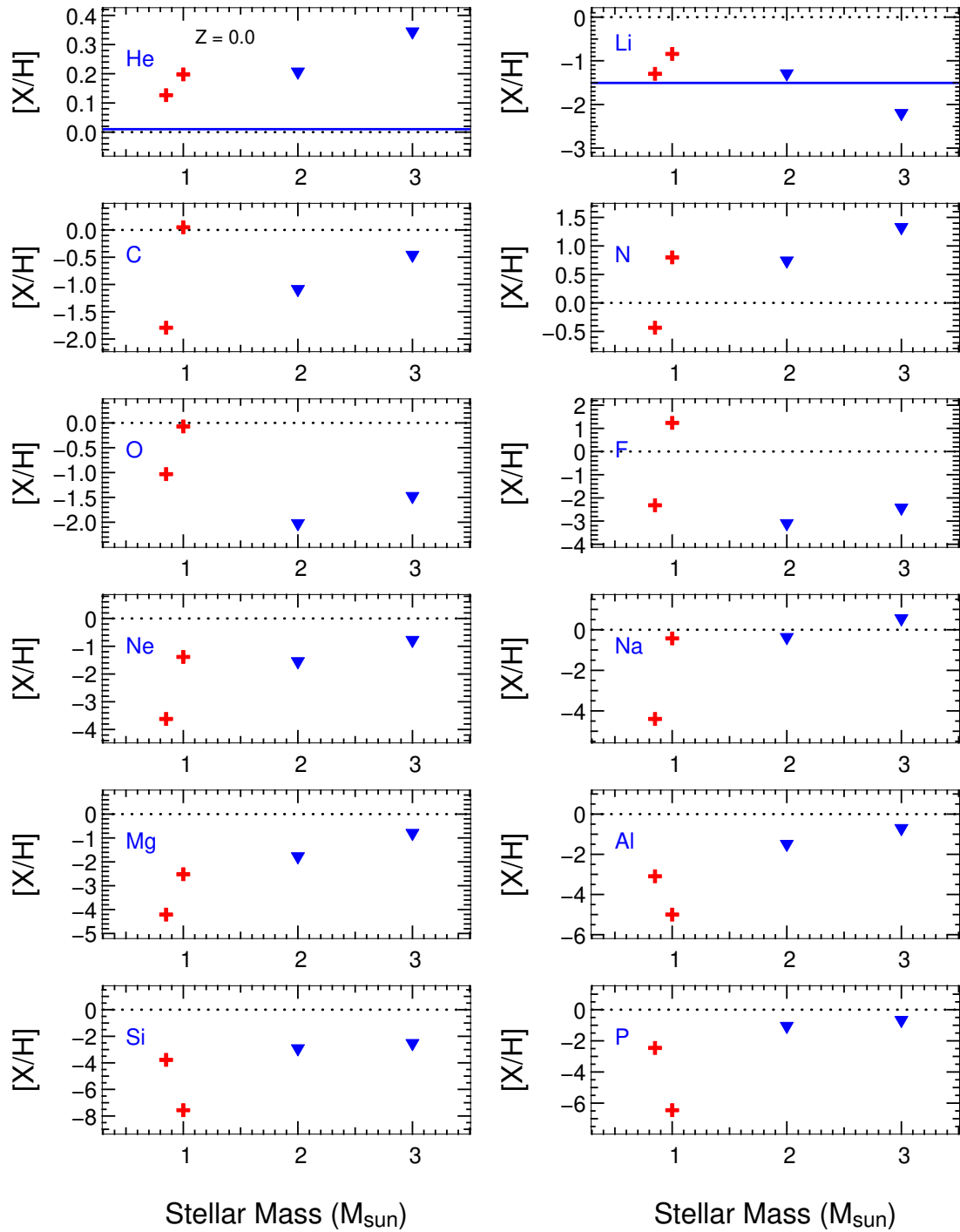


Figure A.1: Selected elemental yields for all the $Z = 0$ models, given as relative to solar against initial stellar mass. Red crosses indicate models that experienced a dual core flash (at the top of the RGB), whilst blue triangles indicate models that experienced a dual shell flash (at the beginning of the AGB). Solid horizontal lines (blue) indicate initial abundances, but are often not visible due to their relative paucity. The horizontal dotted (black) lines at $[X/H] = 0$ indicate the solar abundances (Solar abundances are from [Lodders 2003](#)).

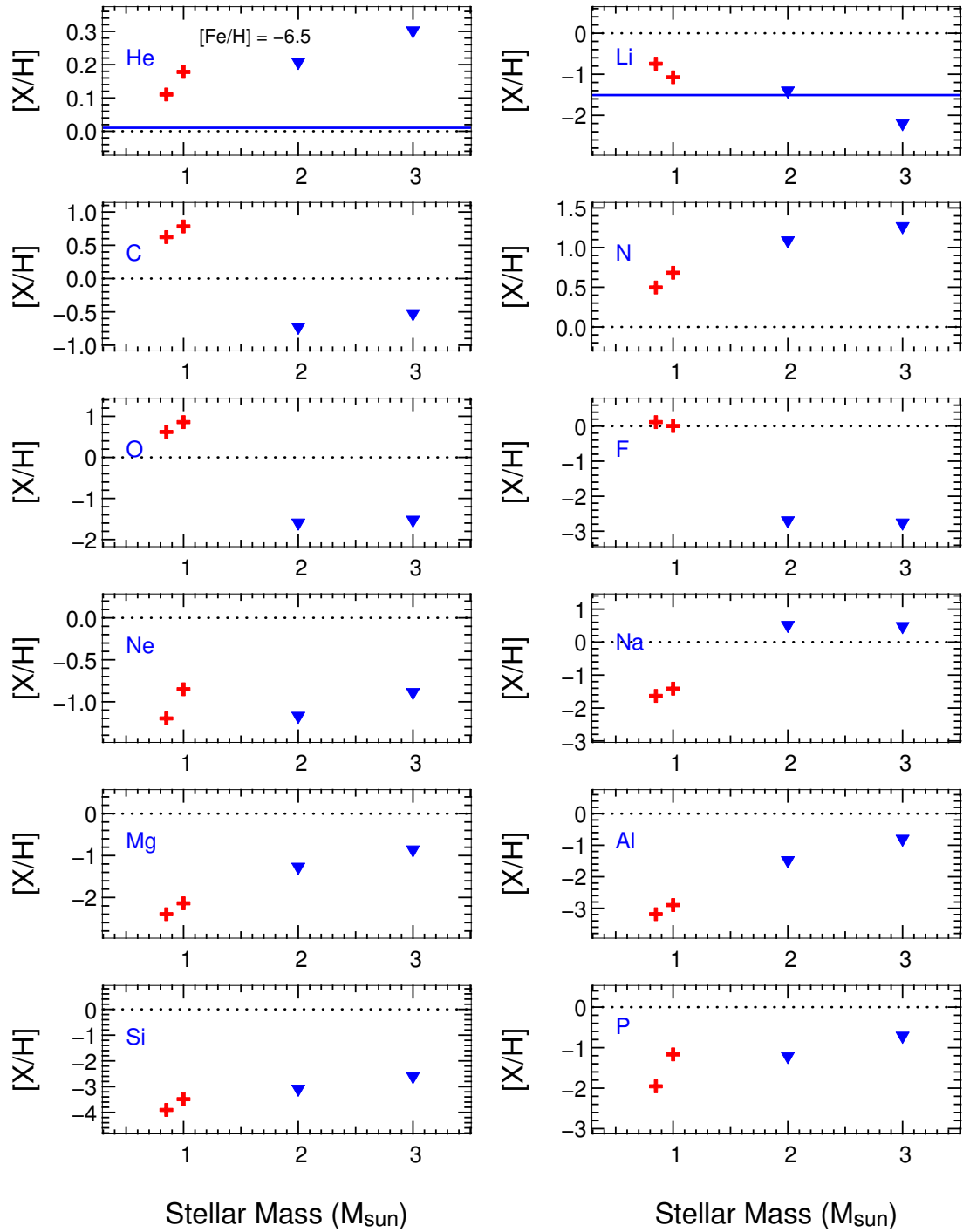


Figure A.2: Same as Figure A.1, but for the $[\text{Fe}/\text{H}] = -6.5$ models.

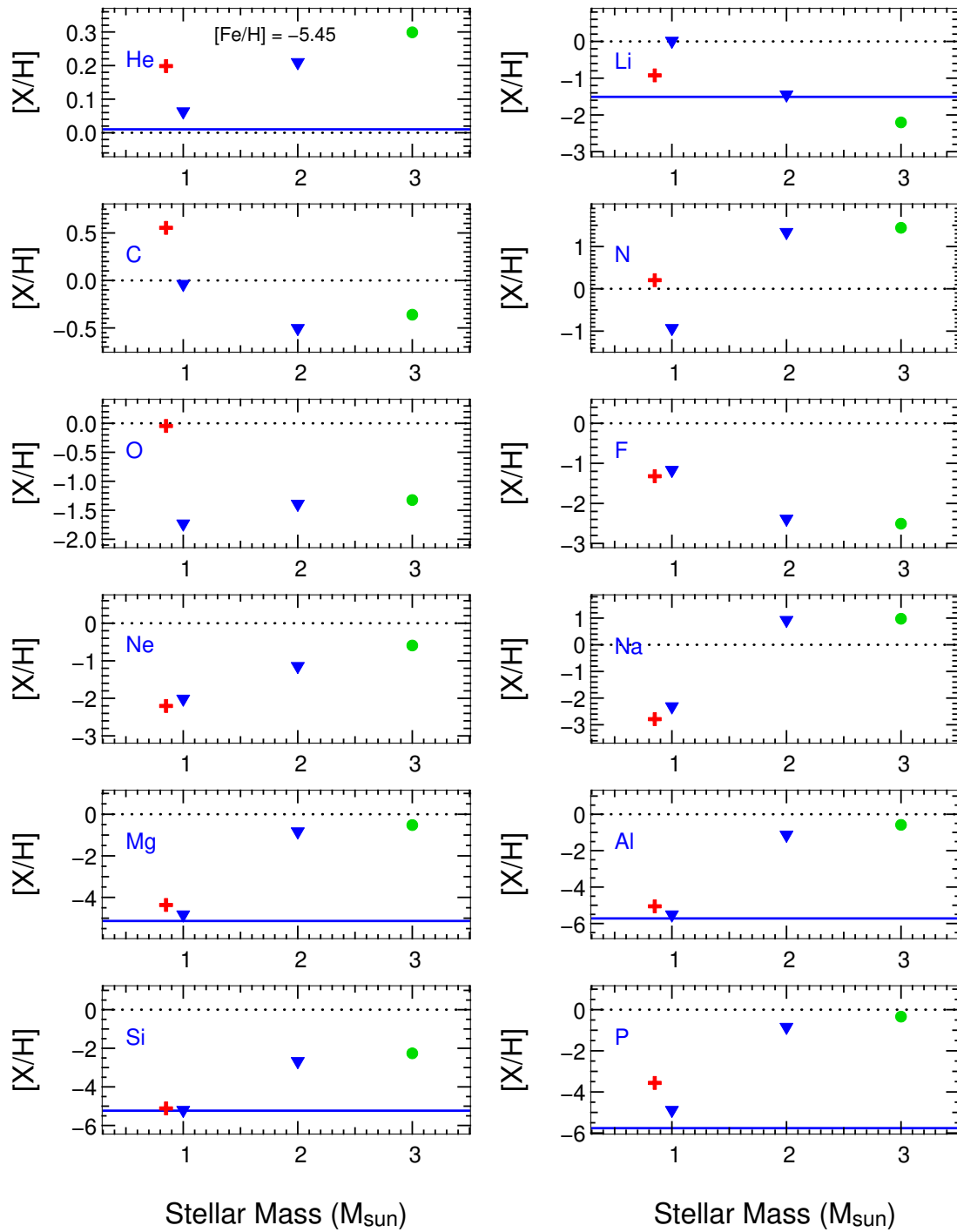


Figure A.3: Same as Figure A.1, but for the $[Fe/H] = -5.45$ models. Green dots indicate that the model did not experience a DCF or a DSF.

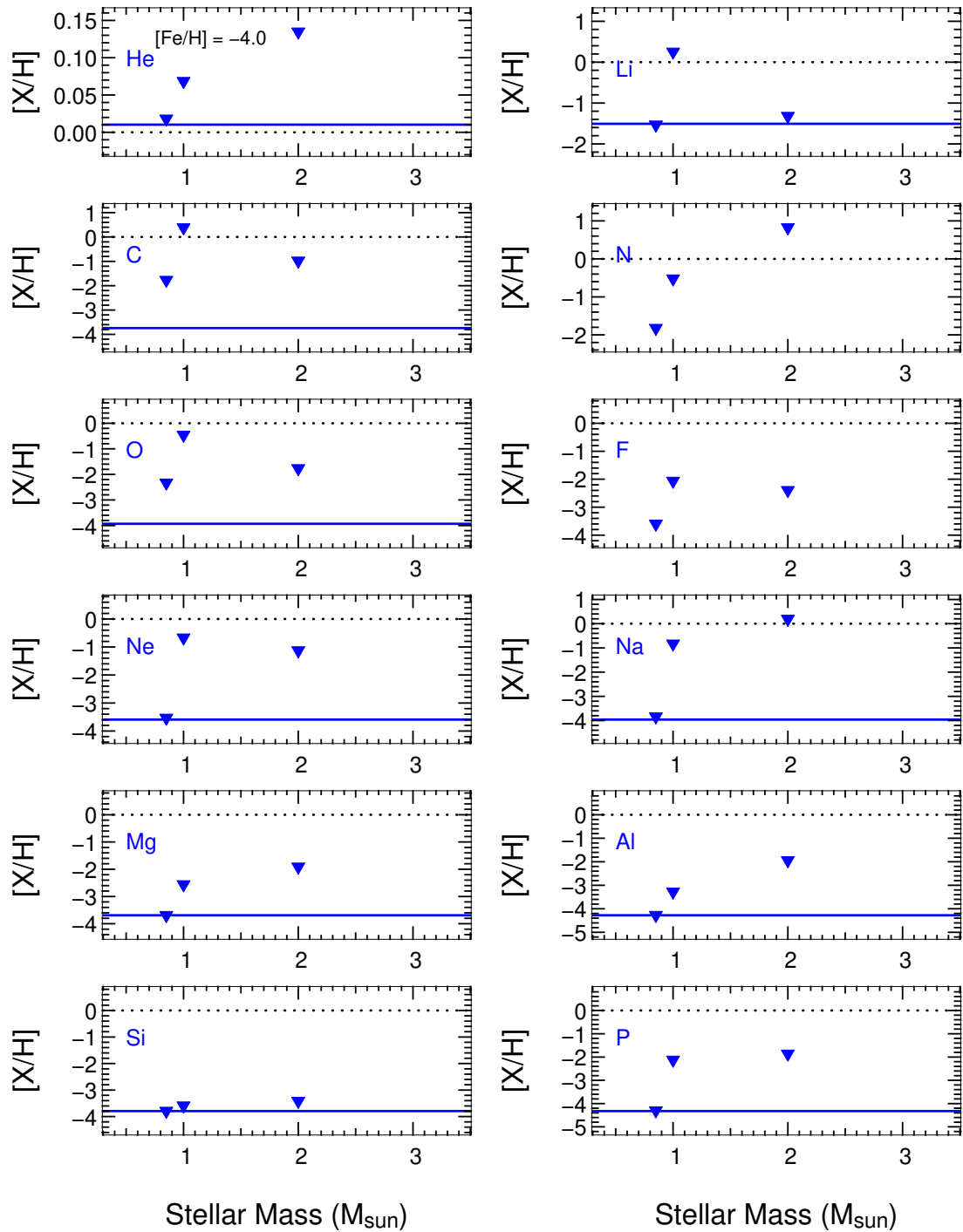


Figure A.4: Same as Figure A.1, but for the $[Fe/H] = -4.0$ models.

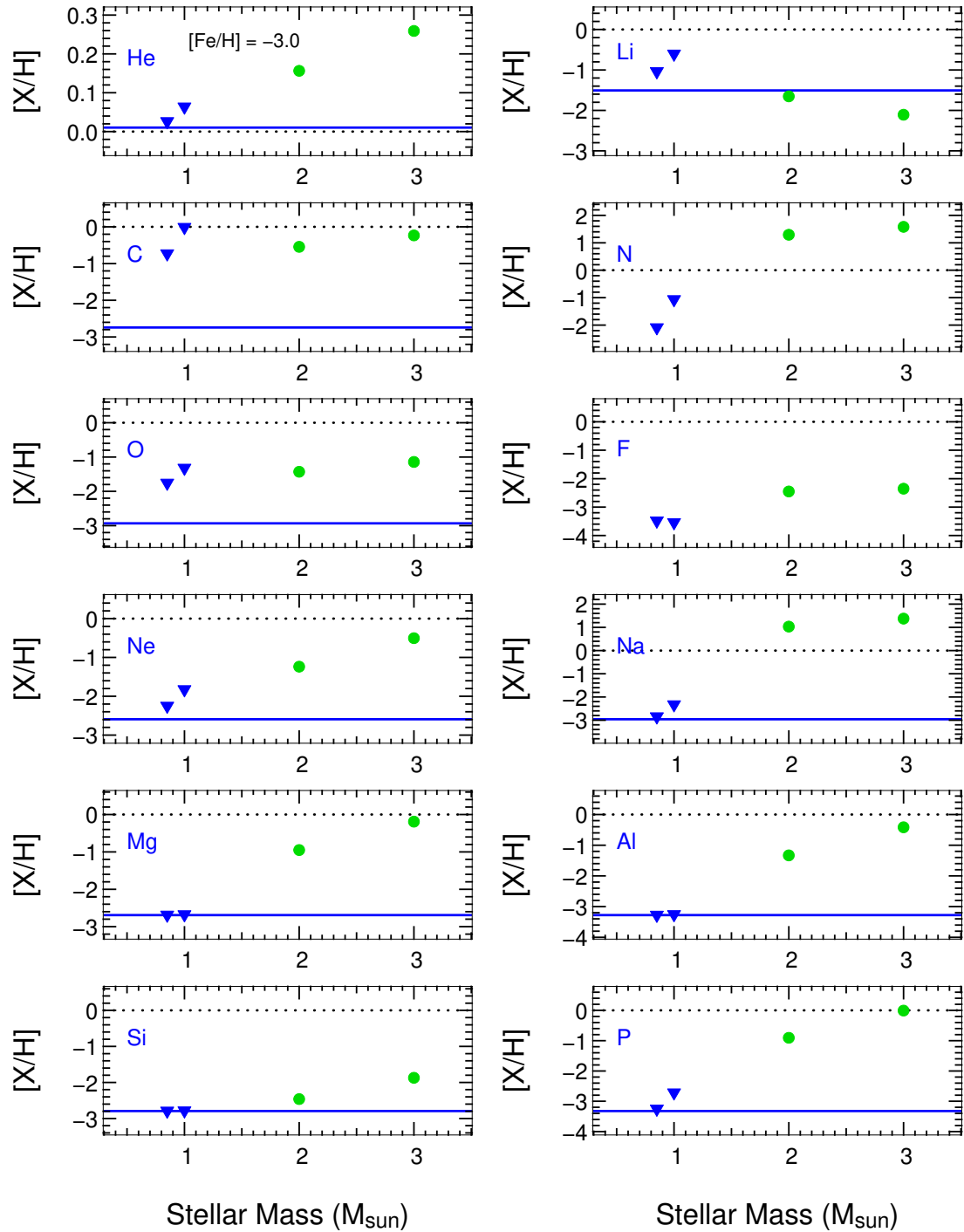


Figure A.5: Same as Figure A.1, but for the $[Fe/H] = -3.0$ models. Green dots indicate that the model did not experience a DCF or a DSF.

A.2 Plots: Elemental Yields Versus [Fe/H]

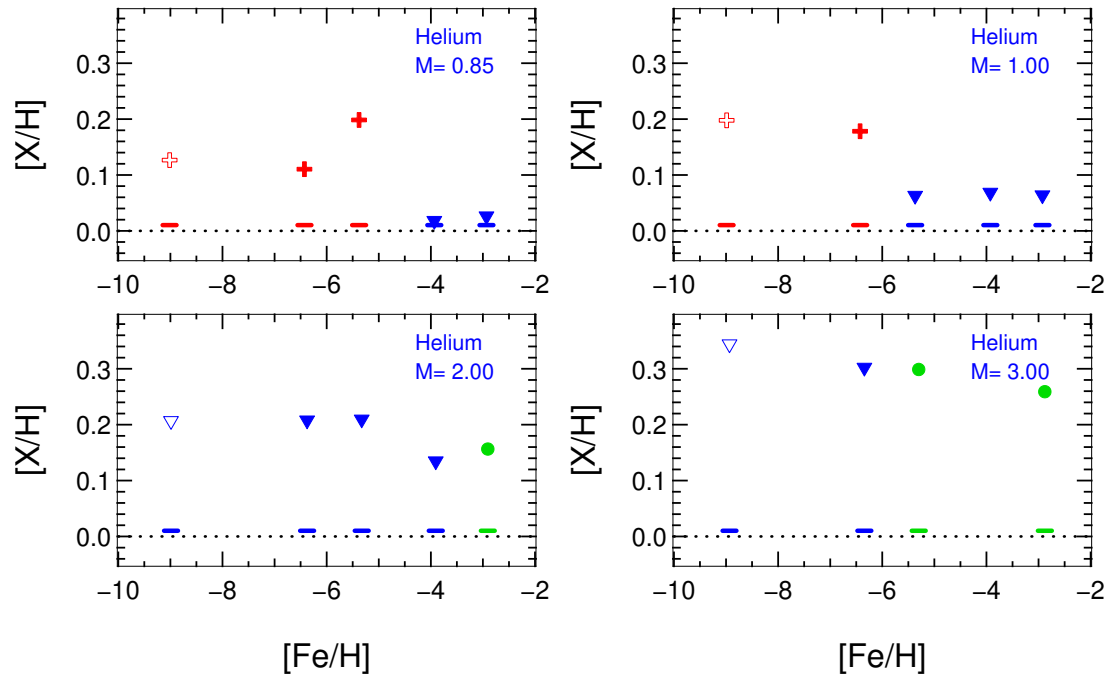


Figure A.6: Helium yields versus initial $[\text{Fe}/\text{H}]$ for all the models in the grid, grouped by initial mass. The $Z = 0$ models have also been included for comparison (they have been given an artificial Fe abundance corresponding to $[\text{Fe}/\text{H}] = -9$ for display purposes). Red crosses indicate models that experienced a dual core flash (at the top of the RGB), blue triangles models that experienced a dual shell flash (at the beginning of the AGB) and green dots indicate models that experienced neither. Short horizontal lines indicate the initial abundance for each model (which are well below the scale of the bottom panel). Note that within each group of four plots the vertical axes are identical to allow direct comparison.

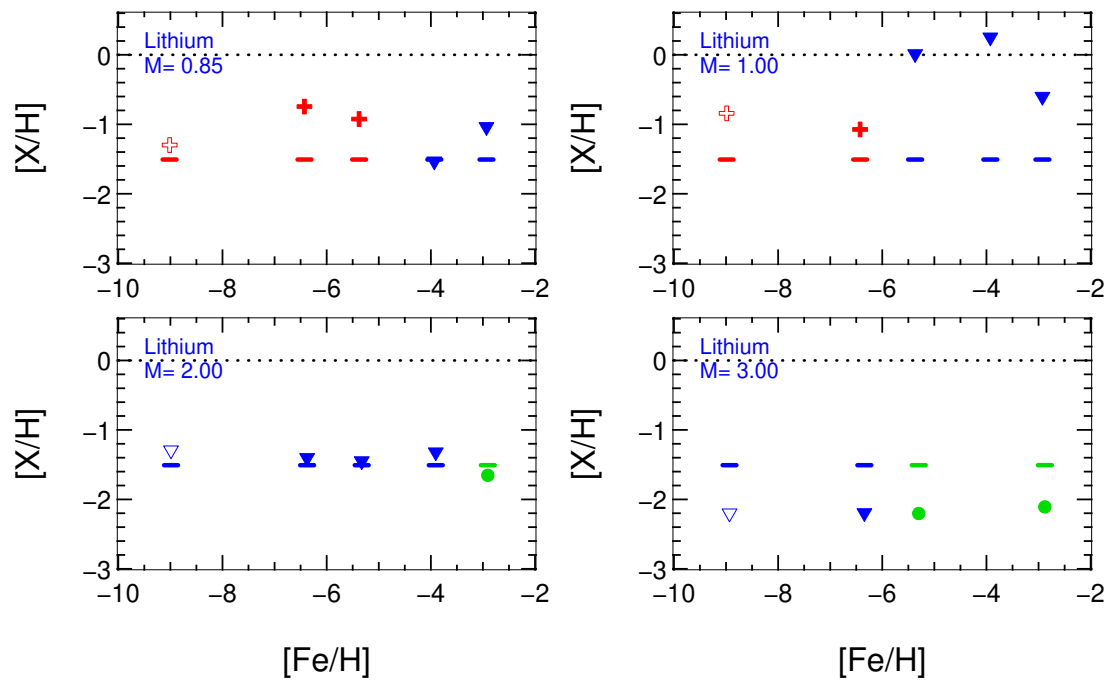


Figure A.7: Same as Figure A.6 except for lithium.

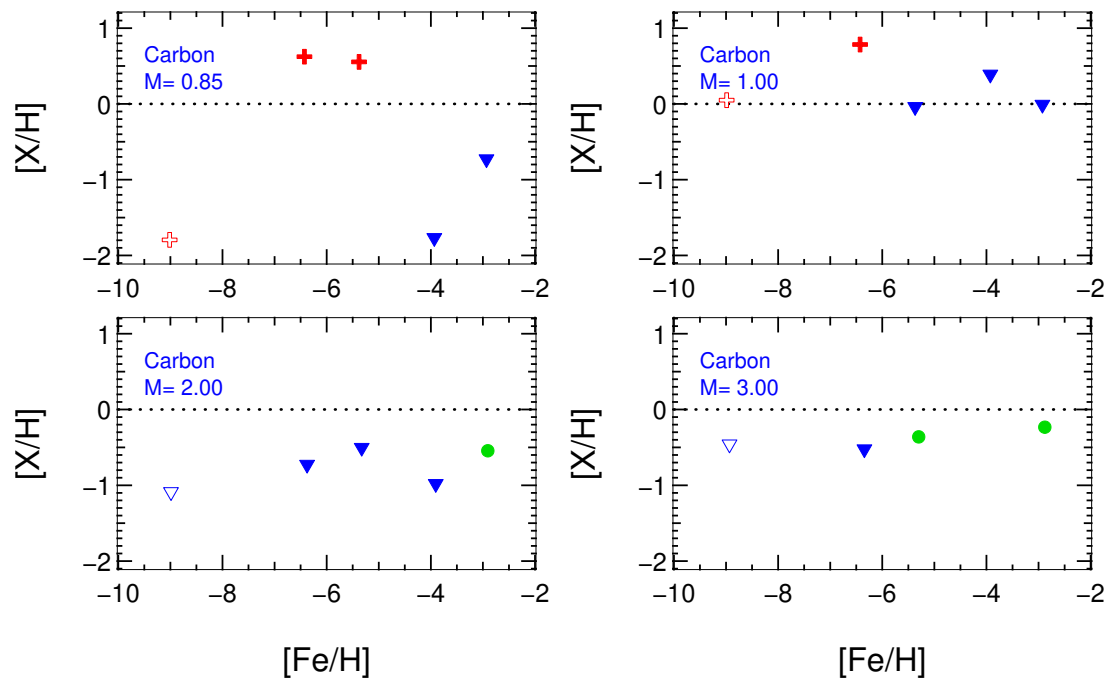


Figure A.8: Same as Figure A.6 except for carbon.

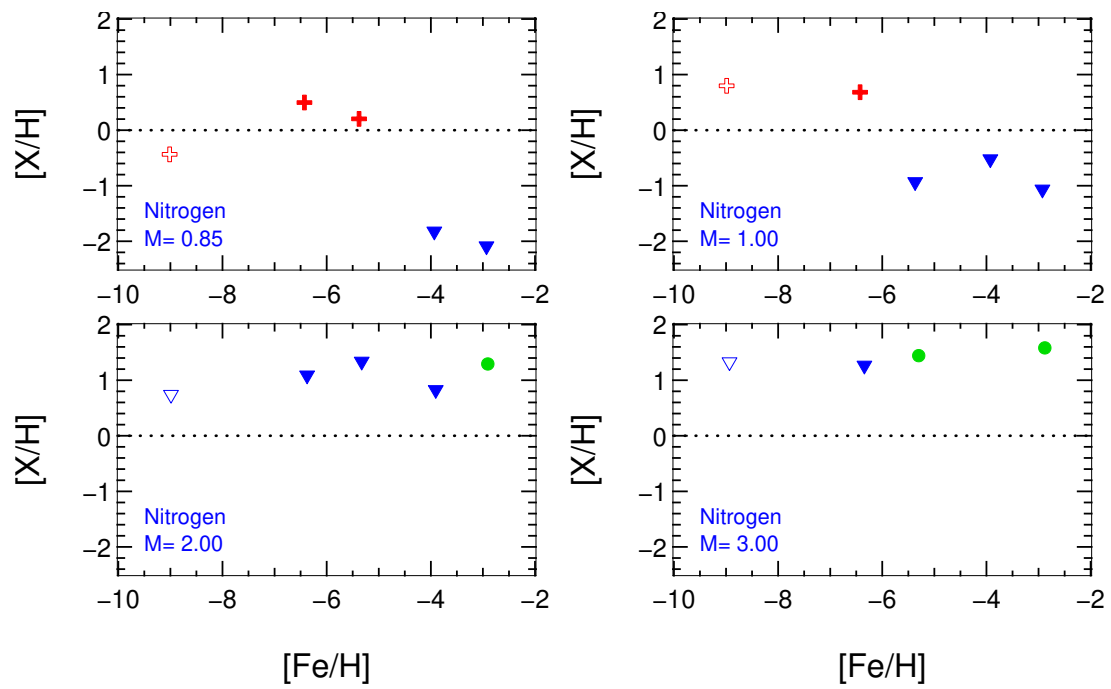


Figure A.9: Same as Figure A.6 except for nitrogen.

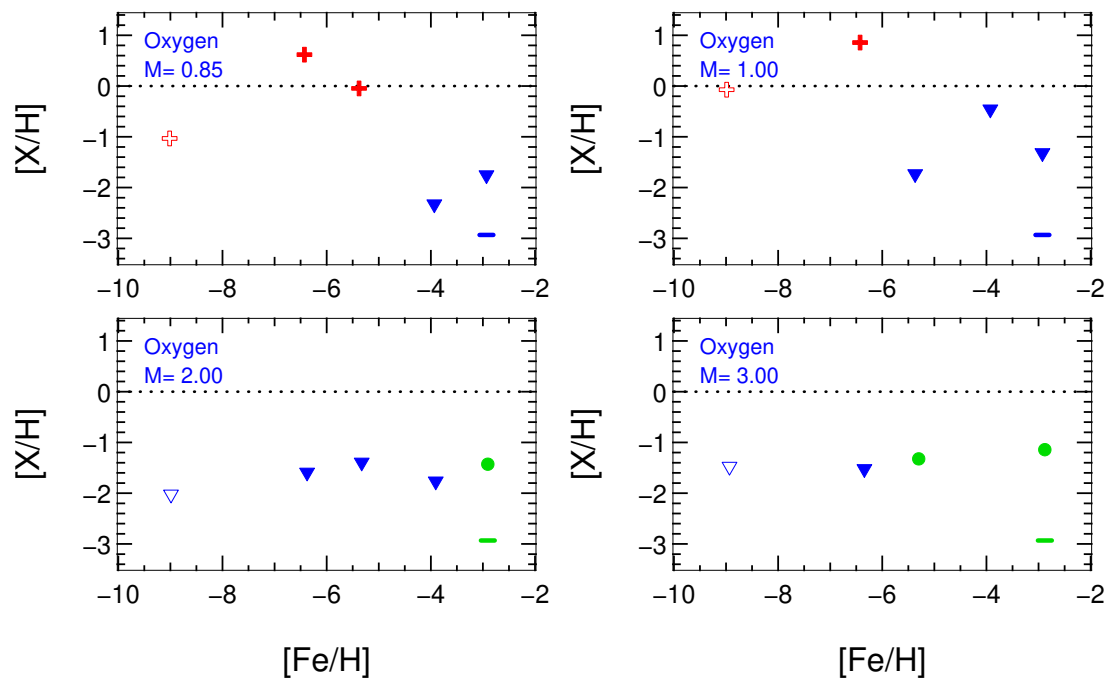


Figure A.10: Same as Figure A.6 except for oxygen.

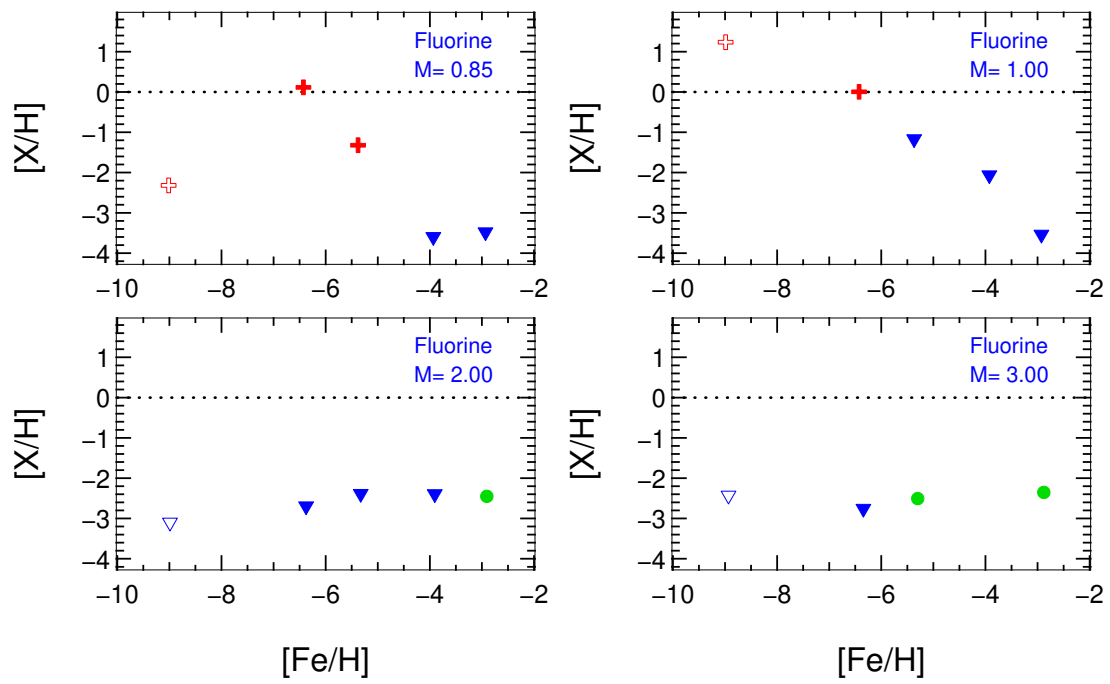


Figure A.11: Same as Figure A.6 except for fluorine.

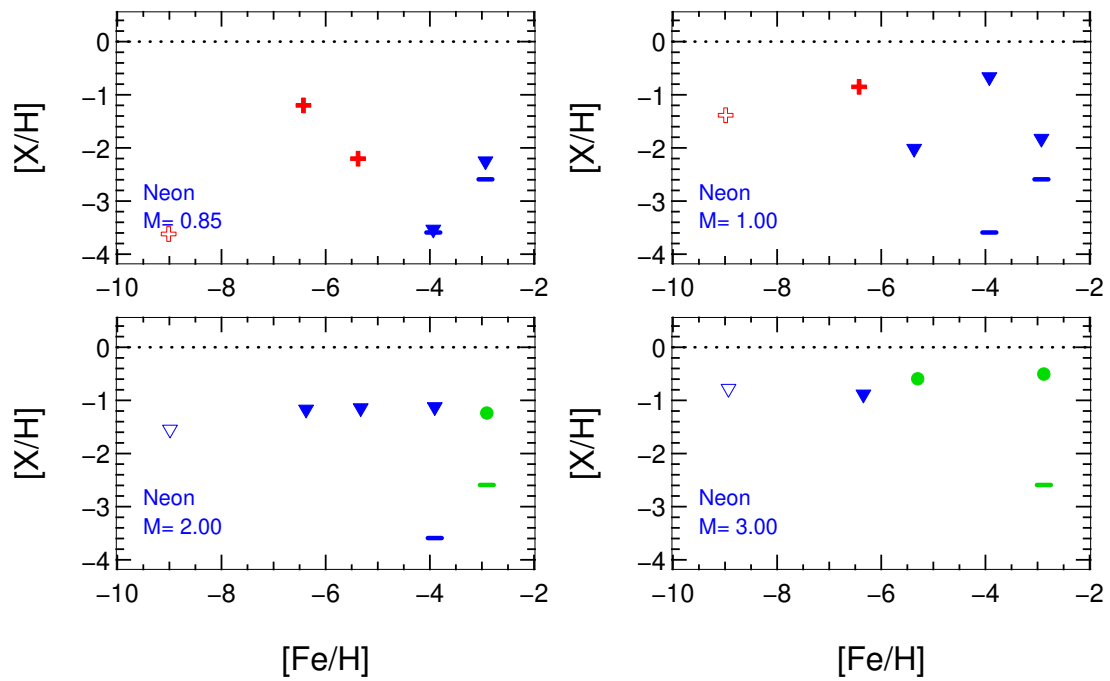


Figure A.12: Same as Figure A.6 except for neon.

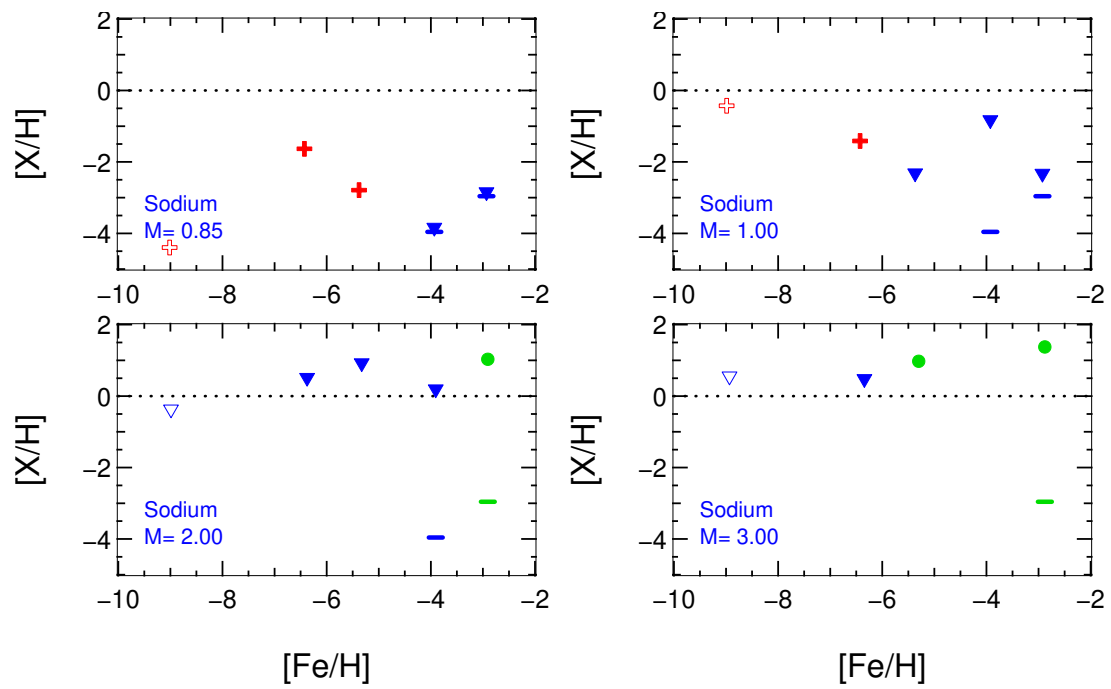


Figure A.13: Same as Figure A.6 except for sodium.

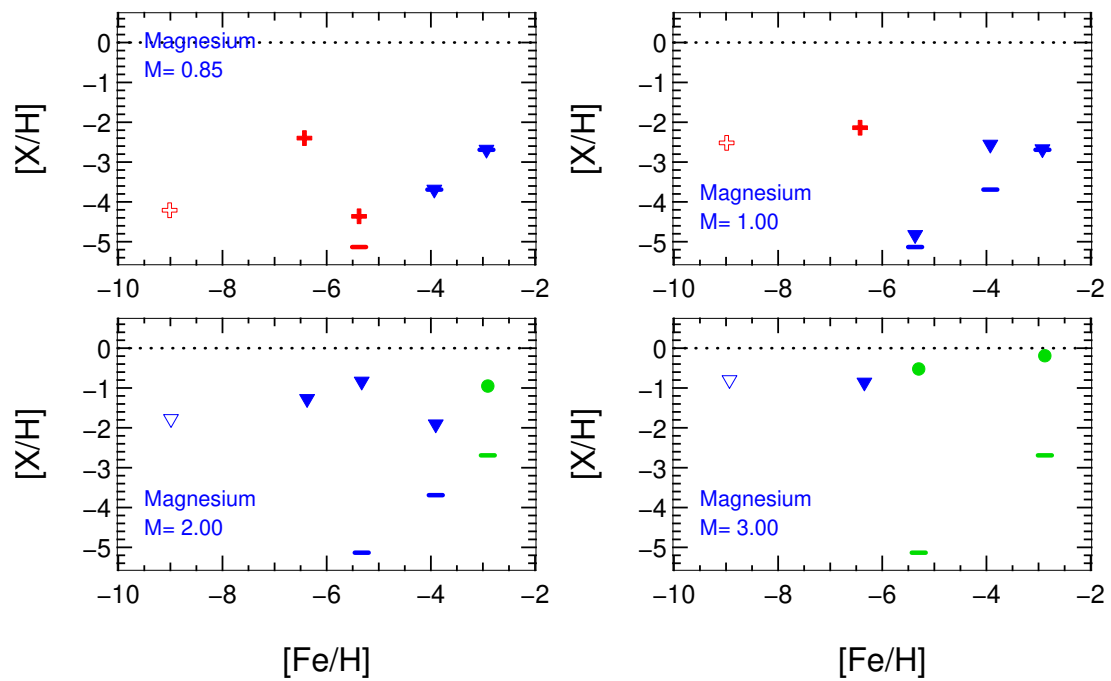


Figure A.14: Same as Figure A.6 except for magnesium.

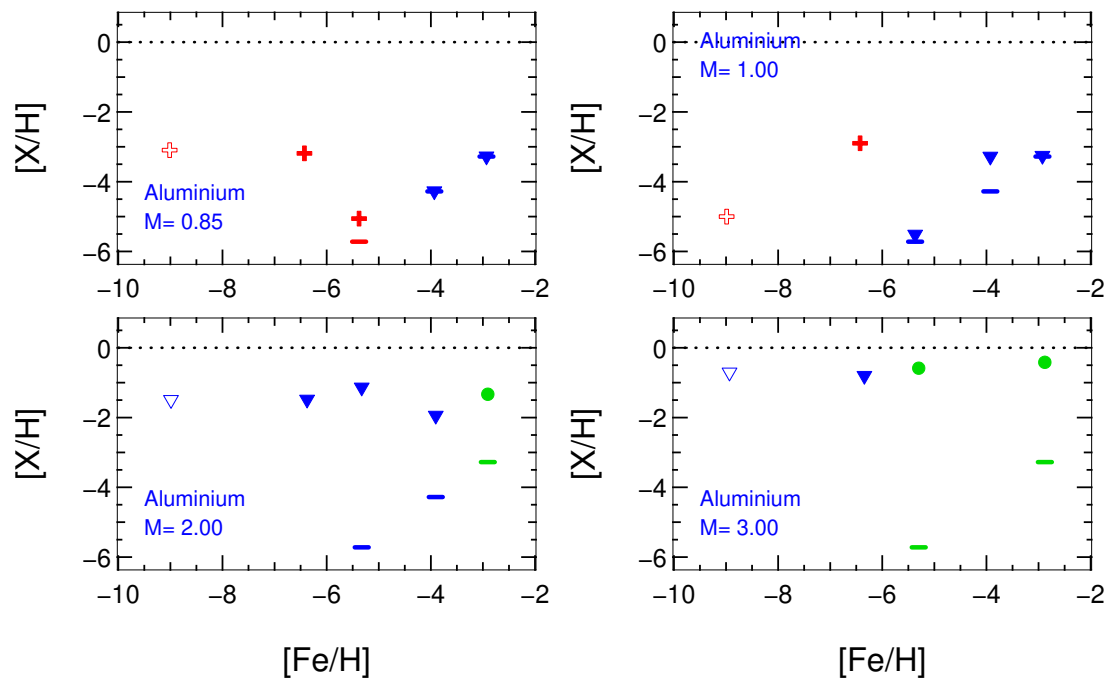


Figure A.15: Same as Figure A.6 except for aluminium.

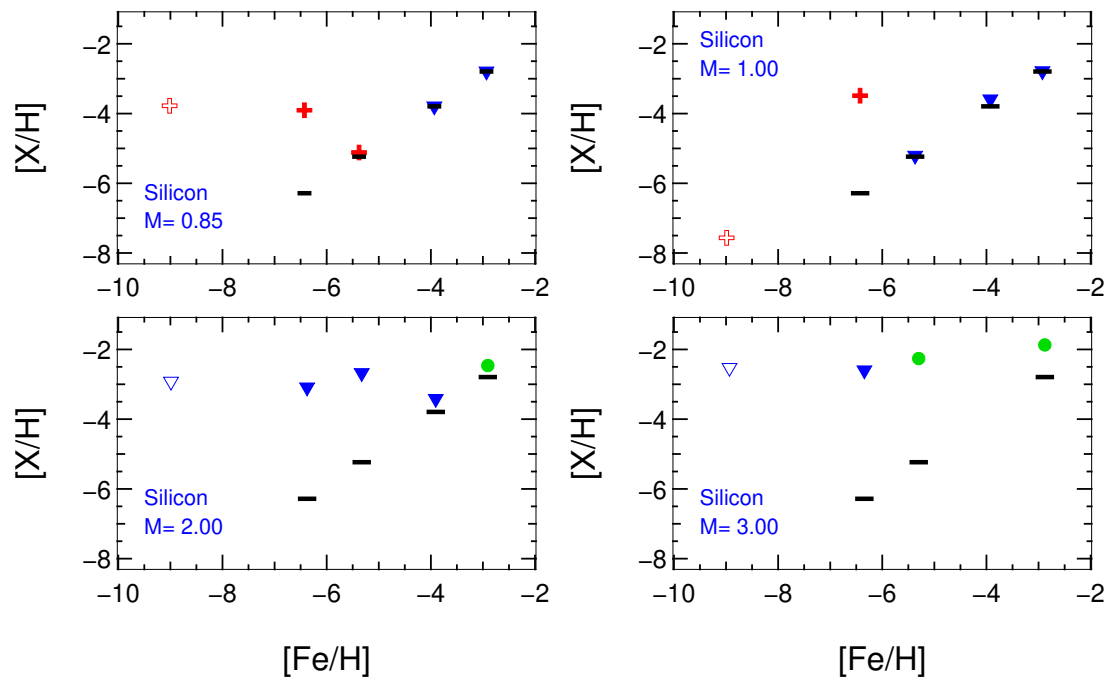


Figure A.16: Same as Figure A.6 except for silicon.

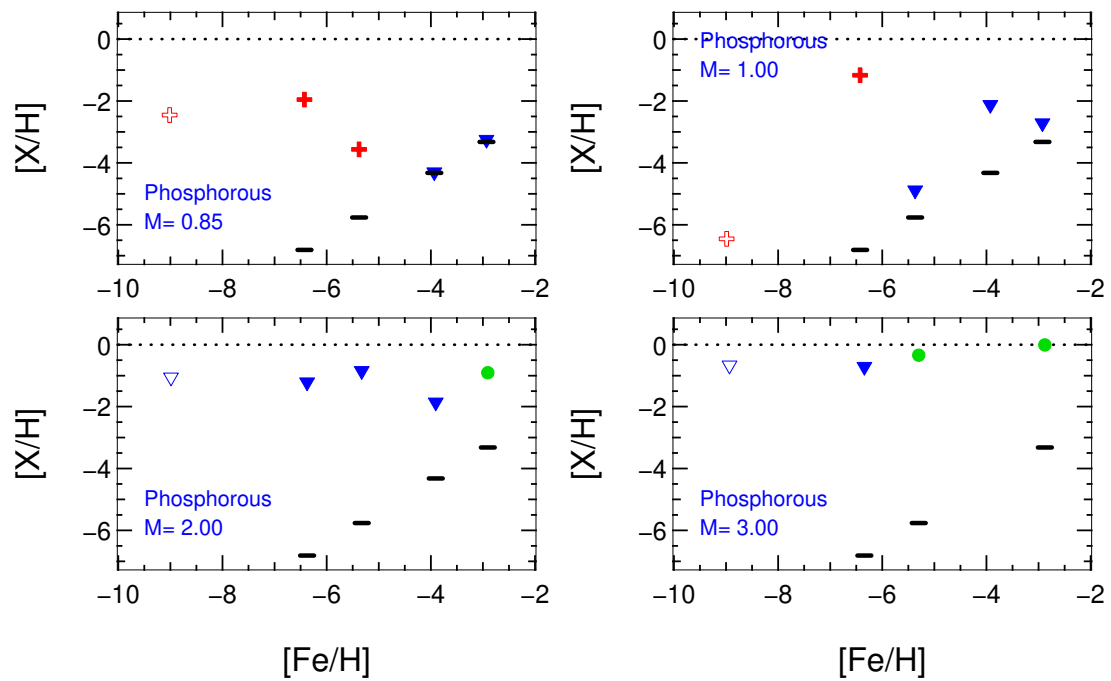


Figure A.17: Same as Figure A.6 except for phosphorous.

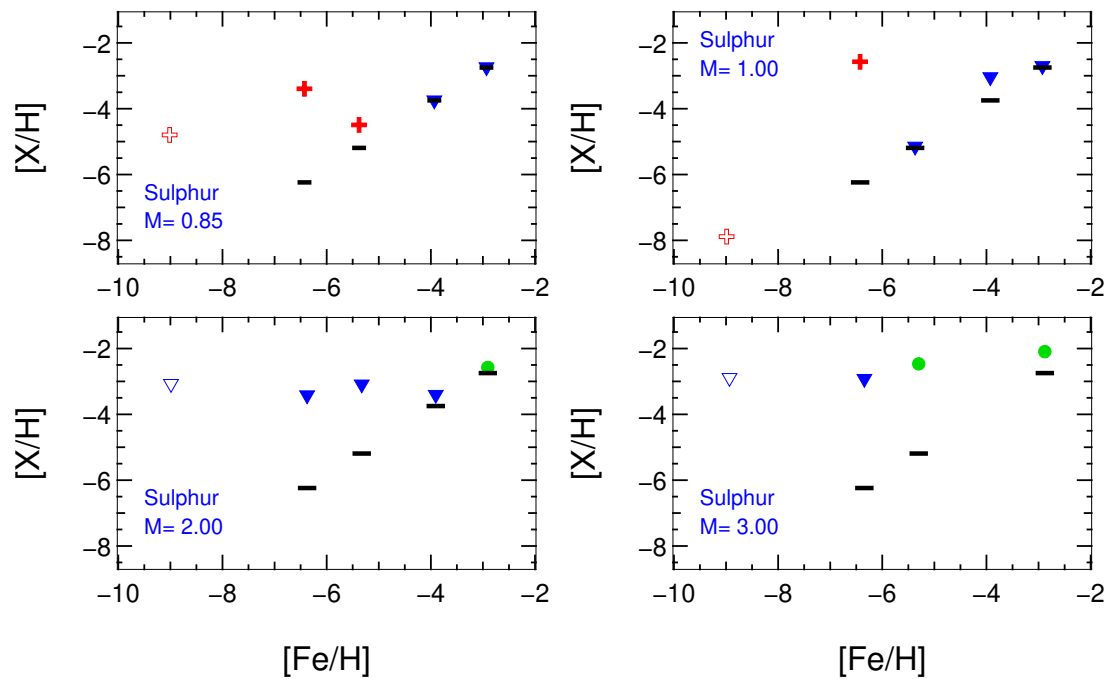


Figure A.18: Same as Figure A.6 except for sulphur.

A.3 Tables: Nuclidic Yields by Mass Fraction

Table A.1: Yields and initial composition for all the $Z = 0$ models. All species in the network are listed. Abundances are in mass fraction, normalised to 1.0. The remnant masses (white dwarf masses) are in brackets below the initial stellar masses in the table header.

Nuclide	Initial Abund. ^a	0.85 M _⊙ (0.776)	1.0 M _⊙ (0.843)	2.0 M _⊙ (1.080)	3.0 M _⊙ (1.101)
h1	0.7548	0.701	0.660	0.660	0.581
h2	1.960E-04	1.57E-04	9.17E-05	2.02E-08	3.34E-18
he3	7.851E-06	4.04E-05	1.60E-04	2.95E-07	1.16E-08
he4	0.2450	0.298	0.330	0.337	0.407
li7	3.130E-10	4.70E-10	1.26E-09	4.49E-10	4.88E-11
be7	0.0	2.73E-14	2.68E-14	5.27E-15	4.61E-14
b8	0.0	1.65E-27	7.54E-27	6.34E-27	1.50E-27
c12	0.0	2.60E-05	1.84E-03	1.31E-04	4.88E-04
c13	0.0	7.78E-06	3.62E-04	3.03E-05	1.15E-04
c14	0.0	3.72E-12	3.37E-09	6.09E-12	8.53E-11
n13	0.0	0.0	0.0	0.0	0.0
n14	0.0	2.44E-04	3.92E-03	3.43E-03	1.17E-02
n15	0.0	9.10E-09	1.14E-06	1.49E-07	7.41E-07
o14	0.0	0.0	0.0	0.0	0.0
o15	0.0	0.0	0.0	0.0	0.0
o16	0.0	5.03E-04	4.33E-03	4.88E-05	1.52E-04
o17	0.0	7.40E-06	4.55E-05	1.40E-07	6.13E-07
o18	0.0	3.25E-08	1.46E-05	7.03E-11	2.42E-10
o19	0.0	0.0	0.0	0.0	0.0
fl7	0.0	0.0	0.0	0.0	0.0
fl8	0.0	0.0	0.0	0.0	0.0
fl9	0.0	1.85E-09	6.22E-06	2.88E-10	1.19E-09
f20	0.0	0.0	0.0	0.0	0.0
ne19	0.0	0.0	0.0	0.0	0.0
ne20	0.0	2.48E-07	1.73E-06	2.74E-05	1.39E-04
ne21	0.0	6.77E-12	4.64E-08	1.81E-09	3.73E-09
ne22	0.0	8.33E-10	4.24E-05	4.74E-07	5.32E-06
na21	0.0	0.0	0.0	0.0	0.0
na22	0.0	2.30E-26	4.86E-17	1.81E-12	2.99E-11
na23	0.0	1.29E-09	1.13E-05	1.29E-05	9.54E-05
na24	0.0	0.0	0.0	0.0	0.0
mg23	0.0	0.0	0.0	0.0	0.0
mg24	0.0	3.84E-11	1.36E-06	1.86E-07	2.63E-07
mg25	0.0	1.46E-08	3.17E-07	1.76E-06	1.56E-05
mg26	0.0	2.47E-08	4.06E-08	8.16E-06	6.89E-05
mg27	0.0	0.0	0.0	0.0	0.0
al25	0.0	0.0	0.0	0.0	0.0
al-6	0.0	3.18E-11	3.36E-10	3.08E-07	1.49E-06
al*6	0.0	0.0	0.0	0.0	0.0
al27	0.0	4.39E-08	1.63E-10	1.34E-06	7.36E-06
al28	0.0	0.0	0.0	0.0	0.0
si27	0.0	0.0	0.0	0.0	0.0
si28	0.0	1.00E-07	1.65E-11	6.17E-07	1.31E-06
si29	0.0	1.16E-08	8.23E-13	1.27E-07	3.06E-07
si30	0.0	2.77E-09	1.83E-13	3.34E-08	7.49E-08
si31	0.0	0.0	0.0	0.0	0.0
si32	0.0	8.70E-21	7.99E-25	6.37E-13	2.20E-12
si33	0.0	0.0	0.0	0.0	0.0
p29	0.0	0.0	0.0	0.0	0.0
p30	0.0	0.0	0.0	0.0	0.0
p31	0.0	2.20E-08	2.07E-12	5.22E-07	1.12E-06
p32	0.0	3.38E-24	3.10E-28	2.47E-16	8.55E-16
p33	0.0	0.0	0.0	4.75E-24	4.23E-22

Continued on next page...

Table A.1 – continued from previous page.

Nuclide	Initial Abund.	0.85 M _⊙ (0.776)	1.0 M _⊙ (0.843)	2.0 M _⊙ (1.080)	3.0 M _⊙ (1.101)
p34	0.0	0.0	0.0	0.0	0.0
s32	0.0	4.38E-09	1.22E-12	1.87E-07	2.66E-07
s33	0.0	6.24E-10	3.36E-14	9.23E-09	1.54E-08
s34	0.0	2.19E-10	1.32E-13	5.56E-09	1.42E-08
s35	0.0	3.98E-10	3.13E-12	8.31E-08	8.31E-08
fe56	0.0	0.0	0.0	0.0	0.0
fe57	0.0	0.0	0.0	0.0	0.0
fe58	0.0	0.0	0.0	0.0	0.0
fe59	0.0	0.0	0.0	0.0	0.0
fe60	0.0	0.0	0.0	0.0	0.0
fe61	0.0	0.0	0.0	0.0	0.0
co59	0.0	0.0	0.0	0.0	0.0
co60	0.0	0.0	0.0	0.0	0.0
co61	0.0	0.0	0.0	0.0	0.0
ni58	0.0	0.0	0.0	0.0	0.0
ni59	0.0	0.0	0.0	0.0	0.0
ni60	0.0	0.0	0.0	0.0	0.0
ni61	0.0	0.0	0.0	0.0	0.0
ni62	0.0	0.0	0.0	0.0	0.0
g	0.0	0.0	0.0	0.0	0.0

Table A.2: Yields and initial composition for all the $[\text{Fe}/\text{H}] = -6.5$ models. All species in the network are listed except for neutrons. Abundances are in mass fraction, normalised to 1.0. The remnant masses (white dwarf masses) are in brackets below the initial stellar masses in the table header.

Nuclide	Initial [Fe/H] = -6.5	0.85 M _⊙ (0.758)	1.0 M _⊙ (0.846)	2.0 M _⊙ (1.066)	3.0 M _⊙ (1.107)
h1	0.7548	0.686	0.642	0.656	0.604
h2	0.00E+00	3.44E-19	2.08E-18	3.99E-18	3.53E-18
he3	7.85E-06	1.33E-05	1.62E-04	1.61E-07	1.72E-08
he4	0.2450	0.280	0.307	0.336	0.384
li7	3.13E-10	1.65E-09	7.22E-10	3.46E-10	5.14E-11
be7	0.00E+00	5.26E-16	7.96E-15	6.63E-14	3.71E-14
b8	0.00E+00	5.04E-26	4.00E-27	1.04E-26	5.32E-27
c12	1.30E-09	7.59E-03	1.04E-02	2.99E-04	4.38E-04
c13	1.33E-16	9.74E-04	1.18E-03	6.86E-05	1.04E-04
c14	0.00E+00	8.58E-07	2.07E-07	4.84E-11	6.76E-11
n13	0.00E+00	0.00E+00	0.00E+00	0.00E+00	0.00E+00
n14	2.27E-16	2.03E-03	2.92E-03	7.60E-03	1.06E-02
n15	1.30E-18	7.36E-06	8.92E-06	3.09E-07	7.02E-07
o14	0.00E+00	0.00E+00	0.00E+00	0.00E+00	0.00E+00
o15	0.00E+00	0.00E+00	0.00E+00	7.86E-37	0.00E+00
o16	2.23E-09	2.10E-02	3.03E-02	1.32E-04	1.42E-04
o17	3.39E-17	1.37E-03	6.21E-03	3.45E-07	5.70E-07
o18	2.26E-16	8.12E-05	1.64E-05	1.47E-10	2.30E-10
o19	0.00E+00	0.00E+00	0.00E+00	0.00E+00	0.00E+00
fl7	0.00E+00	0.00E+00	0.00E+00	1.41E-42	0.00E+00
fl8	0.00E+00	0.00E+00	0.00E+00	2.79E-34	0.00E+00
fl9	3.92E-18	4.90E-07	3.55E-07	7.24E-10	5.80E-10
f20	0.00E+00	0.00E+00	0.00E+00	0.00E+00	0.00E+00
ne19	0.00E+00	0.00E+00	0.00E+00	0.00E+00	0.00E+00
ne20	9.24E-10	3.34E-05	6.73E-05	6.12E-05	1.11E-04
ne21	2.06E-13	2.48E-06	6.69E-06	1.04E-08	2.60E-09
ne22	4.64E-14	3.14E-05	6.66E-05	5.05E-06	5.36E-06
na21	0.00E+00	0.00E+00	0.00E+00	0.00E+00	0.00E+00
na22	0.00E+00	3.24E-30	1.92E-17	4.83E-12	2.30E-11
na23	1.23E-11	7.33E-07	1.14E-06	9.86E-05	8.39E-05
na24	0.00E+00	0.00E+00	0.00E+00	6.93E-37	0.00E+00
mg23	0.00E+00	0.00E+00	0.00E+00	0.00E+00	0.00E+00
mg24	4.13E-10	4.81E-07	4.82E-07	1.89E-07	2.08E-07
mg25	4.49E-12	3.22E-07	2.44E-07	5.74E-06	1.39E-05
mg26	4.95E-12	1.68E-06	3.53E-06	2.62E-05	6.25E-05
mg27	0.00E+00	0.00E+00	0.00E+00	0.00E+00	0.00E+00
al25	0.00E+00	0.00E+00	0.00E+00	0.00E+00	0.00E+00
al-6	0.00E+00	1.66E-12	2.48E-11	4.16E-07	1.17E-06
al*6	0.00E+00	0.00E+00	0.00E+00	0.00E+00	0.00E+00
al27	1.00E-11	3.47E-08	6.31E-08	1.25E-06	6.22E-06
al28	0.00E+00	0.00E+00	0.00E+00	0.00E+00	0.00E+00
si27	0.00E+00	0.00E+00	0.00E+00	0.00E+00	0.00E+00
si28	3.75E-10	6.64E-08	1.62E-07	4.00E-07	1.16E-06
si29	3.95E-12	1.17E-08	2.77E-08	1.01E-07	2.74E-07
si30	2.78E-12	5.61E-09	1.45E-08	2.55E-08	6.90E-08
si31	0.00E+00	0.00E+00	0.00E+00	1.70E-41	0.00E+00
si32	0.00E+00	3.02E-16	2.30E-17	6.52E-12	4.98E-12
si33	0.00E+00	0.00E+00	0.00E+00	0.00E+00	0.00E+00
p29	0.00E+00	0.00E+00	0.00E+00	0.00E+00	0.00E+00
p30	0.00E+00	0.00E+00	0.00E+00	0.00E+00	0.00E+00
p31	1.04E-12	6.82E-08	3.91E-07	3.59E-07	1.05E-06
p32	0.00E+00	1.17E-19	8.91E-21	2.53E-15	1.93E-15
p33	0.00E+00	-3.08E-44	0.00E+00	1.17E-23	4.58E-22

Continued on next page...

Table A.2 – continued from previous page

Nuclide	Initial [Fe/H] = -6.5	0.85 M _⊙ (0.758)	1.0 M _⊙ (0.846)	2.0 M _⊙ (1.066)	3.0 M _⊙ (1.107)
p34	0.00E+00	0.00E+00	0.00E+00	0.00E+00	0.00E+00
s32	1.65E-10	2.61E-08	2.05E-07	7.95E-08	2.47E-07
s33	7.78E-13	1.95E-09	2.86E-09	9.74E-09	1.63E-08
s34	5.30E-11	3.19E-09	6.39E-09	6.35E-09	1.56E-08
s35	0.00E+00	1.16E-07	6.94E-07	3.22E-08	9.27E-08
fe56	4.54E-10	4.13E-10	3.86E-10	4.42E-10	4.39E-10
fe57	1.37E-11	1.25E-11	1.17E-11	1.35E-11	1.34E-11
fe58	2.79E-18	8.97E-15	1.33E-15	4.87E-13	5.27E-13
fe59	0.00E+00	0.00E+00	0.00E+00	0.00E+00	5.86E-31
fe60	0.00E+00	5.60E-16	1.19E-16	3.35E-13	4.94E-13
fe61	0.00E+00	0.00E+00	0.00E+00	0.00E+00	0.00E+00
co59	7.22E-12	6.57E-12	6.14E-12	7.29E-12	7.24E-12
co60	0.00E+00	4.87E-20	1.04E-20	2.92E-17	4.30E-17
co61	0.00E+00	0.00E+00	0.00E+00	0.00E+00	0.00E+00
ni58	6.41E-12	5.83E-12	5.46E-12	6.24E-12	6.20E-12
ni59	0.00E+00	1.01E-18	1.93E-24	4.61E-19	1.06E-18
ni60	7.43E-15	4.18E-14	1.66E-14	1.44E-12	1.53E-12
ni61	4.00E-17	4.69E-11	7.68E-11	1.06E-11	1.40E-11
ni62	2.38E-20	2.04E-20	1.28E-20	1.99E-24	2.05E-25
g ^a	4.67E-16	6.35E-08	3.16E-07	1.41E-09	6.38E-10

Table A.3: Yields and initial composition for all the $[\text{Fe}/\text{H}] = -5.45$ models. All species in the network are listed except for neutrons. Abundances are in mass fraction, normalised to 1.0. The remnant masses (white dwarf masses) are in brackets below the initial stellar masses in the table header.

Nuclide	Initial [Fe/H]= -5.45	0.85 M _⊙ (0.744)	1.0 M _⊙ (0.873)	2.0 M _⊙ (1.058)	3.0 M _⊙ (1.097)
h1	0.7548	0.658	0.730	0.651	0.603
h2	0.00E+00	4.47E-19	3.78E-18	4.04E-18	3.54E-18
he3	7.85E-06	6.21E-05	1.68E-04	1.71E-07	1.89E-08
he4	0.2450	0.329	0.267	0.334	0.380
li7	3.13E-10	1.05E-09	1.00E-08	3.09E-10	5.03E-11
be7	0.00E+00	0.00E+00	2.17E-14	5.37E-14	1.40E-14
b8	0.00E+00	7.29E-20	2.35E-25	3.13E-26	2.28E-25
c12	1.46E-08	6.05E-03	1.84E-03	4.96E-04	6.35E-04
c13	1.49E-15	9.68E-04	1.42E-04	1.14E-04	1.49E-04
c14	0.00E+00	3.26E-08	5.12E-12	1.14E-10	1.30E-10
n13	0.00E+00	0.00E+00	0.00E+00	0.00E+00	0.00E+00
n14	2.54E-15	9.96E-04	8.08E-05	1.34E-02	1.58E-02
n15	1.45E-17	2.91E-07	2.81E-09	5.27E-07	9.22E-07
o14	0.00E+00	0.00E+00	0.00E+00	0.00E+00	0.00E+00
o15	0.00E+00	0.00E+00	0.00E+00	0.00E+00	0.00E+00
o16	2.50E-08	3.89E-03	1.04E-04	2.06E-04	2.23E-04
o17	3.80E-16	7.93E-04	2.18E-06	5.04E-07	8.00E-07
o18	2.53E-15	1.22E-06	2.29E-09	2.10E-10	2.43E-10
o19	0.00E+00	0.00E+00	0.00E+00	0.00E+00	0.00E+00
fl7	0.00E+00	0.00E+00	0.00E+00	0.00E+00	0.00E+00
fl8	0.00E+00	0.00E+00	0.00E+00	0.00E+00	0.00E+00
fl9	4.39E-17	1.72E-08	2.72E-08	1.46E-09	1.03E-09
f20	0.00E+00	0.00E+00	0.00E+00	0.00E+00	0.00E+00
ne19	0.00E+00	0.00E+00	0.00E+00	0.00E+00	0.00E+00
ne20	1.03E-08	2.95E-06	3.80E-06	5.82E-05	2.17E-04
ne21	2.31E-12	4.80E-07	6.12E-07	4.40E-09	5.21E-09
ne22	5.19E-13	2.97E-06	6.72E-06	1.20E-05	1.23E-05
na21	0.00E+00	0.00E+00	0.00E+00	0.00E+00	0.00E+00
na22	0.00E+00	0.00E+00	7.61E-16	3.97E-12	2.88E-11
na23	1.37E-10	4.90E-08	1.62E-07	2.50E-04	2.61E-04
na24	0.00E+00	0.00E+00	0.00E+00	0.00E+00	0.00E+00
mg23	0.00E+00	0.00E+00	0.00E+00	0.00E+00	0.00E+00
mg24	4.62E-09	5.13E-09	5.94E-09	3.10E-07	6.03E-07
mg25	5.02E-11	7.54E-10	9.44E-10	1.72E-05	3.02E-05
mg26	5.54E-11	2.00E-08	2.58E-09	6.96E-05	1.35E-04
mg27	0.00E+00	0.00E+00	0.00E+00	0.00E+00	0.00E+00
al25	0.00E+00	0.00E+00	0.00E+00	0.00E+00	0.00E+00
al-6	0.00E+00	1.50E-14	1.16E-11	1.04E-06	2.32E-06
al*6	0.00E+00	0.00E+00	0.00E+00	0.00E+00	0.00E+00
al27	1.12E-10	4.48E-10	1.62E-10	2.63E-06	9.79E-06
al28	0.00E+00	0.00E+00	0.00E+00	0.00E+00	0.00E+00
si27	0.00E+00	0.00E+00	0.00E+00	0.00E+00	0.00E+00
si28	4.19E-09	4.60E-09	4.32E-09	1.02E-06	2.43E-06
si29	4.42E-11	1.95E-10	7.43E-11	2.67E-07	6.44E-07
si30	3.12E-11	9.94E-11	3.71E-11	6.29E-08	1.62E-07
si31	0.00E+00	0.00E+00	0.00E+00	0.00E+00	0.00E+00
si32	0.00E+00	9.95E-18	1.21E-15	1.14E-11	7.41E-12
si33	0.00E+00	0.00E+00	0.00E+00	0.00E+00	0.00E+00
p29	0.00E+00	0.00E+00	0.00E+00	0.00E+00	0.00E+00
p30	0.00E+00	0.00E+00	0.00E+00	0.00E+00	0.00E+00
p31	1.16E-11	1.61E-09	8.49E-11	8.33E-07	2.47E-06
p32	0.00E+00	3.86E-21	4.71E-19	4.41E-15	2.88E-15
p33	0.00E+00	0.00E+00	0.00E+00	1.41E-23	3.14E-22

Continued on next page...

Table A.3 – continued from previous page

Nuclide	Initial [Fe/H]= -5.45	0.85 M _⊙ (0.744)	1.0 M _⊙ (0.873)	2.0 M _⊙ (1.058)	3.0 M _⊙ (1.097)
p34	0.00E+00	0.00E+00	0.00E+00	0.00E+00	0.00E+00
s32	1.84E-09	2.35E-09	1.84E-09	1.82E-07	5.96E-07
s33	8.71E-12	8.49E-11	2.19E-11	1.58E-08	3.32E-08
s34	5.93E-10	5.67E-10	5.87E-10	1.31E-08	3.62E-08
s35	0.00E+00	8.21E-09	1.81E-10	5.97E-08	3.89E-07
fe56	5.08E-09	4.43E-09	5.00E-09	4.90E-09	4.82E-09
fe57	1.54E-10	1.34E-10	1.52E-10	1.51E-10	1.48E-10
fe58	3.12E-17	2.75E-17	3.98E-12	1.30E-11	8.79E-12
fe59	0.00E+00	0.00E+00	0.00E+00	6.65E-30	5.35E-31
fe60	0.00E+00	2.01E-18	1.06E-14	5.61E-12	6.16E-12
fe61	0.00E+00	0.00E+00	0.00E+00	0.00E+00	0.00E+00
co59	8.08E-11	7.05E-11	8.21E-11	8.41E-11	8.09E-11
co60	0.00E+00	1.75E-22	9.19E-19	4.90E-16	5.36E-16
co61	0.00E+00	0.00E+00	0.00E+00	0.00E+00	0.00E+00
ni58	7.17E-11	6.25E-11	7.07E-11	6.92E-11	6.80E-11
ni59	0.00E+00	1.79E-25	1.91E-19	4.08E-17	1.03E-17
ni60	8.32E-14	7.26E-14	1.48E-11	2.46E-11	2.97E-11
ni61	4.47E-16	7.48E-10	6.14E-11	1.44E-10	2.43E-10
ni62	2.67E-19	2.15E-19	1.08E-19	1.70E-23	6.59E-24
g ^a	5.23E-15	1.95E-06	4.73E-08	5.28E-09	1.25E-08

Table A.4: Yields and initial composition for all the $[\text{Fe}/\text{H}] = -4.0$ models. All species in the network are listed except for neutrons. Abundances are in mass fraction, normalised to 1.0. The remnant masses (white dwarf masses) are in brackets below the initial stellar masses in the table header. Due to loss of data we were unable to calculate the yield for the $3 M_{\odot}$ model in this case.

Nuclide	Initial [Fe/H] = -4.0	0.85 M_{\odot} (0.761)	1.0 M_{\odot} (0.852)	2.0 M_{\odot} (1.085)
h1	0.7548	0.752	0.724	0.695
h2	0.00E+00	1.70E-18	3.93E-18	4.51E-18
he3	7.85E-06	2.10E-04	2.00E-04	2.74E-06
he4	0.2450	0.248	0.268	0.300
li7	3.13E-10	2.94E-10	1.73E-08	4.43E-10
be7	0.00E+00	4.53E-15	2.53E-15	2.09E-13
b8	0.00E+00	2.59E-27	1.61E-25	1.49E-26
c12	4.04E-07	3.19E-05	4.88E-03	1.77E-04
c13	4.12E-14	6.34E-06	3.69E-04	4.03E-05
c14	0.00E+00	3.02E-10	9.87E-09	2.08E-11
n13	0.00E+00	0.00E+00	0.00E+00	0.00E+00
n14	7.03E-14	1.07E-05	2.06E-04	4.41E-03
n15	4.03E-16	3.35E-09	3.76E-08	1.78E-07
o14	0.00E+00	0.00E+00	0.00E+00	0.00E+00
o15	0.00E+00	0.00E+00	0.00E+00	0.00E+00
o16	6.91E-07	2.48E-05	1.73E-03	9.31E-05
o17	1.05E-14	3.13E-06	2.66E-04	2.71E-07
o18	7.02E-14	7.84E-09	1.90E-07	1.65E-10
o19	0.00E+00	0.00E+00	0.00E+00	0.00E+00
f17	0.00E+00	0.00E+00	0.00E+00	0.00E+00
f18	0.00E+00	0.00E+00	0.00E+00	0.00E+00
f19	1.21E-15	1.05E-10	3.43E-09	1.54E-09
f20	0.00E+00	0.00E+00	3.26E-38	0.00E+00
ne19	0.00E+00	0.00E+00	0.00E+00	0.00E+00
ne20	2.87E-07	3.01E-07	2.06E-05	7.59E-05
ne21	6.39E-11	1.38E-09	2.69E-06	1.68E-08
ne22	1.44E-11	2.61E-08	2.29E-04	1.64E-06
na21	0.00E+00	0.00E+00	0.00E+00	0.00E+00
na22	0.00E+00	-2.22E-29	7.82E-15	3.99E-12
na23	3.81E-09	5.01E-09	4.95E-06	4.97E-05
na24	0.00E+00	0.00E+00	0.00E+00	0.00E+00
mg23	0.00E+00	0.00E+00	0.00E+00	0.00E+00
mg24	1.28E-07	1.28E-07	3.16E-07	2.26E-07
mg25	1.39E-09	1.40E-09	7.57E-08	1.59E-06
mg26	1.54E-09	1.94E-09	1.42E-06	6.00E-06
mg27	0.00E+00	0.00E+00	0.00E+00	0.00E+00
al25	0.00E+00	0.00E+00	0.00E+00	0.00E+00
al-6	0.00E+00	4.17E-13	1.00E-10	1.75E-07
al*6	0.00E+00	0.00E+00	0.00E+00	0.00E+00
al27	3.10E-09	3.13E-09	2.97E-08	4.37E-07
al28	0.00E+00	0.00E+00	0.00E+00	0.00E+00
si27	0.00E+00	0.00E+00	0.00E+00	0.00E+00
si28	1.16E-07	1.16E-07	1.66E-07	2.30E-07
si29	1.22E-09	1.23E-09	1.28E-08	2.45E-08
si30	8.63E-10	8.63E-10	3.06E-09	6.68E-09
si31	0.00E+00	0.00E+00	0.00E+00	0.00E+00
si32	0.00E+00	2.93E-17	1.36E-11	9.56E-13
si33	0.00E+00	0.00E+00	0.00E+00	0.00E+00
p29	0.00E+00	0.00E+00	0.00E+00	0.00E+00
p30	0.00E+00	0.00E+00	0.00E+00	0.00E+00
p31	3.21E-10	3.37E-10	4.88E-08	8.55E-08
p32	0.00E+00	1.14E-20	5.29E-15	3.71E-16

Continued on next page...

Table A.4 – continued from previous page

Nuclide	Initial [Fe/H] = -4.0	0.85 M _⊙ (0.761)	1.0 M _⊙ (0.852)	2.0 M _⊙ (1.085)
p33	0.00E+00	0.00E+00	0.00E+00	1.97E-24
p34	0.00E+00	0.00E+00	0.00E+00	0.00E+00
s32	5.10E-08	5.10E-08	9.01E-08	7.05E-08
s33	2.41E-10	2.51E-10	2.84E-08	7.52E-09
s34	1.64E-08	1.64E-08	2.46E-08	1.87E-08
s35	0.00E+00	5.02E-10	2.06E-07	4.44E-08
fe56	1.41E-07	1.41E-07	1.38E-07	1.38E-07
fe57	4.25E-09	4.25E-09	4.16E-09	4.22E-09
fe58	8.65E-16	2.41E-14	4.30E-14	1.87E-10
fe59	0.00E+00	0.00E+00	0.00E+00	8.39E-27
fe60	0.00E+00	4.56E-17	1.98E-16	4.27E-11
fe61	0.00E+00	0.00E+00	0.00E+00	0.00E+00
co59	2.24E-09	2.24E-09	2.19E-09	2.29E-09
co60	0.00E+00	3.97E-21	1.82E-20	3.73E-15
co61	0.00E+00	0.00E+00	0.00E+00	0.00E+00
ni58	1.99E-09	1.98E-09	1.94E-09	1.95E-09
ni59	0.00E+00	1.51E-19	1.07E-20	1.71E-15
ni60	2.31E-12	2.33E-12	2.43E-12	3.49E-10
ni61	1.24E-14	8.03E-11	3.52E-09	1.86E-09
ni62	7.38E-18	5.48E-18	2.75E-18	1.68E-20
g ^a	1.45E-13	1.59E-07	3.82E-06	9.96E-07

Table A.5: Yields and initial composition for all the $[\text{Fe}/\text{H}] = -3.0$ models. All species in the network are listed except for neutrons. Abundances are in mass fraction, normalised to 1.0. The remnant masses (white dwarf masses) are in brackets below the initial stellar masses in the table header.

Nuclide	Initial [Fe/H] = -3.0	0.85 M _⊙ (0.753)	1.0 M _⊙ (0.855)	2.0 M _⊙ (1.038)	3.0 M _⊙ (1.069)
h1	0.7548	0.748	0.730	0.678	0.619
h2	0.00E+00	2.20E-18	3.87E-18	4.24E-18	3.70E-18
he3	7.85E-06	2.68E-04	2.29E-04	2.56E-06	3.90E-08
he4	0.2450	0.251	0.268	0.308	0.356
li7	3.13E-10	9.15E-10	2.44E-09	2.01E-10	6.43E-11
be7	0.00E+00	0.00E+00	1.43E-14	9.57E-14	1.34E-13
b8	0.00E+00	9.75E-27	2.64E-26	1.04E-26	1.43E-27
c12	4.04E-06	3.93E-04	2.01E-03	4.71E-04	8.76E-04
c13	4.12E-13	2.02E-05	1.07E-04	1.08E-04	2.05E-04
c14	0.00E+00	1.92E-09	1.93E-12	6.84E-11	1.96E-10
n13	0.00E+00	0.00E+00	0.00E+00	0.00E+00	0.00E+00
n14	7.03E-13	5.79E-06	5.94E-05	1.26E-02	2.23E-02
n15	4.03E-15	7.83E-10	2.68E-09	4.70E-07	1.13E-06
o14	0.00E+00	0.00E+00	0.00E+00	0.00E+00	0.00E+00
o15	0.00E+00	0.00E+00	0.00E+00	0.00E+00	0.00E+00
o16	6.91E-06	9.33E-05	2.60E-04	1.98E-04	3.48E-04
o17	1.05E-13	1.05E-05	1.61E-05	4.38E-07	1.08E-06
o18	7.01E-13	8.02E-09	1.73E-08	1.90E-10	2.72E-10
o19	0.00E+00	0.00E+00	0.00E+00	0.00E+00	0.00E+00
fl7	0.00E+00	0.00E+00	0.00E+00	0.00E+00	0.00E+00
fl8	0.00E+00	0.00E+00	0.00E+00	0.00E+00	0.00E+00
fl9	1.21E-14	1.36E-10	1.16E-10	1.32E-09	1.50E-09
f20	0.00E+00	0.00E+00	0.00E+00	0.00E+00	0.00E+00
ne19	0.00E+00	0.00E+00	0.00E+00	0.00E+00	0.00E+00
ne20	2.87E-06	4.20E-06	8.43E-06	4.59E-05	2.58E-04
ne21	6.39E-10	2.50E-07	1.09E-06	6.98E-09	9.33E-09
ne22	1.44E-10	1.99E-06	7.41E-06	1.35E-05	3.23E-05
na21	0.00E+00	0.00E+00	0.00E+00	0.00E+00	0.00E+00
na22	0.00E+00	1.43E-17	4.12E-16	2.49E-12	2.94E-11
na23	3.81E-08	4.91E-08	1.58E-07	3.34E-04	6.74E-04
na24	0.00E+00	0.00E+00	0.00E+00	0.00E+00	0.00E+00
mg23	0.00E+00	0.00E+00	0.00E+00	0.00E+00	0.00E+00
mg24	1.28E-06	1.28E-06	1.27E-06	1.43E-06	1.69E-06
mg25	1.39E-08	1.42E-08	1.42E-08	1.31E-05	6.76E-05
mg26	1.54E-08	2.24E-08	3.52E-08	5.49E-05	2.96E-04
mg27	0.00E+00	0.00E+00	0.00E+00	0.00E+00	0.00E+00
al25	0.00E+00	0.00E+00	0.00E+00	0.00E+00	0.00E+00
al-6	0.00E+00	8.84E-13	4.35E-11	7.02E-07	4.03E-06
al*6	0.00E+00	0.00E+00	0.00E+00	0.00E+00	0.00E+00
al27	3.10E-08	3.11E-08	3.16E-08	1.73E-06	1.43E-05
al28	0.00E+00	0.00E+00	0.00E+00	0.00E+00	0.00E+00
si27	0.00E+00	0.00E+00	0.00E+00	0.00E+00	0.00E+00
si28	1.16E-06	1.16E-06	1.15E-06	1.98E-06	6.30E-06
si29	1.22E-08	1.23E-08	1.23E-08	2.40E-07	1.49E-06
si30	8.63E-09	8.63E-09	9.07E-09	6.33E-08	3.70E-07
si31	0.00E+00	0.00E+00	0.00E+00	0.00E+00	0.00E+00
si32	0.00E+00	3.63E-12	3.61E-13	9.87E-12	6.57E-12
si33	0.00E+00	0.00E+00	0.00E+00	0.00E+00	0.00E+00
p29	0.00E+00	0.00E+00	0.00E+00	0.00E+00	0.00E+00
p30	0.00E+00	0.00E+00	0.00E+00	0.00E+00	0.00E+00
p31	3.21E-09	3.77E-09	1.26E-08	7.54E-07	5.44E-06
p32	0.00E+00	1.41E-15	1.40E-16	3.83E-15	2.55E-15
p33	0.00E+00	0.00E+00	0.00E+00	2.14E-24	2.14E-22

Continued on next page...

Table A.5 – continued from previous page

Nuclide	Initial [Fe/H] = -3.0	0.85 M _⊙ (0.753)	1.0 M _⊙ (0.855)	2.0 M _⊙ (1.038)	3.0 M _⊙ (1.069)
p34	0.00E+00	0.00E+00	0.00E+00	0.00E+00	0.00E+00
s32	5.10E-07	5.09E-07	5.09E-07	6.57E-07	1.70E-06
s33	2.41E-09	2.57E-09	6.10E-09	1.71E-08	5.88E-08
s34	1.64E-07	1.64E-07	1.64E-07	1.69E-07	2.38E-07
s35	0.00E+00	1.35E-08	5.37E-08	6.75E-08	5.21E-07
fe56	1.41E-06	1.40E-06	1.39E-06	1.34E-06	1.31E-06
fe57	4.25E-08	4.25E-08	4.21E-08	4.17E-08	3.99E-08
fe58	8.64E-15	9.64E-14	3.37E-13	4.11E-09	2.41E-09
fe59	0.00E+00	0.00E+00	0.00E+00	8.44E-29	1.01E-29
fe60	0.00E+00	1.24E-15	-2.56E-22	9.75E-10	1.95E-09
fe61	0.00E+00	0.00E+00	0.00E+00	0.00E+00	0.00E+00
co59	2.24E-08	2.23E-08	2.21E-08	2.32E-08	2.20E-08
co60	0.00E+00	2.37E-19	-2.23E-26	8.52E-14	1.70E-13
co61	0.00E+00	0.00E+00	0.00E+00	0.00E+00	0.00E+00
ni58	1.99E-08	1.98E-08	1.96E-08	1.90E-08	1.84E-08
ni59	0.00E+00	1.13E-18	-5.49E-25	6.71E-16	8.40E-16
ni60	2.31E-11	2.32E-11	2.43E-11	8.88E-09	1.10E-08
ni61	1.24E-13	3.10E-09	1.75E-08	5.27E-08	9.81E-08
ni62	7.38E-17	4.89E-17	2.88E-17	2.64E-19	1.09E-21
g ^a	1.45E-12	3.13E-06	9.88E-06	2.27E-06	4.28E-06

Appendix B

Yields: Globular Cluster Models

This appendix holds the yields for the four sets of globular cluster models ($[\text{Fe}/\text{H}] = -1.4$) – the standard models, the models calculated using the NACRE rates (2 masses only), the models calculated using Reimers' mass-loss formula on the AGB (also only 2 masses), and the models with no 3DUP. The yields for every species in the nuclear network (except neutrons) are given, in mass fraction. There are 3 tables in total.

B.1 Tables: Nuclidic Yields by Mass Fraction

Table B.1: Yields and initial composition for all the standard GC models (for NGC 6752, $[\text{Fe}/\text{H}] = -1.4$). By standard models we mean that 3DUP has not been inhibited and we have used the standard mass loss rates and nuclear reaction rates. All species in the network are listed except for neutrons. Abundances are in mass fraction, normalised to 1.0. The remnant masses (white dwarf masses) are in brackets below the initial stellar masses in the table header.

Nuclide	Initial	1.25 M _⊙ (0.645)	2.5 M _⊙ (0.676)	3.5 M _⊙ (0.838)	5.0 M _⊙ (0.915)	6.5 M _⊙ (1.047)
h1	0.76860	0.74035	0.71976	0.73714	0.60457	0.64137
h2	2.26E-20	3.79E-18	4.23E-18	4.45E-18	3.66E-18	3.50E-18
he3	1.27E-09	3.02E-04	1.07E-04	8.97E-05	2.91E-07	1.49E-07
he4	0.22970	0.25644	0.26610	0.25487	0.37499	0.34909
li7	1.15E-14	5.75E-11	1.06E-07	3.90E-09	4.27E-17	2.37E-12
be7	0.00E+00	6.61E-18	2.34E-39	7.38E-14	1.19E-13	6.46E-15
b8	0.00E+00	1.08E-27	1.11E-18	1.73E-24	1.25E-21	9.93E-22
c12	2.10E-04	1.32E-03	9.97E-03	6.04E-03	2.02E-03	1.21E-03
c13	4.68E-10	4.62E-06	5.06E-04	3.32E-05	2.15E-04	1.25E-04
c14	0.00E+00	3.03E-11	1.19E-08	5.83E-10	4.82E-11	4.67E-13
n13	0.00E+00	0.00E+00	0.00E+00	0.00E+00	0.00E+00	0.00E+00
n14	1.45E-07	7.70E-05	1.45E-03	1.36E-04	1.63E-02	7.36E-03
n15	4.74E-12	4.39E-09	5.08E-08	4.86E-09	7.44E-07	6.71E-07
o14	0.00E+00	0.00E+00	0.00E+00	0.00E+00	0.00E+00	0.00E+00
o15	0.00E+00	0.00E+00	0.00E+00	0.00E+00	0.00E+00	0.00E+00
o16	1.11E-03	1.12E-03	1.17E-03	1.13E-03	5.13E-04	2.48E-04
o17	5.73E-11	7.51E-07	5.38E-06	2.73E-06	1.22E-06	1.05E-06
o18	1.05E-10	1.52E-09	1.54E-08	2.24E-09	3.84E-10	8.82E-10
o19	0.00E+00	0.00E+00	0.00E+00	0.00E+00	0.00E+00	0.00E+00
f17	0.00E+00	0.00E+00	0.00E+00	0.00E+00	0.00E+00	0.00E+00
f18	0.00E+00	0.00E+00	0.00E+00	4.08E-39	3.12E-35	4.51E-30
f19	4.22E-12	1.98E-08	1.29E-06	1.02E-07	1.41E-09	1.61E-10
f20	0.00E+00	0.00E+00	0.00E+00	0.00E+00	0.00E+00	0.00E+00
ne19	0.00E+00	0.00E+00	0.00E+00	0.00E+00	0.00E+00	0.00E+00
ne20	9.49E-05	9.48E-05	9.82E-05	9.68E-05	2.24E-04	1.23E-04
ne21	1.12E-08	2.20E-08	3.20E-07	3.05E-07	3.48E-07	9.51E-08
ne22	9.85E-09	1.03E-05	5.27E-04	1.32E-04	1.04E-04	5.52E-06
na21	0.00E+00	0.00E+00	0.00E+00	0.00E+00	0.00E+00	0.00E+00
na22	0.00E+00	2.21E-31	3.33E-32	4.64E-15	3.41E-11	5.84E-11
na23	5.25E-07	7.12E-07	1.09E-05	9.11E-07	2.12E-04	1.44E-05
na24	0.00E+00	0.00E+00	0.00E+00	1.44E-42	6.28E-36	1.43E-30
mg23	0.00E+00	0.00E+00	0.00E+00	0.00E+00	0.00E+00	0.00E+00
mg24	5.67E-05	5.67E-05	5.66E-05	5.54E-05	2.17E-05	9.79E-07
mg25	4.25E-08	8.31E-08	8.68E-06	1.32E-05	1.36E-04	8.03E-05
mg26	4.10E-08	6.65E-08	6.23E-06	2.30E-05	3.49E-04	1.12E-04
mg27	0.00E+00	0.00E+00	0.00E+00	0.00E+00	0.00E+00	0.00E+00
al25	0.00E+00	0.00E+00	0.00E+00	0.00E+00	0.00E+00	0.00E+00
al-6	0.00E+00	1.28E-08	7.09E-09	2.25E-09	8.59E-06	6.85E-06
al*6	0.00E+00	0.00E+00	0.00E+00	0.00E+00	0.00E+00	0.00E+00
al27	4.78E-07	4.96E-07	6.02E-07	1.15E-06	1.55E-05	1.07E-05
al28	0.00E+00	0.00E+00	0.00E+00	0.00E+00	0.00E+00	0.00E+00
si27	0.00E+00	0.00E+00	0.00E+00	0.00E+00	0.00E+00	0.00E+00
si28	1.54E-04	1.54E-04	1.53E-04	1.53E-04	1.59E-04	1.54E-04
si29	7.36E-08	8.72E-08	9.22E-07	7.95E-07	2.74E-06	9.56E-07
si30	4.14E-08	4.27E-08	1.78E-07	1.88E-07	7.38E-07	3.40E-07
si31	0.00E+00	0.00E+00	0.00E+00	0.00E+00	9.81E-45	4.83E-37
si32	0.00E+00	1.51E-18	6.36E-12	6.12E-12	2.28E-10	3.69E-10
si33	0.00E+00	0.00E+00	0.00E+00	0.00E+00	0.00E+00	0.00E+00
p29	0.00E+00	0.00E+00	0.00E+00	0.00E+00	0.00E+00	0.00E+00
p30	0.00E+00	0.00E+00	0.00E+00	0.00E+00	0.00E+00	0.00E+00
p31	2.01E-08	2.08E-08	3.63E-07	8.13E-07	8.46E-06	2.96E-06
p32	0.00E+00	5.84E-22	2.47E-15	2.37E-15	8.85E-14	1.43E-13
p33	0.00E+00	0.00E+00	0.00E+00	0.00E+00	1.05E-18	7.20E-17

Continued on next page...

Table B.1 – continued from previous page

Nuclide	Initial	1.25 M _⊙	2.5 M _⊙	3.5 M _⊙	5.0 M _⊙	6.5 M _⊙
		(0.645)	(0.676)	(0.838)	(0.915)	(1.047)
p34	0.00E+00	0.00E+00	0.00E+00	0.00E+00	0.00E+00	0.00E+00
s32	7.83E-06	7.83E-06	7.76E-06	7.86E-06	9.22E-06	8.29E-06
s33	1.68E-08	1.72E-08	2.29E-08	2.16E-08	9.59E-08	5.05E-08
s34	7.74E-08	2.38E-06	2.33E-06	2.35E-06	2.42E-06	2.41E-06
s35	0.00E+00	1.21E-09	5.44E-08	4.59E-08	6.73E-07	2.61E-07
fe56	5.49E-05	5.48E-05	5.34E-05	5.40E-05	5.21E-05	5.38E-05
fe57	4.82E-07	5.08E-07	8.66E-07	5.48E-07	5.19E-07	5.54E-07
fe58	3.27E-14	1.02E-08	6.14E-07	2.13E-07	1.66E-07	6.15E-08
fe59	0.00E+00	4.63E-45	0.00E+00	5.79E-30	2.80E-45	1.50E-31
fe60	0.00E+00	2.28E-12	3.02E-08	1.20E-07	1.20E-07	9.30E-08
fe61	0.00E+00	0.00E+00	0.00E+00	0.00E+00	0.00E+00	0.00E+00
co59	1.18E-07	1.19E-07	2.80E-07	1.98E-07	1.84E-07	1.43E-07
co60	0.00E+00	1.99E-16	2.63E-12	1.05E-11	1.05E-11	8.10E-12
co61	0.00E+00	0.00E+00	0.00E+00	0.00E+00	0.00E+00	1.83E-42
ni58	2.40E-07	2.39E-07	2.30E-07	2.35E-07	2.27E-07	2.34E-07
ni59	0.00E+00	1.89E-11	4.21E-11	1.61E-11	3.49E-13	5.64E-12
ni60	2.06E-10	7.86E-10	1.51E-07	1.18E-07	3.65E-07	1.01E-07
ni61	3.28E-13	1.51E-10	1.78E-07	3.53E-07	2.20E-06	8.47E-07
ni62	2.87E-16	0.00E+00	9.83E-19	5.95E-19	4.71E-19	3.13E-19
g	7.29E-14	1.16E-10	1.06E-06	6.57E-06	6.28E-05	2.47E-05

Table B.2: Yields and initial composition for all the comparison GC models ($[\text{Fe}/\text{H}] = -1.4$). There are two groups of comparison models. One group has been calculated with Reimers' mass loss formula on the AGB instead of that of VW93, whilst the other has been calculated using some updated rates from NACRE. All species in the network are listed except for neutrons. Abundances are in mass fraction, normalised to 1.0. The remnant masses (white dwarf masses) are in brackets below the initial stellar masses in the table header.

Nuclide	Initial	Reimers' on AGB		NACRE Rates	
		2.5 M _⊙ (0.681)	5.0 M _⊙ (0.914)	2.5 M _⊙ (0.676)	5.0 M _⊙ (0.915)
h1	0.76860	0.75389	0.66114	0.72009	0.61272
h2	2.26E-20	5.99E-18	4.35E-18	5.51E-18	3.71E-18
he3	1.27E-09	1.57E-04	3.73E-06	1.48E-04	3.31E-07
he4	0.22970	0.24173	0.32500	0.26588	0.36692
li7	1.15E-14	2.50E-11	3.24E-09	2.46E-10	0.00E+00
be7	0.00E+00	5.51E-18	6.56E-12	3.97E-19	1.31E-13
b8	0.00E+00	6.92E-28	3.62E-22	5.75E-24	0.00E+00
c12	2.10E-04	2.58E-03	3.49E-03	1.16E-02	2.03E-03
c13	4.68E-10	4.67E-06	2.27E-04	5.16E-06	2.35E-04
c14	0.00E+00	5.92E-11	3.51E-11	2.84E-11	9.27E-14
n13	0.00E+00	0.00E+00	1.54E-44	0.00E+00	0.00E+00
n14	1.45E-07	1.09E-04	8.40E-03	1.30E-04	1.62E-02
n15	4.74E-12	5.07E-09	3.75E-07	7.55E-09	7.53E-07
o14	0.00E+00	0.00E+00	0.00E+00	0.00E+00	0.00E+00
o15	0.00E+00	0.00E+00	0.00E+00	0.00E+00	0.00E+00
o16	1.11E-03	1.12E-03	7.32E-04	1.17E-03	4.96E-04
o17	5.73E-11	6.66E-06	1.60E-06	6.27E-06	1.17E-06
o18	1.05E-10	3.75E-09	9.14E-10	2.86E-09	3.61E-10
o19	0.00E+00	0.00E+00	0.00E+00	0.00E+00	0.00E+00
f17	0.00E+00	0.00E+00	0.00E+00	0.00E+00	0.00E+00
f18	0.00E+00	0.00E+00	1.93E-35	0.00E+00	3.94E-35
f19	4.22E-12	6.40E-08	2.10E-09	1.58E-06	1.63E-09
f20	0.00E+00	0.00E+00	0.00E+00	0.00E+00	0.00E+00
ne19	0.00E+00	0.00E+00	0.00E+00	0.00E+00	0.00E+00
ne20	9.49E-05	9.48E-05	1.31E-04	9.69E-05	1.98E-04
ne21	1.12E-08	2.20E-08	7.33E-07	3.08E-07	2.78E-07
ne22	9.85E-09	2.89E-05	1.35E-04	5.83E-04	1.01E-04
na21	0.00E+00	0.00E+00	0.00E+00	0.00E+00	0.00E+00
na22	0.00E+00	2.42E-26	2.68E-11	0.00E+00	2.96E-11
na23	5.25E-07	7.76E-07	8.93E-05	2.28E-06	1.45E-04
na24	0.00E+00	0.00E+00	8.72E-36	0.00E+00	7.51E-36
mg23	0.00E+00	0.00E+00	0.00E+00	0.00E+00	0.00E+00
mg24	5.67E-05	5.66E-05	3.52E-05	6.11E-05	7.05E-05
mg25	4.25E-08	2.59E-07	9.04E-05	1.06E-05	1.55E-04
mg26	4.10E-08	1.38E-07	2.43E-04	8.88E-06	3.73E-04
mg27	0.00E+00	0.00E+00	0.00E+00	0.00E+00	0.00E+00
al25	0.00E+00	0.00E+00	0.00E+00	0.00E+00	0.00E+00
al-6	0.00E+00	7.19E-09	3.53E-06	1.27E-08	1.20E-05
al*6	0.00E+00	0.00E+00	0.00E+00	0.00E+00	0.00E+00
al27	4.78E-07	5.22E-07	5.83E-06	6.66E-07	1.59E-05
al28	0.00E+00	0.00E+00	0.00E+00	0.00E+00	0.00E+00
si27	0.00E+00	0.00E+00	0.00E+00	0.00E+00	0.00E+00
si28	1.54E-04	1.54E-04	1.54E-04	1.53E-04	1.56E-04
si29	7.36E-08	1.25E-07	1.80E-06	1.06E-06	3.51E-06
si30	4.14E-08	4.72E-08	4.95E-07	4.26E-07	4.90E-06
si31	0.00E+00	0.00E+00	1.20E-44	0.00E+00	1.34E-44
si32	0.00E+00	4.71E-17	7.24E-10	1.09E-12	1.79E-10
si33	0.00E+00	0.00E+00	0.00E+00	0.00E+00	0.00E+00
p29	0.00E+00	0.00E+00	0.00E+00	0.00E+00	0.00E+00
p30	0.00E+00	0.00E+00	0.00E+00	0.00E+00	0.00E+00
p31	2.01E-08	2.46E-08	4.85E-06	1.17E-07	6.98E-06

Continued on next page...

Table B.2 – continued from previous page

Nuclide	Initial	Reimers' on AGB		NACRE Rates	
		2.5 M _⊙ (0.681)	5.0 M _⊙ (0.914)	2.5 M _⊙ (0.676)	5.0 M _⊙ (0.915)
p32	0.00E+00	1.83E-20	2.81E-13	4.22E-16	6.94E-14
p33	0.00E+00	0.00E+00	6.53E-19	3.04E-39	5.76E-19
p34	0.00E+00	0.00E+00	0.00E+00	0.00E+00	0.00E+00
s32	7.83E-06	7.83E-06	8.60E-06	7.75E-06	8.83E-06
s33	1.68E-08	1.79E-08	5.18E-08	2.35E-08	8.55E-08
s34	7.74E-08	2.38E-06	2.40E-06	2.34E-06	2.38E-06
s35	0.00E+00	3.97E-09	4.03E-07	4.72E-08	5.32E-07
fe56	5.49E-05	5.47E-05	5.31E-05	5.36E-05	5.22E-05
fe57	4.82E-07	5.54E-07	5.17E-07	8.88E-07	5.25E-07
fe58	3.27E-14	4.14E-08	1.20E-07	5.42E-07	1.72E-07
fe59	0.00E+00	0.00E+00	0.00E+00	1.49E-37	1.13E-23
fe60	0.00E+00	1.80E-10	1.26E-07	1.81E-08	1.25E-07
fe61	0.00E+00	0.00E+00	0.00E+00	0.00E+00	0.00E+00
co59	1.18E-07	1.23E-07	1.65E-07	2.47E-07	1.87E-07
co60	0.00E+00	1.56E-14	1.10E-11	1.58E-12	1.09E-11
co61	0.00E+00	0.00E+00	0.00E+00	0.00E+00	0.00E+00
ni58	2.40E-07	2.38E-07	2.32E-07	2.30E-07	2.27E-07
ni59	0.00E+00	7.03E-11	5.98E-12	7.97E-11	6.17E-13
ni60	2.06E-10	3.07E-09	1.93E-07	1.06E-07	3.73E-07
ni61	3.28E-13	1.01E-09	1.36E-06	1.05E-07	2.13E-06
ni62	2.87E-16	0.00E+00	0.00E+00	0.00E+00	0.00E+00
g	7.29E-14	1.08E-09	4.13E-05	3.72E-07	4.43E-05

Table B.3: Yields and initial composition for all the GC models without 3DUP ($[\text{Fe}/\text{H}] = -1.4$). All species in the network are listed except for neutrons. Abundances are in mass fraction, normalised to 1.0. The remnant masses (white dwarf masses) are in brackets below the initial stellar masses in the table header.

Nuclide	Initial	2.5 M _⊙	3.5 M _⊙	5.0 M _⊙	6.5 M _⊙
		(0.869)	(0.996)	(1.078)	(1.132)
h1	0.76860	0.75924	0.76286	0.69852	0.66393
h2	2.26E-20	5.88E-18	5.29E-18	4.20E-18	3.84E-18
he3	1.27E-09	1.62E-04	1.15E-06	3.72E-07	1.93E-07
he4	0.22970	0.23889	0.23541	0.29985	0.33447
li7	1.15E-14	6.02E-12	5.41E-10	3.44E-11	2.84E-12
be7	0.00E+00	4.69E-17	2.71E-14	2.08E-14	7.23E-14
b8	0.00E+00	1.92E-29	2.75E-18	2.42E-27	3.28E-26
c12	2.10E-04	1.20E-04	2.18E-05	4.89E-05	5.32E-05
c13	4.68E-10	4.33E-06	4.82E-06	1.22E-05	1.44E-05
c14	0.00E+00	8.17E-25	7.48E-14	4.36E-14	4.89E-13
n13	0.00E+00	0.00E+00	0.00E+00	0.00E+00	0.00E+00
n14	1.45E-07	1.23E-04	5.73E-04	1.16E-03	1.14E-03
n15	4.74E-12	4.80E-09	2.10E-08	8.32E-08	1.52E-07
o14	0.00E+00	0.00E+00	0.00E+00	0.00E+00	0.00E+00
o15	0.00E+00	0.00E+00	0.00E+00	0.00E+00	0.00E+00
o16	1.11E-03	1.08E-03	7.48E-04	3.34E-05	1.59E-05
o17	5.73E-11	6.89E-06	1.86E-06	1.47E-07	8.15E-08
o18	1.05E-10	2.79E-09	1.01E-09	2.34E-10	2.80E-10
o19	0.00E+00	0.00E+00	0.00E+00	0.00E+00	0.00E+00
f17	0.00E+00	0.00E+00	0.00E+00	0.00E+00	0.00E+00
f18	0.00E+00	0.00E+00	0.00E+00	0.00E+00	0.00E+00
f19	4.22E-12	5.41E-10	4.33E-10	2.12E-11	1.50E-11
f20	0.00E+00	0.00E+00	0.00E+00	0.00E+00	0.00E+00
ne19	0.00E+00	0.00E+00	0.00E+00	0.00E+00	0.00E+00
ne20	9.49E-05	9.49E-05	9.47E-05	9.50E-05	9.49E-05
ne21	1.12E-08	1.70E-08	1.90E-09	1.35E-09	1.38E-09
ne22	9.85E-09	1.04E-08	3.56E-08	5.19E-08	7.99E-08
na21	0.00E+00	0.00E+00	0.00E+00	0.00E+00	0.00E+00
na22	0.00E+00	4.39E-15	1.43E-12	4.87E-11	1.06E-10
na23	5.25E-07	5.36E-07	1.05E-06	6.04E-07	4.37E-07
na24	0.00E+00	0.00E+00	0.00E+00	0.00E+00	9.39E-44
mg23	0.00E+00	0.00E+00	0.00E+00	0.00E+00	0.00E+00
mg24	5.67E-05	5.67E-05	5.01E-05	3.72E-07	2.81E-07
mg25	4.25E-08	4.48E-08	6.64E-06	3.66E-05	2.79E-05
mg26	4.10E-08	4.73E-08	1.12E-07	4.12E-06	3.43E-06
mg27	0.00E+00	0.00E+00	0.00E+00	0.00E+00	0.00E+00
al25	0.00E+00	0.00E+00	0.00E+00	0.00E+00	0.00E+00
al-6	0.00E+00	5.40E-09	1.82E-07	7.17E-06	3.26E-06
al*6	0.00E+00	0.00E+00	0.00E+00	0.00E+00	0.00E+00
al27	4.78E-07	4.99E-07	4.94E-07	1.14E-05	1.85E-05
al28	0.00E+00	0.00E+00	0.00E+00	0.00E+00	0.00E+00
si27	0.00E+00	0.00E+00	0.00E+00	0.00E+00	0.00E+00
si28	1.54E-04	1.54E-04	1.54E-04	1.56E-04	1.63E-04
si29	7.36E-08	7.36E-08	7.74E-08	7.80E-08	8.05E-08
si30	4.14E-08	4.14E-08	4.20E-08	4.21E-08	4.20E-08
si31	0.00E+00	0.00E+00	0.00E+00	0.00E+00	0.00E+00
si32	0.00E+00	7.26E-37	1.13E-15	1.40E-16	2.23E-14
si33	0.00E+00	0.00E+00	0.00E+00	0.00E+00	0.00E+00
p29	0.00E+00	0.00E+00	0.00E+00	0.00E+00	0.00E+00
p30	0.00E+00	0.00E+00	0.00E+00	0.00E+00	0.00E+00
p31	2.01E-08	2.01E-08	2.21E-08	2.22E-08	2.14E-08
p32	0.00E+00	2.82E-40	4.40E-19	5.44E-20	8.65E-18
p33	0.00E+00	2.09E-43	2.10E-31	1.53E-26	4.96E-24
p34	0.00E+00	0.00E+00	0.00E+00	0.00E+00	0.00E+00

Continued on next page...

Table B.3 – continued from previous page

Nuclide	Initial	2.5 M _⊙	3.5 M _⊙	5.0 M _⊙	6.5 M _⊙
		(0.869)	(0.996)	(1.078)	(1.132)
s32	7.83E-06	7.83E-06	7.83E-06	7.83E-06	7.83E-06
s33	1.68E-08	1.68E-08	1.68E-08	1.68E-08	1.71E-08
s34	7.74E-08	2.38E-06	2.38E-06	2.38E-06	2.38E-06
s35	0.00E+00	3.80E-19	1.83E-10	2.57E-10	1.77E-09
fe56	5.49E-05	5.49E-05	5.49E-05	5.49E-05	5.48E-05
fe57	4.82E-07	4.82E-07	4.83E-07	4.85E-07	5.32E-07
fe58	3.27E-14	3.27E-14	1.88E-09	1.95E-09	4.03E-09
fe59	0.00E+00	0.00E+00	1.51E-31	1.00E-28	1.68E-27
fe60	0.00E+00	6.03E-38	7.92E-11	1.61E-10	3.18E-10
fe61	0.00E+00	0.00E+00	0.00E+00	0.00E+00	0.00E+00
co59	1.18E-07	1.18E-07	1.19E-07	1.19E-07	1.19E-07
co60	0.00E+00	1.12E-25	6.92E-15	1.40E-14	2.77E-14
co61	0.00E+00	0.00E+00	0.00E+00	0.00E+00	0.00E+00
ni58	2.40E-07	2.40E-07	2.40E-07	2.40E-07	2.39E-07
ni59	0.00E+00	2.32E-20	1.60E-13	3.66E-13	3.24E-13
ni60	2.06E-10	2.06E-10	7.41E-10	7.38E-10	7.34E-10
ni61	3.28E-13	3.28E-13	8.10E-10	1.04E-09	7.11E-10
ni62	2.87E-16	5.02E-19	4.75E-19	3.98E-19	2.83E-19
g	7.29E-14	7.01E-11	5.82E-09	9.19E-09	8.89E-09

Appendix C

Miscellaneous Material

C.1 Surface Opacity Uncertainty in $Z = 0$ AGB Stars

We noted in Section 4.2 on page 79 that the updated low temperature opacities do not contain tables with varying amounts of C and O enhancements, as the OPAL opacities do. This means that any enhancement over the initial abundances (via dredge-up for example) is not taken into account. For this reason we chose to use the low temperature tables over a minimum temperature range only, making use of the OPAL tables down to a temperature of 8000 K. Thus the non-inclusion of the enhancements of CNO elements (for example) only affects the very outermost layers of cool envelopes. To illustrate this we take our $M = 0.85 M_{\odot}$, $Z = 0$ model as an example. In Figure C.1 we show the run of temperature and density in the outer layers of a model on the secondary RGB (see Section 5.2.3 on page 114 for the evolutionary background). It can be seen that the low temperature opacities (from Ferguson et al. 2005) are only used in the extreme outer layers of the model – over a mass range of $\sim 10^{-5} M_{\odot}$.

In an attempt to gauge the effect of neglecting the CNO enrichment through post-dual-flash dredge-up we have run a few tests on this star. The tests involved re-reading the low temperature opacity tables and interpolating in them using a new Z , during run-time. This was done if the Z value of the tables stored in memory differed by more than a factor of two from the Z value at the mesh point currently requiring an opacity value. In this case the surface metallicity increases from $Z = 0$ to $Z = 10^{-3}$ very quickly, so the routine was only called a few times. The new Z value was approximated in three different ways. For case 1 we used $Z = 1 - X - Y$, in case 2 we assumed Z was composed of only C, N and O, whilst in case 3 we assumed Z was entirely ^{16}O (all mass fraction abundances were naturally from the model itself). The reason for this variety of choices is because it is quite uncertain as to which is the dominant factor/species in determining the opacity at such low temperatures. Indeed, the dominant molecular species (in terms of opacity contribution at least) are all oxides (H_2O and TiO are the main ones, assuming scaled-solar composition – see Fig. 4 in Ferguson et al. 2005). This may imply that an oxygen-poor composition may not be as opaque as an oxygen-rich one, hence the $Z = Z_{^{16}\text{O}}$ test. We note however that since opacity is very ‘non-linear’ in terms of varying chemical compositions it is perilous to assume that any of the assumptions for Z that are used to interpolate in the *scaled-solar* mixes provided will necessarily be close to reality. Indeed, the composition of the envelope is very non-solar.

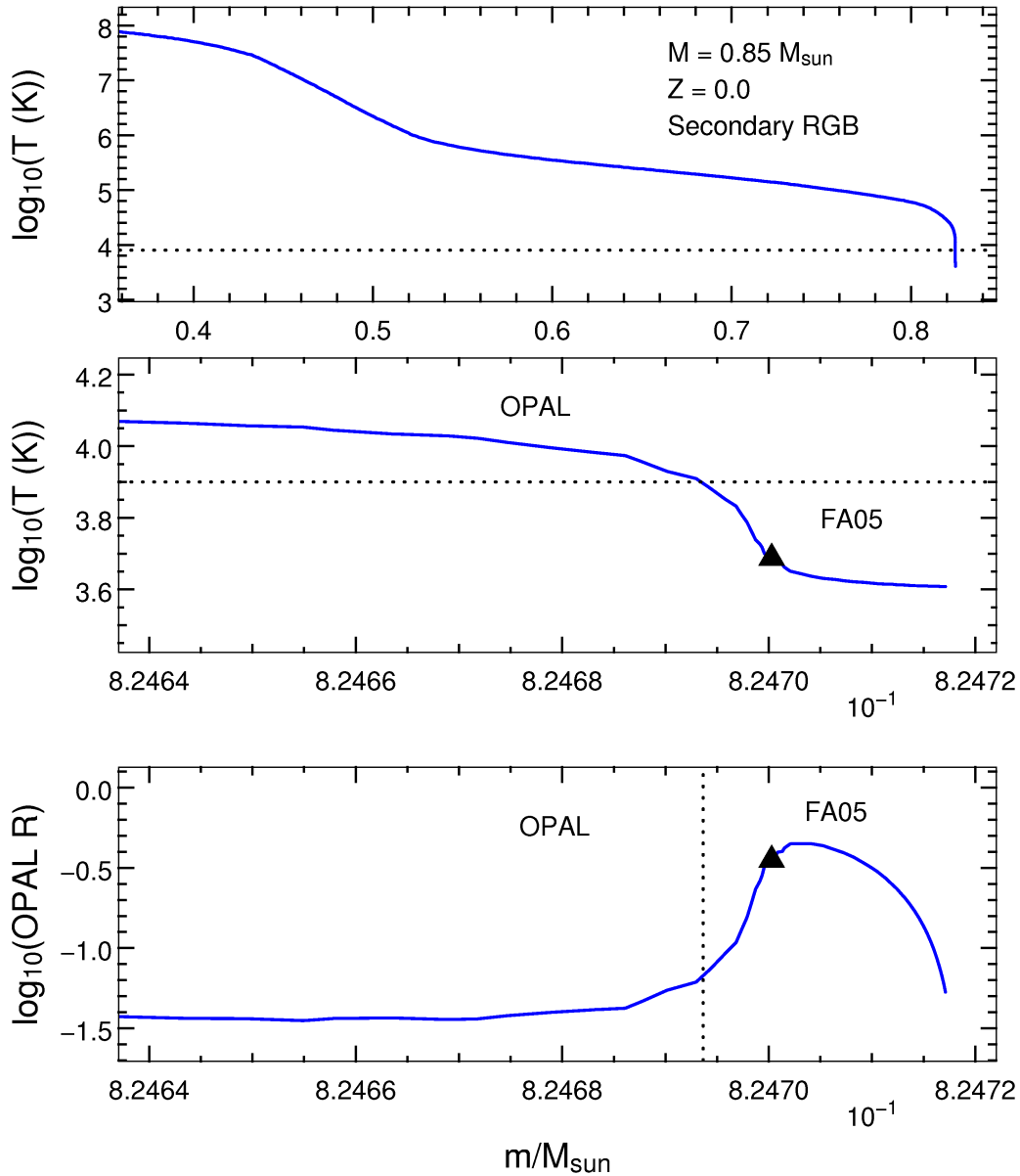


Figure C.1: The run of temperature (top two panels) and density (bottom panel) against mass for our $M = 0.85 M_{\odot}$, $Z = 0$ star during the secondary red giant branch. The top panel is a low resolution plot, showing the temperature for the outer 50% of the star, whilst the bottom two panels zoom in on the very outermost layers. The dotted lines mark where we switch between the OPAL tables (Iglesias and Rogers 1996) and the low temperature opacity tables from Ferguson et al. (2005) (FA05). This occurs at $\log(T) = 3.9$, ie. 8000 K. As can be seen the low temperature tables only come into effect in the extreme outer layers of the model – covering a mass range of only $\sim 10^{-5} M_{\odot}$. The triangles denote the point at which the surface is defined (using optical depth arguments). It is the temperature at these points that we plot in our HR diagrams.

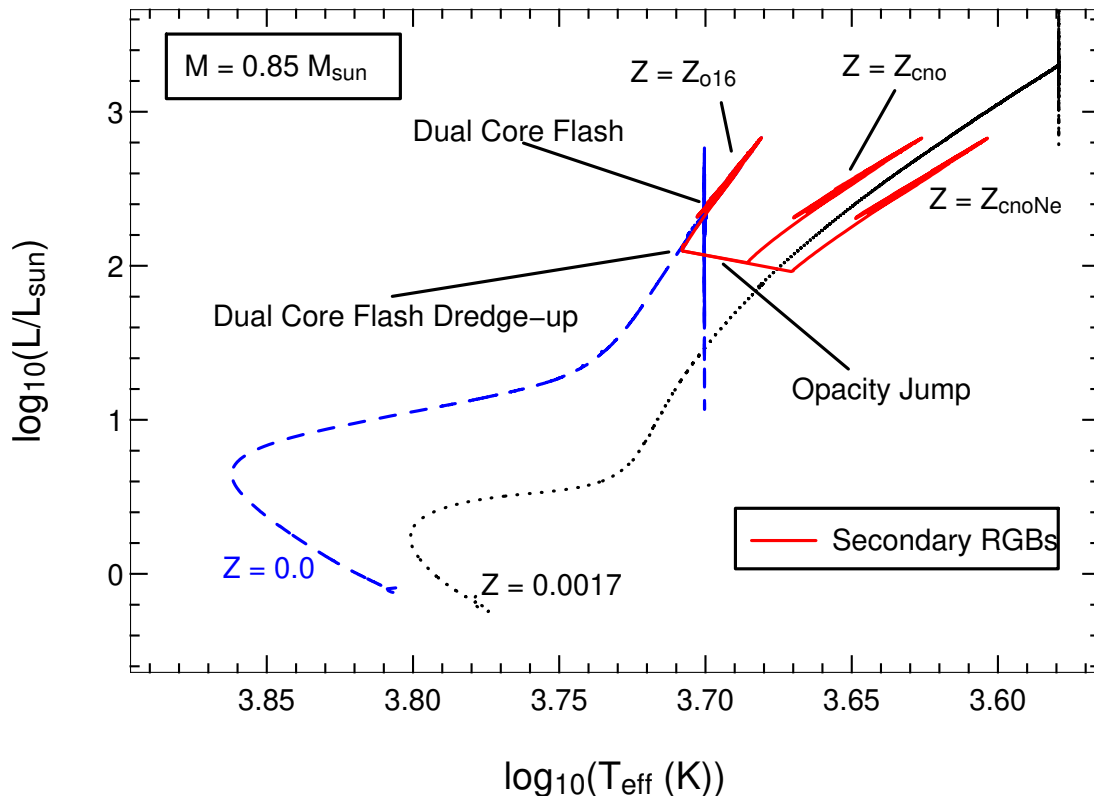


Figure C.2: Evolution of the $0.85 M_{\odot}$, $Z = 0$ model in the HR diagram, from the main sequence to the end of the red giant branch. Also shown is the $Z = 0.0017$ model for reference. The vertical lines (a numerical artefact of this difficult phase of evolution) mark the core He/He-H flashes. Note that the $Z = 0$ model exhibits an extra/secondary RGB above the location of the dual core flash, a feature peculiar to very low metallicity, low mass stars. As mentioned in Section 5.2.2 on page 101 the $Z = 0$ model experiences some dredge-up of CNO-enriched material just after the dual core flash. This means that the surface is enriched (from $Z = 0$ to $Z \sim 10^{-3}$ in this case) on the secondary RGB. The solid lines (red) represent three different evolutionary paths of the SRGB, each using a different makeup of Z for the purposes of the low-temperature opacity calculation (see text for details). As can be seen, the different approximations – and consequently the different scaled-solar low-temperature opacities used – lead to differing colours of the SRGB (and also the AGB). See text for more details.

With this in mind we show the results of our tests on the secondary RGB in Figure C.2. It can be seen that an increase in scaled-solar Z used to obtain new opacities for the surface has a marked effect as Z increases. As soon as the surface is polluted the model jumps discontinuously to cooler temperatures, due to the increase in surface opacity. If we use $Z = Z_{16\text{O}}$ (under the assumption that the opacity is dependent on oxide formation) then the temperature/opacity jump becomes negligible. We note here however that the ^{16}O abundance obtained from the SEV code may be too low as some (energetically negligible) reactions which create ^{16}O are not included. We also note that the models with cooler surfaces continue to be cooler on the AGB. This shift in surface temperature is most likely the main effect of neglecting the CNO enhancements, as the mass range in question is of order $10^{-5} M_{\odot}$, as mentioned above.

We now delve into the issue a bit more deeply. Shown in Figure C.3 is the run of opacities around the region of interest, corresponding to the outermost layers of the SRGB model in Figure C.1. It is interesting to note that the opacity at these temperatures and densities is wholly dominated by H, such that material with up to $Z = 0.02$ has essentially identical opacity to $Z = 0$ material. The situation does however change below ~ 8000 K, when molecules and then grains begin to

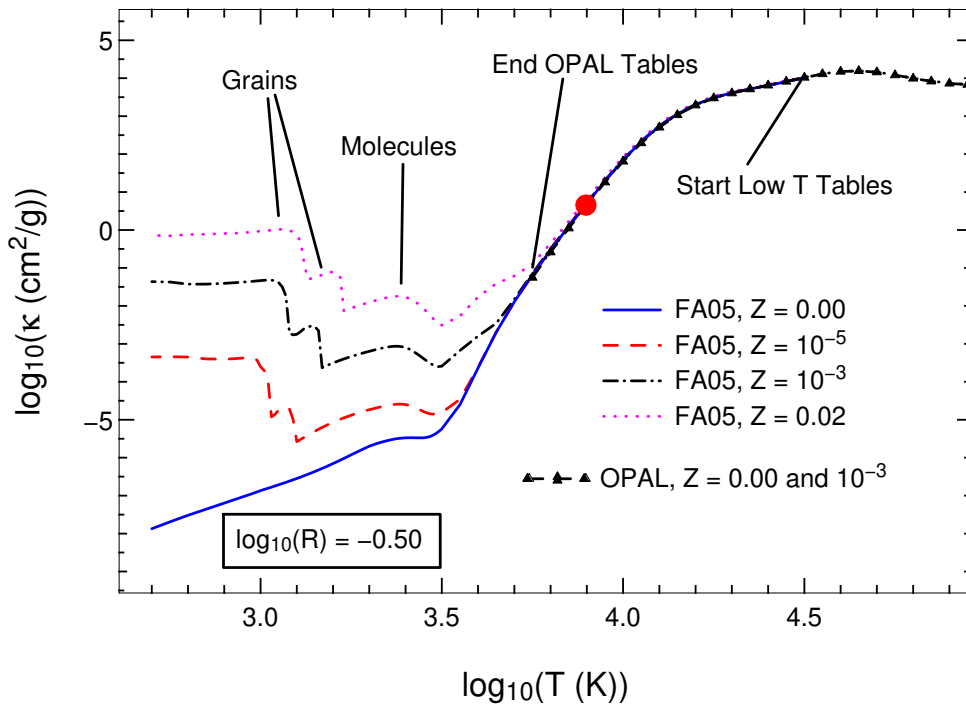


Figure C.3: The run of opacity versus temperature at a $\log(R)$ value of -0.5 , representative of the outermost layers of the model in Figure C.1. We show the low temperature opacities (from Ferguson et al. (2005), FA05) for a range of metallicities and also the low temperature end of the OPAL opacities (Iglesias and Rogers 1996). It can be seen that the two sets overlap. The large dot (red) marks the point at which we change from one set to the next in the SEV code. The tables match up very well in this region. An interesting observation is that the the run of opacities at all the metallicities shown are practically identical to that of the $Z = 0$ case for temperatures above 8000 K – the metals have no tangible effect at these temperatures and densities. The story is different at low temperatures though, when molecules and grains begin to form and dominate the opacity. See text for further discussion.

form and dominate the opacity.

In Figure C.4 we zoom into the region of interest. It is apparent that the region of opacity of most interest is at the intersection of two opacity regimes – the opacity from H is declining rapidly whilst the molecules are beginning to form. However we note that the main molecular contribution (from water vapour and TiO) is yet to peak. It is difficult to ascertain from the Ferguson et al. (2005) or Alexander and Ferguson (1994) papers whether the dominant contribution is from *atomic lines* or molecules in this very particular region (where the opacity just diverges from the $Z = 0$ curve). It seems that our region of interest lies between the figures of monochromatic opacity given in the aforementioned papers. We suggest that our region of interest is the equivalent of 3500 K in Figure 4 of Ferguson et al. (2005), which is a selection of plots for solar metallicity and a lower value of $\log(R)$. Our 3500 K value lies between the their plots of 2000 K and 5000 K. Whether the opacity is dominated by atomic or molecular lines may be important, as different elements are important in each source of opacity. For instance, if iron contributes a significant amount of opacity then it may not be warranted to use $Z = Z_{CNO}$ as an approximation, as the Fe abundance in this star is still zero. Conversely, if the CNO group (or individual elements therein) are important contributors under these conditions then the opacity may be *higher* than that given by scaled-solar mixture opacities. Similar arguments can be made for molecular contributions, particularly noting that oxygen appears to be a key ingredient in the molecular makeup of the gas, in which oxides dominate the opacity (although

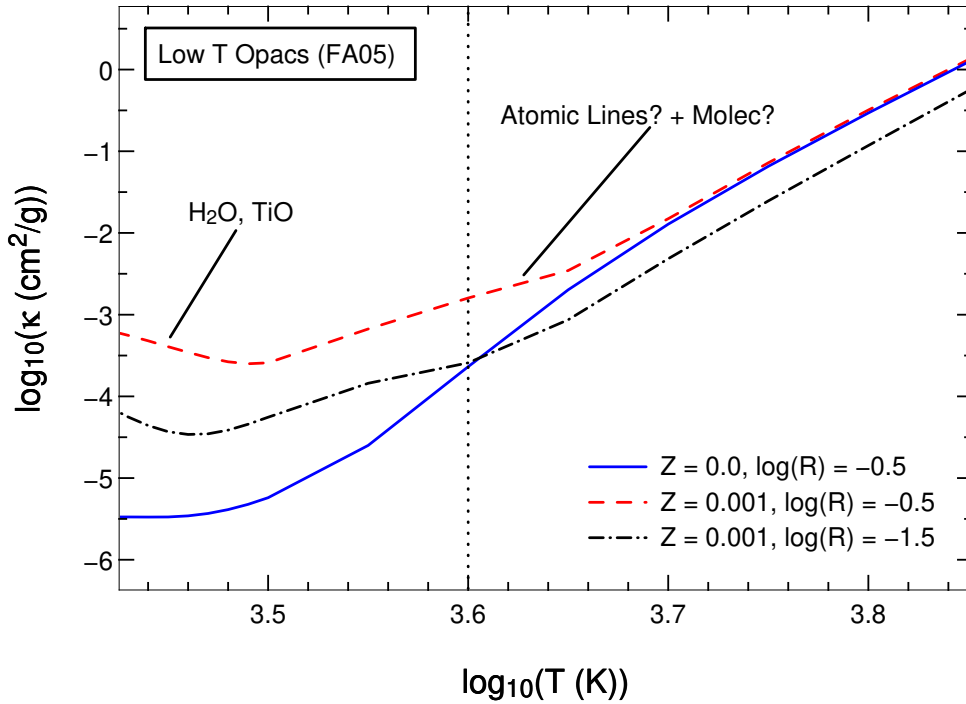


Figure C.4: Zooming in on Figure C.3 but with a reduced number of cases plotted for clarity. We choose to plot $Z = 0$ and $Z = 0.001$ because these are the metallicities of the surface before and after the post-dual-core-flash dredge-up in the model of Figure C.2. We also plot the opacity at $Z = 0.001$ for a $\log(R)$ of -1.5 which is representative of the very outer point of the model (as opposed to the point defined as the surface, see Figure C.1). The temperature of this point is represented by the vertical dotted line. Note that this is the coolest temperature reached in the envelope. It can be seen that the regime of interest is just at the turn-off from the $Z = 0$ curve. As noted in the text we are uncertain whether this turn-off is due mainly to atomic lines or molecular lines, or how sensitive it is to deviations from scaled-solar composition.

this may be a consequence of the large amount of oxygen in the scaled-solar mixture).

In summary we suggest that additional sets of opacity tables are needed at low temperatures in order to follow the evolution of surface temperature in stars such as these. In particular tables with variable C, N, O and possibly Ne are needed. This may also affect the surface temperature evolution of other classes of stars that also increase their CNO abundances due to dredge-up of processed material, such as thermally pulsing AGB stars. We shall contact the Wichita State University group and request these tables which we believe will be adopted widely by the stellar modelling community. We finally note that a more thorough investigation should be made into the feedback effects on the overall evolution of these stars, although it is likely to be small since the mass involved is so small. We shall pursue this in future work.

C.2 Plots from the Journey

Here we display just a small, random selection of figures pertaining to the the past year or so of the Author's candidature.

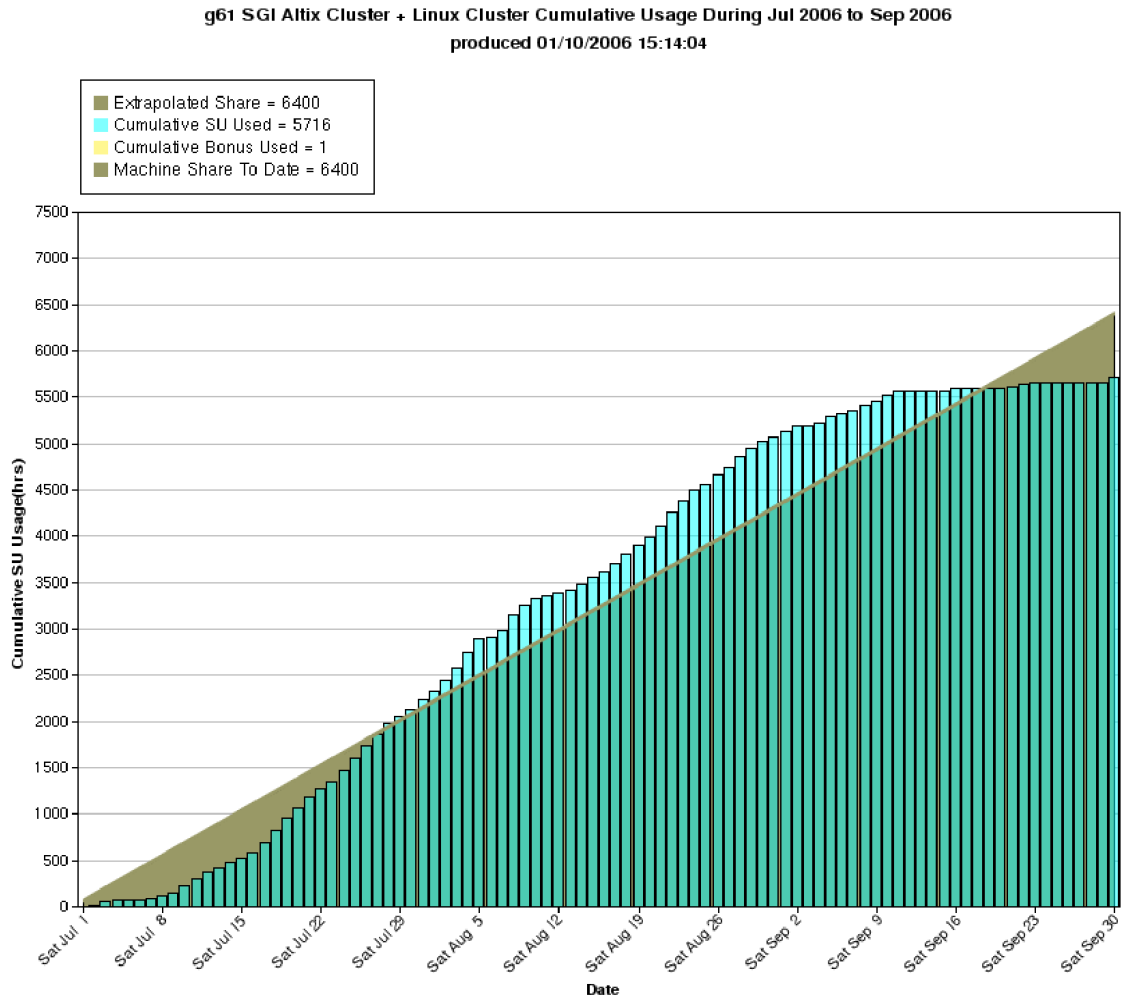


Figure C.5: Cumulative CPU hour usage for the $Z = 0$ and EMP models computed at the Australian Partnership for Advanced Computing (APAC, Canberra, Australia). About 15000 CPU hours were used in total (this graph represents one quarter year, on the x-axis). Note that the y-axis units are in SU, where $1\text{SU} = 2$ hours.

```

Shell No. 4 - Konsole
Shell Shell No. 2 Shell No. 3 Shell No. 4 Shell No. 5
sxc565@lc1:/short/g61/simon/hmps/1.0hmp 63> n
USER sxc565 PROJECT g61
882234 R sxc565 g61 rvhmp3 100 36:48:45 48:00:00 8MB 36MB 100MB 1
882253 R sxc565 g61 rvhmp2 100 35:57:29 48:00:00 8MB 36MB 100MB 1
882477 R sxc565 g61 rsnbb3Ri 100 32:44:58 48:00:00 8MB 37MB 100MB 1
882480 R sxc565 g61 rvmp1 100 32:27:50 48:00:00 7MB 36MB 100MB 1
882864 R sxc565 g61 rvemp2 100 10:48:31 48:00:00 7MB 36MB 100MB 1
882865 R sxc565 g61 rvemp5 100 10:42:25 48:00:00 7MB 36MB 100MB 1
882939 R sxc565 g61 rvemp1 100 09:43:27 48:00:00 7MB 36MB 100MB 1
882974 R sxc565 g61 rvmp2 100 08:57:23 48:00:00 7MB 36MB 100MB 1
883134 R sxc565 g61 rgc0.85 100 02:15:26 48:00:00 7MB 35MB 100MB 1
883137 R sxc565 g61 rN2z0y24 100 02:00:19 48:00:00 45MB 68MB 500MB 1
883138 R sxc565 g61 rsnbb5.0 100 01:47:28 48:00:00 8MB 36MB 100MB 1
883144 R sxc565 g61 rvemp3 100 01:33:30 48:00:00 7MB 36MB 100MB 1
883145 R sxc565 g61 rvmp3 100 01:28:19 48:00:00 7MB 36MB 100MB 1
883146 R sxc565 g61 rsnbb2.0 100 01:25:28 48:00:00 7MB 36MB 100MB 1
883147 R sxc565 g61 rvsnb1 100 01:21:28 48:00:00 7MB 36MB 100MB 1
883174 R sxc565 g61 rvemp85 97 00:04:24 48:00:00 7MB 36MB 100MB 1
883175 R sxc565 g61 rvhmp1 90 00:04:19 48:00:00 8MB 36MB 100MB 1
sxc565@lc1:/short/g61/simon/hmps/1.0hmp 64>

```

Figure C.6: A screengrab of an APAC session showing all the $Z = 0$ and EMP models the Author had running at one time. Both nucleosynthesis and structural evolution calculations can be seen.

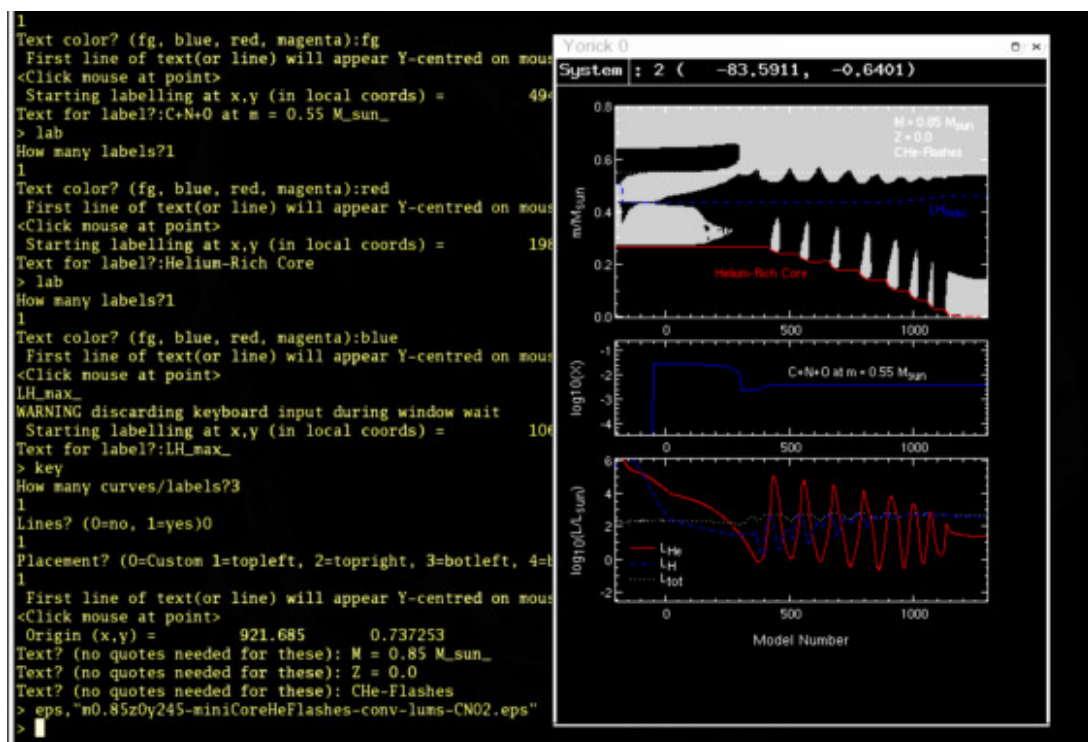


Figure C.7: A screengrab of the Author's laptop computer showing a Yorick plotting session. It can be seen that the plot is of a DCF model, with He minipulses on the SRGB.



Figure C.8: One of the working titles and front covers for the current thesis. The picture is actually a convection plot for one of the $Z = 0$ DCF models (model number versus mass). As can be seen the Author's supervisor has stamped it with his approval.

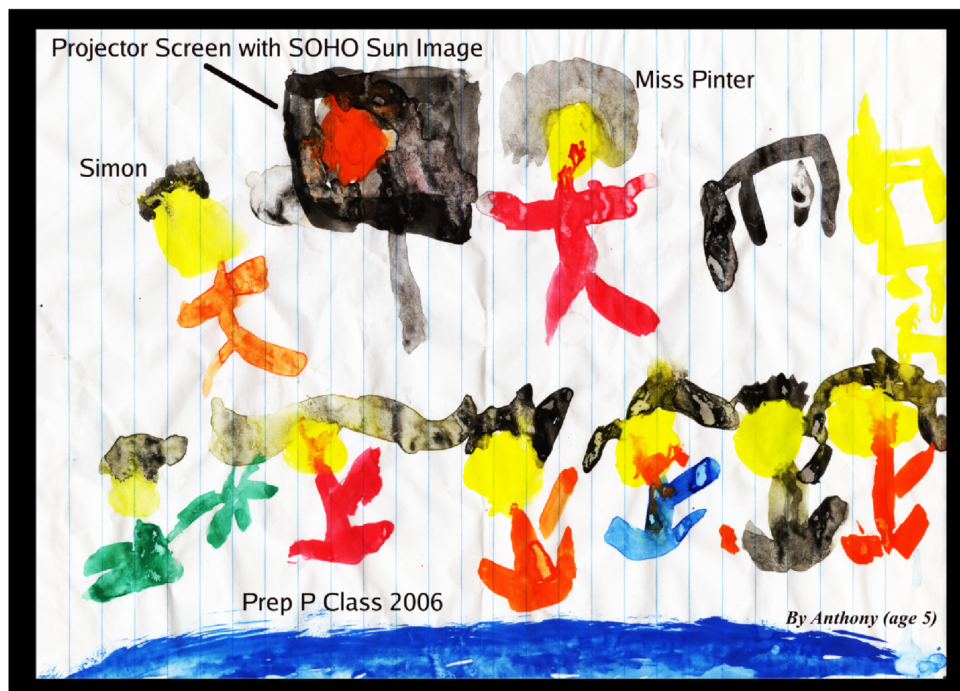


Figure C.9: A painting by a student (Anthony) at a Primary School in Melbourne, Australia. Pictured are Lisa Pinter (teacher) and the Author who was giving an astronomy presentation to the Prep class (5-6 year-olds).

Bibliography

- Adelberger, K. L., Shapley, A. E., Steidel, C. C., Pettini, M., Erb, D. K., and Reddy, N. A. (2005). The Connection between Galaxies and Intergalactic Absorption Lines at Redshift $2 < z < 3$. *ApJ*, 629(2):636–653.
- Alexander, D. R. (1975). Low-Temperature Rosseland Opacity Tables. *ApJS*, 29:363.
- Alexander, D. R. and Ferguson, J. W. (1994). Low-temperature Rosseland opacities. *ApJ*, 437:879–891.
- Alexander, D. R., Rypma, R. L., and Johnson, H. R. (1983). Effect of molecules and grains on Rosseland mean opacities. *ApJ*, 272:773.
- Allende Prieto, C., Beers, T. C., Wilhelm, R., Newberg, H. J., Rockosi, C. M., Yanny, B., and Lee, Y. S. (2006). A Spectroscopic Study of the Ancient Milky Way: F- and G-Type Stars in the Third Data Release of the Sloan Digital Sky Survey. *ApJ*, 636:804–820.
- Angulo, C., Arnould, M., Rayet, M., Descouvemont, P., Baye, D., Leclercq-Willain, C., Coc, A., Barhoumi, S., Aguer, P., Rolfs, C., Kunz, R., Hammer, J. W., Mayer, A., Paradellis, T., Kossionides, S., Chronidou, C., Spyrou, K., degl’Innocenti, S., Fiorentini, G., Ricci, B., Zavatarelli, S., Providencia, C., Wolters, H., Soares, J., Grama, C., Rahighi, J., Shotton, A., and Laméhi Rachti, M. (1999). A compilation of charged-particle induced thermonuclear reaction rates. *Nuclear Physics A*, 656:3–183.
- Aoki, W., Beers, T. C., Christlieb, N., Norris, J. E., Ryan, S. G., and Tsangarides, S. (2007). Carbon-enhanced Metal-poor Stars. I. Chemical Compositions of 26 Stars. *ApJ*, 655:492–521.
- Aoki, W., Frebel, A., Christlieb, N., Norris, J. E., Beers, T. C., Minezaki, T., Barklem, P. S., Honda, S., Takada-Hidai, M., Asplund, M., Ryan, S. G., Tsangarides, S., Eriksson, K., Steinhauer, A., Deliyannis, C. P., Nomoto, K., Fujimoto, M. Y., Ando, H., Yoshii, Y., and Kajino, T. (2006). HE 1327-2326, an Unevolved Star with $[\text{Fe}/\text{H}] < -5.0$. I. A Comprehensive Abundance Analysis. *ApJ*, 639:897–917.
- Arnould, M., Goriely, S., and Jorissen, A. (1999). Non-explosive hydrogen and helium burnings: abundance predictions from the NACRE reaction rate compilation. *A&A*, 347:572–582.
- Asplund, M., Grevesse, N., and Sauval, A. J. (2005). The Solar Chemical Composition. In Barnes, III, T. G. and Bash, F. N., editors, *ASP Conf. Ser. 336: Cosmic Abundances as Records of Stellar Evolution and Nucleosynthesis*, page 25.
- Baerentzen, J. (1965). The Adiabatic Temperature-gradient and the Specific Heat c_p in Outer Hydrogen-Helium Convection Zones. *Zeitschrift für Astrophysik*, 62:221.
- Beaudet, G., Petrosian, V., and Salpeter, E. E. (1967). Energy Losses due to Neutrino Processes. *ApJ*, 150:979.
- Beers, T. and Christlieb, N. (2005). The Discovery and Analysis of Very Metal-Poor Stars in the Galaxy. *ARA&A*, 43(1):531–580.
- Beers, T. C., Allende Prieto, C., Wilhelm, R., Norris, J. E., Yanny, B., Newberg, H. J., Rockosi, C., Thirupathi, S., and Lee, Y. (2005). Low Metallicity Stars in SDSS and SEGUE. *American Astronomical Society Meeting Abstracts*, 207:147.04.
- Beers, T. C., Christlieb, N., Norris, J. E., Bessell, M. S., Wilhelm, R., Allende P. C., and et al. (2005). The Metallicity Distribution Function of the Halo of the Milky Way. *IAUS*, 228:175–183.
- Beers, T. C., Preston, G. W., and Shectman, S. A. (1985). A search for stars of very low metal abundance. I. *AJ*, 90:2089–2102.
- Beers, T. C., Preston, G. W., and Shectman, S. A. (1992). A search for stars of very low metal abundance. II. *AJ*, 103(6):1987–2034.

- Beers, T. C., Sivarani, T., Marsteller, B., Lee, Y., Rossi, S., and Plez, B. (2007). Near-Infrared Spectroscopy of Carbon-Enhanced Metal-Poor Stars. I. A SOAR/OSIRIS Pilot Study. *AJ*, 133:1193–1203.
- Bekki, K., Campbell, S. W., Lattanzio, J. C., and Norris, J. E. (2007). Origin of Abundance Inhomogeneity in Globular Clusters. *MNRAS (accepted Jan. 2007)*.
- Bell, R. A. and Dickens, R. J. (1974). The CNO abundances of the CH stars in omega Cen. *MNRAS*, 166:89–99.
- Bessell, M. S., Brett, J. M., Wood, P. R., and Scholz, M. (1989). Colors of extended static model photospheres of M giants. *A&AS*, 77:1–30.
- Bessell, M. S., Christlieb, N., and Gustafsson, B. (2004). On the Oxygen Abundance of HE 0107-5240. *ApJL*, 612:L61–L63.
- Bessell, M. S. and Norris, J. (1984). The ultra-metal-deficient (Population III?) red giant CD 38.245 deg. *ApJ*, 285:622–636.
- Bethe, H. A. (1939). Energy Production in Stars. *Physical Review*, 55:434–456.
- Bica, E., Bonatto, C., Barbuy, B., and Ortolani, S. (2006). Globular cluster system and Milky Way properties revisited. *A&A*, 450:105–115.
- Biello, J. A. (2001). Layer formation in semiconvection. *Ph.D. Thesis*.
- Biermann, L. (1951). Bemerkungen über das Rotationsgesetz in irdischen und stellaren Instabilitätszonen. Mit 1 Textabbildung. *Zeitschrift für Astrophysik*, 28:304.
- Boesgaard, A. M. and King, J. R. (1993). Galactic evolution of Beryllium. *AJ*, 106(6):2309–2323.
- Boesgaard, A. M. and Steigman, G. (1985). Big Bang Nucleosynthesis: Theories and Observations. *Annual Review of Astronomy and Astrophysics*, 23:319–378.
- Böhm-Vitense, E. (1958). Über die Wasserstoffkonvektionszone in Sternen verschiedener Effektivtemperaturen und Leuchtkräfte. Mit 5 Textabbildungen. *Zeitschrift für Astrophysik*, 46:108.
- Böhm-Vitense, E. (1992). *Introduction to stellar astrophysics. Vol. 3 - Stellar structure and evolution*. Cambridge, England and New York, Cambridge University Press, 1992, 300 p.
- Bond, H. E. (1981). Where is Population III. *ApJ*, 248:606–611.
- Bono, G., Caputo, F., Cassisi, S., Castellani, V., and Marconi, M. (1997). Evolutionary and Pulsational Constraints for Super-Metal-rich Stars with $Z = 0.04$. *ApJ*, 489:822.
- Boyer, R., Henoux, J. C., and Sotirovski, P. (1971). Isotopes of Magnesium in the Solar Atmosphere. *SoPh*, 19:330.
- Briley, M. M., Smith, G. H., Hesser, J. E., and Bell, R. A. (1993). CN and CH variations in the globular cluster M55. *AJ*, 106:142–153.
- Brodie, J. P. and Strader, J. (2006). Extragalactic Globular Clusters and Galaxy Formation. *Annual Review of Astronomy and Astrophysics*, 44:193–267.
- Burbidge, E. M., Burbidge, G. R., Fowler, W. A., and Hoyle, F. (1957). Synthesis of the Elements in Stars. *Reviews of Modern Physics*, 29:547–650.
- Cameron, A. G. W. and Fowler, W. A. (1971). Lithium and the s-PROCESS in Red-Giant Stars. *ApJ*, 164:111.
- Cannon, R. C. (1993). Massive Thorne-Zytkow Objects - Structure and Nucleosynthesis. *MNRAS*, 263:817.
- Cannon, R. D., Croke, B. F. W., Bell, R. A., Hesser, J. E., and Stathakis, R. A. (1998). Carbon and nitrogen abundance variations on the main sequence of 47 Tucanae. *MNRAS*, 298:601–624.
- Canuto, V. M., Goldman, I., and Mazzitelli, I. (1996). Stellar Turbulent Convection: A Self-consistent Model. *ApJ*, 473:550.
- Cary, N. (1974). Main sequence models for massive zero-metal stars. *Ap&SS*, 31:3–10.
- Cassisi, S. and Castellani, V. (1993). An evolutionary scenario for primeval stellar populations. *ApJS*, 88:509–527.
- Cassisi, S., Castellani, V., and Tornambe, A. (1996). The Evolutionary Properties and Peculiar Thermal Pulses of Metal-deficient Low-Mass Stars. *ApJ*, 459:298.

- Castellani, V., Chieffi, A., Tornambe, A., and Pulone, L. (1985). Helium-burning evolutionary phases in population II stars. I Breathing pulses in horizontal branch stars. *ApJ*, 296:204–212.
- Castellani, V., Giannone, P., and Renzini, A. (1971). Induced Semi-Convection in Helium-Burning Horizontal-Branch Stars II. *AP&SS*, 10:355.
- Castellani, V. and Paolicchi, P. (1975). Zero-population stars. *Ap&SS*, 35:185–196.
- Caughlan, G. R. and Fowler, W. A. (1988). Thermonuclear Reaction Rates V. *Atomic Data and Nuclear Data Tables*, 40:283.
- Chieffi, A., Domínguez, I., Limongi, M., and Straniero, O. (2001). Evolution and Nucleosynthesis of Zero-Metal Intermediate-Mass Stars. *ApJ*, 554:1159–1174.
- Chieffi, A. and Limongi, M. (2002). The Explosive Yields Produced by the First Generation of Core Collapse Supernovae and the Chemical Composition of Extremely Metal Poor Stars. *ApJ*, 577:281–294.
- Chieffi, A. and Tornambe, A. (1984). On the evolution of an intermediate-mass zero-metal star which does not experience thermal instabilities during the double shell burning phase. *ApJ*, 287:745–748.
- Chiosi, C., Wood, P. R., and Capitanio, N. (1993). Theoretical models of Cepheid variables and their BVI(c) colors and magnitudes. *ApJS*, 86:541.
- Christlieb, N., Bessell, M. S., Beers, T. C., Gustafsson, B., Korn, A., Barklem, P. S., Karlsson, T., Mizuno-Wiedner, M., and Rossi, S. (2002). A stellar relic from the early Milky Way. *Nature*, 419:904–906.
- Christlieb, N., Gustafsson, B., Korn, A. J., Barklem, P. S., Beers, T. C., Bessell, M. S., Karlsson, T., and Mizuno-Wiedner, M. (2004). HE 0107-5240, a Chemically Ancient Star. I. A Detailed Abundance Analysis. *ApJ*, 603:708–728.
- Christlieb, N., Wisotzki, L., Reimers, D., Gehren, T., Reetz, J., and Beers, T. C. (1999). An Automated Search for Metal-Poor Halo Stars in the Hamburg/ESO Objective-Prism Survey. *ASPC*, 165:259.
- Clayton, D. D. (1983). *Principles of stellar evolution and nucleosynthesis*. Chicago: University of Chicago Press, 1983.
- Coc, A., Vangioni-Flam, E., Descouvemont, P., Adahchour, A., and Angulo, C. (2004). Updated Big Bang Nucleosynthesis Compared with Wilkinson Microwave Anisotropy Probe Observations and the Abundance of Light Elements. *ApJ*, 600:544–552.
- Cohen, J. G., McWilliam, A., Shectman, S., Thompson, I., Christlieb, N., Melendez, J., Ramirez, S., Swenson, A., and Zickgraf, F.-J. (2006). Carbon Stars in the Hamburg/ESO Survey: Abundances. *AJ*, 132:137–160.
- Cohen, J. G., Shectman, S., Thompson, I., McWilliam, A., Christlieb, N., Melendez, J., Zickgraf, F.-J., Ramírez, S., and Swenson, A. (2005). The Frequency of Carbon Stars among Extremely Metal-poor Stars. *ApJL*, 633:L109–L112.
- Cottrell, P. L. and Da Costa, G. S. (1981). Correlated cyanogen and sodium anomalies in the globular clusters 47 Tuc and NGC 6752. *ApJL*, 245:L79–L82.
- Cox, A. N. and Stewart, J. N. (1970). Rosseland Opacity Tables for Population II Compositions. *ApJS*, 19:261.
- Cybart, R. H., Fields, B. D., and Olive, K. A. (2002). Primordial nucleosynthesis with CMB inputs: probing the early universe and light element astrophysics. *Aph*, 17(1):87–100.
- Da Costa, G. S. and Cottrell, P. L. (1980). Carbon and nitrogen abundances on the first giant branch of NGC 6752. *ApJL*, 236:L83–L86.
- Dahn, C. C., Liebert, J., Kron, R. G., Spinrad, H., and Hintzen, P. M. (1977). G77-61 - A dwarf carbon star. *ApJ*, 216:757–766. Provided by the Smithsonian/NASA Astrophysics Data System.
- D’Antona, F. and Mazzetelli, I. (1982). Evolution of low mass zero metal giants up to the helium flash. *A&A*, 115:L1–L3.
- Dearborn, D. S. P., Bazan, G., Castor, J., Cavallo, R., Cohl, H., Cook, K., Dossa, D., Eastman, R., Eggleton, P. P., Eltgroth, P., Keller, S., Murray, S., Taylor, A., Turcotte, S., and Djehuty Team (2001). Djehuty: A 3D Hydrodynamic Stellar Evolution Code. *Bulletin of the American Astronomical Society*, 33:886.
- Dearborn, D. S. P., Liebert, J., Aaronson, M., Dahn, C. C., Harrington, R., Mould, J., and Greenstein, J. L. (1986). On the nature of the dwarf carbon star G77-61. *ApJ*, 300:314–324.

- Denissenkov, P. A. and Herwig, F. (2003). The Abundance Evolution of Oxygen, Sodium, and Magnesium in Extremely Metal Poor Intermediate-Mass Stars: Implications for the Self-Pollution Scenario in Globular Clusters. *ApJ*, 590:L99–L102.
- Denissenkov, P. A., Weiss, A., and Wagenhuber, J. (1997). Could intermediate-mass AGB stars produce star-to-star abundance variations in globular-cluster red giants? *A&A*, 320:115–124.
- Denker, A., Drotleff, H. W., Grosse, M., Knee, H., Kunz, R., Mayer, A., Seidel, R., Soiné, M., Wöohr, A., Wolf, G., and Hammer, J. W. (1995). Neutron Producing Reactions in Stars. In Busso, M., Raiteri, C. M., and Gallino, R., editors, *AIP Conf. Proc. 327: Nuclei in the Cosmos III*, page 255.
- Dicus, D. A., Kolb, E. W., Schramm, D. N., and Tubbs, D. L. (1976). Neutrino pair bremsstrahlung including neutral current effects. *ApJ*, 210:481.
- Doherty, C. L. and Lattanzio, J. C. (2006). Evolution and nucleosynthesis in super-AGB stars. *Memorie della Societa Astronomica Italiana*, 77:828.
- Dominguez, I., Straniero, O., Limongi, M., and Chieffi, A. (2000). Do zero metals intermediate mass stars experience thermal pulses? *Memorie della Societa Astronomica Italiana*, 71:781.
- Eddington, A. S. (1919). The sources of stellar energy. *The Observatory*, 42:371–376.
- Eddington, A. S. (1920). The internal constitution of the stars. *The Observatory*, 43:341–358.
- Eggleton, P. P. (1972). Composition changes during stellar evolution. *MNRAS*, 156:361.
- El Eid, M. F. and Champagne, A. E. (1995). Sodium Enrichment in A–F Type Supergiants. *ApJ*, 451:298.
- Eryurt-Ezer, D. (1981). Advanced evolutionary phase of a first-generation star. *Ap&SS*, 79:265–287.
- Eryurt-Ezer, D. and Kiziloglu, N. (1985). The evolutionary behaviour of Population III intermediate mass stars. *Ap&SS*, 117:95–109.
- Ezer, D. (1961). Models of Massive Pure Hydrogen Stars. *ApJ*, 133:159.
- Ezer, D. (1972). Theoretical Evolution of a Hydrogen-Helium Star of $3 M_{\odot}$ from the Pre-Main Sequence to the Core Helium-Exhaustion Phase. *Ap&SS*, 18:226.
- Ezer, D. and Cameron, A. G. W. (1971). The Evolution of Hydrogen-Helium Stars. *Ap&SS*, 14:399.
- Fan, X., Strauss, M. A., Schneider, D. P., Becker, R. H., White, R. L., and Haiman, Z. (2003). A Survey of $z > 5.7$ Quasars in the Sloan Digital Sky Survey. II. Discovery of Three Additional Quasars at $z > 6$. *AJ*, 125(4):1649–1659.
- Faulkner, D. J. (1968). The evolution of helium shell-burning stars. *MNRAS*, 140:223. Original Evoln paper!
- Faulkner, D. J. and Wood, P. R. (1972). Thermal pulses in He shell-burning stars. *ApJ*, 178:207.
- Fenner, Y., Campbell, S., Karakas, A. I., Lattanzio, J. C., and Gibson, B. K. (2004). Modelling self-pollution of globular clusters from asymptotic giant branch stars. *MNRAS*, 353:789–795.
- Ferguson, J. W., Alexander, D. R., Allard, F., Barman, T., Bodnarik, J. G., Hauschildt, P. H., Heffner-Wong, A., and Tamanai, A. (2005). Low-Temperature Opacities. *ApJ*, 623:585–596.
- Fernando, H. J. S. (1989). Buoyancy transfer across a diffusive interface. *Journal of Fluid Mechanics*, 209:1–34.
- Festa, G. G. and Ruderman, M. A. (1969). Neutrino-Pair Bremsstrahlung from a Degenerate Electron Gas. *Physical Review*, 180:1227–1231.
- Fick, A. (1855). *Phil. Mag.*, 10:30.
- Frebel, A., Aoki, W., Christlieb, N., Ando, H., Asplund, M., Barklem, P. S., Beers, T. C., Eriksson, K., Fechner, C., Fujimoto, M. Y., Honda, S., Kajino, T., Minezaki, T., Nomoto, K., Norris, J. E., Ryan, S. G., Takada-Hidai, M., Tsangarides, S., and Yoshii, Y. (2005a). Nucleosynthetic signatures of the first stars. *Nature*, 434:871–873.
- Frebel, A., Aoki, W., Christlieb, N., Ando, H., Asplund, M., Barklem, P. S., Beers, T. C., Eriksson, K., Fechner, C., Fujimoto, M. Y., Honda, S., Kajino, T., Minezaki, T., Nomoto, K., Norris, J. E., Ryan, S. G., Takada-Hidai, M., Tsangarides, S., and Yoshii, Y. (2005b). The new record holder for the most iron-poor star: HE 1327 2326, a dwarf or subgiant with $[Fe/H] = -5.4$. In Hill, V., François, P., and Primas, F., editors, *IAU Symposium*, pages 207–212.

- Frebel, A., Christlieb, N., Norris, J. E., Aoki, W., and Asplund, M. (2006a). The Oxygen Abundance of HE 1327-2326. *ApJL*, 638:L17–L20.
- Frebel, A., Christlieb, N., Norris, J. E., Beers, T. C., Bessell, M. S., Rhee, J., Fechner, C., Marsteller, B., Rossi, S., Thom, C., Wisotzki, L., and Reimers, D. (2006b). Bright Metal-poor Stars from the Hamburg/ESO Survey. I. Selection and Follow-up Observations from 329 Fields. *ApJ*, 652:1585–1603.
- Freytag, B., Ludwig, H.-G., and Steffen, M. (1996). Hydrodynamical models of stellar convection. The role of overshoot in DA white dwarfs, A-type stars, and the Sun. *A&A*, 313:497–516.
- Frost, C. A., Cannon, R. C., Lattanzio, J. C., Wood, P. R., and Forestini, M. (1998). The brightest carbon stars. *AAP*, 332:L17.
- Frost, C. A. and Lattanzio, J. C. (1996). On the Numerical Treatment and Dependence of the Third Dredge-up Phenomenon. *ApJ*, 473:383–+.
- Fujimoto, M. Y. and Iben, Jr., I. (1998). The peculiar evolution of metal-free stars and the search for Population III stars. In Bedding, T. R., Booth, A. J., and Davis, J., editors, *IAU Symp. 189: Fundamental Stellar Properties*, page 150P.
- Fujimoto, M. Y., Iben, Jr., I., Chieffi, A., and Tornambe, A. (1984). Hydrogen and helium burning in zero-metal asymptotic giant branch stars and the existence of thresholds (in core mass and CNO abundance) for the occurrence of helium shell flashes. *ApJ*, 287:749–760.
- Fujimoto, M. Y., Iben, I. J., and Hollowell, D. (1990). Helium flashes and hydrogen mixing in low-mass population III stars. *ApJ*, 349:580–592.
- Fujimoto, M. Y., Ikeda, Y., and Iben, I. J. (2000). The Origin of Extremely Metal-poor Carbon Stars and the Search for Population III. *ApJ*, 529:L25–L28.
- Fynbo, J. P. U., Starling, R. L. C., Ledoux, C., Wiersema, K., Thöne, C. C., and Sollerman, J. (2006). Probing cosmic chemical evolution with gamma-ray bursts: GRB 060206 at $z = 4.048$. *A&A*, 451(3):L47–L50.
- García-Berro, E., Gil-Pons, P., and Gutiérrez, J. (2006). The evolution of primordial Super-AGB stars. *Memorie della Societa Astronomica Italiana*, 77:834.
- Gass, H., Wehrse, R., and Liebert, J. (1988). Spectrum analysis of the extremely metal-poor carbon dwarf star G 77-61. *A&A*, 189:194–198.
- Giancoli, D. C. (1988). *Physics for scientists and engineers*. Prentice-Hall, Englewood Cliffs, N.J., 2nd edition.
- Gil-Pons, P., Gutierrez, J., and Garcia-Berro, E. (2006). The late stages of the evolution of intermediate-mass primordial stars: the effects of overshooting. *ArXiv Astrophysics eprints*.
- Gingold, R. A. (1974). Asymptotic Giant-Branch Evolution of a $0.6 M_{\odot}$ Star. *ApJ*, 193:177.
- Gnedin, N. Y. (1998). Metal enrichment of the intergalactic medium. *MNRAS*, 294:407.
- Goriely, S. and Siess, L. (2001). Nucleosynthesis of s-elements in zero-metal AGB stars. *A&A*, 378:L25–L28.
- Goriely, S. and Siess, L. (2004). S-process in hot AGB stars: A complex interplay between diffusive mixing and nuclear burning. *A&A*, 421:L25–L28.
- Gratton, R. G., Bonifacio, P., Bragaglia, A., Carretta, E., Castellani, V., Centurion, M., Chieffi, A., Claudi, R., Clementini, G., D'Antona, F., Desidera, S., François, P., Grundahl, F., Lucatello, S., Molaro, P., Pasquini, L., Sneden, C., Spite, F., and Straniero, O. (2001). The O-Na and Mg-Al anticorrelations in turn-off and early subgiants in globular clusters. *A&A*, 369:87–98.
- Gratton, R. G., Sneden, C., Carretta, E., and Bragaglia, A. (2000). Mixing along the red giant branch in metal-poor field stars. *A&A*, 354:169–187.
- Grevesse, N. and Noels, A. (1993). Cosmic Abundances of the Elements. In Prantzos, N., Vangioni-Flam, E., and Casse, M., editors, *Origin and evolution of the elements: Conference proceedings*, page 14.
- Grevesse, N. and Sauval, A. J. (1998). Standard Solar Composition. *Space Science Reviews*, 85:161–174.
- Grossman, S. A. and Taam, R. E. (1996). Double-Diffusive Mixing-Length Theory, Semiconvection and Massive Star Evolution. *MNRAS*, 283:1165–1178.

- Grundahl, F., Briley, M., Nissen, P. E., and Feltzing, S. (2002). Abundances of RGB stars in NGC 6752. *A&A*, 385:L14–L17.
- Guenther, D. B. and Demarque, P. (1983). Evolution of a population III star of low mass. *A&A*, 118:262–266.
- Guesten, R. and Mezger, P. G. (1982). Star formation and abundance gradients in the galaxy. *Vistas in Astronomy*, 26:159–224.
- Habing, H. J. and Olofsson, H., editors (2003). *Asymptotic giant branch stars*.
- Hansen, C. J. and Kawaler, S. D. (1994). *Stellar Interiors. Physical Principles, Structure, and Evolution*. Stellar Interiors. Physical Principles, Structure, and Evolution, XIII. Springer-Verlag Berlin Heidelberg New York.
- Harris, M. J., Fowler, W. A., Caughlan, G. R., and Zimmerman, B. A. (1983). Thermonuclear reaction rates. III. *ARAA*, 21:165.
- Harris, W. E. (1996). A Catalog of Parameters for Globular Clusters in the Milky Way. *AJ*, 112:1487.
- Haselgrove, C. B. and Hoyle, F. (1956). A mathematical discussion of the problem of stellar evolution, with reference to the use of an automatic digital computer. *MNRAS*, 116:515.
- Heney, L. G., Forbes, J. E., and Gould, N. L. (1964). A New Method of Automatic Computation of Stellar Evolution. *ApJ*, 139:306. Paper 2.
- Heney, L. G., Wilets, L., Böhm, K. H., Lelevier, R., and Levee, R. D. (1959). A Method for Atomic Computation of Stellar Evolution. *ApJ*, 129:628. Paper I.
- Herwig, F. (2003). CNO in Low- and Zero-Metallicity AGB Stars. In Charbonnel, C., Schaerer, D., and Meynet, G., editors, *Astronomical Society of the Pacific Conference Series*, page 318.
- Herwig, F. (2004). Dredge-up and Envelope Burning in Intermediate-Mass Giants of Very Low Metallicity. *ApJ*, 605:425–435.
- Herwig, F. (2004). Evolution and Yields of Extremely Metal-poor Intermediate-Mass Stars. *ApJS*, 155:651–666.
- Herwig, F., Bloeker, T., Schoenberner, D., and El Eid, M. (1997). Stellar evolution of low and intermediate-mass stars. IV. Hydrodynamically-based overshoot and nucleosynthesis in AGB stars. *A&A*, 324:L81–L84.
- Herwig, F., Freytag, B., Hueckstaedt, R. M., and Timmes, F. X. (2006). Hydrodynamic Simulations of He Shell Flash Convection. *ApJ*, 642:1057–1074.
- Hollowell, D., Iben, I. J., and Fujimoto, M. Y. (1990). Hydrogen burning and dredge-up during the major core helium flash in a $Z = 0$ model star. *ApJ*, 351:245–257.
- Hoppe, P., Amari, S., Zinner, E., and Lewis, R. S. (1995). Isotopic compositions of C, N, O, Mg, and Si, trace element abundances, and morphologies of single circumstellar graphite grains in four density fractions from the Murchison meteorite. *GeCoA*, 59:4029–4056.
- Hubbard, W. B. and Lampe, M. (1969). Thermal Conduction by Electrons in Stellar Matter. *ApJS*, 18:297.
- Huebner, W., Merts, A., Magee Jr, N., Argo, M., and 1977 (1977). Astrophysical Opacity Library. *Los Alamos Scientific Laboratory, LA-6760-M*.
- Iben, Jr., I. (1975). Thermal pulses; p-capture, alpha-capture, s-process nucleosynthesis; and convective mixing in a star of intermediate mass. *ApJ*, 196:525.
- Iben, Jr., I. (1977). Thermal pulse and interpulse properties of intermediate-mass stellar models with carbon-oxygen cores of mass 0.96, 1.16, and 1.36 solar masses. *ApJ*, 217:788–798.
- Iben, Jr., I. and Renzini, A. (1983). Asymptotic giant branch evolution and beyond. *ARA&A*, 21:271–342.
- Iglesias, C. A. and Rogers, F. J. (1996). Updated Opal Opacities. *ApJ*, 464:943.
- Iliadis, C., Buchmann, L., Endt, P. M., Herndl, H., and Wiescher, M. (1996). New stellar reaction rates for $^{25}\text{Mg}(p,\gamma)^{26}\text{Al}$ and $^{25}\text{Al}(p,\gamma)^{26}\text{Si}$. *PhRvC*, 53:475–496.
- Iliadis, C., Schange, T., Rolfs, C., Schröder, U., Somorjai, E., Trautvetter, H. P., Wolke, K., Endt, P. M., Kikstra, S. W., Champagne, A. E., Arnould, M., and Paulus, G. (1990). Low-energy resonances in $^{25}\text{Mg}(p,\gamma)^{26}\text{Al}$, $^{26}\text{Mg}(p,\gamma)^{27}\text{Al}$ and $^{27}\text{Al}(p,\gamma)^{28}\text{Si}$. *Nuclear Physics A*, 512:509–530.

- Israelian, G., Shchukina, N., Rebolo, R., Basri, G., González Hernández, J. I., and Kajino, T. (2004). Oxygen and magnesium abundance in the ultra-metal-poor giants CS 22949-037 and CS 29498-043: Challenges in models of atmospheres. *A&A*, 419:1095–1109.
- Itoh, N., Mitake, S., Iyetomi, H., and Ichimaru, S. (1983). Electrical and thermal conductivities of dense matter in the liquid metal phase. I - High-temperature results. *ApJ*, 273:774.
- Ivans, I. I., Sneden, C., Kraft, R. P., Suntzeff, N. B., Smith, V. V., Langer, G. E., and Fulbright, J. P. (1999). Star-to-Star Abundance Variations among Bright Giants in the Mildly Metal-poor Globular Cluster M4. *AJ*, 118:1273–1300.
- Iwamoto, N., Kajino, T., Mathews, G. J., Fujimoto, M. Y., and Aoki, W. (2004). Flash-Driven Convective Mixing in Low-Mass, Metal-deficient Asymptotic Giant Branch Stars: A New Paradigm for Lithium Enrichment and a Possible s-Process. *ApJ*, 602:377–388.
- Izotov, Y. I. and Thuan, T. X. (1999). Heavy-Element Abundances in Blue Compact Galaxies. *ApJ*, 511(2):639–659.
- Jorissen, A. and Arnould, M. (1989). Proton mixing in He-rich layers - The C-13(alpha,n)O-16 neutron source and associated nucleosynthesis. *A&A*, 221:161–179.
- Kaeppler, F., Wiescher, M., Giesen, U., Goerres, J., Baraffe, I., El Eid, M., Raiteri, C. M., Busso, M., Gallino, R., Limongi, M., and Chieffi, A. (1994). Reaction rates for O-18(alpha, gamma)Ne-22, Ne-22(alpha, gamma)Mg-26, and Ne-22(alpha, n)Mg-25 in stellar helium burning and s-process nucleosynthesis in massive stars. *ApJ*, 437:396–409.
- Karakas, A. I. (2003). *Asymptotic Giant Branch Stars: Their Influence on Binary Systems and the Interstellar Medium*. PhD thesis, Monash University, Australia.
- Karakas, A. I. and Lattanzio, J. C. (2003). Production of Aluminium and the Heavy Magnesium Isotopes in Asymptotic Giant Branch Stars. *Publications of the Astronomical Society of Australia*, 20:279–293.
- Karakas, A. I., Lattanzio, J. C., and Pols, O. R. (2002). Parameterising the Third Dredge-up in Asymptotic Giant Branch Stars. *Publications of the Astronomical Society of Australia*, 19:515–526.
- Kato, S. (1966). Overstable Convection in a Medium Stratified in Mean Molecular Weight. *PASJ*, 18:374.
- Kirchhoff, G. and Bunsen, R. (1860). Chemische Analyse durch Spectralbeobachtungen. *Annalen der Physik*, 186:161–189.
- Kiziloglu, N. and Eryurt-Ezer, D. (1987). Pregalactic-primordial low-mass stars. *Ap&SS*, 136:83–90.
- Kraft, R. P., Sneden, C., Langer, G. E., and Prosser, C. F. (1992). Oxygen abundances in halo giants. II - Giants in the globular clusters M13 and M3 and the intermediately metal-poor halo field. *AJ*, 104:645–668.
- Kraft, R. P., Sneden, C., Smith, G. H., Shetrone, M. D., Langer, G. E., and Pilachowski, C. A. (1997). Proton Capture Chains in Globular Cluster Stars. II. Oxygen, Sodium, Magnesium, and Aluminum Abundances in M13 Giants Brighter Than the Horizontal Branch. *AJ*, 113:279.
- Kroupa, P., Tout, C. A., and Gilmore, G. (1993). The distribution of low-mass stars in the Galactic disc. *MNRAS*, 262:545–587.
- Kunth, D. and Östlin, G. (2000). The most metal-poor galaxies. *A&ARv*, 10(1):1–79.
- Langer, N., El Eid, M. F., and Fricke, K. J. (1985). Evolution of massive stars with semiconvective diffusion. *A&A*, 145:179–191.
- Laor, A., Bahcall, J. N., Jannuzi, B. T., Schneider, D. P., and Green, R. F. (1995). The Ultraviolet Emission Properties of 13 Quasars. *ApJS*, 99:1.
- Lara, J. F., Kajino, T., and Mathews, G. J. (2006). Inhomogeneous big bang nucleosynthesis revisited. *PhRvD*, 78(8).
- Lattanzio, J. C. (1984). *The Evolution of Initially Inhomogeneous Stars and Low Mass AGB Stars*. PhD thesis, Monash University, Australia, School of Mathematical Sciences. Lattanzio's PhD Thesis.
- Lattanzio, J. C. (1986). The asymptotic giant branch evolution of 1.0-3.0 solar mass stars as a function of mass and composition. *ApJ*, 311:708–730. JL's thesis paper.

- Lattanzio, J. C. (1989). Carbon dredge-up in low-mass stars and solar metallicity stars. *ApJL*, 344:L25.
- Lattanzio, J. C. (1992). Hot bottom burning in a 5 solar mass model. *Proceedings of the Astronomical Society of Australia*, 10:120.
- Ledoux, W. P. (1947). Stellar Models with Convection and with Discontinuity of the Mean Molecular. *ApJ*, 105:305.
- Lee, S. G. (2000). CN and CH Band Strengths of Bright Giants in the Globular Cluster M15. *Journal of Korean Astronomical Society*, 33:137–142.
- Levshakov, S. A., Kegel, W. H., and Agafonova, I. I. (2001). Argon, silicon and iron abundances in the damped Ly-alpha system I Zw 18. *A&A*, 373:836–842.
- Limongi, M., Chieffi, A., and Bonifacio, P. (2003). On the Origin of HE 0107-5240, the Most Iron-deficient Star Presently Known. *ApJL*, 594:L123–L126.
- Lodders, K. (2003). Solar System Abundances and Condensation Temperatures of the Elements. *ApJ*, 591:1220–1247.
- Lucatello, S., Beers, T. C., Christlieb, N., Barklem, P. S., Rossi, S., Marsteller, B., Sivarani, T., and Lee, Y. S. (2006). The Frequency of Carbon-enhanced Metal-poor Stars in the Galaxy from the HERES Sample. *ApJL*, 652:L37–L40.
- Lucatello, S., Tsangarides, S., Beers, T. C., Carretta, E., Gratton, R. G., and Ryan, S. G. (2005). The Binary Frequency Among Carbon-enhanced, s-Process-rich, Metal-poor Stars. *ApJ*, 625:825–832.
- Luck, R. E. and Bond, H. E. (1991). Subgiant CH stars. II - Chemical compositions and the evolutionary connection with barium stars. *ApJS*, 77:515–540.
- Lugaro, M. (2001). *Nucleosynthesis in AGB Stars*. PhD thesis, Monash University, Australia.
- Maeder, A. (1975). Stellar evolution. III - The overshooting from convective cores. *A&A*, 40:303–310.
- Maeder, A. (1976). Stellar evolution. V - Evolutionary models of population I stars with or without overshooting from convective cores. *A&A*, 47:389–400.
- Maeder, A. and Meynet, G. (2006). On the origin of the high helium sequence in ω Centauri. *A&A*, 448:L37–L41.
- Mallia, E. A. (1978). Spectra of asymptotic giant branch stars in four southern globular clusters. *A&A*, 70:115–123.
- Marigo, P., Girardi, L., Chiosi, C., and Wood, P. R. (2001). Zero-metallicity stars. I. Evolution at constant mass. *A&A*, 371:152–173.
- Matsuura, S., Fujimoto, S., Nishimura, S., Hashimoto, M., and Sato, K. (2005). Heavy element production in inhomogeneous big bang nucleosynthesis. *PhsRevD*, 72(12).
- Merryfield, W. J. (1995). Hydrodynamics of semiconvection. *ApJ*, 444:318–337.
- Messenger, B. (2000). Abundance anomalies in globular cluster red giant stars. (Thesis abstract). *Publications of the Astronomical Society of Australia*, 17:284–284.
- Meynet, G., Maeder, A., and Mowlavi, N. (2004). Diffusion in stellar interiors: Critical tests of three numerical methods. *A&A*, 416:1023–1036.
- Mitake, S., Ichimaru, S., and Itoh, N. (1984). Electrical and thermal conductivities of dense matter in the liquid metal phase. II - Low-temperature quantum corrections. *ApJ*, 277:375.
- Molaro, P. and Castelli, F. (1990). A new ultra metal-deficient star - CS 22876. *A&A*, 228:426–442.
- Nakamura, F. and Umemura, M. (2001). On the Initial Mass Function of Population III Stars. *ApJ*, 548:19–32.
- Nordlund, A. and Dravins, D. (1990). Stellar granulation. III - Hydrodynamic model atmospheres. IV - Line formation in inhomogeneous stellar photospheres. V - Synthetic spectral lines in disk-integrated starlight. *A&A*, 228:155–217.
- Norris, J., Cottrell, P. L., Freeman, K. C., and Da Costa, G. S. (1981). The abundance spread in the giants of NGC 6752. *ApJ*, 244:205–220.

- Ödman, C. J. and Izzard, R. G. (2004). Stellardb: A Stellar Abundances Database. *Memorie della Societa Astronomica Italiana*, 75:631.
- Olive, K. A. and Skillman, E. D. (2004). A Realistic Determination of the Error on the Primordial Helium Abundance: Steps toward Nonparametric Nebular Helium Abundances. *ApJ*, 617(1):29–49.
- Olszewski, E. W. (1993). The Age and Metallicity Distributions Among the Magellanic Cloud Clusters. In Smith, G. H. and Brodie, J. P., editors, *ASP Conf. Ser. 48: The Globular Cluster-Galaxy Connection*, page 351.
- Olszewski, E. W., Suntzeff, N. B., and Mateo, M. (1996). Old and Intermediate-Age Stellar Populations in the Magellanic Clouds. *ARA&A*, 34:511–550.
- Parmentier, G., Jehin, E., Magain, P., Neuforge, C., Noels, A., and Thoul, A. A. (1999). The self-enrichment of galactic halo globular clusters. A clue to their formation? *A&A*, 352:138–148.
- Peebles, P. J. E. (1966). Primordial Helium Abundance and the Primordial Fireball. II. *ApJ*, 146:542.
- Pettini, M. (2004). Element abundances through the cosmic ages. In: *Cosmochemistry. The melting pot of the elements. XIII Canary Islands Winter School of Astrophysics*, page 275.
- Picardi, I., Chieffi, A., Limongi, M., Pisanti, O., Miele, G., Mangano, G., and Imbriani, G. (2004). Evolution and Nucleosynthesis of Primordial Low-Mass Stars. *ApJ*, 609:1035–1044.
- Pilachowski, C. A. (1988). The abundance of oxygen in M92 giant stars. *ApJL*, 326:L57–L60.
- Pilachowski, C. A., Sneden, C., and Kraft, R. P. (1996a). Sodium Abundances in Field Metal-Poor Stars. *AJ*, 111:1689.
- Pilachowski, C. A., Sneden, C., Kraft, R. P., and Langer, G. E. (1996b). Proton Capture Chains in Globular Cluster Stars. I. Evidence for Deep Mixing Based on Sodium and Magnesium Abundances in M13 Giants. *AJ*, 112:545.
- Plez, B. and Cohen, J. G. (2005). Analysis of the carbon-rich very metal-poor dwarf G77-61. *A&A*, 434:1117–1124.
- Poelarends, A. J. T., Izzard, R. G., Herwig, F., Langer, N., and Heger, A. (2006). Supernovae from massive AGB stars. *Memorie della Societa Astronomica Italiana*, 77:846.
- Pols, O. R. and Tout, C. A. (2001). Thermal pulses and dredge-up in AGB stars with a consistent solution for stellar structure and composition: dependence on convection prescriptions. *Memorie della Societa Astronomica Italiana*, 72:299–308.
- Powell, D. C., Iliadis, C., Champagne, A. E., Grossmann, C. A., Hale, S. E., Hansper, V. Y., and McLean, L. K. (1999). Reaction rate of $^{24}\text{Mg}(p, \gamma)^{25}\text{Al}$. *Nuclear Physics A*, 660(3):349.
- Prandtl, L. (1925). *Zs. Angew. Math. Mech.*, 5:136.
- Press, W. H., Teukolsky, S. A., Vetterling, W. T., and Flannery, B. P. (1992). *Numerical recipes in FORTRAN. The art of scientific computing*. Cambridge: University Press, 2nd ed.
- Prochaska, J. X., Gawiser, E., Wolfe, A. M., Cooke, J., and Gelino, D. (2003). The ESI/Keck II Damped Ly α Abundance Database. *ApJS*, 147:227–264.
- Raikh, M. E. and Iakovlev, D. G. (1982). Thermal and electrical conductivities of crystals in neutron stars and degenerate dwarfs. *Ap&SS*, 87:193–203.
- Ramadurai, S. (1976). Neutral current and the onset of the helium flash. *MNRAS*, 176:9.
- Reimers, D. (1975). Circumstellar absorption lines and mass loss from red giants. *Memoires of the Societe Royale des Sciences de Liege*, 8:369–382.
- Renzini, A. (1987). Some embarrassments in current treatments of convective overshooting. *A&A*, 188:49–54.
- Ritossa, C., Garcia-Berror, E., and Iben, Jr., I. (1996). On the evolution of super AGB stars with ONE degenerate cores: the case of a 10 M_{\odot} model. *Memorie della Societa Astronomica Italiana*, 67:675.
- Robertson, J. W. and Faulkner, D. J. (1972). Semiconvection in the Core-Helium Phase of Stellar Evolution. *ApJ*, 171:309.
- Rogers, F. J., Swenson, F. J., and Iglesias, C. A. (1996). OPAL Equation-of-State Tables for Astrophysical Applications. *ApJ*, 456:902.

- Sackmann, I.-J. and Boothroyd, A. I. (1992). The creation of superrich lithium giants. *ApJL*, 392:L71–L74.
- Sackmann, I. J., Smith, R. L., and Despain, K. H. (1974). Carbon and eruptive stars : surface enrichment of lithium, carbon, nitrogen, and C13 by deep mixing. *ApJ*, 187:555–574.
- Sandquist, E. L. and Bolte, M. (2004). Exploring the Upper Red Giant and Asymptotic Giant Branches: The Globular Cluster M5. *ApJ*, 611:323–337.
- Schlattl, H., Cassisi, S., Salaris, M., and Weiss, A. (2001). On the Helium Flash in Low-Mass Population III Red Giant Stars. *ApJ*, 559:1082–1093.
- Schlattl, H., Salaris, M., Cassisi, S., and Weiss, A. (2002). The surface carbon and nitrogen abundances in models of ultra metal-poor stars. *A&A*, 395:77–83.
- Schwarzschild, I. M. and Selberg, H. (1962). Red Giants of Population II. *ApJ*, 136:150.
- Schwarzschild, K. (1906). *Gott. Nach.*, 1:41.
- Schwarzschild, M. (1958). *Structure and evolution of the stars*. Princeton, Princeton University Press, 1958.
- Schwarzschild, M. and Härm, R. (1958). Evolution of Very Massive Stars. *ApJ*, 128:348.
- Schwarzschild, M. and Härm, R. (1965). Thermal Instability in Non-Degenerate Stars. *ApJ*, 142:855.
- Schwarzschild, M. and Härm, R. (1967). Hydrogen Mixing by Helium-Shell Flashes. *ApJ*, 150:961.
- Searle, L. and Sargent, W. L. W. (1972). Inferences from the Composition of Two Dwarf Blue Galaxies. *ApJ*, 173:25.
- Sears, R. L. (1959). An Evolutionary Sequence of Solar Models. *ApJ*, 129:489.
- Seaton, M. J., Zeippen, C. J., Tully, J. A., Pradhan, A. K., Mendoza, C., Hibbert, A., and Berrington, K. A. (1992). The Opacity Project - Computation of Atomic Data. *Revista Mexicana de Astronomia y Astrofisica*, vol. 23, 23:19.
- Shaviv, G. and Salpeter, E. E. (1973). Convective Overshooting in Stellar Interior Models. *ApJ*, 184:191–200.
- Shetrone, M. D. (2003). Carbon Isotopes in Globular Clusters Down to the Bump in the Luminosity Function. *ApJL*, 585:L45–L48.
- Shigeyama, T. and Tsujimoto, T. (1998). Fossil Imprints of the First-Generation Supernova Ejecta in Extremely Metal-deficient Stars. *ApJL*, 507:L135–L139.
- Siess, L., Livio, M., and Lattanzio, J. (2002). Structure, Evolution, and Nucleosynthesis of Primordial Stars. *ApJ*, 570:329–343.
- Simpson, E. E. (1971). Evolutionary Models of Stars of 15 and 30 M_{\odot} . *ApJ*, 165:295.
- Singh, H. P., Roxburgh, I. W., and Chan, K. L. (1995). Three-dimensional simulation of penetrative convection: penetration below a convection zone. *A&A*, 295:703.
- Smith, G. H. (2002). The Incidence of CN-strong Giants in Globular Clusters. *PASP*, 114:1215–1221.
- Smith, G. H. and Norris, J. E. (1993). CN variations among asymptotic giant branch and horizontal branch stars in the intermediate metallicity globular clusters M5, M4, and NGC 6752. *AJ*, 105:173–183.
- Smith, G. H., Shetrone, M. D., Bell, R. A., Churchill, C. W., and Briley, M. M. (1996). CNO Abundances of Bright Giants in the Globular Clusters M3 and M13. *AJ*, 112:1511.
- Sneden, C., Ivans, I. I., and Kraft, R. P. (2000). Do AGB stars differ chemically from RGB stars in globular clusters? *Memorie della Societa Astronomica Italiana*, 71:657–665.
- Songaila, A. (2001). The Minimum Universal Metal Density between Redshifts of 1.5 and 5.5. *ApJ*, 561(2):L153–L156.
- Songaila, A. and Cowie, L. L. (1996). Metal enrichment and Ionization Balance in the Lyman Alpha Forest at $Z = 3$. *AJ*, 112:335.
- Spiegel, E. A. (1971). Convection in Stars: I. Basic Boussinesq Convection. *ARA&A*, 9:323.

- Spite, F. and Spite, M. (1982). Abundance of lithium in unevolved halo stars and old disk stars - Interpretation and consequences. *A&A*, 115(2):357–366.
- Spite, M., Cayrel, R., Hill, V., Spite, F., François, P., Plez, B., Bonifacio, P., Molaro, P., Depagne, E., Andersen, J., Barbuy, B., Beers, T. C., Nordström, B., and Primas, F. (2006). First stars IX - Mixing in extremely metal-poor giants. Variation of the $^{12}\text{C}/^{13}\text{C}$, [Na/Mg] and [Al/Mg] ratios. *A&A*, 455:291–301.
- Spruit, H. C. (1992). The rate of mixing in semiconvective zones. *A&A*, 253:131–138.
- Sreenivasan, S. R. and Ziebarth, K. E. (1971). The Evolution of a $20 M_{\odot}$ Star. *BAAS*, 3:394.
- Stancliffe, R. J., Glebbeek, E., Izzard, R. G., and Pols, O. R. (2007). Carbon-enhanced metal-poor stars and thermohaline mixing. *ArXiv Astrophysics e-prints*.
- Stancliffe, R. J., Izzard, R. G., and Tout, C. A. (2005). Third dredge-up in low-mass stars: solving the Large Magellanic Cloud carbon star mystery. *MNRAS*, 356:L1–L5.
- Stothers, R. B. and Chin, C.-W. (1994). Galactic stars applied to tests of the criterion for convection and semiconvection in an inhomogeneous star. *ApJ*, 431:797–805.
- Straniero, O., Chieffi, A., Limongi, M., Busso, M., Gallino, R., and Arlandini, C. (1996). The third dredge-up and carbon star formation in population I low mass stars. *Memorie della Societa Astronomica Italiana*, 67:651.
- Straniero, O., Domínguez, I., Imbriani, G., and Piersanti, L. (2003). The Chemical Composition of White Dwarfs as a Test of Convective Efficiency during Core Helium Burning. *ApJ*, 583:878–884.
- Suda, T., Aikawa, M., Machida, M. N., Fujimoto, M. Y., and Iben, I. J. (2004). Is HE 0107-5240 A Primordial Star? The Characteristics of Extremely Metal-Poor Carbon-Rich Stars. *ApJ*, 611:476–493.
- Suntzeff, N. B. (1981). Carbon and nitrogen abundances in the giant stars of the globular clusters M3 and M13. *ApJS*, 47:1–32.
- Suntzeff, N. B. and Smith, V. V. (1991). Carbon isotopic abundances in giant stars in the CN-bimodal globular clusters NGC 6752 and M4. *ApJ*, 381:160–172.
- Sweigart, A. V. (1991). Horizontal-branch evolution with time-dependent convective overshooting. In Janes, K., editor, *Asp conf. ser. 13: the formation and evolution of star clusters*, pages 299–301.
- Sweigart, A. V., Lattanzio, J. C., Gray, J. P., and Tout, C. A. (2000). Gravitational instabilities in post-horizontal-branch stars. In Noels, A., Magain, P., Caro, D., Jehin, E., Parmentier, G., and Thoul, A. A., editors, *Liege international astrophysical colloquia*, page 529.
- Thielemann, F., Arnould, M., and Truran, J. W. (1987). in *Vangioni-Flam E., Audouze J., Casse M., Chieze J. P., Tran Thanh Van J., (eds.), Advances of Nuclear Astrophysics. Editions Frontieres, France.*, page 525.
- Tornambe, A. and Chieffi, A. (1986). Extremely metal-deficient stars. II - Evolution of intermediate-mass stars up to carbon ignition or core degeneracy. *MNRAS*, 220:529–547.
- Turner, J. and Stommel, H. (1964). A new case of convection in the presence of vertical salinity and temperature gradients. *Proc. Natl Acad. Sci.*, 52:49–53.
- Umeda, H. and Nomoto, K. (2002). Nucleosynthesis of Zinc and Iron Peak Elements in Population III Type II Supernovae: Comparison with Abundances of Very Metal Poor Halo Stars. *ApJ*, 565:385–404.
- Umeda, H. and Nomoto, K. (2003). First-generation black-hole-forming supernovae and the metal abundance pattern of a very iron-poor star. *Nature*, 422:871–873.
- Vangioni-Flam, E., Coc, A., and Cassé, M. (2000). Big bang nucleosynthesis updated with the NACRE compilation. *A&A*, 360:15–23.
- Vassiliadis, E. and Wood, P. R. (1993). Evolution of low- and intermediate-mass stars to the end of the asymptotic giant branch with mass loss. *ApJ*, 413:641–657.
- Ventura, P., Castellani, M., and Straka, C. W. (2005). Diffusive convective overshoot in core He-burning intermediate mass stars. I. The LMC metallicity. *A&A*, 440:623–636.
- Ventura, P. and D’Antona, F. (2005a). Full computation of massive AGB evolution. I. The large impact of convection on nucleosynthesis. *A&A*, 431:279–288.

- Ventura, P. and D'Antona, F. (2005b). Toward a Working Model for the Abundance Variations in Stars within Globular Clusters. *ApJL*, 635:L149–L152.
- Ventura, P. and D'Antona, F. (2006). Does the oxygen-sodium anticorrelation in globular clusters require a lowering of the $^{23}\text{Na}(p,\alpha)^{20}\text{Ne}$ reaction rate? *A&A*, 457:995–1001.
- Ventura, P., D'Antona, F., and Mazzitelli, I. (2004). New AGB models to explore the spread of abundances in Globular Clusters. *Memorie della Societa Astronomica Italiana*, 75:335.
- Wagner, R. L. (1974). Theoretical Evolution of Extremely Metal-Poor Stars. *ApJ*, 191:173–182.
- Wagoner, R. V. (1973). Big-Bang Nucleosynthesis Revisited. *ApJ*, 179:343–360.
- Weiss, A., Cassisi, S., Schlattl, H., and Salaris, M. (2000). Evolution of Low-Mass Metal-Free Stars including Effects of Diffusion and External Pollution. *ApJ*, 533:413–423.
- Weiss, A., Schlattl, H., Salaris, M., and Cassisi, S. (2004). Models for extremely metal-poor halo stars. *A&A*, 422:217–223.
- Wisotzki, L., Koehler, T., Groote, D., and Reimers, D. (1996). The Hamburg/ESO survey for bright QSOs. I. Survey design and candidate selection procedure. *A&AS*, 115:227.
- Wolfe, A. M., Turnshek, D. A., Smith, H. E., and Cohen, R. D. (1986). Damped Lyman-alpha absorption by disk galaxies with large redshifts. I - The Lick survey. *ApJS*, 61:249–304.
- Wood, P. R. (1981). On the entropy of mixing, with particular reference to its effect on dredge-up during helium shell flashes. *ApJ*, 248:311–314.
- Wood, P. R. and Zarro, D. M. (1981). Helium-shell flashing in low-mass stars and period changes in mira variables. *ApJ*, 247:247–256.
- Xiong, D. R. (1985). Convective overshooting in stellar internal models. *A&A*, 150:133–138.
- Yong, D., Grundahl, F., Lambert, D. L., Nissen, P. E., and Shetrone, M. D. (2003). Mg isotopic ratios in giant stars of the globular cluster NGC 6752. *A&A*, 402:985–1001.
- York, D. G., Adelman, J., Anderson, J. E. J., Anderson, S. F., Annis, J., and Bahcall, N. A. (2000). The Sloan Digital Sky Survey: Technical Summary. *AJ*, 120(3):1579–1587.
- Zhao, G. (2005). Search for Metal-poor Stars with LAMOST. In Mikolajewska, J. and Olech, A., editors, *AIP Conf. Proc. 752: Stellar Astrophysics with the World's Largest Telescopes*, pages 155–158.
- Zijlstra, A. A. (2004). Low-mass supernovae in the early Galactic halo: source of the double r/s-process enriched halo stars? *MNRAS*, 348:L23–L27.